UNIVERSIDAD DE CHILE
FACULTAD DE CIENCIAS FÍSICAS Y MATEMÁTICAS
DEPARTAMENTO DE GEOLOGÍA

ORIGEN Y NATURALEZA DE LOS FLUIDOS EN LOS SISTEMAS VOLCÁNICOS E HIDROTERMALES ACTIVOS DE LOS ANDES DE CHILE CENTRAL (32.5-36°S)

TESIS PARA OPTAR AL GRADO DE DOCTOR EN CIENCIAS MENCIÓN GEOLOGÍA

OSCAR MATÍAS BENAVENTE ZOLEZZI

PROFESOR GUÍA:
MARTIN REICH MORALES

MIEMBROS DE LA COMISIÓN:
FRANCO TASSI
FELIPE AGUILERA BARRAZA
DIEGO MORATA CÉSPEDES
MARCELO FARÍAS THIERS

SANTIAGO DE CHILE
2015

RESUMEN DE LA TESIS
PARA OPTAR AL GRADO DE
DOCTOR EN CIENCIAS MENCION GEOLOGIA
POR: Oscar Matías Benavente Zolezzi
PROF. GUIA: Martin Reich

ORIGEN Y NATURALEZA DE LOS FLUIDOS VOLCÁNICOS E HIDROTERMALES DE CHILE CENTRAL (32,5-36ºS)

En el presente trabajo se realizó un amplio estudio geoquímico de gases y aguas desde las distintas manifestaciones termales emitidas por los volcanes Tupungatito y Planchón-Peteroa, y desde las diferentes áreas geotermales localizadas a lo largo de la Cordillera Principal (CP) de Chile Central, con el fin de determinar el ***origen y naturaleza*** de dichos fluidos.

Los sistemas volcánicos de Chile Central están caracterizados por la presencia de fumarolas, suelos humeantes y lagunas cratéricas híper-ácidas (pH<2) e híper-salinas (TDS<35,000 mgL^{-1}) en sus cumbres. Los fluidos fumarólicos están dominados por contribuciones de origen magmático (SO_2, HCl y HF) e hidrotermales (H_2S, H_2 y CH_4), las que al ascender a través los conductos volcánicos se mezclan con fluidos de origen meteórico. Las razones de N_2/Ar (<1500) y R/R_a (<7.11), al igual que la composición isotópica de H_2O_V de las descargas fumarólicas relaciona directamente el origen de dichos fluidos con la deshidratación del slab y la consecuente fusión parcial del manto astenosférico. Sin embargo, las descargas fumarólicas del volcán Planchón-Peteroa respecto a las del Tupungatito se caracterizan por mayores concentraciones de ^3He, SO_2, HCl, y HF; mayores temperaturas (de 220° a >350°C) y estados de oxidación (R_H desde -3 a -5) subsuperficiales; y mayores razones de R/R_a y valores de $\delta^{13}C\text{-}CO_2$ (de 6.09Ra y -5.31 ‰ V-PDB, a 7.11Ra y -2.02 ‰ V-PDB).

Las variaciones regionales de los tipos de manifestaciones hidrotermales (manantiales fríos y calientes, piscinas burbujeantes y de barro, fumarolas), así como en el contenido relativo de los principales aniones (Cl^-, HCO_3^-, SO_4^{2-}) y cationes (Na^+, K^+, Ca^{2+}, Mg^{2+}) de las aguas termales, sugieren la existencia de tres dominios hidrotermales a lo largo de la CP. En el dominio Oeste (CPO), las aguas termales son emitidas desde manantiales fríos y calientes (<32°C) caracterizados por un TSD<700 mgL^{-1}, un pH neutro a alcalino, y una composición $Ca\text{-}HCO_3(SO_4)$ a $Na\text{-}HCO_3(SO_4)$. Aguas termales neutras son emitidas desde manantiales calientes (<45,7°C) en el dominio Central (CPC). Estas aguas levemente salinas (TSD<15.000 mgL^{-1}) se caracterizan por su composición Na(Ca)-Cl a Ca-Cl. El basamento de la CPO y CPC se caracteriza por rocas volcánicas y volcanoclásticas de composición basáltica a andesítica. El dominio Este (CPE), caracterizado por un basamento sedimentario marino-continental (calizas, areniscas y conglomerados), hospeda aguas termales salinas (TSD<57.000 mgL^{-1}) con un pH neutro a ácido (>2) y una composición variable entre Na-Cl, $Ca\text{-}HCO_3$, $Na\text{-}HCO_3$, $Ca\text{-}SO_4$ y acido-SO_4. Estas aguas son descargadas desde manantiales calientes, piscinas burbujeantes y piscinas de barros (<94,5°C), las que espacialmente se encuentran asociadas a los volcanes Holocenos. En los tres dominios las fuentes termales se emergen en zonas deformadas por los sistemas de falla inversas responsables del alzamiento de la CP. El contenido de δD y $\delta^{18}O$ en las aguas termales sugiere los sistemas hidrotermales de Chile Central son alimentados principalmente por agua meteórica proveniente del derretimiento de la nieve acumulada en la CP (entre 2000 y 3000 m s.n.m). No obstante, los gases fumarólicos presentan una composición de δD y $\delta^{18}O$ que evidencia una adición de agua andesítica (<5%), como también es sugerido por el estado redox estimado de los gases hidrotermales (R_H entre -4.9 y -2.5), y la presencia de He (R/R_a hasta 6) y CO_2 ($\delta^{13}C\text{-}CO_2$ entre -8,9 y -5,72 ‰ V-PDB) de origen mantélico. La interacción de gases de origen mantélico con las secuencias marinas ricas en carbonatos y materia orgánica existentes a lo largo de la CPE explica los amplios valores de $\delta^{13}C\text{-}CO_2$ (-14.3 y -6.03‰ V-PDB) y R/R_a (0.47 y 6.2) medidos en los gases hidrotermales. Al norte del oroclino del Maipo el miembro extremo magmático no supera el 2% (carbonatos + materia orgánica >98%), mientras que al sur la contribución magmática en las manifestaciones hidrotermales alcanza ~35%.

En términos globales, el origen de los sistemas volcánicos e hidrotermales de la región está íntimamente relacionado a la subducción de la placa de Nazca bajo el continente Sudamericano, la cual es responsable del (i) magmatismo de arco, y en consecuencia de la transferencia de masa y calor desde las cámaras magmáticas hacia la superficie permitiendo el desarrollo de los sistemas volcánicos y sistemas hidrotermales del tipo ígneo; así como de (ii) la orogénesis en la zona, cuya consecuencia directa es la actividad hidrotermal dominada por fluidos meteóricos impulsados por los significativos gradientes topográficos que caracterizan los Andes de Chile Central. Tanto la distribución regional del contenido de pCO_2 en las aguas termales y de los valores promedios del flujo calórico cortical, como la temperatura de emisión de los fluidos, el tipo de manifestaciones termales y las razones R/R_a de los fluidos indican que a lo largo de los tres dominios hidrotermales, la contribución de fluidos profundos aumenta abruptamente al sur del oroclino del Maipo. Al norte del oroclino, la mayor carga hidráulica regional creada por las mayores diferencias topográficas y la menor permeabilidad vertical de las zonas de fallas debido a su orientación desfavorable respecto al campo de estrés compresivo (E-O) suprime parcialmente la advección vertical de fluidos profundos y o la convección de agua meteórica en las zonas de fallas, dando como resultados fluidos hidrotermales con una fuerte signatura meteórica. Al sur del oroclino, la menor carga hidráulica regional generada por la disminución de la topografía, así como la mayor permeabilidad vertical de las fallas debido a su orientación favorable (rumbo NNE-SSO) respecto a la cinemática de deformación transcurrente de rumbo dextral (de orientación NE-SO), genera condiciones favorables para la formación de celdas convectivas de agua meteórica y/o la advección vertical de fluidos profundos (magmáticos y/o hidrotermales). Lo anterior también explicaría la mayor contribución magmática vs. hidrotermal en las descargas fumarólicas del volcán Planchón-Peteroa respecto a las del volcán Tupungatito.

Los resultados indican que al sur del oroclino del Maipo la interacción entre volcanismo y tectónica favorece la existencia de sistemas geotermales de alta entalpía en la CPE (ej. Calerías, Tinguiririca, Calabozos, Estero del Volcán, Mariposas). Estos sistemas debiesen ser considerados para su incorporación a la matriz eléctrica del país debido a su promisorio potencial energético (~1700 MWe), ya que en su conjunto podrían abastecer de electricidad cerca de 2.000.000 de viviendas en Chile. El aprovechamiento directo de los recursos geotérmicos parece ser factible en la totalidad de las manifestaciones termales estudiadas, sin embargo el desarrollo de este tipo de proyecto tiene que estar vinculado a los deseos de desarrollo local de los pobladores.

…Naturaleza, esencia, causa y origen

La naturaleza, en cuanto modo de ser tanto permanente como propio de las cosas, se identifica con lo que se denomina con el nombre de esencia. Empero, existe una importante diferencia de matiz resultante de ese carácter dinámico de la naturaleza que ya ha sido señalada: la esencia es la manera de ser permanente y única de las diferentes cosas por oposición a los aspectos cambiantes y variables.

Mientras que la esencia prescinde de los aspectos cambiantes y variables de las cosas, la naturaleza explica precisamente esos cambios y variaciones diversas. Y es que este concepto tiende un puente entre las oposiciones en referencia al conocimiento permanente de las cosas, en cuanto los cambios es lo que verdaderamente sostiene a una idea en movimiento.

*La pregunta de los filósofos griegos es una pregunta por la naturaleza–**physis**. La pregunta, por tanto, busca el principio de la totalidad y completitud de lo real, presentando así, una doble característica fundamentada en: su universalidad, pues aspira a alcanzar el principio o principios de todo lo real; y por su radicalidad, dado que pretende alcanzar principio o principios originarios y últimos.*

Así, preguntar por la naturaleza de las cosas es preguntar por lo que las cosas son; sin embargo la respuesta, al fundamentarse en procesos, movimientos y evoluciones, sólo puede explicar la esencia–origen de las cosas en un punto particular del espacio–tiempo, abriendo más preguntas aún…

Mt

AGRADECIMIENTOS

Diversas personas e instituciones han colaborado durante el desarrollo de este trabajo de Tesis, espero que estas pocas palabras logren transmitir mis sinceros agradecimientos a todas ellas.

Deseo agradecer en primer lugar al Programa de Mejoramiento de la Calidad y Equidad de la Educación (MECESUP) por el apoyo económico a través de la beca de doctorado. También quiero agradecer al Centro de Excelencia en Geotermia de los Andes (CEGA; Fondap n°. 15090013) por brindarme todo su apoyo económico por el cual se financiaron campañas de terreno, análisis químicos, envío de muestras y congresos. Deseo agradecer además a la Università degli Studi di Firenze (Florencia, Italia) y en particular a Franco Tassi, en donde me acogieron por seis meses para la realización de una pasantía para discutir sobre los aspectos que involucra la geoquímica de fluidos de sistemas volcánicos e hidrotermales, además de realizar gran parte de los análisis químicos e isotópicos reportados en esta tesis. Por lo mismo me gustaría agradecer a la Comisión Nacional de Ciencia y Tecnología (CONICYT) quien financió esta estadía en Florencia a través del PROGRAMA DE PASANTÍAS EN EL EXTRANJERO. También agradecer a CONICYT por financiar parte de los terrenos realizados en esta tesis a través del proyecto PBCT-PDA07 y el FONDECYT de iniciación N°11100372 *Role of climate, continental crust and subducted sediments in the degassing style and fluid composition of Andean volcanoes*. Me gustaría agradecer además al IAVCEI por haber financiado mi asistencia al congreso internacional IAVCEI General Assembly 2013 (Kagoshima-Japan).

Agradezco al Departamento de Geología de la Universidad de Chile por haberme acogido en el programa de Postgrado. Agradezco, muy especialmente, a profesor guía Martin Reich que siempre me ayudo a reflexionar acerca de los aspectos científicos y humanos de mis pensamientos, sobretodo en momentos donde las ideas se confunden y la voluntad decae. Del mismo modo, agradezco las observaciones a este trabajo realizadas por la comisión examinadora, conformada por los académicos del Departamento de Geología Dr. Diego Morata y Dr. Marcelo Farías y por los integrantes invitados Dr. Felipe Aguilera (SERNAGEOMIN) y Dr. Franco Tassi (Università degli Studi di Firenze). En particular quisiera brindarle toda mi gratitud a Franco por haberme aceptado como discípulo en el camino de la geoquímica de fluidos sin pedir nada más que una buena pizza. A Francisco Gutiérrez, que a pesar de no aparecer en la portada de esta tesis, su ayuda en el campo junto con las infinitas discusiones sostenidas fueron también fundamentales para el despertar de las ideas. También agradezco la cooperación, asistencia y tiempo de otras personas del Departamento de Geología. En especial a sus profesores por las conversaciones científicas que me ayudaron a ver que la Tierra vive por sí sola. Además quiero agradecer a Verónica, Maritza, Bernardette, Sofía, William, Carlos, Rosita y Kilo por el apoyo que recibí desde que comencé. Y como no recordar a mis grandes compañeros Fernanda, Alida, Fofito, Pablo, Coni, Checho, Daniele, Pita, Viole, Tapia y el resto de contertulios que comparten esa hermosa sala de postgrado donde se mezclan los pensamientos y la juerga, el encanto y el estrés, y todas las otras luces y sombras que acompañan al proceso creativo. Agradecer también a Jacopo, Francesco y Jaime por su dedicación en los numerosos análisis y por las hermosas discusiones sobre las máquinas y la química. A Ítalo Payacán, Roberto Valles, Benjamín Oberreuter, Cristobal Bayer, y los arrieros y sus caballos, por la ayuda y compañía en los terrenos, además de esas conversaciones mágicas sostenidas en los cerros pasmosos de los Ándes. A mi "familia italiana" Los Tardani, por su amistad y presencia profunda durante todo el periodo en Firenze…

Agradezco a mis amigos de la vida Javier, Rumel, Diego, Felipe, Iván, Aarón, Carla, Ataxia, Martin; ustedes han escrito nuestra historia en inmemorables recuerdos de risas, pensamientos, llantos, *Tzukis* y *Mawashis*, además de los diversos actos psicomágicos que hemos realizado en conjunto con el fin de atentar en contra de las palabras impuestas por el otro...

Quisiera terminar agradeciendo a mi familia… por todo. A mi mami, papi, Feña, Ange, Cristian, Ricardo, Susana, Sandra, Augusto, Coni, Isi, Cami, Renato, Anto, Augustito, mi madrina, tía Gloria y tío Damián, porque son mi punto de inicio, respiro en mí transitar, y quiero que sean por siempre mi punto de llegada luego de cada éxodo desde paraísos e infiernos… No soy capaz de verbalizar cuanto los he extrañado en estos últimos 3 años…

Y como olvidarme de ti… A Javi por llenar mi ser de alegría con su simpleza y cariño, con su abrazo y presencia, con sus ojitos profundos, con su sinceridad intransable, desde cerca y lejos... cada día...

Muchas gracias a todos…

TABLA DE CONTENIDO

CAPÍTULO III: METODOLOGÍA DE MUESTREO Y OBTENCIÓN DE DATOS

CAPITULO V: GEOCHEMISTRY OF FLUIDS ASSOCIATED WITH THE 2010-2011 UNREST EPISODE OF PETEROA VOLCANO: AN EXAMPLE OF DYNAMIC INTERACTION OF MAGMATIC, HYDROTHERMAL AND METEORIC FLUID RESERVOIRS

CAPÍTULO VI: THE OROGENIC AND MAGMATIC ORIGIN OF THE HYDROTHERMAL SYSTEMS OF THE ANDES OF CENTRAL CHILE (32.5-36°S)

CAPÍTULO VIII: CONCLUSIONES

ÍNDICE DE TABLAS

CAPÍTULO VI: THE OROGENIC AND MAGMATIC ORIGIN OF THE HYDROTHERMAL SYSTEMS OF THE ANDES OF CENTRAL CHILE (32.5-36°S)

CAPÍTULO VII: POTENCIAL GEOTÉRMICO DE LOS SISTEMAS HIDROTERMALES DE CHILE CENTRAL

ÍNDICE DE ILUSTRACIONES

CAPÍTULO I: INTRODUCCIÓN

CAPÍTULO II: ANTECENDENTES GEOLÓGICOS Y TECTÓNICOS

CAPÍTULO III: METODOLOGÍA DE MUESTREO Y OBTENCIÓN DE DATOS

CAPÍTULO IV: ORIGIN OF FUMAROLIC FLUIDS FROM TUPUNGATITO VOLCANO (CENTRAL CHILE): INTERPLAY BETWEEN MAGMATIC, HYDROTHERMAL AND SHALLOW METEORIC SOURCES

CAPÍTULO V: GEOCHEMISTRY OF FLUIDS ASSOCIATED WITH THE 2010-2011 UNREST EPISODE OF PETEROA VOLCANO: AN EXAMPLE OF DYNAMIC INTERACTION OF MAGMATIC, HYDROTHERMAL AND METEORIC FLUID RESERVOIRS

CAPÍTULO VI: THE OROGENIC AND MAGMATIC ORIGIN OF THE HYDROTHERMAL SYSTEMS OF THE ANDES OF CENTRAL CHILE (32.5-36°S)

CAPÍTULO VII: POTENCIAL GEOTÉRMICO DE LOS SISTEMAS HIDROTERMALES DE CHILE CENTRAL

CAPÍTULO I

INTRODUCCIÓN

I.1 MOTIVACIÓN Y PRESENTACIÓN

Los Andes de Chile representan una de las provincias geotérmicas sin desarrollar más grandes del planeta, cuyo potencial geotérmico estimado varía entre 3.350 (Figura I-1; *Soffia 2004*) y 16.000 MW (*Lahsen 1988*), siendo estos valores equivalentes al ~20 y 90% de la capacidad eléctrica instalada a la fecha en Chile, respectivamente (~19.000 MW; *CNE 2015*). A pesar de presentar importantes ventajas comparativas respecto a las energías termo- e hidroeléctrica, entre los que se incluyen los bajos costos operacionales, bajos impactos ambientales, y la alta seguridad que brinda al suministro energético (*Gupta y Roy 2007*), actualmente la participación de la energía geotérmica en el abastecimiento eléctrico de Chile es nula. Existen diversas razones de carácter económico, político y tecnológico que explican el por qué no se ha desarrollado la energía geotérmica en Chile, dentro de las cuales destacan los altos costos y riesgos asociados con el proceso de exploración y perforación, la alta inversión relacionada con la implementación de líneas de transmisión y la falta general de incentivos a la inversión en energía geotérmica (*CNE 2010; Dufey 2010; Hodgson 2013*). A esto se le suma el limitado conocimiento geoquímico, geológico y geofísico básico orientado a la exploración de los sistemas geotermales Andinos (*Lahsen et al. 2010; Barnett 2012*), el cual ha impactado de manera negativa la exploración del recurso geotermal en Chile al aumentar el riesgo económico inherente a la prospección de estos recursos (ej. *Entingh 2000*; *Jennejohn 2009*; *Moghaddam et al. 2013*).

Sorprendentemente, y considerando tanto su cercanía con los mayores centros urbanos del país (Figura I-2) como los resultados promisorios de las exploraciones profundas llevadas a cabo en los proyectos de Tinguiririca y Mariposa (Tabla I-1), los sistemas hidrotermales de Chile Central han sido uno de los menos estudiados desde el punto de vista geotérmico (ej. *Grunder et al. 1987; Hauser 1997).* Esta falta de conocimiento parece relacionarse directamente al estado de desarrollo geotérmico de

dicho segmento, ya que en la actualidad no existen proyectos en fase de evaluación ambiental para su explotación (Tabla I-1), a diferencia de las zonas más estudiadas del país (norte y sur de Chile; *Hilton et al. 1993; Hauser 1997; Perez 1999; Varekamp et al. 2001; Sepúlveda et al. 2004; Tassi et al. 2005; Sepúlveda et al. 2007; Ray et al. 2009; Tassi et al. 2009; 2010; Capaccioni et al. 2011; Risarcher et al. 2011; Tassi et al. 2011; Aguilera et al 2012; Agusto et al. 2013; Dobson et al. 2013; Sánchez et al. 2013*) donde sí existen proyectos geotermales que están siendo evaluados (Pampa Apacheta y Tolhuaca; *Hodgson 2013*)

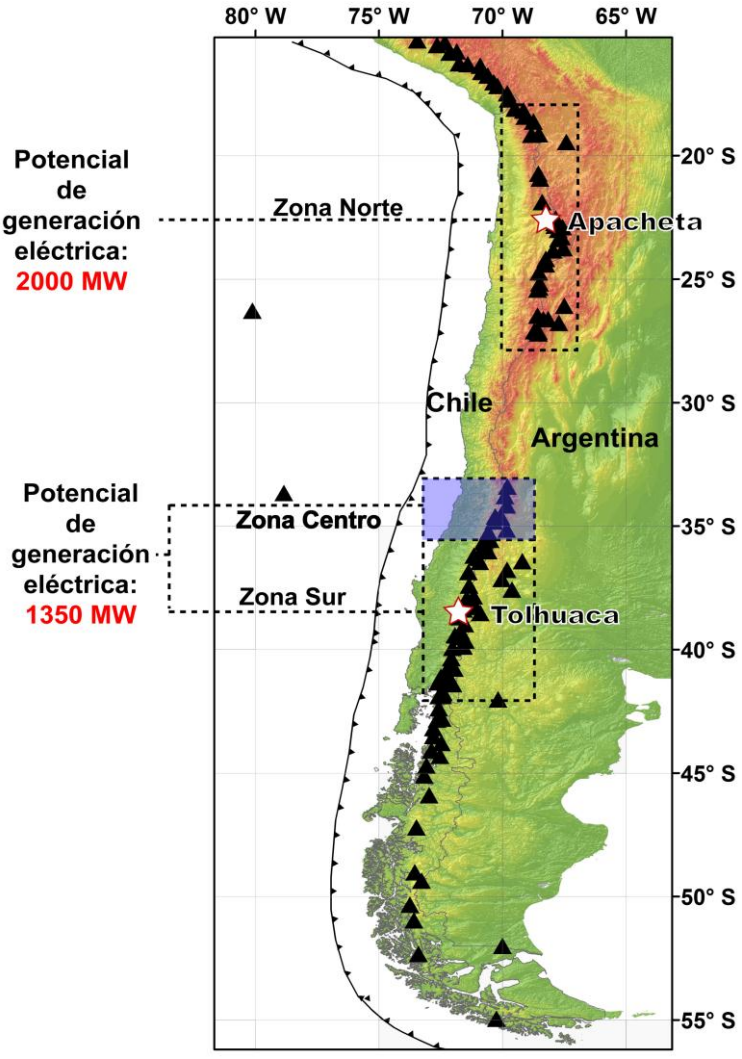

Figura I-1: Potencial geotérmico estimado para las zonas norte, centro y sur de Chile (*Soffia 2004*). Volcanes con actividad Holocena en triángulos (*Stern et al. 2007*).

Dentro de este contexto, la investigación expuesta en la presente Tesis de Doctorado se enfoca en determinar las características químicas y físicas de los sistemas geotermales de los Andes de Chile Central (32,5-36ºS). Por otra parte, en la últimas dos décadas se han realizado numerosos avances en el conocimiento geológico, tectónico, geofísico y volcanológico en Chile Central (ej. *Tassara et al. 2006; Farías et al. 2008; Cembrano y Lara 2009; Farías et al. 2010; Arriagada et al.*

2013; Tassara y Morales 2013; Giambiagi et al. 2014), los cuales proporcionan una base geológica sólida al estudio comparativo de las condiciones físico-químicas de los sistemas volcánicos e hidrotermales, siendo éste el primer paso necesario para la conceptualización de los sistemas geotermales de Chile Central (ej. *Giggenbach y Soto 1992; Giggenbach 1995; Reyes et al. 2010*).

Esta tesis está organizada en 8 capítulos. En las secciones siguientes se exponen las características generales de la región de estudio, la formulación del problema científico, los objetivos del estudio y una revisión breve de la productividad científica relacionada a la tesis de doctorado. En el Capítulo II se presenta una revisión de los antecedentes geotectónicos de la zona de estudio, entre los que se incluye el contexto tectónico de los Andes de Chile Central, dando énfasis al marco geodinámico bajo el cual se forman los actuales sistemas volcánicos e hidrotermales de esta área. Además, en este capítulo se revisan los antecedentes volcanológicos del área de estudio, con énfasis en aquellos sistemas que presentan actividad fumarólica. En el Capítulo III se reportan las técnicas de muestreo de gases y agua en manantiales termales, piscinas burbujeantes y fumarolas, junto con la metodología analítica utilizada en la determinación de diferentes elementos químicos y sus isótopos. En el Capítulo IV y V se presenta y discute el origen y naturaleza de los fluidos emitidos desde los volcanes con actividad fumarólica de la región (volcanes Tupungatito y Planchón-Peteroa, respectivamente), mientras que el origen y naturaleza de los fluidos en los sistemas hidrotermales activos de Chile Central se presentan en el Capítulo VI. En el Capítulo VII se discute el potencial geotérmico de los sistemas hidrotermales de Chile Central. Finalmente, las conclusiones globales se realizan en el Capítulo VIII.

I.2 CARACTERÍSTICAS GENERALES DE LA ZONA DE ESTUDIO

I.2.1 Ubicación y accesos

En este estudio, por Chile Central nos referimos a la porción continental de Chile localizada entre los 32,5 y 36°S de latitud (Figura I-1 y I-2). La zona de estudio coincide con 4 regiones del país, que de norte a sur corresponden a: Región de Valparaíso (V), Región Metropolitana (XIII), VI Región del Libertador General Bernardo O'Higgins (VI) y Región del Maule (VII). Tanto los volcanes como la mayoría de las manifestaciones termales reportadas por *Hauser (1997)* se encuentran localizados en el sector cordillerano colindante con Argentina (Figura I-2). El acceso a las diferentes zonas de estudio se hace a través de vehículo motorizado y, si es necesario, mediante el uso de caballos y/o caminatas.

Tabla I-1: Concesiones geotérmica de los Andes de Chile Central (*SERNAGEOMIN 2014*). Coordenadas en UTM. Datum: PSAD-56 (19S).

Nombre	Titular	Tipo concesión	Esquina NO: N	Esquina NO: E	Esquina SE: N	Esquina SE: E	Observaciones
Valle Nevado	SERVILAND MINERGY S.A	Exploración	6328627	370816	6291627	397816	-
San José II	Ormat Andina Energía LTDA.	Exploración	6303000	402000	6270000	418000	-
San José I	Enel Latin America (Chile) LTDA.	Exploración	6292000	380000	6258000	402000	-
Yeguas Muertas	Enel Latin America (Chile) LTDA.	Exploración	6256500	384000	6217500	403000	-
Colimapu	COLBUN S.A.	Exploración	6250000	403000	6225000	414000	-
Galo	HOT ROCK CHILE S.A.	Exploración	6241000	384000	6203000	368000	-
San Carlos	EDC ENERGIA VERDE CHILE S.A.	Exploración	6235000	352000	6210000	368000	-
Calerías	EDC ENERGIA VERDE CHILE S.A.	Exploración	6216990	384785	6192990	402785	-
Tinguiririca	ANTOFAGASTA MINERALS S.A.	Explotación	6145128	369817	6012623	349815	Pozo tipo *slimhole.* Temperatura máxima medida 235°C. Profundidad ~800 m (Clavero *et al*. 2011; Droguett *et al*. 2012).
Tinguiririca B	ANTOFAGASTA MINERALS S.A.	Exploración	6134000	357000	6128000	377000	-
Necul	Empresa Nacional de Geotermia S.A.	Exploración	6128000	347000	6109000	370000	-
Calabozo	Empresa Nacional de Geotermia S.A	Exploración	6088000	336000	6063000	366000	No existe información del pozo perforado
Pellado	ENERCO	Exploración	6055000	325000	6005000	345000	-
Laguna del Maule	MAGMA ENERGY CHILE LTDA.	Explotación	6020623	344815	6012623	349815	Tres pozos tipo *slimhole.* Temperaturas máximas medidas entre 190 y 204°C. Profundidad de los pozos 659, 897 y 1074 m (Hickson *et al*. 2011).
Santa Edita	HOT ROCK CHILE S.A.	Exploración	6007000	306000	5975000	325000	-
Santa Alejandra	HOT ROCK CHILE S.A.	Exploración	6001000	282000	5967000	306000	-
Los Cristales	MAGMA ENERGY CHILE LTDA.	Exploración	6000500	325000	5971000	345000	-

I.2.2 Geografía

Los Andes de Chile Central en promedio tienen una elevación de 4000 m s.n.m., con una altitud máxima promedio cercana a los 5000 m s.n.m. y diversos altos topográficos que superan los 6000 m s.n.m. Fisiográficamente, la región se puede dividir en tres provincias longitudinales, que de oeste a este corresponden a la Cordillera de la Costa (CC), Depresión Central (DC) y Cordillera Principal (CP; Figura I-2). Tanto la altitud promedio de la Andes de Chile Central, como la extensión longitudinal de ésta disminuyen de norte a sur (*Farías et al. 2008*).

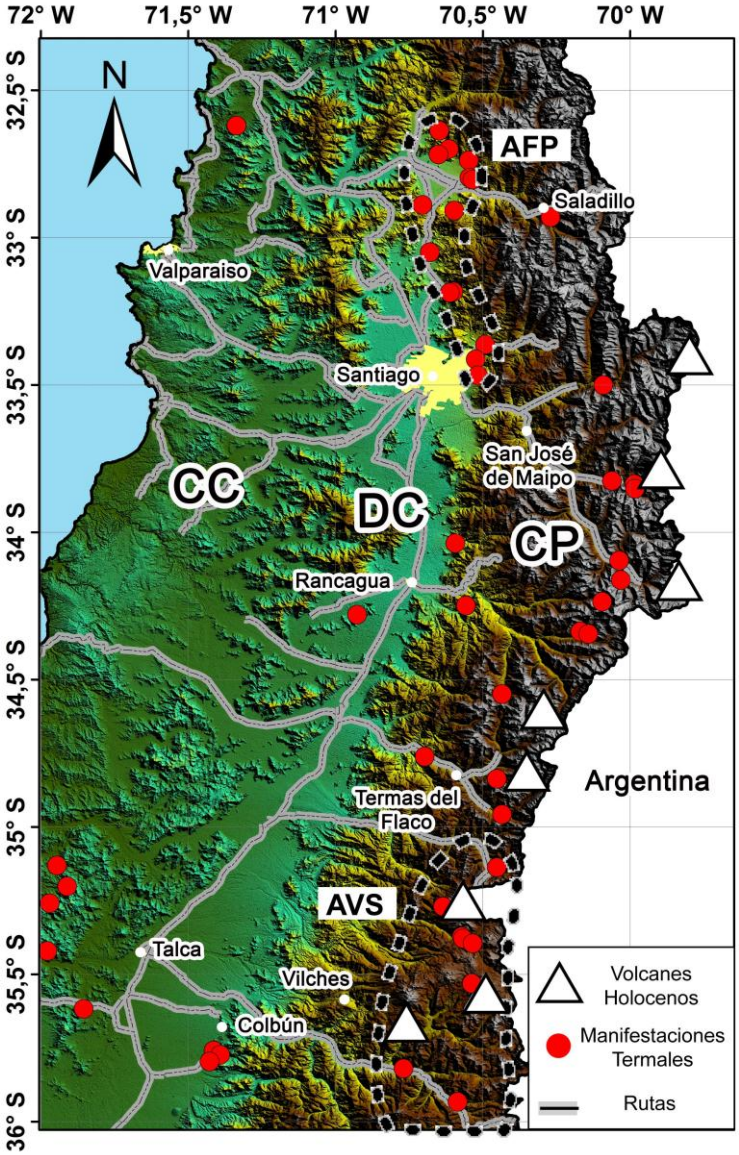

Figura I-2: Ubicación del área de estudio en Chile Central. Se indican los principales rasgos morfológicos, los estratovolcanes Holocenos, las vías de acceso, las principales ciudades y las manifestaciones termales reportadas por *Hauser (1997)*. Volcanes con actividad Holocena en triángulos (*Stern et al. 2007*). Las llíneas segmentadas delimitan los dos ambientes termales definidos por *Hauser (1997)* [AFP-Ambiente Falla Pocuro; AVS-Ambiente Volcánico Sur].

I.2.3 Clima

Los Andes de Chile Central presentan un clima mediterráneo de estación seca prolongada, controlado principalmente por la interacción entre la posición de la transición de los vientos que transportan humedad desde el Océano Pacífico al Océano Atlántico y vice-versa, y la gran altitud de los Andes en estas latitudes (*Hock et al. 2013*). En promedio, la transición de los vientos se localiza cercano a los 32°S, sin embargo su posición es altamente variable (±2°S), dependiendo tanto de fluctuaciones estacionales (invierno-verano) como de variaciones interanualmente (ej. fenómeno de "El Niño" y "La Niña"; *Garreaud 2009*). Como resultado de estas variaciones anuales, las precipitaciones en Chile Central son en promedio del orden de aproximadamente 50 mm durante los meses de verano, mientras que en los meses de invierno aumentan en promedio hasta 400 mm en la DC y 800 mm en la Cordillera Principal (Figura I-3; *Garreaud 2009; Hock et al. 2013*). Las variaciones interanuales producto de los fenómenos de "El Niño" y "La Niña" generan un aumento y una disminución de las precipitaciones a lo largo de Chile Central, respectivamente (*Garreaud 2009*).

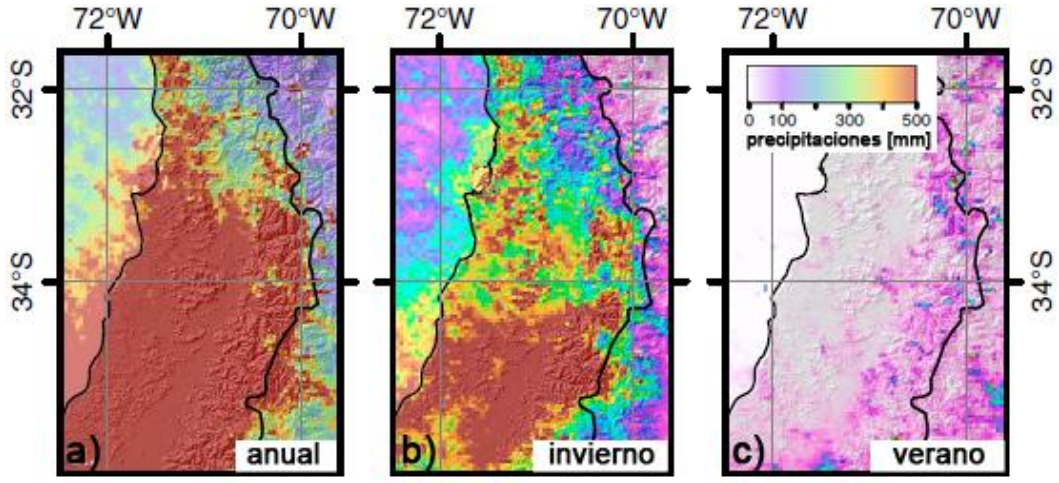

Figura I-3: Patrón de precipitación a) anual, b) invernal, y c) estival de Chile Central entre los años 1998 y 2009. Modificado de *Hock et al. (2013).*

I.3 FORMULACIÓN DEL PROBLEMA

Al igual que en otras zonas del Cinturón de Fuego del Pacífico, los Andes de Chile Central se caracterizan por la presencia de actividad tectónica, sísmica, volcánica e hidrotermal (*Barazangi e Isacks 1976*; *Hildreth y Moorbath 1988*; *Hauser 1997*) controlada principalmente por la subducción de la placa de Nazca bajo el continente Sudamericano (Figura I-1). La mayoría de las manifestaciones termales de Chile Central se localizan en los valles de la escarpada topografía de la CP y

corresponden a manantiales fríos, manantiales calientes, piscinas burbujeantes, piscinas de barro y fumarolas. Dichas manifestaciones se relacionan espacialmente tanto a la traza de los sistemas de falla responsables del alzamiento andino como a los volcanes pertenecientes a la porción norte de la Zona Volcánica Sur (ZVS; Figuras I-2 y I-4). A diferencia del amplio conocimiento relacionado a la petrología y geoquímica de los productos volcánicos de los centros eruptivos de Chile Central (ej. *López-Escobar et al. 1977; Hickey et al. 1986; Futa y Stern 1988; Hildreth y Moorbath 1988; Stern 1991; Tormey et al. 1991, 1995; Kay et al. 2005; Cembrano y Lara 2009*), sólo existen seis trabajos relacionados a las características físico-químicas de la fase fluida emitida por las manifestaciones termales volcánicas y no volcánicas de la zona (*Grunder et al. 1987; Hilton et al. 1993; Hauser 1997; Gately et al. 2004a and b; Dobson et al. 2013*), siendo el catastro de las aguas termales realizado por *Hauser (1997)* el más completo a la fecha.

En base a las características geoquímicas de las aguas termales y su posición a lo largo de la CP, *Hauser (1997)* reconoció la existencia de dos dominios hidrotermales en Chile Central (Figura I-2). El primer dominio corresponde a los manantiales calientes (T<30°C) asociados al Ambiente Falla Pocuro (AFP; Figura I-2) cuyas aguas son levemente alcalinas (pH entre 7 y 8), relativamente diluidas (TSD<1.500 mgL^{-1}) y con una composición variable entre aguas calcio-bicarbonatadas (Ca-HCO_3) y calcio-sulfatadas (Ca-SO_4). El segundo dominio corresponde a la manifestaciones termales (T>25°C) asociadas al Arco Volcánico Sur (AVS; Figura I-2) las cuales son levemente ácidas (pH entre 5 y 7), contienen un gran concentración de sólidos disueltos (TSD<24.200 mgL^{-1}) y tienen una composición variable entre aguas sodio-cloruradas (Na-Cl), calcio-bicarbonatadas (Ca-HCO_3) y calcio-sulfatadas (Ca-SO_4). Además de las variaciones geoquímicas existente entre ambos dominios, una serie de evidencias geofísicas y geoquímicas indican un incremento, hacia el Este y Sur, del transporte advectivo y/o convectivo de calor en la CP (Figura I-4), dentro de las que se incluyen: (i) el incremento de la temperatura de las manifestaciones termales y el flujo calórico promedio hacia el Este y Sur (*Hamza y Muñoz 1996; Hauser 1997*); (ii) la aparición de campos fumarólicos en las laderas de los volcanes Holocenos y a lo largo de las trazas de las fallas inversas, al sur de los 34,5°S (*Grunder et al. 1987; Hauser 1997; Clavero et al. 2011; Hickson et al. 2011*); (iii) el incremento, hacia el sur, de la razón $^3He/^4He$ de las manifestaciones termales emplazadas a lo largo del arco volcánico (*Hilton et al. 1993; Clavero et al. 2011; Dobson et al. 2013*); y (iv) un aumento de la profundidad de las isotermas hacia el sur según el modelo termal conductivo reportado por *Tassara y Morales (2013)*. Si bien los estudios antes mencionados han reportado

diferencias significativas en las características físico-químicas de la actividad hidrotermal en Chile Central, el origen y naturaleza de estas variaciones permanecen inciertos.

Tal como se ha observado en diferentes áreas con volcanismo y/o hidrotermalismo activo (ej. *Craw 1989; Giggenbach y Soto 1992; Giggenbach 1995; Vaselli et al. 2002; Tassi et al. 2006*; *Reyes et al. 2010; Rowland y Simmons 2012*), variaciones espaciales de las características físicas, químicas e isotópicas de los fluidos termales superficiales, son el resultado de diferencias tanto en los tipos de fluidos primarios involucrados en la alimentación de las manifestaciones termales (ej. magmáticos, hidrotermales, metamórficos, sedimentarios; ***factores de primer orden***) como de los procesos físicos-químicos (y biológicos) que los fluidos pueden experimentar durante su circulación por la corteza (ej. separación de fases, enfriamiento y reequilibrio, interacción gas-agua-roca, actividad microbiana, interacción con fluidos meteóricos; ***factores de segundo orden***). En zonas de subducción, los factores de primer y segundo orden se encuentran constreñidos por las características particulares de la configuración de un margen convergente (ej. *Reyes et al. 2010*). Así, por ejemplo, contrastes en la composición geoquímica de los fluidos emitidos desde sistemas volcánicos e hidrotermales emplazados a lo largo de un mismo arco volcánico han sido relacionados a variaciones de la edad y estado termal de la corteza oceánica (*Leeman y Carr 1995*), la tasa y ángulo de subducción (*Snyder et al. 2001; 2003*), y el volumen y tipo de material subductado (*Patino et al. 2000; Fischer et al. 2002*), los que en su conjunto condicionan las características químicas e isotópicas de los volátiles generados (ej. CO_2, H_2O, N_2 y los gases nobles) desde la deshidratación parcial de los sedimentos y basaltos subductados (*Snyder et al. 2001*). De la misma manera, variaciones en el espesor de la cuña astenosférica y de la litósfera sobreyacente al slab (*Snyder et al. 2001; Saginor et al. 2013*), en la litología y composición química de la corteza continental (*Giggenbach 1995; Reyes et al. 2010*), la naturaleza de las estructuras y su relación con el campo de estrés cortical (*Rowland y Sibson 2004; Sánchez et al. 2013),* y en la topografía *(Minissale 2004; Craw et al. 2013*), también han sido relacionados a contrastes de las características físicas, químicas e isotópicas de los fluidos termales superficiales. Esto último se debe a que los factores antes mencionados condicionan la evolución físico-química de los fluidos primarios en su tránsito por la astenósfera y litósfera (*Person y Baumgartner 1995; Cox 2010*).

Producto de su evolución geológica, la configuración geotectónica de Chile Central se caracteriza por importantes variaciones tanto a lo largo del margen de

subducción (ej. cambio del ángulo de subducción, del volumen de material subductado y edad de la placa oceánica; *Tebbens et al. 1997; Völker et al. 2013*) como a lo largo y ancho de la litósfera continental (ej. cambios en la orientación de la fosa y la cadena Andina, disminución de la topografía y espesor cortical hacia el sur, cambio de la cinemática de deformación cortical, cambios en la composición de la corteza; *Cembrano y Lara 2009; Farías et al. 2010*). Contrastes en la petrología y geoquímica de los productos volcánicos holocenos en Chile Central (*López-Escobar et al. 1977; Futa y Stern 1988; Hildreth y Moorbath 1988; Stern 1989, 1991*) han sido atribuidos, por ejemplo, a un aumento del espesor cortical hacia el norte (*Hildreth y Moobarth 1988*), cambio del tensor de estrés actual y del rumbo de las fallas inversas donde se emplazan los centros eruptivos (*Cembrano y Lara 2009*), y a un incremento relativo del material cortical subductado causado por un menor volumen de material mantélico en la cuña astenosférica hacia el norte y/o un aumento del material cortical subductado ya sea por erosión continental o desde el prisma de acreción (*Stern 1989, 1991*). De la misma manera es esperable que las variaciones geotectónicas presentes en Chile Central, además de las variaciones temporales asociadas a la propia actividad volcánica de cada centro eruptivo, sean responsables de las características físicas, químicas e isotópicas de los fluidos emitidos por los volcanes activos, al igual que de las diferencias físico-químicas de la actividad hidrotermal a lo largo y ancho de Chile Central (Figura I-4).

En relación a lo presentado, se plantean para el área de estudio una serie de interrogantes fundamentales para la comprensión del comportamiento de los fluidos que alimentan los sistemas volcánicos e hidrotermales de Chile Central como: ¿Qué procesos controlan el origen y naturaleza de los fluidos en las distintas áreas hidrotermales y volcánicas de la región?, ¿Cómo afectan estos procesos al comportamiento físico-químico actual de cada sistema?, ¿Son estos procesos indicadores del estado de actividad de los sistemas en subsuperficie?, ¿Están los sistemas volcánicos relacionados con los sistemas hidrotermales?, y si es así, ¿Tienen procesos comunes entre sí?. Considerando además la directa relación existente entre las variaciones geotectónicas a lo largo de Chile Central y la evolución de los magmas en esta zona, ¿Existe alguna relación entre los fluidos emitidos por los sistemas volcánicos e hidrotermales y las variaciones geotectónicas?, y de ser así, ¿Qué control ejercen estas variaciones en las características físicas, químicas e isotópicas de los fluidos emitidos por estos sistemas? Finalmente, ¿Existen zonas más favorables para la existencia de sistemas geotermales de alta entalpía a lo largo de Chile Central?

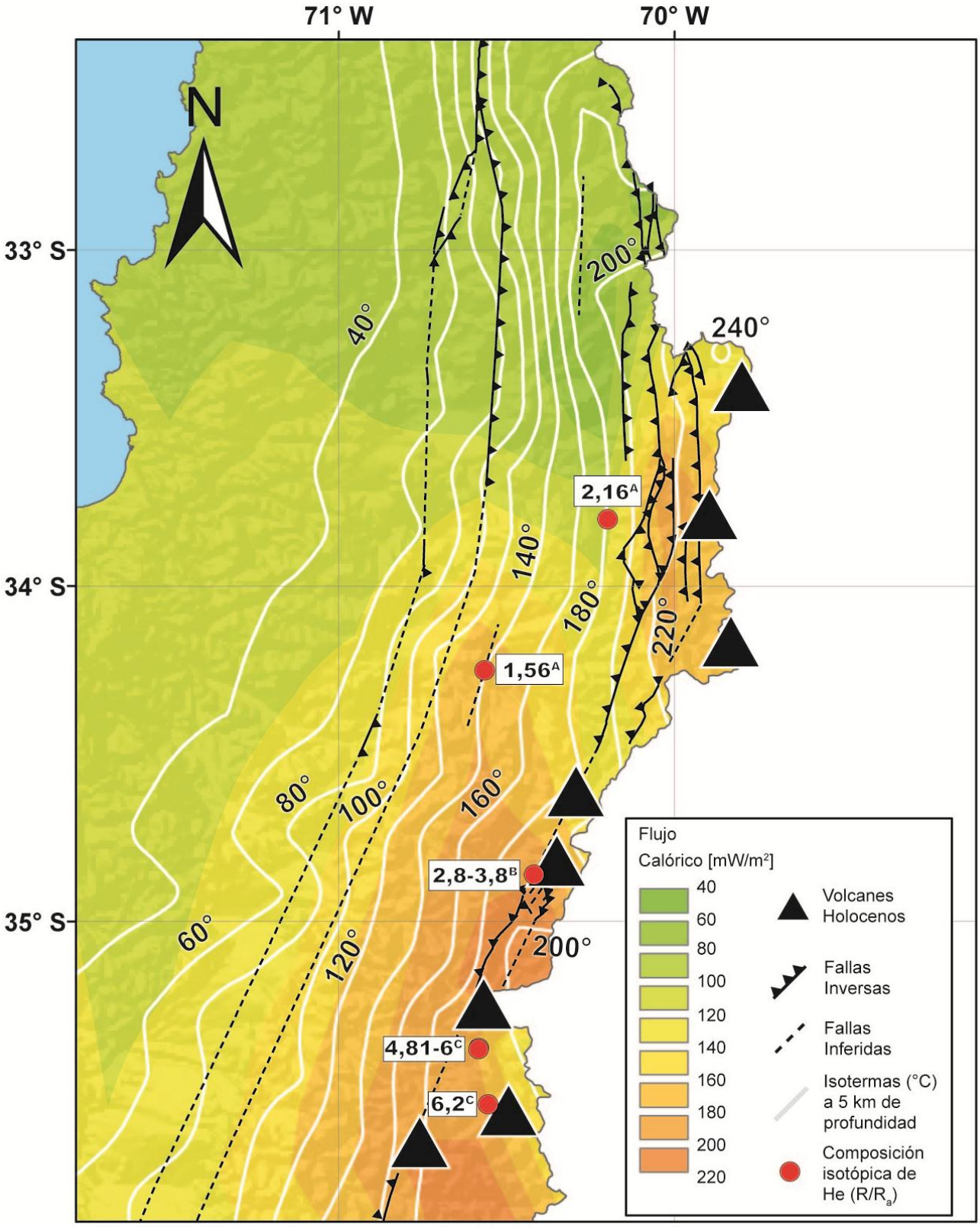

Figura I-4: Principales rasgos relacionados al transporte de fluidos y calor en los Andes de Chile Central. Se reporta la distribución superficial del flujo calórico promedio (*Hamza y Muñoz 1996*), las isotermas (°C) a 5 km de profundidad (*Tassara y Morales 2013*), los volcanes con actividad holocena (*Stern et al. 2007*), los principales sistemas de falla (*Farías et al. 2010*) y las razones isotópicas de Helio reportados en estudios previos (A: *Hilton et al. 1993*; B: *Clavero et al. 2011*; C: *Dobson et al. 2013*).

I.4 OBJETIVOS

Este estudio tiene como **objetivo principal** *determinar el origen y naturaleza de los fluidos asociados a los sistemas volcánicos e hidrotermales de Chile Central (32.5-36°S).*

Complementariamente, los objetivos **específicos** son:

1) Determinar las variables y procesos termodinámicos que actúan sobre los diferentes tipos de manifestaciones termales de la zona, tales como temperatura, condiciones redox, interacción fluido-roca e interacción gas-agua.
2) Identificar desde un punto de vista geoquímico los distintos subsistemas presentes a lo largo de Chile Central (magmático, magmático-hidrotermal e hidrotermal).
3) Determinar el grado de actividad de los diferentes subsistemas identificados y el tipo de interacción existentes entre ellos, en caso de existir.
4) Evaluar la relación entre las variaciones geotectónicas y las características físico-químicas de los diferentes subsistemas reconocidos a lo largo de la zona de estudio.

I.5 PRODUCTIVIDAD CIENTÍFICA (Anexo)

I.5.1 Publicaciones y resúmenes en conferencias resultantes de esta tesis

- **Publicaciones ISI**

Benavente O., Tassi F., Gutiérrez F., Vaselli O., Aguilera F., Reich M. (2013)**.** Origin of fumarolic fluids from Tupungatito Volcano (Central Chile): Interplay between magmatic, hydrothermal and shallow meteoric sources, Bulletin of Volcanology, Volumen 75, Issue 8, pp. 1-15.

Benavente O., Tassi F., Gutiérrez F., Vaselli O., Aguilera F., Reich M. (to be submitted). Regional variation in the fluid geochemistry and the chemical-physical conditions of the hydrothermal systems at the Andes of Central Chile (32.5-36°S): insights towards Andean geothermal systems.

- **Resúmenes en conferencias**

Benavente O., Tassi F., Gutiérrez F., Vaselli O., Aguilera F., Reich M. (2013)**.** The origin of fumarolic fluids from Tupungatito Volcano (Central Chile): insight of the

Chilean arc variation in its volatiles composition. IAVCEI scientific assemblage. Kagoshima, Japan.

Benavente O.,Tassi F., Aguilera F., Agusto M., Caselli M., Gutiérrez F., Vaselli O., Reich M. (2013). Preliminary geochemical investigation of Tupungatito and Planchón-Peteroa (Argentina-Chile) hyperacidic crater lakes. Crater Volcanic Lakes Workshop. Ozu, Japan.

Benavente O., Aguilera F., Gutiérrez F., Tassi F., Reich M., Vaselli O. (2012). Los Sistemas hidrotermales de Chile central (33-36°S). XIII Congreso Geológico Chileno, Antofagasta, Chile.

Benavente O., Gutiérrez F., Aguilera F., Reich M., Tassi F., Vaselli O. (2012). El sistema magmático-hidrotermal asociado al volcán Tupungatito, Región Metropolitana, Chile. XIII Congreso Geológico Chileno, Antofagasta, Chile.

Saltori O., Aguilera F., Augusto M., **Benavente O.**, Tassi F., Caselli A., Gutiérrez F., Pizarro M. (2012). Fluids Geochemistry from Planchón-Peteroa-Azufre volcanic Complex, Southern Volcanic Zone, Chile. Congreso Geológico Chileno.

Aguilera F., Romero J., Gutiérrez F., Augusto M., Saltori O., **Benavente O.**, Caselli A., Pizarro M. (2012). Eruptive activity of Peteroa Volcano for period 2010-2011, Southern Volcanic Zone, Chile. Congreso Geológico Chileno.

Benavente O., Gutiérrez F., Tassi F., Reich M. (2011). Magmato-hydrothermal systems associated to Planchón-Petero and Descabezado Grande-Quizapu-Cerro Azul volcanic complex, VII Region, Chile. SGA.

Benavente O., Gutiérrez F. (2011). Nueva temperatura estimada para el sistema hidrotermal asociado a los Complejos Volcánicos Planchón-Peteroa y Descabezado Grande-Quizapu-Azul, 35º36ºS, Chile. Congreso Geológico Argentino.

Aguilera F., **Benavente O.**, Tassi F., Gutiérrez F. (2011). Distribution of gas-water discharges and current geochemical survey along Planchón-Peteroa-Azufre volcanic complex, Southern Chile. 11th Gas Workshop. Kamtchatka, Rusia

I.5.2 Publicaciones y resúmenes en conferencias resultantes de proyectos de investigación paralelos

- **Publicaciones ISI**

Gutiérrez F., Lemus M., Parada M., **Benavente O**., Aguilera F. (2012). Contribution of ground surface altitude difference to thermal anomaly detection using satellite images: Application to volcanic/geothermal complexes in the Andes of Central Chile. Journal of Volcanology and Geothermal Research, Issue 237-238, pp. 69-80.

- **Resúmenes en conferencias**

Calabrese S., Cabassi J., Bitettoa M., Capecchiacci F., **Benavente O.**, Tassi F., D'Alessandro W., Parelloa F., Vaselli O. (2013). Real-time measurements of gaseous elemental mercury at the summit area of Mt. Etna volcano (Italy): preliminary results. International Conference on Mercury as a Global Pollutant (ICMGP), Edinburgh.

BIBLIOGRAFÍA

Agusto M, Tassi F, Caselli A T, Vaselli O, Rouwet D, Capaccioni B, Caliro S, Chiodini G, Darrah T (2013). Gas geochemistry of the magmatic-hydrothermal fluid reservoir in the Copahue-Caviahue Volcanic Complex (Argentina). Journal of Volcanology and Geothermal Research 257(0): 44-56.

Aguilera F, Tassi F, Darrah T, Moune S, Vaselli O (2012). Geochemical model of a magmatic hydrothermal system at the Lastarria volcano, northern Chile. Bull Volcanology. Bull. Volcanol 74:119–134.

Arriagada C., Ferrando R., Cordova L., Morata D., Roperch P. (2013) The Maipo Orocline: A first scale structural feature in the Miocene to Recent geodynamic evolution in the central Chilean Andes. Andean Geology 40(3): 419-437.

Barazangi, M. and B. L. Isacks (1976). Spatial distribution of earthquakes and subduction of the Nazca plate beneath South America. Geology 4(11): 686-692.

Barnett P (2012). Geothermal Projects in South America of Hot Rock Limited. Chilean International Renewable Energy Congress, Santiago, Chile.

Capaccioni B, Aguilera F, Tassi F, Darrah T, Poreda RJ, Vaselli O (2011) Geochemical and isotopic evidences of magmatic inputs in the hydrothermal reservoir feeding the fumarolic discharges of Tacora volcano (northern Chile). J Volcanol Geotherm Res 208:77–85.

Cembrano, J. and L. Lara (2009). The link between volcanism and tectonics in the southern volcanic zone of the Chilean Andes: A review. Tectonophysics 471(1-2): 96-113.

Clavero, J., C. Pineda, C. Mayorga, A. Giavelli, I. Aguirre, S. Simmons, S. Martini, J. Soffia, R. Arriaza, E. Polando and L. Achurra (2011). Geological, Geochemical, Geophysical and First Drilling Data from Tinguiririca Geothermal Area, Central Chile. Geothermal Resources Council Transactions (GRC). San Diego, California, Geothermal Resources Council. 35: 731-734.

CNE (2010). Identificación de dificultades en la tramitación de permisos de proyectos del sector eléctrico. Comisión Nacional de Energía de Chile. [en línea] http://www.minenergia.cl/documentos/estudios/2010/identificacion-de-dificultades-en-la.html

CNE [en línea] http://www.cne.cl/estadisticas/energia/electricidad [consulta : 23 Marzo 2015].

Cox, S. (2010). The application of failure mode diagrams for exploring the roles of fluid pressure and stress states in controlling styles of fracture-controlled permeability enhancement in faults and shear zones: Geofluids, v. 10, p. 217–233.

Craw D (1988) Shallow-level metamorphic fluids in a high uplift rate mountain belt, Alpine Schist, New Zealand. J Metamorph Geol 6:1–16

Dobson P., Kennedy M., Reich M., Sanchez P., Morata D. (2013). Effects of volcanism, crustal thickness, and large scale faulting on the He isotope signatures of geothermal systems in Chile. Thirty-Eighth Workshop on Geothermal Reservoir Engineering Stanford University, Stanford, California, February 11-13, SGP-TR-198

Dufey A. (2010) Opportunities and Domestic Barriers to Clean Energy Investment in Chile. IISD: Trade, Investment and Climate Change Series. [en línea] http://www.iisd.org/pdf/2010/bali_2_copenhagen_Chile_Jun2010.pdf

Entingh D.J. (2000). Enhanced Geothermal Systems (EGS) R&D Program. Princeton Energy Resources, International, Rockville, MD.

Farías M., Charrier R. et al. (2008). Late Miocene high and rapid surface uplift and its erosional response in the Andes of central Chile (338–358S). Tectonics, 27, TC1005, http://dx.doi.org/10.1029/2006TC002046.

Farías M., Comte D. et al. (2010). Crustal-scale structural architecture in central Chile based on seismicity and surface geology: implications for Andean mountain building. Tectonics, 29, TC3006, http://dx.doi.org/10.1029/2009TC002480.

Fischer, T. P., Hilton, D. R., Zimmer, M. M., Shaw, A. M., Sharp, Z., Walker, J. A. (2002). Subduction and recycling of nitrogen along the Central American margin, Science, Vol. 297, p. 1154–1157.

Futa K. and Stern C.R. (1988). Sr and Nd isotopic and trace element compositions of Quaternary volcanic centers of the southern Andes: Earth and Planetary Science Letters, v. 88, p. 253–263, doi: 10.1016/0012-821X(88)90082-9.

Garreaud R.D. (2009). The Andes climate and weather. Advances in Geosciences 22: 3-11.

Gately, C., Sruoga, P., Gomberg, A., Varekamp, J. (2004a). Hypersaline brines in hot spring fluids from Peteroa volcano, South Andes. IAVCEI General Assembly 2004. 1 p.

Gately, C., Gomberg, A., Sruoga, P., Varekamp, J. (2004b). Geochemistry of the Hydrothermal System of Peteroa Volcano, Chile-Argentina. American Geophysical Union, Spring Meeting 2004. 1 p.

Giambiagi L., Tassara A. et al. (2014). Evolution of shallow and deep structures along the Maipo–Tunuyan transect (33°40′S): from the Pacific coast to the Andean foreland. In: Sepúlveda S. A., Giambiagi L. B., Moreiras S. M., Pinto L., Tunik M., Hoke G. D. y Farías, M. (eds) Geodynamic Processes in the Andes of Central Chile and Argentina. Geological Society, London, Special Publications, 399. http://dx.doi.org/10.1144/SP399.14

Giggenbach, W. F., and R. C. Soto (1992) Isotopic and chemical composition of water and steam discharges from volcanic-magmatic-hydrothermal systems of the Guanacaste Geothermal Province, Costa Rica, Appl. Geochem., 7. 309–332, 1992.

Giggenbach, W.F (1995) Variations in the chemical and isotopic composition of fluids discharged from the Taupo Volcanic Zone, New Zealand. Journal of Volcanology and Geothermal Research 68, 89-116.

Grunder, A. L., J. M. Thompson, et al. (1987). The hydrothermal system of the Calabozos caldera, central Chilean Andes. Journal of Volcanology and Geothermal Research 32(4): 287-298.

Gupta H. y S. Roy (2007). Chapter 4 - Geothermal systems and resources. Geothermal Energy. Amsterdam, Elsevier: 49-59.

Hamza V. M. y M. Muñoz (1996). Heat flow map of South America. Geothermics 25(6): 599-621.

Hauser A. (1997). Catastro y caracterización de las fuentes de aguas minerales y termales de Chile Santiago, Chile, Servicio Nacional de Geología y Minería (SERNAGEOMIN). Boletín 50: 70 p.

Hickey R.L., Frey F.A., Gerlach D.C., and López-Escobar L. (1986). Multiple sources for basaltic arc rocks from the southern volcanic zone of the Andes (34°41'S): Trace element and isotopic evidence for contributions from subducted oceanic crust, mantle and continental crust. Journal of Geophysical Research, v. 91, p. 5963–5983.

Hickson, C. J., F. Ferraris, C. Rodriquez, G. Sielfeld, R. Henriquez, T. Gislason, J. Selters, D. Benoit, P. White, J. Southon, G. Ussher, C. J., A. Smith, B. Lovelock, J. Lawless, P. Quinliven, L. Smith and R. Yehia (2011). The Mariposa Geothermal System, Chile Geothermal Resources Council Transactions (GRC). San Diego, California, Geothermal Resources Council. 35: 817-825.

Hildreth W. y Moorbath S. (1988). Crustal contributions to arc magmatism in the Andes of Central Chile: Contributions to Mineralogy and Petrology, v. 98, p. 455–489.

Hilton, D., Hammerschmidt, K., Teufel, S., Friedrichsen, H. (1993). Helium isotope characteristics of Andean geothermal fluids and lavas. Earth and Planetary Sciences Letters, Vol. 120, p. 265 – 282

Hodgson S (2013). Focus on Chile Parts I-II-III. Geothermal Resources Council Bulletin (GRC) 47(1).

Hoke, G. D., J. N. Aranibar, M. Viale, D. C. Araneo y C. Llano (2013). Seasonal moisture sources and the isotopic composition of precipitation, rivers, and carbonates across the Andes at 32.5–35.5°S. Geochemistry, Geophysics, Geosystems 14(4): 962-978.

Jennejohn D. (2009). Research and Development in Geothermal Exploration and Drilling. Geothermal Energy Association.

Kay S. M., Godoy E. and Kurtz A (2005). Episodic arc migration, crustal thickening, subduction erosion, and magmatism in the South-Central Andes. Geological Society of America Bulletin 117, 67-88.

Lahsen A. (1986). Origen y potencial de energía geotérmica en los Andes de Chile. En: Geología y Recursos Minerales de Chile, Univ. de Concepción, 423–438. J.Frutos, R. Oyarzún, and M. Pincheira (Eds)

Lahsen, A., Muñoz, N. and Parada, M.A. (2010). Geothermal Development in Chile. Proceedings World Geothermal Congress, Bali, Indonesia.

Leeman, W., Carr, M. (1995). Geochemical constraints on subduction processes in the Central American Volcanic Arc: Implications of Boron Geochemistry, in Geologic and Tectonic Development of the Caribbean Plate Boundary in Southern Central America, edited by P. Mann, p. 57– 73, Spec. Pap. 295, Geol. Soc. Am., Boulder, Colo.

López-Escobar L., Frey F.A., and Vergara M., (1977). Andesites and high-alumina basalts from the central-south Chile high Andes: Geochemical evidence bearing on their petrogenesis. Contributions to Mineralogy and Petrology, v. 63, p. 199–228.

Patino, L., Carr, M., and Feigenson, M. (2000). Local and regional variations in Central American arc lavas controlled by variations in subducted sediment input, Contribution to Mineralogy and Petrology, Vol. 138, p.265–283

Pérez Y. (1999). Fuentes de Aguas Termales de la Cordillera Andina del centro - sur de Chile (39-42◦ Sur): Servicio Nacional de Geología y Minería Boletín, v. 54, p. 65.

Person, M., Baumgartner, L. (1995) New evidence for long-distance fluid migration within the Earth's crust. Reviews of Geophysics, Volume 33, Issue S2, pp. 1083-1091

Minissale A. (2004). Origin, transport and discharge of CO2 in central Italy. Earth-Science Reviews 66(1-2): 89-141.

Moghaddam M. K., Y. Noorollahi, F. Samadzadegan, M. A. Sharifi and R. Itoi (2013). Spatial data analysis for exploration of regional scale geothermal resources. Journal of Volcanology and Geothermal Research 266(0): 69-83.

Ray M, Hilton D, Muñoz J, Fischer T, Shaw A (2009). The effects of volatile recycling, degassing and crustal contamination on the helium and carbon geochemistry of hydrothermal fluids from the Southern Volcanic Zone of Chile. Chem Geol 266(1–2):38–49.

Reyes, A.G., Christenson, B.W., and Faure, K. (2010). Sources of solutes and heat in low-enthalpy mineral waters and their relation to tectonic setting, New Zealand: Journal of Volcanology and Geothermal Research, v. 192, no. 3–4, p. 117–141. doi:10.1016/j.jvolgeores.2010.02.015

Risacher F., Fritz B. and Hauser A. (2011). Origin of components in Chilean thermal waters: Journal of South American Earth Sciences, v. 31, no. 1, p. 153–170. doi:10.1016/j.jsames.2010.07.002

Rowland J.V. and Sibson R.H. (2004) Structural controls on hydrothermal flow in a segmented rift system, Taupo Volcanic Zone, New Zealand: Geofluids, v. 4, no. 4, p. 259–283.

Rowland J. y Simmons, S. F. (2012). Hydrologic, magmatic, and tectonic controls on hydrothermal flow, Taupo Volcanic Zone, New Zealand: Implications for the formation of epithermal vein deposits: Economic Geology, v.107, p. 427-457.

Saginor I., Gazel E., Condie C., Carr M.J. (2013). Evolution of geochemical variations along the Central American Volcanic Front. Geochemistry, Geophysics, Geosystems. V-14, I-10, pages 4504–4522.

Sánchez, P., P. Pérez-Flores, G. Arancibia, J. Cembrano and M. Reich (2013). Crustal deformation effects on the chemical evolution of geothermal systems: the intra-arc Liquiñe-Ofqui fault system, Southern Andes. International Geology Review 55(11): 1384-1400.

Sepulveda, F., Lahsen, A., Powell, T. (2004). Chemical and isotopic composition of geothermal discharges from the Puyehue-Cordón Caulle area (40.5ºS), Southern Chile. Geothermics, Vol. 33, p. 655-673.

Sepulveda, F., Lahsen, A., Powell, T. (2007). Gas geochemistry of the Cordon Caulle geothermal system, Southern Chile. Geothermics, Vol. 36, p. 389-420.

SERNAGEOMIN-Servicio Nacional de Geología y Minería de Chile [en línea]. http://www.sernageomin.cl/mineria-geotermia.php [consulta: 23 Marzo 2015].

Snyder, G., Poreda, R., Hunt, A., Fehn, U. (2001). Regional variations in volatile composition: Isotopic evidence for carbonate recycling in the Central American volcanic arc. Geochemistry, Geophysics, Geosystems, Vol. 2, DOI: 10.1029/2001GC000163

Snyder, G., Poreda, R., Fehn, U., Hunt, A. (2003). Sources of nitrogen and methane in Central American geothermal settings: Noble gas and 129I evidence for crustal and magmatic volatile components. Geochemistry, Geophysics, Geosystems, Vol. 4. DOI 10.1029/2002GC000363

Soffia (2004). Perspectivas de Desarrollo de la Energía Geotérmica en Chile. En: Seminario Latinoamericano sobre energías renovables: Hacia la Conferencia Mundial de Bonn – 2004. Programa Chile Sustentable. 93–100. M. [en línea] http://www.archivochile.com/Chile_actual/patag_sin_repre/06/chact_hidroay-6%2000011.pdf.

Stern, C.R. (1989). Pliocene to present migration of the volcanic front, Andean Southern Volcanic Zone: Revista Geológica de Chile, v. 16, p. 145–162.

Stern C.R. (1991). Role of subduction erosion in the generation of Andean magmas: Geology, v. 19, p. 78–81, doi:10.1130/0091-7613(1991)0192.3.CO:2.

Stern C., H. Moreno, L., López-Escobar, J.E., Clavero, L.E. Lara, J.A. Naranjo, M.A. Parada, M.A. Skewes. (2007). Chilean Volcanoes. In: The Geology of Chile. Geological Society of Chile. Pag.156-157.

Tassara, A., Goïtze, H-J., Schmidt, S. y Hackney, R. (2006). Three-dimensional density model of the Nazca plate and the Andean continental margin. Journal of Geophysical Research, 111, B09404, http://dx.doi.org/10.1029/2005JB003976.

Tassara, A. y Morales, D. (2013). 3D temperature model of south-western South America. Annual Meeting of the European Geosciences Union, Viena, Austria. Geophysical Research Abstracts, V15,EGU2013–945.

Tassi, F.,Martinez, C., Vaselli, O., Capaccioni, B., Viramonte, J. (2005). The light hydrocarbons as newgeoindicators of equilibrium temperatures and redox conditions of geothermal fields: evidence from El Tatio (northern Chile). Appl. Geochem. 20, 2049–2062.

Tassi F., O. Vaselli, G. Moratti, L. Piccardi, A. Minissale, R. Poreda, A. Delgado Huertas, A. Bendkik, M. Chenakeb, and D. Tedesco (2006). Fluid geochemistry versus tectonic setting: the case study of Morocco. Geological Society, London, Special Publications, 262:131-145, doi:10.1144/GSL.SP.2006.262.01.08

Tassi F, Aguilera F, Vaselli O, Medina E, Tedesco D, Delgado Huertas A, Poreda R, Kojima S (2009) The magmatic- and hydrothermal-dominated fumarolic system at the Active Crater of Lascar volcano, northern Chile. Bull Volcanol 71:171–183.

Tassi, F., Aguilera, F., Darrah, T., Vaselli, O., Capaccioni, B., Poreda, R J., Huertas, A Delgado. (2010). Fluid geochemistry of hydrothermal systems in the Arica-Parinacota , Tarapacá and Antofagasta regions (northern Chile). Journal of Volcanology and Geothermal Research. Vol 192. 1-15.

Tassi F, Aguilera F, Vaselli O, Darrah T, Medina E (2011) Gas discharges from four remote volcanoes (Putana, Olca, Irruputuncu and Alitar) in northern Chile: a geochemical and isotopic survey. Ann Geophys 54:121–136.

Tebbens, S.F., Cande, S.C., Kovacs, L., Parra, J.C., LaBrecque, J.L., Vergara, H., (1997). The Chile ridge: a tectonic framework. Journal of Geophysical Research 102 (B6), 12035–12060, http://dx.doi.org/10.1029/96JB02581.

Tormey D.R., Hickey-Vargas R., Frey F.A. and López-Escobar L. (1991). Recent lavas from the Andean volcanic front (33 to 42°S): Interpretations of along arc compositional variations, in Harmon, R.S., and Rapela, C.W., eds., Andean magmatism and its tectonic setting: Geological Society of America Special Paper 265, p. 57–78.

Tormey D.R., Frey F. and López-Escobar L. (1995). Geochemistry of the active Azufre-Planchón-Peteroa volcanic complex, Chile (35°15′S): Evidence for multiple sources and processes in a Cordilleran arc magmatic system: Journal of Petrology, v. 36, p. 265–298.

Varekamp, J.C. Ouimette, A.P., Herman, S.W., Bermúdez, A., Delpino, D. (2001). Hydrothermal element fluxes from Copahue, Argentina, a 'beehive' volcano in turmoil. Geology, Vol. 29, p. 1059-1062.

Vaselli, O., A. Minissale, F. Tassi, G. Magro, I. Seghedi, D. Ioane and A. Szakacs (2002). A geochemical traverse across the Eastern Carpathians (Romania): constraints on the origin and evolution of the mineral water and gas discharges. Chemical Geology 182(2-4): 637-654.

Völker D., Geersen J. M., Contreras-Reyes E., Reichert C. (2013) Sedimentary fill of the Chile Trench (32–46°S): volumetric distribution and causal factors Journal of the Geological Society London, 170 . pp. 723-736. DOI 10.1144/jgs2012-119.

CAPÍTULO II

ANTECENDENTES GEOLÓGICOS Y TECTÓNICOS

II.1 INTRODUCCIÓN

La Cordillera de los Andes es el resultado del engrosamiento cortical del borde occidental de la placa Sudamericana producto del acortamiento tectónico y adición magmática generado por la subducción de la placa oceánica de Farallón-Nazca (*Mpodozis y Ramos 1989; Jordan et al. 1983; Ramos et al. 2002; Kay et al. 2005; Charrier et al. 2007; Farias et al. 2010*). Aún cuando el proceso de subducción ha sido relativamente continuo desde el Jurásico, los mayores rasgos morfoestructurales que se aprecian hoy en día a lo largo del margen Andino (ej. variaciones en la altura y grosor de la corteza continental, flexuramiento del continente) se produjeron durante el Cenozoico, particularmente desde el Oligoceno Superior cuando el vector de convergencia entre ambas placas aumentó y se hizo prácticamente ortogonal al margen continental (*Pardo-Casas y Molnar 1987; Isacks 1988; Allmendinger et al. 1997; Somoza 1998; Charrier et al. 2002*).

Actualmente uno de los rasgos morfológicos más importantes a lo largo de la cadena Andina corresponde a la segmentación del arco volcánico (Zonas Volcánicas Norte, Central, Sur y Austral; Figura II-1), siendo el resultado de la ocurrencia de zonas donde la Placa de Nazca no alcanza la temperatura necesaria para su deshidratación y/o su fusión parcial, imposibilitando la fusión del manto y el consecuente magmatismo de arco (*Uyeda y Kanamori 1979)*. Estas zonas sin volcanismo coinciden con segmentos del margen donde él ángulo de subducción entre las placas de Nazca y Sudamericanas disminuye de ~30° hasta <10° a profundidades >90 km (*Stern et al. 2007*), lo cual ha sido explicado como el resultado de la interacción mecánica entre la subducción de dorsales oceánicas (ej. dorsal de Nazca, de Juan Fernández y de Chile;

Yáñez et al. 2001, 2002) y la reología propia de la corteza continental a esas latitudes (*Tassara et al. 2006*).

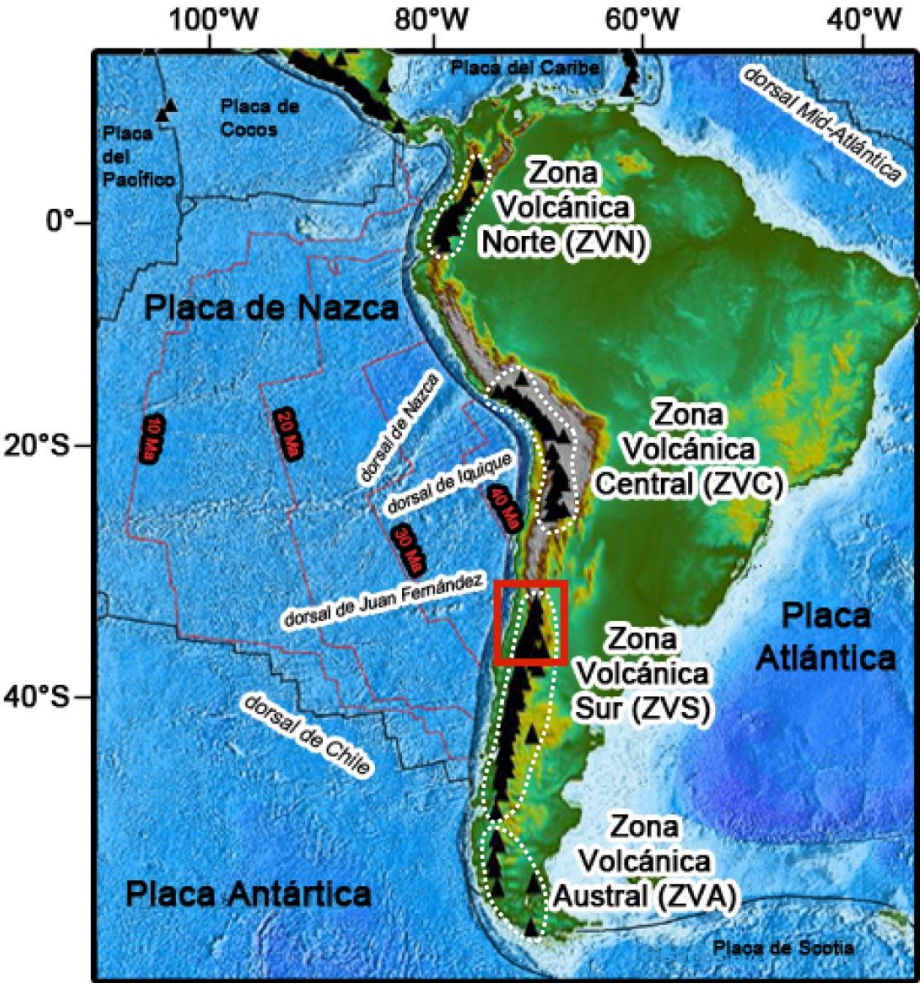

Figura II-1: Características tectónicas y morfológicas principales de Sudamérica. Zona de estudio en rojo. La topografía y batimetría están basadas en ETOPO2 (http://www.ngdc.noaa.gov). La separación de los segmentos volcánicos Andinos está basada en *Stern et al. (2007)*.

El área de estudio abarcada en esta investigación corresponde a los Andes de Chile Central (32.5-36°S), la cual está localizada al sur de la zona de subducción plana asociada a la dorsal de Juan Fernández (Figura II-1 y II-2). Chile Central se caracteriza por presentar un inusual arreglo geotectónico en donde tanto la configuración del margen de subducción como la configuración de la astenósfera y litósfera continental son altamente variables latitudinalmente. Entre estas características se destacan cambio del ángulo de subducción, variaciones del volumen de material subductado y la edad de la placa oceánica, cambios en la orientación de la fosa y la cadena Andina, disminución del espesor cortical y de la elevación de los rasgos topográficos hacia el sur, y variaciones en la cinemática de deformación cortical (*Tebbens et al. 1997; Cembrano y Lara 2009; Farías et al. 2010; Völker et al. 2013*).

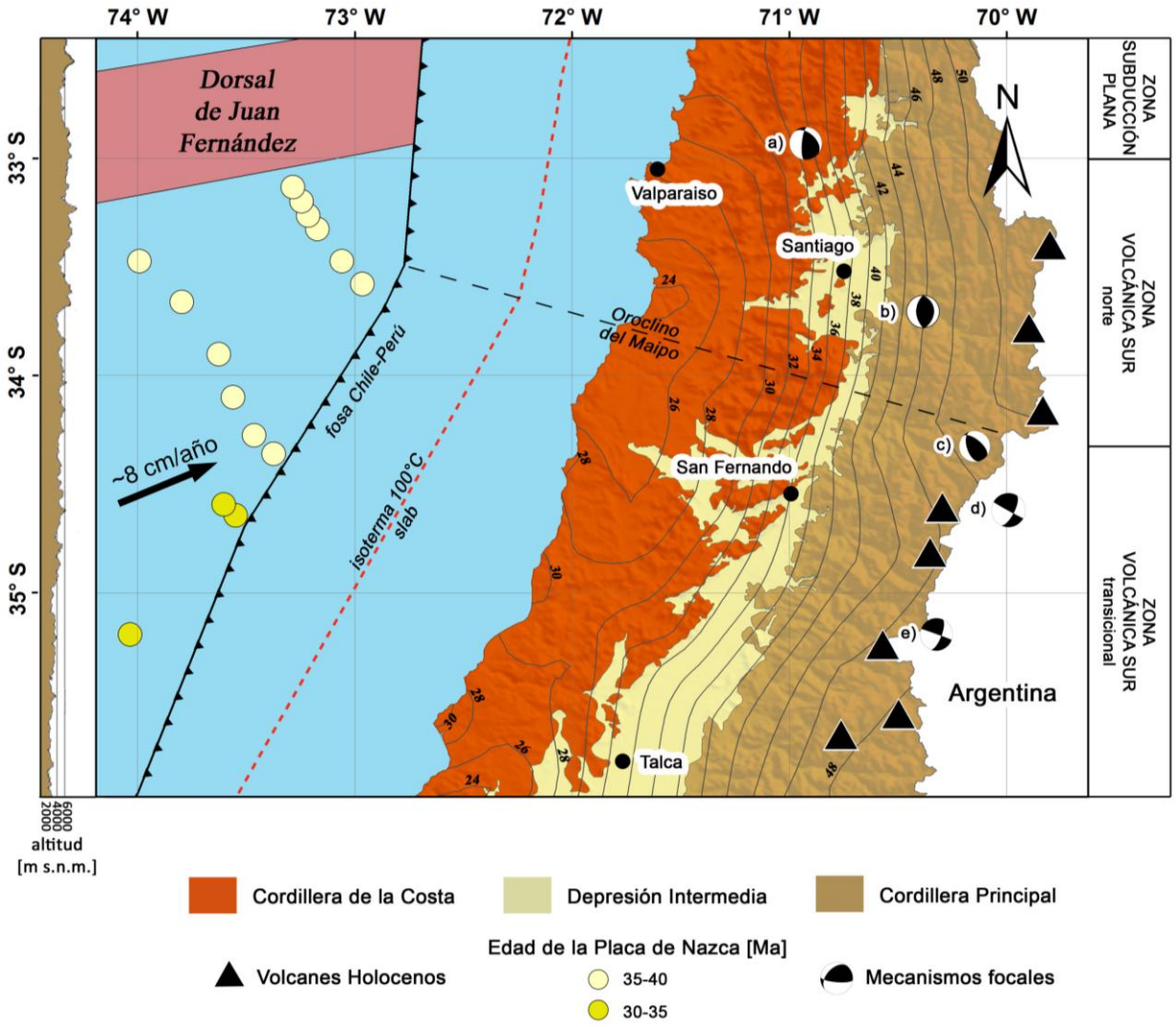

Figura II-2: Principales rasgos morfológicos de Chile Central (ej. segmentación andina, volcanes activos, dorsal de Juan Fernández). La subducción de la placa de Nazca bajo el continente Sudamericano constituye el proceso más importante a lo largo de la cadena andina. Se reporta la tasa y dirección (N78°E) de convergencia relativa de ambas placas (*Pardo-Casas y Molnar 1987; Somoza 1998*), al igual que las variaciones del espesor cortical como curvas de nivel, variaciones en la edad de la placa de Nazca, isoterma 100° de la losa oceánica, y topografía a lo largo de la Cordillera Principal (*Tebbens et al. 1997*; *Tassara et al. 2006; Greveyemer et al. 2003*). Los mecanismos focales reportados corresponden a sismos someros (<50 km) con una M_W>5 (a [2001], c [2004], d [1987], y e [2004]; estimados por Harvard CMT y *Farías et al. 2006*) y M_W<5 (b [2005]; *Pardo et al. 2006*).

Diversos autores coinciden que estas diferencias latitudinales son el resultado directo o indirecto de la subducción de la dorsal de Juan Fernández (*Mpodozis y Ramos 1989; Ramos et al. 2004; Kay et al. 2005; Farías et al. 2008; Arriagada et al. 2013*), la cual subducta cercano a los 32.5°S desde hace ~10 Ma (Figura II-2; *Martinod et al. 2010*). Sin embargo el segmento de Chile Central también ha sido afectado por otros eventos previos a éste (ej. acreción continental durante el Proterozoico Superior-Pérmico, extensión continental durante el Pérmico Superior-Jurásico Inferior; *Charrier et al. 2007*), los cuales han determinado, por ejemplo, el tipo de rocas que conforman la corteza continental y la ubicación de las zonas de debilidad cortical.

De este modo, con el fin de comprender los procesos relacionados al origen y naturaleza de los fluidos volcánicos e hidrotermales de Chile Central, resulta necesario conocer y entender la actual configuración de los Andes de Chile Central, ya que es ésta la que determina la naturaleza de las fuentes de calor, fluidos y solutos que dan origen a los sistemas volcánicos e hidrotermales de la región, así como la existencia de zonas corticales de mayor permeabilidad tales como fallas, fracturas y contactos litológicos, capaces de focalizar el transporte de fluido y calor en la zona.

II.2 CONFIGURACIÓN GEOTECTÓNICA DE LOS ANDES DE CHILE CENTRAL

II.2.1 Características de la corteza oceánica y la fosa

El segmento de la placa de Nazca correspondiente a Chile Central se encuentra limitado hacia el norte y sur por la dorsal de Juan Fernández (~32°S) y la zona de fractura de Mocha (ZFM ~38°S), respectivamente (*Contreras-Reyes et al. 2013*). Al norte de los 34.5°S, el basamento oceánico habría sido formado en la dorsal Pacífico-Nazca hace 35-40 Ma; mientras que entre los 34.5-38°S, se habría formado en la dorsal Nazca-Antártica hace 30-35 Ma (Figura II-2; *Tebbens et al. 1997*). Como resultado de esta diferencia de edad y posteriores procesos de enfriamiento, la placa de Nazca se hace levemente más fría hacia el norte (Figura II-2; *Grevemeyer et al. 2003*), resultando en una placa oceánica menos boyante y más profunda hacia el norte (Figura II-4a; *Völker et al. 2013*).

La porción marina del antearco de Chile Central habría experimentado erosión por subducción durante el Paleógeno, sin embargo durante el Mioceno Medio (*Kukowski y Oncken 2006*) y Plioceno (*Melnick y Echtler 2006*) este régimen habría

cambiado a uno de acreción de sedimentos, resultando en el actual prisma de acreción a lo largo del margen de la Zona Volcánica Sur (ZVS). Este cambio estaría relacionado a la erosión causada por los eventos de glaciación, lo que habría aumentado el flujo de sedimentos desde el continente hacia la fosa (i.e. turbiditas; *Bangs y Cande 1997; Melnick y Echtler 2006).* Mediante un análisis de perfiles sísmicos, *Völker et al. (2013)* determinó que el volumen de sedimentos a lo largo de la fosa (prisma de acreción) tiene una tendencia creciente hacia el sur (de 5 a ~40km^3/km entre los 32.5 y 36°S; Figura II-3b), lo cual se relaciona directamente tanto a las mayores precipitaciones registradas de norte a sur (Sección I.2.3; *Hoke et al. 2013*), así como con la mayor disponibilidad de sedimentos que existe hacia el sur producto de la mayor densidad de centros eruptivos (*Stern et al. 2007; Völker et al. 2013*).

II.2.2 Geometría del margen de subducción y la placa continental de Chile Central

La geometría del margen Andino de Chile Central es ilustrada a través 4 perfiles E-O reportados en la Figura II-3 (32.5, 33.5, 34.5 y 35.5ºS). Estos perfiles fueron construidos en base a los datos reportados en el trabajo de *Tassara et al. (2006)*, quien generó un modelo 3D del margen continental Andino en base a una modelación directa de las anomalías de Bouguer constreñidas a la petrología de la corteza y el manto, profundidades de sismos, tomografías sísmicas y flujo calórico a lo largo y ancho de los Andes.

En los perfiles se ve como el ángulo de subducción, entre 100-150 km de profundidad, aumenta progresivamente desde ~10º a los 32.5ºS, ~25º entre los 33-34.5ºS, hasta ~30º al sur de los 34.5ºS. Este progresivo aumento del ángulo de subducción hacia el sur es acompañado por un aumento del espesor del manto astenosférico (desde ~20 km a los 32.5ºS, ~50 km entre los 33.5ºS, hasta ~70 km al sur de los 34.5ºS; Figura II-3) y una leve disminución del espesor cortical (desde 50 a 48 km entre los 32.5 y 36ºS; Figura II-2 y II-3).

En superficie, los rasgos geométricos más relevantes corresponden al cambio en la orientación de la fosa y la cadena andina (Oroclino del Maipo) de N-S vs. NNE-SSO al sur y norte de los 34.5°S, respectivamente, la aparición de la Depresión Central al sur de los 33°S, y la disminución de la altitud promedio del orógeno hacia el sur (Figura II-2 y II-3).

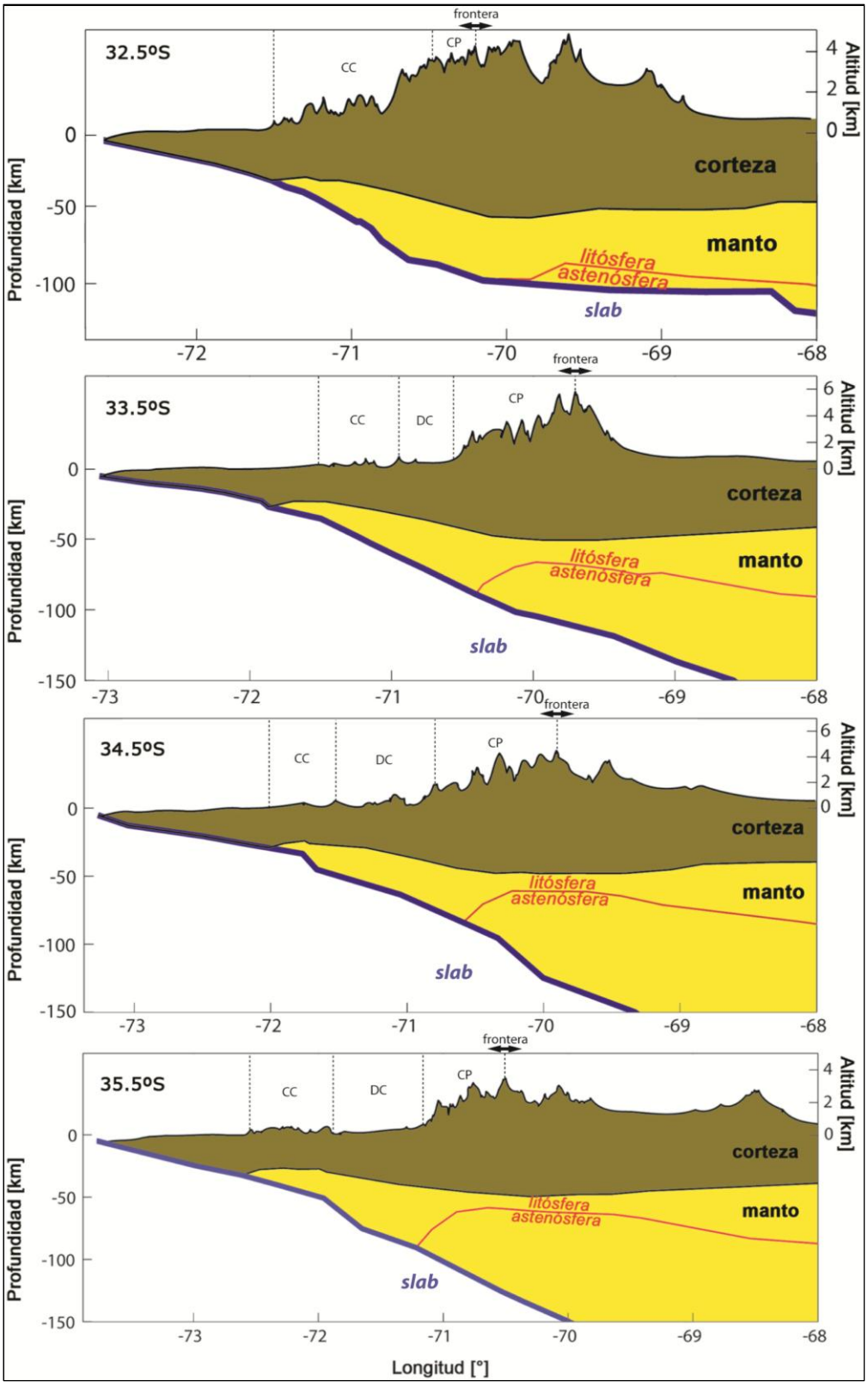

Figura II-3: Perfiles E-O del margen Andino entre los 33.5 y 35.5ºS donde se muestra la profundidad del slab, el límite litósfera-astenósfera, la profundidad de la corteza continental, y la altitud de la corteza. Estos límites fueron tomados del modelo 3D del margen Andino reportado por *Tassara et al. (2006).* CC, DC y CP indican los límites en superficie de la Cordillera de la Costa, Depresión Central y Cordillera Principal reportados en la Figura II-2.

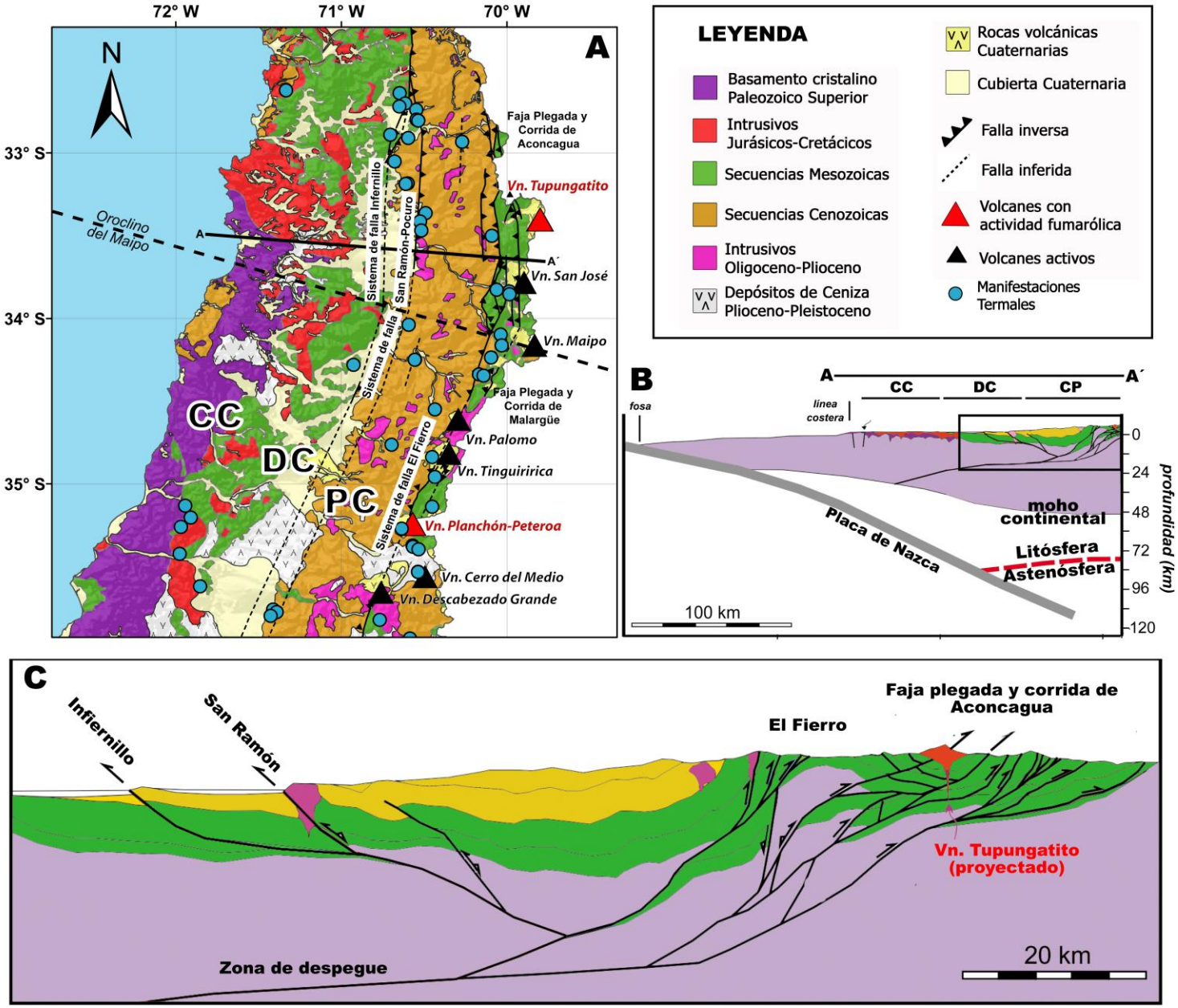

Figura II-4: a) Mapa geológico simplificado de Chile Central. Solo las zonas de fallas activas durante el neógeno han sido reportadas. Modificado de *SERNAGEOMIN (2002)*, *Farías et al. (2010) y Tapia (2010).* b) Sección balanceada A-A´ desde la fosa hasta la cadena volcánica. Se muestran las tres unidades morfoestructurales: Cordillera de la Costa (CC), Depresión Central (DC) y Cordillera Principal (CP). Rasgos geofísicos tomados desde *Tassara et al. (2006).* c) Detalle de la sección balanceada reportada en (b) para el sector de la CP y DC. Figuras b) y c) modificadas de *Giambiagi et al. (2014).*

II.2.3 Geología

En el segmento de Chile Central se aprecian 3 unidades morfoestructurales principales, dispuestas en franjas orientadas N-S, que de oeste a este corresponden a: Cordillera de la Costa (CC), Depresión Central (DC) y Cordillera Principal (CP) [Figura II-2, II-3, II-4a, b y c]. La mayoría de las manifestaciones termales se localizan en la CP y en el borde oriental DC (Figura II-4a).

II.2.3.1 Cordillera de la Costa

La CC se separa de la CP como una unidad geomorfológica independiente a partir de la depresión de Santiago hacia el sur debido a la aparición de la DC (Figura II-3 y 4). En general, la CC se puede dividir en un sector oriental y uno occidental de acuerdo con sus rasgos morfológicos y geológicos: su parte occidental se caracteriza por sus suaves relieves levemente incididos que han sido interpretados como terrazas de abrasión y acumulación marina plio-pleistocenas (*Wall et al. 1996*). El sector occidental está constituido por un basamento cristalino y metamórfico Paleozoico en las cercanías de la costa, mientras que hacia el Este afloran rocas cristalinas del Mesozoico Inferior (Figura II-4). La relación de contacto entre el basamento cristalino-metamórfico y las secuencias estratificadas es fundamentalmente por medio de una amplia discordancia de erosión (*Thomas 1958*). La CC oriental, por otro lado, está compuesta por rocas estratificadas con edades que fluctúan entre el Triásico y el Cretácico Superior, dispuestas monótonamente en un homoclinal inclinado hacia el Este con pliegues que no modifican mayormente su disposición (Figura II-4). Un cordón de cuerpos intrusivos de edad Cretácica Superior marca el borde oriental de la CC. Estos cuerpos intrusivos se presentan principalmente en el margen del valle de Santiago, existiendo solamente algunos cuerpos hacia el Sur (Figura II-4).

II.2.3.2 Depresión Central

La DC está constituida por depósitos aluviales Pleistocenos a Holocenos principalmente, los cuales superan los 500 m de espesor localmente (*Thiele 1980; Rauld 2002*). Su basamento aflora parcialmente en cerros islas y cordones que rodean la DC, los que alcanzan altitudes de hasta 650 m s.n.m. (Figura II-3). La DC limita hacia el este con la CP mediante un sistema de fallas inversas de vergencia oeste (Falla San Ramón-Pocuro en Santiago; *Rauld 2002; Fock 2005; Rauld et al. 2006; Farías et al. 2010*), sin embargo, la expresión morfológica de estas fallas no es continua a lo largo de esta región de Chile Central (Figura II-4c). De acuerdo con los autores previamente citados, la actividad de este sistema de estructuras sería de larga

data, destacando su desarrollo como una estructura normal durante la extensión de la cuenca de Abanico (Eoceno-Oligoceno), su inversión durante el Mioceno inferior, y su reactivación como falla inversa desde el Mioceno hasta el presente (*Fock et al. 2006; Farías et al. 2010*).

II.2.3.3 Cordillera Principal

El área de la CP está dominada por afloramientos de rocas cuyas edades abarcan desde el Mesozoico hasta la actualidad. Las unidades Mesozoicas y Cenozoicas, hasta el Mioceno-Plioceno, se distribuyen en franjas de dirección elongada Norte-Sur que, en términos generales, se hacen progresivamente más jóvenes hacia el Oeste (Figure II-4a). La CP puede ser subdividida en tres franjas de acuerdo con sus rasgos estructurales y litológicos las que de este a oeste corresponde a las franjas occidental, central y oriental (*Fock et al. 2006; Farías et al. 2010*).

La franja occidental de la CP está conformada por rocas volcanoclásticas de la Formación Abanico (Eoceno Superior?-Mioceno Inferior), las que se encuentran deformadas en apretados pliegues en el frente cordillerano *(Farías et al. 2010;* Figura II-4). Inmediatamente al Este de este cordón de rocas deformadas se ubica la Formación Farellones (Mioceno Inferior-Mioceno Superior); a diferencia de la Formación Abanico, estas rocas volcánicas y volcanoclásticas están débilmente deformadas, salvo sus niveles inferiores *(Fock et al. 2006; Farías et al. 2010)*. La Formación Farellones está intruida por distintos cuerpos miocenos y está parcialmente cubierta por unidades volcánicas. Estos cuerpos del Mioceno Superior presentan en algunos casos mineralización de cobre, conformando la franja de pórfidos cupríferos de Chile Central (constituido por El Teniente y Río Blanco-Los Bronces; *Muñoz et al. 2013*). La franja occidental de la CP (CPO) está limitada hacia el Este por un amplio cordón de intrusivos de edad Mioceno Inferior (ej. La Gloria, San Gabriel, Cortaderal; Figura II-4a). Al Este de este cordón de intrusivos comienza la franja central de la CP (CPC), la cual comprende los afloramientos de los niveles basales de la Formación Farellones que sobreyacen progresivamente discordantes a los apretados pliegues y fallas desarrollados en la Formación Abanico oriental (Figura II-4a; *Farías et al. 2010*). Hacia el Este, las capas de la Formación Abanico se ponen en contacto con el basamento Mesozoico por medio de un sistema de fallas de vergencia al este (Falla El Fierro) y retrocorrimientos (*Farías et al. 2010; Giambiagi et al. 2014)* [Figure II-4c]. Este sistema de fallas delimita orientalmente la franja central de la Cordillera Principal (CPC). La franja oriental de la CP (CPE), en cambio, está constituida por unidades sedimentarias marinas (calizas y secuencias de yeso) y continentales (conglomerados y areniscas) Mesozoicas (Jurásico-Cretácico Medio) organizadas de más antigua a

más joven hacia el Este (Figura II-4a). Entre algunos bloques imbricados se observan depósitos del Mioceno Inferior relacionados con el desarrollo de una cuenca de antepaís (*Giambiagi et al. 2003).* Las unidades mesozoicas se encuentran afectadas por un sistema de fallas inversas de vergencia al Este pertenecientes a las fajas plegadas y corridas de Aconcagua (al norte de los 34º15'S) y de Malargüe (al sur de los 34º15'S; *Ramos et al. 2002; Giambiagi et al. 2003*) [Figura II-4c].

II.3 CINEMÁTICA ACTUAL EN LOS ANDES DE CHILE CENTRAL

Como bien ha sido detallado por *Giambiagi y Ramos (2002), Giambiagi et al. (2003), Farías (2007), Farías et al. (2010)* y *Giambiagi et al. (2014)*, la deformación compresiva habría sido la responsable de la construcción de la Cordillera Principal hasta los ~4 Ma, correspondiendo a la edad donde los Andes alcanzó su máxima elevación (*Farías et al. 2007*). Posterior a los 4 Ma, la deformación compresiva habría migrado hacia el antepaís, lo que queda de manifiesto por la serie de cuerpos intrusivos que sellan las fallas de la CP, las fallas fuera de secuencia generadas en la FPCA y las fallas responsables del alzamiento de la Cordillera Frontal al oeste de la CP (*Giambiagi et al. 2003; Farías et al. 2010)* [Figura II-4a-c].

La cinemática que domina la deformación actual de la CP se puede observar mediante la comparación de los mecanismos focales de los sismos ocurridos a lo largo de la zona (Figura II-2). Los mecanismos focales determinados por Harvard CMT (*Harvard Centroid Moment Tensor Catalog*) y *Pardo et al. (2006)* muestran que la CP, al sur del oroclino del Maipo (34.5-36°S), tiene una cinemática predominantemente de rumbo dextral; mientras que al norte del oroclino (32.5-34.5°S), los mecanismos focales concuerdan con un cinemática compresiva de rumbo E-O, lo cual ha sido confirmado en trabajos posteriores (*Pérez et al. 2014).* El comportamiento compresivo y transcurrente que dominaría la cinemática actual de la CP al norte y sur de los 34.5°S, respectivamente, coincide con un aumento, hacia el sur, del ángulo de convergencia de la placa de Nazca (de 13 a 36°), lo que a su vez es resultado del cambio abrupto en la orientación de la fosa y la cadena Andina a los 34.5°S (Figura II-5). Una cinemática de rumbo dextral al sur del oroclino del Maipo, implicaría un avance del antearco hacia el N-NE, mientras que al norte de los 34.5°S, el antearco tendría un movimiento dominante hacia el E. Este movimiento diferencial del antearco explicaría de buena manera la respuesta compresiva del mecanismo focal reportado para el sismo c (Figura II-2; *Farías et al. 2006*), cuyo epicentro se encuentra en las cercanías

del oroclino del Maipo, y su mecanismo tiene una solución cuyo rumbo (NO-SE) coincide con la orientación del oroclino (Figura II-5).

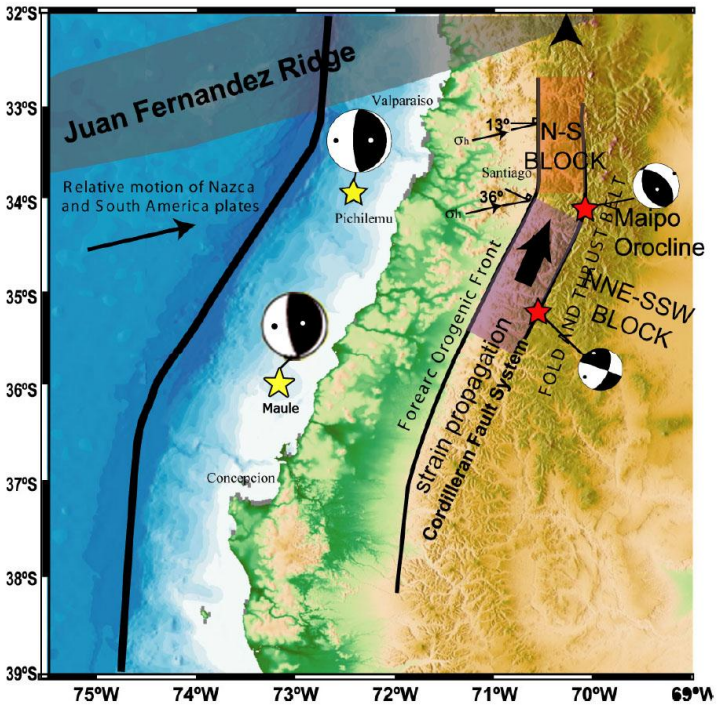

Figura II-5: Modelo de cinemática actual en los Andes de Chile Central (*Farías 2007*). Se reportan las soluciones de los mecanismos focales para los sismos c y e (Figura II-2) además de los mecanismo focales para el terremoto de 1985 (Valparaíso) y 2010 (Maule).

II.4 VOLCANISMO PLEISTOCENO-HOLOCENO DE CHILE CENTRAL

Debido al control tectónico que afecta tanto la distribución de los centros volcánicos, como también las características geoquímicas y petrológicas propias de los productos volcánicos emitidos por estos centros, diversos autores han agrupado los volcanes de edad pleistoceno-holoceno de Chile Central en dos segmentos (Figura II-2), los que de norte a sur corresponden a las Zona Volcánica Sur - Norte (ZVS-N; 33.3-34.4°S) y - Transicional (ZVS-T; 34.4-36°S) [ej. *Tormey et al. 1991; López-Escobar et al. 1995; Stern 2004*].

II.4.1 Zona Volcánica Sur-Norte (ZVS-N)

La ZVS-N está formada por nueve estratovolcanes compuestos y la caldera El Diamante, esta última localizada en territorio argentino. Estos centros eruptivos se disponen sobre las secuencias mesozoicas de la franja oriental de la CP, estando alineados con una orientación N-S. De norte a sur, los centros eruptivos más antiguos

(Pleistoceno Medio) corresponden a los volcanes Nevados de Piuquenes (6.019 m s.n.m.), Marmolejo (6.108 m s.n.m.) y Castillo (5.485 m s.n.m.), la caldera El Diamante (área ~10 x 20 km^2), y los volcanes Listado (4.250 m s.n.m.) y Picos del Barroso (5.000 m s.n.m.). Todos ellos se encuentran fuertemente erosionados, aunque sólo los que están más al norte se encuentran colapsados lateralmente producto de la inestabilidad causada por sus grandes altitudes, la fuerte alteración hidrotermal que los afecta y las altas tasas de erosión de esta zona (*Stern et al. 2007; Farías et al. 2008*). Por el contrario, los centros volcánicos más jóvenes (Pleistoceno Superior-Holoceno) se caracterizan por sus estratoconos bien preservados, que de norte a sur corresponden a los volcanes Tupungato (6.570 m s.n.m.), Tupungatito (5.682 m s.n.m.), San José (5.856 m s.n.m.) y Maipo (5.264 m s.n.m.) [Figura II-4a]. Entre los volcanes más jóvenes, sólo los tres últimos han tenido actividad histórica (*González-Ferrán 1995; Stern et al. 2007*), y sólo los volcanes Tupungatito y San José muestran una actividad fumarólica permanente (*González-Ferrán 1995; SERNAGEOMIN-OVDAS 2012*).

Los depósitos asociados a los centros eruptivos más jóvenes están formados por coladas de lava frescas de composición basalto-andesíticas a dacíticas, con intercalaciones de brechas volcánicas y depósitos piroclásticos menores (*Thiele 1980; Stern et al. 1984*). Las únicas rocas de composición riolítica en la zona corresponden a los flujos piroclásticos de la Ignimbrita Pudahuel, cuyo origen se asocia a la actividad de la caldera El Diamante (*Stern et al. 1984*). Entre los volcanes de esta zona, el complejo Marmolejo-San José comprende cerca de 95 km^3 de material eruptado, mientras que el resto de los volcanes tienen un volumen de material emitido variable entre 5 y 55 km^3 (*Hildreth y Moorbath 1988*).

II.4.2 Zona Volcánica Sur-Transicional (ZVS-T)

La ZVS-T de Chile Central se caracteriza por presentar estratovolcanes compuestos, grandes complejos volcánicos y calderas gigantes alineadas en una dirección NNE-SSO a lo largo de los sistemas de falla regionales (Falla El Fierro) que ponen en contacto las secuencias sedimentarias cenozoicas y mesozoicas de la CP (*Farías et al. 2010*). De norte a sur, los centros eruptivos más importantes de esta zona corresponden a (Figura II-4a): Volcán Palomo (4.850 m s.n.m.), complejo Tinguiririca (4.300 m s.n.m.), Complejo Volcánico Planchón-Peteroa-Azufre (4.107 m s.n.m.), Complejo Volcánico del Medio (3.508 m s.n.m.), Complejo Volcánico Descabezado Grande-Quizapu-Cerro Azul (3.953 m s.n.m.) y la caldera Calabozos. A diferencia del segmento norte de la ZVS, la ZVS-T se ensancha considerablemente

hacia el este (~200 km), debido a la presencia de un volcanismo tanto de arco en la frontera Chile-Argentina, como de trasarco en Argentina (*Stern et al. 2007*). En el arco, los edificios volcánicos tienen una altura neta que no supera los 1900 m al medirlo desde sus bases, el cual es mucho menor a las diferencias de altura existente en la ZVS-N (~3.600 m; *Stern et al 2007*). El volumen de material erupcionado desde estos volcanes varía entre 3 y 60 km^3 (*Hildreth y Moorbath 1984*), aunque el volumen total estimado para los eventos eruptivos de la caldera Calabozos alcanzaría los ~1000 km^3 (*Hildreth et al. 1984; Grunder 1987*). Entre los volcanes del arco, los centros con mayor actividad histórica corresponden a los volcanes Tinguiririca, Planchón-Peteroa y Descabezado Grande-Quizapu, los que también presentan actividad fumarólica permanente (*González-Ferrán 1995; Stern et al. 2007*).

Los depósitos volcánicos de este segmento varían en composición desde basaltos toleíticos a riolítas de alto K, siendo las andesitas la composición más común entre las rocas de la zona (*Hildreth y Moorbath 1984*). Por lo general, las lavas de composición basáltica aumentan en proporción tanto hacia el sur de esta zona como entre las unidades más antiguas del arco volcánico (*Cembrano y Lara 2009*). Grandes volúmenes de rocas de composición riolítica fueron erupcionadas por la caldera Calabozos durante el Pleistoceno Medio (0.8 y 0.15 Ma), cuyo origen involucró la participación de magmas generados por la fusión parcial de la corteza según las características isotópicas de estas rocas (*Hildreth et al. 1984; Grunder 1987*). Rocas basálticas alcalinas son encontradas en la zona del trasarco (ej. conos de escoria de Llancanelo, campo volcánico de Payún Matru; *Risso et al. 2008*).

II.4.3 Influencia de la configuración geotectónica sobre las características geoquímicas de los magmas de Chile Central.

Investigaciones previas acerca de la geoquímica de los productos volcánicos holocenos en el arco de Chile Central (*Stern et al. 1984; López-Escobar et al. 1985; Futa y Stern 1988; Hildreth y Moorbath 1988; Stern 1988,1989, 1991*) han reportado un aumento progresivo tanto en los contenidos de K, Rb, Sr, Ba, La, Th y U, como en la razón de los elementos incompatibles vs. compatibles (ej. $^{87}Sr/^{86}Sr$, $^{143}Nd/^{144}Nd$, Rb/Cs, La/Yb, K/La, Rb/La, Ba/La, Hf/Lu) de sur a norte, lo cual indica una mayor participación de material cortical en la génesis de los magmas erupcionados hacia el norte. Sin embargo, aún no existe consenso entre los diferentes investigadores en cómo este material cortical ha sido incorporado, sin embargo, todos los estudios coinciden que es resultado de las variaciones geotectónicas a lo largo de Chile Central.

Hildreth y Moobarth (1988) propusieron que el aporte cortical estaría relacionado directamente al aumento del espesor cortical a lo largo de Chile Central (desde 46 hasta ~50 km a los 36 y 33°S respectivamente; *Tassara et al. 2006*), lo que aumentaría los tiempos de residencia de los magmas en la corteza, facilitando así los procesos MASH (*Melting, Assimilation, Storage, Homogenization; Hildreth y Moobarth 1988*) de los magmas en la base de la corteza. Sin embargo, y luego de la publicación de importantes trabajos relacionados con el arreglo estructural y la deformación cortical actual de Chile Central (ej. *Fock et al. 2006*; *Farías 2007; Farías et al. 2008; Farías et al. 2010*), *Cembrano y Lara (2009)* argumentarían que el aumento en los tiempos de residencia de los magmas no sólo sería efecto del aumento del espesor cortical de sur a norte, sino que también se debería a la orientación de las fallas inversas regionales (N-S vs. NNE-SSO al norte y sur del oroclino del Maipo, respectivamente), respecto a la cinemática de deformación cortical a lo largo del arco volcánico (desde una deformación sinestral de rumbo NNE-SSO a una deformación netamente compresiva de rumbo E-O, al sur y norte del Oroclino del Maipo respectivamente) [ver mecanismos focales; Figura II-3]. De esta manera se favorecería el almacenamiento y permanencia de los magmas en la corteza superior al norte del oroclino del Maipo (permeabilidad secundaria horizontal ~dirección de σ_2), y por el contrario se favorecería el ascenso de los magmas a través de grietas tensionales de orientación NNE-SSO al sur de esta zona (σ_2 vertical), lo que disminuiría tanto los tiempos de residencia de los magmas en la corteza como el grado de diferenciación de éstos (*Cembrano y Lara 2009*).

Por otro lado, *Stern et al. (1984) y Stern (1988, 1991)* notaron que la composición isotópica de Sr y Nd en los magmas no se relacionaba con el contenido de SiO_2 de éstos, sugiriendo que la signatura cortical de los magmas en la zona norte de Chile Central se debería a un incremento relativo del material subductado en la región mantélica causado por (i) un menor volumen de material mantélico en la cuña astenosférica hacia el norte, y/o por (ii) un aumento del material subductado ya sea por erosión continental o desde el prisma de acreción (Figura II-3). Una disminución del grado de fusión parcial del manto astenosférico, hacia el norte, como consecuencia de un slab más frío (Figura II-2), también ha sido sugerida como una explicación plausible para la signatura cortical dominante en los magmas de la ZVS-N respecto a los de la ZVS-T (*López-Escobar et al. 1977; Tormey et al. 1991; Stern 1991*).

II.4.4 Sistemas Volcánicos con actividad fumarólica y termal

A diferencia del conocimiento que se tiene sobre la petrología y geoquímica de productos volcánicos a lo largo de la ZVS norte y transicional, la información acerca de las características físico-químicas de los fluidos emitidos por estos volcanes es limitada, consistiendo sólo en dos resúmenes de congreso donde se caracteriza la actividad fumarólica y termal asociada al volcán Planchón-Peteroa (ej. *Gately et al. 2004a y b*). Además del volcán Planchón-Peteroa, según *González-Ferrán (1995) y Stern et al. (2007*) los centros eruptivos que presentan actividad fumarólica permanente a lo largo de Chile Central corresponden a los volcanes Tupungatito, San José, Tinguiririca, y Quizapu. Sin embargo, luego de visitar en terreno estos 5 volcanes entre los años 2010 y 2013, se ha verificado que sólo los volcanes Tupungatito y Planchón-Peteroa presentan actividad fumarólica y termal de forma permanente.

A continuación se presenta una breve descripción de las características morfológicas y los antecedentes de actividad histórica de ambos volcanes.

II.4.4.1 Volcán Tupungatito (33°23'14''S-69°48'49''O/5603 m s.n.m.)

El volcán Tupungatito está ubicado en las nacientes del río Colorado (afluente del río Maipo) aproximadamente a 100 km al este de la ciudad de Santiago. Posee ocho cráteres bien preservados, donde se ha concentrado la actividad eruptiva histórica y la actividad fumarólica, los que se localizan en el extremo norte de una depresión semi-circular de 4 km de diámetro. Esta estructura ha sido interpretada como un anfiteatro de deslizamiento (*Moreno y Naranjo 1991*) o como una caldera volcánica compuesta (*González-Ferrán 1995*). Dentro de esta depresión se ha desarrollado un extenso y potente glaciar que descarga hacia el río Colorado con un espesor de entre 15 y 190 m (*Zamora et al. 2011*).

Este volcán es relativamente joven (<55±17 ka), habiéndose desarrollado con posterioridad a su vecino más antiguo, el volcán Tupungato. Los productos asociados al volcán Tupungatito tienen una composición basalto-andesítica a dacítica (*Hildreth y Moobarth 1988*), e incluyen lavas, lahares y flujos piroclásticos que cubren el flanco noroeste del volcán y rellenan el valle del río Colorado (hasta 19 km en el caso de las lavas y hasta 12 km en el caso de un flujo de escoria y subsecuente lahar; *González-Ferrán 1995*). Adicionalmente, depósitos piroclásticos se disponen en torno a los cráteres (*González-Ferrán 1995*). Los registros de erupciones históricas varían entre 19 eventos desde 1829 (*González-Ferrán 1995*) y 25 eventos desde 1646 (*Petit-Breuilh 2004*). Estos eventos han tenido índices de explosividad volcánica (IEV) <2, los

que se asocian a una mayor actividad fumarólica, explosiones, y columnas de gases y cenizas (*González-Ferrán 1995; Petit-Breuilh 2004*). Su última erupción con depósitos importantes ocurrió en 1959-1960, involucrando la deposición de una colada de lava de 1,85 km de longitud y caída de ceniza en Argentina (*Casertano 1963*); mientras que su última reactivación menor ocurrió en 1986, involucrando una débil columna de cenizas negras que cubrieron levemente una pequeña área de sus glaciares (*González-Ferrán 1995; Petit-Breuilh 2004*).

Figura II-6: Vista hacia el suroeste de los cráteres activos del volcán Tupungatito (Febrero 2011). La laguna color turquesa de la foto corresponde al lago hiperácido ubicado en el cráter activo más septentrional, el cuál fue formado durante la erupción de 1961 (González-Ferrán 1995).

Actualmente la actividad volcánica está caracterizada por diversos campos fumarólicos y tres lagunas cratéricas (Figura II-6). Equipos de monitoreo sísmico del OVDAS registraron 88 sismos entre febrero y mayo de 2012, los cuales fueron interpretados como la interacción de los fluidos volcánicos y la dinámica propia de los sistemas de fallas locales. Estos niveles de actividad fueron considerados bajos (*SERNAGEOMIN-OVDAS 2012*).

II.4.4.2 Volcán Planchón-Peteroa (35°14,5'S-70°34,4'O/3977 m s.n.m.)

El complejo volcánico Planchón-Peteroa se localiza a 70 km al este de la ciudad de Curicó en la frontera con Argentina. Está conformado por los extintos volcanes Azufre y Planchón, y sobre éstos se construye actualmente el volcán Peteroa, con 4 cráteres principales (150-500 m de diámetro) y un cono de escoria (150 y 60 m de diámetro y alto, respectivamente; *Tormey 1989; Haller et al. 1994; Naranjo et al. 1999; Naranjo y Haller 2002; Tormey 2010*).

La historia de este complejo se inicia hace aproximadamente 1 Ma (Pleistoceno Medio-Superior) con la formación del volcán Azufre ubicado en el extremo sur del complejo, el cual está constituido por ~69 km^3 de lavas y flujos piroclásticos de composición andesítico-basálticas a dacitas (*Tormey 1989; Naranjo y Haller 2002)*. La actividad del volcán Planchón, ubicado 6 km al norte del volcán Azufre, comienza durante el Pleistoceno Superior (~14-7 ka). Su actividad está caracterizada por la emisión de basaltos y andesitas basálticas generados en tres etapas definidas por el establecimiento de un primer edificio volcánico (Planchón I), la avalancha de detritos generada por el colapso del flanco oeste de dicho edificio y la formación de una nueva estructura volcánica (Planchón II; *Tormey 1989; Haller et al. 1994, Tormey et al. 1995)*. Finalmente, el volcán Peteroa se constituye entre los volcanes Azufre y Planchón hace aproximadamente 7 ka, estando constituido por lavas andesítico-basálticas a andesitas y flujos piroclásticos basalto-andesíticos a dacíticos principalmente (*Tormey 1989; Naranjo et al. 1999; Haller y Risso 2011).*

Dentro del registro de actividad histórica del volcán Peteroa, se puede mencionar una veintena de eventos eruptivos, mayormente débiles (IEV<3) dentro de los cuales destacan:

- En Febrero de 1837, posterior al mega-sismo de 1835, se registró la única erupción histórica (estromboliana) de lava del Planchón, la cual alcanzó un volumen cercano a los $6x10^{-3}$ km^3 y tuvo una composición basáltica a basáltica-andesítica (*Naranjo et al. 1999*). Asociada a la erupción se registraron lahares que arrastraron bloques de hielo hacia el río Teno (*Petit-Breuilh 2004)*
- En 1991 se registró la última actividad considerable la que consistió en una erupción freato-magmática que generaron 2 nuevos cráteres de explosión. La columna eruptiva fue baja, expulsando cenizas a kilómetros de distancia y provocando contaminación en las aguas del río Claro (*Naranjo y Haller 2002*).

- En 1998 se registraron explosiones freáticas menores que erupcionaron un escaso volumen de cenizas finas con un alto grado de alteración argílica (*Naranjo et al. 1999*).
- Finalmente, entre Septiembre del 2010 y Mayo del 2011, se produjeron las eyecciones más importantes del ciclo eruptivo que sucedió al mega-sismo del 27 de Febrero del 2010 (8.8 M_W). Este ciclo se caracterizó por una actividad explosiva freática a freático-magmática, donde el material juvenil eyectado tiene una composición similar a las lavas de la erupción de 1837 (*Naranjo et al. 2012*).

En la actualidad los cráteres activos del volcán Peteroa hospeda lagunas cratéricas, y sólo 3 de estos 4 cráteres presentan actividad fumarólica permanente (Figura II-7).

Figura II-7: Vista hacia el sur de los cráteres activos del Complejo Volcánico Planchón-Peteroa (Marzo 2010). En la foto se aprecia una columna blanca de gas y vapor generada durante la serie de explosiones freáticas de baja intensidad que se desarrollaron principalmente en el sector SO del volcán Peteroa durante Enero y Agosto del 2010.

BIBLIOGRAFÍA

Allmendinger, R. W., T. E. Jordan, S. M. Kay, and B. L. Isacks (1997), The evolution of the Altiplano-Puna plateau of the Central Andes, Annual Review of Earth and Planetary Sciences, 25, 139-174.

Arriagada C., Ferrando R., Cordova L., Morata D., Roperch P. (2013) The Maipo Orocline: A first scale structural feature in the Miocene to Recent geodynamic evolution in the central Chilean Andes. Andean Geology 40(3): 419-437.

Bangs N.L. and Cande S.C. (1997). Episodic development of a convergent margin inferred from structures and processes along the southern Chilean margin. Tectonics, 16, 489–503.

Casertano L. (1963). General characteristics of active Andean volcanoes and a summary of their activities during recent centuries. Bulletin of the Seismological Society of America, Vol. 53, Nº6, pp. 1415-1433.

Charrier, R., O. Baeza, S. Elgueta, J. J. Flynn, P. Gans, S. M. Kay, N. Muñoz, A. R. Wyss, and E. Zurita (2002), Evidence for Cenozoic extensional basin development and tectonic inversion south of the flat-slab segment, southern Central Andes, Chile (33°-36°S.L.), J S Am Earth Sci, 15(1), 117-139.

Charrier, R., L. Pinto, and M. P. Rodríguez (2007), Tectonostratigraphic evolution of the Andean Orogen in Chile, in Geological Society Special Publication: The Andes of Chile, edited, pp. 21-114.

Cembrano, J. and L. Lara (2009). The link between volcanism and tectonics in the southern volcanic zone of the Chilean Andes: A review. Tectonophysics 471(1-2): 96-113.

Farías M., Comte D., Charrier R. (2006). Sismicidad superficial en Chile Central: implicancias para el estado cortical y crecimiento de los Andes centrales australes. Actas XI Congreso Geológico Chileno, vol. 1, pp. 403–406.

Farías M. (2007). Tectónica de la erosión en la evolución del relieve de los Andes de Chile Central durante el Neógeno. Tesis de Ph.D., Departamento de Geología, Universidad de Chile. 194 p. Santiago.

Farías M., Charrier R. et al. (2008). Late Miocene high and rapid surface uplift and its erosional response in the Andes of central Chile (338–358S). Tectonics, 27, TC1005, http://dx.doi.org/10.1029/2006TC002046.

Farías M., Comte D. et al. (2010). Crustal-scale structural architecture in central Chile based on seismicity and surface geology: implications for Andean mountain building. Tectonics, 29, TC3006, http://dx.doi.org/10.1029/2009TC002480.

Fock A. (2005). Cronología y tectónica de la exhumación en el Neógeno de los Andes de Chile central entre los 33º y los 34ºS. Tesis de Ms.C., Departamento de Geología, Universidad de Chile. 179 p. Santiago.

Fock A., Charrier R., Farías M., Muñoz M. (2006). Fallas de vergencia oeste en la Cordillera Principal de Chile central: inversión de la cuenca de Abanico (33º-34ºS). Revista de la Asociación Geológica Argentina, Serie D, Publicación especial No. 10: 48-55.

Futa K. and Stern C.R. (1988). Sr and Nd isotopic and trace element compositions of Quaternary volcanic centers of the southern Andes: Earth and Planetary Science Letters, v. 88, p. 253–263, doi: 10.1016/0012-821X(88)90082-9.

Gately, C., Sruoga, P., Gomberg, A., Varekamp, J. (2004a). Hypersaline brines in hot spring fluids from Peteroa volcano, South Andes. IAVCEI General Assembly 2004. 1 p.

Gately, C., Gomberg, A., Sruoga, P., Varekamp, J. (2004b). Geochemistry of the Hydrothermal System of Peteroa Volcano, Chile-Argentina. American Geophysical Union, Spring Meeting 2004. 1 p

Giambiagi L. B. and V. A. Ramos (2002). Structural evolution of the Andes in a transitional zone between flat and normal subduction (33º30'-33º45'S), Argentina and Chile, J S Am Earth Sci, 15(1), 101-116.

Giambiagi L.B., Ramos V., Godoy E., Álvares P., Orts S. (2003). Cenozoic deformation and tectonic style of the Andes, between 33° and 34°S. Tectonics (22): 1041-1059. doi: 10.1029/2001TC001354.

Giambiagi L., Tassara A. et al. (2014). Evolution of shallow and deep structures along the Maipo–Tunuyan transect (33°40′S): from the Pacific coast to the Andean foreland. In: Sepúlveda S. A., Giambiagi L. B., Moreiras S. M., Pinto L., Tunik M., Hoke G. D. y Farías, M. (eds) Geodynamic Processes in the Andes of Central Chile and Argentina. Geological Society, London, Special Publications, 399. http://dx.doi.org/10.1144/SP399.14

Grevemeyer I., Diaz-Naveas J. L., Ranero C. R., Villinger H., Ocean Drilling ProgramLeg 202 Scienti¢c Party (2003). Heat flow over the descending Nazca plate in central Chile, 32°S to 41°S: observations from ODP Leg 202 and the occurrence of natural gas hydrates. Earth and Planetary Science Letters 213, 285-298.

Haller, M., Risso, C. (2011) La erupción del volcán Peteroa 35º15' S, 70º18' O) del 4 de Septiembre de 2010. Revista de la Asociación Geológica Argentina, 68(2):295-305.

Hickey R.L., Frey F.A., Gerlach D.C., and López-Escobar L. (1986). Multiple sources for basaltic arc rocks from the southern volcanic zone of the Andes (34°41'S): Trace element and isotopic evidence for contributions from subducted oceanic crust, mantle and continental crust. Journal of Geophysical Research, v. 91, p. 5963–5983.

Hildreth W. y Moorbath S. (1988). Crustal contributions to arc magmatism in the Andes of Central Chile: Contributions to Mineralogy and Petrology, v. 98, p. 455–489.

Hoke, G. D., J. N. Aranibar, M. Viale, D. C. Araneo y C. Llano (2013). Seasonal moisture sources and the isotopic composition of precipitation, rivers, and carbonates across the Andes at 32.5–35.5°S. Geochemistry, Geophysics, Geosystems 14(4): 962-978.

Isacks, B. L. (1988), Uplift of the central Andean Plateau and bending of the Bolivian Orocline, Journal of Geophysical Research, 93(B4), 3211-3231.

Jordan, T.E., Isacks, B.L., Allmendinger, R.W., Brewer, J.A., Ramos, V.A. & Ando, C.J. (1983). Andean tectonics related to geometry of subducted Nazca plate. Geological Society of America Bulletin (94): 341-361.

Kay S. M., Godoy E. and Kurtz A (2005). Episodic arc migration, crustal thickening, subduction erosion, and magmatism in the South-Central Andes. Geological Society of America Bulletin 117, 67-88.

Kukowski N. and Oncken O. (2006). Subduction erosion—the 'normal' mode of fore-arc material transfer along the Chilean margin? In: Oncken, O., Chong, G., Franz, G., Giese, P., Götze, H.-J., Ramos, V.A., Strecker, M.R. & Wigger, P. (eds) The Andes—Active Subduction Orogeny, Frontiers in Earth Sciences. Springer, Berlin, 213–232.

López-Escobar L., Frey F.A., and Vergara M., (1977). Andesites and high-alumina basalts from the central-south Chile high Andes: Geochemical evidence bearing on their petrogenesis. Contributions to Mineralogy and Petrology, v. 63, p. 199–228.

López-Escobar L., Cembrano J. y Moreno H. (1995). Geochemistry and tectonics of the chilean Southern Andes basaltic Quaternary volcanism (37º–46ºS). Revista Geológica de Chile, 22, 219–234.

Martinod, J. Husson, L. Roperch, P. Guillaume, B. Espurt, N. (2010). Horizontal subduction zones, convergence velocity and the building of the Andes. Earth and Planetary Science Letters 300 (3-4): 299-309.

Melnick, D., Echtler, H. (2006). Inversion of forearc basins in south-central Chile caused by rapid glacial age trench fill. Geology 34 (9), 709–712.

Moreno H and Naranjo JA (1991). The southern Andes volcanoes (33°-41° 30' S), Chile. 6th Geol Cong Chile, Excur PC-3, pp. 26.

Moreno H., Thiele, R., Varela J., (1988). Estudio preliminar del riesgo geológico en la Alta Cordillera, proyecto Alfalfal. Chilectra Generación S.A. ejecutado por Departamento de Geología y Geofísica, Universidad de Chile.

Mpodozis, C., and V. A. Ramos (1989). The Andes of Chile and Argentina. In Geology of the Andes and its relation to Hydrocarbon and Mineral Resources, in Circumpacific Council for Energy and Mineral Resources, edited by G. E. Ericksen, et al., pp. 59-90.

Naranjo J, Haller M, Ostera H, Pesce A, Sruoga P. (1999). Geología y Peligros del Complejo Volcánico Planchón-Peteroa, Andes del Sur (35º15´S), Región del Maule, Chile- Provincia de Mendoza, Argentina. Serv Nac Geol Min, 52

Naranjo J, Haller M (2002). Erupciones principalmente explosivas del volcán Planchón, Andes del sur (35º15'S). Rev Geol Chile 29:93-113

Naranjo J (2012) Principales etapas evolutivas holocenas del volcán Planchón y su reactivación relacionada al megasismo del 27 de Febrero de 2010. XIII Chilean Geologic Congress 5-9 August, Antofagasta, Chile, pp. 440–441

Pardo, M., E. Vera, T. Monfret, G. Yáñez, and A. Eisenberg (2006), Sismicidad cortical superficial bajo Santiago: Implicaciones en la tectónica andina y evaluación del peligro sísmico, paper presented at XI Congreso Geológico Chileno, Antofagasta, Chile.

Pardo-Casas, F., and P. Molnar (1987), Relative motion of the Nazca (Farallon) and South American plates since late Cretaceous time, Tectonics, 6(3), 233-248.

Petit-Breuilh M. E. (2004).La historia eruptiva de los volcanes hispanoamericanos (siglos XVI al XX). Serie Casa de los Volcanes Nº8, Exmo. Cabildo Insular de Lanzarote, España, 431 p.

Pérez A., J. A. Ruiz, G. Vargas, R. Rauld, S. Rebolledo, J. Campos (2014). Improving seismotectonics and seismic hazard assessment along the San Ramón Fault at the eastern border of Santiago city, Chile. Natural Hazards. Volume 71, Issue 1, pp. 243-274. http://dx.doi.org/10.1007/s11069-013-0908-3.

Ramos, V.A., Cristallini, E. & Pérez, D. (2002). The Pampean flat-slab of the central Andes. Journal of South American Earth Sciences (15): 59-78.

Ramos V. A., T. Zapata, E. Cristallini, and A. Introcaso (2004). The Andean thrust system— Latitudinal variations in structural styles and orogenic shortening, in K. R. McClay, ed., Thrust tectonics and hydrocarbon systems: AAPG Memoir 82, p. 30– 50.

Rauld R. (2002). Análisis morfoestructural del frente cordillerano Santiago Oriente entre el río Mapocho y la Quebrada de Macul. Tesis de Título, Departamento de Geología, Universidad de Chile. 57 p. Santiago.

Rauld, R., Vargas, G., Armijo, R., Ormeño, A., Valderas, C. & Campos, J. (2006). Cuantificación de escarpes y deformación reciente en el frente cordillerano de Santiago. Actas XI Congreso Geológico Chileno: 447-450. Antofagasta.

SERNAGEOMIN (2002). Mapa Geológico de Chile, Servicio Nacional de Geología y Minería, Carta Geológica de Chile, Serie Geología Básica No. 75, 1 mapa en 3 hojas, escala 1:1.000.000. Santiago.

SERNAGEOMIN - Red Nacional de Vigilancia Volcánica - OVDAS (2012). Reportes de actividad volcánica Región Metr opolitana Nº4, 5, 6, 7 y 8.

Somoza, R. (1998), Updated Nazca (Farallon) - South America relative motions during the last 40 My: implications for mountain building in the central Andean region, J S Am Earth Sci, 11(3), 211-215.

Stern C. R., Amini H., Charrier R., Godoy E., Hervé F. y Varela J. (1984). Petrochemistry and age of rhyolitic pyroclastics flows which occur along the drainage valleys of the Río Maipo and Río Cachapoal (Chile) and the Río Chaucha and Río Papagayos (Argentina). Revista Geológica de Chile, 23, 39–52.

Stern, C.R. (1989). Pliocene to present migration of the volcanic front, Andean Southern Volcanic Zone: Revista Geológica de Chile, v. 16, p. 145–162.

Stern C.R. (1991). Role of subduction erosion in the generation of Andean magmas: Geology, v. 19, p. 78–81, doi:10.1130/0091-7613(1991)0192.3.CO:2.

Stern C. R. (2004). Active Andean volcanism: its geologic and tectonic setting. Revista Geológica de Chile, 31, 161–208.

Stern C., H. Moreno, L.López-Escobar,J.E. Clavero, L.E. Lara, J.A. Naranjo, M.A. Parada, M.A. Skewes. (2007). Chilean Volcanoes. In: The Geology of Chile. Geological Society of Chile. Pag.156-157.

Tassara, A., Goïtze, H-J., Schmidt, S. y Hackney, R. (2006). Three-dimensional density model of the Nazca plate and the Andean continental margin. Journal of Geophysical Research, 111, B09404, http://dx.doi.org/10.1029/2005JB003976.

Tebbens, S.F., Cande, S.C., Kovacs, L., Parra, J.C., LaBrecque, J.L., Vergara, H., (1997). The Chile ridge: a tectonic framework. Journal of Geophysical Research 102 (B6), 12035–12060, http://dx.doi.org/10.1029/96JB02581.

Thiele R. (1980). Hoja Santiago. Carta Geológica de Chile No. 39, Instituto de Investigaciones Geológicas, 21 p., 1 mapa. Santiago.

Thomas, H. (1958). Geología de la Cordillera de la Costa entre el Valle de La Ligua y la Cuesta de Barriga, Instituto de Investigaciones Geológicas, Boletín, 2, 1-86.

Tormey, D. (1989) Geology and Chemistry of the Active Azufre-Planchón-Peteroa Volcanic omplex 35º 15' S, Southern Andes : Implications for cordilleran Arc magmatism. Tesis para optar al grado de Doctor (inédita), Instituto Tecnológico de Massachusetts, Massachusetts, Estados Unidos, 331 p.

Tormey D., Frey F., y López-Escobar, L. (1989) Geologic history of the active Azufre-Planchón-Peteroa volcanic center 35º15' S, southern Andes), with implications for the development of compositional gas. Asociación Geológica Argentina, 44(1-4):420-430.

Tormey D.R., Hickey-Vargas R., Frey F.A. and López-Escobar L. (1991). Recent lavas from the Andean volcanic front (33 to 42°S): Interpretations of alongarc compositional variations, in Harmon, R.S., and Rapela, C.W., eds., Andean magmatism and its tectonic setting: Geological Society of America Special Paper 265, p. 57–78.

Tormey D.R., Frey F. and López-Escobar L. (1995). Geochemistry of the active Azufre-Planchón-Peteroa volcanic complex, Chile (35°15′S): Evidence for multiple sources and processes in a Cordilleran arc magmatic system: Journal of Petrology, v. 36, p. 265–298.

Tormey, D. (2010) Managing the effects of accelerated glacial melting on volcanic collapse and debris flows: Planchon-Peteroa volcano, southern Andes. Global Planetary Change, 74(2):82-90.

Uyeda, S., and H. Kanamori (1979), Back-arc opening and the mode of subduction, Journal of Geophysical Research, 84, 1049-1062.

Wall, R., P. Gana, and A. Gutiérrez (1996). Geología de la Hoja Santiago, área de San Antonio-Melipilla, regiones de Valparaíso, Metropolitana y del Libertador General Bernardo O'Higgins, Servicio Nacional de Geología y Minería, Mapas Geológicos, 2.

Yáñez, G., C. R. Ranero, R. Von Huene, and J. Díaz (2001), Magnetic anomaly interpretation across the southern central Andes (32°-34°S): The role of the Juan Fernández Ridge in the late Tertiary evolution of the margin, Journal of Geophysical Research B: Solid Earth, 106(B4), 6325-6345.

Yáñez, G., J. Cembrano, M. Pardo, C. Ranero, and D. Selles (2002), The Challenger-Juan Fernández-Maipo major tectonic transition of the Nazca-Andean subduction system at 33-34°S: Geodynamic evidence and implications, J S Am Earth Sci, 15(1), 23-38.

Völker D., Geersen J. M., Contreras-Reyes E., Reichert C. (2013) Sedimentary fill of the Chile Trench (32–46°S): volumetric distribution and causal factors Journal of the Geological Society London, 170 . pp. 723-736. DOI 10.1144/jgs2012-119.

Zamora, R., Uribe, J., Casassa, G., Potocki, M., Grigholm, B., Mayewski, P., Kurbatov, A., Dixon, D. & Morrison, M. (2011). Radar surveys of ice thickness and snow stratigraphy at Tupungatito Glacier, a high altitude ice core site in the central Chilean Andes. WCRP OSC Climate Research in Service to Society, 24-28 October 2011, Denver, USA.

CAPÍTULO III

METODOLOGÍA DE MUESTREO Y ANÁLISIS

III.1 METODOLOGÍAS E INSTRUMENTAL DE MUESTREO

Debido a las características físicas y químicas de los fluidos termales naturalmente emitidos en superficie, los métodos de muestro se dividen en dos grandes grupos dependiendo si se utiliza para la toma de muestras **líquidas** o **gaseosas**. Las metodologías empleadas para el muestreo de la fase gaseosa también varían según las características fisicoquímicas de la manifestación, del tipo de manifestación termal y de la especie e isótopo que se desea analizar. En cambio, las metodologías empleadas en el muestreo de la fase líquida son uniformes a todos los tipos de manifestaciones, sólo presentando variaciones en la recolección y almacenamiento dependiendo de las especies e isótopos que se desean analizar. A continuación, se describen en detalle las técnicas de muestreo de gases y líquidos, las cuales han sido previamente reportadas por *Montegrossi et al. (2001), Tassi (2004), Vaselli et al. (2006)* y *Tassi et al. (2012).*

III.1.1 Muestreo de las emisiones gaseosas

III.1.1.1 Ampollas de muestreo

El muestreo de la fase gaseosa realizado desde emisiones fumarólicas, piscinas burbujeantes, y de aguas termales (es decir gases disueltos en el agua) requiere el empleo de ampollas de vidrio borosilicatado (ej. Pyrex, DURAN, Kimax; Figura III-1a, b y c) evacuadas al vacío, en donde el gas de la manifestación termal será colectado para su posterior análisis. Las ampollas pueden o no contener una solución alcalina sintética según sea el tipo de manifestación a muestrear y las especies e isótopos que se desean analizar. Además de las ampollas, se utilizan frascos al vacío donde el gas es muestreado para el análisis de hidrocarburos (ej. *vacutainer*; Figura III-1d, *Capecchiacci 2012*) y botellas opacas de 50 ml para almacenar los condensados fumarólicos.

La principal ampolla de muestreo utilizada en este estudio tiene un volumen de 60-80 ml y posee una válvula de alto vacío (ej. Figura III-1a, Thorio o Rotaflo; *Giggenbach 1975*). A esta ampolla se le agrega, previo al muestreo, 30 ml de una solución alcalina sintética compuesta por 4N NaOH + 0.15N $Cd(OH)_2$, lo que permite atrapar los gases condensables y ácidos tales como el H_2O, CO_2, HCl, HF, HBr, H_3BO_3 y especies de S, y separarlos así de los gases no-reactivos que residen en el espacio libre de la ampolla (ej. N_2, H_2, O_2, He, Ar, Ne, CO, CH_4, hidrocarburos C_2-C_7).

Las principales especies gaseosas reactivas sufren los siguientes cambios químicos al entrar en contacto con la solución alcalina dentro de la ampolla de muestreo:

$$CO_{2(g)} + 2OH^-_{(aq)} = {CO_3}^{-2}_{(aq)} + H_2O \quad \text{(III.1)}$$

$$4SO_{2(g)} + 7OH^-_{(aq)} = 3{SO_4}^{-2}_{(aq)} + HS^-_{(aq)} + H_2O \quad \text{(III.2)}$$

$$HCl_{(g)} + OH^-_{(aq)} = Cl^-_{(aq)} + H_2O \quad \text{(III.3)}$$

$$HF_{(g)} + OH^-_{(aq)} = F^-_{(aq)} + H_2O \quad \text{(III.4)}$$

Debido a que la solución alcalina se compone de hidróxido de Cd y de Na, es posible separar las dos principales especies de S en los gases (H_2S y SO_2). Es así como el H_2S reaccionará preferentemente con el $Cd(OH)_2$, formando un sólido de color amarillo (CdS), el cual permanecerá insoluble en la solución de hidróxido de sodio. La reacción que da lugar a la separación del H_2S como fase sólida es la siguiente:

$$Cd(OH)_2 + H_2S = CdS + 2H_2O \quad \text{(III.5)}$$

En cambio, la especie SO_2 reaccionará con el NaOH, permaneciendo en solución en la forma de SO_3^{-2}, SO_4^{-2} y S^0 (reacción III.2). La separación de las especies sulfuradas es necesaria, ya que ambas especies reaccionan entre sí cambiando tanto sus concentraciones como el estado redox del sistema dentro de la ampolla (*Montegrossi et al. 2001*).

Para el análisis isotópico de $^3He/^4He$ y $^{40}Ar/^{36}Ar$ de la muestra gaseosa, solo se requiere que los gases ácidos sean retenidos en la solución alcalina, así los gases inertes puedan enriquecerse en la porción vacía de la ampolla. Por este motivo la solución alcalina de la ampolla empleada para el análisis isotópico de He y Ar no necesariamente debe contener $Cd(OH)_2$, ya que la sola presencia de NaOH cumple con la función de separar los gases solubles de los insolubles.

Para el análisis isotópico de $\delta^{13}C\text{-}CO_2$ y el muestreo de gases disueltos en agua (Figura III-1b y 1c, respectivamente), es necesario que el muestreo de gas sea realizado con ampollas al vacío sin solución alguna en su interior y con un volumen de 30 y 1000 ml, respectivamente.

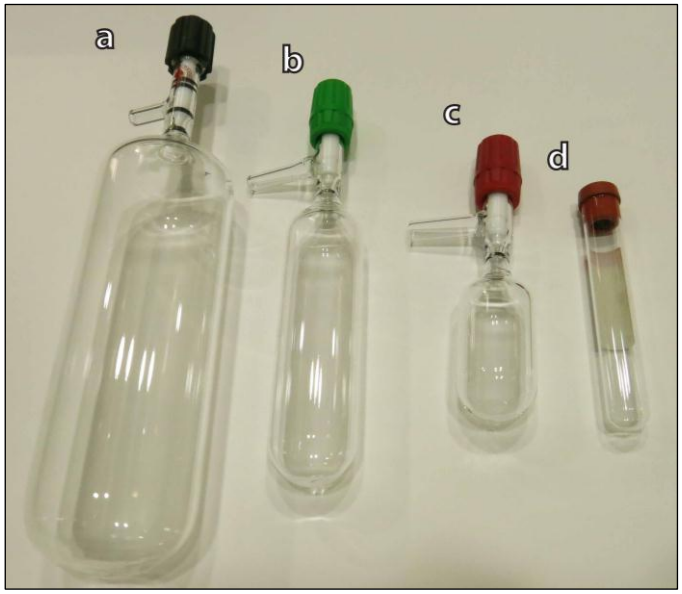

Figura III-1: Ampollas para el muestreo de gases. a) Ampolla para el muestreo de gases disueltos. b) Ampolla para el determinación de la composición química total, y composición isotópica de He y Ar. c) Ampolla para el muestreo de la composición isotópica de C en CO_2. d) *Vacutainer* para el muestreo de hidrocarburos C_2-C_7.

III.1.1.2 Preparación de la solución alcalina

La solución alcalina utilizada en el muestreo está compuesta por una concentración de 4N NaOH + 0.15N $Cd(OH)_2$.

La preparación de la solución 4N NaOH requiere de 160 gr de NaOH que se disuelven en 200 ml de agua destilada de alta pureza (Ultra High Quality, UHQ) sobre un plato caliente (~200°C). La disolución toma alrededor de 2,5 hr, y se debe agitar cada 30 minutos. Una vez disuelto el NaOH, se debe agregar agua UHQ hasta completar 1 litro de solución.

La preparación de la solución 0.15N $Cd(OH)_2$, requiere de 64.87 gr de Cd metálico, los cuales se disponen en una matraz de 500 ml junto con 100 ml de agua UHQ y 100 ml de ácido perclórico ($HClO_4$ al 70%). Esta solución se deja sobre un plato caliente (~200°C) por 2,5 hr, tiempo que toma la disolución del Cd metálico. Este proceso debe ser controlado cada 20 minutos, donde se debe revolver y agregar agua UHQ si la evaporación de la solución es importante. Una vez que el Cd metálico esté disuelto debe ser transferido a un matraz de 1000 ml, y se le debe agregar agua UHQ hasta alcanzar los 500 ml. A esta solución se le vierte NaOH hasta alcanzar un pH~14. Este paso es sumamente delicado, ya que los 500 ml de solución son extremadamente ácidos, por lo que la adición de NaOH puede ser explosiva.

Una vez que se alcanza el pH adecuado (~14), todo el Cd metálico debiese encontrarse como $Cd(OH)_2$, el cual es inmiscible en la solución restante de H_2O+NaOH+NaCl. Su separación desde la solución requiere de centrifugado en tres etapas. Cada paso de centrifugado se realiza a 4000 rpm por 30 minutos. Una vez separado, todo el $Cd(OH)_2$ es vertido en un vaso de precipitado de 1 litro junto con la solución de 4N NaOH. Esta nueva solución se dispone sobre un plato caliente (~200°C) hasta que todo el $Cd(OH)_2$ esté disuelto.

III.1.1.3 Incorporación de la solución alcalina a las ampollas

El proceso de carga de las ampollas consiste en someter a la ampolla a un vacío parcial, lo que permite a cada ampolla succionar la solución alcalina. Una vez que la solución alcalina es introducida, la ampolla es sometida a vacío por unos 10 a 20 minutos, mediante el uso de una bomba de vacío de rotación con una capacidad de 3 litros como mínimo (Figura III-2). Las bajas presiones dentro de la ampolla, posterior al vaciado, son indicadas por el característico sonido similar a partículas sólidas dentro de la ampolla al ser esta agitada. Terminado el proceso de vacío, la boquilla libre de la ampolla es llenada con agua destilada de alta pureza. La ampolla debe ser pesada con una balanza de 0,01 gr de precisión y finalmente la boquilla debe ser sellada con *Parafilm*. La inserción de agua y el sellado de la boquilla evitan el ingreso de aire dentro de la ampolla.

III.1.1.4 Utilización de las ampollas en el muestreo

En el proceso de muestreo, la ampolla es conectada al extremo final de la línea de muestreo mediante un tubo de silicona. El ingreso de gas a la ampolla es controlado por la apertura de la válvula de alto vacío. Durante el muestreo, la ampolla debe estar en posición vertical, con la válvula de alto vacío mirando hacia abajo, así se logra chequear que el gas está ingresando a la ampolla mediante el burbujeo generado en la solución alcalina. El volumen de gases que pueden ser muestreados está limitado por: (i) el consumo total de la solución alcalina, frecuente en soluciones gaseosas ricas en especies ácidas, (ii) la finalización del vacío, frecuente en fluidos ricos en gases no reactivos, (iii) el consumo del espacio vacío, frecuente en fluidos ricos en vapor de agua (*Marini 2000*). Inmediatamente finalizado el muestreo, la boquilla debe ser nuevamente rellenada con agua UHQ, y sellada con *Parafilm*. Finalmente, la muestra debe ser rotulada con código, fecha de muestreo y la temperatura de la emisión. Existen ocasiones donde la solución alcalina puede comenzar a ebullir dada la temperatura del gas muestreado. En estos casos, la presión dentro de la ampolla aumenta considerablemente, acabando con el vacío parcial de la ampolla. Para minimizar este efecto, la ampolla debe ser envuelta en

papel húmedo, manteniendo la temperatura de la ampolla bajo el punto de ebullición (*Marini 2000*).

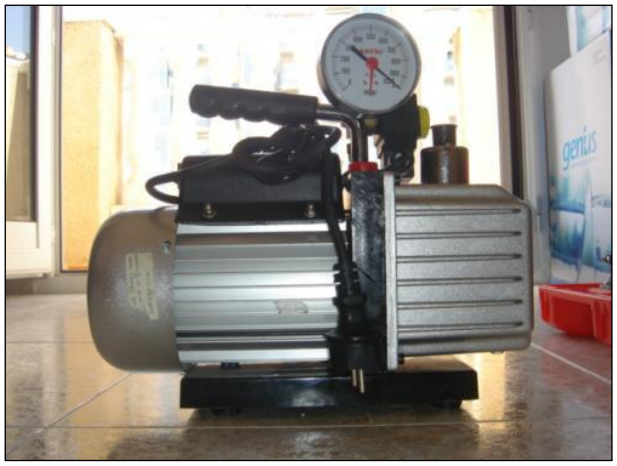

Figura III-2: Bomba de vacío para la preparación de las ampollas de muestreo de gases.

El muestreo con la ampolla para determinación de isótopos de carbono se realiza de la misma manera explicada anteriormente. Sin embargo, el tiempo de muestreo es mucho menor ya que esta ampolla no contiene solución alcalina, por lo que el vacío de la ampolla se completa por la totalidad de los gases sean éstos insolubles y/o solubles.

El proceso de muestreo de gases disueltos comienza cuando se sumerge la ampolla de 1000 ml bajo el agua en la manifestación termal. Una vez que la gran mayoría de las burbujas generadas por el ingreso de la ampolla bajo el agua desaparecen, se procede a abrir la válvula de alto vacío, permitiendo el ingreso de agua hasta completar los ¾ de la ampolla (750 ml). El ingreso de agua a la ampolla genera que los gases disueltos se exsuelvan, quedándose en el espacio sin agua de la ampolla. Para minimizar los efectos de la contaminación atmosférica, la ampolla debe sumergirse en las zonas más profundas del manantial que se quiere muestrear.

Posterior al muestreo, las ampollas deben ser nuevamente pesadas sin el Parafilm y sin el agua UHQ en la boquilla de la ampolla. De esta manera, la diferencia entre la masa pre y post muestreo, entregará la cantidad de gas recolectado.

III.1.1.5 Captura de gases desde las manifestaciones termales

Un punto clave del proceso de muestreo es el encausamiento del flujo gaseoso emanado desde las diferentes manifestaciones termales hacia las ampollas. Existen diferentes metodologías que involucran distintos tipos de líneas de muestreo que se utilizarán dependiendo principalmente del tipo de manifestación y del flujo de gas emitido por ésta.

III.1.1.5.1 Fumarolas de alta temperatura

En el caso de fumarolas de alta temperatura y/o altos flujos de emisión, se inserta un tubo de titanio en el punto de emisión, el cual dirige el flujo gaseoso desde la fumarola hacia el extremo del tubo (Figura III-3). Este flujo gaseoso es redirigido hacia la ampolla mediante una extensión de vidrio borosilicatado, la cual está conectada al tubo de titanio mediante un anillo de teflón (Figura III-3)

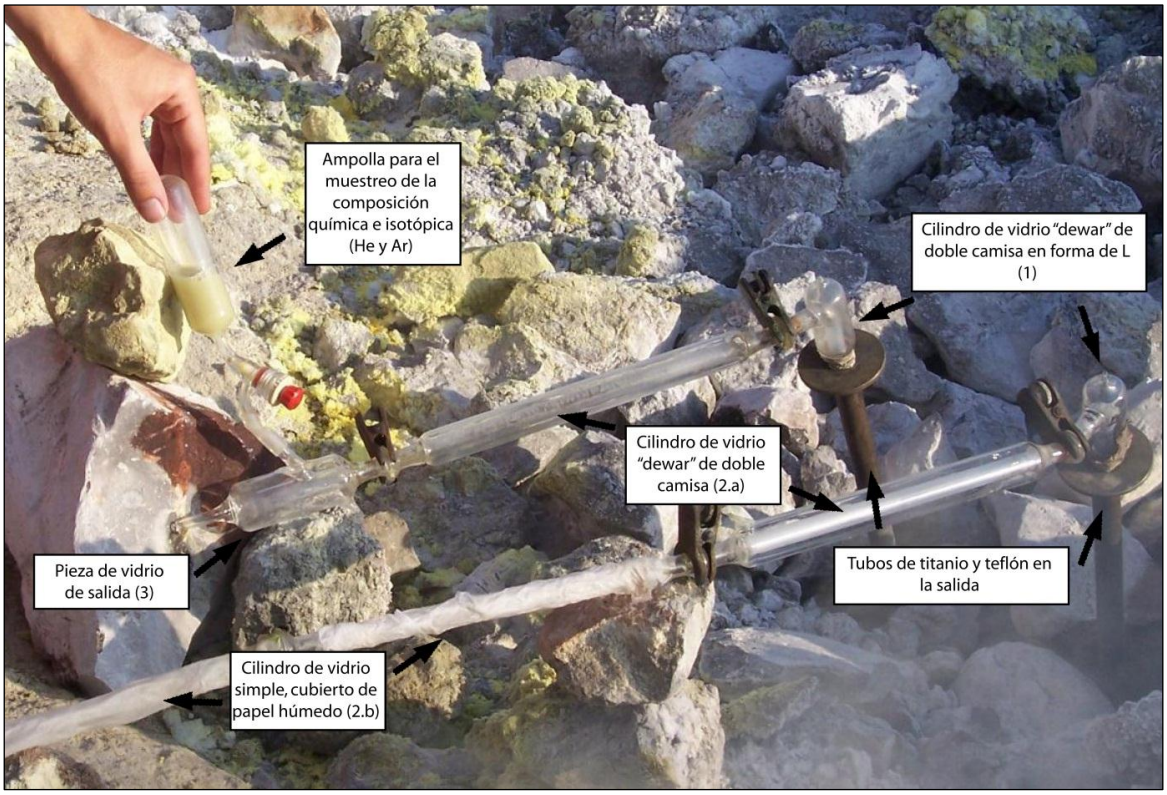

Figura III-3: Tubos de titanio y de Pyrex. En la figura se precisan las diferentes partes de la línea de muestreo.

La utilización del tubo de titanio se debe a que a temperaturas <600°C, el titanio no reacciona con el fluido emitido por las fumarolas, por lo que no altera las características químicas e isotópicas del fluido. En el caso de fumarolas con temperaturas >600°C, el titanio se vuelve reactivo según la siguiente reacción (*Symmonds et al. 1994*):

$$Ti_{(s)} + 2H_2O = TiO_{2(S)} + 2H_2 \qquad \text{(III.6)}$$

por lo que se recomienda utilizar un tubo de cuarzo o de cualquier material que sea altamente refractario a dichas temperaturas (ej. mullita).

El anillo de teflón se utiliza por tres razones. Debido a que el teflón es un material auto-lubricante, permite rotar de manera segura la línea de vidrio durante el muestreo. Por otro lado, la forma del anillo evita tanto el ingreso de aire dentro del tubo

de titanio (contaminación de la muestra) como el rompimiento de la línea de vidrio durante el muestreo, esto último, debido a la expansión repentina del vidrio por calentamiento.

La extensión de vidrio borosilicatado está compuesta por 4 piezas, las cuales se pueden conectar entre sí mediante pinzas metálicas dependiendo del tipo de muestra que se quiere tomar (Figura III-3):

1) La pieza que va inserta directamente en el anillo de teflón corresponde a un cilindro de vidrio "*dewar*" de doble camisa en forma de "L". Estas dos camisas se encuentran separadas entre sí por un espacio vacío. Esta se utiliza debido a que el espacio vacío evita cambios bruscos en la temperatura, por lo tanto impide cambios físicos (condensación de vapor de agua), químicos (cambios redox) e isotópicos (intercambio de ^{18}O entre CO_2-H_2O) en el gas.
2) En la parte del medio de la línea de muestreo existen dos diferente piezas que pueden ser conectadas dependiendo del tipo de muestra que quiere ser tomada:
   a) Para muestras donde se desea analizar la composición química completa y la composición isotópica de He y Ar, el tubo indicado corresponde a un cilindro de vidrio "dewar" de doble camisa, el que cumple con el mismo principio que el punto 1.
   b) Para muestras donde se requiere la separación de la fase líquida y gaseosa (ej. análisis isotópico de $\delta^{18}O$- y δD-H_2O, y $\delta^{13}C$-CO_2), es necesaria la utilización de un cilindro de vidrio simple, el cual es revestido con papel húmedo para causar un fuerte descenso de la temperatura, y gatillar así la condensación del gas. Dependiendo del flujo y temperatura del gas emanado por la fumarola, es necesario conectar 2 o más tubos simples de manera secuencial, lo que aumenta la tasa de condensación. En caso de fumarolas con alto flujo y alta temperatura es recomendable utilizar el condensador de vidrio. Esta pieza consiste en un tubo de vidrio de unos 10 cm de diámetro que se une a la línea de muestreo y que contiene otra cámara interior de vidrio en forma de serpentín. El serpentín acelera la condensación del gas, que comienza a caer por goteo en una de las dos salidas con las que cuenta. El condensador viene acondicionado con varias boquillas, que permiten conectarle un sistema de circulación de agua fría por el espacio entre las dos cámaras de vidrio.
3) En la parte final de la línea de muestreo, se inserta una pieza de vidrio con doble salida, con el objetivo de obtener un flujo de salida óptimo. La forma particular de este objeto de vidrio impide que el gas al interior del mismo genere vórtices y

reflujos de gas, los que pueden causar fenómenos de condensación del gas o aspiración de aire externo. En la salida diagonal de este objeto es conectada la ampolla de muestreo, mediante un tubo de silicona. En esta salida también se conecta la jeringa mediante un tubo de silicona, la cual es llenada y luego evacuada en el *vacutainer* mediante la utilización de una aguja, mientras que desde la salida horizontal de este objeto se recolecta el líquido correspondiente al condensado del gas, el cual se debe se almacenar en botellas oscuras de ámbar de 50 ml.

Finalmente, al terminar el muestro se debe retirar la extensión de vidrio borosilicatado y proceder a medir la temperatura de muestreo insertando una termocupla en el anillo de teflón.

III.1.1.5.2 Fumarolas con bajo flujo de emisión

En el caso de fumarolas que presentan bajos flujos de emisión, el método más adecuado para acumular y redirigir el gas es mediante el empleo de embudos plásticos y tubos de silicona (Figura III-4).

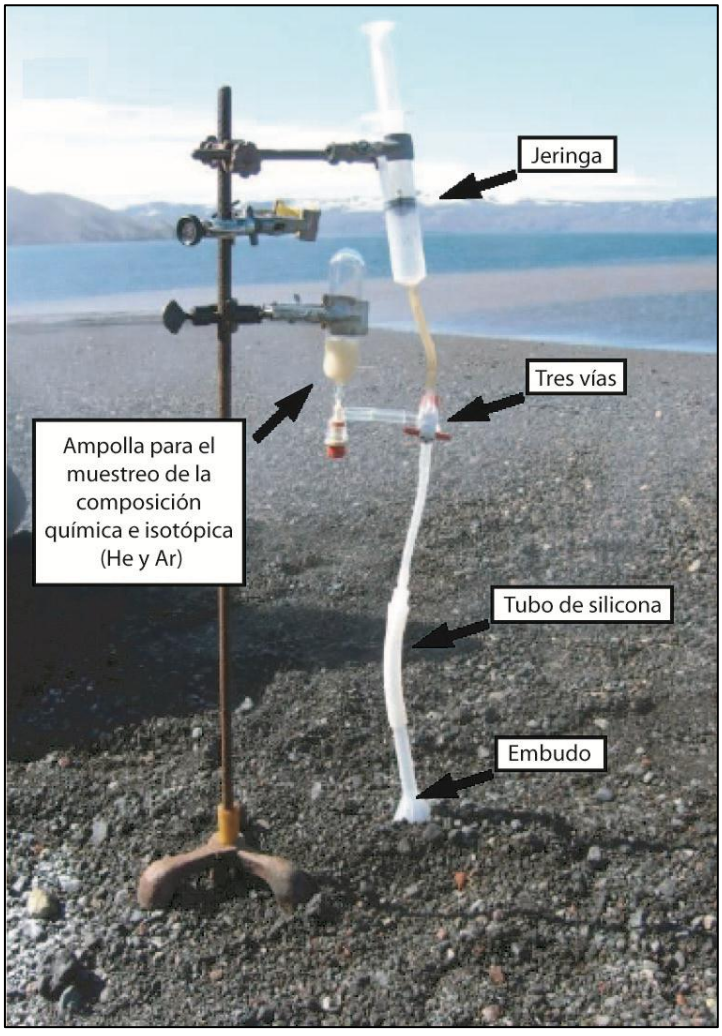

Figura III-4: Línea embudo y tubo de silicona para el muestreo de fumarolas de bajo flujo. En la figura se precisa las diferentes partes de la línea de muestreo.

Una vez identificado el sitio de emisión, se realiza un orificio donde el embudo pueda ser insertado. La boca más grande del embudo debe ser enterrada en el orificio y cubierta con tierra húmeda o lodo de los alrededores, evitando que aire entre al embudo. Previo al muestreo, se debe verificar que exista una cantidad de gas suficiente para muestrear. Para esto se conecta una llave tres vías de teflón en el extremo de salida de la manguera de silicona (Figura III-4). De las dos boquillas libres de dicha válvula una se conecta a la jeringa y la otra se deja libre (Figura III-4). Durante la extracción de gas del sistema (llenado de la jeringa), la válvula de tres vías debe impedir la salida/entrada de gas/aire por la boquilla libre, mientras que durante la expulsión de gas del sistema (vaciado de la jeringa) la válvula de tres vías debe impedir la salida/entrada de gas/aire por la boquilla conectada al embudo por medio de la manguera de silicona. El llenado y vaciado de la jeringa se debe realizar 5 veces, eliminando así todo rastro de aire contenido en el sistema. Una vez realizado ´lo anterior, se procede a la inserción de la(s) ampolla(s) de muestreo (químico e isotópico) por la salida horizontal de la válvula de tres vías (boquilla libre; Figura III-4). El gas acumulado en la jeringa es transferido al *vacutainer* mediante el uso de una aguja.

Para la extracción de condensado fumarólico en este tipo de muestreo, se utiliza un serpentín de vidrio o titanio conectado al extremo de salida del tubo silicona (Figura III-4b). En este caso, para la realización de la operación de condensación se coloca el serpentín en un recipiente con agua y hielo, y se conecta al orificio de salida del serpentín una jeringa para realizar vacío y favorecer el flujo de gas en el sistema. Luego, de la misma forma que con el muestreo anterior, la fracción de condensado destinada para la realización de análisis isotópicos se recolecta en un recipiente de vidrio oscuro. Finalmente, al terminar el muestro se debe retirar el embudo y medir la temperatura del sitio de muestreo.

III.1.1.5.3 Muestreo de gases en piscinas burbujeantes

El muestreo en este tipo de sitios se realiza empleando el mismo sistema de acumulación y redireccionamiento utilizado para el caso de las fumarolas de bajo flujo (Figura III-5). En estos sitios, el embudo plástico debe ser colocado sobre la zona de emisión de las burbujas, de modo tal que la boca de mayor diámetro del embudo capture la mayor parte de las burbujas. En la boca de menor diámetro se conecta el tubo de silicona, el cual redirige el flujo de gas hacia la ampolla. Es muy importante que al inicio del muestreo el embudo sea inmerso completamente en el líquido, asegurándose así de evitar la contaminación atmosférica. Una vez que el embudo está repleto de gas, debe ser liberado a través del tubo de silicona, de manera de prevenir

la contaminación de aire que pueda estar en los tubos. Para esto se conecta una llave de tres vías de teflón en el extremo de salida de la manguera de silicona, y mediante el uso de una jeringa se facilita el ingreso de gas al sistema. Este procedimiento se debe realizar 5 veces, para así eliminar todo rastro de aire contenido en el sistema. Una vez realizado, se procede a la inserción de la(s) ampolla(s) de muestreo, por la salida horizontal de la llave de tres vías. El gas acumulado en la jeringa es trasvasijado al *vacutainer* mediante el uso de una aguja.

Para evitar cualquier tipo de contaminación con aire durante el muestreo es necesario que el embudo siempre se mantenga sumergido y boca abajo. Para ello, y si es posible, previo al muestreo se debe apoyar el embudo en la superficie de donde proviene el burbujeo, y luego por medio de la utilización de rocas, se cubre el embudo hasta que éste quede estable. En casos donde el fondo de la piscina burbujeante esté a mayores profundidades, se puede sostener el embudo de manera manual, o mediante la utilización de varas que permitan sostenerlo a larga distancia. Esto último resulta muy útil en piscinas burbujeantes y/o piscinas de barro donde la temperatura del agua es cercana al punto de ebullición.

Finalmente, al terminar el muestro, se debe retirar el embudo y medir la temperatura en la superficie donde salen las burbujas o en algún lugar cercano a éste.

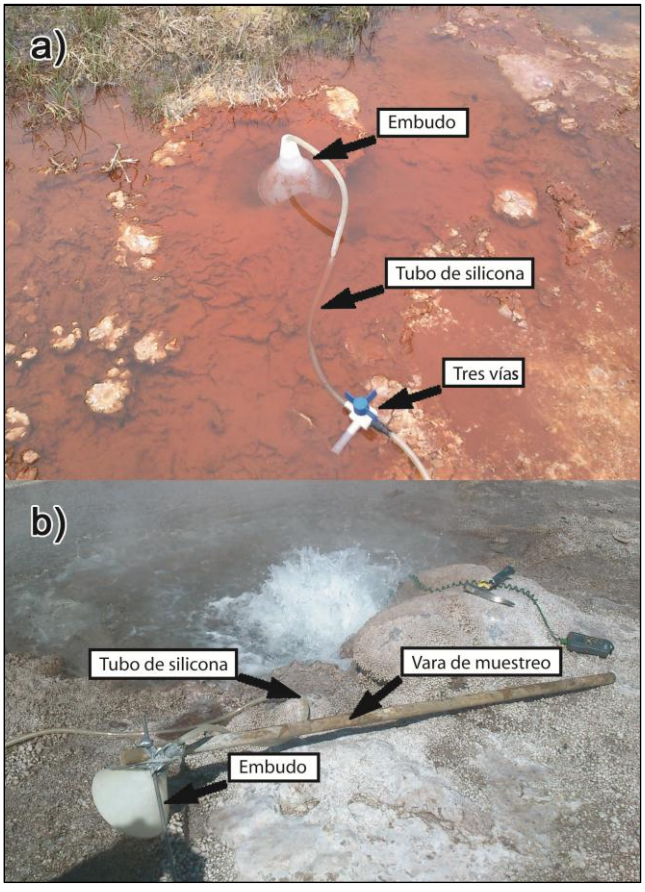

Figura III-5: Línea con embudo y tubo de silicona para el muestreo de gases emitidos en piscinas burbujeantes. Figura a) muestra el embudo apoyado en la superficie de donde proviene el burbujeo, mientras que en la figura b) se muestra el embudo sostenido con la vara de muestreo.

III.1.2 Muestreo de las emisiones líquidas

La técnica de muestreo de aguas es la misma para todos los sitios, no importando el tipo de emisión (ej. piscinas de barro, piscinas burbujeantes, manantiales calientes, manantiales fríos, ríos, arroyos).

Luego de elegir el sitio idóneo para el muestreo (ej. la manifestación termal de mayor temperatura, y la que presenta menor contacto con el suelo y/o con otra fuente de agua) se procede a la medición de:

- Temperatura (°C), mediante el uso de una termocupla digital con resolución de 0.1°C.
- pH, mediante un phímetro digital con resolución 0.01.
- Conductividad eléctrica (µS/cm), la cual es proporcional al contenido total de sólidos disueltos. Esta se mide mediante una sonda multiparámetro con resolución 0.01 µS/cm.
- Alcalinidad, mediante titulación acidimétrica con solución de HCl e indicadores de fenoftaleína (alcalinidad de fenoftaleína) y bromofenol azul (alcalinidad total) así se puede obtener la concentración de CO_3^{-2} y HCO_3^- utilizando el test de alcalinidad.
- Sílice (SiO_2), mediante espectrofotometría con un medidor portátil de radiación UV.

Una vez medidos los parámetros anteriormente mencionados se procede a la toma de la muestra. Para la toma de una muestra líquida representativa, se recomienda que la jeringa plástica a utilizar en la extracción del agua sea ambientada al menos 3 veces. Las botellas varían de acuerdo al tipo de análisis a realizar posteriormente, por lo cual, por cada sitio muestreado deben ser obtenidas 4 muestras, las que corresponden a (Figura III-6):

a) Botella plástica de 100 a 200 ml con tapa y contratapa para el análisis de aniones (HCO_3^-, SO_4^{-2}, Cl^-, NO_3^-, F^-, Br^-). El agua muestreada debe ser filtrada con un filtro de 0.45 µm previo llenado de la botella.
b) Botella plástica de 100 a 200 ml con tapa y contratapa para el análisis de cationes (Na^+, K^+, Ca^{+2}, Mg^{+2}, NH_4^+, Li^+). El agua muestreada debe ser filtrada con un filtro de 0.45 µm previo llenado de la botella. Si el agua muestreada tiene un pH>2 la botella debe ser acidificada con 0,5 ml de HCl (4%).
c) Botella plástica de 100 a 200 ml con tapa y contratapa para el análisis de metales trazas (Al, Sb, As, Ba, B, Cs, Fe, Hg, Mn, Rb, Sr). El agua muestreada debe ser

filtrada con un filtro de 0.45 µm previo llenado de la botella. Si el agua muestreada tiene un pH>2 la botella debe ser acidificada con 1 ml de HNO_3 (67%).

d) Botella de vidrio opaco de 50 ml para el análisis de $^{2}H/^{1}H$ y $^{18}O/^{16}O$. La utilización de vidrio opaco es para evitar fraccionamiento isotópico producto de la exposición a la luz ambiente.

La acidificación de las botellas correspondientes al muestreo de cationes y metales traza tiene por objetivo evitar la precipitación de éstos, debido a una posible saturación una vez el agua se enfríe en la botella. Debido a que el agua está filtrada, la acidificación no debería disolver ningún material suspendido en el agua.

Durante el muestreo es de suma importancia que todas las botellas sean llenadas a su máxima capacidad, evitando dejar burbujas atrapadas una vez cerradas las botellas. Esto se hace ya que cualquier espacio libre en la botella puede producir fraccionamiento de isótopos de O y H, variación en el contenido de HCO_3^- por exsolución de CO_2, y variaciones en las concentraciones absolutas de los cationes y metales traza por evaporación de agua. Una vez realizado el muestreo, las botellas son rotuladas con los datos de T, pH y conductividad eléctrica.

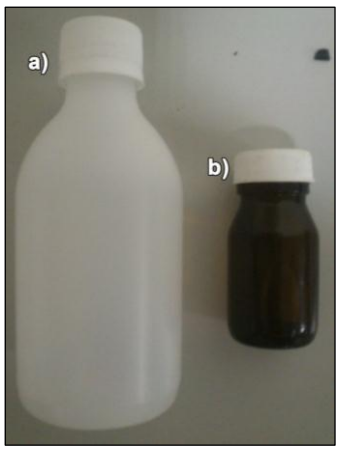

Figura III-6: a) Botellas para el muestreo de cationes, aniones y metales trazas. b) Botellas para el análisis de isotopos estables de aguas y condensados fumarólicos.

III.2 METODOLOGÍAS E INSTRUMENTAL DE ANÁLISIS EN LABORATORIO

El análisis de la composición química de los gases y líquidos de las muestras líquidas y gaseosas, junto con el análisis isotópico de $C\text{-}CO_2$ ($^{13}C/^{12}C$) de éstas, fueron realizados en la Universidad de Florencia, Italia (*Montegrossi et al. 2001; Vaselli et al. 2006; Tassi et al. 2012*). La composición isotópica de He ($^{3}He/^{4}He$) y Ar ($^{40}Ar/^{36}Ar$) en la fase gaseosa se realizaron en la Universidad de Rochester, NY, EEUU (*Poreda y Farley 1992).* Finalmente, los isótopos de O ($^{18}O/^{16}O$) y H ($^{2}H/^{1}H$) en la fase líquida

(H_2O) fueron realizados en los laboratorios *Geokarst Engineering Laboratory*, Trieste, Italia.

III.2.1 Análisis de las emisiones gaseosas

Debido a que la toma de muestras de gases involucra el análisis de hasta tres fases en las ampollas (gases insolubles, gases retenidos por la solución alcalina y gases que precipitan como $CdS_{(s)}$) además del líquido condensado y almacenado en las botellas de vidrio opaco, es necesario un protocolo riguroso y secuencial de extracción y análisis para evitar cualquier alteración de la muestra.

El primer paso corresponde a la extracción y análisis de los gases no solubles que se encuentran en el espacio vacío de la ampolla (III.2.1.1). Una vez finalizada esta etapa, se procede a la extracción y separación de las fases líquida y sólida para determinar los compuestos gaseosos retenidos en ellas (III.2.1.2). La Tabla III-1 muestra un resumen de las técnicas utilizadas para la determinación de los componentes analizados en este trabajo.

III.2.1.1 Análisis de la fase gaseosa de las ampollas y *vacutainer*

La determinación de la composición química e isotópica de la fase gaseosa de las ampollas se realiza por medio de Cromatografía Gaseosa. La conexión de la ampolla a los diferentes cromatógrafos se realizó mediante una manguera de alto vacío que conecta la ampolla a una válvula de seis vías (*six-port valve*; Figura III-7a). El resto de las vías de la válvula están conectadas a la bomba de vacío, a los cromatógrafos de gases y a un vacuómetro. La conexión a los cromatógrafos de gases está implementada mediante un tubo helicoidal de acero inoxidable de 0,5 mm, mientras que la conexión a la bomba de vacío se realiza mediante una manguera de alto vacío (Figura III-7a). Debido a que los diferentes detectores del cromatógrafo se pueden saturar respecto a un cierto compuesto, se procedió a regular la presión de gas previa a la inyección de la muestra al equipo. Esto se realizó mediante la regulación de la apertura de la válvula de alto vacío de las ampollas. Para cada análisis se registró la presión a la que el gas fue inyectado.

Los análisis se realizaron mediante las siguientes técnicas:

- El análisis de H_2 (<5000 ppm vol), He y Ne mediante Cromatografía Gaseosa con detector de conductividad térmica (TCD, *Thermical Conductivity Detector;* Shimadzu 15a) y Ar como gas portador (flujo de 20-30 ml/min). Se emplearon las siguientes condiciones analíticas: $T_{columna}$ = 30ºC, $T_{inyección}$ = 80ºC, $T_{detector}$ = 50°C

- El análisis de H_2 (>5000 ppm vol), O_2 + Ar, N_2, CH_4 (>1000 ppm vol), CO (>350 ppm vol), mediante Cromatografía Gaseosa con detector de conductividad térmica (Shimadzu 15a) y He como gas portador (flujo de 20-30 ml/min). Se emplearon las siguientes condiciones analíticas: $T_{columna}$ = 70ºC, $T_{inyección}$ = 100ºC, $T_{detector}$ = 100°C.
- El análisis de O_2 y Ar mediante Cromatografía Gaseosa con detector de conductividad térmica (Shimadzu 15a) y He como gas portador (flujo de 20-30 ml/min). Se emplearon las siguientes condiciones analíticas: $T_{columna}$ = 0ºC, $T_{inyección}$ = 40ºC, $T_{detector}$ = 50°C
- El análisis de los hidrocarburos C_1 (<1000 ppm vol) a C_5 mediante Cromatografía Gaseosa con detector de ionización de llamas (FID, *Flame Ionization Detector;* Shimadzu 14) y He como gas portador. Se emplearon las siguientes condiciones analíticas: $T_{columna}$ = 50ºC, $T_{inyección}$ = 80ºC, $T_{detector}$ = 90°C.
- El análisis de los hidrocarburos C_5 a C_{10} mediante Cromatografía Gaseosa con detector de ionización de llamas (Shimadzu 15a) y He como gas portador. Se emplearon las siguientes condiciones analíticas: $T_{columna}$ = 30ºC, $T_{inyección}$ = 90ºC, $T_{detector}$ = 90°C
- Análisis del CO (<350 ppm vol) mediante Cromatografía Gaseosa con detector de ionización de llamas (Shimadzu 15a), metanizador (Shimadzu MTN-1) e H_2 como gas portador. Se emplearon las siguientes condiciones analíticas: $T_{columna}$ = 30ºC, $T_{inyección}$ = 90ºC, $T_{detector}$ = 90°C.

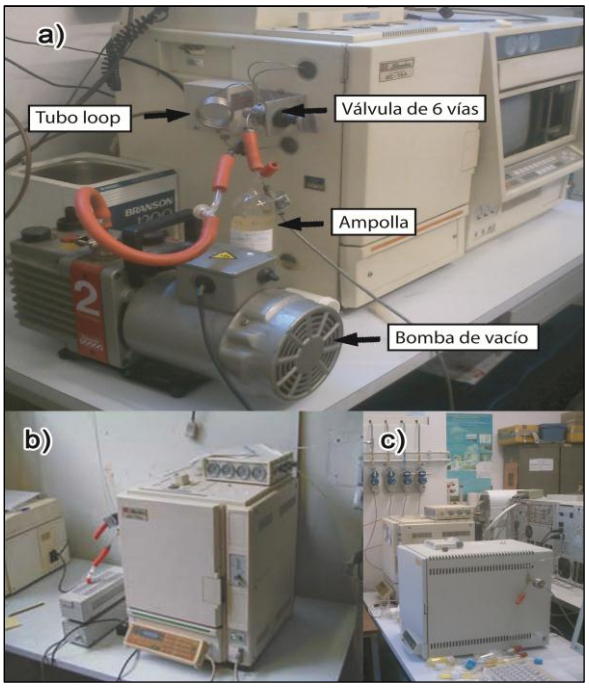

Figura III-7: a) Cromatógrafo gaseoso Shimadzu 15a. En la foto se explicitan los diferentes componentes para la extracción de los gases desde la ampolla. b) Cromatógrafo gaseoso Shimadzu 14a. c) Cromatógrafo gaseoso Carlo Erba 4200. Fotos tomadas en el Laboratorio de Geoquímica de Fluidos y Rocas de la Universidad de Florencia, Italia.

Tabla III-1: Tabla resumen de los métodos utilizados para el análisis químico de los gases (*Montegrossi et al. 2001; Tassi et al. 2004; Vaselli et al. 2006; Tassi et al. 2012*).

Especie	Técnica	Equipo	Nota	Error analítico
He, Ne, H_2 (<5000 ppm vol)	Cromatografía Gaseosa	Shimadzu 15a	Gas Carrier: Ar Detector: TCD Columna: Molecular Sieve (9 m de longitud, 80/100 de malla) Tiempos de retención para el He, Ne y H_2 corresponden a 2.74, 3.11 y 3.63 min, respectivamente	<5%
H_2 (>5000 ppm vol), O_2 + Ar, N_2, CH_4 (>1000 ppm vol), CO (>350 ppm vol)	Cromatografía Gaseosa	Shimadzu 15a	Gas Carrier: He Detector: TCD Columna: Molecular Sieve (9 m de longitud, 80/100 de malla) Tiempos de retención para el H_2, O_2+Ar, N_2, CH_4, CO corresponden a 3.24, 5.16, 7.24, 11.18 y 15.89 min, respectivamente	<5%
C_1-C_{10}	Cromatografía Gaseosa	Shimadzu 14	Gas Carrier: He Detector: FID Columna: Cromosorb 80/100 SP 1700 al 23% Tiempos de retención para los compuestos orgánicos listados en la Tabla III-2	<5%

Continuación de la Tabla III-1.

O_2, Ar	Cromatografía Gaseosa con implante criogénico de CO_2 líquido	Shimadzu 15a	Gas Carrier: He Detector: TCD Columna: Molecular Sieve (9 m de longitud, 80/100 de malla) Tiempos de retención para el O_2 y Ar corresponden a 8.52 y 9.41 min, respectivamente	<5%
C_1-C_{10}	Cromatografía Gaseosa	Shimadzu 14	Gas Carrier: He Detector: FID Columna: Cromosorb 80/100 SP 1700 al 23% Tiempos de retención para los compuestos orgánicos listados en la Tabla III.2	<5%
CO	Cromatografía Gaseosa con metanizador	Shimadzu 14 + Shimadzu MTN-1	Gas Carrier: H_2 Detector: FID Columna: Cromosorb 80/100 SP 1700 al 23% Columna del metanizador de CO: Molecular Sieve 5° y longitud de 5 m. T columna 400°C. Tiempos de retención para el CH_4 original y el derivado del CO corresponden a 7 y 15 min, respectivamente	<5%
SO_2, H_2S y S_8 como SO_4^{2-} HCl como Cl^- HF como F^-	Cromatografía Iónica	Metrohm 761	Eluente: solución de Na_2CO_3+$NaHCO_3$	<5%
CO_2	Titulación	Methrom 794	Titulación con 0.1N HCl	<10%
H_3BO_3	Colorimetría	-	Método Azometina-H	<3%

Tabla III-2: Especies orgánicas analizables y sus respectivos tiempos de retención.

Minuto	10% TCEP	Compuesto	Minuto	23% TCEP	Compuesto
0,4	C_1-C_4		3,15	Metano	CH_4
0,57	c-Pentano	C_5H_{10}	4,14	Etano	C_2H_6
0,705	i-Hexano	C_6H_{14}	4,5	Eteno	C_2H_4
0,78	n-Pentano/Pentadieno	C_5H_{12}/C_5H_8	6,03	Propano	C_3H_8
1,05	i-Heptano	C_7H_{16}	6,93	Propeno	C_3H_6
1,17	n-Hexano	C_6H_{14}	8,55	i-Butano	C_4H_{10}
1,25	i-Octano	C_8H_{18}	11,03	n-Butano	C_4H_{10}
1,64	Metilciclopenteno	C_6H_{10}	13	1-Buteno	C_4H_8
1,87	n-heptano	C_7H_{16}	13,19	i-Buteno	C_4H_8
2,29	Dimetilsulfuro	C_2H_6S	15,14	t-2-Buteno	C_4H_8
2,87	i-nonato	C_9H_20	17,08	c-2-Buteno	C_4H_8
3,14	n-octano	C_8H_{18}	18,6	i-Pentano	C_5H_{12}
4,89	n-nonano	C_9H_{20}	22,7	n-Pentano	C_5H_{12}
6,1	Furano	C_4H_4O	26,4	Penteno	C_5H_{10}
8,69	Benceno	C_6H_6	29,8	2.3	dimetilButano
14,22	Tiofeno	C_4H_4S	38,63	i-hexano	C_6H_{14}
17,67	Tolueno	C_7H_8	46,15	c-Pentano	C_5H_{10}
24,77	Metilfurano	C_5H_7O	49,8	n-hexano	C_6H_{14}
30,61	Metiltiofeno	C_5H_7S	71	i-heptano	C_7H_{16}
32,41	Etilbenceno	C_8H_{10}	95	c-hexano	C_6H_{12}
36,83	Mp-Xileno	C_8H_{10}			

III.2.1.2 Análisis de las fases líquida y sólida de la ampolla

Una vez finalizado el análisis de la fase gaseosa contenida en la ampolla, se procedió a la extracción de las fases líquida y sólida que se encuentran en la ampolla. Esto se hace mediante una bomba de agua, y transferidas mediante un sifón a una cápsula de teflón (tubo PTFE). La solución extraída se debe centrifugar a 4000 rpm durante 30 min, para así obtener una separación completa entre el líquido y el sólido.

III.2.1.2.1 Fase líquida

El líquido es llevado a 100 ml de volumen con la adición de agua UHQ, y es nuevamente centrifugado. La solución final es subdividida en dos partes: i) 25 ml para el análisis de las especies carbonatadas, haciendo de este modo referencia para la determinación del CO_2 presente en el gas, ii) 25 ml para el análisis del Cl^- para la determinación del HCl presente en el gas, y ii) 50 ml para el análisis del SO_4^{2-} para la determinación del SO_2 presente en el gas.

Los procedimientos a realizar en cada uno de estos son:

- El análisis de las especies carbonáticas se realiza mediante titulación acidimétrica (HCl 0,5M) utilizando un titulador automático Methrom 536. La especie carbonática predominante será el CO_3^{2-} debido a los altos valores de pH impuesto por la presencia de la soda. Una vez obtenida la concentración de CO_3^{2-} se puede recalcular pCO_2 en la fase gaseosa.
- El análisis del Cl^- en la solución es realizada mediante cromatografía iónica utilizando el dispositivo Metrom 761. Previo al análisis se le debe agregar 0.05 gr de H_3BO_3 a la solución. Esto tiene como objetivo de crear un efecto tampón que estabilice la solución a un pH cercano a 9,2, esto debido a que un pH excesivamente básico de la solución podría dañar la columna de separación del cromatógrafo.
- El análisis del SO_4^{2-} en la solución es realizada mediante cromatografía iónica (Metrohm 761). Previo al análisis se le debe agregar a los 50 ml de solución 0.05 gr de H_3BO_3 para aumentar el pH a un valor cercano a los 9.2, y 5 ml de H_2O_2 (30-33%) para oxidar todas la especies SO_x que podría estar presente en solución.

III.2.1.2.2 Fase sólida

A la fase sólida se le debe agregar 5 ml de H_2O_2 (30-33%), 0,25 gr de $NaOH_{(s)}$ y 5 ml de agua UHQ, de manera que el azufre del $CdS_{(s)}$, que se encuentra en forma de sulfuro, se transforme a sulfato y pueda solubilizarse. Con el fin de asegurar que todo el sulfuro ha sido oxidado se debe dejar el recipiente reaccionando durante tres días. Se aconseja agitar la solución periódicamente. Pasado los tres días, la solución debe ser llevada a 100 ml para luego ser centrifugada, así separar todos los sólidos residuales de la muestra (ej. $Cd(OH)_2$, S^0, algunas impurezas recolectadas durante el muestreo). El centrifugado se realiza a 4000 rpm durante 30 min. El análisis del SO_4^{2-} en la solución es realizada mediante cromatografía iónica (Metrohm 761). Previo al análisis se le debe agregar 0.05 gr de H_3BO_3 a la muestra para aumentar el pH a un valor cercano a los 9.2. De esta manera se puede determinar el contenido de H_2S en el gas.

Para analizar el S^0, éste debe ser separado de los demás residuos sólidos. Con el fin de lograr esta separación se le agregan 5 ml de CCl_4, el cual sirve para solubilizar el S^0, y algunas gotas de HCl (37%) con el objetivo de disolver el exceso de $Cd(OH)_2$. La disolución es favorecida por la agitación de la solución por algunos minutos. Luego de 1 hora se podrán ver dos fases inmiscibles (H_2O-$CdCl_2$-HCl-impurezas y CCl_4-S^o), las que se pueden separar gravimétricamente mediante el uso de un embudo separador. La solución CCl_4-S^0 es vertida a un frasco de 50 ml al cual se le agregan 20 ml de agua UHQ. Posteriormente se les agrega 0,5 g de $KBrO_3$, 0,5 g

de KOH y 0,02 g de KI. Bajo estas condiciones el I^- se oxida a I_2, donde este último es soluble en CCl_4. Debido a esto el S^o se combina con el I_2, formando el compuesto polar S_2I_2. Este último es removido desde el CCl_4 y pasa a la primera fase inmiscible. Aquí el S_2I_2 se oxida a SO_4^{-2} y I_2. Este último también se disuelve en CCl_4 y se recombina con el S^o hasta que éste sea consumido en su totalidad. El exceso de I_2 otorga al CCl_4 una coloración púrpura, lo cual indica el fin del proceso oxidativo. De esta manera el S^0 puede ser analizado como SO_4^{-2} mediante cromatografía iónica.

III.2.1.3 Análisis de los compuestos gaseosos en la fase líquida del condensado

De las dos botellas de condensados por sitio de muestreo, una de ellas se utiliza para el análisis de la composición química del condensado. Tanto los aniones (F^-, Cl^-, Br^-, NO_3^-, SO_4^{2-}) como los cationes (Na^+, K^+, Ca^{2+}, Mg^{2+}, NH_4^+, Li^+) mayoritarios se analizan mediante cromatografía iónica (cromatógrafos Metrohm modelos 761 y 861, respectivamente).

III.2.2 Reconstrucción de la composición original del gas

Para la reconstrucción de la composición química original de la muestra se requieren los siguientes datos analíticos: i) gases insolubles analizados por cromatografía gaseosa (N_2, H_2, O_2, He, Ar, Ne, CO, CH_4 e hidrocarburos C_2-C_7). ii) gases solubles en la solución alcalina (H_2O, CO_2, HCl, SO_2, H_2S y S^0), y iii) gases solubles en los condensados (B, NH_4, HF y HCl).

III.2.2.1 Concentración molar de los gases analizados en fase líquida

En el caso de los compuestos muestreados con la solución alcalina (H_2O, CO_2, HCl, H_2S, SO_2 y S^0), el cálculo de la molaridad se realiza mediante la división de la concentración de éstos (mg/L) por sus respectivos pesos moleculares. Es importante notar que las concentraciones de HCl, H_2S, SO_2 y S^0 se determinan como iones (HCl como Cl^-, y H_2S, SO_2 y S^0 como SO_4^{2-}), por lo que se debe considerar la relación de los pesos moleculares entra la especie determinada y la especie correspondiente (e.g. HCl/Cl^-=36,45/35,45).

Una vez calculada la molaridad de las especies de S (H_2S, SO_2 y S^0) y el HCl, se procede a recalcular su concentración molar para así descartar el efecto de la dilución. Para llevar a cabo ésto, se utiliza la concentración molar del HCl (estimada como Cl^-) en los condensados. Finalmente, la concentración molar del H_2O, CO_2, HCl, H_2S, SO_2 y S^0 son multiplicados por el volumen de gas muestreado como líquido, el cual se calcula a partir de las diferencias de masa de cada ampolla previo y posterior a la toma de la muestra, obteniéndose la cantidad de moles de cada compuesto en solución.

III.2.2.2 Concentración molar de los gases analizados en fase gaseosa

En el caso de los gases insolubles, los moles de cada compuesto son determinados mediante la ley de los gases ideales (n = PV/RT), utilizando los valores de presión (P) del gas en el espacio superior de la ampolla. Esta presión corresponde a la medida al momento de la inyección del gas en el cromatógrafo de gases. El volumen (V) corresponde al espacio sin líquido de la ampolla, el cual se calcula como la sustracción del volumen original de la ampolla (60-80 ml) menos el volumen inicial de solución alcalina (20-30 ml) menos el volumen de gas muestreado. Este último valor se obtiene restando el peso de cada ampolla antes y después del muestreo. La temperatura (T) corresponde a la temperatura estándar (~25°C).

Una vez obtenida la cantidad total de moles de gas muestreado, es posible calcular cantidad de moles de cada compuesto inerte en base a sus concentraciones relativas medidas por cromatografía gaseosa en el espacio superior de la ampolla.

III.2.2.3 Concentración molar de los gases totales

Para obtener los valores analíticos de cada compuesto gaseoso expresado en µmol/mol, es necesario conocer el número de moles totales de gas muestreado, el cual se calcula como la suma de las contribuciones molares de cada compuesto gaseoso. Así las concentraciones en µmol/mol de cada compuesto gaseoso se obtienen de la relación entre los moles de cada compuesto gaseoso y el número de moles totales muestreados (multiplicados por 1.000.000).

III.2.3 Análisis isotópico de los gases

III.2.3.1 Composición isotópica del C ($^{13}C/^{12}C$) en CO_2

El análisis del $^{13}C/^{12}C$ en el CO_2 es realizado mediante un espectrómetro de masa Finningan modelo 250 delta S de doble inyección. Este instrumento permite el análisis isotópico de carbono en el gas de baja y alta temperatura. Previo a la realización del análisis, la muestra debe ser liberada de $H_2O_{(v)}$ y H_2S. Los procedimientos de extracción estándar y purificación de la mezcla de gas (separación del CO_2 en el gas natural) está basada en los procedimientos de *Evans et al. (1998)*. Las relaciones isotópicas de $^{13}C/^{12}C$ en el CO_2 son finalmente expresadas como razones isotópicas referidas al estándar V-PDB, en valores de ‰ ($\delta^{13}C_{V\text{-}PDB}$ ‰). Los estándares internos (mármoles de Carrara y San Vincenzo) e internacionales (NBS18 y NBS19) son usados para la estimación de la precisión interna. Los errores analíticos son de ±0,05 ‰ y la reproducibilidad de los valores delta (δ) para el C es de ±0,1 ‰.

III.2.3.2 Composición isotópica del Ar ($^{40}Ar/^{36}Ar$) y He ($^{3}He/^{4}He$)

Las relaciones de $^{3}He/^{4}He$ y $^{40}Ar/^{36}Ar$ fueron determinadas utilizando un espectrómetro de masa para gases nobles marca VG modelo 5400, equipado con un multiplicador de electrones Johnston y un contador de pulsos electrónicos en el colector axial. Las muestras de gas fueron procesadas en líneas de alto vacío de acero inoxidable y vidrio Coming-1724. Un paso muy importante es la purificación de los gases, lo cual se realiza removiendo el vapor de agua y CO_2 a -90°C y -195°C, respectivamente, y el N_2 y O_2 haciéndolos reaccionar con una aleación de Zr-Al (SAES-ST-707). El Ar y Ne son absorbidos en carbón activado a -195 y -230 K, respectivamente. El uso de SAES-ST-101, uno en la línea de entrada y dos en el espectrómetro de masa, permite reducir el $^{1}H\text{-}^{2}H^{+}$ de fondo a aproximadamente ~1000 ion/seg

Las razones de $^{3}He/^{4}He$ fueron analizadas mediante una Copa Faraday (resolución de 200 a 5%) y un multiplicador de electrones Johnston (resolución de 600) para el análisis secuencial de los *peaks* de ^{4}He (Copa) y ^{3}He (multiplicador). El espectrómetro de masa mide adecuadamente el ^{3}He sin la interferencia del ^{1}H, ^{2}H y ^{3}H. En el colector axial (resolución de 600) el ^{3}He es completamente separado del $^{1}H\text{-}^{2}H^{+}$ con una línea de base de separación de <2% del *peak* $^{1}H\text{-}^{2}H^{+}$. La contribución del $^{1}H\text{-}^{2}H^{+}$ al *peak* de ^{3}He es de <0,1 ion/seg a 1000 ion/seg de $^{1}H\text{-}^{2}H^{+}$. El error analítico estimado para la razón $^{3}He/^{4}He$ es de aproximadamente 0,3%.

Una vez completado el análisis del He, se miden las relaciones de $^{40}Ar/^{36}Ar$ en un separador de Ar purificado. La sensibilidad del espectrómetro para la medición de Ar es de aproximadamente 4×10^{-4} Amp/torr, mientras que la precisión es de aproximadamente 0,2%.

III.2.4 Análisis de las aguas

III.2.4.1 Composición química

Las muestras de agua fueron analizadas en la Universidades de Florencia y de Chile. Para el primer caso, los análisis se realizaron mediante las siguientes técnicas:

- Aniones mayores (F^-, Cl^-, Br^-, NO_3^-, SO_4^{2-}) se analizan mediante Cromatografía Iónica (Metrohm 761).
- Cationes mayores (Na^+, K^+, Ca^{2+}, Mg^{2+}, Li^+) se analizan mediante Cromatografía Iónica (Metrohm 861).
- Carbonatos ($H_2CO_3^0$, HCO_3^-, CO_3^{2-}) mediante Titulación Automática (Metrohm basic Titrino 794).

- Metales trazas (Al, B, Fe, Mn, Sr) mediante Espectrometría de Masa con fuente de Plasma de Acoplamiento Inductivo (Agilent 7700x ICP-MS).

Las muestras de agua analizadas en la Universidad de Chile se realizaron de forma similar mediante las siguientes técnicas:

- Aniones mayores (F^-, Cl^-, Br^-, NO_3^-, SO_4^{2-}) mediante Cromatografía Iónica con un equipo Metrohm 861- Processor Sample 838.
- Cationes mayores (Na^+, K^+, Ca^{2+}, Mg^2) se analizan mediante Absorción Atómica con un equipo Pin AAcle 900 F-Perkin Elmer.
- Carbonatos ($H_2CO_3^0$, HCO_3^-, CO_3^{2-}) mediante Titulación Manual utilizando la técnica propuesta por *Giggenbach y Goguel (1989*).
- Cationes minoritarios y metales trazas (Al, Fe, Li, Si, Sr) mediante Espectrometría de Emisión Óptica por Plasma de Acoplamiento Inductivo (Optima 7300V- Perkin Elmer).

La Tabla III-3 muestra un resumen de las técnicas utilizadas para la determinación de los componentes analizados en este trabajo, junto con los límites de detección y errores analíticos asociados. La preparación de los estándares de los elementos analizados se hizo acorde a los procedimientos propuestos por *APHA et al. 1998*. Un resumen de las sales y metales empleados para la preparación de los estándares se presenta en la Tabla III-4.

III.2.4.2 Composición isotópica de $^{18}O/^{16}O$ y $^{2}H/^{1}H$ en aguas y condensados

Las relaciones isotópicas de $^{18}O/^{16}O$ y $^{2}H/^{1}H$, expresadas mediante notación delta como $\delta^{18}O$ y δD ‰ V-SMOW, respectivamente, se obtienen mediante espectrometría de masa (equipo Finningan Delta Plus XL). Las razones isotópicas de oxígeno e hidrógeno fueron analizadas de acuerdo a las metodologías de Epstein y Mayeda (1953) y Coleman et al. (1982), respectivamente. El error experimental es de ± 0,1‰ y ± 1‰ para los valores de $\delta^{18}O$ y δD, respectivamente, usando los estándares internos EEZ-3 y EEZ-4, los cuales fueron previamente calibrados como estándares de referencia vs. V-SMOW (Vienna Standard Mean Ocean Water) y SLAP (Standard Light Antartic Precipitation).

Tabla III-3: Tabla resumen de los métodos utilizados para el análisis químico de las aguas.

Especie	Técnica	Equipo	Nota	Error analítico
F^-, Cl^-, Br^-, NO_3^-, SO_4^{2-}	Cromatografía Iónica	Metrohm 761	Eluente: solución carbonato sódico 3.2 mmol/L y bicarbonato sódico1 mmol/L. Tiempos de retención para el F^-, Cl^-, Br^-, NO_3^- y SO_4^{2-} corresponden a 6.27, 10.02, 15.65, 18.15 y 28.24 min, respectivamente. Columna: Metrosep A Sup 2 poliestirenedivinyl benzene polimer Límite de detección para el F^-, Cl^-, Br^-, NO_3^- y SO_4^{2-} corresponden a 2 mg/l.	<5%
Na^+, K^+, Ca^{2+}, Mg^{2+}, Li^+	Cromatografía Iónica	Metrohm 861	Eluente: solución ácido tartárico 4.0 mmol/l y ácido dipicolínico 0.75 mmol/l Tiempos de retención para el Li^+, Na^+, K^+, Ca^{2+} y Mg^{2+} corresponden a 3.91, 4.91, 7.42, 14.21 y 18.71 min, respectivamente Columna: Metrosep C 2-250 silica gel with carboxyl groups Límites de detección para el Li^+, Na^+, K^+, Ca^{2+} y Mg^{2+} corresponden a 0.05, 0.2, 0.5, 0.25 y 0.5 mg/l, respectivamente.	<5%
Na^+, K^+, Ca^{2+}, Mg^{2+}	Absorción Atómica	Pin AAcle 900 F-Perkin Elmer	Límite de detección para el Na^+, K^+, Ca^{2+} y Mg^{2+} corresponde a 0.1 mg/l.	<5%
$H_2CO_3^0$, HCO_3^-, CO_3^{2-}	Titulación (Automática/Manual)	Metrohm 794	Titulación con 0.02N HCl Límite de detección: 1 mg/l	<10%

Continuación de la Tabla III-3.

Al, B, Fe, Mn, Sr	Espectrometría de Masa con fuente de Plasma de Acoplamiento Inductivo	Agilent 7700x ICP-MS	Límites de detección para el Al, B, Fe, Mn y Sr corresponden a 7.9, 15, 1.2 y 2.1 ppt, respectivamente.	<5%
Al, Fe, Li, Si, Sr	Espectrometría de Emisión Óptica por Plasma de Acoplamiento Inductivo	Optima 7300V-Perkin Elmer	Límites de detección para el Al, Fe, Li, Si y Sr corresponden a 0.1, 0.1, 5, 0.1 y 5 ppm, respectivamente.	<5%

Tabla III-4: Tabla resumen de las proporciones de sales, metales y ácidos empleados para la creación de los stocks de estándares (c_i=1000 mg/l) utilizados en el análisis químico de las aguas (*APHA et al. 1998*). Las sales, metales y ácidos fueron diluidos en un matraz de 1000 ml con agua destilada de alta pureza (stocks primarios). Las sales fueron secadas en un horno a 105°C previo a su disolución.

Especie *i*	**Peso de la sal/metal contenedora de la especie *i***	**Especie *i***	**Peso de la sal/metal contenedora de la especie *i***
Cl^-	1.6484 gr de NaCl.	Li^+	12.5156 gr de LiBr
NO_3^-	1.3707 gr de $NaNO_3$	Mg^{2+}	8.3632 gr de $MgCl_2 \cdot 6H_2O$
SO_4^{2-}	1.479 gr de Na_2SO_4	Al	8.3430 gr de $Al_2(SO_4)_3 \cdot 6H_2O$
F^-	2.210 gr de NaF	B	5.7198 gr de H_3BO_3
Br^-	1.287 gr de NaBr	Fe	4.3981 gr de $FeSO_4 \cdot 7H_2O$
Ca^{2+}	1.249 gr de $CaCO_3$	Mn	1 gr de Mn^0 + 100 ml HCl (37%) + 10 ml HNO_3 (35%)
K^+	1.9067 gr de KCl	Sr	1.685 gr de $SrCO_3$ + 100 ml HNO_3 (35%)
Na^+	2.542 gr de NaCl	SiO_2	4.730 gr de $Na_2SiO_3 \cdot 9H_2O$ + 100 ml HNO_3 (35%)

BIBLIOGRAFÍA

American Public Health Association et al. (1998). Standard Methods for the Examination of Water and Wastewater. 20th Ed. American Public Health Association, Washington, D.C. 1183 pp.

Capecchiacci F. (2012). Geochimica dei fluidi vulcanici e idrotermali: Origine delle componenti organiche e loro impatto ambientale.Universita degli Studi di Firenze, Italia, 249 pp.

Coleman, M. L., T. J. Shepherd, J. J. Durham, J. E. Rouse and G. R. Moore (1982). Reduction of water with zinc for hydrogen isotope analysis. Analytical Chemistry 54(6): 993-995.

Epstein, S. and Mayeda, T.K.. (1953). Variation of the 18O/16O ratio in natural waters. Geochimica et Cosmochimica Acta 4, 213–224.

Evans, W., White, L., Rapp, J. (1998). Geochemistry of some gases in hydrothermal fluids from the southern Juan de Fuca ridge. Journal of Geophysical Research, Vol. 15, 305 –313

Giggenbach, W. F. (1975). A simple method for the collection and analysis of volcanic gas samples. Bulletin Volcanologique 39(1): 132-145.

Giggenbach, W., Goguel, R. (1989). Collection and analysis of geothermal and volcanic water and gas discharges, unpublished report. Chemistry Division, Department of Scientific and Industrial Research, Petone, New Zealand, 81 p.

Marini, L. 2000. Geochemical Techniques for the Exploration and Exploitation of Geothermal Energy. Informe Proyecto FONDEF 99I1051, 82 p.

Montegrossi, G., F. Tassi, O. Vaselli, A. Buccianti and K. Garofalo (2001). Sulfur Species in Volcanic Gases. Analytical Chemistry 73(15): 3709-3715.

Poreda, R.. Farley, K. (1992). Rare gases in Samoan xenoliths. Earth and Planetary Earth Sciences Letters, Vol. 113, 129 – 144

Symonds, R., Rose, W., Bluth, G., Gerlach, T. (1994). Volcanic-gas studies: Methods, results, and applications. En Carrol, M., Holloway, J., eds. Volatiles in Magmas, Reviews of Mineralogy, Vol. 30, 1 – 66

Tassi, F. (2004). Fluidi in ambiente vulcanico: Evoluzione temporale dei parametri composizionali e distribuzione degli idrocarburi leggeri in fase gassosa. Tesis para obtener el grado de Doctor, Universitá degli Studi di Firenze, Italia, 356 p.

Tassi, F., J. Fiebig, O. Vaselli and M. Nocentini (2012). Origins of methane discharging from volcanic-hydrothermal, geothermal and cold emissions in Italy. Chemical Geology 310-311(0): 36-48.

Vaselli, O., F. Tassi, G. Montegrossi, B. Capaccioni and L. Giannini (2006). Sampling and analysis of fumarolic gases. Acta Vulcanol. 18: 65-76.

CAPÍTULO IV

ORIGIN OF FUMAROLIC FLUIDS FROM TUPUNGATITO VOLCANO (CENTRAL CHILE): INTERPLAY BETWEEN MAGMATIC, HYDROTHERMAL AND SHALLOW METEORIC SOURCES[1]

IV.1 INTRODUCTION

The chemical and isotopic compositions of fluids naturally discharged into the atmosphere from volcanic systems are the result of the interplay between i) deep processes, e.g. vapor-melt separation, and ii) secondary processes that include gas cooling and re-equilibration, interaction with meteoric water-fed aquifers, reactions with wall-rock minerals, microbial activity, and air contamination (*Giggenbach 1980, 1984, 1987, 1988, 1996; Chiodini and Marini, 1998; Capaccioni and Mangani 2001; Symonds et al. 2001; Taran and Giggenbach 2003*). Geochemical investigations of fumarolic fluids from volcanic systems are commonly aimed at reconstructing fluid sources and chemical-physical conditions occurring along the fluid circulation pattern, to serve as a basis for monitoring purposes and/or evaluation of geothermal energy potential (e.g., *Tedesco and Sabroux 1987; Martini et al. 1991; Giggenbach 1996; Tassi et al. 2005; Sepúlveda et al 2007; Vaselli et al. 2010*).

Tupungatito is an early Pleistocene-Holocene volcano located ~100 km east of Santiago in the High Andes of Central Chile (Figure IV-1a), in the northernmost sector of the South Volcanic Zone (SVZ). This volcano is characterized by a permanent fumarolic activity and the occurrence of three crater lakes at its summit showing intense gas bubbling (*González-Ferrán 1995*). To the best of our knowledge, no geochemical data for these volcanic fluids are currently available. In this study we present and discuss the very first chemical and isotopic ($\delta^{13}C\text{-}CO_2$, $^3He/^4He$, and

[1]Una versión del siguiente capítulo ha sido publicado como: Benavente O., Tassi F., Gutiérrez F., Vaselli O., Aguilera F., Reich M. (2013). Origin of fumarolic fluids from Tupungatito Volcano (Central Chile): Interplay between magmatic, hydrothermal and shallow meteoric sources, Bulletin of Volcanology, Volumen 75, Issue 8, pp. 1-15.

$^{40}Ar/^{36}Ar$) data on the composition of fumarolic gases and steam ($\delta^{18}O$ and δD), as well as the chemical composition of the lake hosted in the 1986-1987 summit crater (Figure IV-1c), using samples collected from this Chilean volcano during two campaigns carried out in February 2011 and 2012. The main aims were to investigate the different fluid source regions and the chemical-physical processes controlling fluid chemistry. These geochemical data are compared with those of fumarolic fluids from other volcanic systems located in the Chilean Andes (Figure IV-1a) that are characterized by different (i) amount and composition of the subducted sediment, (ii) slab thermal state, and (iii) crustal thickness and lithology.

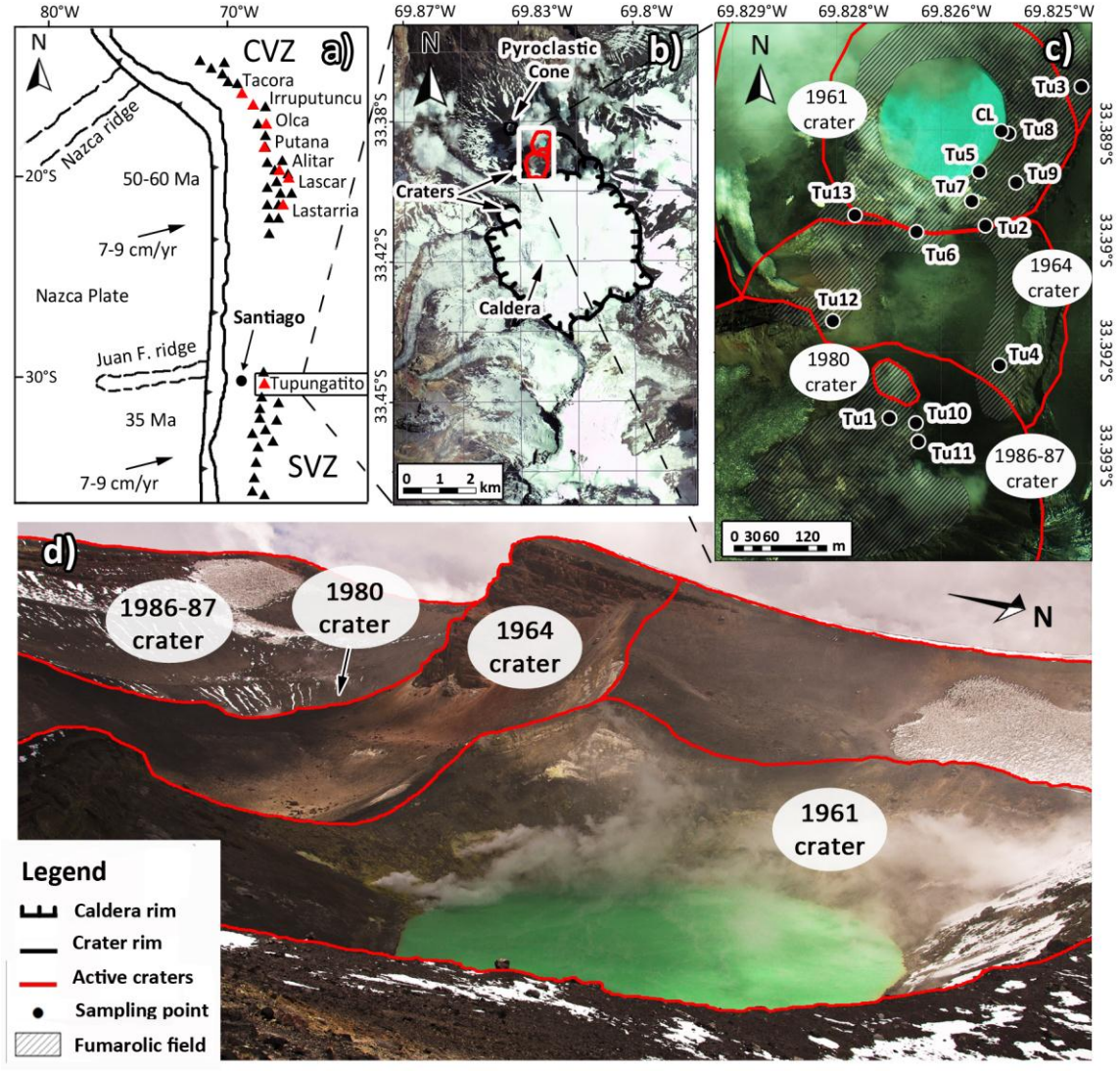

Figure IV-1: (a) Location of the Tupungatito volcano and active and dormant volcanic centers of the Central and Southern Volcanic Zones; (b) aerial image of Tupungatito and Tupungato volcanic complex; (c) summit actives crater of Tupungatito volcano, showing the locations of the fumarolic fields and sampling sites; (d) view from SW of the three main active craters in the Tupungatito summit.

IV.2 GEODYNAMIC, GEOLOGICAL AND VOLCANOLOGICAL SETTINGS

Volcanism in the Andes of Chile is produced by the subduction of the Nazca and Antarctic plates below the South America plate *(Barazangi and Isack 1976; Cande and Leslie 1986, 1987*). The Chilean Volcanic Chain (CVC) consists of three distinct volcanic alignments characterized by a relatively steep subduction angle (>25°): Central (CVZ; 17.5-27°S), Southern (SVZ; 33-46°S) and Austral (AVZ; 49-55°S) Volcanic Zones (Figure IV-1a*; Barazangi and Isacks 1976*).

Tupungatito volcano (33.4°S, 69.8ºW; 5682 m a.s.l.) consists of: i) seven summit craters, ii) a north-westernmost 4 km-wide pyroclastic cone and iii) a 5 km wide caldera with an estimated erupted volume of 6 km^3 that opens westwards (Figure IV-1b; *Hildreth and Moorbath 1988; González-Ferrán 1995; Moreno and Naranjo 1991*). The caldera is covered by glaciers above 5,400 m a.s.l., where the ice-melt waters are discharged into the Colorado-Maipo drainage basin to the west (Fig 1b; Stern et al. 2007). The base of the volcanic edifice (4,700 m a.s.l.) overlies an eroded volcano whose estimated volume is >10 km^3 and consists of dacitic lavas and lithic pyroclastic flows lithologically similar to those of Tupungato stratovolcano (6,550 m a.s.l.), which is located 7 km NW of Tupungatito (*Hildreth and Moorbath 1988*). The sedimentary basement of the Tupungatito volcano is composed of thick Lower Cretaceous marine limestone and evaporitic sequences (*Giambiagi and Ramos 2002*). Upper Cretaceous conglomerate and sandstone beds, and volcanoclastic rocks overlay the Lower Cretaceous sequences, and outcrop ~10 km west from the volcano (*Giambiagi and Ramos 2002*). In this area, the crustal thickness is ~50 km (*Barazangi and Isack 1976; Tassara and Yáñez 2003*). The Tupungatito eruptive products range from basaltic-andesites to dacites (*Hildreth and Moorbath 1988*). Compared to the volcanic rocks of the southern portions of the SVZ, where crustal thickness progressively decreases down to 30 km (*Barazangi and Isack 1976; Tassara and Yáñez 2003*), the Tupungatito magmas, at equivalent SiO_2 contents (~57.5%), has higher contents of K_2O (~2.82 %) and incompatible trace elements (Rb ~80 ppm, Sr ~600 ppm, Ba ~520 ppm and Th ~9 ppm), higher ratios of fluid-mobile elements (Ce/Yb ~45, and Rb/Cs ~30), higher $^{87}Sr/^{86}Sr$ isotope ratios (0.70489), and lower K/Rb and $^{143}Nd/^{144}Nd$ ratios (~250 and 0.511589 respectively) (*Hildreth and Moorbath 1988*). The crustal signature of the Tupungatito volcanic products was interpreted by *Cembrano and Lara (2009)* in terms of advanced magmatic differentiation related to long residence times in the crust of magmas, as they were rising through a thick crust in a compressive tectonic regime.

Table IV-1: Geographical coordinates (UTM), altitude (m), type, outlet temperatures (in °C), and chemical composition of inorganic gases and CH_4 (in mmol/mol) for the Tupungatito gas discharges; b.d.l.: below detection limit.

	Date	Coord N	Coord E	Altitude	T°C	CO_2	HCl	HF	SO_2	H_2S	N_2	CH_4	Ar	O_2	H_2	He	CO	Xgas %
Tu1	14-02-2011	6304903	423082	5236	83,1	970	0,058	0,0060	0,11	19	4,6	0,44	0,0040	0,018	2,4	0,0008	0,0019	27,4
Tu2	14-02-2011	6305161	423203	5233	82,4	970	0,095	0,0080	0,098	20	4,1	0,31	0,0040	0,019	2,0	0,0006	0,0015	24,3
Tu3	14-02-2011	6305359	423316	5261	83,0	970	0,085	0,0069	0,17	20	4,2	0,29	0,0057	0,029	2,2	0,0009	0,0017	27,7
Tu4	14-02-2011	6304982	423211	5267	82,7	970	0,11	0,0076	0,19	22	4,6	0,40	0,0031	0,0046	2,4	0,0008	0,0016	26,3
Tu5	14-02-2011	6305245	423198	5190	82,7	970	0,31	0,026	0,21	20	4,9	0,33	0,0039	0,0081	2,2	0,0008	0,0019	27,5
Tu6	16/02/2012	6305149	423117	5235	83,0	980	0,048	0,0051	0,23	14	4,2	0,23	0,0038	0,011	2,0	0,0006	0,0015	21,8
Tu7	16/02/2012	6305199	423192	5204	83,4	980	0,091	0,0089	0,25	12	4,7	0,31	0,0045	0,0093	2,6	0,0008	0,0022	20,9
Tu8	17/02/2012	6305292	423220	5204	35,2	980	0,051	0,0023	n.r.	11	9,0	0,22	0,032	0,044	0,37	0,001	n.r.	
Tu9	17/02/2012	6305234	423235	5222	83,5	980	0,098	0,0056	0,22	12	5,2	0,19	0,0061	0,011	1,2	0,0006	0,0016	25,6
Tu10	19/02/2012	6304896	423115	5265	83,4	970	0,086	0,0077	0,17	20	5,1	0,36	0,0066	0,012	1,9	0,0007	0,0021	24,7
Tu11	19/02/2012	6304879	423116	5258	83,6	970	0,075	0,0026	0,16	25	4,7	0,39	0,0047	0,0089	1,7	0,0005	0,0015	18,5
Tu12	20/02/2012	6305032	423006	5276	82,7	980	0,022	0,0018	0,14	16	4,7	0,42	0,0058	0,0087	0,80	0,0006	0,0006	18,8
Tu13	20/02/2012	6305178	423033	5258	80,8	980	0,031	0,0019	0,085	16	4,1	0,36	0,0064	0,0087	1,8	0,0007	0,0024	19,4

	C_2H_6	C_2H_4	C_3H_8	C_3H_6	i-C_4H_{10}	n-C_4H_{10}	i-C_4H_8	C_4H_4O	C_6H_6	C_4H_4S	C_7H_8
Tu1	2,0	0,0033	0,14	0,0032	0,0047	0,010	0,085	0,000030	0,26	0,00060	0,0013
Tu2	1,3	0,0026	0,13	0,0025	0,0041	0,0092	0,076	0,000020	0,17	0,00059	0,0012
Tu3	1,4	0,0027	0,12	0,0022	0,0037	0,0087	0,088	0,000028	0,16	0,00065	0,0014
Tu4	1,8	0,0033	0,15	0,0029	0,0040	0,0093	0,090	0,000026	0,20	0,00079	0,0016
Tu5	1,5	0,0029	0,14	0,0027	0,0049	0,0098	0,870	0,000026	0,20	0,00068	0,0015
Tu6	1,7	0,0035	0,18	0,0039	0,0045	0,0085	0,055	0,000056	0,19	0,00056	0,0015
Tu7	1,9	0,0026	0,15	0,0042	0,0078	0,0025	0,066	0,000078	0,29	0,00066	0,0013
Tu8	2,1	0,0011	0,17	0,0036	0,0028	0,0048	0,021	n.r.	0,16	0,00011	0,0018
Tu9	2,1	0,0018	0,18	0,0023	0,0015	0,0041	0,074	0,000059	0,12	0,00017	0,0021
Tu10	2,5	0,0041	0,12	0,0027	0,0039	0,0027	0,052	0,000047	0,21	0,00031	0,0026
Tu11	1,9	0,0024	0,14	0,0024	0,0047	0,0028	0,056	0,000066	0,17	0,00025	0,0015
Tu12	1,7	0,0031	0,19	0,0042	0,0056	0,0036	0,047	0,000079	0,18	0,00029	0,0008
Tu13	1,8	0,0028	0,12	0,0032	0,0042	0,0029	0,053	0,000038	0,16	0,00017	0,0011

Table IV-2: C_2-C_7 hydrocarbons contents (in mmol/mol) for the Tupungatito gas discharges; b.d.l.: below detection limit.

Tupungatito volcano is one of the most active volcanoes in the SVZ, having experienced nineteen historical eruptions between 1829 and 1987 (*Moreno and Naranjo 1991; González-Ferrán 1995*). Historical eruptions were characterized by a VEI <2 and occurred in the NW portion of the caldera, where eight active craters were formed (Figure IV-1c; *González-Ferrán 1995*). Currently, four NS-oriented summit craters are characterized by permanent fumarolic activity and host three crater lakes (Figure IV-1c-d), which show a vigorous gas bubbling. The turquoise-colored crater lake, hosted in the northernmost active crater formed in 1961 (Figure IV-1c-d; *González-Ferrán 1995*), has an extremely low pH (<1), caused by dissolution of acidic gases. Fumaroles were also recognized along the eastern and western rims of the central crater that was produced by an explosive eruption occurred in 1964 (Figure IV-1c; *González-Ferrán 1995*). The last three eruptions (1980, 1986 and 1987), mainly consisting of phreatic activity, occurred in the third crater (Figure IV-1c; *Moreno and Naranjo 1991; González-Ferrán 1995*), which hosts two inaccessible small crater lakes located at the bottom of the 1980 and 1986-87 craters and several fumarolic vents (Figure IV-1c).

IV.3 SAMPLING AND ANALYTICAL METHODS

IV.3.1 Gas and water sampling

Gas samples from fumarolic vents and bubbling pools were collected using pre-evacuated, 60-mL, glass Giggenbach-like (*Giggenbach 1975*) flasks filled with 20 mL of 4N NaOH and a 0.15M $Cd(OH)_2$ suspension (*Montegrossi et al. 2001; Vaselli et al. 2006*). Gas samples from fumarolic vents were conveyed into the sampling flasks using a 1-m-long titanium tube (*Ø* = 2.5 cm) that was inserted into the fumarolic vent and connected through glass dewar tubes. A gas sample from one of the many bubbling emissions in the northernmost crater lake was also collected using a plastic funnel upside-down positioned and connected to the sampling flasks through tygon tubes. At each sampling point, a 60 mL glass pre-evacuated gas vial was used to collect a sample for the analysis of carbon isotopes in CO_2 using the same sampling apparatus adopted for the soda flasks. Fumarolic condensates were collected using an ice-cooled glass condensing system connected to the gas sampling glass line.

A filtered (at 0.45 μm) water sample was collected from the crater lake and stored in 200 mL sterile polyethylene bottles.

	R/Ra	$^{40}Ar/^{36}Ar$	^{36}Ar	$^{40}Ar^*$	$^{40}Ar^*/^{4}He$	He/Ne	$\delta^{13}C\text{-}CO_2$	δD	$\delta^{18}O$	$CO_2/^{3}He$	$CH_4/^{3}He$
Tu1	5,45	327	0,000012	0,00039	0,470	56	-7,65	-68	-2,9	1,54E+11	6,99E+07
Tu2	n.a.	n.a.	n.a.	n.a.	n.a.	n.a.	-6,92	-72	-3,3	n.a.	n.a.
Tu3	5,19	374	0,000015	0,0012	1,281	38	-8,16	-55	0,8	1,43E+11	4,32E+07
Tu4	n.a.	n.a.	n.a.	n.a.	n.a.	n.a.	-6,84	-50	-0,6	n.a.	n.a.
Tu5	5,26	415	0,000009	0,00113	1,490	551	-7,11	-67	-2,2	1,75E+11	5,90E+07
Tu6	5,23	366	0,000010	0,00073	1,284	105	-6,12	-65	-1,8	2,37E+11	5,50E+07
Tu7	6,09	352	0,000013	0,00072	0,881	326	-6,74	-53	-1,1	1,41E+11	4,42E+07
Tu8	5,06	304	0,000104	0,00088	0,803	37	-0,30	n.a.	n.a.	1,27E+11	2,79E+07
Tu9	5,16	415	0,000015	0,00176	3,137	212	-5,31	-75	-3,3	2,44E+11	4,66E+07
Tu10	5,41	461	0,000014	0,00237	3,590	336	-6,29	-50	-0,5	1,95E+11	7,27E+07
Tu11	n.a.	n.a.	n.a.	n.a.	n.a.	n.a.	-6,56	-70	-3,1	n.a.	n.a.
Tu12	5,78	388	0,000015	0,00138	2,426	195	-6,67	-54	-0,8	2,14E+11	9,06E+07
Tu13	n.a.	n.a.	n.a.	n.a.	n.a.	n.a.	-7,31	n.a.	n.a.	n.a.	n.a.

Table IV-3: Isotopic composition of steam ($\delta^{18}O$ and δD in ‰ vs. V-SMOW), carbon in CO_2 ($\delta^{13}C$ in ‰ vs. V-PDB), helium (as R/Ra, where R is the measured ratio and Ra is that of the air: $1.39x10^{-6}$; *Mamiryn and Tolstikhin, 1984*), and argon ($^{40}Ar/^{36}Ar$) for the Tupungatito thermal discharges; n.a.: not analyzed. $\delta^{18}O$ and δD values of local precipitations (MW), as well as ^{36}Ar and radiogenic Ar ($^{40}Ar^*$) concentrations and He/Ne, $^{40}Ar^*/^{4}He$, $CO_2/^{3}He$ and $CH_4/^{3}He$ ratios, are also reported.

Table IV-4: Temperature (in °C), pH and chemical composition (in mg/L) of the Tupungatito crater lake (CL).

	Date	Coord. N	Coord E	Altitude	T	pH	F^-	Cl^-	SO_4^{2-}	Br^-	Na^+	NH_4^+	K^+	Mg^{2+}	Ca^{2+}
CL	16-02-2011	6305292	423220	5204	32,2	0,34	210	12500	12600	21	590	240	360	310	1100

IV.3.2 Chemical and isotopic (R/Ra, δ^{13}C-CO2 and ^{40}Ar/^{36}Ar) analysis of gases and steam δ^{18}O and δD)

Inorganic gases (N_2, O_2, H_2, He, Ar, CO and Ne) in the sampling flask headspace were analyzed using a Shimadzu 15A gas chromatograph (GC) equipped with a 10 m long 5A molecular sieve column and a thermal conductivity detector (TCD). To allow a complete separation of Ar and O_2 peaks the oven temperature was lowered to -10 °C by means of a cryogenic liquid CO_2 cooling loop (Shimadzu CRG-15). Hydrocarbons, including CH_4, were determined by using a Shimadzu 14A gas chromatograph (GC) equipped with a 10-m-long stainless steel column packed with Chromosorb PAW 80/100 mesh coated with 23% SP 1700 and a flame ionization detector (FID). The alkaline suspension was centrifuged at 4,000 rpm for 30 min to separate the solid precipitate from the solution. The latter was used to analyze (i) CO_2, as CO_3^{2-}, by titration (Metrohm Basic Titrino) with a 0.5 N HCl solution; (ii) HCl, as Cl^-, by ion chromatography (IC) (Metrohm Basic761); (iii) SO_2, as SO_4^{2-}, after oxidation with 5 ml H_2O_2 (33%) by ion chromatography. Using 5 ml H_2O_2 (33%), CdS in the solid precipitate was oxidized to SO_4^{2-} that was analyzed by IC for determining H_2S concentrations (*Montegrossi et al. 2001*). Condensate samples for F^- and Cl^- were also analyzed by IC. HF concentrations were calculated on the basis of F^- and Cl^- concentrations in the condensate samples and the alkaline solution samples. The analytical error for titration, GC and IC analyses is <5%.

The analysis of $^{13}C/^{12}C$ ratios of CO_2 (hereafter expressed as $\delta^{13}C\text{-}CO_2$‰ vs. V-PDB) stored in the pre-evacuated sampling flasks were carried out with a Finningan Delta S mass spectrometer after standard extraction and purification procedures of the gas mixtures (*Evans et al. 1998; Vaselli et al. 2006*). Internal (Carrara and San Vincenzo marbles) and international (NBS18 and NBS19) standards were used for estimation of external precision. The analytical error and the reproducibility were ±0.05‰ and ±0.1‰, respectively.

Helium (expressed as R/Ra, where R is the $^3He/^4He$ measured ratio and Ra is the $^3He/^4He$ ratio in the air: 1.39×10^{-6}; *Mamyrin and Tolstikhin 1984*) and argon ($^{40}Ar/^{36}Ar$) isotopic ratios were determined on gas aliquots transferred from the flask headspace into pre-evacuated 50 mL flasks. A double collector mass spectrometer (VG 5400-TFT) was used according to the method described by *Inguaggiato and Rizzo (2004)*. The analytical uncertainty for the determination of R/Ra and $^{40}Ar/^{36}Ar$ was ≤0.3%.

The $^{18}O/^{16}O$ and $^{2}H/^{1}H$ isotopic ratios of the condensate samples (hereafter expressed as $\delta^{18}O\text{-}H_2O‰$ and $\delta D\text{-}H_2O‰$ vs. V-SMOW, respectively) were analyzed using a Finningan Delta Plus XL mass spectrometer at the Geokarst Engineering Laboratory (Trieste, Italy). Oxygen isotopes were analyzed according to the method described by *Epstein and Mayeda (1953).* Hydrogen isotopes were analyzed on H_2 generated by the reaction of 10 µL water with metallic zinc at 500 ˚C, according to the analytical procedure described by Coleman et al. (1982). V-SMOW and SLAP were used as analytical standards and AR-1 as an internal standard. The analytical error is ±0.1‰ for $\delta^{18}O$ and ±0.1‰ for δD.

IV.3.3 Chemical analysis of water

Temperature and pH of lake water were measured *in situ.* Major cations (Na^+, K^+, Ca^{2+}, Mg^{2+}, and NH_4^+) and anions (F^-, Cl^- SO_4^{2-}, Br^-) of the lake water sample collected from the 1961 crater were analyzed by ion chromatography (Metrohm 861 and Metrohm 761, respectively). The analytical error for IC is ≤5%.

Helium (expressed as R/Ra, where R is the $^{3}He/^{4}He$ measured ratio and Ra is the $^{3}He/^{4}He$ ratio in the air: 1.39×10^{-6}; *Mamyrin and Tolstikhin 1984*) and argon ($^{40}Ar/^{36}Ar$) isotopic ratios were determined on gas aliquots transferred from the flask headspace into pre-evacuated 50 mL flasks. A double collector mass spectrometer (VG 5400-TFT) was used according to the method described by *Inguaggiato and Rizzo (2004)*. The analytical uncertainty for the determination of R/Ra and $^{40}Ar/^{36}Ar$ was ≤0.3%.

The $^{18}O/^{16}O$ and $^{2}H/^{1}H$ isotopic ratios of the condensate samples (hereafter expressed as $\delta^{18}O\text{-}H_2O‰$ and $\delta D\text{-}H_2O‰$ vs. V-SMOW, respectively) were analyzed using a Finningan Delta Plus XL mass spectrometer at the Geokarst Engineering Laboratory (Trieste, Italy). Oxygen isotopes were analyzed according to the method described by *Epstein and Mayeda (1953).* Hydrogen isotopes were analyzed on H_2 generated by the reaction of 10 µL water with metallic zinc at 500 ˚C, according to the analytical procedure described by Coleman et al. (1982). V-SMOW and SLAP were used as analytical standards and AR-1 as an internal standard. The analytical error is ±0.1‰ for $\delta^{18}O$ and ±0.1‰ for δD.

IV.4 RESULTS

IV.4.1 Chemical analysis of gases

The measured temperatures of the fumaroles at Tupungatito are between 81° and 84 °C (Table IV-1). Steam is the main fumarolic component, whilst the dry gas fraction, whose molar concentration ranges from 18.5% to 27.7%, is dominated by CO_2 (up to 980 mmol/mol) and has relatively high concentrations of H_2S (up to 25 mmol/mol), and low but detectable concentrations of acidic components, such as HCl (up to 0.31 mmol/mol), SO_2 (up to 0.248 mmol/mol) and HF (0.026 mmol/mol). Nitrogen (up to 5.187 mmol/mol) and H_2 (up to 2.61 mmol/mol) constitute a significant portion of the dry gas fraction, whereas CH_4, O_2, Ar, CO and He have concentrations up to 0.439, 0.028, 0.0066, 0.0024 and 0.0009 mmol/mol, respectively (Table IV-1). The sum of the light hydrocarbons (C_2-C_7) is ≤2.9 µmol/mol (Table IV-2).

The chemical composition of the gas sample collected from the lake (Tu8) is similar to that of the fumaroles (Tables IV-1 and 2), with the exception of CO concentration, which is below the detection limit (<0.005 mmol/mol; Table IV-1).

IV.4.2 Isotopic composition of gases (R/R_a, $\delta^{13}C$-CO_2, $^{40}Ar/^{36}Ar$) and steam ($\delta^{18}O$ and δD)

The isotopic compositions of water vapor ($\delta^{18}O$-H_2O and δD-H_2O), CO_2 ($\delta^{13}C$-CO_2), He (R/R_a), and Ar ($^{40}Ar/^{36}Ar$) isotopic ratios are reported in Table IV-3. The $\delta^{18}O$ and δD values range from -3.3 to 0.8‰ and from -75‰ to -50‰ vs. V-SMOW, respectively. The $\delta^{13}C$-CO_2 values, with the exception of that of sample Tu8 (-0.30‰ vs. V-PDB), are from –8.16‰ to -5.31‰ vs. V-PDB, i.e. in the range of mantle-type CO_2 (Taylor 1986). The R/R_a values range from 5.06 to 6.09, while the $^{40}Ar/^{36}Ar$ ratios are up to 461.

IV.4.3 Chemical composition of water

Temperature, pH and chemical composition of the crater lake are reported in Table IV-4. Temperature and pH are 32.2 °C and 0.34, respectively. The lake chemistry is dominated by SO_4^{2-} and Cl^- (12,600 mg/L and 12,500 mg/L, respectively), whereas Ca^{2+} is the most abundant cation (1,100 mg/L), followed by Na^+ (590 mg/L), K^+ (360 mg/L) and Mg^{2+} (310 mg/L). The concentrations of NH_4^+, F^- and Br^- are relatively high (240, 210 and 21 mg/L, respectively).

IV.5 DISCUSSION

IV.5.1 Crater lake chemistry

The hyperacid lake hosted in the 1961 summit crater shows compositional features typical of volcanic lakes acting as condensers and calorimeters for acid volatiles and heat released from hydrothermal-magmatic degassing (Brantley et al. 1993). Fumarolic gases bubbling in the lake partially dissolve, producing high concentrations of F^-, Cl^-, SO_4^{2-} and NH_4^+, relatively high water temperature and extremely low pH values (Table IV-4). Water-rock interactions, which are favored at low pH, explain the relatively high Ca^{2+}, Na^+, K^+ and Mg^{2+} concentrations (Table IV-4). According to the classification based on the main physical-chemical parameters proposed by *Pasternack & Varekamp (1997)* and *Varekamp et al. (2000),* the Tupungatito lake can be defined as a "high-activity lake", similar to those of other active volcanic systems, such as Ruapheu (New Zealand; Christenson and Wood 1993), Kawah (Indonesia; *Delmelle et al. 2000*) Poàs and Rincon de la Vieja (Costa Rica, *Tassi et al. 2009b*) and Copahue (Argentina, *Varekamp et al. 2006*).

IV.5.2 Chemical-physical conditions at the fluid source

Chemical-physical conditions of hydrothermal-magmatic fluid reservoirs can be investigated by applying techniques developed for the interpretation of gas compositions regulated by gas-gas and gas-rock reactions that at increasing temperatures tend to approach equilibrium (*Giggenbach 1987, 1993, 1996, 1997; Chiodini and Marini 1998; Taran and Giggenbach, 2003*). The log-ratio between the molar concentrations of H_2 and H_2O (R_H) is considered the most suitable parameter for describing the redox state of volcanic fluids (*Giggenbach 1987*). The temperature independent FeO-$FeO_{1.5}$ redox pair, which is considered the most reliable redox buffer for hydrothermal systems, produces a R_H of -2.8, whereas in a magmatic gas-dominated environment the SO_2-H_2S redox pair causes, at temperatures <700 °C, more oxidizing conditions (R_H <-2.8) (*Giggenbach 1987*).

Hydrogen and CO rapidly respond to changes of temperature-redox conditions (*Giggenbach 1987*), thus their concentrations tend to re-adjust during the uprising of hydrothermal-magmatic gases toward the surface, according to the following pressure-independent reaction:

$$CO_2 + H_2 \leftrightarrow CO + H_2O \qquad \text{(IV.1)}$$

The temperature dependence of the equilibrium constant of reaction *(IV.1)* is given by (*Giggenbach 1996*):

$$\log(X_{CO}/X_{CO2}) - \log(X_{H2}/X_{H2O}) = 2.49 - 2248/T \qquad (IV.2)$$

, where T is in K, and X_{CO}, X_{CO2}, X_{H2} and X_{H2O} are the molar fractions of CO, CO_2, H_2 and H_2O, respectively. As shown in Figure IV-2, CO and H_2 seem to attain equilibrium in a single vapor phase at temperatures between 160° and 200 °C and R_H values ranging from -3 to -3.5. The relatively low H_2 and CO concentrations of the Tu12 sample, which plots far from the other Tupungatito gases, are likely related to the extremely low flux of this fumarole, which favors oxidation of these highly reactive gas compounds at shallow depth. The R_H values controlling the equilibrium of reaction *(IV.1)* are slightly more negative than that inferred by the FeO-$FeO_{1.5}$ "rock" buffer (-2.8). This difference is presumably caused by the presence of SO_2 (Table IV-1), which is reduced to H_2S at lower R_H values (*Giggenbach 1987*). However, steam condensation, which has likely affected these low temperature gas discharges, may also control the H_2/H_2O ratios, as H_2 can be partitioned between water and saturated vapor water according to its distribution coefficient (B_{H2}), which ranges from 4.84 (at 100 °C) to 0 at the critical point. In this way, to produce a R_H decrease of 0.2-0.7 (i.e. the difference between -2.8 and the measured R_H values) at the H_2-CO equilibrium temperatures (from 160° to 200 °C), the fraction (*c*) of separated condensed steam (a parameter that ranges from 0 to 1) would have to be in the range from 0.05 to 0.20.

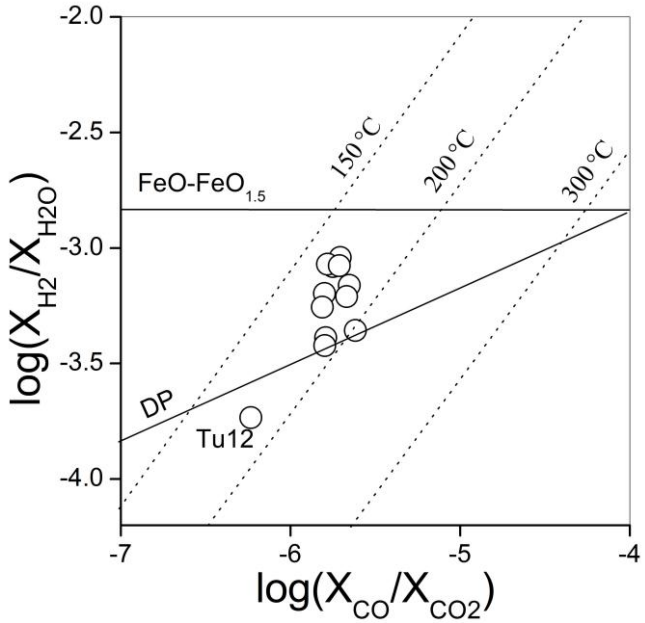

Figure IV-2: $Log(X_{CO}/X_{CO2})$ vs. log(XH2/XH2O) binary diagram. Solid curves refer to the DP (*D'Amore and Panichi 1980*) and FeO-$FeO_{1.5}$ (*Giggenbach, 1987*) redox buffers.

Application of equilibrium thermodynamics in the H_2-CO_2-CO-CH_4-H_2O system can provide useful insights for evaluating temperature and redox conditions that control hydrothermal-magmatic fluids (*Chiodini and Marini 1998*). This approach is based on reaction *(IV.1)* and other four reactions, as follows:

$$3CO_2 + CH_4 \leftrightarrow 4CO + 2H_2O \quad \text{(IV.3)}$$

$$CH_4 + 2H_2O \leftrightarrow 4H_2 + CO_2 \quad \text{(IV.4)}$$

$$CH_4 + H_2O \leftrightarrow 3H_2 + CO \quad \text{(IV.5)}$$

$$CH_4 + CO_2 \leftrightarrow 2H_2 + 2CO \quad \text{(IV.6)}$$

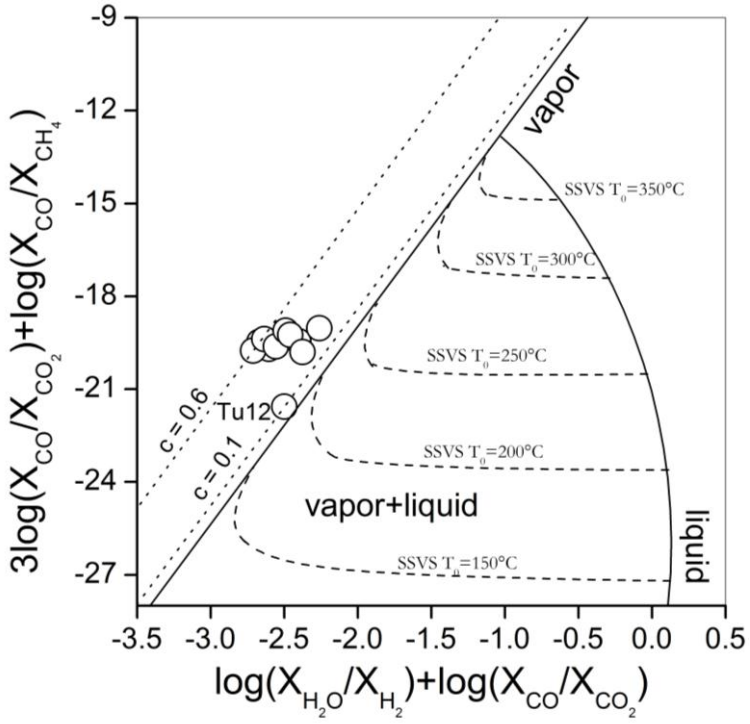

Figure IV-3: $3\log(X_{CO}/X_{CO2}) + \log(X_{CO}/X_{CH4})$ vs. $\log(X_{CO}/X_{CO2}) - \log(X_{H2}/X_{H2O})$ binary diagram. The theoretical values for a single saturated vapor phase (vapor) and single saturated liquid phase (liquid) are shown. Compositions of i) vapors separated in a single step from boiling liquids at T_o = 150°, 200°, 250°, 300° and 350 °C (dashed lines), and ii) single vapor phase affected by separation at T = 100 °C of different fractions (c = 0.3 and c = 0.7) of condensed steam (dotted lines), are also reported.

The equations describing the dependence on temperature of reactions *(IV.1), (IV.3), (IV.4), (IV.5)* and *(IV.6)* can be combined in the redox independent $[\log(X_{CO}/X_{CO2}) + \log(X_{H2O}/X_{H2})]$ and $[3\log(X_{CO}/X_{CO2}) + \log(X_{CO}/X_{CH4})]$ functions. In the $[\log(X_{CO}/X_{CO2}) + \log(X_{H2O}/X_{H2})]$ vs. $[3\log(X_{CO}/X_{CO2}) + \log(X_{CO}/X_{CH4})]$ binary diagram (Figure IV-3) the theoretical compositions of: (i) single saturated vapor phase (vapor), (ii) single saturated liquid phase (liquid), (iii) vapors produced by single-step vapor

separation (SSVP) from boiling liquids of original temperature T_o = 150°, 200°, 250°, 300° and 350 °C (dashed lines), and (iv) single saturated vapor phase after separation at T = 100 °C of different fractions (*c*) of condensed steam (dotted lines), are reported (*Chiodini and Marini 1998*). According to this approach, the Tupungatito fumaroles, with the exception of the Tu12 sample, seem to equilibrate in a single vapor phase at ~220 °C. These calculated temperatures are significantly higher than those calculated on the basis of eq. *(IV.2)*, since reactions *(IV.3)-(IV.6)*, which include CH_4, have a slower kinetics with respect to that of reaction *(IV.1)* (*Giggenbach 1997; Taran and Giggenbach 2003*). Although the fractions of condensed steam, ranging from 0.1 to 0.6, are higher than those evaluated on the basis of water-vapor distribution coefficient of H_2 values (i.e. possibly due to uncertainties in the assumptions of the two approaches), both results show that steam condensation is a significant process affecting the hydrothermal-magmatic fluids feeding the Tupungatito fumaroles.

Dehydrogenation processes involving the C_2 and C_3 alkene-alkane pairs may also be used to obtain insights on chemical-physical conditions of the deep fluid source regions (*Capaccioni and Mangani 2001; Seewald et al. 2001; Taran and Giggenbach 2003; Tassi et al. 2005b*). Dehydrogenation of C_2H_6 and C_3H_8 to produce C_2H_4 and C_3H_6, respectively, are given by:

$$C_2H_6 \leftrightarrow C_2H_4 + H_2 \quad \text{(IV.7)}$$

$$C_3H_8 \leftrightarrow C_3H_6 + H_2 \quad \text{(IV.8)}$$

Using thermochemical data reported by *Reid et al. (1987), Barin (1989), and Domalski and Hearing (1993)*, in the equilibrated vapor the temperature dependence of equilibrium constant for reactions *(IV.7)* and *(IV.8)* are (*Capaccioni et al. 2004*):

$$\log(P_{C2H4}/P_{C2H6}) = 7.43 - 7809/T - \log P_{H2} \quad \text{(IV.9)}$$

$$\log(P_{C3H6}/P_{C3H8}) = 7.15 - 6000/T - \log P_{H2} \quad \text{(IV.10)}$$

, where T is in K and $P_{H2}=P_{tot}*X_{H2}$. Considering that changes of $\log P_{H2O}$ (P_{tot}~P_{H2O}) with temperature for coexisting vapor and liquid water are described by $\log P_{H2O}$ = 5.51 − 2048/T; Giggenbach, 1980), equations *(9)* and *(10)* can be expressed, as follows:

$$\log(P_{C2H4}/P_{C2H6}) = 1.92 - 5761/T - R_H \quad \text{(IV.11)}$$

$$\log(P_{C3H6}/P_{C3H8}) = 1.64 - 4552/T - R_H \quad \text{(IV.12)}$$

At the equilibrium temperatures calculated on the basis of the H_2-CO_2-CO-CH_4-H_2O system (~220 °C), the C_2H_4-C_2H_6 equilibrium is attained at R_H values ranging from -6.5 to -7.1consistentwith those of the SO_2-H_2S redox buffer for SO_2/H_2S ratio of 10, i.e. three orders of magnitude higher than the measured SO_2/H_2S ratio (0.005 to 0.02) (Figure IV-4). The C_3H_6-C_3H_8 pair equilibrates at more reducing conditions (R_H = -5.7 ÷ -6) than those of the C_2H_4-C_2H_6 pair (Figure IV-5), possibly because the C_3-C_3 pair attained equilibrium at shallower depth, i.e. where the influence of magmatic gases is less, than the C_2-C_2 pair, being reaction *(IV.9)* characterized by a slower kinetics with respect to reaction *(IV.10)* (*Lide 2001; Seewald, 2001; Capaccioni et al. 2004*).

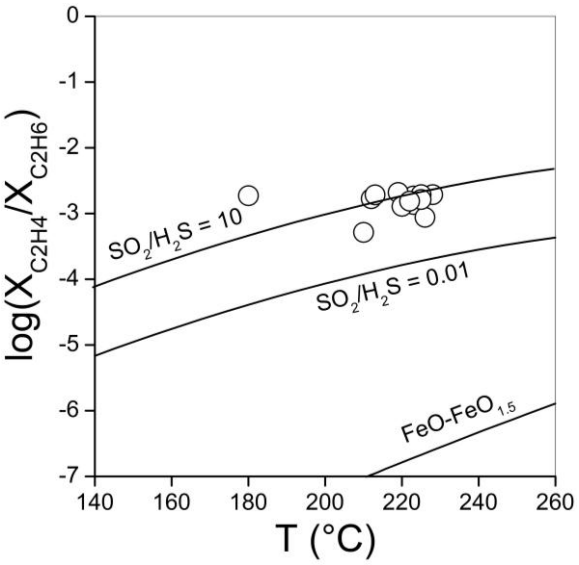

Figure IV-4: Binary diagram of $\log(X_{C2H4}/X_{C2H6})$ vs. calculated temperatures (°C) in the H_2-CO_2-CO-CH_4-H_2O system. Solid curves refer to SO_2-H_2S (SO_2/H_2S equal to 10 and 0.01) and FeO-$FeO_{1.5}$ redox buffer (*Giggenbach 1996*).

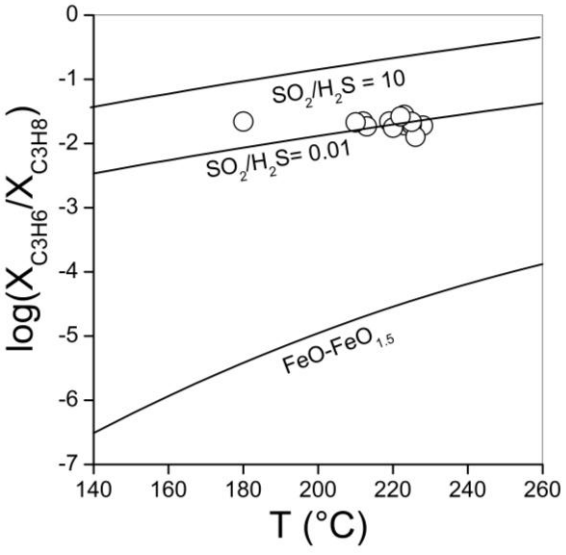

Figure IV-5: Binary diagram of $\log(X_{C3H6}/X_{C3H8})$ vs. calculated temperatures (°C) in the H_2-CO_2-CO-CH_4-H_2O system. Solid curves refer to SO_2-H_2S (SO_2/H_2S equal to 10 and 0.01) and FeO-$FeO_{1.5}$ redox buffer (*Giggenbach 1996*).

IV.5.3 Fumarolic fluid sources

The relatively low outlet temperatures of the Tupungatito fumaroles (from 80.8° to 83.6 °C), which are close to the boiling point of water at 5,200 m a.s.l. (~82.3 °C), unequivocally indicate that liquid water occurs at shallow depth, likely as a result of steam condensation affecting the uprising fluids (*Stevenson 1993*), although a mixture of both hot magmatic gases and groundwater, forming a boiling solution, which at its turn separates at shallow depth, cannot be excluded (*Taran et al. 1997*). The $\delta D\text{-}H_2O$ vs. $\delta^{18}O\text{-}H_2O$ binary diagram (Figure IV-6a), where the Global Meteoric Water Line (GMWL; *Craig 1961*) is reported, shows that the origin of water vapor of the Tupungatito fumaroles, as well as those from Alitar, Irrupucuntu, Lascar, Lastarria, Olca, Putana and Tacora volcanoes (*Tassi et al. 2009, 2011; Aguilera et al. 2011; Capaccioni et al. 2011*), are related to mixing processes between meteoric (MW) and "andesitic" (*Taran et al. 1989; Giggenbach 1992a*) water. If we assume that steam is produced by a simple mixing between these two end-members, the position of the Tupungatito samples in Figure IV-6a apparently corresponds to 52-69% of magmatic water. However, if steam condensation occurs, both the chemical composition (e.g. CO_2/H_2O ratio) and the isotopic signature of water vapor in the fumarolic discharges are expected to be affected (e.g., *Taran et al. 1997; Chiodini et al. 2001; Ohba 2007; Ohba et al. 2011a, 2011b; Shinohara et al. 2011*). The composition of the gas phase after the partial condensation of the water vapor can be modeled by the Rayleigh fractionation process, expressed by:

$$\delta = (\delta_i+1000)F^{\alpha-1}-1000 \quad \text{(IV.13)}$$

$$r = r_iF^{(1/\beta-1)} \quad \text{(IV.14)}$$

, where δ indicates the delta notation of D/H and $^{18}O/^{16}O$ of H_2O, F is the fraction of H_2O vapor left after condensation, α is the isotope fractionation factor between liquid water and vapor for O and H isotopes (1.00509 and 1.0283 at 100 °C respectively; *Horita and Wesolowski 1994*), r is the CO_2/H_2O molar ratio, β corresponds to the CO_2/H_2O distribution factor between liquid water and vapor (0.000215 at 100 °C; *Giggenbach 1980*), and the subscript i is the initial value of the gas before condensation.

Assuming a CO_2/H_2O ratio for meteoric water equal to zero (*Taran et al. 1997*) and considering the fumarolic gases from Lastarria as the most representative end-member of "Andesitic water" for the Andean volcanoes due to its physical-chemical characteristics (e.g. T up to 400 °C, CO_2/H_2O up to 0.2, δD up to -18.1, $\delta^{18}O$ up to

10.7) (Aguilera et al. 2011), Figure IV-6b and 6c show the change in the CO_2/H_2O ratio and δD-$\delta^{18}O$ of H_2O due to condensation. According to this approach, the Tupungatito fumaroles are distributed between the condensation curves that represent initial mixtures between 60 and 90% of magmatic vapor with condensed steam fraction values (c=1-F) ranging from 0.2 to 0.6 (F ranging between 0.4 and 0.8), similar to those obtained in section IV.5.2. Figure 6b and 6c also show the "Primary steam" (PS) line, which represents the composition of steam generated at shallow depth (100 °C) by mixing of meteoric water and magmatic vapor (at 10 and 900 °C, respectively) (*Giggenbach and Stewart, 1992*). The Tupungatito fumaroles could also be explained as a mixture between Andesitic water and 10 to 20% of PS. However, this cannot simply be evaluated with a mixing line, because a mixture between >50% magmatic fluids and "Primary Steam", as calculated for the Tupungatito samples (Figure IV-6b-c), will not produce a fumarolic gas at boiling temperatures (~82 °C). Thus, the hypothesis of a mixing between magmatic fluids and vapor derived from a shallow evaporated aquifer can likely be discarded. The higher condensed steam fraction values and lower initial mixtures calculated in the CO_2/H_2O-$\delta^{18}O$-H_2O plot (Fig 6c) with respect to Figure IV-6b can be attributed to ^{18}O re-equilibration between H_2O-CO_2 (Figure IV-6d), which shifts the initial $\delta^{18}O$ data to lower values. Following the approach proposed by *Chiodini et al. (2000),* isotopic fractionation related to H_2O-CO_2 interactions were calculated according to the following equation:

$$\delta^{18}O\text{-}H_2O_{ini} = \delta^{18}O\text{-}H_2O + [2X_{CO2}/(1 + X_{CO2})] \times [1000\ln\alpha\ (T_i) - 1000\ln\alpha\ (T_{meas})] \quad (IV.15)$$

, where T_i is 220 °C (which is the average of the H_2-CO_2-CO-CH_4-H_2O equilibrium temperatures excluding the Tu12 sample; Figure IV-3), $\delta^{18}O$-H_2O_{ini} represents the $\delta^{18}O$-H_2O composition of steam at the H_2-CO_2-CO-CH_4-H_2O equilibrium conditions, T_{meas} is the fumarolic outlet temperature, X_{CO2} is the CO_2 molar fraction, and α is the oxygen isotope fractionation factor between $CO_{2(g)}$ and $H_2O_{(g)}$, whose temperature dependence can be described, as follows (*Chiodini et al. 2000*):

$$1000\ln\alpha = -5.7232 + 20.303(10^3/T) - 11.977(10^6/T^2) + 3.7432(10^9/T^3) \quad (IV.16)$$

Equation *(IV.15)* shows that the initial $\delta^{18}O$-H_2O value depends on both $\delta^{18}O$-H_2O and X_{CO2} values, which at their turn depend on the fraction of H_2O vapour left after condensation (F). Using eq. *(IV.13)*, the initial values of the gas before condensation were calculated and plotted in Figure IV-6d (solid red lines). The fractionation lines (dotted black lines) on Figure IV-6d were constructed by applying eq. *(15)*, using the

$\delta^{18}O\text{-}H_2O$ and X_{CO2} values calculated for the effects of steam condensation by eq. *(IV.13)* and *(IV.14)* (blue solid lines). The X_{CO2} values were calculated considering that water vapor and CO_2 are the most common gases in volcanic systems (X_{CO2}+ X_{H2O}~1; *Giggenbach 1980*). The interceptions between solid blue lines and the MW-andesitic water mixing line (solid black line) (Figure IV-6d), indicate that (i) the fraction of magmatic water in vapors equilibrated in the $H_2\text{-}CO_2\text{-}CO\text{-}CH_4\text{-}H_2O$ system ranges from 78% to 99% (samples Tu11 and Tu3 respectively), and (ii) *c* ranges from 0.45 to 0.78 (samples Tu7 and Tu9 respectively), consistent with the condensate fraction values estimated above (Figure IV-3, 6b and 6c).

The dominant magmatic signature of the vapor isotopes is consistent with the occurrence of SO_2, HCl and HF in the fumarolic fluids (Table IV-1). Hence, the liquid dominated system, whose boiling produces vapors feeding the Tupungatito fumaroles, is not able to completely scrub the highly soluble and reactive gases released from the magmatic source, possibly because it is not well developed and has a low pH (*Symonds et al. 2001*). The $CH_4/(C_2H_6+C_3H_8)$ ratios (from 83 to 223) of the fumarolic fluids are significantly higher than those typically measured in hydrothermal fluids (<100) from sedimentary and volcanic domains (e.g. *Oremland et al. 1987; Whiticar and Suess 1990; Jenden et al. 1993; Whiticar 1999; Zelenski and Taran 2001; Tassi et al. 2012*). The CH_4-excess may be caused by the relatively low stability of C_{2+} compounds with respect to that of CH_4 under relatively high temperatures. The occurrence of comparable amounts of (i) alkenes (C_2H_4, C_3H_6 and C_4H_8) and furan (C_4H_4O), formed at oxidizing conditions and relatively high temperatures (Capaccioni et al. 1995), and (ii) aromatics (C_6H_6 and C_7H_8) and thiophene (C_4H_4S), produced by catalytic reactions favored at reducing conditions (*Tassi et al. 2010*), corroborate the hypothesis that the Tupungatito gas discharges are mostly sourced by magmatic fluids interacting with a limited hydrothermal aquifer, which is not able to reduce all the gas species formed at oxidizing conditions.

The ternary N_2-Ar-He diagram (Figure IV-7) proposed by *Giggenbach (1992b)* is commonly used to constrain potential sources of these gases, such as crustal and mantle fluids, and air contamination. The Tupungatito fumaroles show very high N_2/Ar ratios (up to 1,479) relative to air (83.6), typical of arc volcanoes including those of CVZ (*Tassi et al. 2009a, 2011; Aguilera et al. 2011; Capaccioni et al. 2011*). This indicates a non-atmospheric source for N_2, suggesting that (i) the mantle source is affected by contamination of organic-rich sediments in the subducted slab (*Matsuo et al. 1978; Jenden et al. 1988; Giggenbach 1997; Snyder et al. 2003*) and, (ii) possible addition of

crustal fluids to the magmatic system. This hypothesis is also supported by the helium isotopic composition (R/Ra from 5.06 to 6.09), which is consistent with the wide R/Ra range characterizing fluids related to continental and arc volcanoes (between 3 and 8) (*Craig and Lupton 1976; Poreda and Craig 1989; Ballentine et al. 2002; Hilton et al. 2002*).

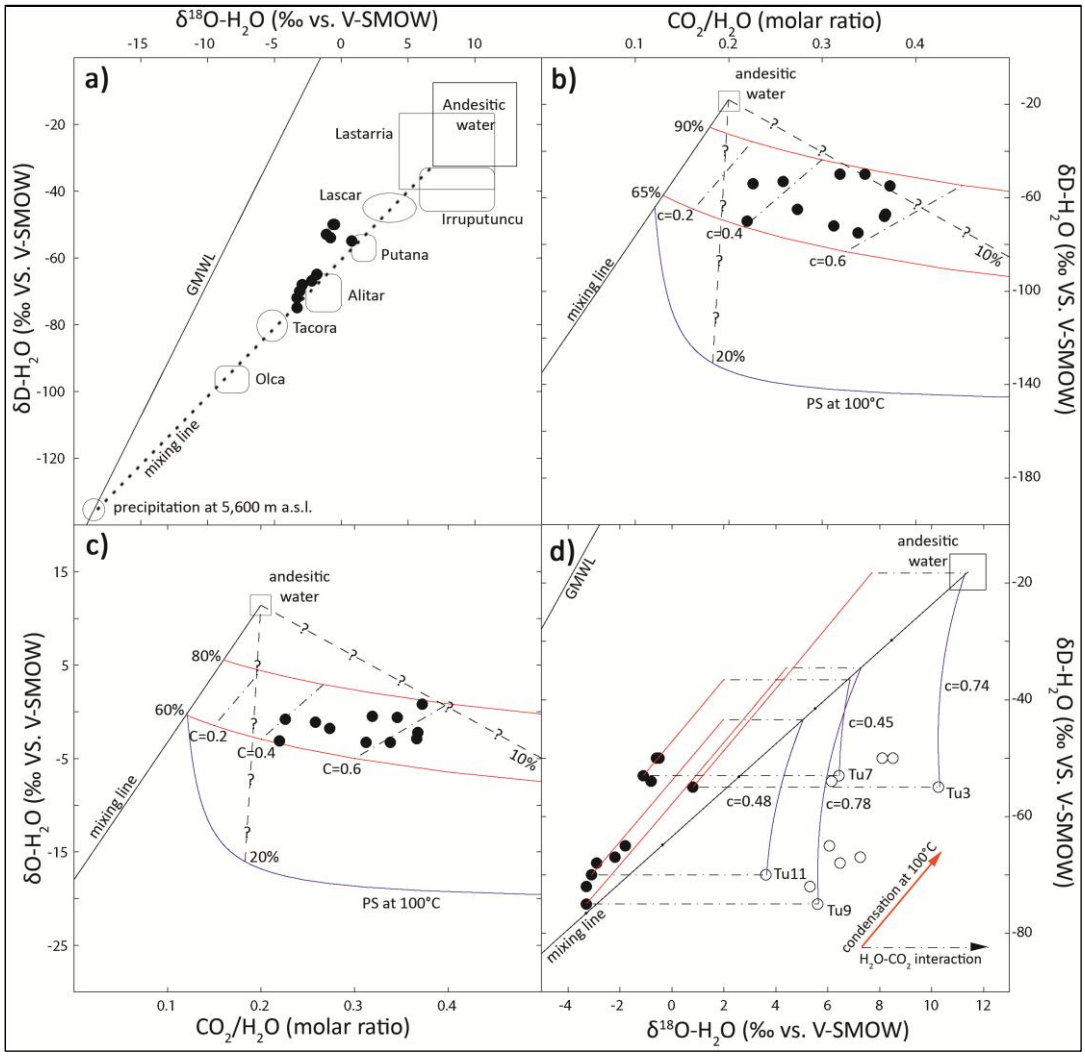

Figure IV-6: (a) $\delta^{18}O$-H_2O vs. δD-H_2O diagram of steam from the Tupungatito fumaroles. Andesitic water field (*Taran et al., 1989; Giggenbach, 1992*), Global Meteoric Water Line (GMWL; *Craig, 1961*), isotopic composition of the meteoric water (MW) at 5,600 m a.s.l. (δD~-135‰ and $\delta^{18}O$~-18‰; *Capaccioni et al. 2011*), mixing line between meteoric and Andesitic water, and isotopic composition of Alitar, Irrupucuntu, Lascar, Lastarria, Olca, Putana and Tacora volcanoes (*Tassi et al. 2009, 2011; Aguilera et al. 2011; Capaccioni et al. 2011*) are reported. (b)-(c) CO_2/H_2O molar ratio vs. δD-H_2O and CO_2/H_2O molar ratio vs. $\delta^{18}O$-H_2O diagrams of steam from the Tupungatito fumaroles. Andesitic water field (Aguilera et al. 2012), mixing line between meteoric and Andesitic water, condensation curves which represent initial mixture of 65 and 90% magmatic vapor, condensed steam fraction ranging from 0 .2 to 0.6, "Primary Steam" line at 100°C (Taran et al. 1997), and mixing lines between Andesitic water and 10 and 20% of "Primary Steam" are reported. (d) Detail of the $\delta^{18}O$-H_2O vs. δD-H_2O diagram of steam from the Tupungatito fumaroles. Isotopic compositions produced by i) steam condensation at 100 °C (solid red line) and ii) H_2O-CO_2 isotopic exchange from 220 °C to outlet temperatures, calculated for condensed steam fraction (*c*) ranging from 0 to 0.78, were also reported (solid blue line).

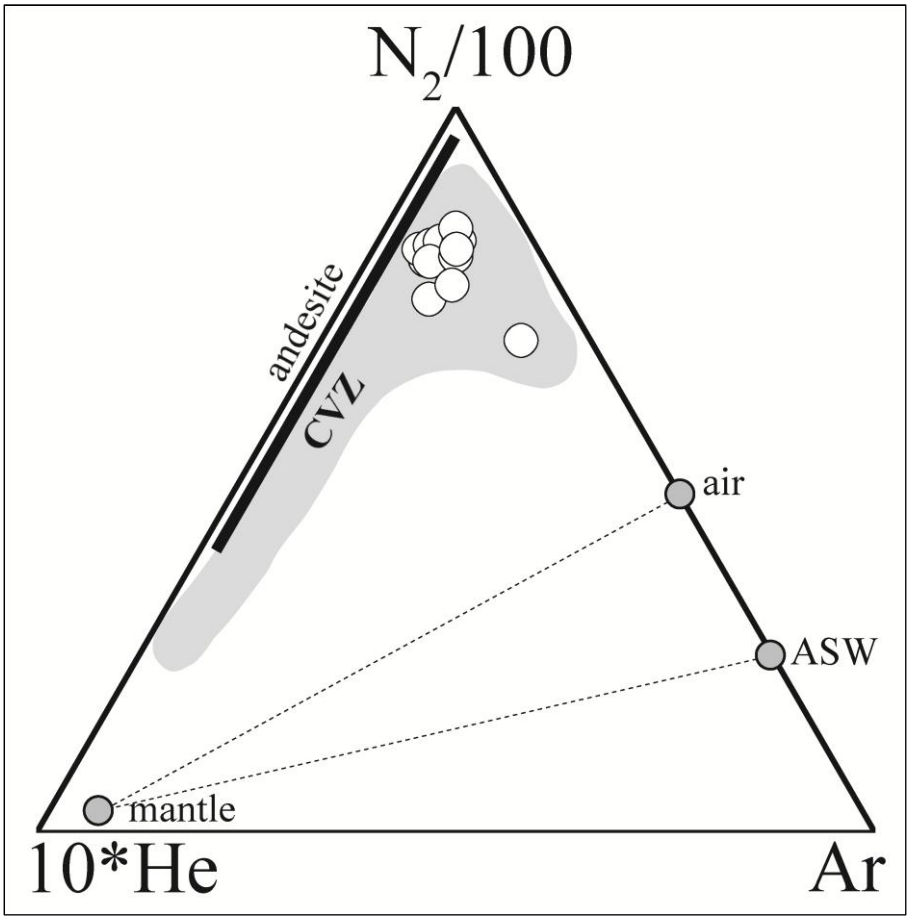

Figure IV-7: N_2/100-Ar-He*10 diagram for the Tupungatito thermal discharges (*Giggenbach 1992b*). Air and Air Saturated Waters (ASW) compositions and convergent plate boundaries ("andesite") field (*Giggenbach 1996*) are also reported. The compositional fields (SVZ) of the Lastarria, Lascar, Irrupucuntu, Putana, Alitar, Olca and Tacora fumarolic gases (*Tassi et al. 2009a, 2011; Aguilera et al. 2011; Capaccioni et al. 2011*) are plotted for comparison.

The $CH_4/^3He$ ratios (2.79 to 9.06 x 10^7; Table IV-3) are significantly higher than those measured in sediment-free mid-ocean ridge environment (between 1×10^5 and 1×10^6; *Snyder et al. 2003*), suggesting significant contribution of crustal fluids rich in both thermogenic and/or biogenic CH_4, which is consistent with the "crustal signatures" of the Tupungatito lavas (Section IV-2) Unfortunately, isotope data of CH_4, which are useful to discriminate different mechanisms for the origin of this compound (e.g., *Schoell 1980, 1988*), are not available for the Tupungatito gases.

The $^{40}Ar/^{36}Ar$ ratios (from 304 to 461) are higher than that of air (295.5), indicating that 3 to 36% of the Ar is likely related to the radiogenic decay of ^{40}K, the latter being typically enriched in the crust. Fluids from the upper mantle can also be considered an important source of ^{40}Ar-enriched fluids, although ^{40}Ar concentrations are not

homogeneously distributed in the mantle since MORB lavas are characterized by $^{40}Ar/^{36}Ar$ ratios up to 28,000 (*Sarda et al. 1985; Farley and Poreda 1993*). By assuming that ^{36}Ar is entirely derived from air and $^{40}Ar/^{36}Ar$ ratio in air = 295.5, the concentration of radiogenic Ar ($^{40}Ar^*$) in gas samples can be calculated, as follows:

$$^{40}Ar^* = {}^{40}Ar - 295.5 \times {}^{36}Ar \qquad \text{(IV.17)}$$

The $^{40}Ar^*/^4He$ ratio is a useful tracer of noble gas fractionation during volatile exsolution from magma (*Marty 1995; Sarda and Moreira 2002*). The $^{40}Ar^*/^4He$ ratio produced by the present-day radiogenic decaying process in the mantle, calculated on the basis of measured K/(U+Th) ratios in MORB and the "bulk earth" value of 0.55 for 4.5 Ga of radiogenic production, is ~0.27 ±0.02 (*Jochum et al. 1983*), a value slightly lower than those of Tupungatito gases (from 0.47 to 3.59; Table IV-3).

The $CO_2/^3He$ ratios and the $\delta^{13}C\text{-}CO_2$ values are commonly used as diagnostic parameters to distinguish fluid contributions from crust, mantle and atmosphere (Marty and Jambon 1987; O'Nions and Oxburg 1988). The $CO_2/^3He$ ratios in the Tupungatito fumaroles range from 1.27×10^{11} to 2.44×10^{11} (Table IV-3), i.e. more than one order of magnitude higher than the MORB ratio (1.41×10^9*; Marty and Jambon 1987; Sano and Marty, 1995*). This suggests that CO_2 is not only related to mantle (M) degassing, but it partially derives from limestone (L) and/or organic-rich sediments (S). The relative contribution of each one of these potential CO_2 sources can be evaluated, as follows (*Sano and Marty 1995*):

$$M + S + L = 1 \qquad \text{(IV.18)}$$

$$(\delta^{13}C\text{-}CO_2)_{meas} = M(\delta^{13}C\text{-}CO_2)_{MORB} + L(\delta^{13}C\text{-}CO_2)_{Lim} + S(\delta^{13}C\text{-}CO_2) \qquad \text{(IV.19)}$$

$$[1/(CO_2/^3He)]_{meas} = [M/(CO_2/^3He)]_{MORB} + [L/(CO_2/^3He)]_{Lim} + [S/(CO_2/^3He)]_{Sed} \qquad \text{(IV.20)}$$

, where subscripts *meas*, *MORB*, *Lim* and *Sed* refer to the sample, MORB (a proxy to the upper mantle), limestone and organic sediment, respectively.

Following *Sano and Marty (1995),* we assume that the end members have the following values:

$(\delta^{13}C\text{-}CO_2)_{MORB}$ = -5‰; $(\delta^{13}C\text{-}CO_2)_{Sed}$ = -30‰; $(\delta^{13}C\text{-}CO_2)_{Lim}$ = 0‰; $(CO_2/^3He)_{MORB} = 1.5 \times 10^9$; $(CO_2/^3He)_{Sed} = 1 \times 10^{13}$; $(CO_2/^3He)_{Lim} = 1 \times 10^{13}$.

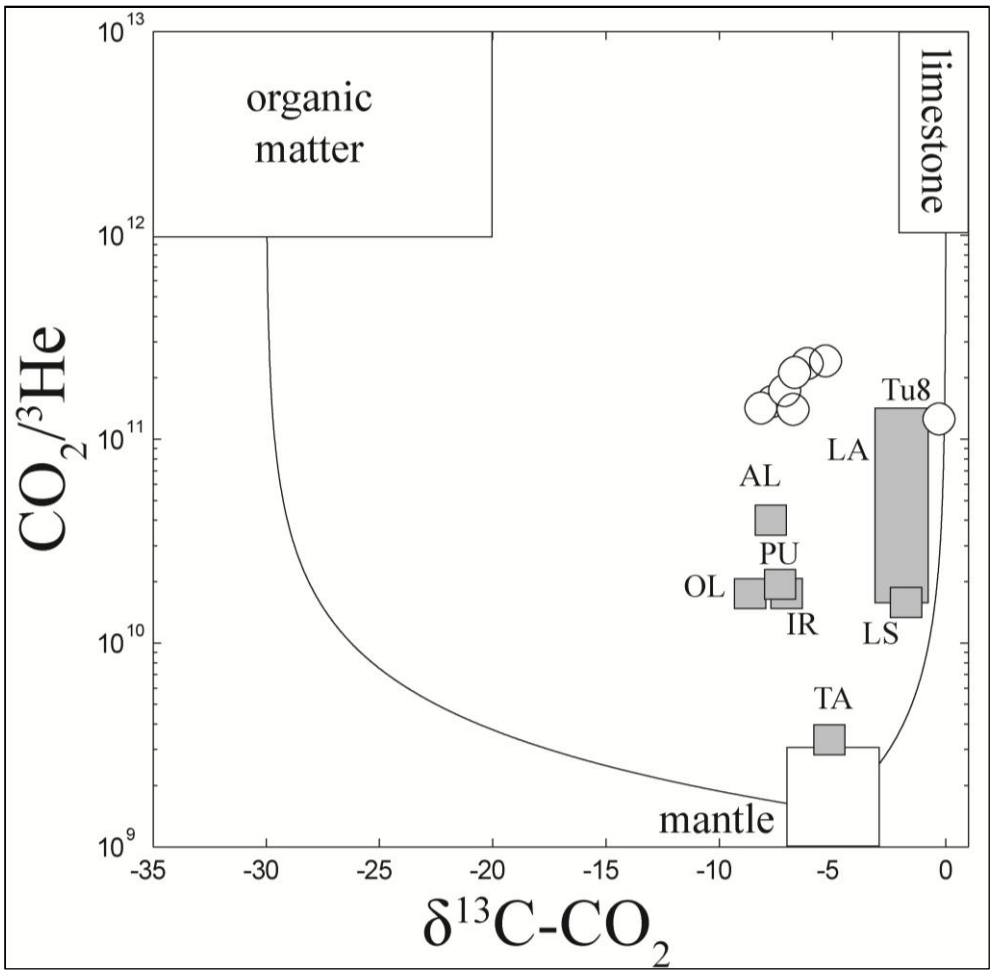

Figure IV-8: $CO_2/^3He$ vs. $\delta^{13}C\text{-}CO_2$ diagram for the Tupungatito gas discharges. Gases from organic-rich sediments (S), limestone (L) and mantle (M) (Sano and Marty 1995) are reported. The compositional fields of the Lastarria (LS), Lascar (LA), Irrupucuntu (IR), Putana (PU), Alitar (AL), Olca (OL) and Tacora (TA) volcanoes (*Tassi et al. 2009a; Aguilera et al. 2011; Capaccioni et al. 2011; Tassi et al. 2011*) gases are plotted for comparison.

According to eqs. *(IV.18)*, *(IV.19)* and *(IV.20)*, CO_2 is mostly produced from carbonates of the subducting slab and the basement (L from ~64% to ~90%), whereas sediments are to be regarded as a secondary CO_2 source. These results are consistent with those of fluid discharges from several volcanoes of the CVZ, such as Alitar (AL), Olca (OL), Putana (PU) and Irrupucuntu (IR) (*Tassi et al. 2011*), whereas gases from Tacora (TA), Lascar (LA) and Lastarria volcanoes (LS) (*Tassi et al. 2009a; 2011; Aguilera et al. 2011; Capaccioni et al. 2011*), which are located in the same area, plot between M and L CO_2 sources with S <10% (Figure IV-8). This implies that subducted slab age (Eocene at 17.5°S to Quaternary at 46°S*; Ramos et al. 2004*), slab thermal state (*Grevemeyer et al. 2003*), and type and amount of material subducted (*von Huene and Scholl 1991; Strand 1995; Contreras-Reyes et al. 2010*), which significantly

change from north to south along the Chilean margin, do not have a significant influence on the $CO_2/^3He$ and $\delta^{13}C\text{-}CO_2$ ratios. In contrast, the relative proportions of hydrothermal and magmatic gases, a feature peculiar to each volcano that depends on its state of activity and fluid circulation pattern, seem to exert a strong control on chemical and isotopic compositions of He and CO_2. Separation of solid (such as calcite) and liquid phases likely occurring during fluid uprising may explain the measured variations of the $\delta^{13}C\text{-}CO_2$ values in the Tupungatito fumaroles (from -8.16‰ to -5.31‰ vs. V-PDB; Table IV-3) (e.g., *Ray et al. 2009; de Leeuw et al. 2010*). The high $\delta^{13}C\text{-}CO_2$ value (-0.30‰ vs. V-PDB; Table IV-3) of the bubbling gas sample (Tu8) might be due to kinetic fractionation processes related to the lake degassing temperature (>30 °C) and relative proportions of the different carbon species (e.g. *Mook et al 1974*) dissolved in the lake and not to a different carbon source.

IV.6 CONCLUSIONS

The fumarolic activity at Tupungatito volcano is related to uprising of magmatic fluids partially scrubbed by a hydrothermal aquifer, whose boiling produces vapors that are affected by steam condensation as they approach the surface. The $\delta^{13}C\text{-}CO_2$ and $CO_2/^3He$ ratios suggest (i) mantle contamination by limestone from the subducting Nazca Plate and/or (ii) interaction between the magmatic source and the crustal basement. However, the helium isotopic composition (R/Ra from 5.06 to 6.09), $CH_4/^3He$ ratios (2.8 to 9.1 x 10^6) as well as the “crustal signatures” of the Tupungatito lavas, suggest that the contribution of crustal fluids is likely an important process controlling the composition of the Tupungatito fluids.

A conceptual geochemical model of the Tupungatito fluid circulation pattern, showing fluid source regions and chemical physical conditions inferred by chemical equilibrium regulating the composition of gases at different depths, is plotted in Figure IV-9. Primary fluids originating from magma degassing are partially “filtered” by an overlying aquifer whose boiling produces gases enriched in reduced gas species, such as H_2, CO, CH_4 and H_2S. Fumarolic fluids show the signature of a magmatic source (CO_2, He, N_2, SO_2 HCl, HF and andesitic water), notwithstanding the fact that they are affected by condensation of a significant (up to 0.78) steam fraction. Chemical reactions in the $H_2O\text{-}CO_2\text{-}CH_4\text{-}CO\text{-}H_2$ system attain equilibrium in a separated vapor phase at a temperature ~220 °C, where the C_2 alkane-alkene pair also equilibrates under redox conditions typical of an environment dominated by magmatic fluids. On the contrary, dehydrogenation of C_3H_8 re-equilibrates at more reducing conditions and/or

lower temperatures. Chemical reactions regulating H_2 and CO, rapidly responding to changes of chemical-physical conditions affecting the uprising hydrothermal-magmatic vapors, record temperatures down to 160 °C and redox conditions approaching those of the hydrothermal “rock” buffer.

The results presented in this work can be used for future geochemical monitoring programs due to the recent and relatively intense volcanic activity showed by Tupungatito volcano in the last 180 years.

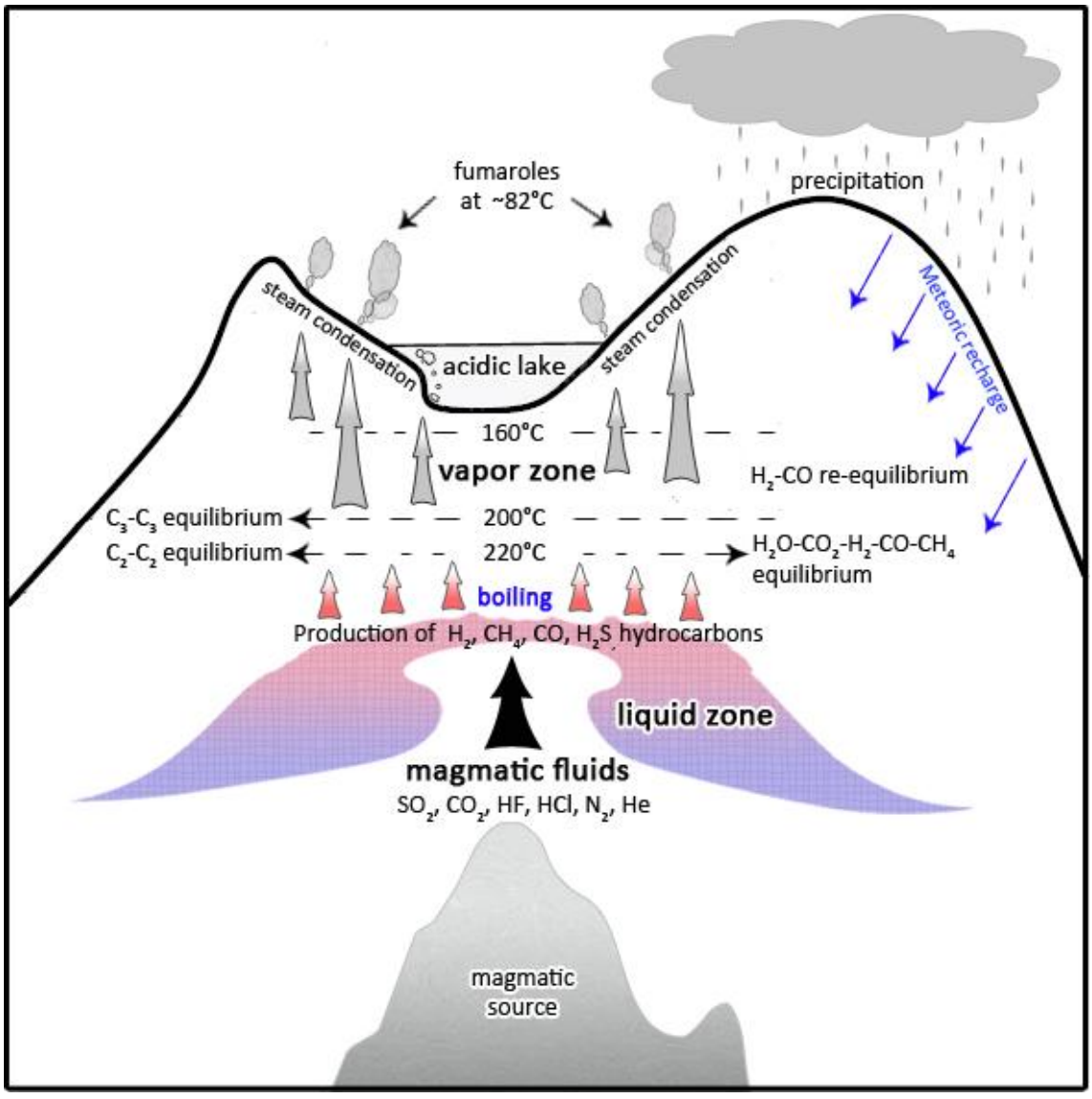

Figure IV-9: Conceptual geochemical model of fluid circulation at the Tupungatito volcanic system.

REFERENCES

Aguilera F, Tassi F, Darrah T, Moune S, Vaselli O (2012). Geochemical model of a magmatic hydrothermal system at the Lastarria volcano, northern Chile. Bull Volcanology. Bull. Volcanol 74:119–134.

Ballentine CJ, Sherwood Lollar B (2002) Regional groundwater focusing of nitrogen and noble gases into the Hugoton-Panhandle giant gas field, USA. Geochim Cosmoch Acta 66–14:2483–2497.

Barazangi M, Isacks B (1976) Spatial distribution of earthquakes and subduction of the Nazca plate beneath. South America. Geology 4:606–692.

Barin I (1989) Thermochemical Data on Pure Substances. Vol. 1, VCH, Wenheim.

Botcharnikov R, Shmulovich K, Tkachenko I, Korzhinsky A, Rybin V (2003) Hydrogen isotope geochemistry and heat balance of a fumarolic system: Kudriavy volcano, Kuriles. J Volcanol Geotherm Res 124(1–2):45–66.

Brantley SL, Agustsdottir AM, Rowe GL (1993) Crater lakes reveal volcanic heat and volatile fluxes. Geol Soc Am Today 3:175–178.

Cande S, Leslie R (1986) Late Cenozoic tectonics of the southern Chile Trench. J Geophys Res 91:471–496.

Cande S, Leslie R (1987) Interaction between the Chile Ridge and Chile Trench: geophysical and geothermal evidence. J Geophys Res 92:495–520.

Capaccioni B, Martini M, Mangani F (1995) Light hydrocarbons in hydrothermal and magmatic fumaroles: hints of catalytic and thermal reactions. Bull Volcanol 56:593–600.

Capaccioni B, Mangani F (2001) Monitoring of active but quiescent volcanoes using light hydrocarbon distribution in volcanic gases: the results of 4 years of discontinuous monitoring in the Campi Flegrei (Italy). Earth Planet Sci Lett 188:543–555.

Capaccioni B, Taran Y, Tassi F, Vaselli O, Mangani G, Macias JL (2004) Source conditions and degradation processes of light hydrocarbons in volcanic gases: an example from El Chichón volcano (Chiapas State, Mexico). Chem Geol 206:81–96.

Capaccioni B, Aguilera F, Tassi F, Darrah T, Poreda RJ, Vaselli O (2011) Geochemical and isotopic evidences of magmatic inputs in the hydrothermal reservoir feeding the fumarolic discharges of Tacora volcano (northern Chile). J Volcanol Geotherm Res 208:77–85.

Chiodini G, Marini L (1998) Hydrothermal gas equilibria: The H2O-H2-CO2-CO-CH4 system. Geochim Cosmochim Acta 62:2673–2687.

Chiodini G, Allard P, Caliro S, Parello F (2000) 18O Exchange between steam and carbon dioxide in volcanic and hydrothermal gases: Isotopic and genetic implications. Geochim Cosmochim Acta 64:2479–2488.

Chiodini G, Marini L, Russo M (2001) Geochemical evidence for the existence of high-temperature hydrothermal brines at Vesuvio volcano, Italy. Geochim Cosmochim Acta 65:2129–2147.

Christenson BW, Wood CP (1993) Evolution of a vent hosted hydrothermal system beneath Ruapehu crater. NZ. Bull Volcanol 55:547–565.

Coleman ML, Shepherd TJ, Rouse JE, Moore GR (1982) Reduction of water with zinc for hydrogen isotope analysis. Anal Chem 54:993–995

Contreras-reyes E, Flueh ER, Grevemeyer I (2010) Tectonic control on sediment accretion and subduction off south-central Chile: Implications for coseismic rupture processes of the 1960 and 2010 megathrust earthquakes. Tectonics 29:1–32.

Craig H (1961) Isotopic variations in meteoric waters. Science 133:1702–1703.

Craig H, Lupton JE (1976) Primordial neon, helium and hydrogen in oceanic basalts. Earth Planet Sci Lett 31:369–385.

D'Amore F, Panichi C (1980) Evaluation of deep temperature of hydrothermal systems by a new gas-geothermometer. Geochim Cosmochim Acta 44:549–556.

Delmelle P, Bernard A, Kusakabe M, Fisher TP, Takano B (2000) Geochemistry of the magmatic-hydrothermal system of Kawah Ijen volcano, East Java, Indonesia. J Volcanol Geotherm Res 97:31–53.

Domalski ES, Hearing ED (1993) Estimation of the thermodynamic properties of C–H–N–O–S–halogen compounds at 298.15 K. J Phys Chem Ref 22:805–1159.

Epstein S, Mayeda TK (1953) Variation of the 18O/16O ratio in natural waters. Geochim Cosmochim Acta 4:213–224.

Evans WC, White LD, Rapp JB (1998) Geochemistry of some gases in hydrothermal fluids from the southern Juan de Fuca ridge. J Geophys Res 15:305–313.

Farley KA, Poreda RJ (1993) Mantle neon and atmospheric contamination. Earth Planet Sci Lett 114:325–339.

Garreaud R (2009) The Andes climate and weather. Adv Geosc 7:1–9.

Giambiagi LB, Ramos VA (2002) Structural evolution of the Andes in a transitional zone between flat and normal subduction (33°30'-33°45′S), Argentina and Chile. J South Am Earth Sci 15:101–116.

Giggenbach W.F. (1975). A simple method for the collection and analysis of volcanic gas samples. Bull Volcanol 39: 132-145.

Giggenbach WF (1980) Geothermal gas equilibria. Geochim Cosmochim Acta 44:2021–2032.

Giggenbach WF (1984) Mass transfer in hydrothermal alteration systems-A conceptual approach. Geochim Cosmochim Acta 48:2693–2711.

Giggenbach WF (1987) Redox processes governing the chemistry of fumarolic gas discharges from White island, New Zealand. Appl Geochem 2:143–161.

Giggenbach WF (1988) Geothermal solute equilibria, derivation of Na-K-Mg-Ca geoindicators. Geochim Cosmochim Acta 52:2749–2765.

Giggenbach WF (1992a) Isotopic shifts in waters from geothermal and volcanic systems along margins, and their origin. Earth Planet Sci Lett 113:495–510.

Giggenbach W F (1992b) The composition of gases in geothermal and volcanic systems as a function of tectonic setting. Proc Int Symp Water-Rock Interaction, WRI-8, 873–878.

Giggenbach WF (1993) Redox control of gas compositions in Philippine volcanic-hydrothermal systems. Geothermics 22:575–587.

Giggenbach WF (1996) Chemical composition of volcanic gases. In: Scarpa M, Tilling R (eds) Monitoring and Mitigation of Volcanic Hazards, Springer, Berlin, pp. 221–256.

Giggenbach WF (1997) The origin and evolution of fluids in magmatic-hydrothermal systems. in Barnes HL (ed) Geochemistry of hydrothermal ore deposits, 3rd edition, New York, John Wiley, pp. 737–796.

González-Ferrán O (1995) Volcanes de Chile. Instituto Geográfico Militar, Santiago, Chile, 639 pp.

Grevemeyer I, Juan L Diaz-Naveas, Cesar R Ranero, Heinrich W Villinger, Ocean Drilling Program Leg 202 Scientific Party (2003) Heat flow over the descending Nazca plate in central Chile, 32°S to 41°S: observations from ODP Leg 202 and the occurrence of natural gas hydrates. Earth Planet Sci Lett 213:285–298.

Hildreth W, Moorbath S (1988) Crustal contributions to arc magmatism in the Andes of Central Chile. Contrib Mineral Petrol 98:455–489.

Hilton DR, Fischer TP, Marty B (2002) Noble Gases and Volatile Recycling at Subduction Zones. Rev Mineral Geochem 47:319–370.

Horita J, Cole DR, Wesolowski DJ (1994) Liquid-vapor fractionation of oxygen and hydrogen isotopes of water from the freezing to the critical temperature. Geochim. Cosmochim. Acta, 58:3425–3437, 1994.

Jenden PD, Kaplan IR, Poreda RJ, Craig H (1988) Origin of nitrogen-rich gases in the Californis Great Valley: evidence from helium, carbón and nitrogen isotope ratios. Geochim Cosmochim Acta 52:851–861.

Jenden PD, Hilton DR, Kaplan IR, Craig H (1993) Abiogenic hydrocarbons and mantle helium in oil and gas fields. In: Howell DG (ed) The Future of Energy Gases, US Geological Survey Professional Paper, 1570, pp. 31–56.

Jochum KP, Hokman AW, Ito E, Seufert HM, White WM (1983) K, U, and Th in mid-ocean ridge basalt glasses and heat production, K/U and K/Rb in the mantle. Nature 306:431–436.

de Leeuw GMA, Hilton GA, Gulec DR, Mutlu N (2010) Regional and temporal variations in CO2/3He, 3He/4He and d13C along the North Anatolian Fault Zone, Turkey. Appl Geochem 25:524–539.

Lide DR (2001) Handbook of chemistry and physics, 82nd edn. CRC, Boca Raton, Florida, USA

Mamyrin BA, Tolstikhin IN (1984) Helium isotopes in nature. In: Fyfe WS (eds) Development in geochemistry, Elsevier, Amsterdam, pp. 288

Martini M, Giannini L, Buccianti A, Prati F, Cellini-Le- gittimo P, Iozzelli P, Capaccioni B (1991) 1980-1990: Ten years of geochemical investigation at Phlegrean Fields (Italy). J Volcanol Geotherm Res 48:161–171.

Marty B, Jambon A (1987) C/3He in volatile fluxes from the solid earth—implications for carbon geodynamics. Earth Planet Sci Lett 83:16–26.

Matsuo S, Suzuki J, Mitzutani Y (1978) Nitrogen to argon ratio in volcanic gases. In: Alexander EC, Ozima M. (eds) Terrestrial Rare Gases. Japan Science Society Press, Tokyo, pp. 17–25.

Montegrossi G, Tassi F, Vaselli O, Buccianti A, Garofalo K (2001) Sulfur species in volcanic gases. Anal Chem 73:3709 – 3715.

Mook WG, Bemmerson JC, Steverman WH (1974) Carbon isotope fractionation between dissolved bicarbonate and gaseous carbon dioxide. Earth Planet Sci Lett 22:169–176.

Moreno H, Naranjo JA (1991) The southern Andes volcanoes (33°-41° 30' S), Chile. 6th Geol Cong Chile, Excur PC-3, pp. 26.

Ohba T (2007) Formation process of recent fumarolic gases at the Mt. Mihara summit peak of the Izu-Oshima volcano, Japan. Earth Planets Space 59:1127–1133.

Ohba T, Daita Y, Sawa T, Taira N, Kakuage Y (2011a) Coseismic changes in the chemical composition of volcanic gases from the Owakudani geothermal area on Hakone volcano, Japan. Bull Volcanol 73:457–469.

Ohba T, Nogami K, Hirabayashi J, Sawa T, Kazahaya K, Morikawa N, Ohwada M (2011) Chemical and isotopic composition of fumarolic gases at Iwate volcano, Japan, during and after seismic activity in 1998: implications for the modification of ascending volcanic gases. Ann Geophys 54(2):187–197.

Oremland RS, Miller LG, Whiticar MJ (1987) Sources and flux of natural gases from Mono Lake, California. Geochim Cosmochim Acta 51:2915–2929.

Pasternack GB, Varekamp JC (1997) Volcanic lake systematics I. Physical constraints. Bull Volcanol 58:528–538.

Poreda R, Craig H (1989) Helium isotope ratios in Circum-Pacific volcanic arcs. Nature 338:473–478.

Ramos VA, Cristallini E, Introcaso A (2004) The Andean thrust system latitudinal variations in structural styles and orogenic shortening. AAPG Spec Vol Memoir 82: Thrust tectonics and hydrocarbon systems, pp. 30–50.

Ray M, Hilton D, Muñoz J, Fischer T, Shaw A (2009). The effects of volatile recycling, degassing and crustal contamination on the helium and carbon geochemistry of hydrothermal fluids from the Southern Volcanic Zone of Chile. Chem Geol 266(1–2):38–49.

Reid RC, Prausnitz JM, Poling BE, (1987) The Properties of Gases and Liquids. McGraw-Hill, New York, pp. 768.

Sano Y, Marty B (1995) Origin of carbon in fumarolic gas from island arcs. Chem Geol 119:265–274.

Sarda P, Staudacher T, Allegre CJ (1985) 40Ar/36Ar in MORB glasses: Constraints on atmosphere mantle evolution. Earth Planet Sci Lett 72:357–375.

Schoell M (1980) The hydrogen and carbon isotopic composition of methane from natural gases of various origins. Geochim Cosmochim Acta 44:649–661.

Schoell M (1988) Multiple origins of methane in the Earth. Chem Geol 71:1–10.

Seewald JS (2001) Aqueous geochemistry of low molecular weight hydrocarbons at elevated temperatures and pressures: constraints from mineral buffered laboratory experiments. Geochim Cosmochim Acta 65:1641–1664.

Sepúlveda F, Lahsen A, Powell T (2007) Gas geochemistry of the Cordón Caulle geothermal system, Southern Chile. Geothermics 36: 389-420

Shinohara H, Hirabayashi J, Nogami K, Igushi M (2011) Evolution of volcanic gas composition during repeated culmination of volcanic activity at Kuchinoerabujima volcano, Japan. J Volcanol Geoth Res 202:107–116.

Snyder G, Poreda R, Fehn U, Hunt A (2003) Sources of nitrogen and methane in Central American geothermal settings: Noble gas and 129I evidence for crustal and magmatic volatile components. Geochem Geophys Geosyst 4, doi:10.1029/2002GC000363.

Stern C, Moreno H, López-Escobar L, Clavero J, Lara L, Naranjo J, Parada M, Skewes A (2007) Chilean Volcanoes. In: Moreno T, Gibbons W (ed) Geology of Chile, Geol. Soc. London, pp. 309–328.

Stevenson S (1993) Physical models of fumarolic flow. J Volcanol Geotherm 57(3–4):139–156.

Strand K (1995) Semmicrostructural analysis of a volcanogenic sediment component in a trench.slope basin of the Chile margin. In: Lewis SD, Behrmann JH, Musgrave RJ, Cande SC (eds) Proceedings of the Ocean Drilling Program, Scientific Results, 141, pp. 169–180.

Symonds R, Gerlach T, Reed M (2001) Magmatic gas scrubbing: implications for volcano monitoring. J Volcanol Geotherm Res 108:303–341.

Taran YA, Giggenbach WF (2003) Geochemistry of light hydrocarbons in subduction related volcanic and hydrothermal fluids. Soc Econ Geol 10:61–74.

Taran YA, Pokrovsky B, Esikov A (1989) Deuterium and oxygen-18 in fumarolic steam and amphiboles from some Kamchatka volcanoes: "andesitic waters". Doklady Akademii nauk SSSR 304:440–443.

Taran YA, Connor CB, Shapar VN, Ovsyannikov AA, Bilichenko AA (1997) Fumarolic activity of Avachinsky and Koryaksky volcanoes, Kamchetka, from 1993 to 1994. Bull Volcanol 58:441–448.

Tassara A, Yáñez G (2003) Relación entre el espesor elástico de la litósfera y la segmentación tectónica del margen andino (15-47°S). Rev Geol Chile 32:159–186.

Tassi F, Martinez C, Vaselli O, Capaccioni B, Viramonte J (2005a) Light hydrocarbons as redox and temperature indicators in the geothermal field of El Tatio (northern Chile). Appl Geochem 20:2049–2062.

Tassi F, Vaselli O, Capaccioni B, Giolito C, Duarte E, Fernandez E, Minissale A, Magro G (2005b) The hydrothermal-volcanicsystem of Rincon de la Vieja volcano (Costa Rica): a combined (inorganic and organic) geochemical approach to understanding the origin of the fluid discharges and its possible application to volcanic surveillance. J Volcanol Geotherm Res 148:315–333.

Tassi F, Aguilera F, Vaselli O, Medina E, Tedesco D, Delgado Huertas A, Poreda R, Kojima S (2009a) The magmatic- and hydrothermal-dominated fumarolic system at the Active Crater of Lascar volcano, northern Chile. Bull Volcanol 71:171–183.

Tassi F, Vaselli O, Fernandez E, Duarte E, Martinez M, Delgado Huertas A, Bergamaschi F (2009b). Morphological and geochemical features of crater lakes in Costa Rica: an overview. J Limnol 68(2):1–13.

Tassi F, Montegrossi G, Capaccioni B, Vaselli O (2010) Origin and distribution of thiophenes and furans in thermal fluid discharges from active volcanoes and geothermal systems. Int J Mol Sci 11:1434–1457.

Tassi F, Aguilera F, Vaselli O, Darrah T, Medina E (2011) Gas discharges from four remote volcanoes (Putana, Olca, Irruputuncu and Alitar) in northern Chile: a geochemical and isotopic survey. Ann Geophys 54:121–136.

Tassi F, Fiebig J, Vaselli O, Nocentini M (2012) Origins of methane discharging from volcanic, hydrothermal and cold emissions in Italy. Chem Geol 310-311:36–48.

Taylor BE (1986) magmatic volatiles: Isotopic variation of C, H and S. Rev Mineral 16:185–225.

Tedesco D, Sabroux JC (1987) The determination of deep temperatures by means of the CO-CO2-H2-H2O geothermometer: an example using fumaroles in the Campi Flegrei, Italy. Bull Volcanol 49:381–387.

Varekamp, JC, Pasternack GB, Rowe GL (2000) Volcanic lake systematics II. Chemical constraints. J. Volcanol Geotherm Res 97:161–179.

Varekamp JC, deMoor JM, Merrill MD, Colvin AS, Goss AR, Vroon PZ, Hilton DR (2006) Geochemistry and isotopic characteristics of the Caviahue-Copahue volcanic complex, Province of Neuquen, Argentina. Geol Soc Am 407:317–342.

Vaselli O, Tassi F, Montegrossi G, Capaccioni B, Giannini L (2006) Sampling and analysis of fumarolic gases. Acta Vulcanol 18:65–76.

Vaselli O, Tassi F, Duarte E, Fernandez E, Poreda RJ, A Delgado Huertas (2010) Evolution of fluid geochemistry at the Turrialba volcano (Costa Rica) from 1998 to 2008. Bull Volcanol 72:397–410.

von Huene R, Scholl DW (1991) Observations at convergent margins concerning sediment subduction, subduction erosion, and the growth of continental crust. Rev Geophys 29:279–316.

Whiticar MJ, Suess E (1990) Hydrothermal hydrocarbon gases in the sediments of the King-George Basin, Bransfield Strait, Antarctica. Appl Geochem 5:135–147.

Whiticar MJ (1999) Carbon and hydrogen isotope systematics of bacterial formation and oxidation of methane. Chem Geol 161:291–314.

Zelenski M, Taran Y (2011) Geochemistry of volcanic and hydrothermal gases of Mutnovsky volcano, Kamchactka: evidence for mantle, slab and atmosphere contributions to fluids of a typical arc volcano. Bull Volcanol 73:373–394.

CAPÍTULO V

GEOCHEMISTRY OF FLUIDS ASSOCIATED WITH THE 2010-2011 UNREST EPISODE OF PETEROA VOLCANO: AN EXAMPLE OF DYNAMIC INTERACTION OF MAGMATIC, HYDROTHERMAL AND METEORIC FLUID RESERVOIRS

V.1 INTRODUCTION

The Peteroa volcano is an active composite stratovolcano located in the Transitional Southern Volcanic Zone (TSVZ), in the center of a NNE-SSW trending volcanic chain named Planchón-Peteroa-Azufre Volcanic Complex (PPAVC) in Central Chile (*Tormey et al. 1995; Naranjo et al. 1999*) (Figure V-1). The volcanic edifice is characterized by a ~5 km diameter caldera-type crater, where four minor craters and a scoria cone are hosted (Figure V-2). The craters present diameters between 150 to 500 m and depths ranging from 50 to 150 m, and are characterized by the occurrence of acidic crater lakes and permanent fumarolic activity (Figure V-2). Glaciers are hosted in the summit caldera and in the valleys that dissect the volcanic complex (*Tormey 2010*).

Since the Peteroa volcano was the only system along the TSVZ having volcanic activity within months of the 27th February 2010 MW 8.8 Maule earthquake (Figure V-1), its recent eruptive cycle during January 2010-July 2011 has brought renewed interest from the scientific community and disaster management authorities (*Haller and Risso 2011; Aguilera et al. 2012; Naranjo 2012*). The activity was characterized by phreatic to phreatomagmatic eruptions with a VEI up to 2 (*Aguilera et al. 2012; Naranjo 2012*). Several earthquakes (MW < 3) were recorded beneath the PPAVC during the unrest episode (*SERNAGEOMIN-OVDAS, 2010a, b, c; 2011a, b*), as well as

unprecedented ground deformation (up to 15 cm of subsidence) that affected both the volcanic complex and its surrounding (*Pritchard et al. 2013*). Because neither significant surface thermal enhancement was detected during the eruptive episodes nor ground uplift was observed before January 2010, *Pritchard et al. (2013)* suggested that ground subsidence along the PPAVC was related to co-seismic release of fluids from a hydrothermal reservoir rather than an accumulation of magmatic fluids and its subsequent release. Additionally, *Haller and Risso (2011)* and *Naranjo (2012)* reported that juvenile materials (i.e. cognate lithics) emitted during the unrest episode was chemically similar (SiO_2 varying from 55 to 57.5 wt. %) to the eruptive products from 1837 eruption (*Naranjo and Haller 2002*), suggesting that 2010-2011 eruptive cycles did not involve the injection of a new magmatic batch at depth (*Naranjo 2012*). Even though different authors have reported geophysical, petrological and glaciovolcanic evidence related to the 2010-2011 unrest episode at Peteroa and its surroundings (e.g. *Pritchard et al. 2013; Aguilera et al. 2012; Naranjo 2012, Liaudat et al 2013*), there is no consensus on the fluid sources involved, the possible dynamic interaction between those sources and the mechanisms that triggered this interaction.

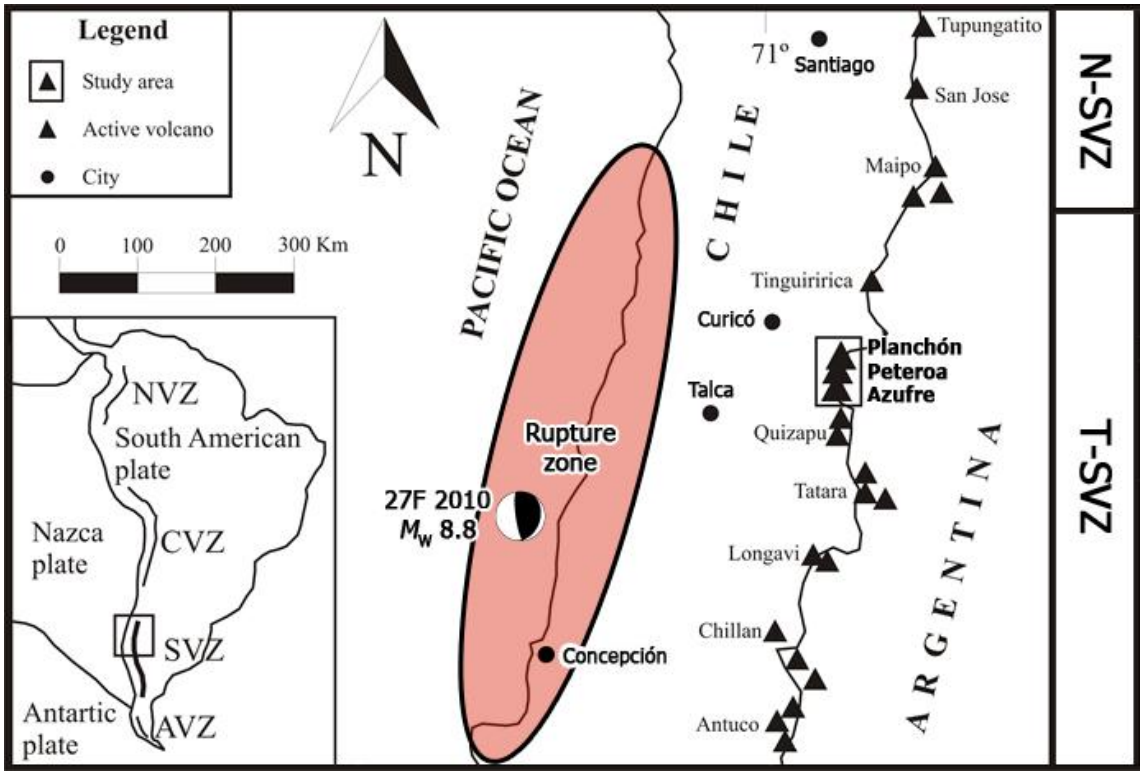

Figure V-1: Schematic map of the Northern and Transitional Southern Andean Volcanic Zone (N- and T-SVZ, respectively) and location of Planchón-Peteroa-Azufre Volcanic Complex (PPAVC). Light red ellipse shows the approximate Maule earthquake rupture zone (*Pritchard et al. 2013*).

In this chapter, I discuss the geochemical and isotopic features ($\delta^{18}O$- and δD-H_2O, $\delta^{13}C$-CO_2, $^{3}He/^{4}He$, $^{40}Ar/^{36}Ar$ and $\delta^{15}N$-N_2) of fumaroles, crater-lake water and thermal fluids sampled at the PPAVC during 2010, 2011 and 2012 (Figure V-2). My aim is to constrain the post-earthquake chemical and isotopic changes of fluid discharges at Peteroa, and their relation with different source regions and mechanisms of co-seismic fluid release.

V.2 GEOLOGICAL AND VOLCANOLOGICAL SETTING

The PPAVC was formed in response to the relatively steep subduction (>25°) of the Nazca beneath the South American plates (*Barazangi and Isack 1976; Cande and Leslie 1986, 1987*). The volcanic complex was built over a basement constituted by Upper Jurassic to Cretaceous continental and marine sediments (limestone, conglomerates, sandstones and gypsum), and Upper Cretaceous continental sediments, pyroclastic rocks, and basaltic to rhyolitic lava flows (*Haller et al 1985; Tormey et al 1989; Tormey et al 1995; Naranjo et al 1999*). The basement successions have been folded and cut by Middle Tertiary dioritic to granodioritic plutons (*Tormey et al 1995*).

Pleistocene-Holocene volcanic rocks in this volcanic complex have been divided into three major volcano-stratigraphic units (*Tormey et al. 1989, 1995; Naranjo et al. 1999; Naranjo and Haller 2002*), ordered from oldest to youngest as follow:

- **Azufre volcano** is the earliest (< 1.20 Ma) and largest (~69 km^3) edifice constituted mainly by basaltic andesite lava and pyroclastic flows, restricted dacitic lava flows and domes, rare andesitic lava and pyroclastic flows, and lahars deposits.
- **Planchón volcano** (6 km to the north of Azufre) was built in 3 different stages: i) Planchón I (~14 to ~12 ka) started its activity during the last stages of Azufre activity and is constituded by ~43 km^3 of basaltic and basaltic andesites lava flows, pyroclastic deposits and very restricted lahars deposits; ii) Planchón–Teno debris avalanche corresponds to a ~10 km^3 deposit formed ~11 ka as a consequence of the collapse of the western flank of Planchón I *(MacPhail 1973; Davidson 1974*; *Hauser 1990, 1993*); iii) Planchón II (~12 to ~7 ka), built within the summit anphitheatre, is a ~5 km^3 edifice made of basaltic to basaltic andesites lava flows and pyroclastic deposits, and lahars deposits.
- **Peteroa volcano**, the smallest (< 1 km^3) and youngest edifice (< 7 ka), is a volcano formed by four vents and a scoria cone scattered between Azufre and

Planchón volcanoes. Peteroa volcanic products are characterized by basaltic andesite to andesitic lava flows and basaltic andesite to dacitic pyroclastic flows, surge and fall deposits.

According to *Tormey et al. (1995),* volcanic products at PPAVC follows an evolution path from a tholeiitic system of basalt and subordinate dacite (Azufre-Planchón) formed at relative moderate-pressure (~4-8 kbar), to a calc-alkaline system with abundant andesite (Peteroa) formed by magma mixing at shallow crustal level.

Basement structures control the orientation of PPAVC features as well as the location of the thermal manifestations (e.g. hot springs, bubbling pools, mud pools, fumaroles, steaming grounds) around the volcanic complex, especially in its N, E and SE sides (*Cembrano and Lara 2009; Aguilera et al 2011; Benavente and Gutierrez 2011; Gutierrez et al. 2012*). These structures are dominated by reverse faults striking approximately NNE-SSW, which were developed in a compressional stress regime as part of the Malargüe fold and thrust belt (*Ramos et al. 1996*).

Fifteen glaciers of different size are hosted in the PPAVC summit and its surroundings, which occupy a total surface of ~20 km^2 (*Liaudat et al. 2013*). Since 1997, the areal variations of the ice bodies were insignificant, although remarkable reduction of the glaciers ice-thickness has been observed in the last years (*Liaudat et al. 2013*).

V.3 ERUPTIVE CHRONOLOGY

V.3.1 Historical activity

The historical activity of PPAVC has been related exclusively to Peteroa volcano and is characterized by a weak, but permanent emission of gas from different fumarolic fields and sporadic strong degassing from craters 2 and 3 (Figure V-2). At least 19 historical eruptions have been observed since 1660, corresponding mainly to phreatic and phreatomagmatic eruptions with a VEI ≤ 4 (*Haller et al 1994; Haller and Risso 2011).* Complete descriptions of the historical eruptive events were made by *Gardeweg (1991), Haller et al (1994), González-Ferrán (1995)* and *Naranjo et al (1999).* The first eruption described corresponds to an explosive suite of events during 1660, whose occurrences still is debatable. Subsequently, explosive eruptions were recorded in November-December 1751. The greatest historical eruption occurred 12th March 1762 (VEI = 4), when the explosive and effusive activity at Peteroa was followed by the partial collapse of the volcanic edifice. This collapse produced several debris

avalanches and lahars that affected the valley of Río Teno. Minor explosive eruptions were documented in 1835, 1837, 1842, 1860, 1869, 1872 an 1878 and 1889-1894. During 1937, an explosive and effusive event formed a scoria cone, from where a single lava flow was emitted. This event was accompanied by generation of lahars. Explosive events also occurred in 1938, 1959, 1960, 1962 and 1967. Strong degassing was observed between 1985 and 1987 with columns reaching up 300 m above crater. In February 1991, a phreatomagmatic eruption produced an eruptive column of 1 km above the crater, which was dispersed 80 km to the east and southeast (*Naranjo and Haller 1997, 2002*). The eruption was accompanied by lahars produced in the western flank of Peteroa and the contamination of the nearby rivers (Teno and Claro rivers) with acid waters from the active craters (*BGVN 1991; Haller et al. 1991*). Two new craters were formed during the 1991 eruption (crater 3 and 4; Fig. 2). The previous explosive eruption was recorded during November 1998 (*BGVN 1999*). Finally, strong degassing was observed in February 2001 (*BGVN 2001*).

V.3.2 Eruptive activity between 2010 and 2011

Previous to the beginning of this new eruptive period, the activity at Peteroa was restricted to fumarolic emission in the sites previously described and no gas column was observed. During a visit in February 2009, crater lakes were present in all craters.

Five eruptive cycles can be recognized for the period comprised between January 2010-July 2011 (Figure V-3):

- **Cycle 1** (4th January to 8th August 2010): White columns varied between 100 and 200 m above crater, constituted only by gas and vapor. Renewed activity was related to the occurrence of low-intensity phreatic explosions in the SW side of crater 3. Acid crater lakes were present in all four craters.
- **Cycle 2** (4th September to 1st November 2010): The more intense period of activity, with an ash column reaching up 3 km above the crater, and plumes travelling frequently E-SE and sporadically NE-NW, reaching up 345 km of distance. Ash fall deposits covered an area of 1,265 km^2. Dark-grey fine ash (<0.5 mm) emitted during the explosions of early September 2010 correspond to non-altered crystals, glassy lava fragments and non-vesiculated juvenile fragments with SiO2 contents (55 to 57.5 wt. %) similar to the volcanic products emitted in the 1837 eruption (*Naranjo 2012*). Observations during November 2010 indicate that the acid lake in crater 3 disappeared (*Tormey, pers. comm.*).

- **Cycle 3** (17th February to 15th April 2011): Permanent emission of ash-free white columns up to 600 m above the crater. Explosions were observed during the third week of February and on March 18th involving columns reaching up 1000 m above the crater and plumes dispersed up to 37 km to E-SE. Tephra deposits associated to these explosions correspond to dark grey coarse to fine ash (2 to <0.063 mm), formed by lithic fragments of poorly vesicular andesitic lava, glassy lava fragments and, quartz, plagioclase and pyroxene crystals with no evidence of hydrothermal alteration (*Aguilera et al. 2012*). Observations carried out by the authors during March 2011 indicate the presence of acid lakes in the crater 3.
- **Cycle 4** (16th April to 20th May 2011): Increasing of activity, emission of columns between 300 and 1500 m above crater, and plumes reaching up 638 km of distance. Ash fall deposits covered an area of 693 km^2.
- **Cycle 5** (17th June to 13th July 2011): Sporadic explosions (columns of 500-2,000 m above crater), with plumes travelling to the SE reaching up 41 km of distance.

Soil (at 45 and 80 cm of depth) and air temperatures at PPAVC have been monitored continuously since 2007 close to the rim of Peteroa (35°14′27″S - 70°33′50″W; 3,489 m a.s.l.; Figure V-2) [*Liaudat et al 2013*]. According to Figure V-3a, the mean monthly soil temperatures (January 2010 and April 2012) clearly follow the general tendency of the mean monthly air temperatures, which in turns depend on seasonal variation (i.e. maximum and minimum air temperatures during summer and winter, respectively). The maximum mean soil temperatures were measured in March 2010, coinciding with the peak of degassing in the 1st cycle (Figure V-3a). Even though no temperature anomalies were detected during 2nd, 3rd, 4th and 5th eruptive cycles, an increase of the difference between soil temperatures measured at 45 and 80 cm, as was documented between April- and September-2010, evidences an increase of the thermal gradient likely related to a major incidence of geothermal heat at Peteroa (*Liaudat et al. 2013*).

Seismic activity during the eruptive periods was detected since September-2010, when the local network began to operate (Figure V-3b; *SERNAGEOMIN-OVDAS, 2010a, b, c; 2011a, b*). Seismic activity was characterized by epicentres located in two main zones, 16-33 km NE and 5-7 km N from active crater, with foci located at 1-30 km and 1-8 km depth, respectively (*SERNAGEOMIN-OVDAS, 2010a, b, c; 2011a, b*). A third zone is located 9-20 km SE from active crater, with foci at 1-15 km depth (*SERNAGEOMIN-OVDAS, 2010a, b, c; 2011a, b*). According to *SERNAGEOMIN-OVDAS (2010a, b, c; 2011a, b),* over 85% of earthquakes are related to rock fracture, while the rest were interpreted as a result of fluid circulation.

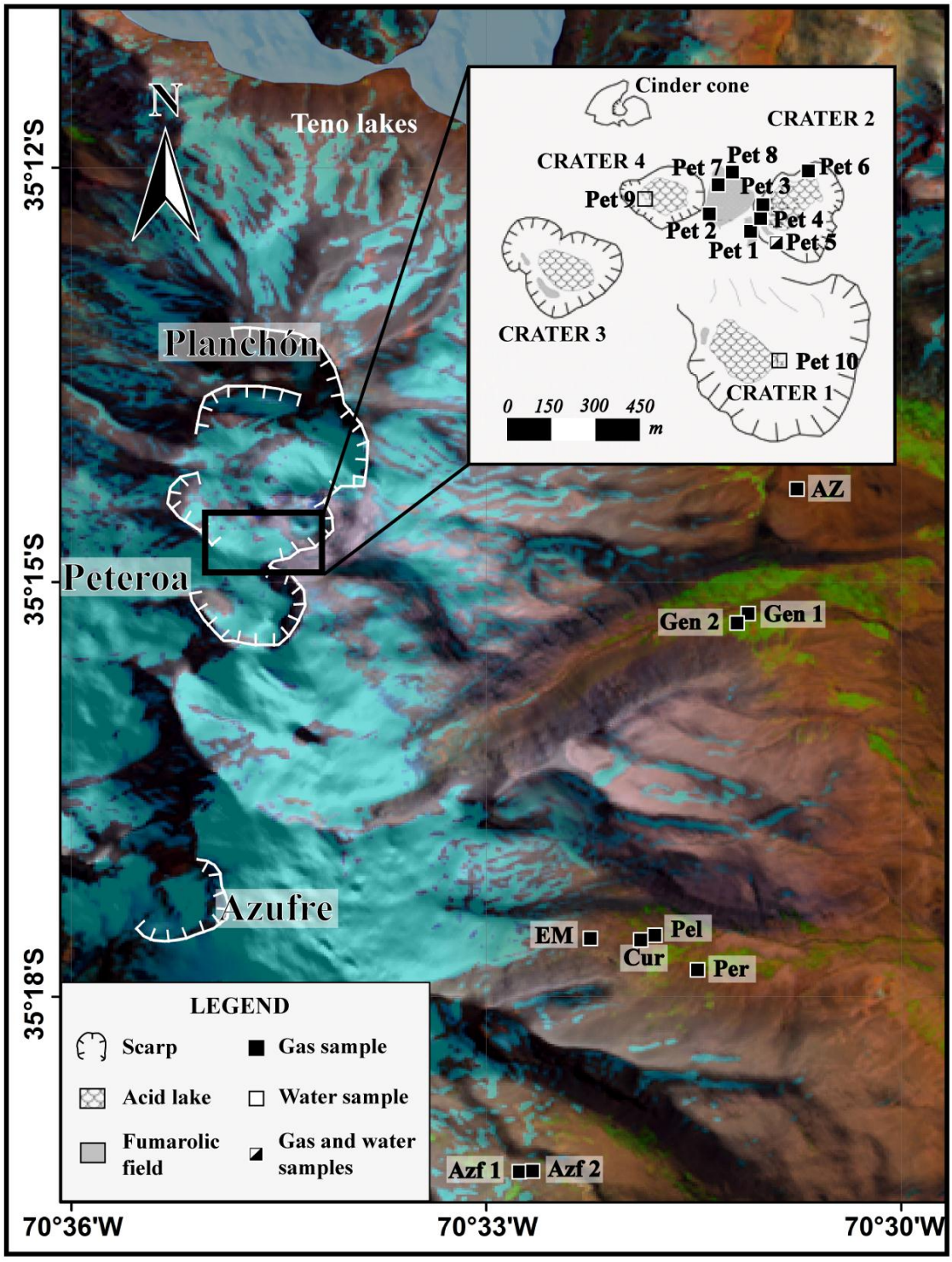

Figure V-2: Map of the Planchón-Peteroa-Azufre Volcanic Complex (PPAVC). Craters zone at Peteroa volcano, fumarolic fields, crater lakes, thermal springs and location of the sampling sites are shown. Red star corresponds to the soil and air temperature monitoring site of *Trombotto-Liaudat et al (2013).*

V.3.3 Activity after 2010-2011 eruptive period

A permanent low height column (50-100 m) was present in the active crater after the 2010-2011 eruptive period. Low frequency seismic activity was present during

August and September 2011 (186 and 274 earthquakes/month, respectively), whereas in October 2011 the seismic frequency increased up to 675 earthquakes/month. From November 2011 to February 2012, seismic activity was variable in a restricted range between 317 and 485 earthquakes/month (Figure V-3b). Despite of increasing of seismic activity, no eruptive events were observed. In fact, the field observations of Peteroa craters during March 2012 indicate that only a weak white column (50 m height) was present, and all craters hosted lakes. However, between February- and March-2013 the difference between soil temperatures measured at 45 and 80 cm increased (Figure V-3a), indicating that a major incidence of geothermal heat was associated with this peak of seismic activity (*Liaudat et al. 2013*).

V.4 SAMPLING AND ANALYTICAL PROCEDURES

V.4.1 Gas and water sampling

Twenty-three gas samples from fumarolic vents and bubbling pools were collected in 5 different sites: 14 samples of fumarolic vents, 12 samples from craters of Peteroa (7 in fumarolic field between crater 2 and 3, 5 samples from crater 2) and 2 samples from SE flank of the Azufre volcano; 9 samples from bubbling pools, 1 sample from the Valenzuela valley, 3 samples from the glacial valley and 5 samples from the Los Azufres valley (Figure V-2).

Gas samples from fumarolic vents were convoyed into sampling flasks using a 1-m-long titanium tube (Ø = 2.5 cm) that was inserted into the fumarolic vent and connected through glass dewar tubes. A plastic funnel was positioned upside-down and connected to the sampling flasks through tygon tubes to collect the gas from bubbling emissions. Gas samples from fumarolic vents and bubbling pools were collected using pre-evacuated 60 mL glass thorion-tapped flask filled with 20 mL of 4N NaOH and 0.15M $Cd(OH)_2$ suspension (*Montegrossi et al. 2001; Vaselli et al. 2006*). Water vapor and the main acidic gas species (CO_2, SO_2, HCl and HF) were trapped in the alkaline solution whereas H_2S formed insoluble CdS at the bottom of the flask. Low-solubility gas species (N_2, O_2, CO, H_2, He, Ar, Ne, CH_4 and light hydrocarbons) were concentrated in the head-space of the sampling flask. Aliquots of fumarolic vapor condensates (for the analysis of $^{18}O/^{16}O$ and D/H ratios in H_2O) and dry gases (for the analysis of CO and $^{13}C/^{12}C$ ratio in CO_2) were sampled using an ice-cooled glass tube connected to the gas sampling line (*Montegrossi et al. 2001; Vaselli et al. 2006*). At 6 sampling points, a 200 mL glass thorion-tapped two valves flask filled with 100 mL of

4N NaOH was used to analyze nitrogen isotopes in N_2 ($\delta^{15}N$), using the same sampling system for the soda flasks.

Finally, 4 water samples from crater lakes hosted in crater 1, 2 and 4 were collected in 200 mL sterile polyethylene bottles, being previously filtered at 0.45 mm. Unfiltered water was collected in 100 ml dark glass bottles for O and H isotopic determination ($\delta^{18}O$ and δD).

V.4.2 Chemical and isotopic (R/R_a, $\delta^{13}C\text{-}CO_2$, $^{40}Ar/^{36}Ar$ and $\delta^{15}N$) analysis of gases and steam ($\delta^{18}O$ and δD)

Inorganic gases in the sampling flask headspace (i.e. N_2, O_2, H_2, He, Ar, CO and Ne) were analyzed using a Shimadzu 15A gas chromatograph (GC) equipped with a 10 m long 5A molecular sieve column and a thermal conductivity detector (TCD). To allow a complete separation of Ar and O_2 peaks the oven temperature was lowered to -10°C by means of a cryogenic cooler (Shimadzu CRG-15) fed by liquid CO_2. A Shimadzu 14A gas chromatograph (GC) equipped with a 10-m-long stainless steel column packed with Chromosorb PAW 80/100 mesh coated with 23% SP 1700 and a flame ionization detector (FID) was used to analyze CH_4 and light hydrocarbons. The alkaline suspension was centrifuged at 4,000 rpm for 30 min to separate the solid precipitate from the solution. The latter was used to analyze 1) CO_2, as CO_3^{2-}, by titration (Metrohm Basic Titrino) with a 0.5N HCl solution; 2) HCl, as Cl^-, by ion chromatography (IC) (Metrohm Basic 761); 3) SO_2, as SO_4^{2-}, after oxidation with 5 ml H_2O_2 (33%) by ion chromatography. Using 5 ml H_2O_2 (33%), CdS in the solid precipitate was oxidized to SO_4^{2-} that was analyzed by IC for determining H_2S concentrations (*Montegrossi et al. 2001*). IC was used to analyze condensate samples for F^- and Cl^-. HF concentrations were calculated on the basis of F^- and Cl^- concentrations in the condensate samples and the alkaline solution samples. The analytical error for titration, GC and IC analyses was <5%.

The analysis of $^{13}C/^{12}C$ ratios of CO_2 (expressed as $\delta^{13}C\text{-}CO_2$‰ vs. V-PDB) stored in the pre-evacuated sampling flasks were carried out with a Finningan Delta S mass spectrometer after standard extraction and purification procedures of the gas mixtures (*Evans et al. 1998; Vaselli et al. 2006*). Standards used for estimation of external precision were Carrara and San Vincenzo marbles (Internal), NBS18 and NBS19 (International). Analytical error and reproducibility were ±0.05‰ and ±0.1‰, respectively.

The $\delta^{15}N$ (expressed as ‰ vs. Air) and $^{40}Ar/^{36}Ar$ ratios in the gas samples were determined at the INGV laboratories of Naples (Italy) using an Agilent 6890 N gas chromatograph (GC) coupled with a Finnigan Delta plus XP continuous-flow mass spectrometer (MS). The GC is equipped with a molecular sieve column (MS 5 Å capillary, 30 m × 0.53 mm × 50 µm; He carrier gas), a TCD detector and a post column switching device (Denswitch) that has the following function: 1) to split the column gas flow to the TCD detector and to the MS, and 2) to invert the column flow after the species of interest (Ar and N_2) has reached the detector, preventing undesirable species (mainly CO and water) from reaching the MS. To allow simultaneous determination of ^{36}Ar and ^{15}N, the MS is equipped with a standard triple collector. Initially, the ion beam is focused to send mass 36 to the more sensitive cup. After recording the mass 36 peak, the magnetic field is switched to focus the ion beams of masses 28, 29 and 30 on the three cups using a jump calibration procedure taking into account any hysteresis of the magnet.

Helium isotopic ratios were determined on gas aliquots transferred from the flask headspace into pre-evacuated 50 mL flasks. Helium ratios were expressed as R/R_a, where R is the measured $^3He/^4He$ ratio and R_a is the $^3He/^4He$ ratio of the air (R_a= 1.39×10^{-6}; *Mamyrin and Tolstikhin 1984*). Isotopic analyses were performed on a double collector mass spectrometer (VG 5400-TFT) using methods described by *Inguaggiato and Rizzo (2004)*. The analytical uncertainty for the R/R_a determination was ≤0.3%.

The $^{18}O/^{16}O$ and $^2H/^1H$ isotopic ratios (hereafter expressed as $\delta^{18}O\text{-}H_2O$‰ and $\delta D\text{-}H_2O$‰ vs. V-SMOW, respectively) of the condensate and water samples were determined using a Finningan Delta Plus XL mass spectrometer at the Geokarst Engineering Laboratory (Trieste, Italy). Oxygen isotopes measurements were performed according to the methods described by *Epstein and Mayeda (1953)*. Hydrogen isotopes were analyzed on the H_2 generated by the reaction of 10 µL water with metallic Zn at 500 ˚C (*Coleman et al 1982*). Analytical errors were ±0.1‰ for $\delta^{18}O$ and ±0.1‰ for δD, using V-SMOW and SLAP as analytical standards and AR-1 as an internal standard.

V.4.3 Chemical analysis of water

Temperature and pH of crater lake waters were determined in the field. Water samples were analyzed for major cations (Na^+, K^+, Ca^{2+}, Mg^{2+}, and NH_4^+) and anions

(F^-, Cl^- SO_4^{2-}, Br^- and NO_3^-) by ion chromatography (Metrohm 861 and Metrohm 761, respectively). The analytical error for IC was ≤5%.

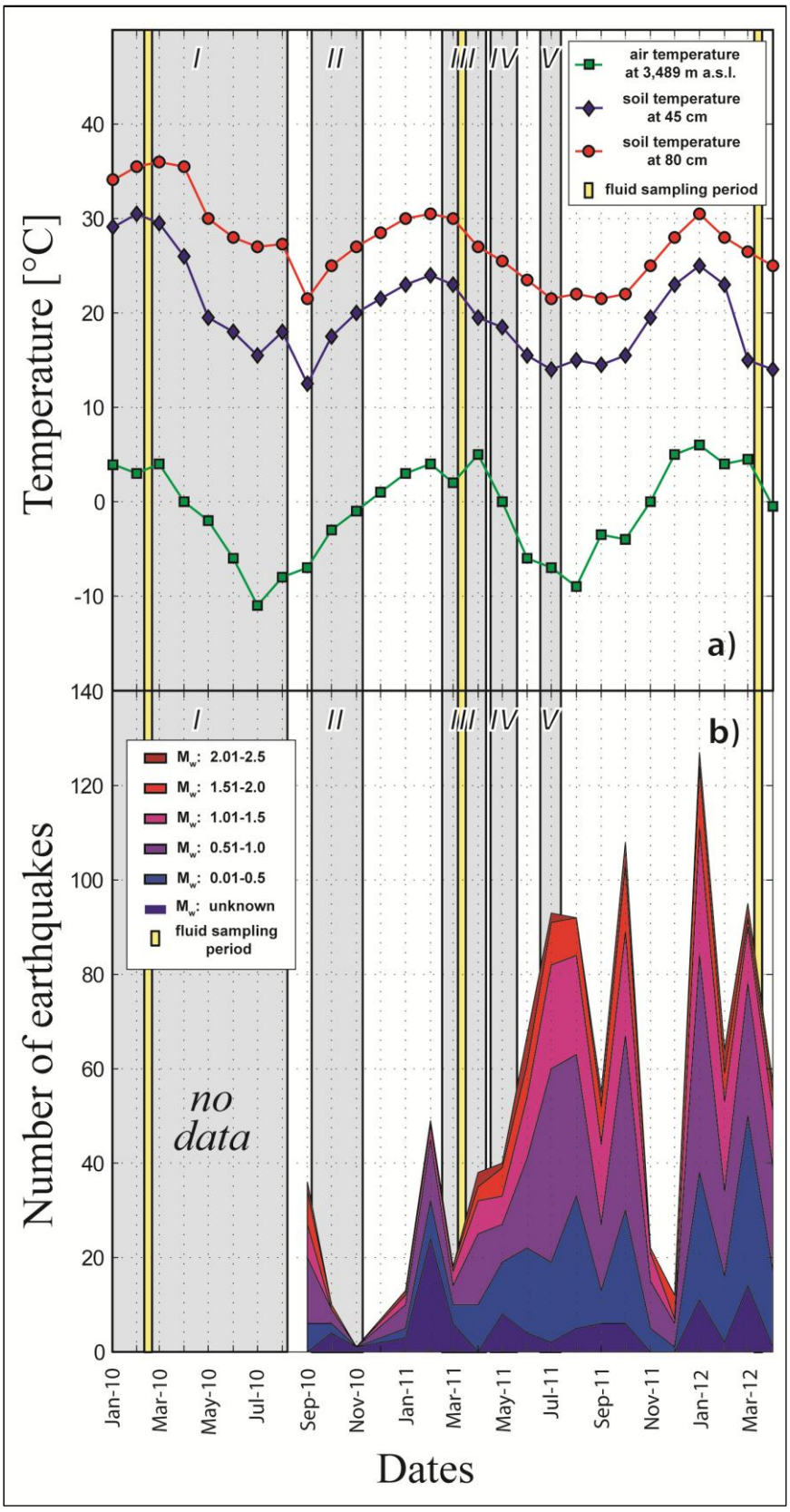

Figure V-3: Mean monthly air (green squares) and soil temperatures at 45 and 80 cm (blue diamonds and red circles, respectively) measured in Peteroa crater area from January 2010 to April 2013 (*Liaudat et al 2013*). Also are indicated the number of earthquakes per month at the PPAVC and its surrounding (*SERNAGEOMIN-OVDAS*). Earthquakes were grouped into 6 groups depending upon their magnitude (M_W). The vertical grey bands represent the five eruptive cycles defined in this work, whereas the vertical yellow bands represent the sampling periods.

Table V-1: Chemical data of inorganic gases and CH_4 (in mmol/mol) from PPAVC gas discharges. Type of sample, date, geographical coordinates (UTM, WGS 85 Zone 19), altitude (m a.s.l.), outlet temperatures (in °C) and total concentration of the dry gas fraction are also reported. b.d.l.: below detection limit.

Achronym	Type	Date	Coord N	Coord E	Altitude	T (°C)	CO_2	HCl	HF	SO_2	H_2S	N_2	CH_4	Ar	O_2	H_2	He	CO	Xgas %
Pet 1	Fumarole	February 2010	6099208	357027	3436	91,8	978	0,246	0,011	0,115	19,3	1,56	0,237	0,026	0,056	0,364	0,0032	0,0026	9,45
Pet 1	Fumarole	March 2011	6099208	357027	3436	87,7	975	0,375	0,010	0,550	21,0	2,62	0,132	0,0043	0,0065	0,245	0,0014	0,015	14,6
Pet 1	Fumarole	March 2012	6099208	357027	3436	87,8	363	14,1	1,31	466	151	7,55	0,009	0,016	0,006	0,612	0,0025	0,0008	3,45
Pet 2	Fumarole	February 2010	6099171	356908	3434	102,1	961	0,189	0,021	0,168	35,4	2,75	0,286	0,024	0,049	0,384	0,0028	0,0031	3,85
Pet 3	Fumarole	March 2011	6099212	357037	3374	88,4	979	0,385	0,012	0,509	18,0	2,26	0,098	0,0016	0,005	0,209	0,0012	0,0092	12,1
Pet 3	Fumarole	March 2012	6099212	357037	3374	89,4	349	12,9	1,29	474	156	6,54	0,012	0,018	0,005	0,533	0,0034	0,0006	4,87
Pet 4	Fumarole	March 2011	6099169	357042	3401	88,4	978	0,318	0,012	0,402	18,1	2,54	0,109	0,0042	0,028	0,177	0,0013	0,0089	14,7
Pet 5	Fumarole	March 2011	6099157	357050	3331	43,2	986	0,235	0,008	0,308	10,8	2,50	0,122	0,0076	0,028	0,131	0,0015	0,0050	21,8
Pet 6	Fumarole	March 2011	6099288	357171	3358	87,9	978	0,314	0,010	0,411	18,9	2,38	0,102	0,0047	0,0068	0,231	0,0015	0,015	15,0
Pet 7	Fumarole	March 2011	6099257	356939	3411	88,3	980	0,383	0,011	0,539	16,2	2,35	0,091	0,0043	0,0010	0,279	0,0022	0,012	15,4
Pet 7	Fumarole	March 2012	6099257	356939	3411	87,9	343	13,3	1,27	475	160	6,89	0,008	0,011	0,007	0,478	0,0043	0,0019	4,11
Pet 8	Fumarole	March 2012	6099317	356996	3446	87,9	351	12,1	1,23	483	146	7,13	0,011	0,014	0,003	0,511	0,0032	0,0022	5,64
Gen 1	Bubbling pool	February 2010	6098170	362325	2472	26,3	990	b.d.l.	b.d.l.	b.d.l.	b.d.l.	8,14	1,365	0,151	0,551	0,0048	0,0078	b.d.l.	98,5
Gen 2	Bubbling pool	February 2010	6098014	362203	2476	28	993	b.d.l.	b.d.l.	b.d.l.	b.d.l.	5,29	1,315	0,117	0,615	0,0061	0,0052	b.d.l.	98,7
Gen 2	Bubbling pool	March 2012	6098014	362203	2476	28	993	b.d.l.	b.d.l.	b.d.l.	b.d.l.	5,29	1,109	0,126	0,615	0,0061	0,0052	b.d.l.	93,5
AZ	Bubbling pool	February 2010	6099896	36287	2435	24	994	b.d.l.	b.d.l.	b.d.l.	b.d.l.	3,84	1,411	0,098	0,485	0,0044	0,0044	b.d.l.	99,1
EM	Bubbling pool	February 2010	6093572	361212	2507	38	996	b.d.l.	b.d.l.	b.d.l.	b.d.l.	2,74	1,019	0,095	0,360	0,0056	0,0056	b.d.l.	97,2
Per	Bubbling pool	February 2010	6093131	361819	2472	37	994	b.d.l.	b.d.l.	b.d.l.	b.d.l.	3,94	1,395	0,126	0,641	0,0049	0,0031	b.d.l.	97,2
Pel	Bubbling pool	February 2010	6093577	361327	2490	43,7	992	b.d.l.	b.d.l.	b.d.l.	b.d.l.	6,52	1,584	0,048	0,115	0,0038	0,0061	b.d.l.	96,5
Pel	Bubbling pool	March 2011	6093577	361327	2490	46,2	996	b.d.l.	b.d.l.	b.d.l.	b.d.l.	1,81	1,438	0,039	0,544	0,0056	0,0026	b.d.l.	97,7
Cur	Bubbling pool	March 2012	6098014	362203	2476	39	991	b.d.l.	b.d.l.	b.d.l.	b.d.l.	6,23	1,778	0,151	0,958	0,0044	0,0004	b.d.l.	91,6
Azf 1	Fumarole	March 2012	6090273	359938	2758	88,7	794	5,3	0,8	38	156	3,21	0,086	0,046	0,011	2,562	0,0011	0,0069	3,11
Azf 2	Fumarole	March 2012	6090246	359912	2766	87,8	781	4,7	0,9	26	181	3,55	0,094	0,041	0,006	3,115	0,0009	0,0087	2,56

Table V-2:C_2-C_7 hydrocarbons contents (in mmol/mol) for the PPAVC gas discharges; b.d.l.: below detection limit.

Samples	C_2H_6	C_2H_4	C_3H_8	C_3H_6	i-C_4H_{10}	n-C_4H_{10}	i-C_4H_8	C_4H_4O	C_6H_6	C_4H_4S	C_7H_8
Peteroa 1	0,0037	0,000049	0,00017	0,00014	b.d.l.	0,00011	0,0026	0,000021	0,0018	0,00069	0,00011
Peteroa 1	0,0054	0,000113	0,00047	0,00029	b.d.l.	0,00011	0,0018	0,000013	0,0025	0,00039	0,00005
Peteroa 1	0,000077	0,000011	0,000003	0,000013	b.d.l.	b.d.l.	b.d.l.	0,00054	0,000012	b.d.l.	b.d.l.
Peteroa 2	0,0042	0,000062	0,00021	0,00015	b.d.l.	0,00012	0,0032	0,000019	0,0021	0,00073	0,00012
Peteroa 3	0,0048	0,000071	0,00037	0,00027	b.d.l.	0,00019	0,0027	0,000016	0,0020	0,00041	0,00005
Peteroa 3	0,000063	0,000011	0,000005	0,000010	b.d.l.	b.d.l.	b.d.l.	0,00043	0,000035	b.d.l.	b.d.l.
Peteroa 4	0,0048	0,000088	0,00039	0,00027	b.d.l.	0,00016	0,0023	0,000014	0,0023	0,00042	0,00008
Peteroa 5	0,0052	0,000091	0,00048	0,00039	b.d.l.	0,00018	0,0022	0,000014	0,0023	0,00037	0,00005
Peteroa 6	0,0064	0,000115	0,00055	0,00041	b.d.l.	0,00012	0,0019	0,000011	0,0022	0,00033	0,00007
Peteroa 7	0,0047	0,000091	0,00047	0,00040	b.d.l.	0,00015	0,0020	0,000010	0,0022	0,00038	0,00005
Peteroa 7	0,000051	0,000013	0,000004	0,000013	b.d.l.	b.d.l.	b.d.l.	0,00044	0,000032	b.d.l.	b.d.l.
Peteroa 8	0,000066	0,000030	0,000004	0,000024	b.d.l.	b.d.l.	b.d.l.	0,00026	0,000012	b.d.l.	b.d.l.
Gendarmeria 1	2,661	b.d.l.	0,116	0,0127	0,019	0,0056	0,0034	b.d.l.	0,0691	b.d.l.	0,0026
Gendarmeria 2	1,746	b.d.l.	0,080	0,0131	0,014	0,0045	0,0048	b.d.l.	0,0588	b.d.l.	0,0023
Gendarmeria 2	1,658	b.d.l.	0,191	0,0566	0,044	0,0123	0,0071	b.d.l.	0,564	b.d.l.	0,0061
Agua del Azufre	1,658	b.d.l.	0,091	0,0122	0,015	0,0061	0,0026	b.d.l.	0,0684	b.d.l.	0,0027
El Macho	2,265	b.d.l.	0,086	0,0095	0,016	0,0075	0,0060	b.d.l.	0,0897	b.d.l.	0,0042
Perticio	2,368	b.d.l.	0,111	0,0124	0,018	0,0079	0,0048	b.d.l.	0,0762	b.d.l.	0,0036
Pelambre	1,897	b.d.l.	0,091	0,0098	0,016	0,0068	0,0026	b.d.l.	0,0745	b.d.l.	0,0021
Pelambre	0,432	b.d.l.	0,0385	0,0081	0,0024	0,0013	0,0004	b.d.l.	0,0003	b.d.l.	b.d.l.
Curicó	2,368	b.d.l.	0,181	0,0624	0,053	0,0135	0,0088	b.d.l.	0,662	b.d.l.	0,0093
Azufre 1	0,000156	0,000021	0,000012	b.d.l.	b.d.l.	b.d.l.	b.d.l.	0,00011	0,000088	b.d.l.	b.d.l.
Azufre 2	0,000161	0,000015	0,000013	0,000029	b.d.l.	b.d.l.	b.d.l.	0,00008	0,000071	b.d.l.	b.d.l.

Sample	Date	R/Ra	$^{40}Ar/^{36}Ar$	He/Ne	$\delta^{13}C$	δD	$\delta^{18}O$	$\delta^{15}N$
Peteroa 1	March 2011	n.a.	n.a.	n.a.	-6,11	-80	-5,9	n.a.
Peteroa 1	March 2012	4,44	313	3,05	-11,18	n.a.	n.a.	4,27
Peteroa 3	March 2011	6,87	455	315	-7,60	-73	-4,3	n.a.
Peteroa 3	March 2012	4,43	337	2,87	-11,15	n.a.	n.a.	4,79
Peteroa 4	March 2011	n.a.	n.a.	n.a.	-3,02	-74	-3,6	n.a.
Peteroa 5	March 2011	7,11	378	289	-3,56	-74	-3,5	n.a.
Peteroa 6	March 2011	n.a.	n.a.	n.a.	-2,02	-80	-4,8	n.a.
Peteroa 7	March 2011	6,59	491	511	-5,82	n.a.	n.a.	n.a.
Peteroa 7	March 2012	4,55	367	4,62	-11,57	-75,5	-10,51	5
Peteroa 8	March 2012	4,43	314	3,98	-11,43	-115,3	-15,67	4,47
Gendarmería 2	March 2012	5,94	285	6,69	-12,58	-102,8	-15,13	1
Pelambre	March 2011	3,69	328	94	-13,21	-106	-14,7	n.a.
Curicó	March 2012	1,19	295	1,38	-12,59	-97,8	-13,36	-0,34
Rain at 4,000 m a.s.l.	March 2011	n.a.	n.a.	n.a.	n.a.	-118	-15,8	n.a.

Table V-3: Isotopic composition of steam ($\delta^{18}O$ and δD in ‰ vs. V-SMOW), carbon in CO_2 ($\delta^{13}C$ in ‰ vs. V-PDB), helium (as R/Ra, where R is the measured ratio and Ra is that of the air: $1.39x10^{-6}$; *Mamryn and Tolstikhin, 1984*), argon ($^{40}Ar/^{36}Ar$), and nitrogen in N_2 ($\delta^{15}N$ in ‰ vs. Air) for the PPAVC gas discharges; n.a.: not analyzed. $\delta^{18}O$ and δD values of local precipitations (Rain) are also reported.

Table V-4: Temperature (in °C), pH, chemical composition (in mg/L) and isotopic composition of water ($\delta^{18}O$ and δD in ‰ vs. V-SMOW) of the PPAVC crater lakes.

Sample	Type	Date	Coord N	Coord E	Altitude	T (°C)	pH	HCO_3	Cl	SO_4	Na	K	Ca	Mg	NO_3	F	Br	Li	NH_4	δD	$\delta^{18}O$
Peteroa 5	Crater lake	March 2011	6099157	357050	3331	43,2	1,49	n.d.	44	3288	82	133	223	140	2,03	5,2	0,06	n.d.	9,98	-74	-9,5
Peteroa 5	Crater lake	March 2012	6099157	357050	3331	30,6	1,5	n.d.	92	2794	63	16	182	95	0,81	2,45	0,52	n.d.	n.d.	n.a.	n.a.
Peteroa 9	Crater lake	March 2011	6099324	356704	3353	19,1	2,73	n.d.	197	3018	182	42	326	377	1,00	9,9	0,77	n.d.	4,92	-80	-9,9
Peteroa 10	Crater lake	March 2011	6098725	357071	3263	7,4	2,91	n.d.	662	2001	145	34	523	182	1,00	39,2	1,43	n.d.	2,63	-80	-10,1

V.5 RESULTS

V.5.1 Chemical composition of gas

Table V-1 shows sample locations and chemical data of fumaroles. For the Peteroa crater and Azufre volcano fumaroles, the measured temperatures range between 43.2 and 102°C. Steam is the main fumarolic component, and the molar concentration of dry gas fraction ranges from 2.56% to 21.8%. Dry gas is dominated by CO_2 (up to 986 mmol/mol), except in samples from Peteroa (March 2012) where CO_2 range between 343 and 363 mmol/mol, followed by H_2S for February 2010 and March 2011 samples (up to 21 mmol/mol), which increased one order of magnitude for March 2012 samples (up to 181 mmol/mol). Acidic components are present in relatively low concentrations in samples taken in February 2010 and March 2011. HCl is up to 0.385 mmol/mol), SO_2 <0.550 mmol/mol and HF<0.021 mmol/mol, but subsequently its concentrations increased by a factor of two (HCl and HF, up to 14.1 and 1.31 mmol/mol, respectively) and three orders of magnitude (SO_2 up to 483 mmol/mol). N_2 and H_2 are present in variable concentrations, ranging from 1.56 to 7.55, and from 0.131 to 3.115 mmol/mol, respectively. CH_4, Ar, O_2, He and CO have concentrations up to 0.286, 0.046, 0.056, 0.0043 and 0.0092 mmol/mol, respectively (Table V-1), while the sum of the light hydrocarbons (C_2-C_7) is ≤0.0121 mmol/mol (Table V-2).

Gas samples collected from bubbling pools have temperatures that range between 24 and 43.7ºC. The chemical composition is characterized by high gas/water vapor ratio (X_g from 91.6 to 99.1%), caused by the strong water condensation at the surface. Dry gas fraction is dominated by CO_2 (up to 996 mmol/mol), while N_2 and CH_4 are present in relative high concentrations (up to 8.14 and 1.78 mmol/mol, respectively). Water-soluble acidic gas species, such as HCl, HF and SO_2, are absent in all bubbling pool gas samples, and also are H_2S-free. CO concentration is below the detection limit (<0.005 mmol/mol; Table V-1) probably related to dissolution of CO in shallow aquifers, which transform to formiate (Shock 1993). H_2, Ar, O_2 and He have concentrations up to 0.0061, 0.0151, 0.958 and 0.0078 mmol/mol, respectively. C_2-C_7 light hydrocarbons present concentration ≤3.36 mmol/mol (Table V-2).

V.5.2 Isotopic composition of gases (R/R_a, $\delta^{13}C$-CO_2, $^{40}Ar/^{36}Ar$, $\delta^{15}N$-N_2) and steam ($\delta^{18}O$ and δD)

The isotopic composition of water vapor ($\delta^{18}O$-H_2O_{VSMOW} and δD-H_2O_{VSMOW}), CO_2 ($\delta^{13}C$-$CO_{2\ PDB}$), He (R/R_a), Ar ($^{40}Ar/^{36}Ar$), and N_2 ($\delta^{15}N$-N_2) is reported in Table V-3. The

$\delta^{18}O$ and δD values range from -15.67 to -3.5‰ and from -115.3‰ to -73‰ vs. V-SMOW, respectively. The $\delta^{13}C$-CO_2 values range from –7.6‰ to -2.02‰ vs. V-PDB for fumarolic gases in March 2011, but highly negative values are measured in gas samples from all bubbling pools and in the fumaroles a year later (March 2012, delta values -13.21‰ and -11.15‰ vs. V-PDB). The R/R_a values of fumarolic gases also show changes for the same period, and range from 6.87 to 7.11 for March 2011 and from 4.43 to 4.55 for March 2012. Samples from bubbling pools present R/R_a values between 1.19 and 3.69. $^{40}Ar/^{36}Ar$ ratios are up to 455, while $\delta^{15}N$-N_2 values range from 4.2 to 4.79‰ vs. Air, except bubbling pool sample (Curicó) which value is -0.34‰ vs. Air.

V.5.3 Chemical and isotopic ($\delta^{18}O$ and δD) composition of crater lake water

Temperature, pH and chemical composition of the crater lakes samples are reported in Table V-4. Temperature and pH range from 7.4 to 43.2°C and from 1.49 to 2.91, respectively. The lake chemistry is dominated by SO_4^{2-} (up to 3,288 mg/L), while Cl^- is present in relative low concentrations (up to 662 mg/L) and HCO_3^- is absent. Ca^{2+} is the most abundant cation (523 mg/L), followed by Mg^{2+} (377 mg/L), Na^+ (182 mg/L) and K^+ (133 mg/L). The concentrations of F^-, NH_4^+, NO_3^- and Br^- are up to 39.2, 9.98, 2.03 and 1.43 mg/L, respectively. The $\delta^{18}O$ and δD values range from -10.1 to -9.5‰ and from -80‰ to -74‰ vs. V-SMOW, respectively.

V.6 DISCUSSION

V.6.1 Fluid source regions

The chemistry of the Peteroa crater fumaroles is related to SO_2-rich fluid degassing from an active deep magmatic system, and fluids are associated to an upper hydrothermal zone where high-temperature gas-water-rock interactions generate reduced reactive gaseous species such as H_2S, H_2 and, at lesser extent, HCl and HF (Table V-1) (e.g. *Giggenbach et al. 1987, 1996; Martini 1993*). The outlet temperatures of most fumaroles in the crater (Table V-1, boiling temperature of pure water at 3,400 m a.s.l. ~88°C) are highly indicative of the presence of a shallow meteoric aquifer. Water-gas interaction and cooling-induced re-equilibration mechanisms most likely play an important role modifying the physico-chemical features of the deep magmatic-hydrothermal fluids while they pass through the aforementioned shallow aquifer (e.g. scrubbing process; *Symonds et al. 2001*). Such process can explain the relatively low

concentration of SO_2, H_2S, HCl, HF and CO in the fumarolic gases in February 2010 and March 2011 (Table V-1), as well as the low pH (<2.91) and high concentration of SO_4^{2-}, Cl^- and F^- (up to 3,288, 662 and 39.2 mg/L, respectively) in all the crater lakes waters (Table V-4), as a consequence of the partial dissolution of the ascending soluble acid magmatic-hydrothermal compounds on the shallow aquifer (*Symonds et al. 2001; Varekamp et al. 2000*). Complete scrubbing of SO_2, H_2S, HCl and HF within the liquid-dominated environment may explain the lack of these compounds at the bubbling pools located in the periphery of the PPAVC. In contrast, the strong flux of ascending fluids feeding the Azufre fumaroles located in the SE side of the PPAVC, did not allow a complete dissolution of the highly soluble magmatic-hydrothermal gases, resulting in deeper geochemical signatures (e.g. *Capaccioni et al. 2007*).

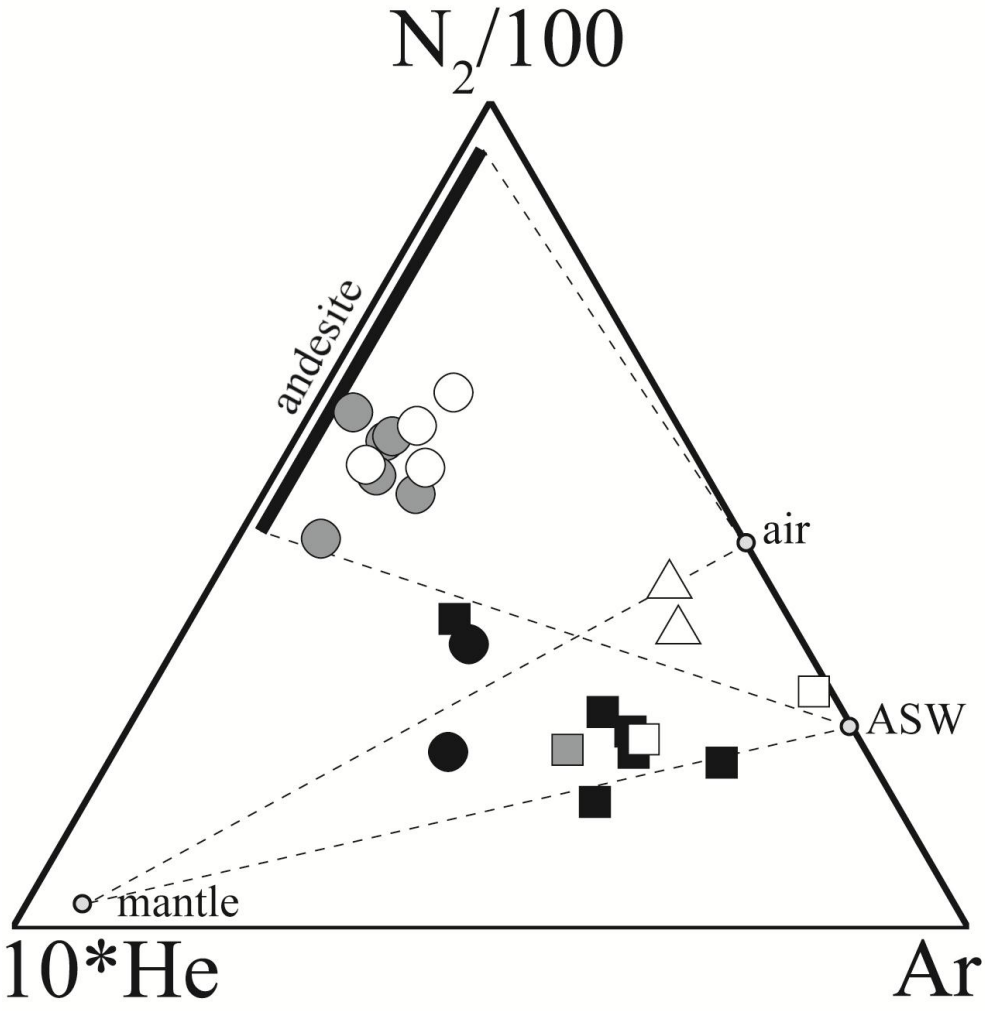

Figure V-4: N_2/100-Ar-He*10 diagram for the thermal discharges sampled at Peteroa volcano and its surrounding (*Giggenbach 1992b*). Air and Air-Saturated Waters (ASW) compositions and convergent plate boundaries ("andesite") field (*Giggenbach 1996*) are also reported. Black-filled circles: crater fumaroles sampled during 2010; grey-filled circles: crater fumaroles sampled during 2011; open-circles: crater fumaroles sampled during 2012; open triangles: Azufre volcano fumaroles; black-filled squares: bubbling pools sampled during 2010; grey-filled squares: bubbling pools sampled during 2011; open squares: bubbling pools sampled during 2012.

Apart from decreasing the concentrations of the most soluble gaseous species, the liquid-dominated environment overlying the degassing magma may add atmospheric-related gaseous compounds such as N_2, O_2 and Ar. This can be evaluated using the ternary N_2-Ar-He diagram (Figure V-4) proposed by *Giggenbach (1992b)*, which is useful to constrain potential sources of gases (e.g. crust, mantle, atmosphere). With the exception of sample Pel-2, the N_2/Ar ratios of the bubbling pools samples (ranging between 28.8 and 53.8) are generally similar to the value of air-saturated water (hereafter ASW; 36.8), suggesting the existence of a fresh ASW component at deeper levels (e.g. *Rouwet et al 2009*). Despite the relatively low O_2 content of the Azufre fumaroles with respect to N_2 (Table V-1), its N_2/Ar ratios (69.7 and 86.5) indicate a major air contribution (N_2/Ar~83.6; *Giggenbach 1993*). It is likely that the Azufre fumaroles were contaminated by air inside the fumarolic conduit (e.g. *Stevenson 1993*), where the atmospheric O_2 is consumed by the oxidation of H_2 and CO at shallow levels. The N_2/Ar ratios measured in most of the crater fumaroles and sample Pel-2 (ranging from 112 to 1,400) are notably higher than those of ASW and air, indicating an additional non-atmospheric N_2 source. Strong N_2-excess is typical of arc volcanoes (Figure V-4), and is commonly related to thermal decomposition of organic material buried in the slab and/or in the continental crust (*Matsuo et al. 1978; Jenden et al. 1988; Giggenbach 1997; Snyder et al. 2003*).

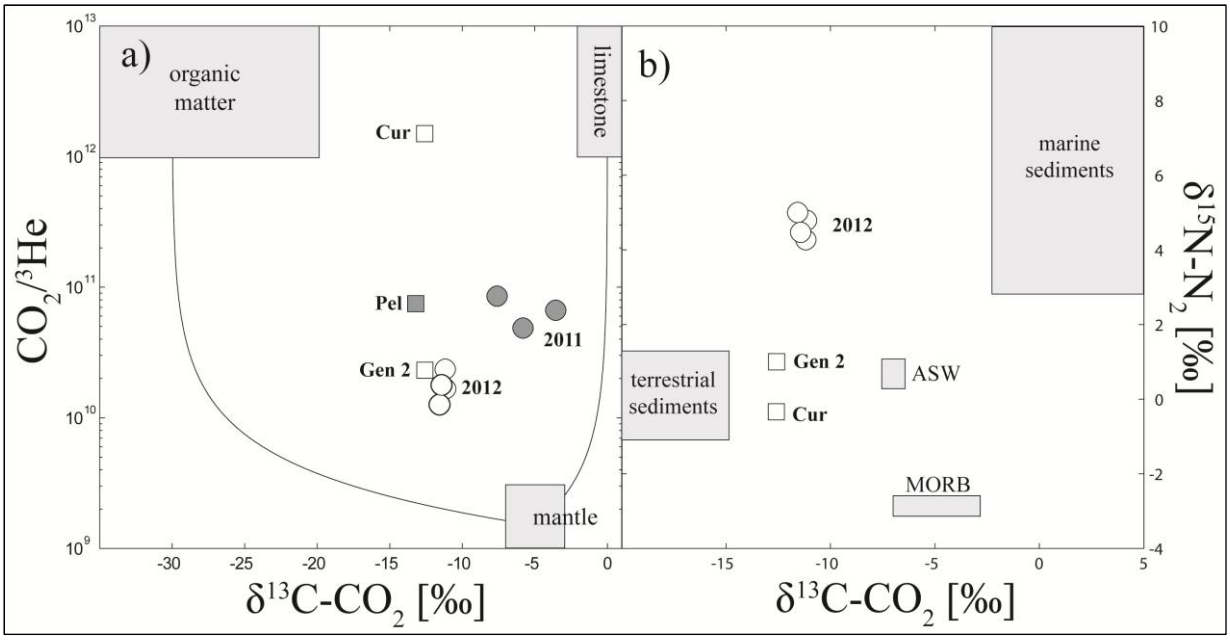

Figure V-5: a) $CO_2/^3He$ vs. $\delta^{13}C\text{-}CO_2$ diagram. Gases from organic-rich sediments (S), limestone (L) and mantle (M) end-members (*Sano and Marty 1995*) are reported. b) $\delta^{15}N_2$ vs. $\delta^{13}C\text{-}CO_2$ diagram after *Fisher et al. (1997)*. Gases from marine and terrestrial sediments, air and MORB end-members are shown *(Sano et al. 2001; Fischer et al. 2002)*. Symbols as in Figure V-4.

The occurrence of significant mantle He in the crater fumarolic fluids, indicated by the relatively high R/R_{air} values (ranging from 4.43 to 7.11), confirms the strong genetic link existing between the crater fumaroles and the magmatic arc system (R/R_{air} values ranging between 3 and 8; *Hilton et al 2002*). R/R_{air} values of bubbling pools are significantly lower than those measured in the crater fumaroles (R/R_{air} between 1.19 and 5.94) which can be explained in terms of atmospheric contribution and/or higher residence times where the interaction between magmatic-hydrothermal fluids and crustal rocks is enhanced. The $^{40}Ar/^{36}Ar$ ratios of samples Gen-2 and Cur (285 and 295, respectively) are close to the value measured in the air (295.5), however the relatively high (>0.29) He/Ne ratios (1.38 and 6.96) exclude any possible air-contamination during the sampling, pointing to the existence of an ASW component that interact with the magmatic-hydrothermal system at depth. Sample Pel and the crater fumaroles samples, on the other hand, have $^{40}Ar/^{36}Ar$ ratios (ranging from 311 to 491) indicating that up to 66% of the total Ar is related to the radiogenic decay of ^{40}K (*Sarda et al. 1985*), the latter being typically enriched in crustal rocks.

The isotopic composition of $\delta^{13}C\text{-}CO_2$ and the $CO_2/^3He$ ratios (Figure V-5a) provide further evidences to distinguish different fluid sources (mantle, limestone and organic-rich sediment) contributing to Peteroa fluid discharges (*Sano and Marty 1995*). Although the $\delta^{13}C\text{-}CO_2$ values of the crater fumaroles (from -11.57 to -3.56‰ V-PDB) partially overlap the range typical of mantle CO_2 (-5‰ ±2‰ V-PDB; *Sano and Marty 1995*), its $CO_2/^3He$ ratios (ranging from $1.26x10^{10}$ to $8.54x10^{10}$) are approximately ten times higher than the value reported for the MORB ($1.41x10^9$; *Sano and Marty 1995*), suggesting that CO_2 is not only related to mantle degassing (2 to 12% of the CO_2) but also to decomposition of both marine carbonates (51 to 86% of the CO_2) and organic-rich sediments (11 to 37%; Figure V-5a). These results can be attributed to a significant contribution of subducted sediments to the magma source (e.g. *Snyder et al. 2003*), although a possible interaction of the magmatic fluids with the carbonate-rich sedimentary sequences beneath the Peteroa volcano is more likely, as suggested by the $\delta^{15}N\text{-}N_2$ values (4.47 to 5‰ vs. Air) of the fumarolic gases (Figure V-5b), as well as by the increased $^{87}Sr/^{86}Sr$ ratios and $\delta^{18}O$ values measured in the PPAVC volcanic products (*Tormey et al. 1995*). The $\delta^{13}C\text{-}CO_2$ bubbling pool values, on the other hand, are slightly more negative (from -13.21 to -12.58‰ V-PDB) than the one measured in the crater fumaroles, and its $CO_2/^3He$ ratios are up to three orders of magnitude higher than those of the MORB (from $2.31x10^{10}$ to $1.49x10^{12}$). These features, coupled with the $\delta^{15}N\text{-}N_2$ values (-1 to 0.34‰ vs. Air) similar to those of terrestrial sediments and ASW, confirm the relatively high residence times that the magmatic-hydrothermal fluids

feeding the bubbling pools have experienced while passing through a carbonate- and organic-rich crustal section.

V.6.2 Temporal and spatial evolution of the physico-chemical characteristics of the Peteroa fluid discharges in 2010-2012

As shown in Figures V-4a and b, the temporal pattern (from 2010 to 2012) of CO_2-HCl-(SO_2+H_2S) and CH_4-SO_2-Ar at the crater fumaroles suggest two distinct phase of volcanic activity at Peteroa. During the 2010-2011 unrest episode, the crater fumaroles had a composition typically of volcanic emissions in magmatic-hydrothermal stages, dominated by CO_2(H_2S) and with comparable amounts of hydrothermal- and magmatic- related components such as CH_4, and SO_2, HCl and HF, respectively (Table V-1; e.g. *Benavente et al. 2013*). The CO_2/CH_4 ratios slightly increased from 3,300-4,100, in February 2010, to 7,400-10,700, in March 2011, likely resulting from the evolution of the hydrothermal-magmatic reservoir to higher temperatures and/or oxidizing conditions (e.g. *Capaccioni et al. 1995; Vaselli et al. 2010*). In March 2012, the SO_2, HCl and HF abundances of the crater fumaroles increased by three orders of magnitude (Table V-1), suggesting that magmatic fluids overwhelmed the previous "hydrothermal-magmatic signature". However, for the same period, a decrease in R/R_{air} ratios (6.59-7.11, in 2011, to 4.43-4.55, in 2012) and CO_2 (961-980 mmol/mol, in 2010-2011, to 343-363 mmol/mol, in 2012) were observed (Table V-1). Such change, from a magmatic-hydrothermal stage to a subsequent phase dominated by magmatic components, can be explained in terms of a degassing episode from a relatively "old" (i.e. highly degassed) magma body, as it has already suggested by *Naranjo (2012)* based on the chemical similarities between the eruptive products emitted during the 2010-2011 cycle and the 1837 unrest episodes. Any He remaining in this "old" magma body would be low in concentration and would, therefore, not be expected to retain its original mantle $^3He/^4He$ signature due to the assimilation of ^4He-rich crustal material (e.g. *Kennedy and Van Soest 2006; de Leeuw et al. 2010*). This process would explain the decrease in R/R_{air} ratios during the magmatic stage.

Despite the overall increase in a potentially magmatic signature of the crater fumaroles in March 2012, the highest outlet temperatures were registered in February 2010 (91.8-102.1°C), whereas in March 2011 and 2012 the outlet temperature did not significantly change from ~88°C. This tendency, also observed in the mean monthly soil temperatures at the Peteroa caldera (Figure V-3a), could be explained as a relatively major release of fluid and heat from the magmatic-hydrothermal reservoir

during the first eruptive cycle. Such fluid release would have caused both enhanced fumarolic activity and elevated ground temperatures, but would have also reduced the fluid pressure within the magmatic-hydrothermal reservoir, causing the surface subsidence of up to 15 cm that was registered in March 2010 at PPAVC and its surrounding by *Pritchard et al (2013)*.

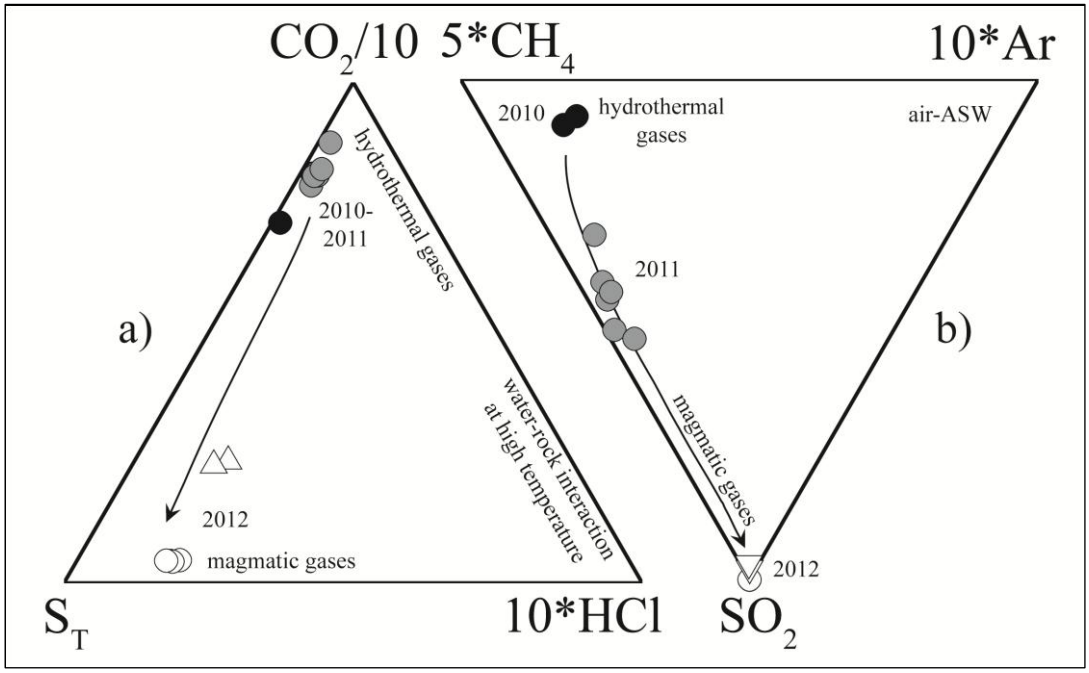

Figure V-6: a) CO_2/10-S_T-HCl*10 diagram for the thermal discharges sampled at Peteroa volcano and its surrounding. Hydrothermal and magmatic gases end members as Fisher et al 1997. b) SO_2-Ar-CH_4*10 diagram. Symbols as in Figure V-4.

As the volcanic activity proceeds, the melting of the glacier is enhanced producing subglacial water that interacts, in different degrees, with the uprising magmatic-hydrothermal fluids, as also suggested by the outlet temperature of the crater fumaroles at the boiling point of water at 3,500 m a.s.l. According to the distribution of the δD- and $\delta^{18}O$-H_2O values for the crater fumaroles (Figure V-7), the samples collected during the magmatic-hydrothermal stage (March 2011) are related to mixing processes between meteoric (MW) and "andesitic" water (*Taran et al. 1989; Giggenbach 1992a*). Contrary to what intuition would indicate, samples collected during the magmatic stage (March 2012), as well as the water samples of the crater lakes and the bubbling pools plot along the local meteoric line. I argue that the δD and $\delta^{18}O$ temporal variations at the crater fumaroles between March 2011 and 2012 (Figure V-7) are related to an episode of minimum and maximum availability of rain water and/or melted glacial water in the shallow aquifer. Field observations of the crater from where the gas condensates were taken in March 2011, which is also near to the sampling

points in March 2012 (crater 2; Figure V-2), indicate the presence of an acid lake only in March 2012, confirming the proposed hypothesis. The occurrence of SO_2, HCl, and HF in the crater fumaroles, even during the magmatic-hydrothermal stage, indicate that the shallow aquifer as well as the underlying hydrothermal systems were not able to completely scrub the highly soluble and reactive gases released from the magmatic reservoir. According to the numerical models carried out by *Symonds et al. (2010*), the latter indicates that the meteoric aquifer and the hydrothermal reservoir are not well developed and/or have an acidic pH (*Symonds et al. 2010*)

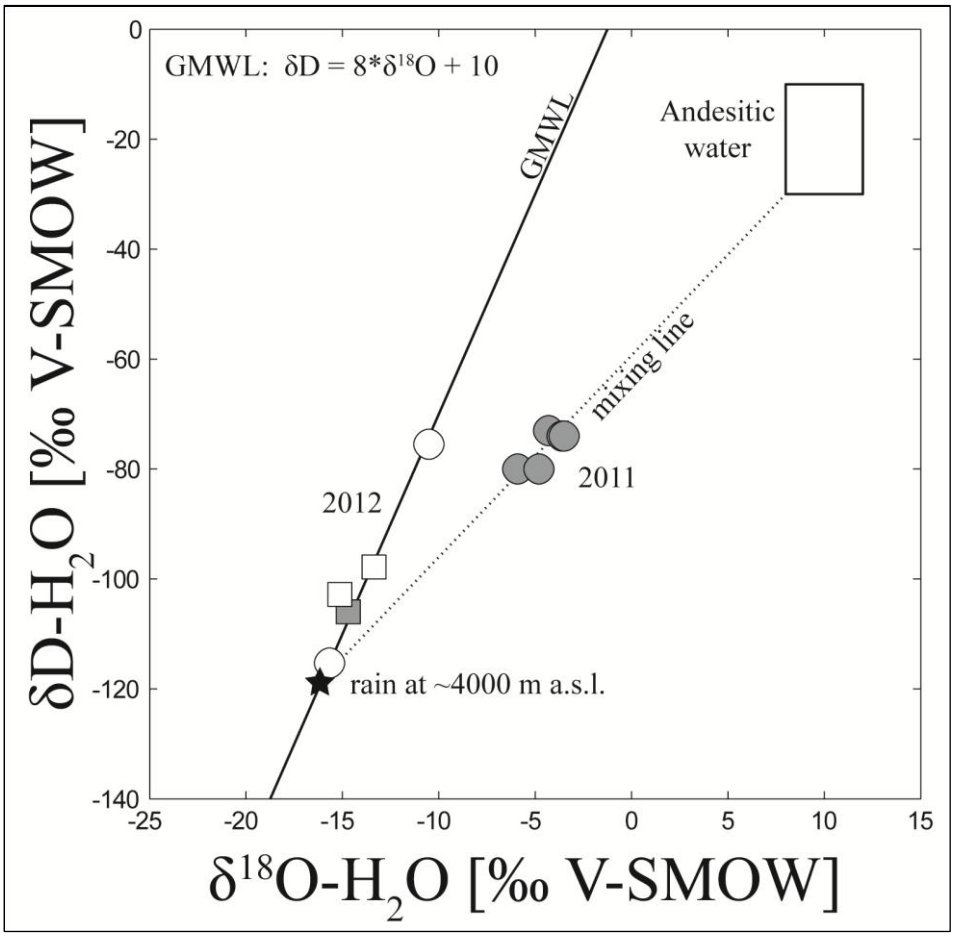

Figure V-7: $\delta^{18}O$-H_2O vs. δD-H_2O diagram of steam and water sampled from thermal discharges at Peteroa volcano and its surroundings. Andesitic water field (Taran et al., 1989; Giggenbach, 1992), Global Meteoric Water Line (GMWL; Craig, 1961), isotopic composition of the meteoric water (MW) at 4,000 m a.s.l. and mixing line between meteoric and andesitic water are reported. Symbols as in Figure V-4.

Even though no significant increase in outlet temperatures at the fumarolic vents and soil temperature at the crater are evident during the magmatic stage, a change in the physico-chemical conditions (temperature, pressure and redox) of fluids at depth is expected (e.g. *Fischer et al 1997; Vaselli et al 2003, 2010; Tassi et al 2013*). According to the approach proposed by *Giggenbach (1993)*, theoretical equilibrium temperatures

of magmatic-hydrothermal fluids in the CH_4-CO_2-H_2 system can be calculated by the following reaction:

$$CH_4 + 2H_2O \leftrightarrow 4H_2 + CO_2 \quad (V.1)$$

The temperature dependence of the equilibrium constant of reaction *(V.1)* in the equilibrated vapor and liquid is given by:

$$\log(X_{CH4}/X_{CO2})_v = 4R_H + 5181/T(K) \quad (V.2)$$

$$\log(X_{CH4}/X_{CO2})_l = 4R_H + 5181/T + \log(B_{CO2}) - \log(B_{CH4}) \quad (V.3)$$

, where $R_H = \log(X_{H2}/X_{H2O})$, $\log(X_{H2O}) \approx \log(f_{H2O}) = 4.9 - (1820/T)$, T is in K, and B_{CO2} and B_{CH4} are the vapor/liquid distribution coefficients of CO_2 and CH_4, respectively (*Giggenbach 1987, 1991*). The B_{CO2} and B_{CH4} values at different temperatures are calculated on the polynomial equations reported by *Sepulveda et al (2007).* Assuming that Ar in magmatic-hydrothermal fluids is of atmospheric origin and is controlled by the equilibrium between the atmosphere and air-saturated water ($\log(r_{Ar}) = -6.52$, where r_{Ar} is the Ar mol-ratio), *Giggenbach (1993)* suggested that under equilibrium conditions, H_2 concentrations in the equilibrated vapor and liquid are related to R_H by the following equations:

$$\log(X_{H2}/X_{Ar})_v = R_H - \log(r_{Ar}) \quad (V.4)$$

$$\log(X_{H2}/X_{Ar})_l = R_H - \log(r_{Ar}) - \log(B_{H2}) \quad (V.5)$$

, where the vapor/liquid distribution coefficients B_{H2} was calculated from the same data sources used for those of CO_2 and CH_4. In Figure V-8a the $\log(X_{H2}/X_{Ar*})$ vs. $\log(X_{CH4}/X_{CO2})$ grid is constructed on the basis of Equations V.2, 3, 4 and 5 at different R_H and temperatures (*Giggenbach and Goguel 1989; Giggenbach 1993*). The Ar* values, used in Figure V-8 instead of the Ar molar concentrations, were calculated as follows:

$$Ar^* = Ar - (O_2/22) \quad (V.6)$$

The O_2/22 values correspond to the amounts of Ar added by atmospheric contamination, because O_2 is completely absent in pristine hydrothermal fluids and only occurs as the result of shallow level atmospheric contamination. The gases collected at the crater during the magmatic-hydrothermal stage plot along the liquid equilibrium curve at R_H values near -3.1, with temperatures ranging from ~290ºC, in February 2010, to ~330ºC in March 2011 (Figure V-8a). Such redox conditions are lower than those dictated by the $FeO/FeO_{1.5}$ "rock" buffer ($R_H = -2.8$) and they can be ascribed to inputs of oxidizing magmatic-related fluids into the hydrothermal reservoir, which agree with the presence of SO_2 in the crater gases (Table V-1; *Giggenbach 1987*). The distribution of the gases sampled during the magmatic stage at Peteroa indicates even higher oxidizing conditions ($R_H \approx -3.25$) with respect to the prior period. However, there is no significant increment of the equilibrium temperature (Figure V-8a). The evolution of equilibrium conditions calculated using the CO_2-CH_4-H_2-Ar systems is consistent with the changes from a magmatic-hydrothermal (in 2010-2011) to a magmatic stage (in 2012).

Chemical equilibria in the H_2-CO_2-CO-CH_4-H_2O system can also be considered for geothermometric evaluation of the Peteroa fumarolic fluids (*Chiodini and Marini 1998*). The equilibrium conditions are adequately described by the following two redox-independent reactions (*Chiodini and Marini 1998*):

$$CO_2 + H_2 \leftrightarrow H_2O + CO \quad (V.7)$$

$$CH_4 + 3CO_2 \leftrightarrow 4CO + 2H_2O \quad (V.8)$$

The analytical expressions of the thermodynamic constants of Equations V.7 and V.8, i.e. $\log(H_2O/H_2)+\log(CO/CO_2)$ and $3\log(CO/CO_2)+\log(CO/CH_4)$, are controlled by the temperature of an original saturate liquid phase (T_o) and either adiabatic single-step steam separation temperature (T_s; Figure V8-b). As shown in Figure V-8b, in spite some spread, fumarolic samples of Peteroa volcano plot within the vapor + liquid field. The evolution of the equilibrium conditions in Figure V-8b indicates an increasing intensity in boiling of the magmatic-hydrothermal reservoir during the unrest episode (2010-2011). In February 2010 vapor phase was separated from a liquid zone (T_o~275°C) at a temperature T_s>200°C and a pressure >16 bar; whereas in March 2011 fumarolic gases plot near the liquid line at T_o~350°C and a T_s<150°C. The relatively low H_2 and CO contents of sample Pet-5 in March 2011 (Table V-1), which plots far from the gases collected in 2011, are likely related to the extremely low gas flux of this fumarole (T~43°C; Table V-1), which favors oxidation of highly reactive gas

species at shallow depth. Fumarolic gases collected during the magmatic stage, on the other hand, plot close to a T_o and T_s up to 325°C and 275°C, respectively (Figure V-8b), evidencing a steam separation at higher pressures (~60 bar).

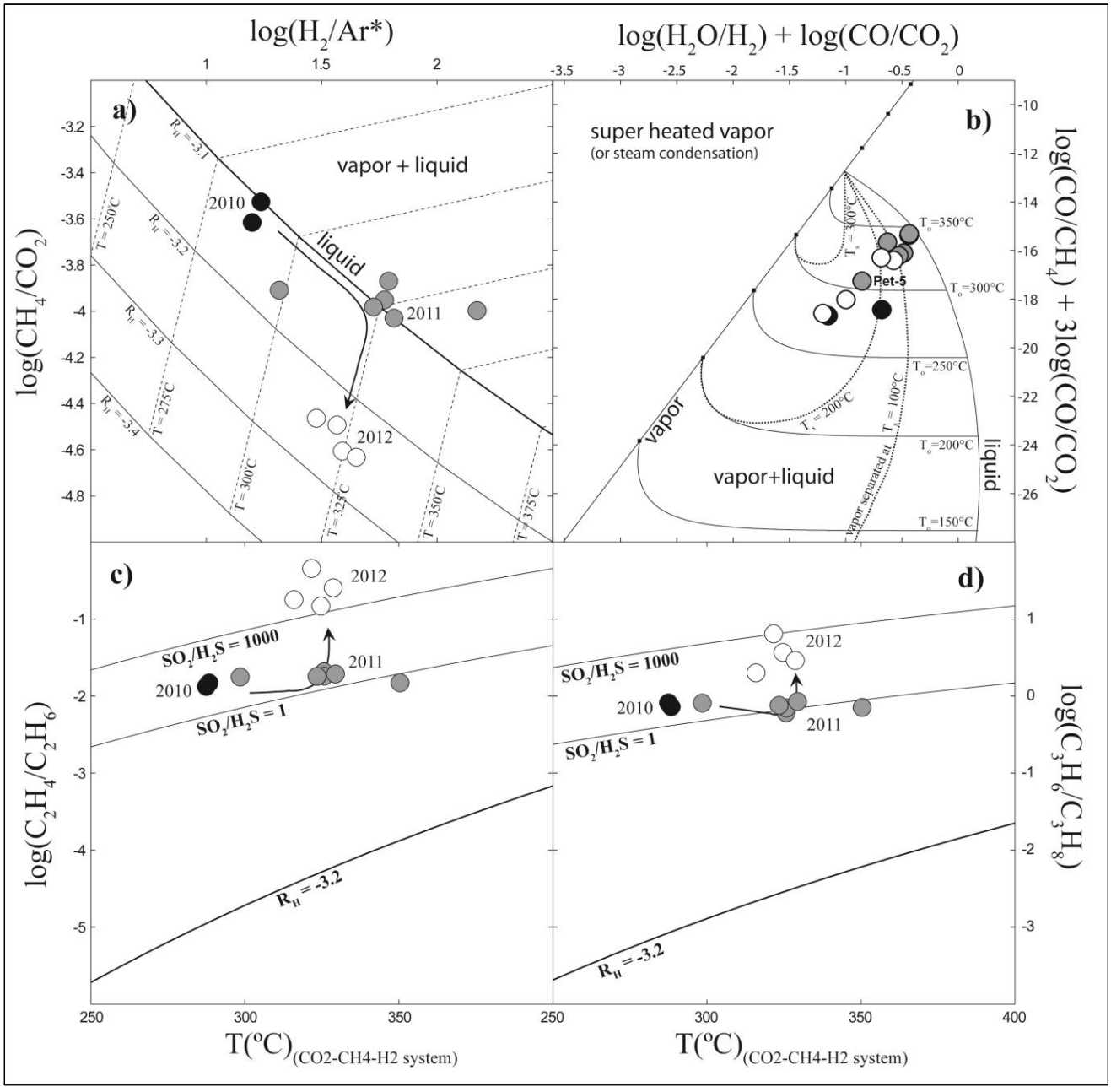

Figure V-8: a) log(H_2/Ar*) vs. log(CH_4/CO_2) diagram for the thermal discharges sampled at Peteroa volcano and its surrounding. Ar*=Ar−O_2/22; R_H=log(H_2/H_2O) (*Giggenbach 1987*). Black solid curve refer to the FeO-$FeO_{1.5}$ (Giggenbach, 1987) redox buffers (R_H=-2.8). b) 3log(CO/CO_2)+log(CO/CH_4) vs. log(H_2O/H_2)+log(CO/CO_2) binary diagram for the Peteroa volcano fumaroles after *Chiodini and Marini (1998)*. Theoretical compositions were calculated considering gases solubilities and thermodynamic data for pure water. Binary diagrams of c) log(C_2H_4/C_2H_6) and d) log(C_3H_6/C_3H_8) vs. calculated temperatures (°C) in the H_2-CO_2-CH_4-Ar system (Figure V-8a). Black solid curves refer to a redox buffer of R_H=-3.2, whereas grey solid curves refer to the SO_2-H_2S redox buffer at SO_2/H_2S ratios equal to 1 and 1000 (Giggenbach 1996). Symbols as in Figure V-4.

I additionally explore the thermodynamic conditions of the deep fluid source regions on the basis of the C_2-C_3 hydrocarbons chemical features (*Cappaccioni and Mangani 2001; Taran and Giggenbach 2003*). De-hydrogenation process involving the C_2 and C_3 alkene-alkane pairs are conveniently described by the following reactions:

$$C_2H_6 \leftrightarrow C_2H_4 + H_2 \quad (V.9)$$

$$C_3H_8 \leftrightarrow C_3H_6 + H_2 \quad (V.10)$$

Using thermochemical data reported by *Barin (1989), Domalski and Hearing (1993) and Reid et al. (1987)*, the temperature dependence of equilibrium constants are:

$$\log(X_{C2H4}/X_{C2H6}) = 7.43 - 7809/T - \log(H_2) \quad (V.11)$$

$$\log(X_{C3H6}/X_{C3H8}) = 7.15 - 6000/T - \log(H_2) \quad (V.12)$$

Equations (V.11) and (V.12) depend, besides of temperature, on $\log(H_2)$. Therefore, the C_2 and C_3 pairs provide information on both thermal and redox conditions of fluid reservoir (e.g. *Tassi et al 2005*). Figure 8c-d shows the $\log(X_{C2H4}/X_{C2H6})$ and $\log(X_{C3H6}/X_{C3H8})$ values plotted vs. temperature (°C) estimates from to the CO_2-CH_4-H_2-Ar system (Figure V-8a). All the gas samples taken at Peteroa crater cluster far from the equilibrium curve $R_H = -3.2$. This suggests that conversion of the C_2 and C_3 alkene to alkane pairs was efficiently controlled at higher oxidizing conditions than those that control the CO_2-CH_4-H_2-Ar equilibrium (Figure V-8a). Such oxidizing conditions could correspond to those of the SO_2-H_2S redox pair, which is the most reliable buffer system in a magmatic-dominated environment (*Giggenbach 1996*). At the equilibrium temperatures calculated on the basis of the CO_2-CH_4-H_2 system, the C_2H_4-C_2H_6 and C_3H_6-C_3H_8 values of the gas samples taken during the hydrothermal-magmatic and magmatic stages attain equilibrium at R_H, consistent to those of the SO_2-H_2S redox buffer for SO_2/H_2S ratio of 1 and ≥1000, respectively. These evidences are in agreement with a strong input of magmatic fluids in the fumarolic gases at Peteroa in March 2012.

V.7 CONCLUSIONS

Despite that seismic activity and surface deformation pattern have not reflected any significant magma movements and eruptive activity at Peteroa ceased after the 2010-2011 unrest episode, the drastic changes in the fluid geochemistry that occurred at the Peteroa fumaroles from the 2010-2011 unrest episode to March 2012 point to the occurrence of a magmatic chamber supplying fluid and heat at depth. A key observation for understanding the mechanisms responsible for the recorded geochemical evolution of the fumarolic fluids at Peteroa is given by the NNE-SSW orientation (Figure V-9a) of the subsidence that affected the volcanic complex within months of the 27th February 2010 MW 8.8 Maule earthquake (*Pritchard et al. 2013*).

The Peteroa volcano is emplaced along a NNE-SSW high-angle (>60°) thrust fault which is favorably oriented for dextral shear with respect to the prevailing stress field affecting the Andean region (i.e. a subhorizontal maximum principal compressive stress-σ_{Hmax} trending N60°E; *Cembrano and Lara 2009* and references therein). Correspondingly, the NNE-SSW orientation of the subsidence reported by *Pritchard et al. (2013)* may reflect the shape of both the hydrothermal-magmatic reservoir and the underlying magmatic systems (Figure V-9b), as deep-sourced fluids would be preferentially transported along NNE-strike vertical tension cracks formed under upper crustal dextral strike-slip deformation (e.g. *Cembrano and Lara 2009*). As *Pritchard et al. (2013)* suggested, the existing NNE-striking magmatic and hydrothermal systems at PPAVC were disturbed by the static and dynamic stress change of the Maule earthquake through the formation and/or reactivation of numerous cracks suitably oriented with respect to the co-seismic stress field (Figure V-9b), allowing fluids and heat to escape from the magmatic and hydrothermal reservoirs. According to this hypothesis, the enhanced fumarolic activity and elevated ground temperatures observed during the 1st eruptive cycle (February 2010) should be a consequence of this intense escape of fluids from a reservoir where vapor and liquid were in equilibrium at a T~275°C, a pressure >60 bar and redox conditions slightly more oxidized (R_H~ -3.1) that those dictated by the $FeO/FeO_{1.5}$ buffer (Figure V-9c). Such fluid releases (<0.029 km^3; *Pritchard et al. 2013*) would have drastically reduced the fluid pressure within the magmatic-hydrothermal reservoir causing both the surface subsidence (~15 cm) registered in March 2010 at PPAVC (*Pritchard et al 2013*), as well as the phreatic eruptions observed during the 1st eruptive cycle (Figure V-3).

In March 2011, the acid gases content at crater fumaroles, as well as the CO_2/CH_4 and N_2/Ar ratios slightly increased compared to those observed in February

2010, whereas R_H values remained relatively constant. These temporal changes suggest that after an almost uninterrupted release of fluids from the magmatic-hydrothermal reservoir during the 2010 unrest episode (Figure V-3), a partial consumption of the liquid-dominated system overlying the magmatic zone would have occurred (e.g. *Chiodini et al. 2004*). Such process is clearly observed in Figure V-8b where fumarolic gases sampled in March 2011 plot close to the pure liquid equilibrium line at To~350°C, being this composition typical of vapors separated from a liquid reservoir when complete vaporization of the liquid zone occurs (e.g. Guagua Pichincha–Ecuador; Montserrat–West Indies, Aguashuca–Salvador, Tambora–Indonesia; *Chiodini and Marini 1998).*

Continuation of the degassing process from the magmatic-hydrothermal reservoir would have led to a total consumption of the liquid-dominated systems, lowering abruptly the load experienced by the underlying magmatic chamber at Peteroa (*Fourier 2010*). *Fournier (2010)* argued that such process may induce rapid vesiculation within the water-saturated magma, resulting in the rupture of the self-sealed zone surrounding the magmatic body (*"sealing carapace"*; *Fisher et al. 1996*). Consequently, a rapid loss of exsolved fluids from the crystallizing magma as well as flashing from any brine that had previously resided in plastic rock beneath the self-sealed zone are expected (Figure V-9d). The increasing seismic activity observed from March 2011 to January 2012 at PPAVC and its surroundings (Figure V-3b) together with the clear magmatic signature observed in March 2012 at the crater fumaroles (Figure V-6) is consistent with this hypothesis. Discharge of magmatic fluid across a narrow ring directly into brittle rock where hydrostatic pressure conditions prevails (Figure V-9d) strongly favors the evolution of SO_2-rich and H_2S-poor fluids, explaining the relatively high SO_2/H_2S ratios measured (>2; Table V-1) and estimated (~1000; Figure V-8c and d) during March 2012 at the crater fumaroles (*Fournier 2010; Liotta et al. 2010*). The relatively low HCl contents (<14.1 mmol/mol) measured during the magmatic stage at the crater fumaroles may be a consequence of the relatively low temperature at which the vapor phase was separated (T_S<275°C), as $HCl_{(0)}$ is preferentially partitioned into the liquid phase at T<400°C (*Fournier 2010*).

A similar scenario would have also occurred during the 2nd eruptive cycle (Figure V-3), where a sudden rupture of the self-sealed zone would have caused the observed phreatic-magmatic eruptions. This is corroborated by the similar SiO_2 contents displayed by the juvenile materials emitted during this eruptive episode (Figure V-3) and those of the eruptive products from 1837 eruption (*Naranjo 2012*), which indicate

that the 2010-2011 unrest episode did not involve the injection of a new batch of magma at depth (Figure V-9d).

The intimate relation between seismic and deformation signals, as well as ground-temperature and geochemical parameters, observed in 2010–2012 demonstrates that monitoring of the crater fumarolic fluids can provide important information on the fluid source regions responsible for the evolution of the volcanic activity at Peteroa volcano. Further efforts should initiate a periodic inventory of the diffuse gas (CO_2) emissions from the soil of the outer flanks of the volcanic edifice, as these may reveal fracturing processes of the edifice. The gas emanations data should be coordinated with improved geophysical measurements such a high definition global positioning system permanent station and remotely measured SO_2 flux, which allows a better interpretation of all the data in terms of eruption forecasting.

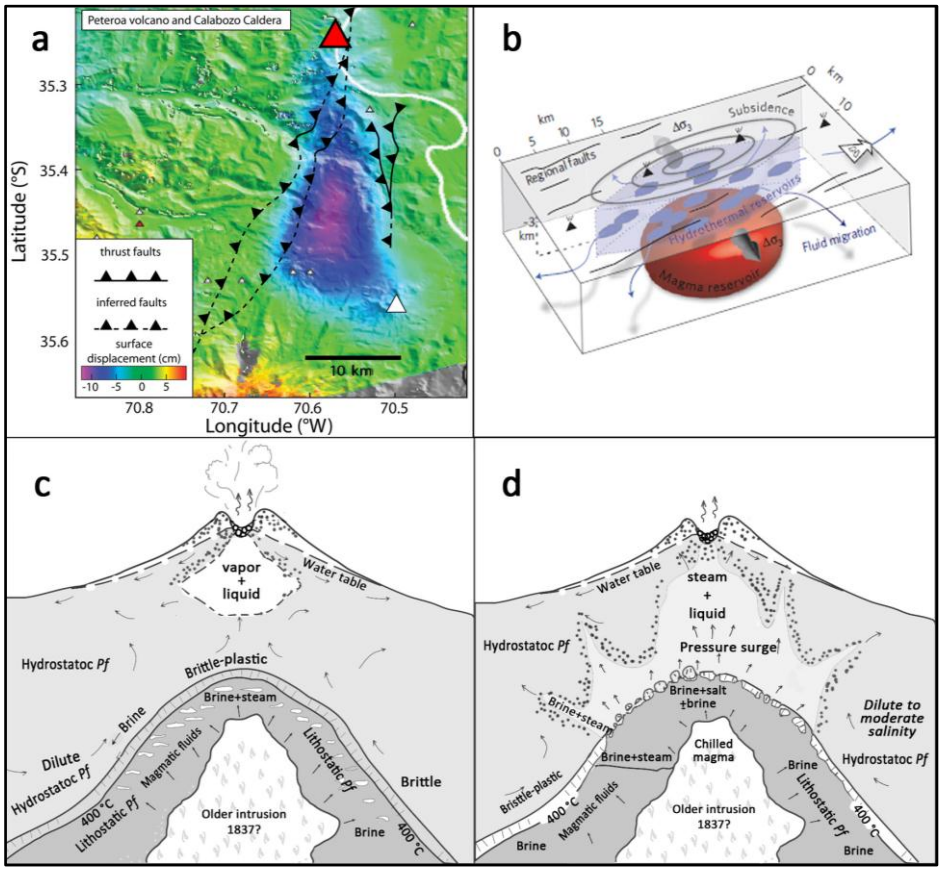

Figure V-9: a) Volcanic ground subsidence at Peteroa volcano and at Calabozo caldera complex observed in the interferogram stacks spanning the earthquake (modified from *Pritchard et al. 2013*). Regional fault systems are reported for comparison (*Benavente and Gutierrez 2011*). b) Conceptual diagram of the mechanism that explains the volcanic subsidence triggered by the Maule earthquake (*Pritchard et al. 2013*). c) and d) Schematic models of the transition from a hydrothermal-magmatic episode (c) to magmatic episode (d) at Peteroa volcano caused by a temporary breaching of a normally self-sealed zone. See text for discussion.

REFERENCES

Aguilera F, Benavente O, Gutierrez F, Agusto M, Caselli A (2011) Distribution of gas-water discharges and current geochemical survey along Planchón-Peteroa-Azufre Volcanic Complex, southern Chile. 11th Gas Workshop 1-10 September, Petropavlosk-Kamchatki, Russia, pp. 5

Aguilera F, Romero J, Gutierrez F, Agusto M, Saltori O, Benavente O, Caselli A, Pizarro M (2012a) Eruptive activity of Peteroa volcano for Period 2010-2011, Southern Volcanic Zone, Chile. XIII Chilean Geologic Congress 5-9 August, Antofagasta, Chile, pp. 600–602

Aguilera F, Tassi F, Darrah T, Moune S, Vaselli O (2012b) Geochemical model of a magmatic-hydrothermal system at the Lastarria volcano, northern Chile. Bulletin of Volcanology 74(1): 119-134.

Agusto M, Tassi F, Caselli A T, Vaselli O, Rouwet D, Capaccioni B, Caliro S, Chiodini G, Darrah T (2013) Gas geochemistry of the magmatic-hydrothermal fluid reservoir in the Copahue-Caviahue Volcanic Complex (Argentina). Journal of Volcanology and Geothermal Research 257(0): 44-56.

Barazangi M, Isacks B (1976) Spatial distribution of earthquakes and subduction of the Nazca plate beneath. South America. Geology 4:606–692.

Barin I (1989) Thermochemical Data on Pure Substances. Vol. 1, VCH, Wenheim.

Benavente O, Gutiérrez F (2011). Nueva temperatura estimada para el sistema hidrotermal asociado a los Complejos Volcánicos Planchón-Peteroa y Descabezado Grande-Quizapu-Azul, 35º36ºS, Chile. XVIII Congreso Geológico Argentino, Neuquen, Argentina.

Benavente O, Tassi F, Gutiérrez F, Vaselli O, Aguilera F, Reich M (2013). Origin of fumarolic fluids from Tupungatito Volcano (Central Chile): interplay between magmatic, hydrothermal, and shallow meteoric sources. Bulletin of Volcanology C7 - 746 75(8): 1-15.

Bulletin of Global Volcanism Program (BGVP 2001) Peteroa, Volcanic Activity Reports, BGVN 26:03. http://www.volcano.si.edu

Cande S, Leslie R (1986) Late Cenozoic tectonics of the southern Chile Trench. J Geophys Res 91:471–496.

Cande S, Leslie R (1987) Interaction between the Chile Ridge and Chile Trench: geophysical and geothermal evidence. J Geophys Res 92:495–520.

Capaccioni B, Mangani F (2001) Monitoring of active but quiescent volcanoes using light hydrocarbon distribution in volcanic gases: the results of 4 years of discontinuous monitoring in the Campi Flegrei (Italy). Earth Planet Sci Lett 188:543–555.

Capaccioni B, Aguilera F, Tassi F, Darrah T, Poreda RJ, Vaselli O (2011) Geochemical and isotopic evidences of magmatic inputs in the hydrothermal reservoir feeding the fumarolic discharges of Tacora volcano (northern Chile). J Volcanol Geotherm Res 208:77–85.

Capaccioni B, Tassi F, Vaselli O, Tedesco D, Poreda R (2007). Submarine gas burst at Panarea Island (southern Italy) on November 3, 2002: a magmatic versus hydrothermal episode. J. Geophys. Res., 112:B05201, doi: 10,1029/2006JB0044359.

Cembrano J, Lara L (2009). The link between volcanism and tectonics in the southern volcanic zone of the Chilean Andes: A review. Tectonophysics 471(1-2): 96-113.

Chiodini G, Marini L (1998) Hydrothermal gas equilibria: The H2O-H2-CO2-CO-CH4 system. Geochim Cosmochim Acta 62:2673–2687.

Chiodini G., Avino R., Brombach T., Caliro S., Cardellini C., De Vita S., Frondini F., Granirei D., Marotta E., Ventura G.(2004). Fumarolic and diffuse soil degassing west of Mount Epomeo, Ischia, Italy. Journal of Volcanology and Geothermal Research V. 133, Issues 1–4, pgs. 291-309.

Coleman M, Shepherd T, Rouse J, Moore G (1982) Reduction of water with zinc for hydrogen isotope analysis. Anal Chem 54:993–995

Davidson J (1974) A Quaternary volcanic mudflow (lahar) down the Claro and Teno valleys from Planchón volcano (Curicó province, Chile). International Symposium on Volcanology Andean and Antartic Volcanology Problems 9-14 September, Santiago, Chile, pp. 14-15.

de Leeuw, G. A. M., D. R. Hilton, N. Gulec, and H. Mutlu (2010). Regional and temporal variations $CO_2/^3He$, $^3He/^4He$ and $\delta^{13}C$ along the North Anatolian Fault Zone, Turkey, Appl. Geochem., 25, 524–539, doi:10.1016/j.apgeochem.2010.01.010.

Domalski ES, Hearing ED (1993) Estimation of the thermodynamic properties of C–H–N–O–S–halogen compounds at 298.15 K. J Phys Chem Ref 22:805–1159.

Elkins L J, Fischer T P, Hilton D R, Sharp Z P, McKnight S, Walker J (2006) Tracing nitrogen in volcanic and geothermal volatiles from the Nicaraguan volcanic front. Geochimica et Cosmochimica Acta 70, 5215–5235.

Epstein S, Mayeda T (1953) Variation of the 18O/16O ratio in natural waters. Geochim Cosmochim Acta 4:213–224

Evans W, White L, Rapp J (1998) Geochemistry of some gases in hydrothermal fluids from the southern Juan de Fuca Ridge. J Geophys Res 15:305–313

Farías M. (2007). Tectónica de la erosión en la evolución del relieve de los Andes de Chile Central durante el Neógeno. Tesis de Ph.D., Departamento de Geología, Universidad de Chile. 194 p. Santiago.

Fischer T P, Arehart G B, Sturchio N C, Williams S N (1996). The relationship between fumarole gas composition and eruptive activity at Galeras Volcano, Colombia. Geology 24(6): 531-534.

Fischer T P, Hilton D R, Zimmer M M, Shaw A M, Sharp Z D, Walker J A (2002) Subduction and recycling of nitrogen along the Central American Margin. Science 297, 1154–1157.

Fischer T P, Sturchio N C, Stix J, Arehart G B, Counce D, Williams S N (1997). The chemical and isotopic composition of fumarolic gases and spring discharges from Galeras Volcano, Colombia. Journal of Volcanology and Geothermal Research 77(1-4): 229-253.

Fourier R. (2006). Hydrothermal systems and volcano geochemistry. Volcano Deformation Springer Praxis Books 2006, pp 323-341.

Gardeweg M (1991) Erupción 1991 volcán Planchón-Peteroa. Serv Nac Geol Min, Report, 1

Giggenbach W F (1987) Redox processes governing the chemistry of fumarolic gas discharges from White island, New Zealand. Appl Geochem 2:143–161.

Giggenbach W F, Goguel R L (1989) Collection and analysis of geothermal and volcanic water and gas discharges. Unpublished report. Chemistry Division, DSIR-Petone, New Zealand, pp 1–81

Giggenbach W F (1991) Chemical techniques in geothermal exploration. In: D'Amore F (ed) Application of geochemistry in geothermal reservoir development. UNITAR, pp 119–144

Giggenbach WF (1992a) Isotopic shifts in waters from geothermal and volcanic systems along margins, and their origin. Earth Planet Sci Lett 113:495–510.

Giggenbach W F (1992b) The composition of gases in geothermal and volcanic systems as a function of tectonic setting. Proc Int Symp Water-Rock Interaction, WRI-8, 873–878.

Giggenbach WF (1993) Redox control of gas compositions in Philippine volcanic-hydrothermal systems. Geothermics 22:575–587.

Giggenbach W F (1996) Chemical composition of volcanic gases. In: Scarpa M, Tilling R (eds) Monitoring and Mitigation of Volcanic Hazards, Springer, Berlin, pp. 221–256.

Giggenbach W F (1997) The origin and evolution of fluids in magmatic-hydrothermal systems. in Barnes HL (ed) Geochemistry of hydrothermal ore deposits, 3rd edition, New York, John Wiley, pp. 737–796.

González-Ferrán O (1995) Volcanes de Chile. Instituto Geográfico Militar, Santiago Militar, 639 p. Santiago

Gutierrez F, Lemus M, Parada M, Benavente O, Aguilera F (2012) Contribution of ground altitude difference to thermal anomaly detection using satellite images: Application to volcanic/geothermal complexes in the Andes of Central Chile. J Volcanol Geotherm Res 237-238:69-80

Haller M, Nullo F, Proserpio C, Parica P, Cagnoni M, Walker J (1985) Major element geochemistry of early Tertiary Andean volcanics (34º-36ºS). Comunicaciones 35:97-100

Haller M, Ostera H, Pesce A, Gardini M, Folguera A (1994) Vulcanoestratigrafía reciente y eruptividad del Volcán Peteroa. VII Chilean Geologic Congress 17-21 October, Concepción, Chile, pp. 319–323

Haller M, Risso C (2011) La erupción del volcán Peteroa (35º15'S, 70º18'O) del 4 de Septiembre de 2010. Rev Asoc Geol Arg 68:295-305

Hauser A (1990) Hoja Rancagua, VI Región. Ser Nac Geol Min, 1

Hauser A (1993) Remosiones en masa en Chile. Ser Nac Geol Min, 45

Hildreth, W, Moobath S (1988) Crustal contribution to arc magmatism in the Andes of central Chile. Contrib Mineral Petrol 98:455-489

Hilton D R, Fischer T P, Marty B (2002) Noble Gases and Volatile Recycling at Subduction Zones. Rev Mineral Geochem 47:319–370.

Inguaggiato S, Rizzo A (2004) Dissolved helium isotope ratios in ground-waters: a new technique based on gas-water reequilibration and its application to stromboli volcanic system. App Geochem 19:665–673

Jenden P D, Kaplan I R, Poreda R J, Craig H (1988) Origin of nitrogen-rich gases in the Californis Great Valley: evidence from helium, carbón and nitrogen isotope ratios. Geochim Cosmochim Acta 52:851–861.

Kennedy, B.M., Van Soest, M.C. (2006). A helium isotope perspective on the Dixie Valley, Nevada, hydrothermal system. Geothermics 35, 26–43.

Liaudat D T, Penas P, Aloy G (2013) Impact of volcanic processes on the cryospheric system of the Peteroa Volcano, Andes of southern Mendoza, Argentina. Geomorphology, http://dx.doi.org/10.1016/j.geomorph.2013.11.016.

Liotta M., A. Paonita, A. Caracausi, M. Martelli, A. Rizzo, R. Favara (2010). Hydrothermal processes governing the geochemistry of the crater fumaroles at Mount Etna volcano (Italy). Chemical Geology. V. 278 pp. 92–104

Mamyrin B, Tolstikhin I (1984) Helium isotopes in nature. In: Fyfe W (eds) Development in geochemistry, Elsevier, Amsterdam, pp. 288

Martini M (1993) Water and fire: Vulcano island from 1977-1991. Geochem J 27:297–303

Marty B, Zimmermann L (1999) Volatiles (He, N, C, Ar) in mid-ocean ridge basalts: assessment of shallow-level fractionation and characterization of source composition. Geochimica et Cosmochimica Acta 63, 3619–3633.

Matsuo S, Suzuki J, Mitzutani Y (1978) Nitrogen to argon ratio in volcanic gases. In: Alexander EC, Ozima M. (eds) Terrestrial Rare Gases. Japan Science Society Press, Tokyo, pp. 17–25.

Montegrossi G, Tassi F, Vaselli O, Buccianti A, Garofalo K (2001) Sulfur species in volcanic gases. Anal Chem 73:3709–3715

Naranjo J (2012) Principales etapas evolutivas holocenas del volcán Planchón y su reactivación relacionada al megasismo del 27 de Febrero de 2010. XIII Chilean Geologic Congress 5-9 August, Antofagasta, Chile, pp. 440–441

Naranjo J, Haller M (2002) Erupciones principalmente explosivas del volcán Planchón, Andes del sur (35º15'S). Rev Geol Chile 29:93-113

Naranjo J, Haller M, Ostera H, Pesce A, Sruoga P (1999) Geología y Peligros del Complejo Volcánico Planchon-Peteroa, Andes del Sur (35º15´S), Región del Maule, Chile- Provincia de Mendoza, Argentina. Serv Nac Geol Min, 52

Pritchard ME, Jay JA, Aron F, Henderson ST, Lara LE (2013) Subsidence at southern Andes volcanoes induced by the 2010 Maule, Chile earthquake. Nature Geosci 6(8): 632-636.

Ramos VA, Cristallini E, Introcaso A (2004) The Andean thrust system latitudinal variations in structural styles and orogenic shortening. AAPG Spec Vol Memoir 82: Thrust tectonics and hydrocarbon systems, pp. 30–50.

Reid RC, Prausnitz JM, Poling BE, (1987) The Properties of Gases and Liquids. McGraw-Hill, New York, pp. 768.

Rouwet D, Inguaggiato S, Taran Y, Varley N, Santiago J A (2009). Chemical and isotopic compositions of thermal springs, fumaroles and bubbling gases at Tacaná Volcano (Mexico-Guatemala): implications for volcanic surveillance. Bulletin of Volcanology 71(3): 319-335.

Sano Y, Marty B (1995) Origin of carbon in fumarolic gases from island arcs. Chemical Geology 119, 265–274.

Sano Y, Takahata N, Nishio Y, Fischer T P, Williams S N (2001). Volcanic flux of nitrogen from the earth. Chemical Geology 171, 263–271.

Sano Y, Takahata N, Nishio Y, Marty B (1998). Nitrogen recycling in subduction zones. Geophysical Research Letters 25, 2289–2292.

Sarda P, Staudacher T, Allegre CJ (1985) 40Ar/36Ar in MORB glasses: Constraints on atmosphere mantle evolution. Earth Planet Sci Lett 72:357–375.

Sepulveda F, Lahsen A, Powell T (2007) Gas geochemistry of the Cordón Caulle geothermal system, southern Chile. Geothermics 36:389–420

SERNAGEOMIN-OVDAS (2010a) Actividad volcánica Región del Maule, Grupo volcánico Planchón-Peteroa. Reporte Especial Actividad Volcánica, 1

SERNAGEOMIN-OVDAS (2010b) Actividad volcánica Región del Maule, Grupo volcánico Planchón-Peteroa. Serv Nac Geol Min, REAV, 4

SERNAGEOMIN-OVDAS (2010c) Actividad volcánica Región del Maule, Grupo volcánico Planchón-Peteroa. RAV, 7

SERNAGEOMIN-OVDAS (2011a) Actividad volcánica Región del Maule, Grupo volcánico Planchón-Peteroa. REAV, 15

SERNAGEOMIN-OVDAS (2011b) Actividad volcánica Región del Maule, Grupo volcánico Planchón-Peteroa. RAV, 23

Shock E (1993) Hydrothermal dehydration of aqueous organic compounds. Geochim Cosmochim Acta 57:3341-3349

Snyder G, Poreda R, Fehn U, Hunt A (2003) Sources of nitrogen and methane in Central American geothermal settings: Noble gas and 129I evidence for crustal and magmatic volatile components. Geochemistry , Geophysics, Geosystems 4(1): 9001.

Stern C, Futa K, Muehelnbachs K, Dobbs F, Muñoz J, Godoy E, Charrier R (1984) Sr, Nd, Pb and O isotope composition of Late Cenozoic volcanics, northernmost SVZ (33-34°S). In: Harmon R, Barriero B, (eds) Andean Magmatism: Chemical and Isotopic Constraints. Shiva Publishing Cheshire, pp 96-105

Stevenson S (1993) Physical models of fumarolic flow. J Volcanol Geotherm 57:139–156

Symonds R, Gerlach T, Reed M (2001) Magmatic gas scrubbing: implications for volcano monitoring. J Volcanol Geotherm Res 108:303–341.

Tassi F, Aguilera F, Vaselli O, Medina E, Tedesco D, Delgado Huertas A, Poreda R, Kojima S (2009) The magmatic- and hydrothermal-dominated fumarolic system at the Active Crater of Lascar volcano, northern Chile. Bull Volcanol 71:171–183.

Tassi F, Aguilera F, Vaselli O, Darrah T, Medina E (2011) Gas discharges from four remote volcanoes (Putana, Olca, Irruputuncu and Alitar) in northern Chile: a geochemical and isotopic survey. Ann Geophys 54:121–136.

Tassi F, Martinez C, Vaselli O, Capaccioni B, Viramonte J (2005) Light hydrocarbons as redox and temperature indicators in the geothermal field of El Tatio (northern Chile). Appl Geochem 20:2049–2062.

Tassi F, Vaselli O, Papazachos C B, Giannini L, Chiodini G, Vougioukalakis G E, Karagianni E, Vamvakaris D, Panagiotopoulos D (2013) Geochemical and isotopic changes in the fumarolic and submerged gas discharges during the 2011-2012 unrest at Santorini caldera (Greece). Bulletin of Volcanology C7 - 711 75(4): 1-15.

Taran Y A, Giggenbach W F (2003) Geochemistry of light hydrocarbons in subduction related volcanic and hydrothermal fluids. Soc Econ Geol 10:61–74.

Taran YA, Pokrovsky B, Esikov A (1989) Deuterium and oxygen-18 in fumarolic steam and amphiboles from some Kamchatka volcanoes: "andesitic waters". Doklady Akademii nauk SSSR 304:440–443.

Tormey D, Frey F, López-Escobar L (1989) Geologic history of the active Azufre-Planchon-Peteroa Volcanic Center (35°15'S, southern Andes) with implications for the development of compositional gaps. Rev Asoc Geol Arg 44:420-430

Tormey D, Frey F, López L (1995) Geochemistry of the Active Azufre-Planchón-Peteroa Volcanic Complex, Chile (35º15'S): Evidence for Multiple Sources and Processes in a Cordilleran Arc Magmatic System. J Petrol 36:265-298

Tormey D (2010) Managing the effects of accelerated glacial melting on volcanic collapse and debris flows: Planchon-Peteroa volcano, southern Andes. Global Planet Change 74:82-90

Varekamp J C, Pasternack G B, Rowe G L (2000) Volcanic lake systematics II. Chemical constraints. J. Volcanol Geotherm Res 97:161–179.

Vaselli O, Tassi F, Montegrossi G, Capaccioni B, Giannini L (2006) Sampling and analysis of fumarolic gases. Acta Vulcanol 18:65–76

Vaselli O, Tassi F, Duarte E, Fernandez E, Poreda R J, Delgado Hueras A (2010) Evolution of fluid geochemistry at the Turrialba volcano (Costa Rica) from 1998 to 2008. Bulletin of Volcanology 72: 397-410.

Vaselli O, Tassi F, Montegrossi G, Duarte E, Fernandez E, Bergamaschi F (2003) Fumarole migration and fluid chemistry at Poás volcano (Costa Rica) from 1998 to 2001. In: Oppeneheimer C, Pyle DM, Barclay J (eds) Special Memory of the Geol. Soc. of London (UK), Special Issue on: "Volcanic degassing", 213, pp 247–262.

CAPÍTULO VI

THE OROGENIC AND MAGMATIC ORIGIN OF THE HYDROTHERMAL SYSTEMS OF THE ANDES OF CENTRAL CHILE (32.5-36°S)

VI.1 INTRODUCTION

The Andes of Central Chile (32.5-36°S) is an active subduction-related mountain belt that hosts eight active volcanoes, more than sixty thermal fluid discharges (cold and hot springs, bubbling pools, mud pools and fumaroles) and dozen mineral deposits including Au-Cu veins, Cu-Skarns, Au-epithermal and Cu-porphyries (Figure VI-1; *Hauser 1997; Maksaev et al. 2007; Stern et al. 2007*). Like in other collisional- and subduction-related orogens (e.g. Southern Alps-New Zealand, Taiwan, Rocky Mountains-Canada, Coast Ranges-Canada, Alps-Europe, Pyrenees-Europe, Central Himalaya, Nanga Parbat-Western Himalaya; *Craw et al. 2002* and references therein), the presence of both mineral deposits and thermal features evidences the extensive hydrothermal circulation that has taken place in the Andean range during its development (*Hauser 1997; Maksaev et al. 2007*). Nowadays, both fluid discharges and heat flow anomalies occur at the Principal Cordillera (PC) of Central Chile in close association with N-S and NE-SW trending thrust faults and active volcanoes (Figure VI-2a and b), suggesting a first-order tectono-magmatic control on their occurrences (*Hamza and Muñoz 1996; Hauser 1997*). Nevertheless, to our knowledge, there is not a comprehensive study regarding the origin and nature of these hydrothermal discharges.

A general assessment of the primary chemical characteristics of thermal waters in Central Chile was carried out by *Hauser (1997)*, who proposed the occurrence of two main fluid domains. The first domain includes cold and hot springs located along the western edge of the PC (32.5-34°S), where Ca-HCO_3 and Ca-SO_4 alkaline waters (pH>7.3) with low TDS (<1000 mgL^{-1}) are closely associated with the Pocuro-San

Ramón fault zone (Figure VI-2a). The second domain (35-36°S) consists of hot springs, bubbling pools, mud pools and fumaroles located close to the Holocene volcanic chain (eastern edge of the PC; Figure VI-2a), with water showing a Na-Cl, Ca(Na)-HCO_3 and Ca(Na)-SO_4 composition, neutral to slightly acidic pH and high TDS values (>1000 mgL^{-1}). The latter has an estimated heat flow up to 220 mW/m^2 (Figure VI-2b), which is ~3.5 times higher than that of the former (down to 60 mW/m^2; *Hamza and Muñoz 1996*). Up to date, the causes of the spatial zonation in heat flow and chemical features of emerging waters, as well as the role of the active fault systems and the volcanic arc in affecting the water geochemistry remain unclear.

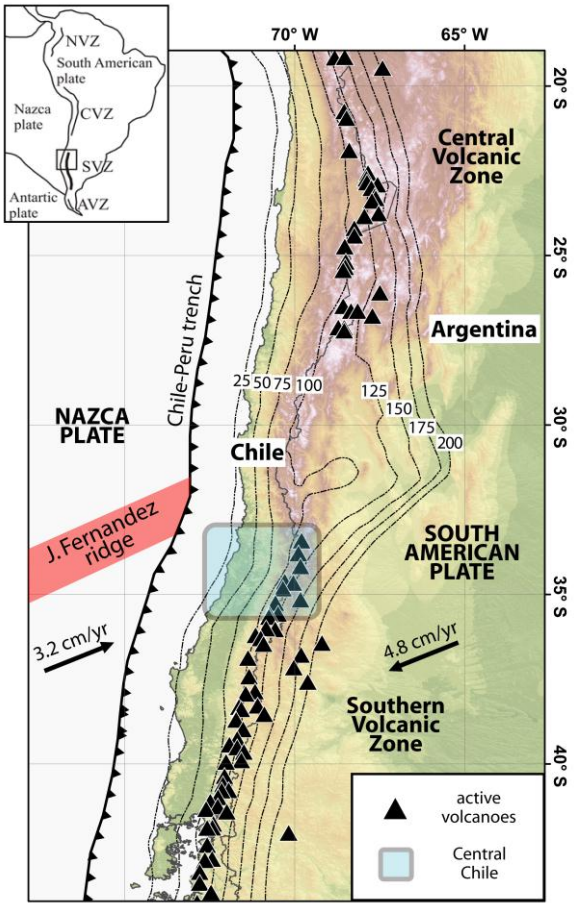

Figure VI-1: Digital elevation model (ASTER GDEM) and tectonic framework of the Andean Margin of Chile. The position of the Holocene volcanoes along the Central and Southern Volcanic Zones, and the Wadatti-Benioff zone contours (km) of the convergent zone are shown (*Tassara et al. 2006; Stern et al. 2007*). Absolute plate motion velocity after *Gripp and Gordon (2002).*

A preliminary evaluation of the geothermal potential in the Andes of Central Chile was carried out by the ENAP (Empresa Nacional del Petróleo; *Soffia 2004*), who estimated a potential varying between 400 and 1300 MW_e along four geothermal areas: Volcán San José, Tinguiririca, Calabozos and Mariposas. So far, Tinguiririca (by Energía Andina S.A.), Calabozos (by ENEL Green Power) and Mariposas (by Energy Developed Corporation) geothermal fields have been explored at depth (Figure VI-2b). A maximum temperature of 235°C was measured in the Tinguiririca field at ~800 m depth (*Clavero et al. 2011; Droguett et al. 2012*). In the Mariposas area, on the other

hand, lower temperatures were measured at the bottom of the three wells drilled down to 659, 897 and 1074 m depth (from 190 to 204°C; *Hickson et al. 2011*). No public information is available for the Calabozos´ well. Despite the significant geothermal potential highlighted by these preliminary explorations, the geothermal resources in Central Chile have not yet been recovered and exploited for electricity generation. Several political and economic reasons have been identified as barriers to the geothermal energy development in Central Chile (e.g. geothermal law issues, ineffective financial mechanism to reduce high risk in exploration stages, lack of drilling equipment, untrained professionals into geothermal techniques; *CNE 2010; Dufey 2010; Hodgson 2013*). The poor information on the geothermal systems of Central Chile, as well as the scientific/technical inexperience of geothermal companies exploring geothermal systems emplaced in active orogens are both considered to represent further obstacles for the development of geothermal projects in this region (*Barnett 2012*).

In this study, exploration geochemical techniques were applied in Central Chile in order to (i) investigate the source(s) region feeding the hydrothermal fluid discharges and (ii) constrain the physico-chemical conditions of the hydrothermal reservoirs feeding the fluid discharges. Water and gas samples, collected from cold and hot springs, bubbling pools, mud pools and fumaroles from different areas located along the western, central and eastern PC (Figure VI-2a and b), were sampled for chemical and isotopic ($^{3}He/^{4}He$, $\delta^{18}O\text{-}H_2O$, $\delta D\text{-}H_2O$, $\delta^{13}C\text{-}CO_2$) analyses. Geochemical data were coupled with the available structural, stratigraphical and geophysical information in order to construct the first conceptual hydrogeochemical model aimed to describe the hydrothermal fluid circulation at the Andes of Central Chile.

VI.2 TECTONIC, GEOLOGICAL AND HYDROLOGICAL SETTING

The Andean Cordillera is a continuous mountain chain along the western edge of South America formed by a uniform process of subduction of the Nazca oceanic plate underneath the continental South America plate (Figure VI-1). Particularly, the study area is located in a transition zone between a sub-horizontal subduction segment (flat-slab zone), where the slab dip is <10° between 100 and 150 km depth (28-32.5°S), and a zone of normal subduction (i.e. slap dip >25° between 100 and 150 km depth), south of 34.5°S (Figure VI-1; *Barazangi and Isacks 1976; Tassara et al. 2006*). The change in the subduction geometry has been invoked to explain the presence of active volcanism south of 33°S (Southern Volcanic Zone, hereafter SVZ) and its absence in the flat-slab

zone (Figure VI-1; *Barazangi and Isacks 1976; Stern et al. 2007*). Additionally, significant along-strike changes in the geotectonic setting of Central Chile appear associated with the subduction of the Juan Fernández ridge (Figure VI-2a, b and c), including a: (i) progressive decrease in mountain elevation and crustal thickness between 32.5 and 36°S, (from <7000 to ~3500 m a.s.l. and from 51 to 48 km, respectively), along with an increase in the asthenospheric mantle wedge thickness from 20 to ~70 km (*Tassara et al. 2006; Farías et al. 2010*); (ii) changes in the orientation of geologic units, major structures and the trench from a N-S trend between 32.5 and 34.5°S, to a NNE-SSW trend south of 34.5°S (hereafter Maipo orocline; *Arriagada et al. 2013*); and (iii) a change in the tectonic regime along the volcanic arc region, from compressional to dextral transpressional north and south of the Maipo orocline, respectively (*Cembrano and Lara 2009 and references therein*).

At a regional scale, the Andes of Central Chile is segmented into three-parallel morphostructural units (*Farías et al. 2010),* from west to east (Figure VI-2a, b and c): the Coastal Cordillera, the Central Depression, and the PC. Most of the hydrothermal manifestations in the region are distributed along the PC throughout three different segments, namely western, central and eastern PC (Figure VI-2a and b). Cenozoic deposits (basaltic to andesitic volcanic-volcanoclastic rocks) are distributed between the eastern side of the Central Depression (ECD) and the western Principal Cordillera (WPC). The main structural systems developed in this area correspond to the west-vergents Infiernillo and Pocuro-San Ramón thrust faults (Figure VI-2c), with the latter having accommodated 0.7 to 1.1 km of surface uplift of the eastern hanging wall at 33°S, and 600 to 800 m at 35°S (*Farías et al. 2008*). Along the central Principal Cordillera (CPC) some folds and faults deform subtly the 5,500 m thick basaltic to andesitic volcanic-volcanoclastic Cenozoic sequences with a predominant west-vergency (Figure VI2-c; *Charrier et al. 2002*). Immediately east of this zone this Cenozoic sequences override Mesozoic sedimentary rocks (conglomerates, sandstones, limestones and gypsum sequences) through the east-vergent high-angle reverse El Fierro fault system (Figure VI2-c; *Farías et al. 2010*). Mesozoic marine and continental sedimentary deposits crop out in the eastern portion of the Principal Cordillera (EPC). These deposits are overlain by Neogene syntectonic foreland-basin deposits and volcanic piles near the Holocene volcanic front. Most of the deformation in the EPC has been accommodated by east-verging thrusts-faults and related backthrust-faults (Figure VI2-c), which represent the westernmost portion of the Aconcagua (32.5-34.5°S) and Malargüe (34.5-36°S) foreland fold-and-thrust belts (*Giambiagi et al. 2003*).

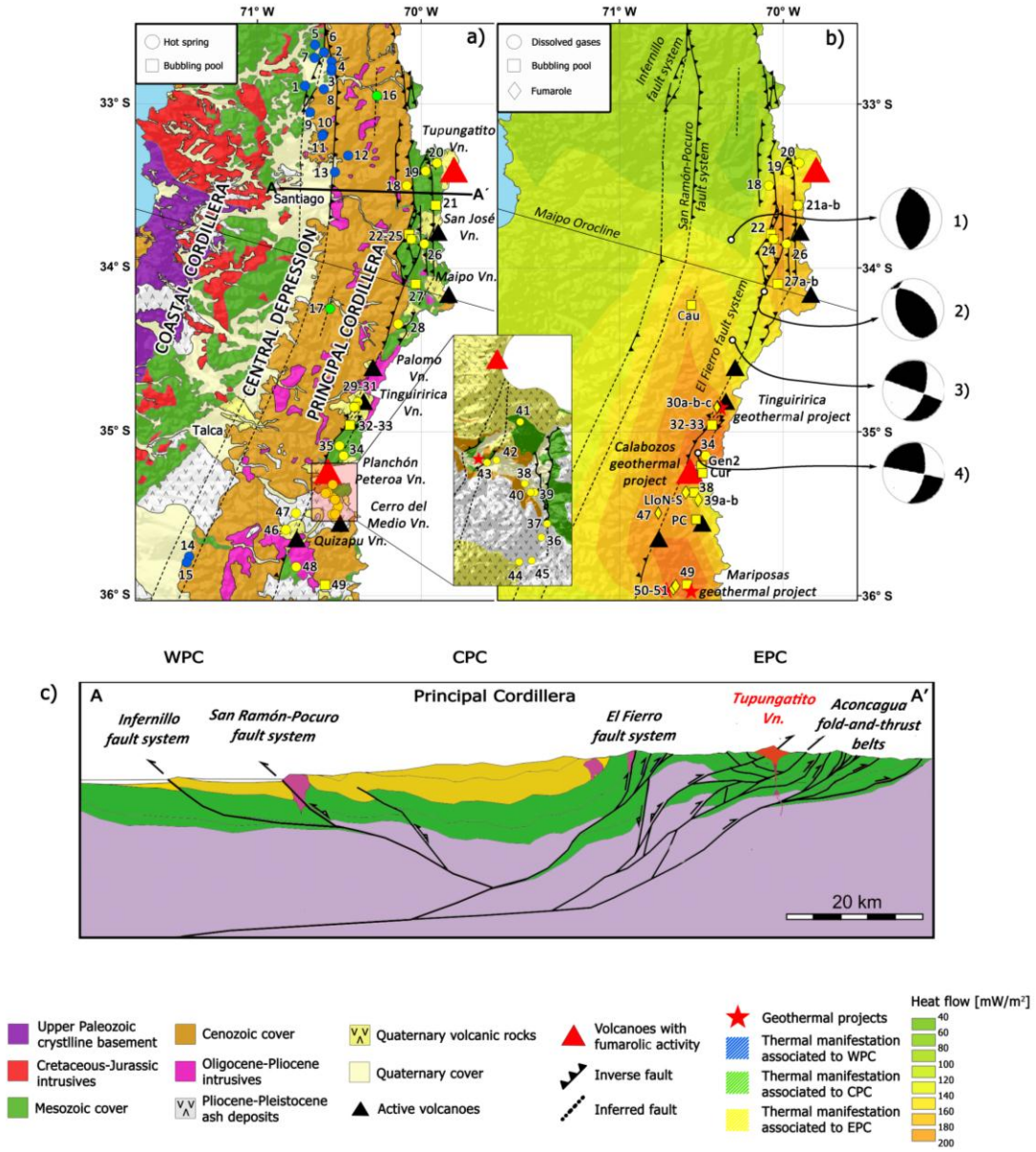

Figure VI-2: (a) Main geological and morphological features of the Andes of Central Chile after Farías et al. (2007; 2009). Hot springs (circles) and bubbling pools (squares) are shown. Colors of the symbols represent the position along the Principal Cordillera, i.e. Western Principal Cordillera (WPC, blue), Central Principal Cordillera (CPC, green) and Eastern Principal Cordillera (EPC, yellow).The active volcanoes of Central Chile with- (red triangles) and without fumarolic activity (black triangles) are also reported. (b) Main tectonic framework and heat flow pattern of Central Chile. Fumaroles (yellow diamonds), bubbling pool (yellow squares), dissolved gases taken from the hot springs (yellow circles), and main geothermal projects (red stars) are shown. A major inflection of the trench and continental margin occurs at 34°30'S (Maipo orocline). Available focal mechanisms of shallow crustal earthquakes in the volcanic arc region suggest a change from partitioned to non-partitioned dextral strike–slip. Data (2004 to 2005) compiled from *Pardo et al. (2006)* (1) and Harvard CMT (2, 3 and 4). (c) Cross section of the Andes of Central Chile. Only inverse faults active during the Neogene are plotted (modified from *Giambiagi et al. 2014*).

The volcanic arc of Central Chile (Figure VI-2a) is built on top of the Mesozoic sedimentary cover between 33 and 34.5°S (northern SVZ: NSVZ), whereas south of 34.5°S, volcanoes are located on the top of the Meso–Cenozoic limit (transitional SVZ: TSVZ). Among the active volcanoes of Central Chile, both Tupungatito and Planchón-Peteroa are characterized by a permanent fumarolic activity and the occurrence of crater lakes at their summit (*Saltori et al. 2012; Benavente et al. 2013*). Quaternary volcanic products emitted by the volcanoes of Central Chile show a wide variety of compositions ranging from tholeiitic basalts to high-K rhyolites (*Stern et al. 2007*). Andesites are the most abundant products, although basalts increase southward (*Hildreth and Moorbath 1988*). Volcanic products of the NSVZ have relatively high contents of incompatible trace elements (K, Rb, Sr, Ba, La, Th and U), higher ratios of fluid-mobile to less fluid-mobile elements (Rb/Cs, La/Yb, K/La, Rb/La, Ba/La and Hf/Lu), higher $^{87}Sr/^{86}Sr$ isotope ratios, and lower K/Rb and $^{143}Nd/^{144}Nd$ with respect to those products from the TSVZ having similar SiO_2 contents (*Hildreth and Moorbath 1988*). According to *Cembrano and Lara (2009)*, this pronounced "crustal signature" characterizing the magmas of Central Chile north of the Maipo orocline is a consequence of the longer residence times in the crust of magmas as they ascend through high-angle thrust faults (>45°) severely misoriented with respect to the prevailing intra-arc compressive stress field (Figure VI-2b; *Sibson 1996, 2007; Cox 2010*). Conversely, the strike–slip deformation affecting the volcanic arc south of the Maipo orocline (Figure VI-2b), would provide subvertical pathways for magma ascent and, therefore, shorter residence times in the crust for magmas (*Cembrano and Lara 2009*). The latter has important implications for the hydrothermal fluid circulation in the study area, because fault systems seem to be acting as vertical pathways for the fluid circulation south of the Maipo orocline, whereas to the north, the thrust fault systems require supralithostatic fluid pressures to become vertical conduits for fluid circulation (e.g. *Sánchez et al. 2013*).

Meteorological and hydrological conditions at the PC of Central Chile are similar to many Mediterranean near semi-arid, mountainous regions of the world, i.e. extremely low precipitation (~50 mm) during the summer months (December-February) results in snowmelt and glacier melt from high altitudes being main sources of meteoric water in the zone (*Hoke et al. 2013; Ohlanders et al. 2013*). Most precipitation, especially at altitudes >2000 m a.s.l., is in solid form because precipitation occurs almost exclusively during the winter season (June-August). Maximum snow accumulation altitude occur around 3000 m a.s.l. on the windward slopes of the Andes

(*Ohlanders et al. 2013*). At higher altitudes, snow depth decreases sharply (*Viale and Nuñez 2011*).

VI.3 SAMPLING AND ANALYTICAL METHODS

VI.3.1 Chemical and isotopic ($\delta^{18}O$ and δD) analysis of water samples

Temperature (±0.1°C), pH (±0.05 units), alkalinity (acidimetric titration with 0.01N HCl) and SiO_2 (molecular spectrophotometry) concentrations were determined in the field. Three water samples were collected and stored in 200 mL sterile high-density polyethylene bottles for the analysis of anions (Cl^- SO_4^{2-}, F^-, Br^- and NO_3^-), cations (Na^+, K^+, Ca^{2+} and Mg^{2+}) and minor and trace elements (B, Li, Al and Fe). Samples were filtered at 0.45 µm. Cations and minor-trace elements samples were acidified with 2 mL of HCl (2%) and ultra-pure HNO_3 (33%), respectively. Major anions and cations were analyzed by ion chromatography (Metrohm 861 and Metrohm 761, respectively) at the Department of Earth Sciences of the University of Florence (Italy). B, Li, Al and Fe were determined by ICP-MS. The analytical error for titration, IC and MS are ≤5% and for IPC-MS is ≤10%.

Samples for determination of $^{18}O/^{16}O$ and $^{2}H/^{1}H$ ratios (hereafter expressed as $\delta^{18}O$-H_2O‰ and δD-H_2O‰ referred V-SMOW, respectively) were collected in 50 ml sterile opaque glass bottles, and analyzed using a Finningan Delta MAT Plus XL spectrometer at the Geokarst Engineering Laboratory (Trieste, Italy). Oxygen and hydrogen isotopes were analyzed according to the method described by Epstein and *Mayeda (1953)* and *Coleman et al. (1982)*, respectively. V-SMOW and SLAP were used as analytical standards and AR-1 as an internal standard. The analytical uncertainties are ±0.1‰ for $\delta^{18}O$ and ±1‰ for δD.

VI.3.2 Sampling methods and chemical and isotopic (R/Ra, $\delta^{13}C$-CO_2) analysis of gases and steam ($\delta^{18}O$- and δD-H_2O‰)

Gas samples from fumarolic vents and bubbling pools were collected using pre-evacuated, 60 mL Giggenbach flasks (*Giggenbach 1975*) filled with 20 mL of 4N NaOH and a 0.15M $Cd(OH)_2$ suspension (*Montegrossi et al. 2001; Vaselli et al. 2006*). Gas samples from fumarolic vents were conveyed into the sampling flasks using a 1-m-long titanium tube (Ø =2.5 cm) that was inserted into the fumarolic vent and connected through glass dewar tubes. Gas samples from bubbling pool were collected using a plastic funnel positioned upside-down and connected to the sampling flasks through

tygon tubes. At each sampling point, a 60 mL glass pre-evacuated gas vial was used to collect a sample for the analysis of carbon isotopes in CO_2 using the same sampling apparatus adopted for the soda flasks. Fumarolic condensates were obtained using an ice-cooled glass condensing system connected to the gas sampling glass line and conveyed into 50 mL sterile opaque glass bottles. Dissolved gases were sampled using pre-evacuated 250 mL glass vials equipped with a Teflon stopcock and connected to the sampling line used to collect water samples. Sampling flasks were filled with water up to ¾ of the flasks inner volume (*Caliro et al. 2008; Tassi et al. 2008*).

Inorganic gases (N_2, O_2, H_2, He, Ar, CO and Ne) in the sampling flask headspace were analyzed using a Shimadzu 15A gas chromatograph (GC) equipped with a 10 m long 5A-molecular sieve column and a thermal conductivity detector (TCD). To allow a complete separation of Ar and O_2 peaks, the oven temperature was lowered to -10 °C by means of a cryogenic liquid CO_2 cooling system (Shimadzu CRG-15). Hydrocarbons, including CH_4, were determined by using a Shimadzu 14A gas chromatograph (GC) equipped with a 10-m-long stainless steel column packed with Chromosorb PAW 80/100 mesh coated with 23% SP 1700 and a flame ionization detector (FID). The alkaline suspension was centrifuged three times at 4,000 rpm for 30 min to separate the solid precipitate from the solution. The latter was used to analyze (i) CO_2, as CO_3^{2-}, by titration (Metrohm Basic Titrino) with a 0.5 N HCl solution; (ii) HCl, as Cl^-, by ion chromatography (IC) (Metrohm Basic 761); (iii) SO_2, as SO_4^{2-}, after oxidation with 5 ml H_2O_2 (33%), by ion chromatography. Using 5 ml H_2O_2 (33%), CdS in the solid precipitate was oxidized to SO_4^{2-} that was analyzed by IC for determining H_2S concentrations (*Montegrossi et al. 2001*). Condensate samples for F^- and Cl^- were also analyzed by IC. HF concentrations were calculated on the basis of F^- and Cl^- concentrations in the condensate samples and the alkaline solution samples. The analytical error for titration, GC and IC analyses is <5%.

The analysis of $^{13}C/^{12}C$ ratios of CO_2 (hereafter expressed as $\delta^{13}C\text{-}CO_2$‰ referred to V-PDB) stored in the pre-evacuated sampling flasks were carried out with a Finningan Delta S mass spectrometer after standard extraction and purification procedures of the gas mixtures by using liquid N_2 and a solid–liquid mixture of liquid N_2 and trichloroethylene (*Evans et al. 1988; Vaselli et al. 2006*). Internal (Carrara and San Vincenzo marbles) and international (NBS18 and NBS19) standards were used for estimation of external precision. The analytical error and the reproducibility are ±0.05‰ and ±0.1‰, respectively. Helium (expressed as R/Ra, where R is the $^3He/^4He$ measured ratio and Ra is the $^3He/^4He$ ratio in the air: 1.39×10^{-6}; *Mamyrin and Tolstikhin 1984*) isotopic ratios were determined on gas aliquots transferred from the

flask headspace into pre-evacuated 50 mL flasks. A double collector mass spectrometer (VG 5400-TFT) was used according to the method described by *Inguaggiato and Rizzo (2004)*. The analytical uncertainty for the determination of R/Ra is ≤0.3%. The $^{18}O/^{16}O$ and $^{2}H/^{1}H$ isotopic ratios of water in the condensates samples were analyzed using the same procedure described for the water samples (Section 3.1).

VI.4 RESULTS

VI.4.1 Chemical and isotopic composition of waters

Outlet temperature, pH values, total dissolved solids (TDS) and contents of major and minor components of 49 water discharges are reported in Table VI-1. As shown in the Piper-type diagram in Figure VI-3, water samples pertain to seven different chemical facies, as follows: Na-Cl, Ca-Cl, Ca-HCO_3, Na-HCO_3, Ca-SO_4, Na-SO_4, and acid-SO_4.

Na-Cl waters, mostly located in EPC with the only exception of sample 16 in CPC, are characterized by neutral pH (from 6.33 to 7.57), relatively high TDS values (2,300 to 35,000 mgL^{-1}), high temperatures (up to 89.4°C), as well as high Li, B and SiO_2 contents (up to 17.1, 40 and 145 mgL^{-1}, respectively). The pCO_2 values, computed by means of the speciation program SpecE8 (*Bethke 2007*), range from 0.03 to 0.4 bar (Fig. 4). Exception is sample 35, showing a low temperature (6°C), high pH (8.6), low TDS (1,550 mgL^{-1}) and a pCO_2 value similar to waters equilibrated with atmospheric CO_2 (Figure VI-4). The Ca-Cl waters, located in WPC and CPC (samples 13 and 17, respectively), have distinct temperatures (21.1 and 45.7°C, respectively), pH (6.3 and 7.7, respectively) and TDS values (840 and 2,540 mgL^{-1}, respectively), although are both characterized by pCO_2 values <0.01 bar (Fig. 4).

Ca-HCO_3 waters are located in both WPC and EPC. The former (samples 1, 2, 3, 5, 7 and 8) are relatively cold (T<18.7°C), slightly alkaline (pH>7.5), and have TDS and pCO_2 values <300 mgL^{-1} and <0.01 bar, respectively. The latter (samples 22, 23, 31, 40, 41, 46 and 47) are characterized by relatively high TDS values (up to 2,200 mgL^{-1}), temperatures (up to ~80°C) and pCO_2 values (up to 3.83 bar; Figure VI-4), whereas their pH values range from 5.4 to 7.5. The Na-HCO_3 water samples (Figure VI-3), collected from springs located at both WPC (sample 15) and EPC (samples 36, 44 and 45) south of the Maipo orocline, have higher temperature (up to 64.9°C) and pH (up to 9.2), and lower pCO_2 values (down to $8.7x10^{-5}$ bar; Figure VI-4) than Ca-HCO_3 springs emerging in the same areas.

ID	Name	type	E	N	h	T	pH	Cond	TDS	Ca	K	Mg	Na	Al	B
1	Auco	spring	340130	6359740	846	18,7	7,73	300	417	65,1	0,2	10,06	29,99	0,02	0,17
2	El Barro	spring	355078	6376500	1060	15,4	7,34	600	552	80,3	0,2	20,05	30,02	0,01	0,085
3	El Corazon	spring	355075	6369980	940	19	7,82	340	366	50,01	0,2	12,4	30,21	0,02	0,05
4	El Lobo	spring	355194	6371960	938	20,1	7,01	890	698	115	0,5	35,3	29,97	0,01	0,06
5	El Parrón	spring	345420	6387650	1910	12,8	7,5	600	295	42	0,5	4	22	0,03	0,07
6	Jahuel	spring	350698	6382649	1127	16,8	7,35	900	538	75	1,9	23	34	0,02	0,1
7	La Higuera	spring	345286	6378760	794	11	7,6	600	467	72,95	0,5	13	15	0,01	0,07
8	La Totora	spring	350908	6357715	1010	12	7,45	610	420	66	0,4	8	24	0,02	0,07
9	Baños de Chacabuco	spring	343311	6341956	741	23,5	7,6	720	338	23,6	0,75	0,92	80,2	0,05	0,6
10	Termas de Colina	spring	351014	6327245	948	29	7,82	630	455	50	0,89	1,2	83	5,7	1,3
11	Baños el Carvajalino	spring	350565	6326085	819	24,9	7,9	830	421	53	0,65	2,2	68,4	0,05	0,16
12	Termas de la Cal	spring	365418	6312927	1167	20	8,1	870	209	27,5	0,25	3,47	24	0,05	2,1
13	Baños de Apoquindo	spring	358122	6301705	857	21,1	7,7	1600	1704	375	1,3	2,6	232	0,03	0,07
14	Termas Panimávida	spring	281522	6039846	970	33,7	9,3	640	337	29,82	1,313	0,033	57,245	0,078	1,57
15	Termas Quinamávida	spring	280284	6035883	970	23,3	9,2	340	296	18,49	1,505	0,151	53,875	0,333	0,42
16	Saladillo	spring	381298	6353643	1716	21,9	7,57	14990	13505	727,5	120,6	44,35	3792,5	0,01	7,19
17	Cauquenes	spring	356744	6209276	756	45,7	6,3	5080	3389	778	9,276	0,253	463,75	0,04	6,3
18	Salinilla	spring	399001	6293034	1680	22,7	7,1	15600	11727	461,18	38,895	45,517	3985	9,922	1,317
19	Baños Azules	spring	409612	6302976	2504	17,8	5,1	2600	2771	612	6,4	62	62	0,032	0,14
20	Termas Tupungato	spring	415987	6308503	2975	24,2	5,1	7520	4097	684	37	126	319	0,1	4,1
21	Termas del Plomo	bubbling pool	415546	6279865	2978	26,8	7,1	16150	8910	518	14	91	2707	0,03	0,83
22	Monumento Morado 1	bubbling pool	400543	6260255	2265	9,1	7,26	2400	3358	633	8	94	39	0,01	0,21
23	Monumento Morado 2	bubbling pool	400649	6260176	2264	10,4	7,5	3400	5005	1094	7	92	42	0,01	2,25
24	Baños Morales P1	bubbling pool	401927	6256821	1812	15,2	6,2	15680	7461	461	83	72	2024	0,01	1,77
25	Baños Morales P2	spring	401927	6256821	1812	28,2	6,2	60000	28680	1093	279	231	9125	165,73	3,34

Table VI-1: Chemical and isotopic data of the water samples taken in Central Chile. Coordinates (WGS 1984; UTM; Zone 19S), altitude (m), type of feature, outlet temperatures (in °C), EC (in μScm^{-2}), TDS (in mgL^{-1}), pH, chemical composition and $\delta^{18}O$ and δD (‰V-SMOW) values of the thermal discharges of Central Chile. Concentrations of solutes are in mg/L; n.a.: not analyzed; b.d.l.: below detection limit; SI: saturation index.

continuation of Table VI-1

ID	Fe	Li	Mn	Sr	SiO_2	F	Cl	Br	NO_3	SO_4	HCO_3	CO3	log f_{CO2}	δD‰	$\delta^{18}O$‰	SI calcite	SI gypsum
1	0,40	0,01	0,00	0,30	30,0	0,14	5,5	0,04	15,00	80,0	180,0	b.d.l.	-2,5	-72,01	-9,59	0,4	-1,8
2	0,60	0,03	0,00	0,40	32,0	0,10	3,3	0,04	20,00	75,0	290,0	b.d.l.	-1,9	-82,1	-10,7	0,3	-1,8
3	0,60	0,03	0,00	0,58	28,5	0,11	8,3	0,05	8,00	38,0	189,0	b.d.l.	-2,5	-76,01	-9,66	0,5	-2,2
4	1,10	0,03	0,03	0,46	38,1	0,05	3,0	0,04	4,00	300,0	170,0	b.d.l.	-1,9	-72,9	-9,26	-0,3	-1,0
5	0,31	0,01	0,00	0,15	32,9	0,05	2,5	0,03	9,60	11,0	170,0	b.d.l.	-2,3	-80,01	-10,91	-0,1	-2,7
6	0,07	0,02	0,02	0,33	33,0	0,15	5,0	0,05	5,10	200,0	160,0	b.d.l.	-2,2	-83,9	-11,01	0,0	-1,4
7	0,58	0,03	0,00	0,20	50,1	0,10	4,5	0,04	3,94	46,0	260,0	b.d.l.	-2,3	-71,5	-9,49	0,3	-1,9
8	0,48	0,02	0,02	0,27	29,1	0,20	13,1	0,02	5,60	92,3	180,0	b.d.l.	-2,3	-91,9	-12,8	0,0	-1,6
9	0,01	0,13	0,01	0,02	16,5	0,01	29,0	1,30	7,80	87,4	89,7	b.d.l.	-2,5	n.a.	n.a.	-0,3	-2,1
10	0,01	0,04	0,00	0,16	24,6	0,12	100,0	0,27	7,87	120,0	60,0	b.d.l.	-3,1	-67,2	-9,02	0,0	-1,8
11	0,01	0,10	0,01	0,07	20,1	0,02	87,1	1,40	4,90	114,7	67,7	b.d.l.	-3,1	n.a.	n.a.	0,1	-1,7
12	0,01	0,18	0,01	0,08	20,3	0,01	14,0	0,05	8,40	21,4	87,3	b.d.l.	-3,1	-68,2	-9,31	0,2	-2,6
13	0,10	0,03	0,40	0,15	20,1	0,01	870,0	4,10	4,80	100,2	93,4	b.d.l.	-2,9	n.a.	n.a.	0,6	-1,2
14	0,02	0,09	0,00	0,01	31,0	0,34	53,1	b.d.l.	1,48	151,5	5,5	3,6	-5,6	-58,6	-8,99	0,3	-1,8
15	0,31	0,15	0,02	0,00	38,2	0,22	3,5	b.d.l.	1,58	8,7	156,2	12,6	-4,1	-50,9	-7,83	1,3	
16	0,30	6,06	0,97	18,21	45,1	0,03	7844,4	14,06	8,19	713,2	162,3	b.d.l.	-2,5	-100,1	-13,78	0,7	-0,7
17	0,06	1,17	0,01	6,86	37,5	0,01	1977,3	8,63	7,66	62,4	30,0	b.d.l.	-2,0	-58,8	-8,6	-0,9	-12,5
18	1,99	5,84	0,03	10,50	49,0	0,26	6385,7	6,19	1,10	480,3	244,1	b.d.l.	-1,9	n.a.	n.a.	0,2	-1,1
19	0,05	0,50	17,22	5,10	43,1	2,20	69,0	0,09	0,50	1063,0	828,0	b.d.l.	-0,5	-95,23	-13,1	-2,1	0,1
20	3,20	1,09	0,20	0,00	64,6	2,04	381,0	0,50	2,52	1762,0	710,0	b.d.l.	-0,5	n.a.	n.a.	-2,1	0,2
21	0,88	3,97	0,37	16,28	29,0	0,01	3763,4	7,37	4,95	1610,1	142,2	b.d.l.	-2,1	-103,6	-15,6	0,1	-0,4
22	0,03	0,68	18,37	4,73	42,3	0,02	19,7	0,01	1,82	440,0	2056,2	b.d.l.	-0,8	-95	-13	1,7	-0,5
23	0,47	0,44	8,49	5,96	61,3	0,02	20,7	b.d.l.	1,47	806,9	2862,9	b.d.l.	-1,3	-101	-13,5	2,0	-0,1
24	0,28	3,67	0,74	6,83	46,0	0,30	3785,3	3,80	5,10	426,5	540,0	b.d.l.	-1,0	-105	-13,6	-0,4	-0,9
25	19,86	14,67	2,67	19,90	86,0	b.d.l.	15183,6	14,60	5,67	1016,1	1420,5	b.d.l.	-0,5	n.a.	n.a.	0,1	-0,7

continuation of Table VI-1

ID	Name	type	E	N	h	T	pH	Cond	TDS	Ca	K	Mg	Na	Al	B
26	Baños Colina	spring	409262	6253744	2545	51,3	6,4	70000	31746	1416	342	314	9950	218,14	19,15
27	Puente de Tierra	bubbling pool	404731	6226554	2148	45	6,47	60600	56807	1626	343	263	18324	0,01	19,40
28	Baños Las Calerías	spring	395156	6199348	2190	61	6,3	13300	9577	730	203	39	2360	0,30	42,00
29	Termas Azufre	spring	373120	6146230	3157	27,5	2,89	900	959	74	2	24	54	2,50	0,03
30	Laguna Humos	bubbling pool	371798	6143023	2974	24	1,8	950	535	60	1	11	21	7,61	0,03
31	Campamento Humos	spring	371250	6142895	2726	59,7	6,77	350	618	61	2	10	50	2,50	1,59
32	Termas del Flaco 1	bubbling pool	368978	6130555	1806	63,7	6,9	5720	3926	139	128	6	1182	0,03	14,12
33	Termas del Flaco 2	bubbling pool	368996	6130555	1732	89,4	6,9	4960	3664	135	119	5	1135	0,10	15,94
34	Termas de San Pedro	spring	365777	6109783	1732	24	7,1	15900	15591	768	729	25	3698	0,10	9,92
35	Termas Romeral	spring	363400	6116454	1433	6	8,6	3100	1818	141	25	7	464	0,05	1,66
36	Termas del Tigre Naciente	spring	362754	6073577	2563	64,9	7,2	1360	754	21	3	1	146	0,04	4,60
37	Termas Potrerillo	spring	363420	6075560	2343	46	7,4	1560	967	65	5	5	180	0,04	0,66
38	Termas del Pellejo	spring	360694	6081288	2129	48,9	6,7	3120	1691	125	21	32	194	0,05	2,50
39	Termas de la Tierra humeante del Colorado	spring	361881	6080029	2154	75	7,4	4600	2796	80	67	6	860	0,05	5,52
40	Termas de la Quebrada de los Colores	spring	361386	6080040	2185	30,2	6,8	4400	2602	292	8	94	220	0,04	1,03
41	Fumaroles del Azufre	bubbling pool	360011	6090191	2738	70	5,4	4080	867	63	11	24	60	0,20	b.d.l.
42	Termas Baños de la Yegua	spring	357295	6084620	1995	54	6,7	4080	3089	314	53	15	605	0,10	7,82
43	Fumarolas de Llolli	bubbling pool	356196	6084260	2002	94,5	2	3600	2162	19	15	28	37	39,72	0,03
44	Termas de Aguas Calientes 1	bubbling pool	360200	6069989	2569	38,9	6,9	900	667	44	4	6	114	0,02	0,89
45	Termas de Aguas Calientes 2	spring	361680	6070203	2563	37,9	7	940	716	45	4	5	98	0,04	1,15
46	Termas del Descabezado Grande	spring	334606	6059316	1880	29,8	5,8	2440	1294	54	24	101	111	0,07	5,44
47	Termas del Valle del estero del Volcán	spring	340000	6070460	1954	79,5	6	1840	971	81	4	23	94	0,09	0,60
48	Termas del Medano	spring	340794	6034171	988	29,5	6,6	1460	988	104	8	5	134	0,08	10,00
49	Termas del Campanario	bubbling pool	356881	6022199	1545	45,7	6,33	15590	21003	1925	340	85	5335	0,03	3,03

continuation of Table VI-1

ID	Fe	Li	Mn	Sr	SiO_2	F	Cl	Br	NO_3	SO_4	HCO_3	CO3	log f_{CO2}	δD‰	$\delta^{18}O$‰	SI calcite	SI gypsum
26	5,50	13,91	0,06	35,76	163,0	b.d.l.	15283,2	b.d.l.	3,31	2964,1	992,1	b.d.l.	-0,4	-96,3	-13,35	0,9	-0,1
27	5,59	44,10	0,90	30,60	60,6	0,02	31806,1	58,49	46,83	2847,5	1304,5	b.d.l.	-0,5	-107	-13,6	1,1	-0,3
28	3,50	10,10	7,50	31,20	80,0	0,20	3590,0	2,20	0,30	1620,0	830,0	b.d.l.	-0,7	-106	-13,25	0,1	-1,3
29	3,40	0,16	0,96	0,08	100,0	2,81	98,0	0,81	0,13	567,0	b.d.l.	b.d.l.	-	-93	-12,9	-	-1,1
30	7,54	0,16	0,96	0,08	75,0	0,29	9,3	b.d.l.	0,19	311,0	b.d.l.	b.d.l.	-	-63	-5,7	-	-1,3
31	0,10	0,21	0,02	0,00	18,9	0,22	9,2	0,81	0,13	37,1	394,2	b.d.l.	-1,1	-90	-12,8	0,2	-2,0
32	0,10	3,89	0,17	6,10	149,0	1,78	1801,2	3,23	1,81	288,5	169,6	b.d.l.	-1,6	-95,1	-12,2	0,1	-1,3
33	0,54	4,30	0,15	5,79	76,0	7,66	1651,8	2,69	1,49	286,7	183,1	b.d.l.	-1,3	-91,1	-11,5	0,5	-1,1
34	6,17	3,15	6,06	9,81	32,1	b.d.l.	8389,9	127,70	11,04	1177,2	564,4	b.d.l.	-1,5	-96,8	-13,28	0,8	-0,5
35	0,03	0,75	0,00	1,78	12,0	0,12	910,9	b.d.l.	2,81	118,6	96,4	b.d.l.	-3,2	-92,3	-13,73	0,3	-1,5
36	0,02	0,44	0,00	0,19	54,4	4,58	95,3	b.d.l.	1,47	110,4	275,2	b.d.l.	-1,5	-95,1	-13,25	0,1	-2,0
37	0,01	0,27	0,00	0,71	54,9	2,98	52,8	b.d.l.	1,47	265,3	295,3	b.d.l.	-1,9	-96,1	-13,53	0,5	-1,3
38	3,37	0,45	0,99	0,89	124,9	2,62	195,3	b.d.l.	1,50	134,7	812,7	b.d.l.	-0,6	-96,3	-13,44	0,8	-1,3
39	0,03	1,90	0,83	1,31	135,3	1,74	1243,7	b.d.l.	1,55	106,2	244,7	b.d.l.	-1,5	-94,4	-12,75	1,0	-1,8
40	9,21	0,68	1,52	1,59	81,8	1,43	39,7	b.d.l.	1,47	374,8	1434,5	b.d.l.	-0,8	-95,5	-13,57	0,8	-0,8
41	0,47	0,15	1,60	0,65	172,2	0,25	3,7	b.d.l.	1,60	2,5	485,1	b.d.l.	0,6	-91,2	-11,13	-0,9	-
42	1,95	1,21	1,71	4,60	136,1	2,06	723,7	b.d.l.	1,53	498,0	680,3	b.d.l.	-0,9	-94,8	-12,98	0,7	-0,7
43	37,20	0,16	0,96	0,08	280,5	0,17	1,7	1,47	1,35	1656,9	b.d.l.	b.d.l.	-	-60,7	-4,23	-	-1,8
44	0,01	0,36	0,00	0,47	45,5	2,11	61,3	b.d.l.	1,89	80,3	262,4	b.d.l.	-1,4	n.a.	n.a.	-0,2	-2,0
45	0,04	0,31	0,00	0,44	43,7	1,66	71,0	b.d.l.	1,65	84,0	314,8	b.d.l.	-1,6	-86,6	-13,31	-0,2	-1,9
46	0,04	0,25	0,01	0,53	100,3	0,35	101,0	b.d.l.	1,53	137,3	612,0	b.d.l.	0,0	-87,3	-13,31	-1,1	-1,8
47	0,07	0,17	0,25	0,29	153,7	b.d.l.	2,4	b.d.l.	1,45	65,3	497,3	b.d.l.	0,1	-83,5	-11,7	0,0	-1,7
48	0,02	0,56	0,00	1,23	41,1	0,67	330,9	b.d.l.	1,55	266,2	36,6	b.d.l.	-2,2	-89,5	-12,4	-1,3	-1,2
49	13,64	17,40	2,50	41,45	67,9	0,03	12061,1	36,93	1,20	508,0	516,8	b.d.l.	-0,9	-100,6	-13,64	0,4	-0,6

Table VI-2: Chemical and isotopic data of the dissolved gases samples taken in Central Chile. Coordinates (WGS 1984; UTM; Zone 19S), altitudes (m), outlet temperatures (in °C). He, H_2, O_2, N_2, CH_4, and CO_2 in µmol/mol; $\delta^{13}C$ as ‰ referred to VPDB; and He isotopic composition as R/R_a, where R is the measured ratio and Ra is that of the air: $1.39x10^{-6}$ (*Mamiryn and Tolstikhin 1984*). X_{gc} calculated gas fraction in %, as defined by *Taran (2005)*. L, S and M are the limestones, organic sediments and mantle end-members (%), as defined by *Sano and Marty (1995).*

ID	Name	N	E	Altitude	T°C	CO_2	N_2	CH_4	Ar	O_2	H_2	He	R/Ra	$\delta^{13}C$-CO_2	X_{gc}	%M	%L	%S	R_H
18	Salinilla	6293034	399001	1680	22,7	465957	519058	66,20	12605,7	2302,77	7,88	2,55	1,03	-12,6	-	1,2	57,0	41,8	-
19	Baños Los Azules	6302976	409612	2504	17,8	521186	467317	2,01	11137,5	316,66	38,52	2,29	0,81	-10,4	0,0001	0,7	64,7	34,5	-10,3
20	Baños Tupungato	6308503	415987	2975	24,2	771761	210234	1,33	4865,5	13115,49	21,72	0,98	1,27	-6,03	0,0033	0,3	79,6	20,0	-9,1
21b	Termas del Plomo	6279865	415546	2978	26,8	523392	443779	10,39	10771,9	22028,77	15,87	1,50	0,68	-9,19	0,0006	0,4	69,0	30,6	-10,0
26	Baños Colina	6253744	409262	2545	51,3	325004	633890	1,86	15580,9	25505,85	14,91	1,81	1,04	-7,15	0,0002	1,2	75,2	23,6	-10,5
34	Termas de San Pedro	6109783	365777	1732	24	356289	618828	3,53	14826,5	10035,04	16,27	1,81	1,06	-14,3	-	1,1	51,4	47,5	-
39b	Termas de la Tierra humeante del Colorado	6080029	361881	2154	75	456099	523296	4,54	12039,5	8534,01	24,64	1,68	0,75	-13,4	0,0008	0,6	54,9	44,6	-9,7

Table VI-3: Chemical and isotopic data of the bubbling pools and fumaroles samples taken in Central Chile. Coordinates (WGS 1984; UTM; Zone 19S), altitude (m), type of feature, outlet temperature (in °C), and chemical and isotopic composition of gas discharges. Gas content are in µmol/mol; $\delta^{13}C\text{-}CO_2$ as ‰ referred to VPDB; He isotopic composition as R/R_a; and $\delta^{18}O$ and δD (‰V-SMOW). X_g and X_{gc} measured and calculated gas fraction (in %), respectively as defined by *Taran (2005)*. The measured $CO_2/^3He$ ratios ($x10^{11}$) in fumaroles, and those calculated in the bubbling pools are also reported. L, S and M are the limestones, organic sediments and mantle end-members (%), as defined by *Sano and Marty (1995)*. * data from *Hilton et al. (1993)*. ** data from *Saltori et al. (2012)*. * data from *Dobson et al. (2013)*. n.a.: not analyzed; n.r.: not reported; b.d.l.: below detection limit.**

ID	Name	Type	N	E	altitude	T	CO_2	H_2S	N_2	CH_4	Ar	O_2	Ne	H_2	He	CO
21a	Termas del Plomo	bubbling pool	6279861	415560	2962	25,2	628281	b.d.l.	355000	146,0	6890,0	9680,0	0,35	b.d.l.	2,8	b.d.l.
22	Monumento el Morado	bubbling pool	6260255	400543	2293	9,1	956172	b.d.l.	41000	21,0	950,0	1850,0	0,05	b.d.l.	6,6	b.d.l.
24a	Baños Morales	bubbling pool	6256802	401926	1852	22,3	739149	b.d.l.	246000	78,0	5880,0	8890,0	0,32	b.d.l.	3,1	b.d.l.
27a	Puente de Tierra 1	bubbling pool	6226554	404731	2148	45	972243	b.d.l.	26000	75,0	490,0	1110,0	0,03	80,0	0,9	b.d.l.
27b	Puente de Tierra 2	bubbling pool	6226548	404754	2140	44,5	965126	b.d.l.	31000	72,0	620,0	3120,0	0,03	60,0	1,1	b.d.l.
32a	Tinguiririca 1	bubbling pool	6130555	368978	1806	63,7	984453	b.d.l.	9156	6218,0	55,3	69,7	b.d.l.	1,6	15,4	b.d.l.
32b	Tinguiririca 2	bubbling pool	6130555	368996	1732	89,4	984385	b.d.l.	8897	6514,0	49,0	110,0	b.d.l.	2,1	11,6	b.d.l.
33	Tinguiririca 3	bubbling pool	6130555	368978	1806	63,7	987550	b.d.l.	7659	4598,0	61,0	95,0	b.d.l.	1,9	13,8	b.d.l.
38	Termas de Pellejo	bubbling pool	6093577	361327	2490	46,2	995971	b.d.l.	1807	1437,6	39,5	544,1	b.d.l.	5,6	2,6	b.d.l.
49a	Termas del Campanario 1	bubbling pool	6022198	356923	1544	38,5	734287	b.d.l.	255000	258,0	4580,0	5870,0	0,25	b.d.l.	4,5	b.d.l.
49b	Termas del Campanario 2	bubbling pool	6022199	356881	1545	45,7	753687	b.d.l.	234000	198,0	5160,0	6950,0	0,29	b.d.l.	4,9	b.d.l.
Gen 2**	Gendarmeria 2	bubbling pool	6098014	362203	2766	87,8	993000	b.d.l.	5290	1315,0	117,0	615,0	b.d.l.	6,1	5,2	b.d.l.
Cur**	Curicó	bubbling pool	6098014	362203	2476	39	990878	b.d.l.	6230	1778,0	151,0	958,0	b.d.l.	4,4	0,4	b.d.l.
PC***	Puesto Calabozos	bubbling pool	6065586	358899	2450	75	n.r.	n.r.	n.r.	n.r.	n.r.	n.r.	n.r.	n.r.	n.r.	n.r.
30a	Baños Los Humos 1	Fumarole	6143073	371828	2981	90,6	925080	112,0	35000	66,0	150,0	90,0	0,01	39500,0	1,5	b.d.l.
30b	Baños Los Humos 2	Fumarole	6143235	371802	2976	90	928639	130,0	26000	58,0	120,0	50,0	0,01	45000,0	2,6	b.d.l.
30c	Baños Los Humos 3	Fumarole	6142687	371534	2879	90,7	922471	140,0	31000	47,0	180,0	160,0	0,01	46000,0	1,7	b.d.l.
39a	Barro Colorado	Fumarole	6079574	361772	2282	94,4	997000	320,0	1570	568,0	3,0	34,0	b.d.l.	114,0	1,5	2,8
47	Estero del Volcán	Fumarole	6070452	339996	1960	112,2	988962	4587,0	6158	141,0	11,4	25,0	b.d.l.	108,0	5,8	1,84
50	La Plata 1	Fumarole	6019525	344668	1953	94,3	901282	24740,9	62302	1575,3	791,5	3,6	0,11	9258,7	40,5	b.d.l.
51	La Plata 2	Fumarole	6019948	344296	2183	93	902435	38532,3	34744	1039,7	542,8	2,8	0,35	22659,0	40,5	b.d.l.
LloN***	Lolli Norte	Fumarole	6084188	356174	1925	93,5	n.r.	n.r.	n.r.	n.r.	n.r.	n.r.	n.r.	n.r.	n.r.	n.r.
LloS***	Lolli Sur	Fumarole	6083788	356099	1800	94	n.r.	n.r.	n.r.	n.r.	n.r.	n.r.	n.r.	n.r.	n.r.	n.r.

continuation of Table VI-3

ID	C_2H_6	C_3H_8	X_g	R/R_a	$\delta^{13}C\text{-}CO_2$	δD‰	$\delta^{18}O$‰	X_{gc}	$CO_2/^3He$ ($x10^{11}$)	%M	%L	%S	R_H
Cau*	n.r.	n.r.	n.r.	1,56	n.r.	n.r.	n.r.	-	-	-	-	-	-
21a	b.d.l.	b.d.l.	-	1,07	-7,76	n.a.	n.a.	0,002	1,512	0,98	73,32	25,70	-
22	5,00E-07	8E-08	-	0,47	-9,76	-101	-13,5	0,023	2,227	0,66	66,92	32,42	-
24a	6E-07	5E-08	-	1,81	-8,6	-105	-13,6	0,002	0,948	1,57	70,03	28,41	-
27a	9,6E-07	7,5E-08	-	n.a.	-10,9	-107	-13,6	0,05	-	-	-	-	-7,4
27b	7,8E-07	7E-08	-	n.a.	n.a.	n.a.	n.a.	0,04	-	-	-	-	-7,6
32a	2,6E-05	1,48E-06	-	n.a.	n.a.	n.a.	n.a.	0,44	-	-	-	-	-8,1
32b	2,6E-05	1,89E-06	-	2,13	-8,34	-95,1	-12,2	0,5	0,288	5,19	67,87	26,93	-7,9
33	1,8E-05	8,7E-07	-	n.a.	-9,77	-91,1	-11,5	0,40	-				-8,1
38	4,32E-06	3,84E-07	-	3,69	-13,21	-106	-14,7	0,62	2,135	1,98	54,32	43,70	-7,5
49a	2,1E-06	1,01E-06	-	0,55	-11,1	-100,6	-13,64	0,0036	0,232	0,69	62,43	36,89	-
49b	2,05E-06	1,05E-06	-	n.a.	-11,1	n.a.	n.a.	0,0031	-	-	-	-	-
Gen 2**	1,74E-05	7,99E-07	-	5,94	-12,58	-102,8	-15,13	0,21	-	6,46	52,69	40,86	-7,9
Cur**	2,36E-05	1,80E-06	-	1,19	-12,59	-97,8	-13,36	0,16	-	0,09	57,96	41,95	-8,1
PC***	n.r.	n.r.	n.r.	6,2	-11,1	-98	-13,5	n.r.	-	n.r.	n.r.	n.r.	n.r.
30a	4,1E-07	9E-08	4,4	n.a.	-8,9	-88	-11,2	-	-	-	-	-	-2,8
30b	3,6E-07	7E-08	5,6	3,9	-8,5	-85	-10,8	-	0,752	2,26	69,78	27,96	-2,6
30c	3,2E-07	6E-08	3,4	3,6	-8,7	-87	-11	-	15,002	1,37	69,86	28,77	-2,8
39a	9,10E-07	6,30E-07	17,3	3,27	-5,72	-89	-11,1	-	0,659	1,01	80,09	18,90	-4,7
47	3,15E-07	3,9E-08	11,78	3,4	-8,12	-80,1	-9,4	-	1,084	4,14	69,48	26,38	-4,8
50	4,21E-06	9,53E-07	0,28	3,8	-8,9	-93,2	-11,8	-	1,462	35,88	40,43	23,69	-4,5
LloN***	n.r.	n.r.	n.r.	3,4	-8,12	-95	-12,6	n.r.	-	n.r.	n.r.	n.r.	n.r.
LloS***	n.r.	n.r.	n.r.	4,81	n.r.	-85	-8,9	n.r.	-	n.r.	n.r.	n.r.	n.r.

Ca-SO_4 waters (Figure VI-3) are located north of the Maipo orocline along the WPC (samples 4 and 6) and EPC (samples 19 and 20). The former have neutral pH (~7) and relatively low temperatures (up to 20°C) and salinities (TDS <450 mgL^{-1}), whereas the latter are slightly acidic (pH~5.8) and show TDS values and temperatures up to 3,760 mgL^{-1} and 24.2°C, respectively. The only Na-SO_4 water, collected south of the Maipo Orocline (sample 14; Figure VI-2a), has the highest temperature (33.7°C) and pH (9.3), and the lowest pCO_2 value ($2.5x10^{-6}$ bar) among the springs located at the WPC.

Acidic (pH <3), SO_4-dominated waters (samples 29, 30 and 43) were collected from spring and bubbling-pools located in EPC south of the Maipo orocline. Analytical data for $\delta^{18}O$-H_2O and δD-H_2O values of water discharges range from -13.78 to -4.23‰ and from -107 to -50.9‰ vs. V-SMOW, respectively (Table VI-1).

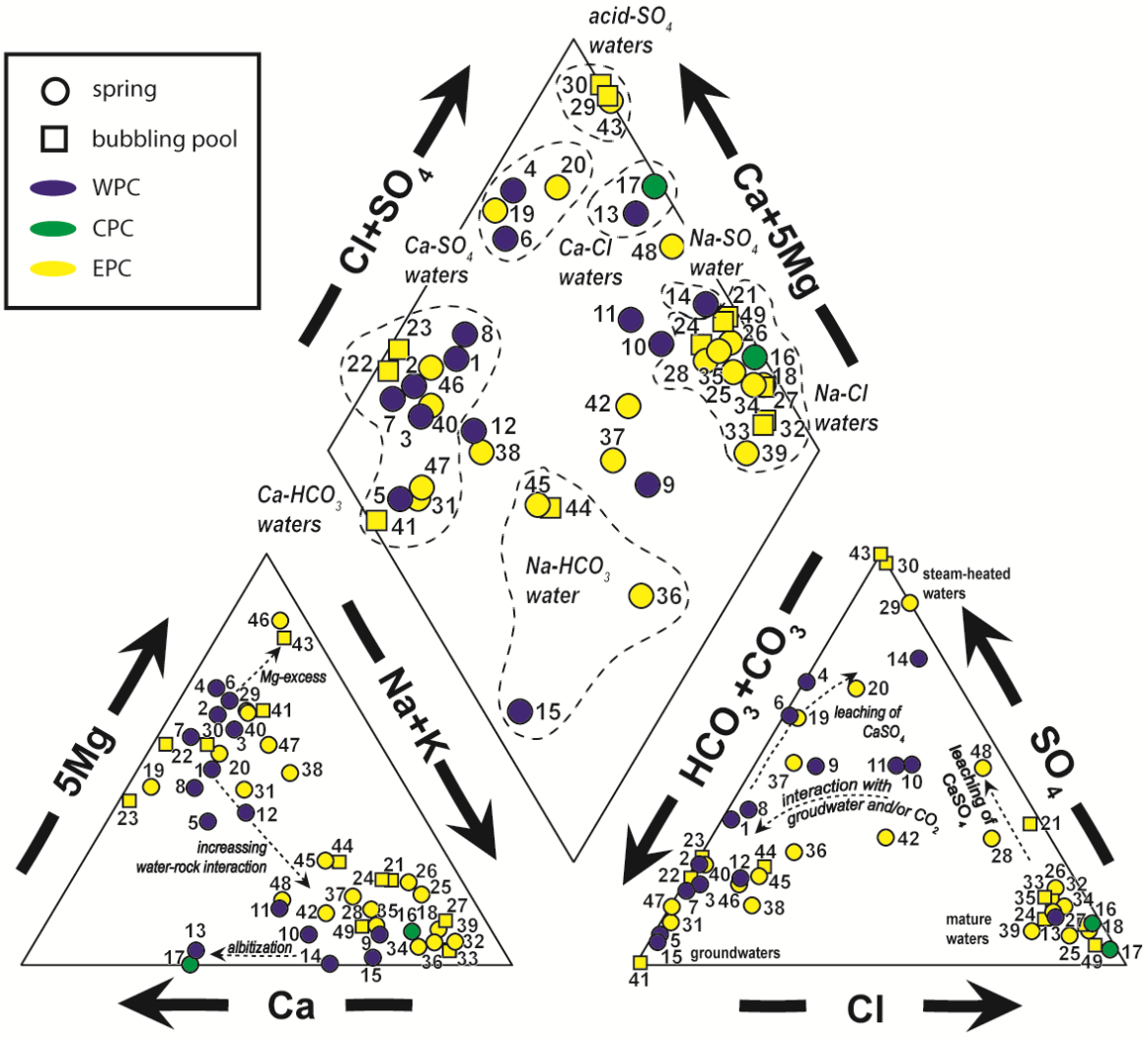

Figure VI-3: Piper-type plot constructed from the (Na-K)-Ca-5Mg and Cl-SO_4-(HCO_3+CO_3) triangles (both in $meqL^{-1}$) of the springs samples investigated.

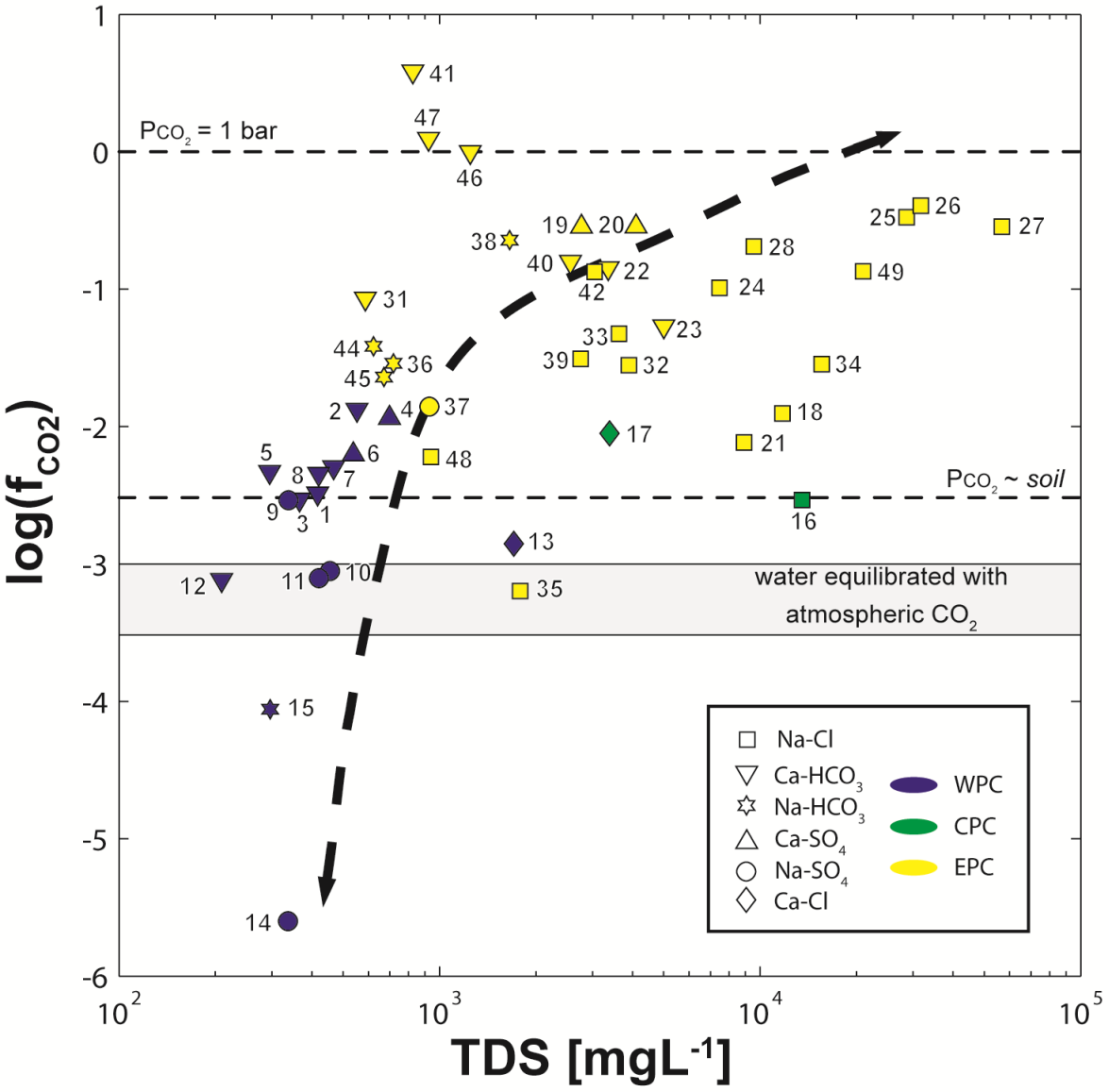

Figure VI-4: log(fCO$_2$) vs. TDS for the spring samples investigated. Dashed lines correspond to the fCO$_2$ equal to both 1 bar and a pressure similar to that generated by input of soil CO$_2$ in places with temperate climates (*Shvartsev 2008*). Also reported is the field representing the water equilibrated with atmospheric CO$_2$ (*Shvartsev 2008*).

VI.4.2 Chemical and isotopic composition of dissolve gases

Outlet temperature and chemical and isotopic compositions (R/Ra and δ^{13}C-CO$_2$) of dissolved gases are reported in Table VI-2. Carbon dioxide (from 32 to 77 %mol/mol) and N_2 (from 21 to 63 %mol/mol) are the most abundant gas species, whereas O_2 varies in a wide range (between 0.03 and 2.55 %mol/mol). Ar, H_2, CH_4 and He have concentrations lower than 1.2, 0.0025, 0.00045 and 0.0002 %mol/mol, respectively.

The $\delta^{13}C\text{-}CO_2$ values range from -14.3 to -6.03‰ vs. V-PDB, whereas R/R_a values range from 0.68 to 1.27.

VI.4.3 Chemical and isotopic composition of gases from bubbling pools and fumaroles

The chemical and isotopic composition of bubbling gases and fumaroles is shown in Table VI-3. Previous data reported by *Hilton et al. (1993), Saltori et al. (2012) and Dobson et al. (2013)* were also reported.

Fumarolic discharges are dominated by water vapor (H_2O_v in the range of 82.7 to 99 %mol/mol). The dry gas fraction of the fumarolic discharges, as well as the composition of bubbling gases are largely dominated by CO_2 (from 628 to 997 mmol/mol) followed by N_2 (from 1.57 to 355 mmol/mol). Methane concentrations are relatively high in some bubbling pools (up to 6.51 mmol/mol), whereas in fumarolic gases they do not exceed 1.57 mmol/mol. Fumarolic gases have higher H_2 concentrations (up to 46 mmol/mol), with respect to those of the bubbling pools (<0.09 mmol/mol). Hydrogen sulphide is present at relatively high concentrations in the fumarolic gases (ranging from 0.112 to 38.53 mmol/mol), whereas the bubbling pools are H_2S-free. Carbon monoxide was detected (up to 0.007 mmol/mol) in two of the seven fumarolic discharges (samples 39a and 47). It is noteworthy to point out that gas samples were analyzed, in average, 1 month after they were taken on the field. Therefore, the very low CO content of gas samples might be attributed to its reaction in alkaline solution to form $COOH^-$ (*Giggenbach and Matsuo 1991*). Water-soluble acidic gas species such as HF, HCl and SO_2, are below the detection limits in all the gas samples. Argon concentrations are low in the fumarolic gases (<0.79 mmol/mol), whereas in bubbling pools vary between 0.039 and 6.89 mmol/mol. Oxygen concentrations vary over a wide range, from <0.16 mmol/mol in fumarolic discharges, up to 9.68 mmol/mol in bubbling pools. Helium has concentrations < 0.0405 mmol/mol, and the sum of C_2H_6 and C_3H_8 species is up to 0.097 mmol/mol.

The $\delta^{13}C\text{-}CO_2$ values of the fumarolic discharges (from -9.3 to -5.72‰) are significantly less negative with respect to those of bubbling gases (from -13.21 to -7.76), whereas their R/Ra values range from 3.4 to 6 and from 0.47 to 6.2, respectively. The $\delta^{18}O\text{-}H_2O$ and $\delta D\text{-}H_2O$ values in steam from the fumarolic discharges range from -12.6 to -8.9‰ and from -95 to -80.1‰ (V-SMOW), respectively.

VI.5 DISCUSSION

VI.5.1 Processes controlling the chemical and isotopic composition of water samples

The δD vs. $\delta^{18}O$ diagram in Figure VI-5a shows that the isotopic signature of most hydrothermal discharges from Central Chile is consistent with that of the Local Meteoric Water Line (LMWL; *Hoke et al. 2013*). The shift to more negative $\delta^{18}O$ values respect to the LMWL for some CO_2-rich bubbling pools (samples 21, 38 and Gen2; Table VI-1) and some HCO_3-rich waters (samples 45 and 46) may be caused by isotopic exchange between CO_2 and H_2O (e.g. *Pauwels et al. 1997; Peiffer et al. 2014*). In contrast, some acid-sulphate (samples 30 and 43), Ca-HCO_3 (sample 41) and Na-Cl waters (samples 24, 27, 32 and 33; Fig. 5a), as well as the fumarolic condensates (Figure VI-5b) show significant enrichment in ^{18}O and ^{2}H likely produced by: (i) fluid–rock interaction, (ii) steam loss through evaporation, and/or (iii) mixing between meteoric and "andesitic" water. In particular, the four Na-Cl samples have a positive $\delta^{18}O$ shift (<1.5‰) without significant variation in δD with respect to local meteoric waters at comparable altitudes, suggesting that water-rock interaction at temperatures >150°C is the dominant process controlling the isotopic fractionation of these waters (*Truesdell and Hulston 1980*). This is also supported by the high Na/Mg ratios and high Li and B contents of these samples, which are indicative of prolonged chemical exchange with the host rock (*Giggenbach 1997a*). Despite their high Li and B contents (up to 14.67 and 42 mgL^{-1}, respectively), the water isotopic data of the others Na-Cl samples (18, 21, 25, 26, 28, 34, 35 and 39) do not differ from local meteoric values (Figure VI-5a) suggesting that water-rock interaction occurred at temperatures <150°C and/or the positive $\delta^{18}O$ shifting was masked through dilution with shallow meteoric water (e.g. *Capaccioni et al. 2013; Peiffer et al. 2014*).

The effect of evaporation on local meteoric water heated by steam released from a deep source can be quantified using the following equation:

$$S=(\delta D_S - \delta D_g + \varepsilon_{2H}) / (\delta^{18}O_S - \delta^{18}O_g + \varepsilon_{18O}) \quad \text{(VI.1)}$$

, where subscripts *s* and *g* referred to steam and groundwater, respectively, and ε is the kinetic isotope factor for evaporation, which is close to 50‰ for hydrogen and 16‰ for oxygen (*Giggenbach and Stewart 1982*). As shown in Figure VI-5a, samples 30, 41 and 43 plot consistently with steam-heated water lines of slopes ~3.7, which is close to the S values (~3.1) calculated for each sample by using Equation VI.1. Such calculation considers an isotopic composition of groundwater similar to that of local

meteoric waters at comparable altitudes, and a deep-steam isotopic composition similar to that of the steam emitted by the fumarolic vents (30b and LloS) located close to samples 30, 41 and 43 (Figure VI-2a and b). The latter implies that these waters derive from the condensation of CO_2- and/or H_2S-rich fumarolic vapors on the local meteoric water, as also supported by their high temperatures (>70°C), high pCO_2 value (up to $10^{0.58}$ bar) and acidic pH (Table VI-1). Lines connecting the fumarolic condensates and local meteoric water at similar altitudes (between 2000 and 3000 m a.s.l.) have slopes (2.3 to 2.7) lower than those calculated for the steam-heated waters (Figure VI-5b). The latter may indicate a possibly contribution (<5%) of "andesitic" waters (*Taran et al. 1989 and Giggenbach 1992*), whose presence was also suggested in fumaroles from the Tupungatito and Planchón-Peteroa volcanoes (Figure VI-5b; *Saltori et al. 2012; Benavente et al. 2013*).

The $\delta^{18}O$ vs. emergence elevation diagram in Figure VI-5c shows that water recharge zones for Central Chile springs lie between ~2,000 and 2,600 m a.s.l, coinciding with the altitude interval where snow accumulates at the PC (from 2000 to 3000 m a.s.l.; *Ohlanders et al. 2013*). Moreover, the high vertical drop (up to ~1000 m) between the infiltrating and emergence altitude of some springs (Fig. 5c) suggests that topographically-driven groundwater, originated from snowmelt at aforementioned altitudes, plays an important role controlling the geochemical characteristics of fluid discharges at Central Chile. As has been observed in other orogens (*e.g. Craw et al. 2002, 2009*), the high topographic gradient of mountain regions induces a limited interaction between the topographically-driven waters and the host rock, which promotes dissolution of carbonates and sulphates over alumino-silicate minerals since the formers dissolved ~2 to 6 order of magnitude faster than the latter depending upon pH (*Shvartsev 2008*). This process would explain the occurrence of thermal waters characterized by Ca(Mg)-HCO_3 and Ca-SO_4 composition with a slightly alkaline pH (<8.1), relatively low TDS (<600 mgL^{-1}) and pCO_2 values similar to those of waters equilibrated with soil (~$10^{-2.5}$ bar) such as samples 1-8 and 12 (Figure VI-3 and 4). On the contrary, bubbling pools and springs from the EPC (samples 19, 20, 22, 23, 31, 40, 41, 46 and 47) having a Ca-HCO_3 composition (Figure VI-3) but higher pCO_2 and TDS values (up to $10^{0.58}$ bar and 2200 mgL^{-1}, respectively; Figure VI-4) could be rather related to dissolution of deep-sourced CO_2 in the topographically-driven groundwater, as this process would induce an acidic pH in the groundwater (down to 5.4) and, consequently, would favor rock dissolution.

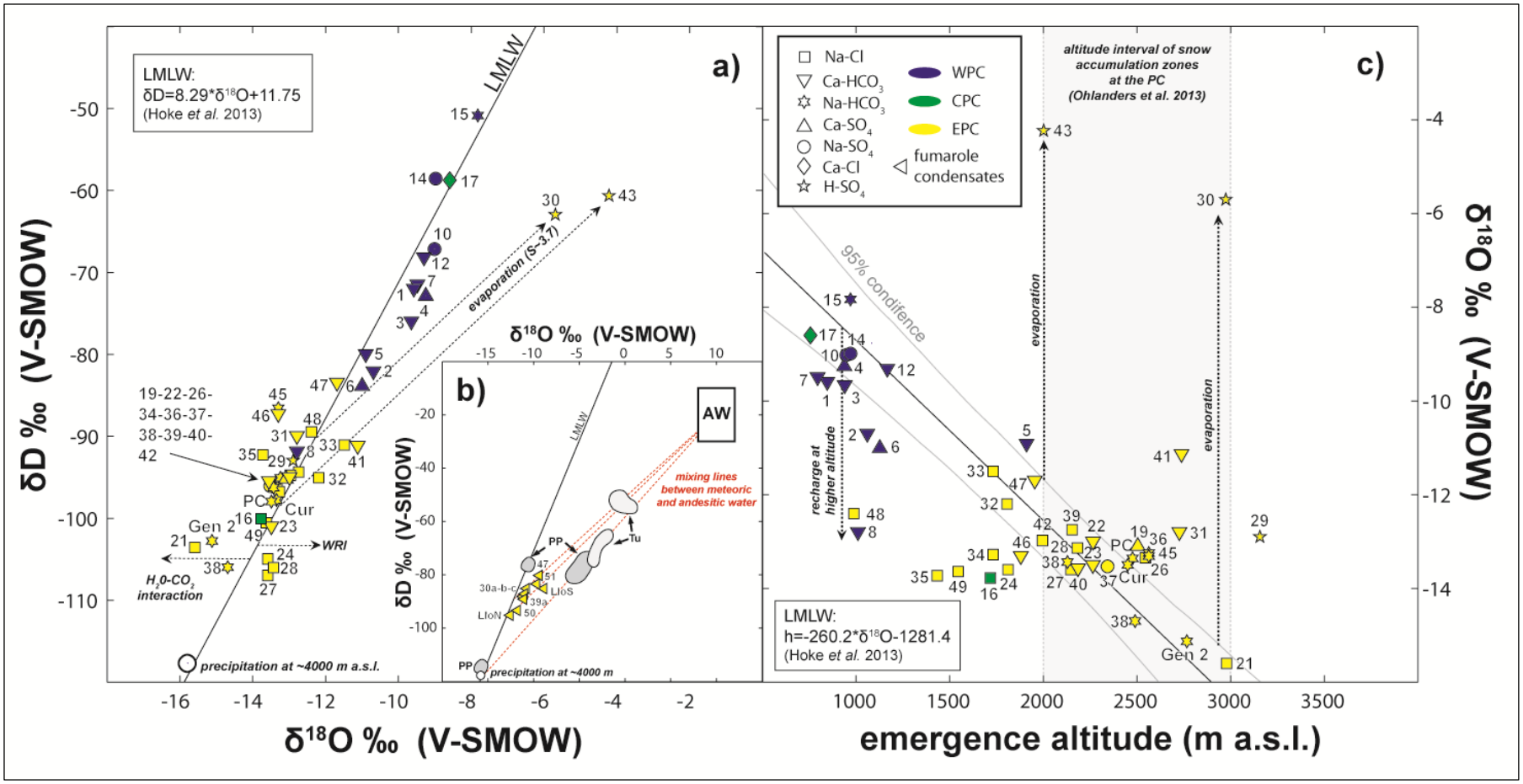

Figure VI-5: $\delta^{18}O$-H_2O vs. δD-H_2O diagrams of water from the hot springs and bubbling pools (a) and fumarole condensates (b). Local Meteoric Water Line (LMWL; *Hoke et al. 2013*), isotopic composition of the precipitation at ~4000 m a.s.l. (*Saltori et al. 2012*), mixing line between meteoric and Andesitic water, evaporation trend, and the isotopic composition of Tupungatito and Planchón-Peteroa volcanoes (*Benavente et al. 2013; Saltori et al. 2012*) are reported. (c) Altitude vs. $\delta^{18}O$-H_2O diagram of water from the hot springs, bubbling pools and fumaroles along Central Chile. Local Meteoric Water Line (black line; *Hoke et al. 2013*) of Central Chile and associated 95% confidence interval (grey line) are reported.

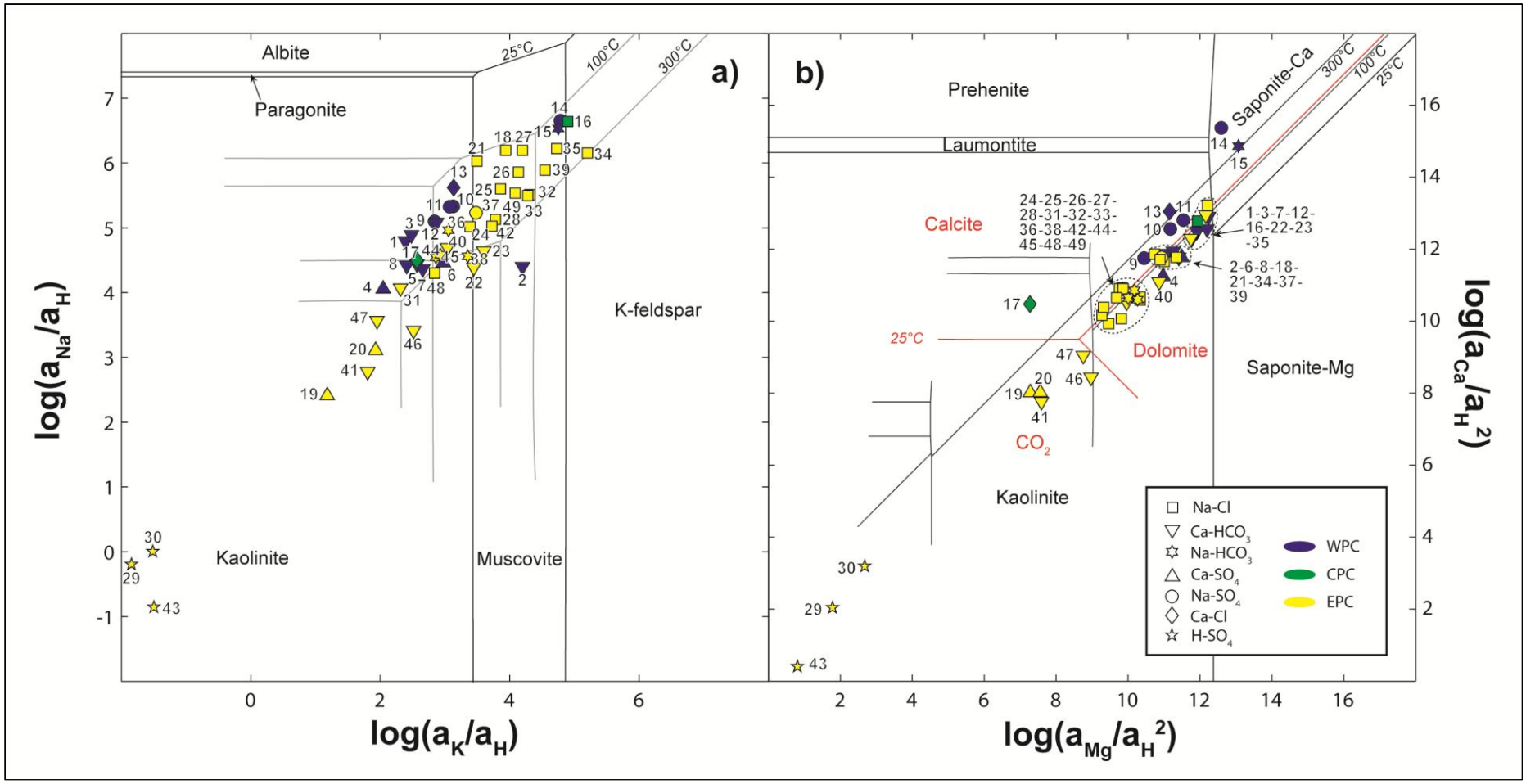

Figure VI-6: (a) $\log(a_{Na+} / a_{H+})$ vs. $\log(a_{K+} / a_{H+})$ activity diagram for the springs collected in Central Chile. The stability fields for alkali-feldspars, muscovite, kaolinite, and paragonite at different T (25, 100 and 300°C) conditions are reported. (b) $\log(a_{Ca2+} / a_{H+}^2)$ vs. $\log(a_{Mg2+} / a_{H+}^2)$ activity diagram for the springs collected in Central Chile showing the stability fields for Ca-Mg saponite, prehnite, laumontite and kaolinite (black lines), and calcite, dolomite and CO_2 (red lines) at different temperatures conditions (25, 100 and 300°C). Activity of quartz = 1.

Bubbling pools and springs from the WPC and EPC having a Na-HCO_3 and Na-SO_4 composition are characterized by a large Ca^{2+} deficiency compared to HCO_3^- and SO_4^{2-} contents, respectively (i.e. Ca/HCO_3 and Ca/SO_4 molar ratios < 1). This indicates that their origin is not related to Na enrichment due to calcite and anhydrite (or gypsum) precipitation (e.g. *Shvartsev 2008*). Conversely, their high temperatures, alkaline pH and low pCO_2 values when comparing with those of Ca-HCO_3 and Ca-SO_4 springs emerging in the same domains (Figure VI-4), likely reflects the occurrence of Ca-Na ion-exchange between Na-bearing silicates (e.g. albite) and Ca-(HCO_3-SO_4) waters. The latter process is commonly attributed to long-lasting water–rock interaction occurring in slow-moving groundwater rising along fault systems (e.g. *Marini et al. 2000; Reyes et al. 2010; Capaccioni et al. 2013*).

The extent of the water–rock interaction is well illustrated by the $\log[K^+]/[H^+]$ vs. $\log[Na^+]/[H^+]$ and $\log[Mg^{++}]/[H^+]^2$ vs. $\log[Ca^{++}]/[H^+]^2$ activity diagrams for both alkaline and alkaline-earth silicates and their alteration products at 25, 100 and 300°C (Figure VI-6a and b, respectively). The stability diagram for carbonate minerals at 25°C is also reported in Figure VI-6b. The use of activity plots also allows a quick evaluation of the effects of mixing in the solid state, as the stability field limits of solid mixture end-members are taken into account (e.g. *Reed 1997; Marini et al. 2000; Marini 2006; Capaccioni et al. 2013; Nissi et al. 2013*). In the $\log[K^+]/[H^+]$ vs. $\log[Na^+]/[H^+]$ activity diagram (Figure VI-6a), acid-SO_4 waters and Ca-SO_4 and Ca-HCO_3 waters with the highest pCO_2 values (Figure VI-4) plot within the stability field of kaolinite at T lower than 100°C. The rest of Ca-HCO_3 as well as some Na-HCO_3, Na-SO_4 and Na-Cl waters plot near the invariant points of stable equilibrium between water and kaolinite-paragonite-muscovite, paragonite-muscovite-albite and K-feldspar-albite-muscovite at T in the range of 100-300°C. Only Na-SO_4, Na-HCO_3 and Na-Cl waters are found along the K-feldspar-albite boundaries at temperature between 100 and 300°C. According to *Reed (1997)* the distribution of the water samples in Figure VI-6a is indicative of an evolution trend from acidic “immature” waters, causing dissolution of the surround rocks and subsequent precipitation of clay minerals, to neutral and slightly alkaline “mature” waters having attained equilibrium with alkaline feldspars.

Further indications on the chemical evolution of the hydrothermal waters circulating in the study area are given by the activity plot of $\log[Mg^{++}]/[H^+]^2$ vs. $\log[Ca^{++}]/[H^+]^2$ (Figure VI-6b). Ca-HCO_3 and Ca-SO_4 waters from the WPC and EPC fall along the calcite-dolomite boundary (at 25°C) in Figure VI-6b, which is consistent with the fact that all these waters are saturated with calcite and dolomite (SI_{cal} is from −0.25

to +0.42 and SI_{dol} is from −0.25 to +0.42, respectively; Table VI-1). Na-HCO_3 and Na-SO_4 waters from the WPC, conversely, plot off the carbonates boundary (Ca/Mg molar ratios >1), near the invariant points of stable equilibrium between laumontite, prehnite and saponite-Ca at T<100°C. The latter is a common compositional feature of "mature" waters caused by the Mg incorporation into secondary Mg-rich phyllosilicate minerals (e.g. chlorites; *Giggenbach 1988*). On the contrary, Na-Cl from the EPC, which are also saturated with respect to calcite and dolomite (SI_{cal} and SI_{dol} values from −1.32 to +2.02 and from −1.32 to +2.02, respectively; Table VI-1) plot along the carbonates boundary in Figure VI-6b like the Ca-HCO_3 and Ca-SO_4 waters from the EPC and WPC do. I propose that the Mesozoic carbonate rocks in the EPC act as a sort of geochemical barrier in determining the possible attainment of equilibrium between mature Na-Cl hydrothermal fluids and the typical Ca-silicates minerals present in "mature" hydrothermal systems (e.g. laumontite, prehnite, anorthite; *Giggenbach 1988*). Basically, the carbonate ions released by the carbonate rocks of the EPC would enhance saturation of Ca- and Mg-carbonates in the water over Ca- and Mg-bearing secondary alumino-silicates, preventing the typical enrichment of dissoved Ca over Mg caused by the precipitation of Mg-rich phyllosilicate (e.g. *Shvartsev 2008; Nissi et al. 2013*). Nevertheless, it is worth noting that most Na-Cl waters plot close to the Ca- and Mg-saponite boundary in Figure VI-6b, and according to the analysis of the secondary minerals present in the well drilled at Tinguiririca geothermal field carried out by *Droguett (2012)*, both minerals are present at depth.

Samples 13 and 17 have an unusual Ca-Cl composition characterized by near-neutral pH and an excess of Ca over SO_4 and HCO_3 (i.e. 2 mol Ca > 2 mol SO_4 + mol HCO_3 +2 mol CO_3; Table VI-1), which suggests that these waters did not acquire their Ca-Cl component through the interaction with the Mesozoic carbonate-evaporite rocks that are expected to be present at the WPC and CPC at >10 km depth (below the basaltic to andesitic volcanic sequences; Figure VI-2c). The Ca-Cl component is a compositional characteristic of some thermal waters occurring in modern rift zones, oil-field brines and some continental hydrothermal systems (e.g. Reykjanes-Iceland, Salton Sea-USA and Oregon Cascada range-USA) as a result of albitization-chloritization of basalt by its interaction with hot Na-Cl solutions (*Hardie et al. 1987; Mariner et al. 2003*). In fact, the albitization-chloritization of mafic volcanic rocks is a common hydrothermal phenomenon at the WPC and CPC (e.g. *Vergara et al. 1993*). *Muñoz et al. (2010)* reported several basaltic to andesitic hydrothermally-altered volcanic outcrops at the WPC and CPC characterized by a secondary mineral assemblage made of chlorite, chalcedony/quartz and secondary albite formed by

partial or complete replacement of primary An-rich plagioclase. Moreover, these hydrothermaly-alterated outcrops are emplaced along the faults and folds that subtly deformed the 5,500 m thick basaltic to andesitic volcanic and volcanoclastic Cenozoic sequences, like samples 13 and 17 do (Figure VI-2a, b and c). This hydrothermal phenomenon involves essentially the transfer of $Na^{+} + Mg^{2+} + SiO_{2(aq)} \leftrightarrow Ca^{2+}$ between Na-Cl solutions and mafic volcanic rocks (*Hardie et al. 1987*), therefore, the occurrence of such process would explain the relatively low Mg and SiO_2 contents of samples 13 and 17 (<2.6 and <37 mgL^{-1} respectively) when compared to those of the Na-Cl waters with similar Cl concentrations (samples 35 and 32, respectively ;Table VI-1).

The sample 16, which is also located in the CPC but north of the Maipo orocline, has a Na(Ca)-Cl composition where at least part of its chloride is balanced by calcium (Table VI-1). Given its geographic position, I speculate that this Na-Ca-Cl composition corresponds to an intermediate step in the evolution of Na Cl waters as they change to Ca-Cl in character. According to *Mariner et al. (1993)*, the latter might reflect an incomplete albitization-chloritization process as consequence of (i) the lower temperatures at which this process might occur and/or (ii) the lower residence times that Na-Cl waters would experience within the mafic volcanic sequences. Unfortunately, there is no tritium data available for the fluid discharges of Central Chile, therefore, it is not possible to confirm or exclude the second hypothesis.

VI.5.2 Controls on the chemical and isotopic composition of gas samples

Potential source regions (limestone, organic sediment, mantle) feeding gas discharges of the EPC can be examined by comparing the isotopic signatures of C-CO_2 and He (Figure VI-7). Gas discharges of Central Chile seem to have at least two different origins: (i) gases associated with mantle degassing (hereafter volcanic environment) producing the relatively high R/Ra ratios (up to 6.2) and the restricted δ^{13}C-CO_2 values (from -8.9 to -5.72‰ V-PDB) characteristic of fumarolic discharges and some bubbling pools (samples 32b, 38 and Gen2), and (ii) gases characterized by relatively low R/Ra ratios (from 0.75 to 1) and a wide range of δ^{13}C-CO_2 values (from -14.3 to -6.03‰ V-PDB) likely originated in the carbonate- and organic-rich Mesozoic sequences that constitute the basement of the EPC (hereafeter sedimentary environment). Intermediate δ^{13}C-CO_2 and R/Ra values likely indicate mixing of these two end-members and/or addition of air.

The relative contribution from these potential C-CO_2 and He sources (limestone, organic sediment and mantle) can be evaluated using the methodology proposed by

Sano and Marty (1995), which considers the $CO_2/^3He$ ratio and the $\delta^{13}C\text{-}CO_2$ value of each gas sample. However, the measured $CO_2/^3He$ ratio for bubbling pool and strip samples cannot be used directly, because CO_2 dissolves in water and the methodology proposed by *Sano and Marty (1995)* considers the total concentration of CO_2 (i.e. free gas phase and dissolved gas). According to *Taran (2005)*, the total CO_2 content (in mole fraction) of bubbling pools and strip samples can be estimated as follow:

$$X_{CO2} = x_{CO2}(X_g + (1+K_{H2CO3}/H^+)*P/Kh_{CO2}) \quad \text{(VI.2)}$$

, where P is the atmospheric pressure (atm) at the elevation of each gas discharge, Kh_{CO2} is the solubility of CO_2 in pure water at the temperature of each gas discharge, H^+ is the activity of hydrogen in the bubbling pool (pH), Kh_{H2CO3} is the first dissociation constant for H_2CO_3, x_{CO2} is the analytical concentration of CO_2 in the bubbling pools and strip samples (in mole fraction) and X_g is the concentration of the free gas phase (i.e. gas/water ratio). For these cases, the gas/water ratio of gas discharges can be calculated using the analytical contents (C_i) of one of the three atmospheric gases (N_2, Ar and/or Ne) as has been shown by *Taran (2005)*. Because the subduction-related gases usually have non-atmospheric nitrogen (N_2/Ar>86), gas/water ratios (in mole fraction) were computed on the basis of the measured Ar content (in mole fraction) as follows:

$$X_g = (1.36/C_{Ar} - 1.05P)/55.51 \quad \text{(VI.3)}$$

, where C_{Ar} is the analytical content of Ar. Equation VI.3 was recalculated from *Taran (2005)* considering that groundwater of Central Chile recharges at a temperature and elevation close to 5°C and 2600 m a.s.l., respectively (Figure VI-5c).

Values of $CO_2/^3He$ considering the free CO_2 gas ($CO_2/^3He$) and the total CO_2 concentration ($CO_{2,total}/^3He$ with Xg correction using Ar) are shown in Table VI-3. Following *Sano and Marty (1995),* the relative contribution from mantle degassing (M), limestone (L) and/or organic-rich sediments (S) can be evaluated as follows:

$$M + S + L = 1 \quad \text{(VI.4)}$$

$$(\delta^{13}C\text{-}CO_2)_{meas} = M(\delta^{13}C\text{-}CO_2)_{MORB} + L(\delta^{13}C\text{-}CO_2)_{Lim} + S(\delta^{13}C\text{-}CO_2) \quad \text{(VI.5)}$$

$$[1/(CO_2/^3He)]_{meas} = [M/(CO_2/^3He)]_{MORB} + [L/(CO_2/^3He)]_{Lim} + [S/(CO_2/^3He)]_{Sed} \quad \text{(VI.6)}$$

, where $(\delta^{13}C\text{-}CO_2)_{MORB}$ = -5‰, $(\delta^{13}C\text{-}CO_2)_{Sed}$ = -30‰, $(\delta^{13}C\text{-}CO_2)_{Lim}$ = 0‰, $(CO_2/^3He)_{MORB} = 1.5\times10^9$, $(CO_2/^3He)_{Sed} = 1\times10^{13}$ and $(CO_2/^3He)_{Lim} = 1\times10^{13}$. As shown in Table VI-3, where the three end-members modeled are reported as percentage, CO_2 of the gas discharges from EPC is mostly produced from carbonates (L from 39.5 to 80%), whereas organic-sediment (S from 18.9 to 47.5%) and mantle degassing (M from 0.1 to 35.9%) are to be regarded as secondary CO_2 sources for samples from the sedimentary and volcanic environments, respectively.

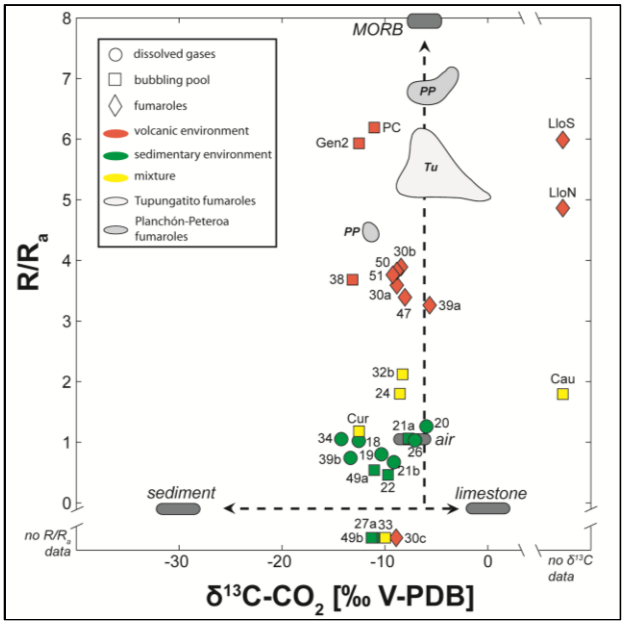

Figure VI-7: $\delta^{13}C\text{-}CO_2$ vs R/R_a plot for thermal fluids in the Central Chile. End-members for MORB, limestone, and organic matter in sediments are $\delta^{13}C$ (CO_2)=−6.5, 0 and −30‰; and R/R_a = 8, 0.02 and 0.02, respectively. For comparison the fields of the fumarolic discharges from Tupungatito and Planchón-Peteroa volcanoes are reported (*Saltori et al. 2012; Benavente et al. 2013*).

As shown by the N_2–He–Ar ternary diagram (Figure VI-8), where the compositional fields of gases from mantle, air-saturated water (ASW), air and the Chilean arc-type gases are reported (*Giggenbach 1996*), gas discharges from the volcanic environment describe a mixing trend between air-ASW and the Chilean arc-type gases end-member (*Tassi et al. 2009, 2011; Aguilera et al. 2011; Capaccioni et al. 2011; Saltori et al. 2012; Agusto et al. 2013; Benavente et al. 2013*). This likely implies the existence of magmatic-related sources feeding these gas discharges, which is consistent with the andesitic water fraction observed (<5%) in the fumarolic discharges (Figure VI-5b) and also with the presence of non-atmospheric N_2 (N_2/Ar ratios up to 540) in most of these samples (Figure VI-8). Given the relatively high contents of hydrothermal-related compounds in these samples (H_2S, H_2 and CH_4; Table VI-3), as well as the absence of water-soluble magmatic gases (SO_2, HCl and HF), such magmatic-related sources may correspond to magmatic-driven hydrothermal systems (*Goff and Janik 2000*). Occurrence of scrubbing processes within the magmatic-driven hydrothermal systems overlying the degassing magmas may explain the absence of acid-soluble magmatic in most of the gas discharges from the volcanic environment

together with the presence of poorly soluble magmatic compounds such us N_2-excess and ^{3}He (*Symonds et al. 2001*).

Samples from the sedimentary environment are plotted between ASW and air end-members in Figure VI-8, indicating that the atmosphere is the only source of N_2 and Ar in these gases. Excluding any sampling artefact, the latter indicates that gases from the sedimentary environment are originated by the interaction of the Mesozoic sequences with a fresh ASW component likely introduced to deeper levels by topographically-driven groundwater (e.g. *Craw et al. 2002*). Such description is consistent with a tectonic-driven origin for these hydrothermal fluids, where the fluid flow is restricted to fault–fracture networks and the heat source is the conductive heat transfer from the host rock (*Goff and Janik 2000*). According to the $CH_4/(C_2H_6+C_3H_8)$ ratios of these samples (between 34 and 85), the interaction between fresh groundwater and the Mesozoic sequences likely occurs at T>150°C, which favors thermogenic production of hydrocarbons from the decomposition of organic matter buried in the sedimentary sequences (*Fiebig et al. 2009*). Samples from the volcanic environment, on the other hand, have $CH_4/(C_2H_6+C_3H_8)$ ratios also consistent with a thermogenic origin for hydrocarbons (between 120 and 400), although the relatively high $CH_4/(C_2H_6+C_3H_8)$ ratios of these samples with respect to those from the sedimentary environment likely indicates that some of the CH_4 is being produced by CO_2 reduction, which is a reaction that is favored under rock-dominated hydrothermal conditions (e.g. *Giggenabach 1997b*).

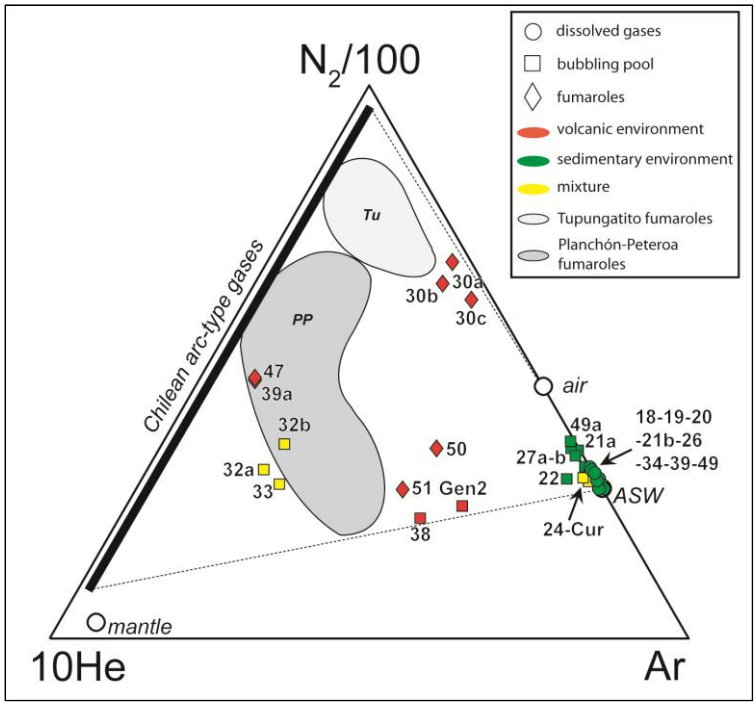

Figure VI-8: N_2/100-10He-Ar ternary diagram. For comparison the fields of the fumarolic discharges from Tupungatito and Planchón-Peteroa volcanoes (*Saltori et al. 2012; Benavente et al. 2013*), Air, Air Saturated Waters (ASW), mantle compositions and convergent plate boundaries ("andesite") field are reported (*Giggenbach 1996*).

VI.5.3 Temperature and redox condition of the gas-water-rock interaction

VI.5.3.1 Water Geothermometry

Evaluation of equilibrium conditions using the relative Na, K, Ca and Mg contents allows estimations of relatively "deep" temperatures due to the slow kinetic of the reactions involved (*Giggenbach 1984, 1988*). Figure VI-9a shows the ionic solute Na-K-Mg-Ca geothermometer (10K/[10K+Na] vs. 10Mg/[10Mg+Ca]), where plotted curves represent water composition expected for "full equilibrium" (black curve) and "isochemical dissolution" of an average crustal rock (*Giggenbach 1988*). As expected, acid-SO_4 waters and Ca-HCO_3 samples with the highest pCO_2 values (samples 41, 43 and 46) plot close the composition of dissolved rocks, whereas Na-HCO_3 and Na-SO_4 waters from the WPC (sample 9, 10, 11, 14 and 15) seem to attain a full equilibrium with an average crustal rock at about 100-160°C. On the contrary, Ca-HCO_3 samples from the WPC and EPC, as well as Na-HCO_3, Ca-SO_4, Na-SO_4 and even Na-Cl waters from the CPC and EPC are scattered in an area far from the rock-water equilibrium curve suggesting that these waters are all partially equilibrated (*Giggenbach 1988*). In the case of the Ca-HCO_3, Ca-SO_4 samples and most Na-HCO_3 and Na-SO_4 waters from the EPC, the latter explanation seems reasonable as these water do not have chemical and isotopic evidences of having experienced a long-lasting water-rock interaction process (Section 5.1). However, the Na-Cl waters from the EPC and CPC have strong evidences that support its chemical and, in some cases, its isotopic "maturity" (e.g. high Li and B contents, positive $\delta^{18}O$ shifting). This indicates that their intermediate positions in Figure VI-9a are likely related to the mineral assemblage that these waters attained equilibrium, which seems to be different to that used by *Giggenbach (1988)* to construct the full equilibrium curve.

According to Figure VI-6a and b, these Na-Cl waters attain equilibrium with albite and K-feldspar, and Ca- and Mg-saponite, respectively. Therefore, the Na/K and Ca/Mg equilibrium ratios can be evaluated according to the following reactions:

$$\text{albite} + K^+ \leftrightarrow \text{K-feldspar} + Na^+ \qquad \text{(VI.7)}$$

$$Ca_{0.165}Mg_3Al_{0.33}Si_{3.67}O_{10}(OH)_2 + 0.165Mg^{2+} \leftrightarrow Mg_{3.165}Al_{0.33}Si_{3.67}O_{10}(OH)^2 + 0.165Ca^{2+}$$

Ca-saponite Mg-saponite (VI.8)

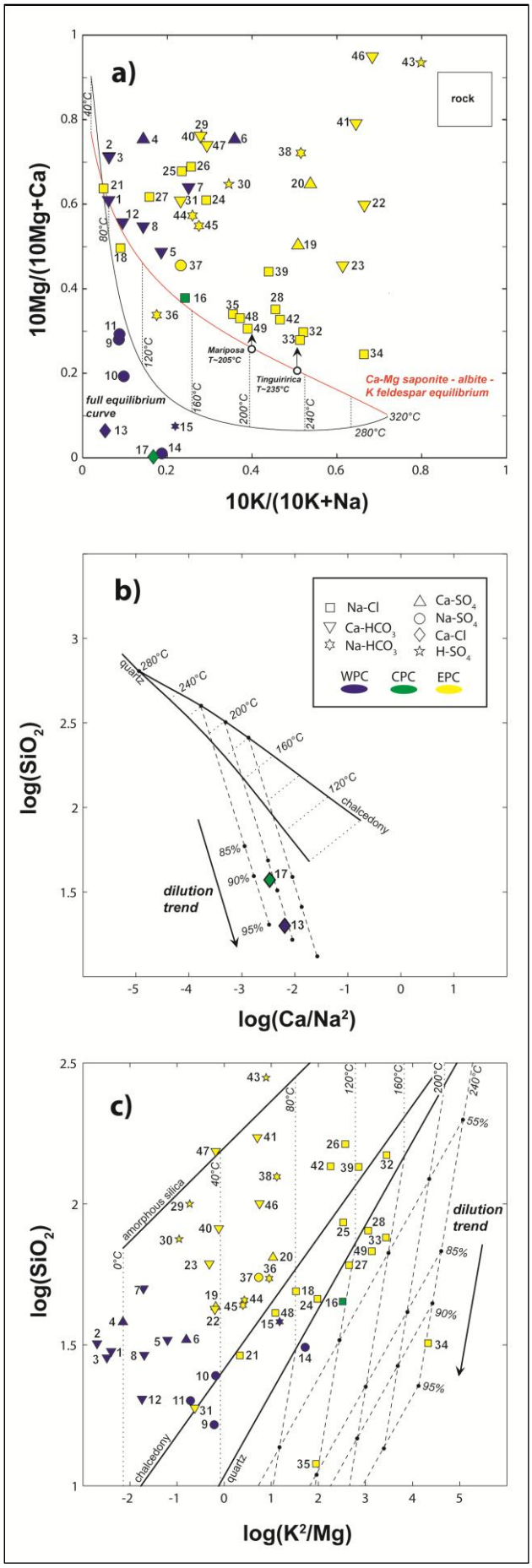

Figure VI-9: (a) plot of 10K/(10K+Na) vs. 10Mg/(10Mg+Ca) for spring samples discharging from Central Chile. Diagram is based on Giggenbach (1988). Rock represents isochemical dissolution of mean crustal rock, curved full line (black line) represents solutions that have attained full equilibrium with the rock as a function of temperature, and red line represents solutions that have attained equilibrium with Ca-Mg saponite and alkali-feldspars as function of temperature (see text). (b) Plot of log(Na^2/Ca) vs. log(SiO_2) for spring samples discharging from Central Chile. The lines are drawn using the temperature-dependent equations for amorphous silica, chalcedony, and quartz from Henley et al. (1984). Temperature in °C. Dilution trends are also shown. (c) Plot of log(K^2/Mg) vs. log(SiO_2) adapted from Giggenbach and Glover (1992) for spring samples discharging from Central Chile. Dilution trends are also shown.

Assuming that activity ratios for the secondary feldspars and saponite solid mixture are close to unity (*Giggenbach 1988; Marini 2006*), and that activity coefficients of monovalent and bi-valent cations are similar (i.e., $\gamma Ca^{2+} \sim \gamma Mg^{2+}$ and $\gamma Na^{+} \sim \gamma K^{+}$), the K/Na and Ca/Mg weight ratios (mg/kg) can be computed using the following temperature-dependent relations (in °C):

$$\log(c_{K+}/c_{Na+}) = 1.75 - (1390/(T+273.15)) \quad \text{(VI.9)}$$

$$\log(c_{Ca2+}/c_{Mg2+}) = 0.0356 + 0.012T - 4.121(T^2/10^5) + 0.848(T^3/10^7) - 0.569(T^4/10^{10}) \quad \text{(VI.10)}$$

Equation VI.9 was obtained from *Giggenbach (1988)* while Equation VI.10 was recalculated from thermodynamic data of *Delany and Lundeen (1991).* Figure VI-9a shows that Na-Cl waters saturated in Ca- and Mg-saponite (samples 18, 21, 32, 33, 34, 35, 42, 48 and 49; Figure VI-6b) plot near the calculated equilibrium line between K-feldspar, albite and Ca- and Mg-saponite phases (red curve) at temperature ranging between 80 to ~280°C. The temperatures estimated by the Na-Cl waters from the Tinguiririca (samples 32 and 33) and Mariposa (samples 48 and 49) geothermal fields in Figure VI-9a are in accordance with those measured at the bottom of the wells drilled in these fields (~234 and ~205°C, respectively; *Clavero et al. 2011; Hickson et al. 2011*).

In Figure VI-9a, Ca-Cl waters also plot close to the full equilibrium curve, but, and as already discussed in Section 5.1, their relatively high Ca/Mg ratios and low Na/K ratios are likely caused by an albitization-like reaction (Equation VI.11) that consumes sodium and releases calcium from/to the aqueous solution (*Mariner et al. 1993*).

$$2Na^{+} + \text{anortithe} + 4SiO_2 \leftrightarrow 2\text{albite} + Ca^{2+} \quad \text{(VI.11)}$$

Equation VI.11 can be evaluated in the $\log(Ca/Na^2)$ vs. $\log(SiO_2)$ diagram (Figure VI-9b) considering that dissolved SiO_2 content is constrained by the precipitation/dissolution of quartz or calcedony (*Henley et al. 1984*), and that $\log(Ca/Na^2)$ and $\log(SiO_2)$ are related by the following temperature-dependent relation:

$$\log(c_{Ca2+}/[c_{Na+}]^2) - \log(c_{SiO2}) = 0.6648 - 0.1323T + 5.454(T^2/10^4) - 1.524(T^3/10^6) + 1.754(T^4/10^9) \quad \text{(VI.12)}$$

, where the c_i corresponds to the concentration of Ca^{2+}, Na^+ and SiO_2 in mg/kg. Equation VI.12 was recalculated from thermodynamic data of *Delany and Lundeen (1991),* assuming that activity coefficients of Ca^{2+} and Na^+ are closely related through $\gamma Ca^{2+} \sim (\gamma Na^+)^2$, and activity ratios for albite and anorthite as well as activity coefficients of SiO_2 are close to unity (*Giggenbach 1988; Marini 2006*). It can be seen from Figure VI-9b that samples 13 and 17 plot below the quartz, chalcedony and amorphous silica solubility lines, likely as a result of a dilution process of "Ca-Cl brines" due to their interaction with groundwater. By assuming a simple dilution model, and that dissolved SiO_2 contents of "Ca-Cl brines" are buffered by the precipitation/dissolution of chalcedony (Section 5.1), samples 13 and 17 seem to derive from the dilution of Ca-Cl brine (95 and 85%, respectively) equilibrated with the host rock at ~200°C. The latter likely implies that samples 13 and 17 have a common parental Ca-Cl brine, whose Cl content (up to ~17000 mgL^{-1}) is similar to that of the saline Na-Cl samples located at the EPC at comparable latitudes (samples 25-27; Figure VI-2a).

The interaction of deep-sourced fluids and topographically-driven groundwater is a process that should affect not only the Ca-Cl waters but also the rest of samples as the hydrothermal activity in Central Chile occurs in an active orogen (e.g. *Craw et al. 2002*). Such process can be evaluated by comparing the dissolved SiO_2 content and K^2/Mg ratios of samples (Figure VI-9c) assuming that both values respond to changes in temperature at a similar rate to each other (e.g. *Giggenbach and Glover 1992*). Disregarding inmature waters (acid-SO_4 and Ca-HCO_3 samples), most data points in Figure VI-9c lie along the quartz solubility line or in between the chalcedony and quartz solubility line at temperatures between 40 and 160°C. Na-Cl samples 34 and 35, and to a lesser extent samples 14, 16, 17, 28 and 49, plot below the quartz solubility line, which is a typical feature of diluted mature hydrothermal waters (e.g. *Reyes et al. 2010*). This is also consistent with the absence of any positive $\delta^{18}O$ shifting of these waters with respect to LMWL in Figure VI-5a. Assuming that the dissolved SiO_2 content of these Na-Cl waters is buffered by precipitation/dissolution of quartz and chalcedony at temperatures greater and lower than 200°C, respectively, samples 14, 16, 17, 28, 34, 35 and 49 likely result from the dilution (up to 95%) of mature Na-Cl waters equilibrated with the host rock at temperature in the range of 100 and 240°C.

The temperatures estimated from Figure VI-9c are as much as 80°C cooler than those estimated from the Na-Ca-K-Mg diagram (Figure VI-9a), which is consistent with the fact that both K-Mg and silica geothermometers reset quickly to cooler temperatures than the Na-K geothermometer (*Giggenbach 1988*). Therefore, such

differences suggest that these Na-Cl waters move laterally a considerable distance from their source before discharging at the surface (e.g. *Mariner et al. 1993*).

VI.5.3.2 Gas Geothermometry

Physico-chemical conditions of hydrothermal gases can be accurately predicted in the $H_2O–CO_2–H_2–CO–CH_4$ system (e.g. *Chiodini and Marini 1998*). Unfortunately, CO was above the detection limit only in two samples (39a and 47; Table VI-3), likely resulting from the interaction between uprising hydrothermal fluids and groundwater which causes dissolution of soluble species such CO, as well as condensation of water vapor (e.g. *Shock 1993; Tassi et al. 2010*). Therefore, in the present study, evaluation of the temperature and redox conditions is restricted to the gas equilibria in the $H_2O–CO_2–CH_4–H_2–Ar$ system, where the H_2O content of gases emitted by bubbling pools and strip samples were estimated taking into account the total gas content X_g calculated by Equation VI.3 (*Taran 2005*).

The log-ratio between the molar concentrations of H_2 and H_2O (R_H) is considered the most suitable parameter for describing the redox state of hydrothermal fluids (*Giggenbach 1987*). Its comparison to another parameter with quick responds to changes in temperature and redox state, such the $\log(Ar^*/H_2O)$, results useful to assess the physico-chemical conditions controlling gas composition near the surface (e.g. *Cinti et al. 2014*). Ar^* values correspond to the air-corrected Ar calculated as follow:

$$Ar^*=Ar-(O_2/22) \quad \text{(VI.13)}$$

, where $O_2/22$ value is the amount of Ar from atmospheric contamination, considering that O_2 is absent in pristine hydrothermal fluids (*Giggenbach 1991*). As shown by the $\log(H_2/H_2O)$ vs. $\log(Ar^*/H_2O)$ diagrams (Figure VI-10a and b), the position of bubbling and strip gases is consistent with $\log(H_2/H_2O)$ and $\log(Ar^*/H_2O)$ values dictated by the $H_2O=H_2+1/2O_2$ reaction occurring in a liquid phase at typical hydrothermal conditions (e.g. *D´amore and Panichi 1980; Giggenbach 1987*). However, equilibrium temperatures of bubbling gases tend to approach those estimated by water geothermometers (Figure VI-9a and c) only at redox conditions dictated by the D´amore and Panichi (DP) hydrothermal buffer (120-180°C; Figure VI-10b). Fumarolic gases, on the other hand, seem to attain equilibrium with liquid (sample 39a), liquid + vapor (samples 47, 50 and 51), vapor (samples 30a-c) at temperatures between 250 and 320°C and redox conditions typical of rock-dominated hydrothermal systems (Figure VI-10a and b).

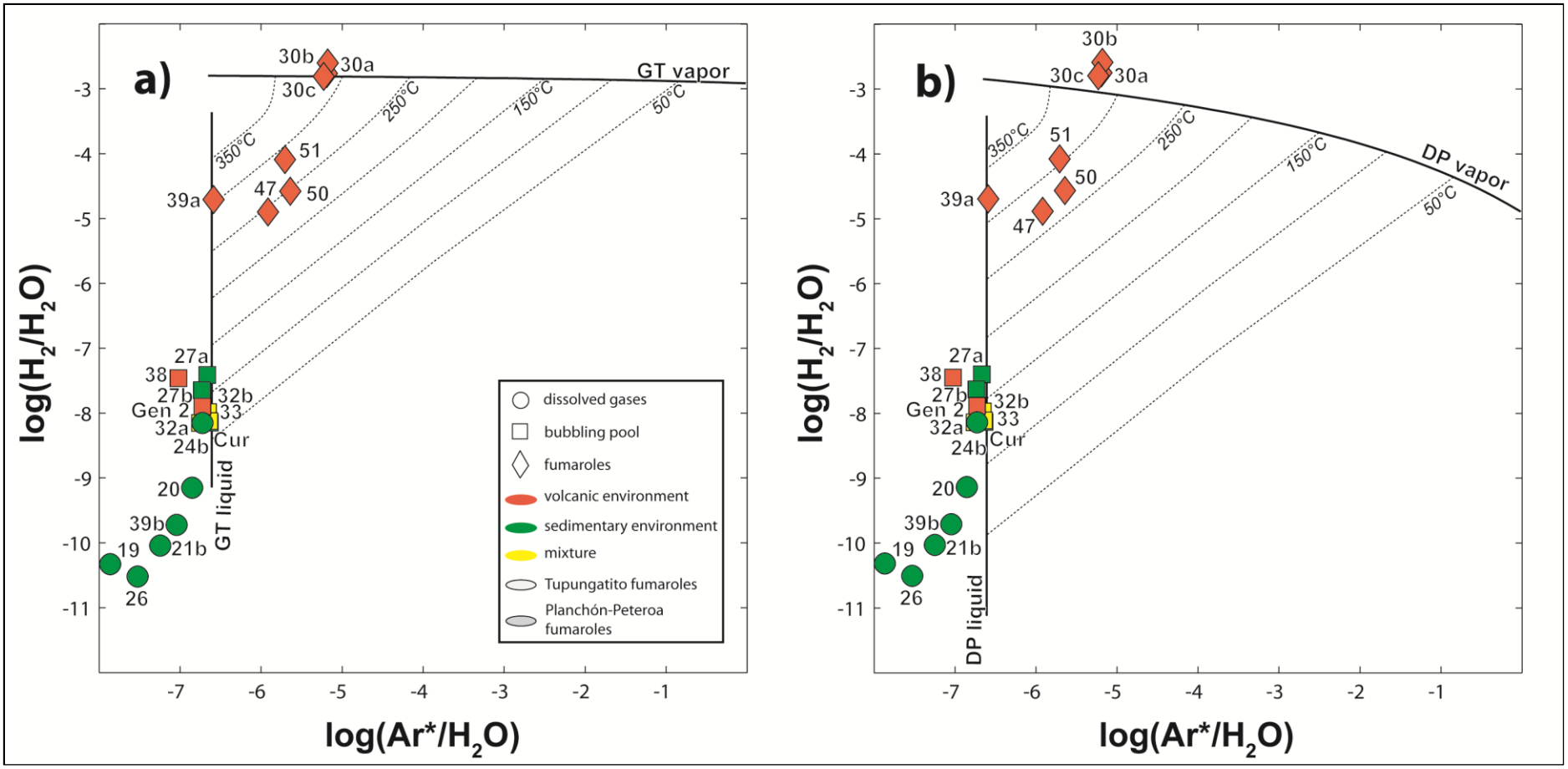

Figure VI-10: Plot of $\log(X_{H2}/X_{H2O})$ vs. $\log(X_{Ar*}/_{XH2O})$. The theoretical grids assume that redox conditions in the gas equilibration zone are controlled by (a) the GT (FeO–FeO1.5) hydrothermal buffer (Giggenbach, 1987) and (b) the DP buffer (D'Amore and Panichi, 1980).

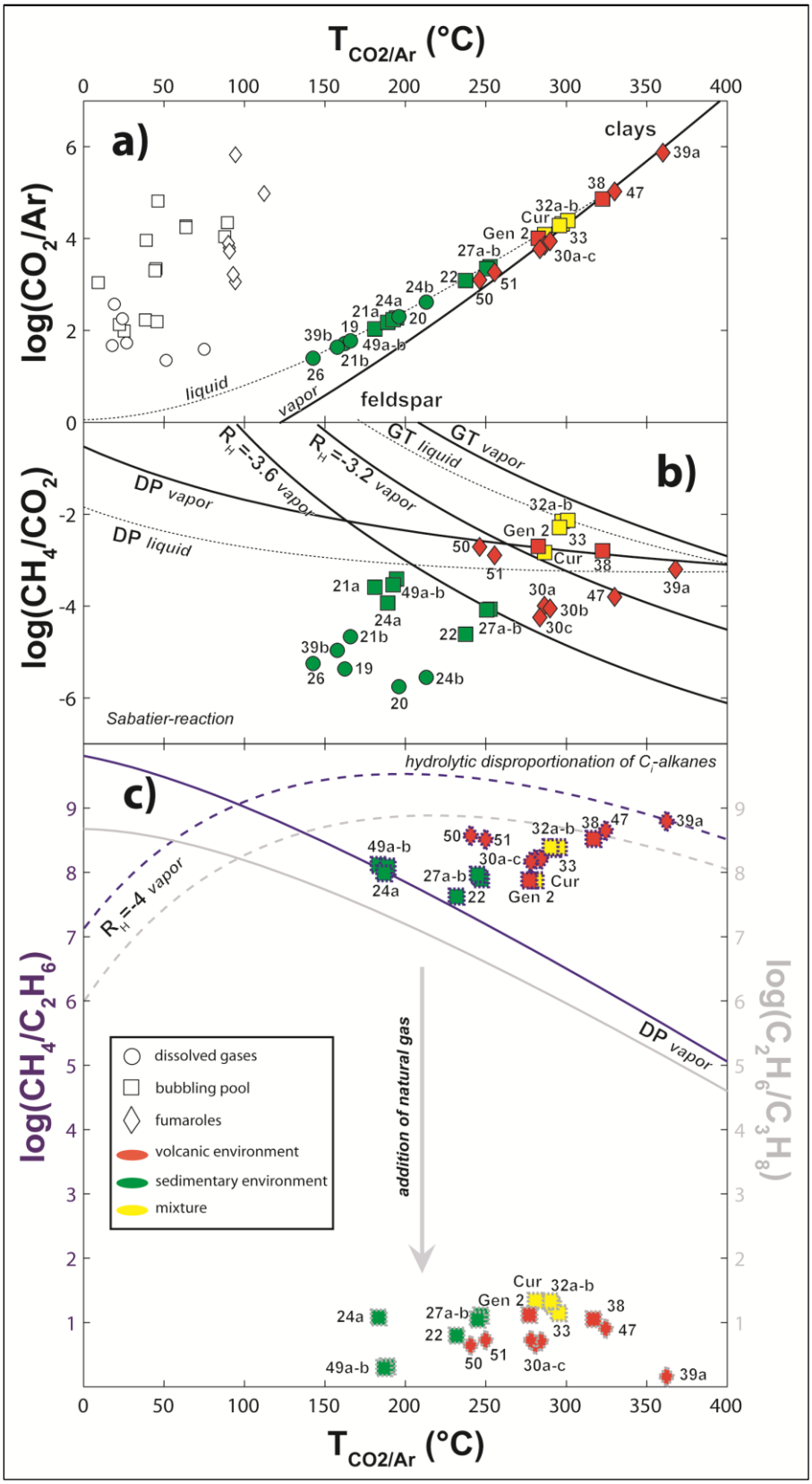

Figure VI-11: (a) Log (CO_2/Ar) of sampled gases versus sampling temperature (empty symbols) and CO_2/Ar equilibrium temperature (colored symbols). (b) Log (CH_4/CO_2) of sampled gases versus CO_2/Ar equilibrium temperature. (c) Log (CH_4/C_2H_6) values (purple outline symbols) and log(C_2H_6/C_3H_8) values (grey outline symbols) of sampled gases versus CO_2/Ar equilibrium temperature. See text for explanation of theoretical curves and equilibrium temperature calculations.

Since sampled waters from the EPC seem to attain equilibrium with Al-silicates, clay minerals and Ca- and Mg-carbonates at deep (Figure VI-9a), chemical equilibria involving CO_2 can be investigated considering the CO_2/Ar geothermometer proposed by *Giggenbach (1991),* which assumes that CO_2 partial pressures of samples are controlled by the interaction between primary silicates (feldspars), secondary clays and calcite, whereas Ar is considered to have a meteoric origin. Figure VI-11a shows the theoretical curves obtained with the CO_2/Ar geothermometer for liquid and gas phases (*Chiodini et al. 2001*), as well as the log values of concentration ratios in sampled gases versus the sampling temperatures (hollow points) and inferred geothermometric temperatures (colour points). The latter temperatures were calculated considering the water phase(s) (i.e liquid, vapor or liquid+vapor) that gas samples are in equilibrium according to Figure VI-10b. Except for the fumaroles, temperatures calculated by the CO_2/Ar geothermometer for bubblig pools and strip samples are as much as ~150°C hotter than those estimated in Figure VI-10b (between 130° and 170°C), probably relflecting the deep conditions of the hydrothermal systems as CO_2/Ar ratio has a slower kinetics upon cooling compared to those of H_2/H_2O and Ar^*/H_2O ratios (*Giggenbach 1991*). This seems to be supported by the fact that there is a good agreement between the estimated CO_2/Ar temperatures of bubbling pools 32a-b, 33 and 38, and those of the fumaroles close to the aforementioned bubbling pools (samples 30a-c and 47; Figure VI-2b).

Like the CO_2/Ar gas couple, the redox- and temperature-dependent CO_2/CH_4 ratio is known for its slow kinetic (e.g. *Giggenbach 1991; Chiodini and Marini 1998*). Therefore, if CO_2 and CH_4 gases are assumed to be equilibrated according to the Sabatier reaction ($CO_2 + 4H_2 \leftrightarrow CH_4 + 2H_2O$), it is possible to investigate the deep redox conditions of the hydrothermal systems by comparing the temperatures fixed by the CO_2-Ar system (Figure VI-11a) and the CO_2/CH_4 ratios of each sample (Figure VI-11b). Gas discharges from the volcanic environment seem to be controlled by the Sabbatier reaction at significantly more oxidizing conditions (R_H down to -3.6) than that of the *Giggenbach (1988)* hydrothermal buffer equilibrated in the vapor phase (GT vapor; Figure VI-11b). Such equilibrium conditions confirm the presence of active magmatic bodies supplying hot, oxidizing fluids to the overlying magmatic-driven hydrothermal systems (Section 5.2). Gas discharges from the sedimentary environment, on the other hand, plot at spurious oxidizing conditions in Figure VI-11b (R_H>3.6) indicating that CH_4 and CO_2 in gases from the sedimentary environment are not in equilibrium under the Sabatier reaction. *Fiebig et al. (2009)* proposed that at low oxygen fugacity, hight CO_2 fugacity and temperatures <250°C, methane might attain

abiogenic equilibrium with ethane and propane, and such equilibrium condition can be computed by considering the hydrolytic hydrocarbon disproportionation reaction:

$$C_nH_{2n+2} + 2H_2O = C_{n-1}H_{2n} + CO_2 + 3H_2 \quad \text{(VI.14)}$$

with

$$\log(C_{n-1}H_{2n}/C_n\,H_{2n+2}) = \log(K_T) - 3R_H - \log(f_{H2O}) - \log(f_{CO2}) \quad \text{(VI.15)}$$

, where K_T is the equilibrium constant of the hydrolytic hydrocarbon disproportionation given by *Taran and Giggenbach (2003)*, R_H is the expression of redox potential, and f_{H2O} and f_{CO2} are the fugacities of water and CO_2, respectively. Figure VI-11c shows a plot of $\log(C_1/C_2)$ and $\log(C_2/C_3)$ values vs. the temperature derived from the CO_2/Ar geothermometer. Equilibrium curves for $\log(C_1/C_2)$ and $\log(C_2/C_3)$ where computed considering that f_{H2O} and f_{CO2} are controlled by coexisting of steam and water, and the equilibrium with primary silicates (feldspars) and secondary clays, respectively (*Giggenbach 1980*). Gas discharges from the sedimentary environment seem to attain equilibrium in the methane/ethane systems at redox conditions given by the DP buffer, which is consistent with the previous findings; however measured $\log(C_2/C_3)$ values are significantly lower with respect to the amounts expected under full equilibrium conditions (Figure VI-11c). A similar pattern is displayed by the gas discharges from the volcanic environment (Figure VI-11c), although such samples attain equilibrium in the methane/ethane systems at considerably more oxidizing redox conditions (R_H values up to 4). The most plausible explanation for the observed pattern consists of assuming entrainment of very minor proportions (~0.00001%) of a natural gas component, which are usually enriched in ethane and propane with respect to methane (e.g. *Giggenbach 1997b; Fiebig et al. 2009*). Such addition would decrease C_2H_6/C_3H_8 ratio in 7 folds without changing the $\log(C_1/C_2)$ values significantly (e.g. *Giggenbach 1997b; Fiebig et al. 2009*). Given the organic–rich nature of the sedimentary basement at the EPC, the presence of natural gas at depth is a feasible possibility (Section VI-2).

VI.5.4 Regional distribution of fluid physical and chemical characteristics

The liquid geothermometer data in Figures VI-9a, b and c show that the equilibrium temperature of thermal springs in Central Chile increase east- and southwards, particularly south of the Maipo orocline, reaching maximum temperatures up to 160, 200 and 280°C in the WPC, CPC and EPC, respectively. This observation

correlates with a similar increase in (i) the average outlet temperatures of the surface manifestations, and (ii) the average crustal heat flow (Figure VI-2b). Moreover, north of Maipo orocline, fumarolic discharges at the EPC are restricted to the Tupungatito volcano, whereas to the south, fumarolic fields are spatially associated with both volcanoes and fault systems (Figure VI-2b). The latter indicates that develop of high-temperature (T>200°C) hydrothermal systems, commonly associated with fumarolic discharges (*Hochstein and Browne 2000*), is facilitated along the EPC, south of the Maipo orocline.

In Figure VI-12a log(pCO_2) values and $^3He/^4He$ ratios (R_m/R_a) of hydrothermal features are contoured and plotted along with the location of active volcanic centers. The data show an increase in pCO_2 values and He ratios that is well-correlated with an eastwards increase in the fluids outlet and subsurface temperatures. This trend is closely related to the location of both the preset-day volcanic chain and the carbonate-rich sedimentary sequences, and in consequence, seems to be the result of the contribution of mass (CO_2 and ^3He) from these sources to the meteoric fluids. North of the Maipo orocline, the sedimentary fingerprint (~98%) dominates the chemical and isotopic composition of the hydrothermal discharges at the EPC, whereas to the south, the magmatic contribution reaches ~35% (Table VI-3). The latter suggests that magmatic intrusions associated to the Quaternary volcanoes acts as heat and mass sources of the hydrothermal systems located south of the Maipo orocline, whereas at north, heat seems to be transferred by conduction from the sedimentary rocks.

Despite of their location in the central part of the PC, the origin of the chloride-rich waters emerging in this area is also attributable to the interaction between the sedimentary rocks of the EPC and deep-circulating meteoric waters. Samples 16 and 17 would derive from a saline member whose Cl concentration (~17.000 mgL^{-1}) is similar to that of the Na-Cl waters located in the CPE at similar latitudes. Basically, these Na-Cl waters would be transported from the EPC through the west-vergence thrust faults that deform the CPC (*Farías et al. 2010; Giambiagi et al. 2014*). The latter is supported by the presence of mantle He in the dissolved gases of sample 17 (R/R_a~1.56; *Hilton et al. 1993*), which indicates that such saline Na-Cl waters interacted with a mantle source (i.e. intrusions associated to the Quaternary volcanoes) and then picked up ^4He from radioactive decay of uranium and thorium in the confining rocks during its transit towards the CPC. As aleady explained, the Ca-Cl component characterizing the hydrothermal waters from the CPC is likely a consequence of an albitization-chloritization process due to the interaction between these Na-Cl saline waters and the mafic volcanic sequences of this area. However, such reaction seems

to be favored near the Maipo orocline, where would occur at higher temperature (~200°C; Figure VI-9b) than north of the Maipo orocline (~140°C; Figure VI-9a and c). The sample 13, located in the WPC, would also derive from the same Na-Cl parental source feeding samples 16 and 17. The latter is consistent with the greater dilution (~94%) that such Na-Cl parental water would experience in its transit from the EPC towards the WPC (Figure VI-9b), compared to the dilution calculated for the sample 17 (~89%), which emerges closer from the EPC than sample 13 (at the CPC and WPC, respectively; Figure VI-2a).

Excluding sample 13, the pCO_2 values of the springs along the WPC decrease towards the south despite that crustal heat flow and fluid temperature increase (Figure VI-12a). Such spatial variation is closely associated to a change in the chemical character of the springs, as well as in the elevation of their recharge zones. The springs located between 32.5 and ~34°S have neutral pH, Ca-HCO_3 to Ca-SO_4 compositions and $\delta^{18}O$-δD values suggesting elevated recharge zones (Figure VI-3 and VI-5c). To the south (~36°S), natural springs have higher pH (up to 9.3) and Na/Ca ratios, and have $\delta^{18}O$-δD values indicating that their recharge zones are at altitudes similar to that of the discharge ones (Figure VI-5c). These chemical and isotopic variations seem to be related to a change in the hydrothermal flow regime at the WPC from one dominated by topographically-driven meteoric water north of the Maipo orocline, to one dominated by buoyancy-driven convection of meteoric water along the San Ramon-Pocuro fault zone, to the south. The latter would favors a long-lasting water-rock interaction process of thermal waters within the Pocuro-San Ramón fault zone, south of Maipo orocline, explaining the higher discharge temperatures of springs to the south, as well as their mature chemical character with respect to the spring waters located north of the Maipo orocline.

VI.5.5 A model of fluid flow in the Andes of Central Chile

Chemical and isotopic compositions of the hydrothermal fluids of Central Chile indicates that the Maipo orocline represents a major along-strike change in the chemical and physical conditions of the natural discharges along the three domains (WPC, CPC and EPC). Nonetheless, an understanding of how and why such changes occur requires a comprehension of the different regional-scale fluid regimes that take place in active orogens (e.g. *Craw et al. 2002*).

The fluid flow models developed for the Southern Alps of New Zealand by *Koons and Craw (1991*) suggest that vigorous hydrothermal systems in active orogens can

develop as a result of their rapid uplift and denudation. Their numerical models show that both processes create a dual-flow system that consists of a flow regime at shallow levels driven by topography and a flow regime at deeper levels driven by buoyancy forces set up in response to lateral thermal gradients. Consequently, there are three principal fluids passing through active collisional mountain belts: (i) meteoric water from rain and snow on the mountains, (ii) basinal fluids from sedimentary sequences caught up in the active deformation zone, and (iii) magmatic and metamorphic fluids which rise from below (*Craw et al. 2002*). Assuming the model above, the geochemical characteristics of thermal fluids and the heat flow patterns suggest that shallow meteoric vs.deep-source fluid ratios decreases south of the Maipo orocline (Figure VI-2a-b and VI-12a). Because precipitation rates along the study area are similar (Hoke et al. 2013), the geochemical differences observed north and south of Maipo orocline should be a consequence of variation in driving forces that facilitate or inhibit the existence of topography- or buoyancy-driven hydrothermal systems, such as the permeability structure of fault systems and topography (e.g. *Koons and Craw 1991*; *López and Smith 1995, 1996; Craw et al. 2002*).

The Principal Cordillera of Central Chile is characterized by a continuous decrease in the elevation from north to south and east to west (Section VI.2.1). As a consequence of this regional topography gradient, the major W-E regional hydraulic head created north of the Maipo Orocline results in a higher regional westward groundwater flow. Additionally, both fault strike and the long-term crustal stress change abruptly at the Maipo Orocline (Figure VI-2a-b; *Farías 2007*). Between 33 and 34°S, the interplay between N-S high angle thrust faults and pure compressive stress conditions (vertical σ_3) would favors the horizontal permeability of fault systems, whereas south of 34°S, favorably-oriented NNE-SSW high angle thrust faults with respect to the dextral strike-slip stress (horizontal σ_3) would favors vertical permeability of fault systems along NNE-SSW transtensional domains (Figure VI-12b and c) [e.g. *Cembrano and Lara 2009; Cox 2010; Sánchez et al. 2013*]. Therefore, north of Maipo Orocline, both the major regional hydraulic head created by the higher differences on topography and the lower vertical permeability of the fault zones suppress advection of deep fluids and convection of groundwater within fault systems. This would explain the low discharge temperatures and the strong meteoric signature of thermal fluids (e.g. $R_m/R_a<1.81$, $N_2/Ar<84$). South of the Maipo Orocline, on the contrary, vertical transport of deep fluids would be favored, explaining the higher temperatures of the fluid discharges, the higher temperatures that fluids attain at depth, and the high R_m/R_a values (up to 6.2) and the N_2-excess measured in the gas discharges.

The fumarolic discharges of Tupungatito volcano, located north of the Maipo Orocline (Figure VI-12a), have characteristics reflecting a clear deep-magmatic source (R_m/R_a and Tup to 5.8 and 220°C, respectively; *Benavente et al. 2013*) like some fluid discharges located south of the Maipo Orocline do. In compressive margins, ascension of deep-sourced fluids through high-angle faults (e.g. north of the Maipo Orocline) require variable fluid-overpressuring (i.e. fluid pressure P_f higher than lithostatic pressure P_l when $\sigma_3 = \sigma_{vertical} = \rho gh = P_l$) capable of reactivate unfavorably oriented thrust faults (e.g. *Sibson 1996; Sibson 2007*). Such fluid-overpressuring condition likely occurs within the hydrothermal-magmatic system associated to the Tupungatito volcano, but not in the hydrothermal system surrounding the volcanic systems, north of Maipo orocline (Figure VI-12a).

VI.6 CONCLUSIONS

Hydrothermal fluids have been sampled at three main zones along the PC of Central Chile (WPC, CPC and EPC) to investigate the source(s) region feeding the hydrothermal fluid discharges and constrain the physico-chemical conditions of the hydrothermal reservoirs feeding these discharges. Overall, the origin of the hydrothermal systems in the study area is related to the subduction of the Nazca plate beneath the South American continent, which is responsible for both: (i) the active orogenesis of the area and, therefore, the coexistence of a dual-flow hydrothermal system that consists of a meteoric flow regime at shallow levels driven by topography and a flow regime at deeper levels driven by buoyancy forces set up in response to the up-lifted thermal gradients; and (ii) the arc magmatism, whose direct consequence is the hydrothermal activity dominated by the transfer of heat and mass from magma intrusions to the deep circulating meteoric water. Regardless the hydrothermal regimen dominating in a particular area of the PC, the hydrothermal systems of Central Chile are mainly recharged by local meteoric water originated from snow melting followed by its infiltration at approximately 2000–2600 m a.s.l. Given the hydrostatic load created by the high topographic differences between the infiltration and discharging altitudes (up to 1000 m), groundwater migrates downward and returns to the surface along the valleys of the PC, often close to thrust-fault systems which are subparallel to these valleys.

Under such context, differences in the chemical and isotopic signatures of the fluid discharges from the WPC, CPC and EPC are mainly related to both the nature of the

rocks that constitute the basement in each zone and the location of the present-day volcanic chain (EPC).

- The WPC hosts diluted waters (<800 mgL^{-1}) having a Ca-HCO_3-SO_4 to Na-HCO_3-SO_4 composition and a neutral to alkaline pH, which results from the interaction between topographically-driven groundwater and the basaltic-andesitic volcanic rocks. Such interaction seems to be favored south of the Maipo orocline, where these waters achieve full chemical equilibrium at depth in the range of 150-160°C. The latter is consistent with the fact that Ca-HCO_3-SO_4 waters have f_{CO2} values associated to open system exchanges with CO_2-rich reservoirs, most likely represented by soils. "Mature" Na-HCO_3-SO_4 waters have instead much lower f_{CO2} values associated to both consumption of CO_2 through continuous rock titration and disconnection with CO_2-rich reservoirs such the carbonate sedimentary sequences and the magmatic system.

- The hydrothermal activity along the EPC, on the contrary, seems to be closely associated to the transfer of heat and mass from both the carbonate-rich sedimentary sequences and the magma intrusions associated to the present-day volcanic arc. North of the Maipo orocline, the sedimentary fingerprint (~98%) dominates the chemical and isotopic composition of the hydrothermal discharges at the EPC as evidenced by the relatively low R/R_a ratios (down to 0.42) and high CO_2/He^3 ratios (up to $2.2x10^{11}$) of the gas discharges, as well as the relatively high TDS values of the Na-Cl brines discharging at surface (up to 35,000 mgL^{-1}). To the south, the magmatic contribution in the hydrothermal systems reaches ~35%, resulting in fluid discharges with higher outlet temperatures (up to 102.5°C), lower CO_2/He^3 ratios ($0.2x10^{11}$) and higher R/R_a and N_2/Ar ratios (up to 6.2 and 540, respectively). Chemical equilibria in the H_2O–CO_2–CH_4–H_2–Ar–C_2H_6–C_3H_8 system indicates that gases north of Maipo orocline tend to equilibrate in a liquid-phase at temperatures <250 °C and redox conditions controlled by the redox buffer proposed by *D'Amore and Panichi (1980)*, whereas to the south, gases equilibrates with both liquid+vapor and vapor at temperatures up to 350°C and redox conditions significantly more oxidizing than that of the *D'Amore and Panichi (1980)* hydrothermal buffer (R_H down to -4), which is consistent with their magmatic-related origin.

- Finally, the origin of the chloride-rich waters emerging in the CPC and WPC are also related to the interaction between the sedimentary rocks of the EPC and

deep-circulating meteoric waters. Na-Cl brines, with a Cl content of ~17,000 mgL^{-1}, would be transported from the EPC through the west-vergence thrust faults that deform the CPC and WPC. Such saline Na-Cl waters interact with the basaltic-andesitic volcanic sequences that constitute the basement of the WPC and CPC, resulting in Ca-Cl waters depleted in Mg and SiO_2 with respect to their parental Na-Cl water as a consequence of an albitization-chloritization hydrothermal process. Such process seems to be favored near the Maipo orocline, where would occurs at higher temperature (~200°C) than north of the Maipo orocline (~140°C).

Along the WPC, CPC and EPC, the geochemical characteristics of thermal fluids and the heat flow patterns suggest that shallow meteoric vs.deep-source fluid ratios decreases south of the Maipo orocline. The continuous decrease in the mountain elevation, as well as the change of both thrust fault systems orientation and long-term crustal stress at the Maipo Orocline favor the ascension of deep-sourced fluids through high-angle faults south of Maipo orocline.

These results provide new insights for the prospection of geothermal resources along Central Chile, indicating that south of the Maipo Orocline the interplay of volcanism and active tectonic favor the existence of magmatic-driven hydrothermal systems (T ranging between 200 to 280°C) in the EPC (Calerías, Tinguiririca, Calabozos and Mariposa geothermal projects) and tectonic-driven hydrothermal system in the CPC (Termas Cauquenes; T~200°C) and WPC (Termas Panimávida and Quinamávida; T~160°C). Given the increasing oil price and the need to reduce the greenhouse gas emissions, the hydrothermal reservoirs of Central Chile are still inexplicably unexploited.

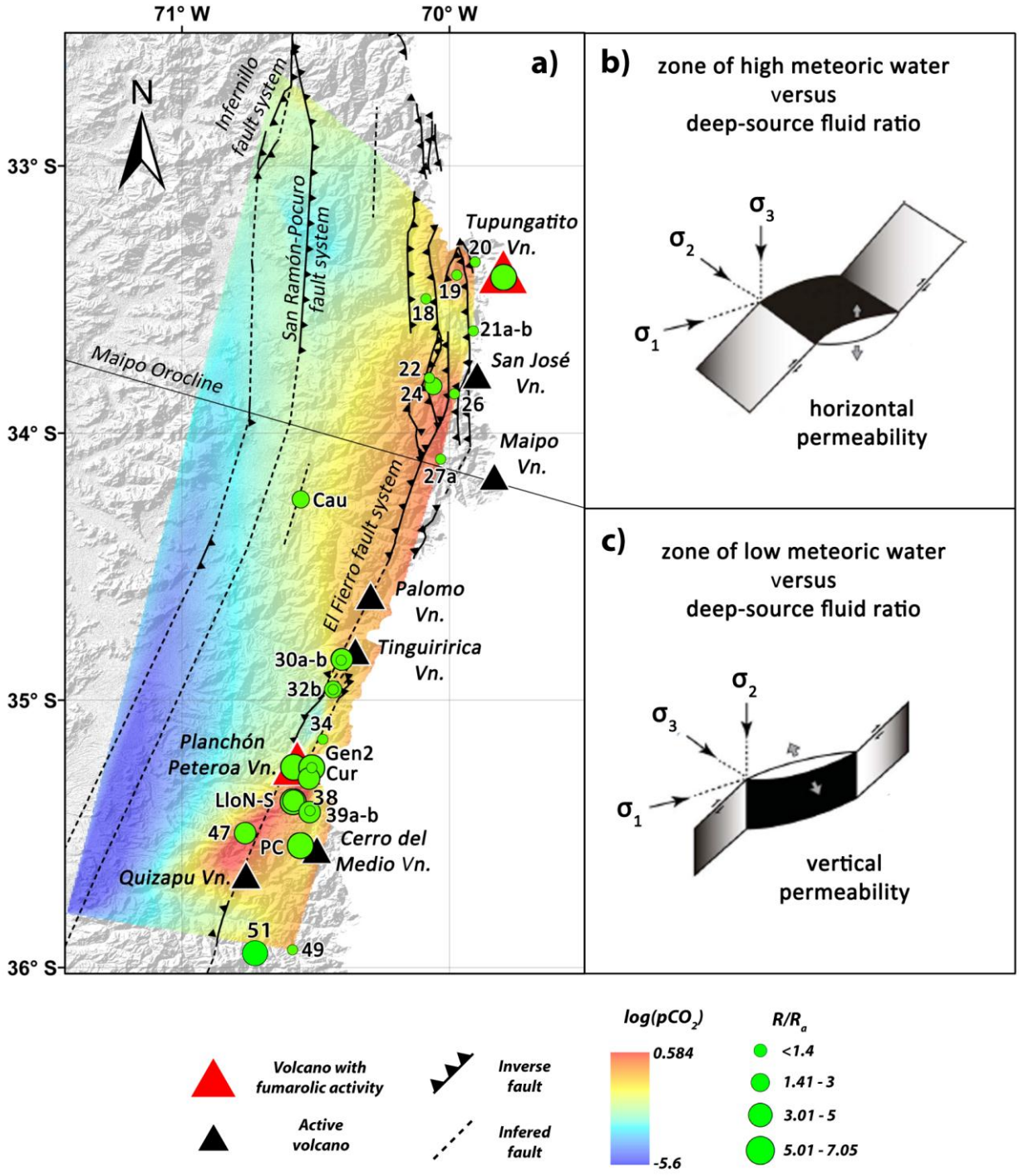

Figure VI-12: Illustration summarizing the physical and chemical processes governing the three hydrothermal domains along the Principal Cordillera of Central Chile, and its differences north and south of the Maipo Orocline. a) Isodistribution map of log(fCO_2) in spring samples, the helium isotopic composition (as R_m/R_a; green circles), volcanoes and the faults systems are also reported. b) North of the Maipo orocline, hydrothermal activity is coeval with current east–west compression which favors the horizontal permeability of fault systems, and therefore inhibiting transfer of fluids from deep sources. c) South of the Maipo orocline, on the contrary, the favorably-oriented NNE-SSW high angle thrust faults with respect to the dextral strike-slip stress would favors vertical permeability of fault systems along NNE-SSW transtensional domains, which in turns enchance vertical transport of deep fluids.

REFERENCES

Aguilera F, Tassi F, Darrah T, Moune S, Vaselli O (2012). Geochemical model of a magmatic hydrothermal system at the Lastarria volcano, northern Chile. Bull Volcanology. Bull. Volcanol 74:119–134.

Agusto M, Tassi F, Caselli A T, Vaselli O, Rouwet D, Capaccioni B, Caliro S, Chiodini G, Darrah T (2013) Gas geochemistry of the magmatic-hydrothermal fluid reservoir in the Copahue-Caviahue Volcanic Complex (Argentina). Journal of Volcanology and Geothermal Research 257(0): 44-56.

Arriagada C., Ferrando R., Cordova L., Morata D., Roperch P. (2013) The Maipo Orocline: A first scale structural feature in the Miocene to Recent geodynamic evolution in the central Chilean Andes. Andean Geology 40(3): 419-437

Barazangi, M. and B. L. Isacks (1976). Spatial distribution of earthquakes and subduction of the Nazca plate beneath South America. Geology 4(11): 686-692.

Barnett P. (2012). Geothermal Projects in South America of Hot Rock Limited. Chilean International Renewable Energy Congress, Santiago, Chile.

Benavente, O., F. Tassi, F. Gutiérrez, O. Vaselli, F. Aguilera and M. Reich (2013). "Origin of fumarolic fluids from Tupungatito Volcano (Central Chile): interplay between magmatic, hydrothermal, and shallow meteoric sources." Bulletin of Volcanology C7 - 746 75(8): 1-15.

Bethke, C. (2007). Geochemical and Biogeochemical Reaction Modeling. New York.

Capaccioni B, Aguilera F, Tassi F, Darrah T, Poreda RJ, Vaselli O (2011) Geochemical and isotopic evidences of magmatic inputs in the hydrothermal reservoir feeding the fumarolic discharges of Tacora volcano (northern Chile). J Volcanol Geotherm Res 208:77–85.

Capaccioni, B., Menichetti, M., Renzulli, A., Tassone, A. (2013). Thermal waters of 'tectonic origin': the alkaline, Na-HCO3 waters of the Rio Valdez geothermal area (Isla Grande de Tierra del Fuego, Argentina). Geofluids (2013) 13, 21–31, doi: 10.1111/gfl.12005

Capasso, G. and Inguaggiato, S. (1998). A simple method for the determination of dissolved gases in natural waters. An application to thermal waters from Vulcano Island. Appl. Geochem. 13, 631–642.

Cembrano, J. and L. Lara (2009). "The link between volcanism and tectonics in the southern volcanic zone of the Chilean Andes: A review." Tectonophysics 471(1-2): 96-113.

Chiodini G, Marini L (1998) Hydrothermal gas equilibria: The H2O-H2-CO2-CO-CH4 system. Geochim Cosmochim Acta 62:2673–2687.

Chiodini G., Marini L., Russo M. (2001). Geochemical evidence for the existence of high-temperature brines at Vesuvio volcano, Italy. Geochim. Cosmochim. Acta 65, 2129-2147.

Charrier, R., O. Baeza, S. Elgueta, J. J. Flynn, P. Gans, S. M. Kay, N. Muñoz, A. R. Wyss, and E. Zurita (2002), Evidence for Cenozoic extensional basin development and tectonic inversion south of the flat-slab segment, southern Central Andes, Chile (33°-36°S.L.), J S Am Earth Sci, 15(1), 117-139.

Clavero, J., C. Pineda, C. Mayorga, A. Giavelli, I. Aguirre, S. Simmons, S. Martini, J. Soffia, R. Arriaza, E. Polando and L. Achurra (2011). Geological, Geochemical, Geophysical and First Drilling Data from Tinguiririca Geothermal Area, Central Chile. Geothermal Resources Council Transactions (GRC). San Diego, California, Geothermal Resources Council. 35: 731-734.

CNE (Chilean Commission of Energy), 2010. Identification of difficulties in the processing of permits for electricity sector projects (In Spanish)

Coleman, M. L., T. J. Shepherd, J. J. Durham, J. E. Rouse and G. R. Moore (1982). Reduction of water with zinc for hydrogen isotope analysis. Analytical Chemistry 54(6): 993-995.

Cox, S. F. (2010). The application of failure mode diagrams for exploring the roles of fluid pressure and stress states in controlling styles of fracture-controlled permeability enhancement in faults and shear zones. Geofluids 10(1-2): 217-233.

Craw, D., Koons, P. O., Horton, T. & Chamberlain, C. P. (2002). Tectonically driven fluid flow and gold mineralisation in active collisional orogenic belts: comparison between New Zealand and western Himalaya. Tectonophysics, 348, 135–153.

D'Amore F. and Panichi C. (1980). Evaluation of deep temperatures of hydrothermal systems by a new gas geothermometer. Geochim. Cosmochim. Acta 44, 549–556.

Delany J. M. and S. R. Lundeen (1991). The LLNL thermochemical data base -- revised data and file format for the EQ3/6 package. Other Information: PBD: Jul 1991: Medium: P; Size: 59 p.

Dobson P., Kennedy M., Reich M., Sanchez P., Morata D. (2013). Effects of volcanism, crustal thickness, and large scale faulting on the He isotope signatures of geothermal systems in Chile. Thirty-Eighth Workshop on Geothermal Reservoir Engineering Stanford University, Stanford, California, February 11-13, SGP-TR-198

Droguett, B., D. Morata, J. Clavero, G. Pineda, S. Morales and F. Carrillo (2012). Mineralogía de alteración en el pozo Pte-1, campo geotermal Tinguiririca, Chile. XIII Congreso Geológico Chileno. E. Medina. Antofagasta, Chile, Universidad Católica del Norte. 13: 500-502. (In Spanish)

Dufey A. (2010) Opportunities and Domestic Barriers to Clean Energy Investment in Chile. IISD: Trade, Investment and Climate Change Series. Available in http://www.iisd.org/pdf/2010/bali_2_copenhagen_Chile_Jun2010.pdf

Epstein, S. and Mayeda, T.K.. (1953). Variation of the 18O/16O ratio in natural waters. Geochimica et Cosmochimica Acta 4, 213–224.

Evans, W. C., L. D. White and J. B. Rapp (1988). Geochemistry of some gases in hydrothermal fluids from the southern Juan de Fuca Ridge. Journal of Geophysical Research: Solid Earth 93(B12): 15305-15313.

Farías, M., R. Charrier, S. Carretier, J. Martinod, A. Fock, D. Campbell, J. Cáceres and D. Comte (2008). "Late Miocene high and rapid surface uplift and its erosional response in the Andes of Central Chile (33º-35ºS)." Tectonics.

Farías, M., D. Comte, R. Charrier, J. Martinod, C. David, A. Tassara, F. Tapia and A. Fock (2010). "Crustal-scale structural architecture in central Chile based on seismicity and surface geology: Implications for Andean mountain building." Tectonics 29: 22.

Fiebig J., Woodland A., D'Alessandro W., Püttmann W. (2009). Excess methane in continental hydrothermal emissions is abiogenic. Geology, v. 37, p. 495-498, doi:10.1130/G25598A.1

Giambiagi, L. B., V. A. Ramos, E. Godoy, P. P. Alvarez and S. Orts (2003). "Cenozoic deformation and tectonic style of the Andes, between 33 degrees and 34 degrees south latitude." Tectonics 22(4): 1041.

Giambiagi L., Tassara A. et al. (2014). Evolution of shallow and deep structures along the Maipo–Tunuyan transect (33°40′S): from the Pacific coast to the Andean foreland. In: Sepúlveda S. A., Giambiagi L. B., Moreiras S. M., Pinto L., Tunik M., Hoke G. D. y Farías, M. (eds) Geodynamic Processes in the Andes of Central Chile and Argentina. Geological Society, London, Special Publications, 399. http://dx.doi.org/10.1144/SP399.14

Giggenbach, W. F. (1975). A simple method for the collection and analysis of volcanic gas samples. Bulletin Volcanologique 39(1): 132-145.

Giggenbach, W. F. (1984). Mass transfer in hydrothermal alteration systems: A conceptual approach. Geochimica et Cosmochimica Acta 48(12): 2693-2711.

Giggenbach, W.F. (1987). Redox processes governing the chemistry of fumarolic gas discharges from White Island, New Zealand. Appl. Geochem. 2, 143–161.

Giggenbach, W. F. (1988). "Geothermal solute equilibria. Derivation of Na-K-Mg-Ca geoindicators." Geochimica et Cosmochimica Acta 52(12): 2749-2765.

Giggenbach W. F. (1992). The composition of gases in geothermal and volcanic systems as a function of tectonic setting. Proc Int Symp Water-Rock Interaction. 8: 873-878.

Giggenbach W.F. (1997a). The Origin and Evolution of Fluids in Magmatic-Hydrothermal Systems, In: Barnes, H.L. (Ed.), Geochemistry of Hydrothermal Ore Deposits, 3rd edition. Wiley, pp. 737–796.

Giggenbach W.F. (1997b). Relative importance of thermodynamic and kinetic processes in governing the chemical and isotopic composition of carbon gases in high-heat flow sedimentary basins: Geochimica et Cosmochimica Acta, v. 61, p. 3763–3785.

Giggenbach W.F. and Stewart, M.K. (1982). Processes controlling the isotopic composition of steam and water discharges from steam vents and steam heated pools in geothermal areas. Geothermics 11, 71–80.

Giggenbach W.F. and Matsuo S. (1991). Evaluation of results from second and third IAVCEI field workshop on volcanic gases, Mt. Usu, Japan and White Island, New Zealand. Appl. Geochem. 6, 125–141.

Giggenbach, W. F. and R. B. Glover (1992). Tectonic regime and major processes governing the chemistry of water and gas discharges from the rotorua geothermal field, New Zealand. Geothermics 21(1-2): 121-140.

Goff, F. and C. J. Janik (2000). Geothermal Systems. Encyclopedia of Volcanoes. H. Sigurdsson, Houghton, B., McNutt, S., Rymer, H., and Stix, J. San Diego, CA, Academic Press: 817-834.

Gupta, H. and S. Roy (2007). Chapter 4 - Geothermal systems and resources. Geothermal Energy. Amsterdam, Elsevier: 49-59.

Hamza, V. M. and M. Muñoz (1996). "Heat flow map of South America." Geothermics 25(6): 599-621.

Hardie, L.A., (1983). Origin of $CaCl_2$ brines by basalt-seawater interaction: Insights provided by some simple mass balance calculations. Contrib. Mineral. Petrol. 82, 205^213.

Hauser, A. (1997). Catastro y caracterización de las fuentes de aguas minerales y termales de Chile Santiago, Chile, Servicio Nacional de Geología y Minería (SERNAGEOMIN). Boletín 50: 70 p. (In Spanish)

Hickson, C. J., F. Ferraris, C. Rodriquez, G. Sielfeld, R. Henriquez, T. Gislason, J. Selters, D. Benoit, P. White, J. Southon, G. Ussher, C. J., A. Smith, B. Lovelock, J. Lawless, P. Quinliven, L. Smith and R. Yehia (2011). The Mariposa Geothermal System, Chile Geothermal Resources Council Transactions (GRC). San Diego, California, Geothermal Resources Council. 35: 817-825.

Hildreth, W. and S. Moorbath (1988). Crustal contributions to arc magmatism in the Andes of Central Chile. Contributions to Mineralogy and Petrology 98(4): 455-489.

Hilton, D. R., K. Hammerschmidt, S. Teufel and H. Friedrichsen (1993). "Helium isotope characteristics of Andean geothermal fluids and lavas." Earth and Planetary Science Letters 120(3-4): 265-282.

Hochstein M., Browne P. (2000). Surface Manifestations of Geothermal Systems with Volcanic Heat Sources. Encyclopedia of Volcanoes. H. Sigurdsson, Houghton, B., McNutt, S., Rymer, H., and Stix, J. San Diego, CA, Academic Press: 835-855.

Hodgson S (2013). Focus on Chile I-II-III. Geothermal Resources Council Bulletin (GRC) 47(1).

Hoke, G. D., J. N. Aranibar, M. Viale, D. C. Araneo and C. Llano (2013). "Seasonal moisture sources and the isotopic composition of precipitation, rivers, and carbonates across the Andes at 32.5–35.5°S." Geochemistry, Geophysics, Geosystems 14(4): 962-978.

Inguaggiato, S. and A. Rizzo (2004). Dissolved helium isotope ratios in ground-waters: a new technique based on gas-water re-equilibration and its application to Stromboli volcanic system. Applied Geochemistry 19(5): 665-673.

Koons P.O., Craw D. (1991). Evolution of fluid driving forces and composition within collisional orogens. Geophys. Res. Lett. 18, 935– 938.

López, D. L. and L. Smith (1995). Fluid Flow in Fault Zones: Analysis of the Interplay of Convective Circulation and Topographically Driven Groundwater Flow. Water Resources Research 31(6): 1489-1503.

López, D. L. and L. Smith (1996). Fluid flow in fault zones: Influence of hydraulic anisotropy and heterogeneity on the fluid flow and heat transfer regime. Water Resources Research 32(10): 3227-3235.

Maksaev V., Townley B., Palacios C., and Camus F. (2007) Metallic ore deposits. In: Moreno, T., and Gibbons, W. (editors): The Geology of Chile. The Geological Society (London), pp. 414.

Mamyrin, B. and I. Tolstikhin (1984). Helium isotopes in nature. Developments in Geochemistry. E. S. Ltd. Amsterdam, Elsevier: 288.

Marini, L., G. Ottonello, M. Canepa and F. Cipolli (2000). "Water-rock interaction in the Bisagno valley (Genoa, Italy): application of an inverse approach to model spring water chemistry." Geochimica et Cosmochimica Acta 64(15): 2617-2635.

Marini, L. (2006). Chapter 5: The product solid phases. Geological sequestration of carbon dioxide: thermodynamics, kinetics, and reaction path modeling. D. i. Geochemistry, Elsevier. Volume 11: 79-167.

Mariner R.H., Presser T.S., Evans W.C. (1993). Geothermometry and water-rock interaction in selected thermal systems in the Cascade Range and Modoc Plateau, western United States. Geothermics 22, 1-15.

Mariner, R.H., Evans, W.C., Presser, T.S. and White L.D. (2003) Excess nitrogen in selected thermal and mineral springs of the Cascade Range in northern California, Oregon and Washington: sedimentary or volcanic in origin? J. Volcanol. Geotherm. Res. 121, 99 - 114.

Minissale, A. (2004). Origin, transport and discharge of CO2 in central Italy. Earth-Science Reviews 66(1-2): 89-141.

Montegrossi, G., F. Tassi, O. Vaselli, A. Buccianti and K. Garofalo (2001). "Sulfur Species in Volcanic Gases." Analytical Chemistry 73(15): 3709-3715.

Muñoz M., Aguirre L., Vergara M., Demant A., Fuentes F., Fock A. (2010). Prehnite-pumpellyite facies metamorphism in the Cenozoic Abanico Formation, Andes of central Chile (33 degrees 50 ‘ S): chemical and scale controls on mineral assemblages, reaction progress and the equilibrium state: Andean Geology, v. 37, no. 1, p. 54-77.

Nisi, B., Vaselli, O., Tassi, F., Elío, J., Delgado, A., Mazadiego, L.F., Ortega, M.F., (2013). Hydrogeochemistry of running and spring waters in the Hontomín-Huermeces area (Burgos Spain). International Journal of Greenhouse Gas Control 14, 151–168.

Ohlanders N, Rodriguez M, McPhee J. (2013). Stable water isotope variation in a Central Andean watershed dominated by glacier and snowmelt. Hydrology and Earth System Sciences 17(3): 1035–1050. doi:10.5194/hess-17-1035-2013

Pauwels, H., Fouillac, C., Goff, F., Vuataz, F.D. (1997). The isotopic and chemical composition of CO_2-rich thermal waters in the Mont-Dore region (Massif-Central, France). Appl. Geochem. 12 (4), 411–427.

Peiffer, L., Bernard-Romero, R., Mazot, A., Taran, Y.A., Guevara, M., Santoyo E. (2014). Fluid geochemistry and soil gas fluxes (CO_2–CH_4–H_2S) at a promissory Hot Dry Rock Geothermal System: The Acoculco caldera, Mexico. Journal of Volcanology and Geothermal Research, 284, 122-137, 2014

Polyak, B. G. and I. N. Tolstikhin (1985). Isotopic composition of the earth's helium and the problem of the motive forces of tectogenesis. Chemical Geology: Isotope Geoscience section 52(1): 9-33.

Reed M.H. (1997). Hydrothermal alteration and its relationship to ore fluid composition, in Barnes, H., ed., Geochemistry of hydrothermal ore deposits: New York, John Wiley and Sons Inc. Publication, p. 303–366.

Reyes, A.G., Christenson, B.W. and Faure, K. (2010). Sources of solutes and heat in low-enthalpy mineral waters and their relation to tectonic setting, New Zealand: Journal of Volcanology and Geothermal Research, v. 192, p. 117-141.

Saltori, O., F. Aguilera, M. Agusto, O. Benavente, F. Tassi, A. Caselli, F. Gutierrez and M. Pizarro (2012). Fluids Geochemistry from Planchón-Peteroa-Azufre volcanic Complex, Southern Volcanic Zone, Chile. XIII Congreso Geológico Chileno. E. Medina. Antofagasta, Chile, Universidad Católica del Norte. 13: 474-476.

Sánchez, P., P. Pérez-Flores, G. Arancibia, J. Cembrano and M. Reich (2013). Crustal deformation effects on the chemical evolution of geothermal systems: the intra-arc Liquiñe-Ofqui fault system, Southern Andes. International Geology Review 55(11): 1384-1400.

Sano, Y. and Marty, B. (1995). Origin of carbon in fumarolic gases from island arcs. Chemical Geoleology. 119, 265–274.

Shvartsev S. L. (2008). Geochemistry of fresh groundwater in the main landscape zones of the Earth. Geochemistry International 46(13): 1285-1398.

Sibson, R. H. (1996). "Structural permeability of fluid-driven fault-fracture meshes." Journal of Structural Geology 18(8): 1031-1042.

Sibson, R. H. (2007). "An episode of fault-valve behaviour during compressional inversion?: The 2004 MJ6.8 Mid-Niigata Prefecture, Japan, earthquake sequence." Earth and Planetary Science Letters 257(1-2): 188-199.

Shock, E.L., (1993) Hydrothermal dehydration of aqueous organic compounds. Geochim. Cosmochim. Acta 57, 3341–3349.

Stern, C. M., H, L. López-Escobar, J. Clavero, L. Lara, J. Naranjo, M. Parada and A. Skewes (2007). Chilean volcanoes. Geological Society Special Publication: The Andes of Chile. Londres: 147-178.

Symonds R.B., Gerlach T.M., Reed M.H. (2001). Magmatic gas scrubbing: implications for volcano monitoring. J. Volcanol. Geochim. Res. 108, 303–341.

Taran Y.A. (2005). A method for determination of the gas–water ratio in bubbling springs. Geophys. Res. Lett. 32, L23403. http://dx.doi.org/10.1029/2005GL024547.

Taran, Y.A., Pokrovsky, B.G., Esikov, A.D. (1989). Deuterium and oxygen-18 in fumarolic steam and amphiboles from some Kamchatka volcanoes: “andesitic waters”. Dokl Akad Nauk SSSR 304, 440–443.

Taran Y.A., Giggenbach W.F. (2003). Geochemistry of light hydrocarbons in subduction-related volcanic and hydrothermal fluids. Soc. Econom. Geol., spec. Public. 10 (Giggenbach Memorial Volume). 61–74.

Tassara, A., H. J. Gotze, S. Schmidt and R. Hackney (2006). Three-dimensional density model of the Nazca plate and the Andean continental margin." Journal of Geophysical Research-Solid Earth 111(B9)

Tassi F, Aguilera F, Vaselli O, Medina E, Tedesco D, Delgado Huertas A, Poreda R, Kojima S (2009) The magmatic- and hydrothermal-dominated fumarolic system at the Active Crater of Lascar volcano, northern Chile. Bull Volcanol 71:171–183.

Tassi, F., Aguilera, F., Darrah, T., Vaselli, O., Capaccioni, B., Poreda, R.J., Delgado, Huertas A. (2010). Fluid geochemistry of hydrothermal systems in the Arica-Parinacota, Tarapacá and Antofagasta regions (northern Chile). J. Volcanol. Geotherm. Res. 192, 1–15.

Tassi F, Aguilera F, Vaselli O, Darrah T, Medina E (2011) Gas discharges from four remote volcanoes (Putana, Olca, Irruputuncu and Alitar) in northern Chile: a geochemical and isotopic survey. Ann Geophys 54:121–136.

Truesdell AH and Hulston JR (1980) Isotopic evidence on environments of geothermal systems. In: Handbook of Environmental Isotope Geochemistry (eds Fritz P, Fontes JCh), vol 1, pp., 179–226. The Terrestrial Environment, A, Elsevier, Amsterdam, the Netherlands.

Vaselli, O., A. Minissale, F. Tassi, G. Magro, I. Seghedi, D. Ioane and A. Szakacs (2002). A geochemical traverse across the Eastern Carpathians (Romania): constraints on the origin and evolution of the mineral water and gas discharges. Chemical Geology 182(2-4): 637-654.

Vaselli, O., F. Tassi, G. Montegrossi, B. Capaccioni and L. Giannini (2006). Sampling and analysis of fumarolic gases. Acta Vulcanol. 18: 65-76.

Vergara M., Levi B., Villarroel R. (1993). Geothermal-type alteration in a burial metamorphosed volcanic pile, central Chile. Journal of Metamorphic Geology 11:449-454

Viale, M. and Nunez, M. N (2011). Climatology of Winter Orographic Precipitation over the Subtropical Central Andes and Associated Synoptic and Regional Characteristics, J. Hydrometeor., 12, 481–507, doi:10.1175/2010JHM1284.1, 2011

CAPÍTULO VII

POTENCIAL GEOTÉRMICO DE LOS SISTEMAS HIDROTERMALES DE CHILE CENTRAL

VII.1 LOS SISTEMAS GEOTERMALES DE CHILE CENTRAL

Al igual que en otros orógenos activos (ej. Alpes del Sur-Nueva Zelandia, Montañas de Taiwan, Montañas Rocosas-Canada, Montaña Costera-Canada, Alpes-Europa, Pirineos-Europa, Nanga Parbat-Himalaya; *Craw et al. 2002; Ehlers 2005*), la rápida exhumación (<2.5 km) que los Andes de Chile Central han experimentado en los últimos 10.5-4.6 Ma habría afectado de manera importante la estructura termal conductiva de la corteza, alzando las isotermas en el bloque colgante (correspondiente a la Cordillera Principal; CP) y deprimiendo éstas en el bloque yacente (Depresión Central; Figura VII-1) [*Farías et al. 2008*]. Lo anterior tiene importantes implicancias para la actividad hidrotermal en la CP (Figura VII-1), ya que el alzamiento generalizado del gradiente geotérmico permite la coexistencia tanto de un régimen hidrotermal somero−dominado por fluidos meteóricos impulsados por los gradientes topográficos que caracterizan los Andes de Chile Central− como de un régimen profundo asociado a la advección y/o convección de fluidos meteóricos, hidrotermales y/o magmáticos (ej. *Koons y Craw 1991; McCaig et al. 1995; Templeton et al. 1999; Craw et al. 2002*). Sin importar el régimen hidrotermal dominante (somero vs. profundo), tanto las manifestaciones termales activas (ej. manantiales fríos y calientes, y piscinas burbujeantes) como los depósitos hidrotermales asociados a manifestaciones termales inactivas se localizan, por lo general, a lo largo de las zonas de falla que cortan los valles de la CP. Esto último ocurre porque dichas zonas (i) tienen generalmente una mayor permeabilidad que la roca caja permitiendo el ascenso de fluidos termales a través de estas estructuras, pero también porque (ii) el nivel freático en los valles es cercano a la superficie, posibilitando hidráulicamente la presencia agua en superficie (*López y Smith 1995, 1996*; *Ehlers 2005*).

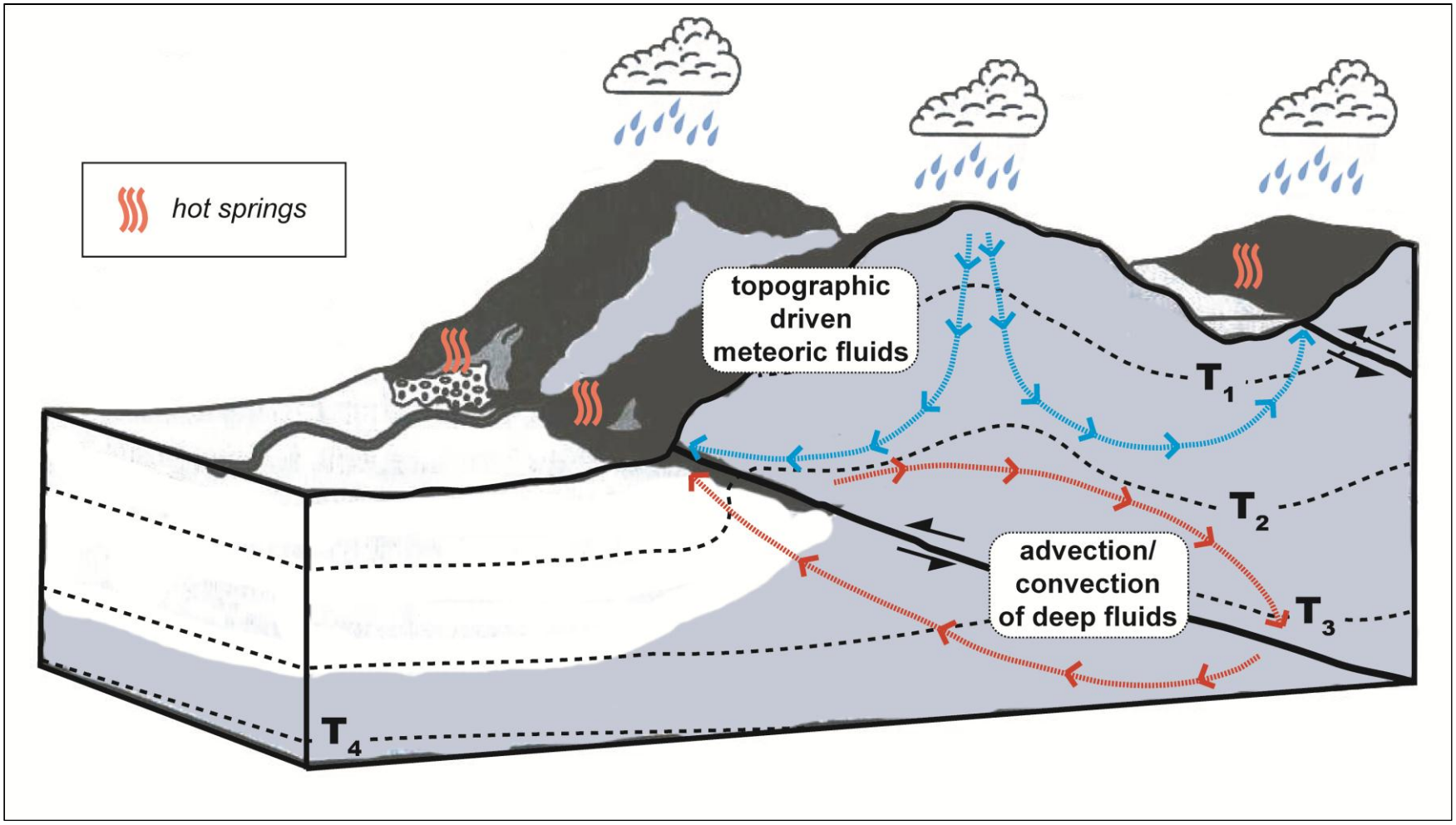

Figura VII-1: Esquema de los regímenes hidrotermales presentes en orógenos activos. El esquema muestra un orógeno emplazado en un ambiente compresivo caracterizado por fallas inversas donde las isotermas ($T_1<T_2<T_3<T_4$) se alzan en el bloque colgante mientras que en el bloque yacente se deprimen. Las manifestaciones termales se encuentran localizadas a lo largo de las trazas de las fallas en superficie. Modificado de *Ehlers (2005).*

La interpretación conjunta de las características químicas e isotópicas de los fluidos hidrotermales y los patrones de flujo calórico propuestos por *Hamza y Muñoz (1996)* sugieren que la razón fluido somero vs. profundo disminuye al sur del oroclino del Maipo a lo largo de los tres dominios hidrotermales de la CP (CPO, CPC y CPE). Lo anterior apunta a que el desarrollo de sistemas geotermales de alta temperatura debiese estar facilitado al sur del oroclino del Maipo, donde tanto la menor carga hidráulica regional asociada a la disminución de la topografía (*Farías et al. 2008*) así como a la orientación de los sistemas de falla respecto a la cinemática campo de transcurrente dextral (*Cembrano y Lara 2009*) generan condiciones favorables para la formación de celdas convectivas de agua meteórica y/o la advección vertical de fluidos metamórficos y/o magmáticos-hidrotermales. Sin embargo, la sola presencia de calor y agua no son factores suficientes para la generación de un sistema geotermal, debido a que el desarrollo de dichos sistemas necesariamente requiere la presencia de zonas permeables en la corteza (reservorio geotermal) donde el calor y el fluido puedan acumularse (*Gupta y Roy 2007*).

Desde el punto de vista del estudio de la geoquímica de fluidos hidrotermales, la presencia de aguas Na-Cl maduras – comúnmente asociadas a zonas de descarga laterales en sistemas geotermales hospedados en volcanes andesíticos (*outflows zones; Goff y Janik 2000*) – es un indicador clásico de la existencia de un reservorio geotermal (*Giggenbach 1997*). Si adicionalmente existen descargas fumarólicas asociadas (*upflows zones*), y éstas tienen una signatura química hidrotermal (ej. $R_H \sim -2.8$*; Giggenbach 1997*), dicho reservorio estaría parcial o totalmente dominado por vapor, dando cuenta de un sistema geotermal de alta temperatura (>200°C; *Hochstein y Browne 2000*). Sobre la base de lo analizado en el Capítulo VI, en Chile Central existirían nueve zonas con presencia de aguas Na-Cl parcialmente maduras. Estas áreas corresponden, de norte a sur, a: Saladillo, Salinilla, Plomo, Morales-Colina, Puente de Tierra, Calería, Tinguiririca, Peteroa-Calabozos y Mariposas (Figura VII-2). Del total de las áreas sólo tres están asociadas a descargas fumarólicas "hidrotermales" (Tinguiririca, Peteroa-Calabozos, Mariposas). A lo anterior se suma el área Estero del Volcán donde existen fumarolas hidrotermales, pero no se encontraron descargas de aguas Na-Cl en sus alrededores. En la Tabla VII-1 se muestra un resumen de las temperaturas estimadas mediante diferentes geotermómetros líquidos y gaseosos para cada una de las áreas (Capítulo VI).

En Chile Central, los posibles sistemas geotérmicos al norte y sur del oroclino del Maipo presentan claras diferencias en su origen y potencial geotérmico, las cuales

están evidenciadas por la geoquímica de los fluidos y la naturaleza de las manifestaciones termales superficiales asociadas.

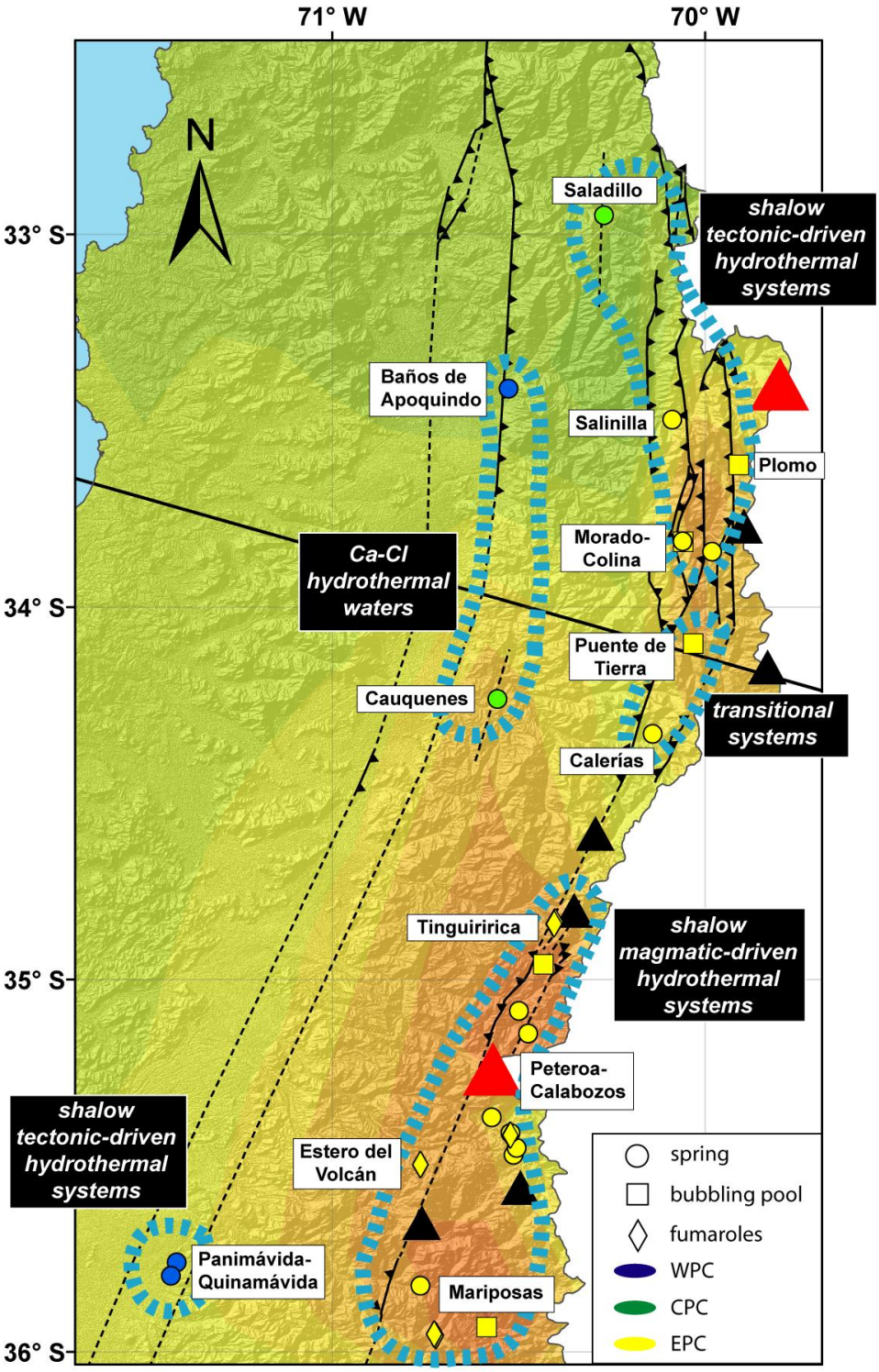

Figura VII-2: Posibles zonas geotermales y su relación genética con el contexto geotectónico de Chile Central.

Tabla VII-1: Resumen de las temperaturas estimadas mediante los geotermómetros de agua y gases según lo analizado en el Capítulo VI. $T_{(K\text{-}Mg\ vs.\ SiO2)}$: geotermómetro de agua que evalúa conjuntamente la razón K^2/Mg y la concentración de SiO_2. $T_{(Na\text{-}K\text{-}Ca\text{-}Mg)}$: geotermómetro de agua que evalúa conjuntamente la razón Ca/Mg y Na/K. $T_{(Ca\text{-}Na)}$: geotermómetro de agua que evalúa la razón Ca/Na^2. $T_{(H2\text{-}H2O\text{-}Ar)}$: geotermómetro de gas que evalúa conjuntamente la razón H_2/ H_2O y Ar/H_2O. $T_{(CO2/Ar)}$: geotermómetro de gas que evalúa la razón CO_2/Ar. Temperaturas en °C.

Localidad	Muestras	$T_{(K\text{-}Mg\ vs.\ SiO2)}$	$T_{(Na\text{-}K\text{-}Ca\text{-}Mg)}$	$T_{(Ca\text{-}Na)}$	$T_{(H2\text{-}H2O\text{-}Ar)}$	$T_{(CO2/Ar)}$
Baños de Apoquindo	13			205		
Termas Panimávida	14	80	140			
Termas Quinamávida	15	70	150			
Saladillo	16	120	150			
Cauquenes	17			205		
Salinilla	18	80	90			
Termas del Plomo	21	50	60		50	160
Baños Morales	24	100	160		120	200
	25	120	160			
Termas Colina	26	110	160		40	150
Puente de Tierra	27	120	120		160	250
Baños Calerías	28	130	220			
Tinguiririca	32-33	160	240		130-300	300
Peteroa	34-35	70-240	140-290		150-160	280-320
Peteroa-Calabozo	36-37-38-42	100	220		260	330
Estero del Volcán	39				320	350
Mariposa	48-49-50-51	140	200		260-300	250

Los sistemas geotermales localizados al norte del oroclino del Maipo (Salinilla, Termas del Plomo, Baños Morales y Termas Colina) parecen estar asociados a reservorios que alcanzan temperaturas de equilibrio <150°C (Tabla VII-1) y sus manifestaciones termales superficiales se restringen a manantiales calientes y piscinas burbujeantes. La signatura isotópica (R/R_a < 1.81 y $\delta^{13}C\text{-}CO_2$ ~ -8.6‰) y química (R_H ~ -3) de los gases indica que el origen de estos sistemas está relacionado a la interacción de fluidos meteóricos y rocas sedimentarias, lo que explicaría las altas concentraciones de solutos que alcanzan las aguas Na-Cl (TSD<57000 mgL^{-1}). Sobre la base de lo analizado en el Capítulo VI, el componente magmático en estos fluidos es despreciable (<2%), por lo que la fuente de calor de estos sistemas geotermales se restringe a las isotermas alzadas producto de la actividad orogénica. Sin embargo, aunque no exista una transferencia de materia evidente desde el sistema magmático hacia estos sistemas geotermales, es esperable que cercano a los centros eruptivos Holocenos (volcanes Tupungatito, San José y Maipo) las isotermas puedan estar aún

más someras (ej. *Hochstein y Browne 2000*). Actualmente, la existencia de estos reservorios geotermales no ha sido "confirmada" a través de métodos geofísicos de resistividad – específicamente el método MT-TDEM (*Magnetotelluric and Time Domain Electromagnetic Methods*) – ni por sondajes profundos. No obstante, de existir dichos reservorios geotermales, estos debiesen estar restringidos a lo largo de los sistemas de falla y sus respectivas zonas de daño (Figura VII-3).

Al sur del oroclino del Maipo, por el contrario, los geotermómetros de agua y gases apuntan a la existencia de reservorios geotermales de alta temperaturas (<350°C) cuya manifestaciones superficiales incluyen manantiales calientes, piscinas burbujeantes, piscinas de barro y fumarolas. Estos sistemas geotermales parecen estar genéticamente ligados a la transferencia de calor y, en menor medida, de masa desde los cuerpos magmáticos asociados a los volcanes aledaños. Lo anterior está evidenciado por las altas razones isotópicas de He (R/R_a<6.2), la presencia de agua andesítica (<5%) y N_2 en exceso (N_2/Ar>100) en las fumarolas, además de las condiciones redox que los fluidos alcanzarían en profundidad (-4<R_H<-3; Capítulo VII). Es importante notar que la concentración de gases magmáticos ácidos (HCl, SO_2 y HF) en las descargas fumarólicas es menor al límite de detección, sugiriendo que dichos gases fueron condensados en las partes profundas de los reservorios geotermales y posteriormente neutralizados con la roca caja. Lo anterior tiene implicancias positivas para un posible desarrollo productivo de estos sistemas geotermales, ya que en caso de existir fluidos ácidos en profundidad, la producción económica de fluidos geotermales requiere de una inversión adicional para la neutralización de estos fluidos (ej. *Rivera et al. 2000; Sanchez et al. 2001; Brondial 2005*).

A diferencia de los reservorios geotermales al norte del oroclino del Maipo, la existencia de reservorios de alta temperatura sí ha sido inferida indirectamente a través de sondeos MT-TDEM en las zonas de Tinguiririca y Mariposa (*Clavero et al. 2011; Hickson et al. 2011*). De acuerdo a los perfiles reportados para ambas zonas (Figura VII-4), se observa la presencia de zonas de alta resistividad (~100Ωm^{-1}) bajo una secuencia de baja resistividad con forma de campana (<10Ωm^{-1}), lo cual es típico de reservorios geotermales neutros con halo de alteración fílica (*clay cap*; *Giggenbach 1997*). A pesar de que ambos proyectos geotermales han sido sondeados utilizando pozos delgados (*slim holes*), los respectivos reservorios geotermales no fueron alcanzados en ninguna de las perforaciones, ya que tanto la mineralogía (zona rica en esméctitas) como el perfil de temperatura (zona conductiva) que se encontró en

profundidad es típica de la capa de arcilla que sobreyace al reservorio (*Hickson et al. 2011; Clavero et al. 2011; Droguet 2013)*.

La zona Planchón-Calabozos también fue sondeada mediante MT-TDEM (*Urzúa, comunicación personal*), sin embargo no existen reportes publicados de los resultados obtenidos. Tampoco existen reportes publicados sobre el pozo delgado perforado en esta zona. No obstante, la existencia de zonas de acumulación de fluido y calor en profundidad en el área Peteroa-Calabozo fue indirectamente inferida por *Pritchard et al. (2013),* quien reportó una subsidencia de 8 cm en esta área posiblemente asociada a la despresurización de los reservorios geotermales (Figura VII-5). Evidencia similares fueron observados tanto el área del Estero del Volcán como la del Tinguiririca, (Figura VII-5; *Pritchard et al. 2013*).

Además de indicar la posible presencia de reservorios geotermales en profundidad, la subsidencia de estas áreas hidrotermales también evidencia la extensión y forma de los reservorios geotermales (*Pritchard et al. 2013*). Como se observa en la Figura VII-5, las áreas afectadas por la subsidencia (Tinguiririca, Peteroa-Calabozos y Estero del Volcán) tienen una dirección similar a la de los sistemas de falla que deforman la CP al sur del oroclino del Maipo (NNE-SSO). Lo anterior indicaría que los fluidos magmáticos-hidrotermales en estas zonas son transferidos desde profundidades a través de las zonas de falla. Sin embargo, la acumulación de estos fluidos hidrotermales no sólo se restringiría a la zona de daño de la falla (Figura VII-5). Como se observa en la Figura VII-6, la cual muestra los modelos conceptuales de las áreas hidrotermales al sur del oroclino del Maipo, estas zonas de acumulación podrían corresponder tanto (i) a los contactos discordantes entre las secuencias Meso-Cenozoicas deformadas y las secuencias volcánicas de edad Mioceno medio a Pleistoceno (ii) como a las secuencias volcánicas Cuaternarias emitidas por los centros eruptivos que hospedan dichos sistemas hidrotermales.

Las áreas Puente de Tierra y Calerías – ubicadas al norte y sur del oroclino del Maipo, respectivamente (Figura VII-2) – parecen localizarse en una zona de transición entre los sistemas geotermales tectónicos y magmáticos antes mencionados. Por un lado, la temperatura máxima (T~250°C) estimada para el posible reservorio geotermal en el área Puente de Tierra es cerca de 100°C mayor que la estimada en las áreas Salinilla, Termas del Plomo, Baños Morales y Termas Colina. Mientras que en la zona de Calería, si bien los geotermómetros de agua entregan temperaturas similares a las estimadas en las áreas Tinguiririca, Peteroa-Calabozos y Mariposa, no se han

reportados descargas fumarólicas asociadas a este sistema geotermal (*Hauser 1997; HotRock 2011*).

De estas dos áreas sólo Calerías ha sido sondeada mediante un MT-TDEM (Figura VII-4; *HotRock 2011*). La Figura VII-4 sugiere que de existir un reservorio geotermal en Calerías, éste debiese estar restringido a lo largo de la zona de falla y sus respectivas zonas de daño, similar a lo propuesto para los sistemas geotermales localizados al norte del oroclino del Maipo. No obstante, debido a la temperatura que alcanzaría el reservorio en el área de Calerías, es probable que el gradiente geotermal de dicha área esté parcialmente incrementado por la presencia de la cámara magmática inactiva asociada al volcán Picos del Barroso de edad Plioceno Medio (*González-Ferrán 1995*; *Stern et al. 2007*). En el caso de Puente de Tierra, el calor remanente de los intrusivos Alfalfalito (~11 Ma) y/o Cerro Catedral (~3 Ma.) – localizados a <8 km de Puente de Tierra (*Muñoz 2011*) – serían los posibles responsables del alzamiento de las isotermas en esta área. De esta manera, el origen de los sistemas geotermales en la zona de transición estaría relacionado tanto a las isotermas alzadas producto de la actividad orogénica como al calor remanente de los intrusivos Plio-Pleistocenos.

A los sistemas geotermales indicados anteriormente, se suman tres áreas donde, de acuerdo al Capítulo VI, se evidencian procesos de interacción agua-roca que generan aguas geotermales (Ca-Cl, Na-SO_4 y Na-HCO_3) químicamente maduras (Baños Apoquindo, Cauquenes y Panimávida-Quinamávida). Lo anterior indicaría la posible existencia de reservorios donde las aguas alcanzan equilibrio químico con la roca caja. En Baños Apoquindo y Cauquenes el proceso de equilibrio involucra aguas Na-Cl híper salinas – posiblemente generadas en la parte Este de la CP – y las rocas volcánicas máficas de la parte Oeste y Central de la CP (Capítulo VI). De esta manera, el proceso de interacción agua-roca estaría constreñido a los primeros 10 km de la corteza donde se encontrarían estas rocas. En el área Panimávida-Quinamávida, por otro lado, la interacción agua–roca estaría constreñida a la zona de falla Pocuro-San Ramón donde el agua meteórica (Ca-HCO_3 a Ca-SO_4) circularía por convección hasta profundidades podrían alcanzar cerca de 13 km de profundidad (ej. *Craw et al. 2002*). De acuerdo a las temperaturas de equilibrio estimadas para estas aguas (entre 160 y 200°C) el recurso geotérmico en dichas áreas podría ser aprovechado para generación eléctrica de baja entalpía o usos directos (*Lund et al. 2005; Gupta y Roy 2007*). Sin embargo, a la fecha, la existencia de reservorios en dichas zonas no ha sido corroborada a través de estudios geofísicos ni perforaciones.

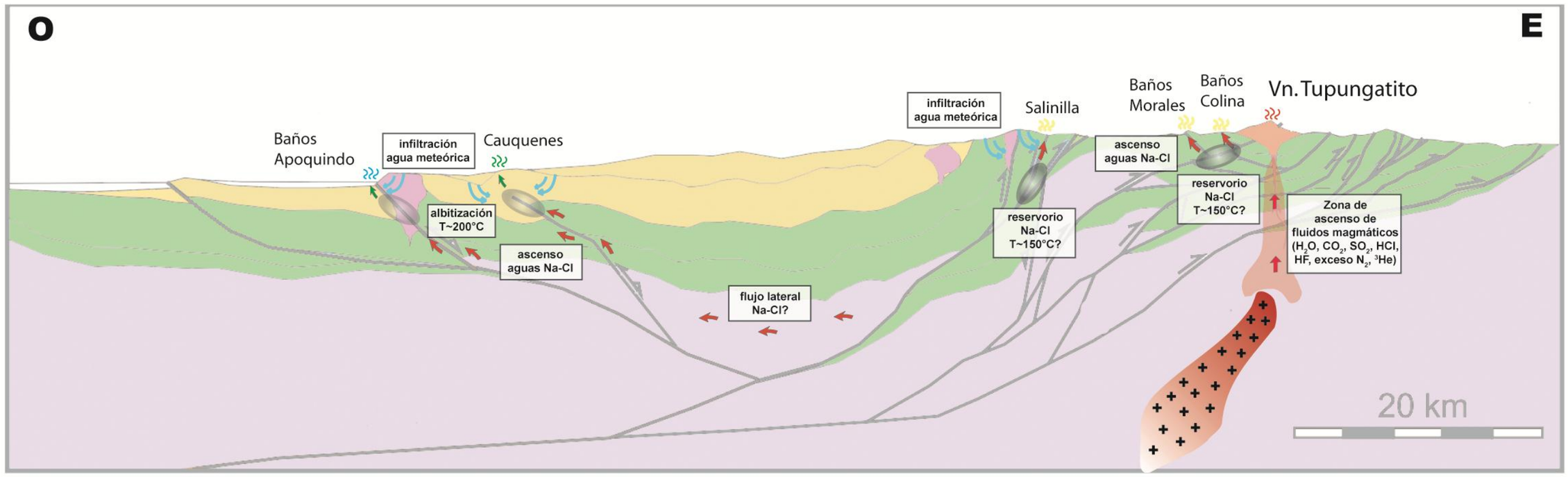

Figura VII-3: Perfiles del modelo conceptual de los sistemas geotermales localizados al norte del oroclino del Maipo. Perfil modificado de *Giambiagi et al. 2014*.

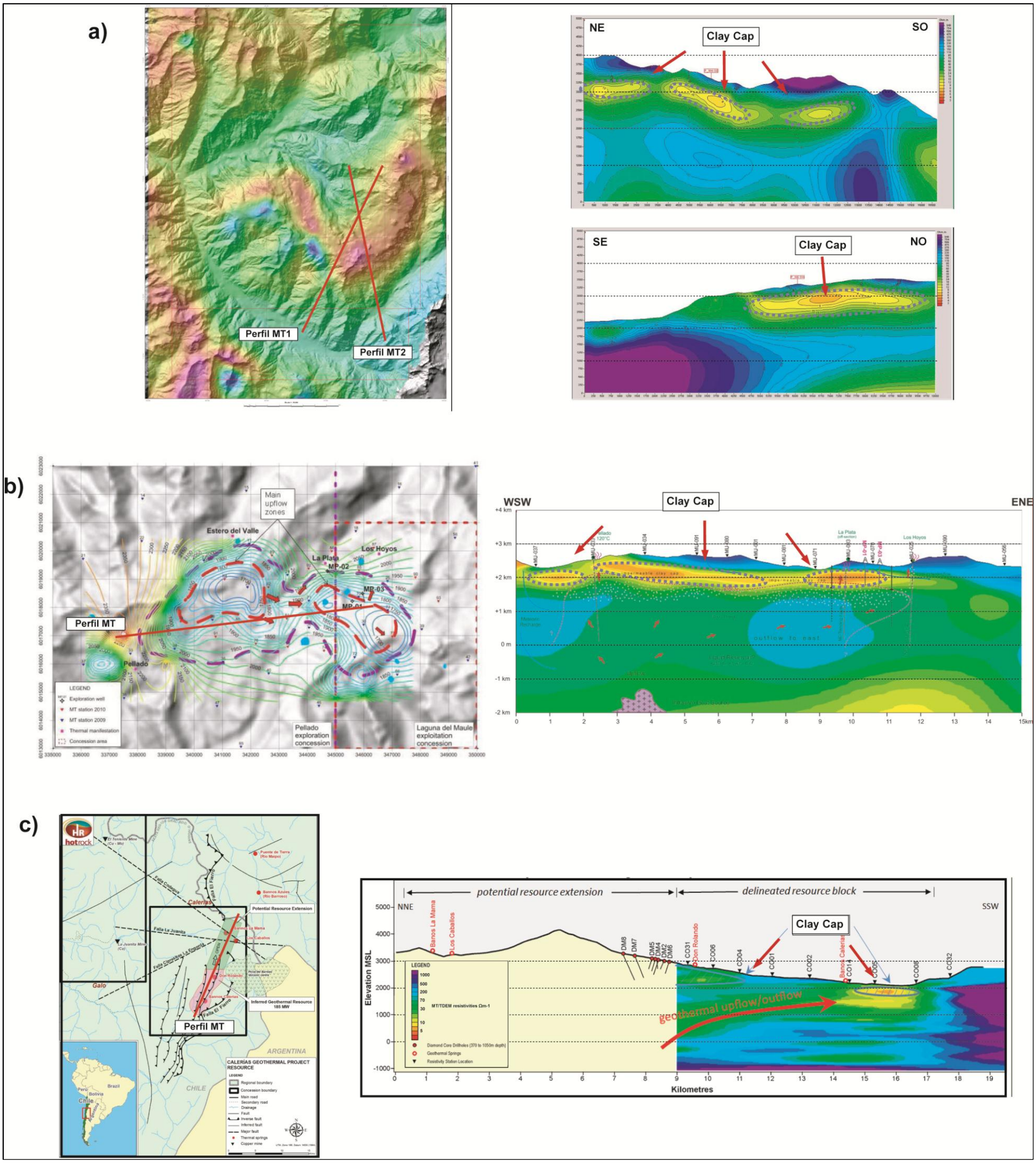

Figura VII-4: Mapa y perfiles de las áreas geotermales (a) Tinguiririca, (b) Mariposa y (c) Calerías donde se muestran los modelos MT realizados (*Clavero et al. 2011; HotRock 2011; Hickson et al. 2011*). En los mapas asociados se muestra la orientación aproximada de los perfiles reportados

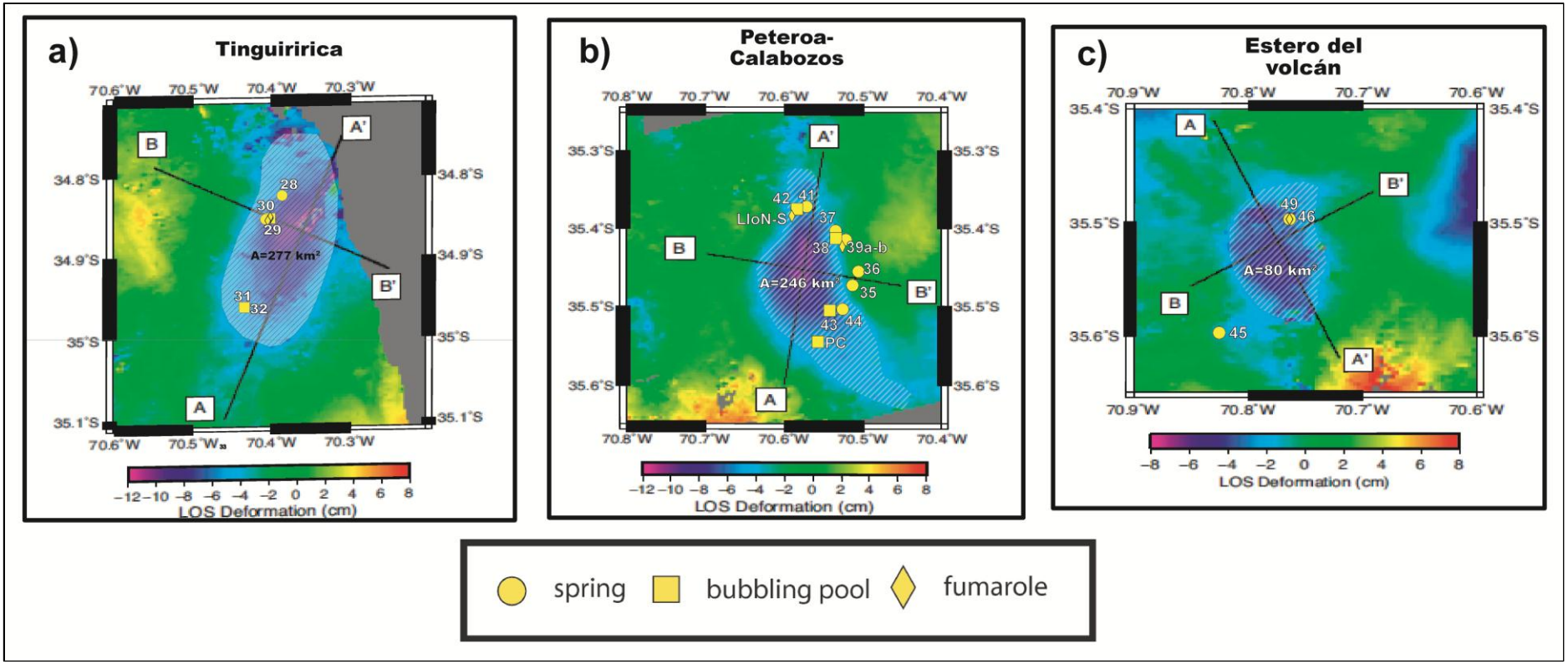

Figura VII-5: Áreas afectadas por la subsidencia cosísmica luego del terremoto 8.8 M_w del Maule (27 de Febrero 2010). Modificado de *Pritchard et al. (2013)*.

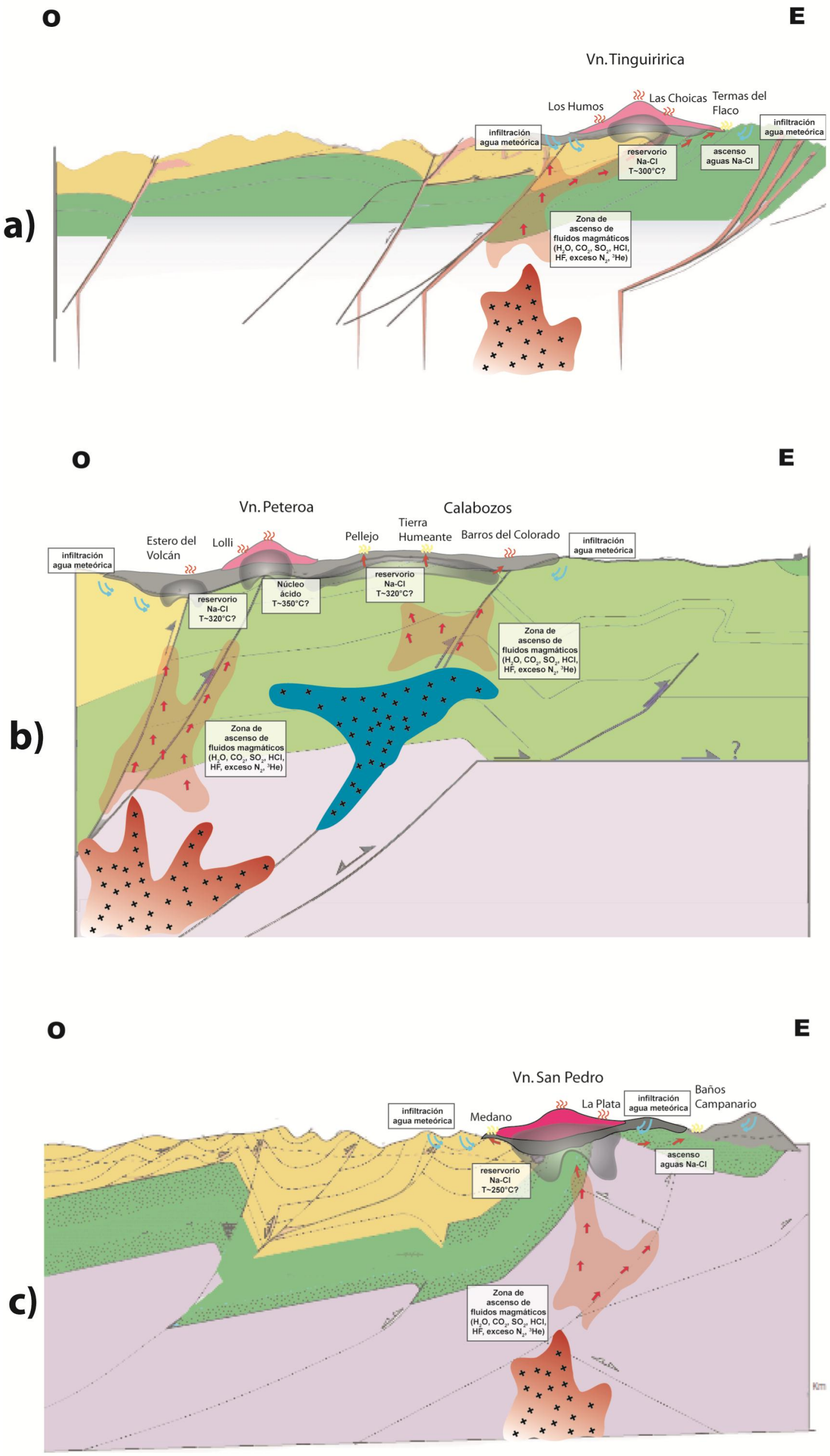

Figura VII-6: Perfiles de los modelos conceptuales de los sistemas geotermales Tinguiririca (a), Peteroa-Calabozos-Estero del Volcán (b), y Mariposas (c). Los perfiles fueron modificados de Radic (2010) y Droguet (2012) [a], Tapia (2010) [b], y Astaburuaga (2014) [c].

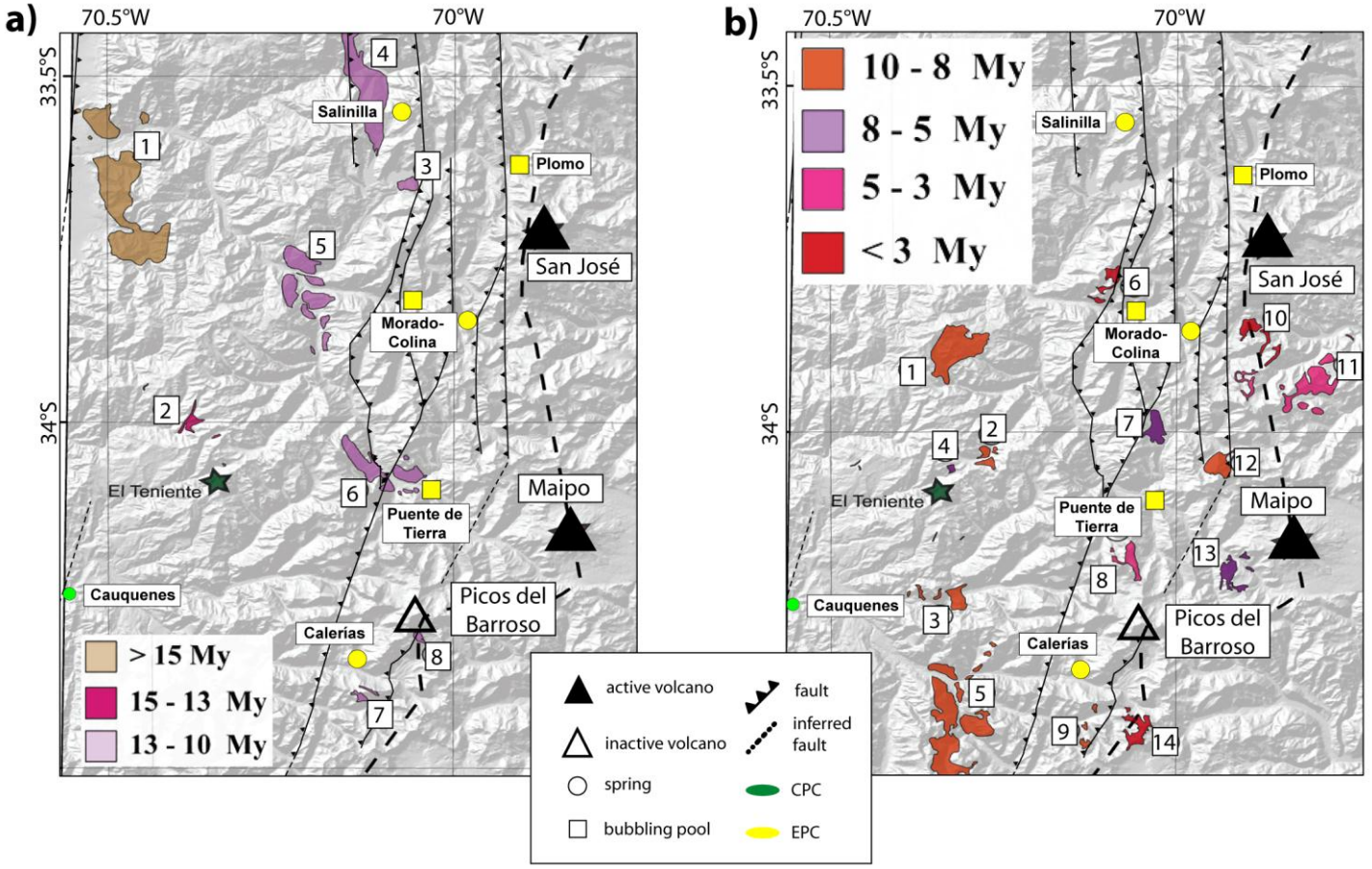

Figura VII-7: Posición de los intrusivos Neógenos en los Ándes de Chile Central (Modificado de *Muñoz et al. 2009*). a) Intrusivos de edad mayor a 10 Ma: (1) La Obra (~19-20 Ma), (2) Diorita Maqui (~14 Ma), (3) Cerro Mesón Alto (~11-12 Ma), (4) La Gloria (~10 Ma), (5) San Gabriel (~11 Ma), (6) Alfalfalito (~12 Ma), (7) Diques Blancos de Las Leñas (~12-13 Ma), (8) Cachapoal (~11-12 Ma). b) Intrusivos de edad entre 1 y 10 Ma: (1) La Carlota (~9 Ma), (2) Extravío (~8 Ma), (3) Mina Juanita (~9 Ma), (4) Laguna Negra (~7 Ma), (5) Nacientes del Cortaderal (~8 Ma), (5) Santa Rosa de Rengo (~8-9 Ma, [8]); (6) Los Lunes (~1 Ma), (7) Jeria (~6-7 Ma), (8) Cerro Catedral (~3 Ma), (9) Estero Crucero (~8-10 Ma), (10) Paso Colina (~1.3 Ma), (11) Arroyo Colina (~3-4 Ma), (12) Río Negro (~8 Ma), (13) Cruz de Piedra (~5-6 Ma), y (14) Portezuelo Arriaza (~1.6 Ma).

VII.2 ESTIMACIÓN DEL POTENCIAL GEOTÉRMICO

VII.2.1 Metodología

A partir de los modelos conceptuales mencionados en la sección anterior, es posible estimar –de manera simplificada– el potencial geotermal de los reservorios geotermales inferidos (Calerías, Tinguiririca, Peteroa-Calabozos, Estero del Volcán y Mariposa). De acuerdo a los datos disponibles en cada una de estas áreas (lito-estratigráfico, geoquímico y geofísico), el método de la estimación del calor almacenado es el procedimiento más adecuado para la estimación del potencial geotérmico (*AGRC 2010*).

El principio básico de éste método consiste en la estimación el calor almacenado dentro de un volumen de reservorio definido. La estimación considera el calor almacenado en tanto en la roca como en el fluido. A partir de calor total calculado, se estima cuanto de este calor puede ser razonablemente extraído y convertido en electricidad utilizando la tecnología actual.

El volumen del reservorio es generalmente definido como el área del recurso multiplicado por su profundidad. La ecuación usada para calcular el calor almacenado es la siguiente:

$$Q = A*h*\{\underbrace{[C_r*\rho_r*(1-f)*(T_i - T_f)]}_{\text{calor acumulado en las rocas}} + \underbrace{[\rho_{si}.\phi*(1-S_w).(h_{si} - h_{wf})]}_{\text{calor acumulado en el vapor}} + \underbrace{[\rho_{wi}*\phi*S_w*(h_{wi} - h_{wf})]}_{\text{calor acumulado en el agua}}\} \quad \text{(VII.1)}$$

, donde:

Q := calor almacenado total

h := espesor del reservorio

T_i := Temperatura promedio del reservorio.

ρ_{si}, ρ_{wi} := densidades de vapor y agua a temperatura del reservorio

Φ := porosidad

A := Área del reservorio

C_r := calor especifico de la roca a condiciones del reservorio

T_f := Temperatura base

h_{si}, h_{wf} := entalpías del agua a temperatura base

S_w := Saturación del agua

La estimación del potencial eléctrico (en MWe) de un probable desarrollo geotermal debe considerar factores adicionales al valor de calor almacenado estimado mediante la Ecuación VII.1, incluyendo:

- **Factor de recuperación:** Este factor está controlado principalmente por la eficiencia de la recarga del sistema geotérmico inducida naturalmente, la cual, a si vez, es función de la hidrología así como de la estructura de permeabilidad fuera y dentro del reservorio. Teóricamente, este factor puede oscilar entre 1 (completa recarga del reservorio) y 0,1 (recarga limitada del reservorio; *Williams et al. 2008*). En este trabajo este valor ha sido considerado como una función de la porosidad (2.5*Φ; *Muffler and Cataldi 1978*)
- **Factor de conversión de eficiencia:** Este factor describe la razón entre la energía calórica consumida por la planta de generación (por unidad de vapor) y la energía eléctrica producida. Éste valor depende principalmente de la temperatura del reservorio y del ambiente. En la mayoría de plantas geotermales este factor es del orden del 15%.
- **Tiempo de vida económica del proyecto:** Utilizada para dividir el potencial energético total a lo largo del tiempo de vida del proyecto, para así obtener un valor promedio del potencial energético. En este caso se han considerado 30 años de vida económica del proyecto (*AGRC 2010*).
- **Factor de Planta:** Este factor describe la razón entre la capacidad instalada de la planta y la capacidad real de generación por unidad de tiempo (ej. 1 año). El factor de planta está determinado por la frecuencia de las operaciones de mantenimiento y por su prioridad para ingresar al sistema interconectado eléctrico (*AGRC 2010)*. En la mayoría de plantas geotermales el factor de planta varía entre 90% a 95%. En este caso consideraremos un escenario conservador del 90%.

El cálculo final de potencial de electricidad en MWe se realiza usando la siguiente ecuación:

$$E = (Q * R_f * \eta_c)/(F * L) \qquad \text{(VII.2)}$$

, donde:

E := capacidad energética de la planta (MWe)
$\boldsymbol{R_f}$:= factor de recuperación (fracción de calor almacenado extraíble)
F := factor de planta.
Q := calor almacenado total
$\boldsymbol{\eta_c}$:= factor de recuperación
L := vida económica del proyecto

La metodología descrita anteriormente usa una aproximación determinística para estimar las reservas, no obstante en la práctica es más realista definir un rango de valores para muchas de estas variables (*AGRC 2010*). Lo anterior se realiza

asignándole una distribución de probabilidad a las variables de manera de tomar en cuenta la incertidumbre inherente a mucho de los parámetros utilizados en la estimación de recursos (ej. temperatura del reservorio, profundidad del reservorio). Hay un gran número de distribuciones probabilísticas que pueden ser utilizadas para describir cada una de las variables, sin embargo las más utilizadas en la estimación de recursos corresponden a las distribuciones triangulares, rectangulares y logarítmico-normales (*AGRC 2010*). Una vez definidos los rangos y sus distribuciones de probabilidad se procede al cálculo del calor acumulado (VII.1) y el potencial eléctrico (VII.2) mediante una simulación de Montecarlo. De acuerdo al *AGRC (2010)*, el cálculo de las reservas a través de una simulación de Montecarlo requiere un número mínimo de 10000 iteraciones.

VII.2.2 Resultados y Discusiones

Debido a que los modelos MT-TDEM realizados en las áreas Calerías, Tinguiririca, Peteroa-Calabozos y Mariposa no se encuentran publicados no es posible separar los reservorios geotermales asociados en zonas vapor- y líquido-dominantes (Figura VII-4). De esta manera, para la estimación del calor acumulado de los sistemas Tinguiririca, Pereroa-Calabozos, Estero del Volcán y Mariposas–caracterizados por la presencia de fumarolas–se asumirá la existencia de un único nivel vapor dominante caracterizado por una fracción de vapor del 50% (*ej. Sepúlveda 2005*). En el caso del sistema Calerías, donde no se han reportado fumarolas asociadas, se asumirá la existencia de un único nivel líquido-dominado (fracción de vapor=0%). Los parámetros comunes a cada simulación se reportan en la Tabla VII-2.

Tabla VII-2: Parámetros comunes seleccionados para el cálculo de potencial energético.

Parámetros comunes	
Vida económica del proyecto (años)	30
Factor de Planta (%)	90
Densidad de la roca (kg/m³)	2700
Temperatura ambiente (°C)	10

VII.2.2.1 Calerías

En la Tabla VII-3 se muestran los parámetros específicos al sistema geotermal Calerías. La extensión lateral mínima (31 km^2) ha sido seleccionada en base al área reportada por *HotRock (2011)*, mientras que la máxima ha sido estimada en base a la distribución superficial de las manifestaciones termales junto con el marco estructural de la zona de estudio (55 km^2; Figura VI-4c). La extensión vertical mínima (800 m) y

máxima (1400 m) del reservorio ha sido estimada en base al espesor de la capa resistiva del perfil reportado por *HotRock (2011)* [Figura VI-4c]. La temperatura mínima del reservorio ha sido estimada mediante los geotermómetros de mayor cinética de reacción ($\mathbf{T_{K\text{-}Mg\ vs.\ SiO2}}$), mientras que la temperatura máxima consideró los cálculos reportados por *HotRock (2011)*, ya que este reporte consideran cuatro manifestaciones termales para su análisis, mientras que en este trabajo sólo se pudo acceder a una de estas manifestaciones (Baños Calerías). Para la temperatura base se ha considerado la temperatura mínima estimada por los geotermómetros (Tabla VII-1). El rango de porosidad utilizado en la estimación es el esperado para reservorios líquido dominados (ej. *Williams et al. 2008*).

Tabla VII-3: Parámetros y tipo de distribuciones para el cálculo de potencial energético de sistema Calerías.

Variables	Min	Probable	Max	Tipo de Distribución
Área de reservorio (km^2)	31	33	55	Triangular
Espesor (m)	800	1200	1400	Triangular
Porosidad (%)	3%	6%	10%	Triangular
Temperatura (°C)	160	220	250	Triangular
Temperatura Base (°C)	160	160	160	Constante
Capacidad calorífica de la roca (kJ/kg°C)	0,915	0,946	0,957	Triangular
Saturación del Líquido en el reservorio (%)	100%	100%	100%	Constante
Factor de recuperación (%)	7,5%	15,0%	25,0%	Triangular
Eficiencia (%)	14,0%	15,0%	16,0%	Triangular

Los resultados de estimación de potencial se muestran en la Figura VII-9. Estos resultados preliminares sugieren la presencia de un recurso geotérmico de interés en el área (5.900 PJ y **165 MWe**). Los resultados son comparables a los reportados por *HotRock (2011)* quienes estimaron un calor acumulado de 7.400 PJ y 185 MWe de potencial de generación eléctrica. El potencial de generación eléctrica estimado podría suplir la demanda energética de ~222.750 viviendas en Chile, asumiendo que cada vivienda en Chile consume 740 W (*Romero 2011*).

VII.2.2.2 Tinguiririca

En la Tabla VII-4 se muestran los parámetros específicos al sistema geotermal Tinguiririca. La extensión lateral mínima (40 km^2) ha sido seleccionada en base al área reportada por *Clavero et al. (2011)*, mientras que la máxima ha sido estimada en base al área afectada por la subsidencia según *Pritchard et al. (2013*) [277 km^2; Figura VI-5a]. La extensión vertical mínima (1000 m) y máxima (1500 m) del reservorio ha sido

estimada en base al espesor de la capa resistiva de los perfiles reportados por *Clavero et al. (2011)* [Figura VI-4a]. La temperatura mínima del reservorio ha sido estimada mediante los geotermómetros de mayor cinética de reacción ($T_{K\text{-}Mg\ vs.\ SiO2}$), mientras que la máxima consideró la temperatura estimada por los geotermómetros de menor cinética de reacción ($T_{CO2/Ar}$; Tabla VI-1). La temperatura base ha sido estimada como la temperatura mínima estimada para el reservorio El rango de porosidad utilizado en la estimación es el esperado para reservorios vapor dominados (ej. *Williams et al. 2008*).

Tabla VII-4: Parámetros y tipo de distribuciones para el cálculo de potencial energético de sistema Tinguiririca.

Variable	Min	Probable	Max	Tipo de Distribución
Área de reservorio (km^2)	40	55	277	Triangular
Espesor (m)	1000	1250	1500	Triangular
Porosidad (%)	2%	5%	8%	Triangular
Temperatura (°C)	220	240	300	Triangular
Temperatura Base (°C)	220	220	220	Constante
Capacidad calorífica de la roca (kJ/kg°C)	0,946	0,954	0,974	Triangular
Saturación del Líquido en el reservorio (%)	50%	50%	50%	Constante
Factor de recuperación (%)	5,0%	12,5%	20,0%	Triangular
Eficiencia (%)	14,0%	15,0%	16,0%	Triangular

Los resultados de estimación de potencial se muestran en la Figura VII-10. Estos resultados preliminares sugieren la presencia de un recurso geotérmico de interés en el área (13.400 PJ y **294 MWe**), el cual podría suplir las necesidades de ~397.300 viviendas en Chile. El potencial eléctrico estimado es 6 veces mayor al reportado por ENAP (~50 MWe; *Soffía 2004*).

VII.2.2.3 Peteroa-Calabozos

En la Tabla VII-5 se muestran los parámetros específicos al sistema geotermal Peteroa-Calabozos. La extensión lateral mínima (142 km^2) ha sido calculada en base a la distribución espacial de las manifestaciones hidrotermales, mientras que la máxima ha sido estimada en base al área afectada por la subsidencia según *Pritchard et al. (2013*) [246 km^2; Figura VI-5b]. No existen datos publicados sobre el MT-TDEM de esta área, por lo que no se puede constreñir la extensión vertical del reservorio. Sin embargo, y con el fin de llevar a cabo el cálculo de las reservas, se considerará una extensión vertical similar a la estimada en el área de Tinguiririca. La temperatura mínima del reservorio ha sido estimada mediante los geotermómetros de mayor

cinética de reacción ($T_{K\text{-}Mg\ vs.\ SiO2}$), mientras que la máxima consideró la temperatura estimada por los geotermómetros de menor cinética de reacción ($T_{CO2/Ar}$; Tabla VI-1). La temperatura base ha sido estimada como la temperatura mínima estimada para el reservorio. El rango de porosidad utilizado en la estimación es el esperado para reservorios vapor dominados (ej. *Williams et al. 2008*).

Tabla VII-5: Parámetros y tipo de distribuciones para el cálculo de potencial energético de sistema Peteroa-Calabozos.

Variable	Min	Probable	Max	Tipo de Distribución
Área de reservorio (km^2)	142	150	246	Triangular
Espesor (m)	1000	1250	1500	Triangular
Porosidad (%)	2%	5%	8%	Triangular
Temperatura (°C)	220	240	320	Triangular
Temperatura Base (°C)	220	220	220	Constante
Capacidad calorífica de la roca (kJ/kg°C)	0,946	0,954	0,974	Triangular
Saturación del Líquido en el reservorio (%)	50%	50%	50%	Constante
Factor de recuperación (%)	5,0%	12,5%	20,0%	Triangular
Eficiencia (%)	14,0%	15,0%	16,0%	Triangular

Los resultados de estimación de potencial se muestran en la Figura VII-11. Estos resultados preliminares sugieren la presencia de un recurso geotérmico de interés en el área (23.280 PJ y **510 MWe**), el cual podría suplir las necesidades de ~689.200 viviendas en Chile. El potencial eléctrico calculado es similar (~625 MWe) al estimado por *Aravena (2012)*, y se encuentra en el rango del potencial estimado por ENAP (300 a 1.000 MWe; *Soffía 2004*).

VII.2.2.4 Estero del Volcán

En la Tabla VII-6 se muestran los parámetros específicos al sistema geotermal Estero del Volcán. La extensión lateral ha sido calculada sólo en base al área afectada por la subsidencia según *Pritchard et al. (2013*) [80 km^2; Figura VI-5c]. No existen manantiales Na-Cl catastrados en esta zona, por lo que no fue posible constreñir la extensión lateral en base a la distribución de las manifestaciones termales. No han sido realizados sondeos MT-TDEM en el área, por lo que no se puede constreñir la extensión vertical del reservorio. Sin embargo, y con el fin de llevar a cabo el cálculo de las reservas, se considerará una extensión vertical similar a la estimada en el área de Tinguiririca. La temperatura mínima del reservorio ha sido estimada mediante los geotermómetros de mayor cinética de reacción ($T_{H2\text{-}Ar\text{-}H2O}$), mientras que la máxima consideró la temperatura estimada por los geotermómetros de menor cinética de

reacción ($T_{CO2/Ar}$; Tabla VI-1). La temperatura base ha sido estimada como la temperatura mínima estimada para el reservorio. El rango de porosidad utilizado en la estimación es el esperado para reservorios vapor dominados (ej. *Williams et al. 2008*).

Tabla VII-6: Parámetros y tipo de distribuciones para el cálculo de potencial energético de sistema Estero del Volcán.

Variable	Min	Probable	Max	Tipo de Distribución
Área de reservorio (km^2)	80	80	80	Constante
Espesor (m)	1000	1250	1500	Triangular
Porosidad (%)	2%	5%	8%	Triangular
Temperatura (°C)	320	330	350	Triangular
Temperatura Base (°C)	300	300	300	Constante
Capacidad calorífica de la roca (kJ/kg°C)	0,946	0,954	0,974	Triangular
Saturación del Líquido en el reservorio (%)	50%	50%	50%	Constante
Factor de recuperación (%)	5,0%	12,5%	20,0%	Triangular
Eficiencia (%)	14,0%	15,0%	16,0%	Triangular

Los resultados de estimación de potencial se muestran en la Figura VII-12. Estos resultados preliminares sugieren la presencia de un recurso geotérmico de interés en el área (9.009 PJ y **198 MWe**), el cual podría suplir las necesidades de ~268.000 viviendas en Chile. El potencial eléctrico calculado es similar (~177 MWe) al estimado por *Aravena (2012)*.

VII.2.2.5 Mariposa

En la Tabla VII-7 se muestran los parámetros específicos al sistema geotermal Mariposa. La extensión lateral mínima (28 km^2) ha sido seleccionada en base al área reportada por *Hickson et al. (2011)*, mientras que la máxima ha sido estimada en base a la extensión de las manifestaciones termales asociadas (~239 km^2). La extensión vertical mínima (1500 m) y máxima (2000 m) del reservorio ha sido estimada en base al espesor de la capa resistiva de los perfiles reportados por *Hickson et al. (2011)* [Figura VI-4b]. La temperatura mínima del reservorio ha sido estimada mediante los geotermómetros de mayor cinética de reacción ($T_{K\text{-}Mg\ vs.\ SiO2}$), mientras que la máxima consideró la temperatura estimada por los geotermómetros de menor cinética de reacción ($T_{CO2/Ar}$; Tabla VI-1). La temperatura base ha sido estimada como la temperatura mínima estimada para el reservorio. El rango de porosidad utilizado en la estimación es el esperado para reservorios vapor dominados (ej. *Williams et al. 2008*).

Tabla VII-7: Parámetros y tipo de distribuciones para el cálculo de potencial energético de sistema Mariposas

Variable	Min	Probable	Max	Tipo de Distribución
Área de reservorio (km^2)	28	40	239	Triangular
Espesor (m)	1500	1750	2000	Triangular
Porosidad (%)	2%	5%	8%	Triangular
Temperatura (°C)	200	250	300	Triangular
Temperatura Base (°C)	200	200	200	Constante
Capacidad calorífica de la roca (kJ/kg°C)	0,946	0,954	0,974	Triangular
Saturación del Líquido en el reservorio (%)	50%	50%	50%	Constante
Factor de recuperación (%)	5,0%	12,5%	20,0%	Triangular
Eficiencia (%)	14,0%	15,0%	16,0%	Triangular

Los resultados de estimación de potencial se muestran en la Figura VII-13. Estos resultados preliminares sugieren la presencia de un recurso geotérmico de interés en el área (23.075 PJ y **509 MWe**), el cual podría suplir las necesidades de ~688.000 viviendas en Chile. El potencial eléctrico calculado es mayor al estimado por *Hickson et al. (2011)* y *Aravena (2012)* [320 and 346 MWe, respectivamente].

VII.2.3 Limitaciones de la estimación

Si bien el cálculo de almacenamiento de calor ha demostrado ser válido cuando se ha aplicado a campos geotérmicos desarrollados con una historia conocida de producción (*Williams et al. 2008*), las estimaciones realizadas en áreas geotermales en fase de exploración sólo deben considerarse un aproximación gruesa del calor almacenado y del potencial energético de dichas áreas.

Es importante notar que las estimaciones del calor acumulado en este trabajo consideraron como la extensión lateral de los reservorios las áreas dadas por (i) la distribución de las manifestaciones termales y (ii) la zona de subsidencia reportada por *Pritchard et al. (2013)*, donde ambos valores podrían estar sobreestimando la extensión real de éstos. Lo anterior explicaría la diferencia entre el potencial energético estimado en este trabajo para el sistema Mariposa y los reportados por *Hickson et al. (2011)* y *Aravena (2012).* Estas incertezas podrían dilucidarse mediante la delimitación de la extensión horizontal y vertical del reservorio utilizando un modelo MT-TDEM para cada sistema (*Williams et al. 2008*).

Las estimaciones anteriores tampoco consideran factores como:

- Permeabilidad
- Productividad individual de los pozos
- Problemas durante la perforación
- Problemas derivados del fluido geotermal como incrustaciones o entrada de fluidos ácidos.
- Contenido de gas
- Limitaciones de acceso en superficie
- Ingreso de agua fría al reservorio u otros problemas de producción
- Limitaciones medio ambientales

Si bien las estimaciones del potencial energético muestran resultados promisorios en las áreas Calerías, Tinguiririca, Peteroa-Calabozos, Estero del Volcán y Mariposa; estos sistemas sólo podrán ser considerados viables para la producción de electricidad una vez hayan sido perforados y probados a través de la exploración de pozos profundos que permitan confirmar las condiciones del reservorio y la productividad de los pozos.

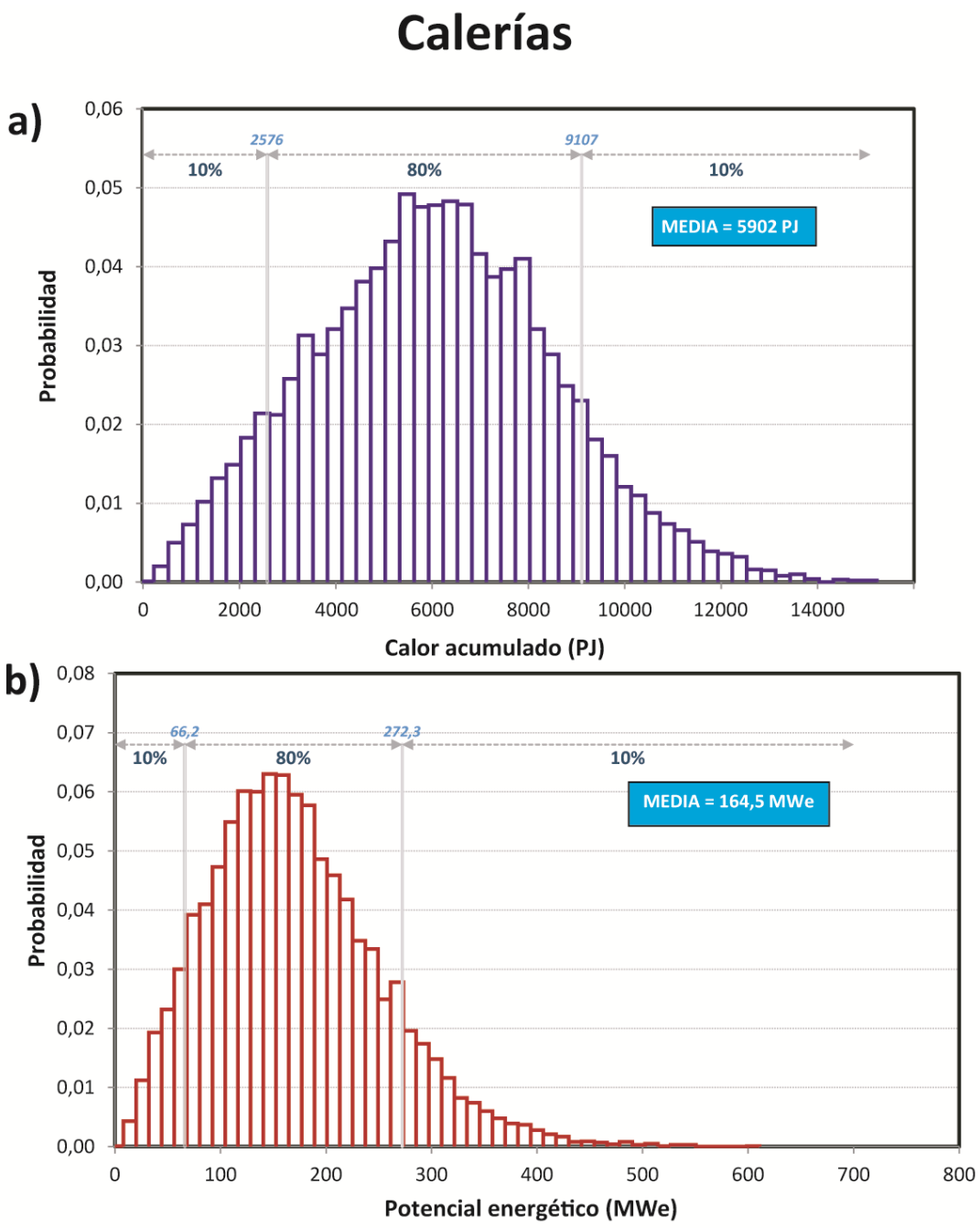

Figura VII-8: Distribuciones de frecuencia para el cálculo de calor almacenado (a) y potencial energético (b) en el área Calerías. Se reporta los valores de los percentiles 10 y 90, al igual que la media.

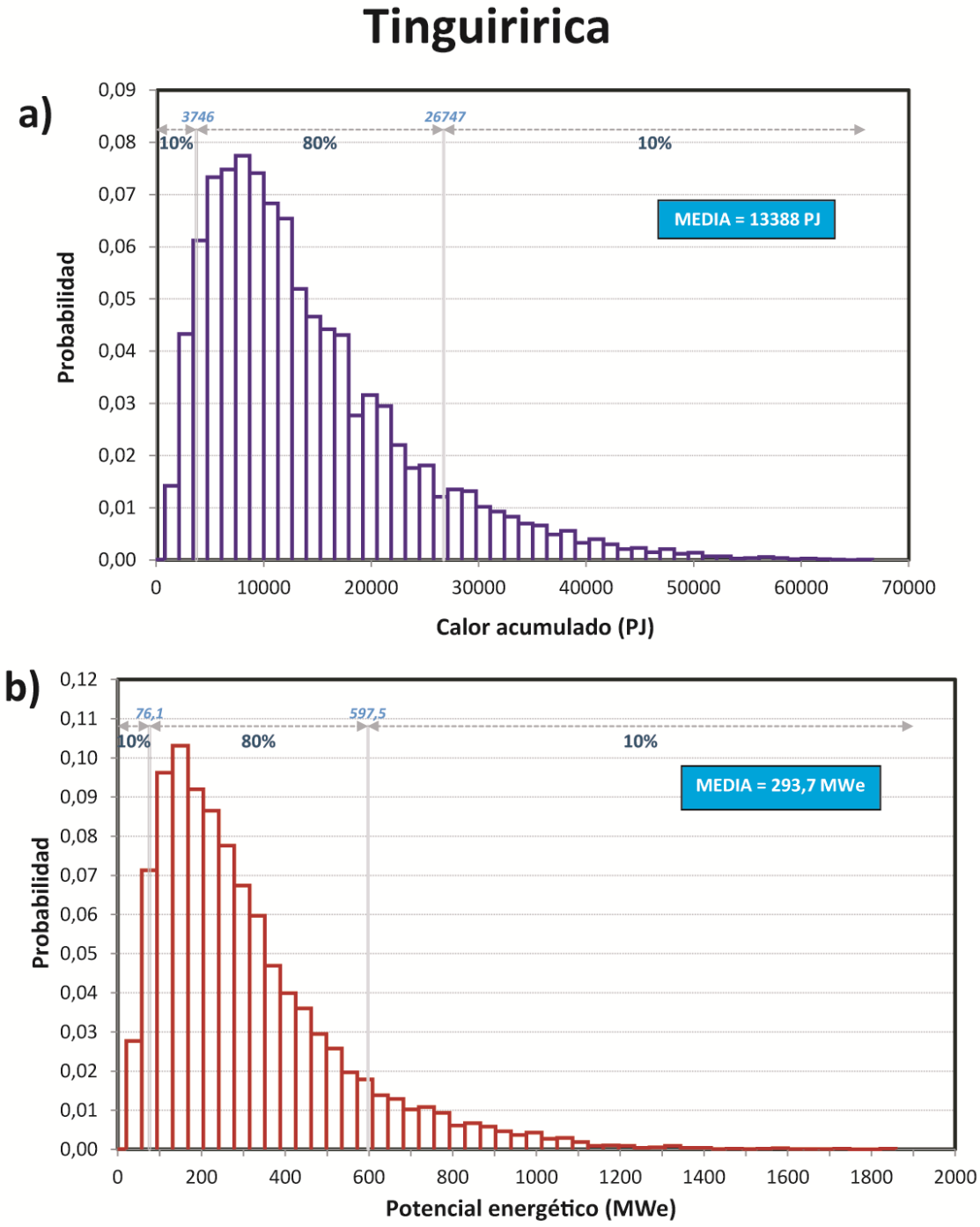

Figura VII-9: Distribuciones de frecuencia para el cálculo de calor almacenado (a) y potencial energético (b) en el área Tinguiririca. Se reporta los valores de los percentiles 10 y 90, al igual que la media.

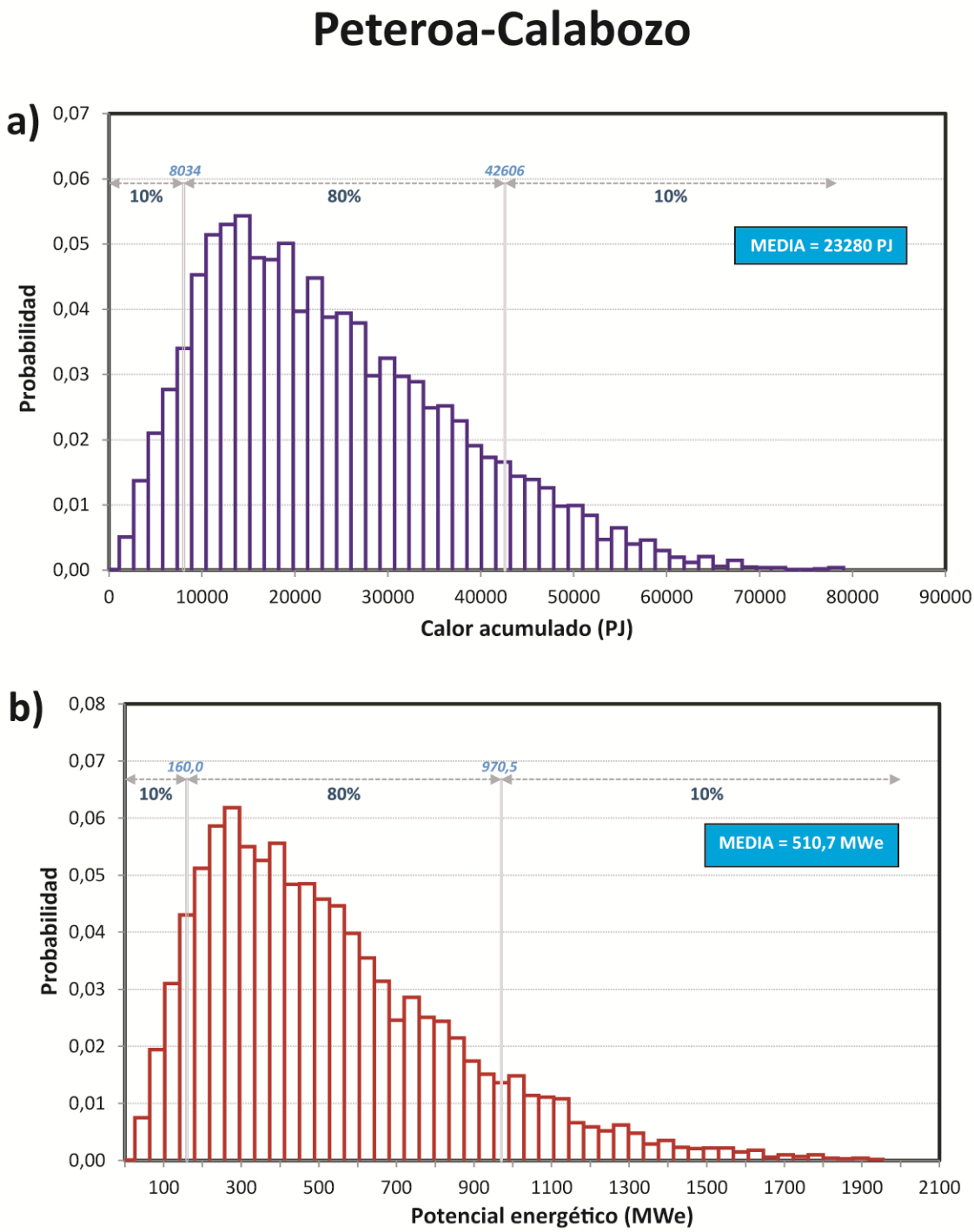

Figura VII-10: Distribuciones de frecuencia para el cálculo de calor almacenado (a) y potencial energético (b) en el área Peteroa-Calabozos. Se reporta los valores de los percentiles 10 y 90, al igual que la media.

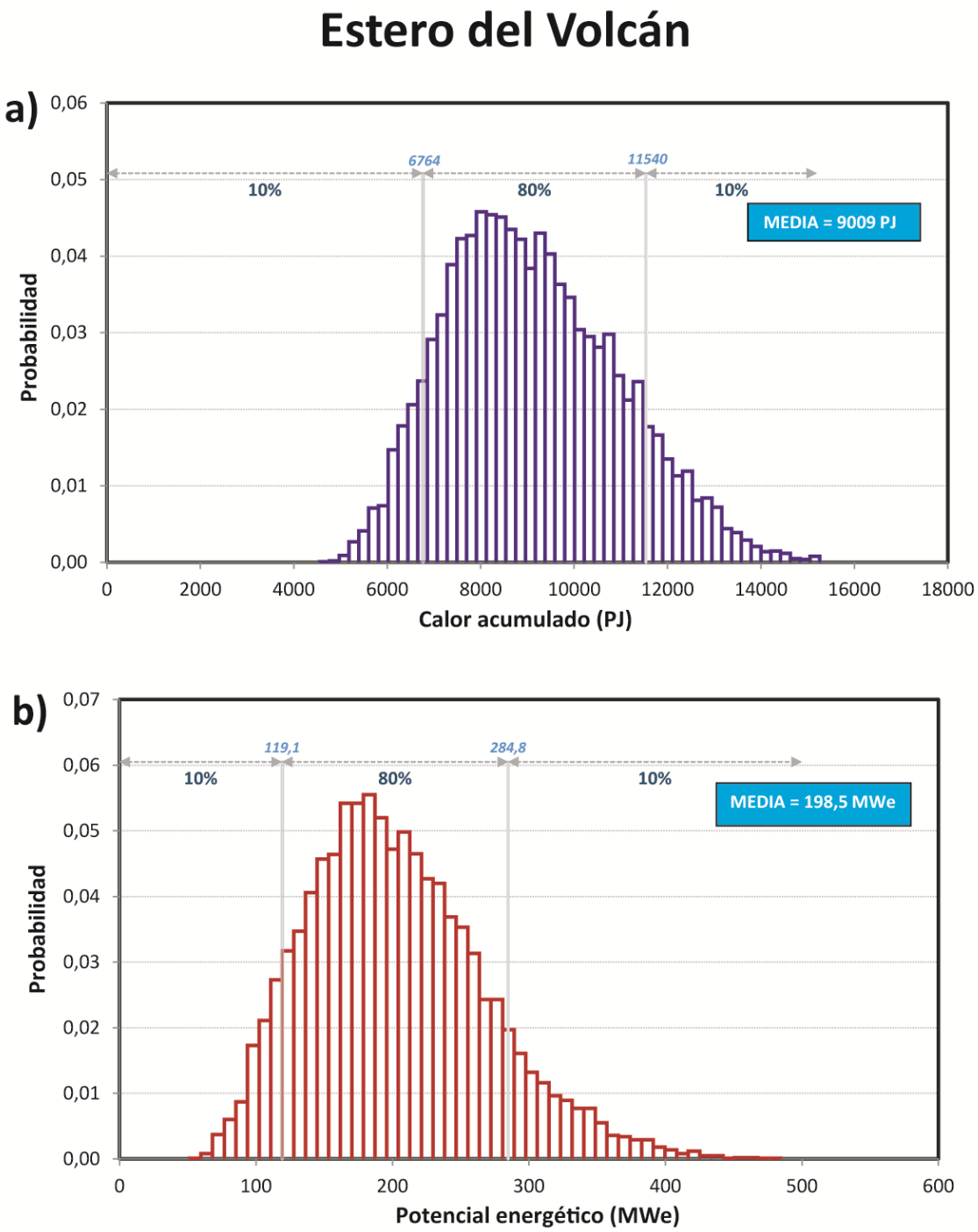

Figura VII-11: Distribuciones de frecuencia para el cálculo de calor almacenado (a) y potencial energético (b) en el área Estero del Volcán. Se reporta los valores de los percentiles 10 y 90, al igual que la media.

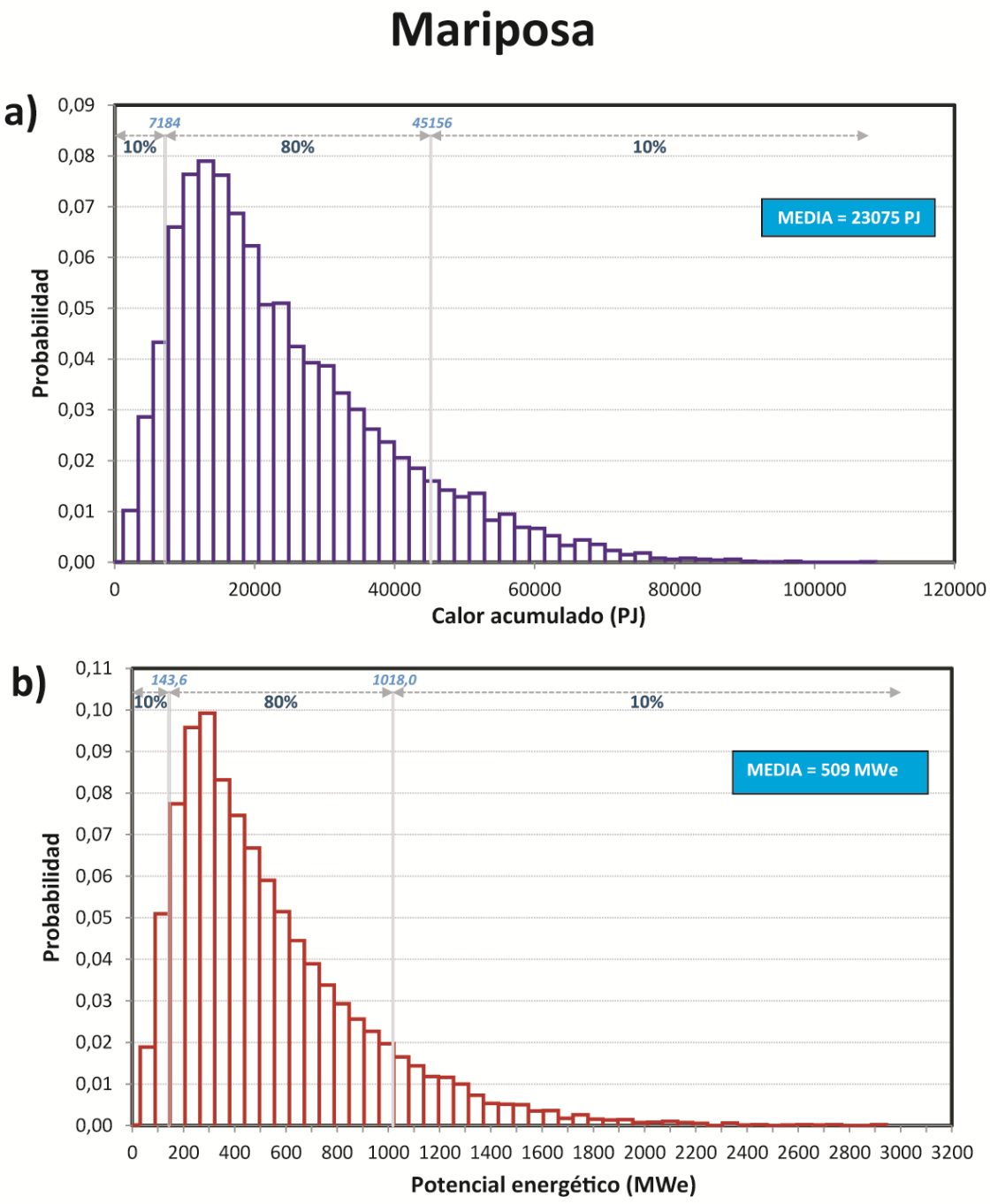

Figura VII-12: Distribuciones de frecuencia para el cálculo de calor almacenado (a) y potencial energético (b) en el área Mariposa. Se reporta los valores de los percentiles 10 y 90, al igual que la media.

BIBLIOGRAFÍA

AGEG,. (2010). Code for geothermal resources and reserves reporting. 2nd Edition. Australian Geothermal Energy Group – Geothermal Code Committee.

Aravena, D. (2012). Desarrollo de metodología para estimación de potencial geotérmico explotable en la región del Maule, Zona Volcánica Sur, Chile. Memoria para optar al título de Geólogo. Departamento de Geología, Universidad de Chile.

Astaburuaga, D. (2014). Evolución estructural del límite Mesozoico-Cenozoico de la Cordillera Principal entre 35°30´Y 36°S, Región del Maule, Chile.

Análisis structural del sector occidental de la Faja Plegada y Corrida de Malargue en el área de Valle Grande, región del Maule. Chile (35º23'S). Memoria para optar al título de Geólogo. Departamento de Geología, Universidad de Chile.

Brondial Y. (2005). Commercialization of Acidic Geothermal Wells by pH Buffering. Asian Journal of Energy and Environment, 6(03), 175-185.

Droguet, B. (2012). Alteración hidrotermal en el campo geotérmico del sistema volcánico Tinguiririca, VI Región, Chile. Memoria para optar al título de Geólogo. Departamento de Geología, Universidad de Chile.

Clavero, J., C. Pineda, C. Mayorga, A. Giavelli, I. Aguirre, S. Simmons, S. Martini, J. Soffia, R. Arriaza, E. Polando and L. Achurra (2011). Geological, Geochemical, Geophysical and First Drilling Data from Tinguiririca Geothermal Area, Central Chile. Geothermal Resources Council Transactions (GRC). San Diego, California, Geothermal Resources Council. 35: 731-734.

Cembrano, J. and L. Lara (2009). The link between volcanism and tectonics in the southern volcanic zone of the Chilean Andes: A review. Tectonophysics 471(1-2): 96-113.

Craw, D., Koons, P. O., Horton, T. & Chamberlain, C. P. (2002). Tectonically driven fluid flow and gold mineralisation in active collisional orogenic belts: comparison between New Zealand and western Himalaya. Tectonophysics, 348, 135–153.

Droguet B. (2012). Alteración hidrotermal en el campo geotérmico del sistema volcánico Tinguiririca, VI Región, Chile. Memoria para optar al título de Geólogo. Departamento de Geología, Universidad de Chile.

Ehlers TA (2005) Crustal thermal processes and the interpretation of thermochronometer data. Rev Mineral Geochem 58:315-350.

Farías M., Charrier R. et al. (2008). Late Miocene high and rapid surface uplift and its erosional response in the Andes of central Chile (338–358S). Tectonics, 27, TC1005, http://dx.doi.org/10.1029/2006TC002046.

Giggenbach, W.F. (1997), The origin and evolution of fluids in magmatic-hydrothermal systems, in Barnes, H.L., ed., Geochemistry of hydrothermal ore deposits, 3rd edition: New York, John Wiley, p. 737-796.

González-Ferrán O (1995) Volcanes de Chile. Instituto Geográfico Militar, Santiago Militar, 639 p. Santiago

Goff, F. and C. J. Janik (2000). Geothermal Systems. Encyclopedia of Volcanoes. H. Sigurdsson, Houghton, B., McNutt, S., Rymer, H., and Stix, J. San Diego, CA, Academic Press: 817-834.

Gupta, H. and S. Roy (2007). Chapter 4 - Geothermal systems and resources. Geothermal Energy. Amsterdam, Elsevier: 49-59.

Hamza V. M. and M. Muñoz (1996). Heat flow map of South America. Geothermics 25(6): 599-621.

Hauser A. (1997). Catastro y caracterización de las fuentes de aguas minerales y termales de Chile Santiago, Chile, Servicio Nacional de Geología y Minería (SERNAGEOMIN). Boletín 50: 70 p.

Hickson, C. J., F. Ferraris, C. Rodriquez, G. Sielfeld, R. Henriquez, T. Gislason, J. Selters, D. Benoit, P. White, J. Southon, G. Ussher, C. J., A. Smith, B. Lovelock, J. Lawless, P. Quinliven, L. Smith and R. Yehia (2011). The Mariposa Geothermal System, Chile Geothermal Resources Council Transactions (GRC). San Diego, California, Geothermal Resources Council. 35: 817-825.

Hochstein M. P. and Browne P. R. L. (2000). Surface manifestations of geothermal systems with volcanic heat sources, in Encyclopedia of Volcanoes, edited by H. Sigurdsson, pp. 835-865, Academic Press, San Diego.

HotRock (2011). Hot Rock Announces Maiden Geothermal Resource in Chile [en línea] http://www.asx.com.au/asxpdf/20110725/pdf/41zy3dttdyg5zw.pdf [consulta : 31 Noviembre 2014].

Koons, P.O. and Craw, D. (1991). Evolution of fluid driving forces and composition within collisional orogens. Geophys. Res. Lett. 18, 935– 938.

Lund, J., Freeston, J., Boyd, T., (2005). World-Wide Direct Uses of Geothermal Energy 2005 In: Proceedings of the World Geothermal Congress 2005, Antalya, Turkey, 24-29 April 2005.

McCaig, A.M., Wayne, D.M., Marshall, J.D., Banks, D., Henderson, I. (1995). Isotopic and fluid inclusion studies of fluid movement along the Gavarnie Thrust, central Pyrenees: reaction fronts in carbonate mylonites. Am. J. Sci. 295, 309– 343.

Muffler L.P.J. and Cataldi R. (1978). Methods for regional assessment of geothermal resources: Geothermics, v. 7, p. 53-89.

Muñoz M., Charrier R., Maksaev V., Fanning C.M., Deckart, K. (2009). New geochronological data on Neogene-Quaternary intrusive rocks from the high Andes of central Chile (33º45'-34º30'S). Actas XII Congreso Geológico Chileno. Santiago.

Pritchard ME, Jay JA, Aron F, Henderson ST, Lara LE (2013) Subsidence at southern Andes volcanoes induced by the 2010 Maule, Chile earthquake. Nature Geosci 6(8): 632-636.

Radic, J. P. (2010) Informe inédito. Energía Andina.

Rivera E.S., Sequeira H.G, Ruiz O.V. (2000). Commercial Production of Acid Wells at the Miravalles Geothermal Field, Costa Rica. Proceedings of the World Geothermal Congress 2000, Kyushu-Tohoku, Japan, May 28-June 10, 2000.

Romero N. (2011). Consumo de energía a nivel residencial en Chile y análisis de eficiencia energética en calefacción. Memoria para optar al título de Ingeniero Civil. Departamento de Geología, Universidad de Chile.

Sanchez, D.R., Herras, E.B., Siega, F.L., Salonga, N.D., Nogara, J.B. and San, B.G. (2001). Evaluation of NaOH injection into Acid Wells of Leyte Geothermal Production Field and Mindanao I Geothermal Project : The Case of MG 9D and KN2DWells. Proceedings of the 22nd Annual PNOC-EDC Geothermal Conference, 13-14 March 2001, Makati City, Philippines.

Sepúlveda F. (2005). El sistema geotérmico de Cordón Caullet, Sur de Chile: caracterización geológica y geoquímica. Tesis de Ph.D., Departamento de Geología, Universidad de Chile. 191 p. Santiago.

Soffia (2004). Perspectivas de Desarrollo de la Energía Geotérmica en Chile. En: Seminario Latinoamericano sobre energías renovables: Hacia la Conferencia Mundial de Bonn – 2004. Programa Chile Sustentable. 93–100. M. [en línea] http://www.archivochile.com/Chile_actual/patag_sin_repre/06/chact_hidroay-6%2000011.pdf.

Tapia, F. (2010). Análisis structural del sector occidental de la Faja Plegada y Corrida de Malargue en el área de Valle Grande, región del Maule. Chile (35º23'S). Memoria para optar al título de Geólogo. Departamento de Geología, Universidad de Chile.

Williams, C.F., Reed, M.J. and Mariner, R.H. (2008). A review of methods applied by the US Geological Survey in the assessment of identified geothermal resources. US Geological Survey Open File Report 2008-1296.

CAPÍTULO VIII

CONCLUSIONES

En el presente trabajo se realizó un amplio estudio geoquímico de gases y aguas desde las distintas manifestaciones termales emitidas por los volcanes Tupungatito y Planchón-Peteroa, y desde las diferentes áreas geotermales localizadas a lo largo de la Cordillera Principal de Chile Central. Estos datos geoquímicos fueron evaluados con el objetivo de determinar el origen y naturaleza de las manifestaciones termales localizadas en la región, así lograr una identificación general de: (i) los factores y procesos geoquímicos y termodinámicos que actúan sobre las manifestaciones termales, (ii) los distintos subsistemas presentes a lo largo de la zona, (iii) los procesos geotectónicos de escala regional y local que controlan las características físicas, químicas e isotópicas composicionales de las emisiones de la zona de estudio, y (iv) las áreas más prometedoras para la explotación de los recursos geotermales en Chile Central.

En términos globales, el origen de los sistemas volcánicos e hidrotermales de la región está íntimamente relacionado a la subducción de la placa de Nazca bajo el continente Sudamericano, la cual es responsable de: (i) el magmatismo de arco (*Hildreth y Moorbath 1988*), y en consecuencia de la transferencia de masa y calor desde las cámaras magmáticas hacia la superficie permitiendo el desarrollo de los sistemas volcánicos e hidrotermales del tipo ígneo (*Goff y Janik 2000*); así como de (ii) la orogénesis en la zona (*Farías et al. 2010*), cuya consecuencia directa es la actividad hidrotermal dominada por fluidos meteóricos impulsados por los significativos gradientes topográficos que caracterizan los Andes de Chile Central (i.e. sistemas hidrotermales del tipo tectónicos; *Goff y Janik 2000*). Bajo este contexto, la naturaleza de los sistemas volcánicos e hidrotermales de los Andes de Chile Central está controlada por diferencias E-O y/o N-S en la configuración geotectónica de la corteza continental superior (ej. litología, topografía, arquitectura de las estructuras, tipo de deformación cortical; *Cembrano y Lara 2009; Farías et al. 2010*), las cuales son responsables de: (i) diferencias en los tipos de fluidos primarios involucrados en la alimentación de las manifestaciones termales superficiales, (ii) diferencias en los procesos físico-químicos que afectan a los fluidos mientras circulan por la corteza, y

(iii) de la forma y orientación de los reservorios magmáticos e hidrotermales de la zona.

Si bien los sistemas volcánicos e hidrotermales de los Andes de Chile Central comparten procesos comunes en su origen y naturaleza, la abundancia relativa de las especies constituyentes de los fluidos emitidos desde estos sistemas, así como los procesos físicos-químicos que afectan a los fluidos, presentan importantes diferencias.

VIII.1 SISTEMAS VOLCÁNICOS

Los sistemas volcánicos con actividad termal (Tupungatito y Planchón-Peteroa) están caracterizados por la presencia de fumarolas, suelos humeantes y lagunas cratéricas híper-ácidas (pH<2) e híper-salinas (TDS<35,000 mgL^{-1}) en sus cumbres. Este tipo de manifestaciones termales son típicas de volcanes donde el sistema meteórico actúa como condensador de los gases ácidos y el calor liberado desde un reservorio magmático-hidrotermal activo (ej. *Brantley et al. 1993; Pasternack y Varekamp 1997*; *Varekamp et al. 2000*). Lo anterior es concordante con las características químicas e isotópicas de los fluidos fumarólicos emitidos por dichos volcanes, donde se evidencian contribuciones variables de origen magmático (SO_2, HCl y HF), hidrotermal (H_2S, H_2 y CH_4), y meteórico (Ar, Ne y N_2/Ar<90). La presencia de cantidades comparables de: (i) alquenos (C_2H_4, C_3H_6 y C_4H_8) y furano (C_4H_4O), formados en condiciones oxidantes y bajo temperaturas relativamente altas (*Capaccioni et al. 1995*), y (ii) compuestos aromáticos (C_6H_6 y C_7H_8) y tiofeno (C_4H_4S), producidos por reacciones catalíticas favorecidas en condiciones reductoras y de menor temperatura (*Tassi et al. 2010*), corroboran que las emisiones gaseosas de los volcanes Tupungatito y Planchón-Peteroa son el resultado de la interacción de fluidos magmáticos con un acuífero hidrotermal limitado, el cual no es capaz de reducir todas las especies formadas en condiciones oxidantes.

Las razones de N_2/Ar (<1500) y $^3He/^4He_{medido}/^3He/^4He_{aire}$ (R/R_a<7.11), al igual que la composición isotópica del vapor de H_2O emitido por estos volcanes – la cual es similar a la del agua andesítica (*Taran 1989; Giggenbach 1992*) – relaciona directamente el origen de los fluidos fumarólicos de ambos volcanes con la deshidratación del slab y la consecuente fusión parcial del manto astenosférico. El aumento de la razón R/R_a junto con el incremento en la composición isotópica de $\delta^{13}C$-CO_2 en las fumarolas del volcán Planchón-Peteroa (7.11R_a y -2.02 ‰ V-PDB, respectivamente) en comparación a las del volcán Tupungatito (6.09R_a y -5.31 ‰ V-PDB, respectivamente), es consistente con lo reportado por investigaciones previas

acerca de la geoquímica de los productos volcánicos holocenos en el arco de Chile Central (*Futa y Stern 1988; Hildreth y Moorbath 1988; Stern 1988, 1991*). A contenidos de SiO_2 similares, tanto las concentraciones de K, Rb, Sr, Ba, La, Th y U, como la razón de los elementos incompatibles vs. compatibles (ej. $^{87}Sr/^{86}Sr$, $^{143}Nd/^{144}Nd$, Rb/Cs, La/Yb, K/La, Rb/La, Ba/La, Hf/Lu) disminuyen de norte a sur, indicando una mayor contribución mantélica respecto a la contribución cortical en la génesis de los magmas hacia el sur.

Los antecedentes estudiados indican que el aumento relativo de la contribución mantélica en la generación de los magmas hacia el sur, es en gran medida una característica resultante de diferencias en la configuración del margen de subducción y la litósfera continental a lo largo de Chile Central (*Kay et al. 2005*). Así por ejemplo, *López-Escobar et al. (1977), Stern (1988, 1991)* y *Tormey et al. (1991)* postularon que esta signatura cortical sería el resultado conjunto de: (i) una disminución del grado de fusión parcial del manto astenosférico como consecuencia de un slab más frío hacia el norte (Figura II-2); y (ii) a un incremento relativo del material cortical subductado en la región mantélica causado por un menor volumen de material mantélico en la cuña astenosférica (Figura II-3 y II-4). Sin embargo, y tal como fue discutido en el Capítulo IV, pareciera que variaciones en la edad y el estado termal de la placa de Nazca, al igual que en la composición y volumen de material subductado, tienen una influencia menor en la composición isotópica de He y $\delta^{13}C\text{-}CO_2$ de los fluidos fumarólicos a lo largo de Chile. Esto es debido a que las fumarolas de los volcanes chilenos pertenecientes a la Zona Volcánica Central (ej. Alitar, Lastarria, Lascar, Irrupucuntu, Olca, Putana, Tacora; *Tassi et al. 2009; Aguilera et al. 2011; Capaccioni et al. 2011; Tassi et al. 2011*) presentan una composición isotópica de He y $\delta^{13}C\text{-}CO_2$ similar a las medidas en los volcanes Tupungatito y Planchón-Peteroa, aun cuando tanto la edad y estado termal del slab (*Grevemeyer et al. 2003; Ramos et al. 2004*), como el volumen y tipo de material subductado (*von Huene y Scholl 1991; Strand 1995; Contreras-Reyes et al. 2010*) difieren considerablemente respecto a los reportados para la ZVS-N y –T (Capítulo II). Por el contrario, las proporciones relativas de gases hidrotermales y magmáticos involucrados, una característica peculiar de cada volcán que depende de su estado de actividad y del patrón de circulación de los fluidos en la litósfera continental (ej. *Delmelle y Stix 2000*), pareciera ser el principal responsable de las diferencias en la composición isotópica de He y $\delta^{13}C\text{-}CO_2$ de las fumarolas volcánicas en los Andes de Chile Central. Lo anterior se sustenta en que el incremento de los valores de R/R_a y $\delta^{13}C\text{-}CO_2$ reportados para las fumarolas del volcán Planchón-Peteroa vs. a las del volcán Tupungatito está acompañado por: (i) un incremento de

las concentraciones de SO_2, HCl, y HF, (ii) un aumento del estado de oxidación (disminución de los valores de $\log[H_2/H_2O]$ desde -3 a -5) y de la temperatura de equilibrio (de 220° a >300°C) de los fluidos en sus respectivos reservorios magmático-hidrotermales, y (iii) un cambio en las fases fluidas en equilibrio que caracterizan los reservorios magmático-hidrotermales que alimentan las descargas fumarólicas superficiales, dominado por líquido en el volcán Tupungatito a uno dominado por vapor+líquido en el volcán Planchón-Peteroa.

Si bien la marcada signatura magmática evidenciada por el Planchón-Peteroa podría ser sólo un episodio puntual debido al ciclo eruptivo que afectó a este volcán durante el desarrollo de la tesis (Capítulo V), tanto la cantidad de eventos eruptivos históricos que ha experimentado dicho volcán (~30), como el volumen de material ígneo asociado a dichas erupciones (IEV≤3), son mayores que lo reportado para el volcán Tupungatito (>25 y IEV<3, respectivamente; *Casertano 1963; González-Ferrán 1995; Naranjo et al. 1999; Naranjo y Haller 2002; Petit-Breuilh 2004*). Lo anterior sugiere la existencia de mecanismos que facilitan la transferencia de masa y energía desde la cámara magmática hacia la superficie en el volcán Planchón-Peteroa respecto al volcán Tupungatito. Una observación clave para entender los procesos que intervienen en el ascenso diferencial de fluidos magmáticos observado en ambos volcanes, está dado por la orientación (NNE-SSO) de la subsidencia (<15 cm) que afectó al volcán Planchón-Peteroa y sus alrededores (Figura V-9a) a semanas de haber ocurrido el terremoto del Maule (8.8 M_W 27F-2010; *Pritchard et al. 2013*).

Tal como fue explicado en los Capítulos II y V, el volcán Planchón-Peteroa junto a los otros volcanes pertenecientes a la ZVS-T, se encuentran emplazados a lo largo del sistema de falla inversa El Fierro, el cual está favorablemente orientado (NNE-SSO) respecto al campo de estrés presente a lo largo de la ZVS-T (σ_{Hmax}~36°; *Cembrano y Lara 2009*). Lo anterior permite un desplazamiento dextral del antearco a lo largo de su traza (Figura II-5). De esta manera, la orientación de la subsidencia reportada por *Pritchard et al. (2013)* reflejaría la forma del reservorio magmático e hidrotermal hospedado en la estructura volcánica del Planchón-Peteroa (Figure V-9b), debido a que los fluidos magmáticos serían transportados verticalmente (paralelo a σ_2) a lo largo de grietas tensionales de rumbo NNE-SSO (*Sibson 2004; Cox 2010*). Dichas grietas serían generadas a presiones hidro- a lito-estáticas producto de la deformación de rumbo dextral imperante al sur del oroclino del Maipo (ej. *Cembrano y Lara 2009*). Por el contrario, el ascenso de fluidos magmáticos en el volcán Tupungatito – al igual que en los otros volcanes pertenecientes en la ZVS-N (Capítulo II) – estaría limitado, debido a que dicho ascenso sólo ocurriría cuando la presión de fluido en los

reservorios magmático-hidrotermal supera la presión lito-estática (*Sibson 2004; Cox 2010*). Lo anterior ocurre debido a que los volcanes de la ZVS-N se encuentran emplazados a lo largo de fallas inversas de alto ángulo (>60°) las cuales se encuentran desfavorablemente orientadas (rumbo N-S) respecto al campo de estrés compresivo (σ_{Hmax}~10°) dominante al norte del oroclino del Maipo (Figura II-5; *Cembrano y Lara 2009*).

Es importante notar que rotaciones en el tensor de esfuerzos corticales, relacionados por ejemplo a una extensión cosísmica en el arco, también puede inducir un ascenso abrupto de fluidos magmáticos hacia la superficie. Este ascenso ocurriría siempre y cuando el vector de máxima extensión sea perpendicular al rumbo de las fallas que controlan espacialmente los reservorios magmático-hidrotermales (ej. *Lara et al., 2004*). El ciclo eruptivo del volcán Planchón-Peteroa durante el 2010 y 2011 (Capítulo V), junto con la subsidencia que afectó a diferentes sistemas volcánicos e hidrotermales de la ZVS-T (ej. Caldera del Atuel, Tinguiririca, Planchón-Peteroa, Calabozos) posterior al terremoto del Maule (8.8 M_W 27F-2010), parece ser un claro ejemplo de dicho mecanismo (*Pritchard et al. 2013*).

VIII.2 SISTEMAS HIDROTERMALES

Las variaciones regionales de los tipos de manifestaciones termales no volcánicas (ej. manantiales fríos y calientes, piscinas burbujeantes y de barro, fumarolas), así como en el contenido relativo de los principales aniones (Cl^-, HCO_3^-, SO_4^{2-}) y cationes (Na^+, K^+, Ca^{2+}, Mg^{2+}) de las aguas termales, apuntan a la existencia de tres dominios hidrotermales a lo largo de los Andes de Chile Central. En el dominio Oeste de la Cordillera Principal (CPO) las aguas termales son emitidas desde manantiales fríos y calientes (T<32°C) caracterizados por un contenido total de sólidos disueltos (TSD) menor a 700 mgL^{-1}, un pH neutro a alcalino, y una composición química variable entre Ca-$HCO_3(SO_4)$ y Na-$HCO_3(SO_4)$. En el área Baños Apoquindo, por el contrario, se descargan aguas Ca-Cl con una salinidad que alcanzan los 1700 mgL^{-1}. Estas manifestaciones termales se encuentran espacialmente asociadas al sistema de fallas San Ramón-Pocuro, el cual deforma rocas volcánicas y volcanoclásticas andesíticas (*Farías et al. 2010; Giambiagi et al. 2014*).

El dominio Central de la Cordillera Principal (CPC) se caracteriza por aguas termales de composición Na-Ca-Cl y Ca-Cl emitidas desde manantiales calientes (T<45,7°C). Estas aguas son levemente salinas (TSD<13.500 mgL^{-1}) y de pH neutro, y se encuentran espacialmente asociadas a fallas inversas de vergencia Oeste que

deforman las rocas volcánicas y volcanoclásticas andesíticas asociadas a las formaciones Abanico y Farellones. Por el contrario, el dominio Este de la Cordillera Principal (CPE), caracterizado por un basamento sedimentario marino-continental (*Farías et al. 2010; Giambiagi et al. 2014*), hospeda aguas termales salinas (TSD<57.000 mgL^{-1}) con un pH neutro a ácido (>2) y una composición variable entre Na-Cl, Ca-HCO_3, Na-HCO_3, Ca-SO_4 y ácido-sulfatada. Estas aguas son descargadas desde manantiales calientes, piscinas burbujeantes y piscinas de barros (T<94,5°C), las que espacialmente se encuentran asociadas a los volcanes Cuaternarios y a las fallas inversas de las fajas plegadas y corridas de Aconcagua y Malargüe (*Farías et al. 2010; Giambiagi et al. 2014*).

El contenido de δD y $\delta^{18}O$ en las aguas termales sugiere que los sistemas hidrotermales de Chile Central son alimentados principalmente por agua meteórica proveniente del derretimiento de la nieve que se acumula entre los 2000 y 3000 m s.n.m. en la CP (Capítulo VI). No obstante, los gases fumarólicos presentan valores de δD y $\delta^{18}O$ que manifiestan una adición de fluidos desde una fuente magmática (<5%). Lo anterior también es sugerido por el estado redox de los gases (R_H entre -4.9 y -2.5), así como la presencia de He (R/R_a < 6) y CO_2 ($\delta^{13}C$-CO_2 entre -8,9 y -5,72 ‰ V-PDB) de origen mantélico. La interacción de gases de origen mantélico con las secuencias marinas ricas en carbonatos y materia orgánica que caracteriza el basamento de la CPE explicaría los amplios valores de $\delta^{13}C$-CO_2 (-14.3 y -6.03‰ V-PDB) y R/R_a (0.47 y 6.2) medidos tanto en los gases emitidos desde las piscinas burbujeantes como en los gases disueltos.

La distribución regional del contenido de pCO_2 en las aguas termales se encuentra bien correlacionada con un aumento tanto de la temperatura de emisión de los fluidos, como en los valores promedio del flujo calórico (<220 mW/m^2) hacia el Este. Esta tendencia parece relacionarse directamente a la ubicación del arco volcánico y de los sedimentos marinos ricos en carbonatos, y en consecuencia es el resultado de una contribución desde ambas fuentes hacia el sistema meteórico de circulación profunda que alimenta los sistemas hidrotermales emplazados en la CPE (ej. *Goff y Janik 2000*). Según lo analizado en el Capítulo VI, al norte del oroclino del Maipo el miembro extremo magmático no supera el 2% (carbonatos + materia orgánica >98%), mientras que al sur del oroclino la contribución magmática en las manifestaciones termales alcanza cerca del 35% (contribución sedimentaria ~65%).

A pesar de estar localizadas en la parte central de la CP, el origen de las aguas cloruradas salinas pertenecientes a este dominio también radica en la interacción de

las secuencias sedimentarias y aguas meteóricas de origen profundo. De acuerdo a lo analizado en el Capítulo VI, estas aguas derivan de un miembro parental híper-salino cuya concentración de Cl calculada (~17.000 mgL^{-1}) es similar al de las aguas Na-Cl localizadas en la CPE a latitudes similares (ej. Baños Morales, Baños Colina, Puente de Tierra). Estas aguas Na-Cl serían transportadas desde la CPE a través de las fallas inversas de vergencia Oeste que deforman la CPC (*Farías et al. 2010; Giambiagi et al. 2014*). Lo anterior explicaría la presencia de He mantélico en los fluidos de las Termas de Cauquenes (R/R_a~1.56; *Hilton et al. 1993*). La interacción de estas aguas Na-Cl salinas con las rocas volcánicas máficas de la CPC explicaría el componente Ca-Cl que caracteriza las aguas hidrotermales del dominio Central (ej. *Mariner et al. 1993*). Las descargas Ca-Cl en el área Baños de Apoquindo tendrían un origen similar, lo que es consistente con la mayor dilución que estos fluidos experimentan en su tránsito desde la CPE (94%), respecto a la dilución estimada para las descargas de la CPC (89%; Capítulo VI).

El resto de las manifestaciones termales de la CPO se encuentran desconectadas del sistema hidrotermal imperante en la CPE. Lo anterior queda en evidencia por la disminución del contenido de pCO_2 hacia el sur (hasta $10^{-5,6}$ bar) a pesar de que el flujo calórico (*Hamza y Muñoz 1996*) y las temperaturas de descarga de las manifestaciones aumentan en la misma dirección. Esta variación espacial estaría relacionada a un aumento de los tiempos de residencia de los fluidos meteóricos dentro del sistema de fallas San Ramón-Pocuro hacia el sur, lo que favorecería el proceso de interacción agua-roca en la zona de falla (ej. *Marini et al. 2000*). Dicha interacción ocurriría en ausencia de una fuente de CO_2 (magmática y/o sedimentaria), lo que explicaría el carácter maduro de las aguas Na-HCO_3 y Na-SO_4 en las áreas Panimávida y Quinamávida, además de la baja salinidad y pH alcalino de dichas descargas hidrotermales.

A lo largo del arco volcánico y de los tres dominios hidrotermales de Chile Central (CPO, CPC y CPE), el oroclino del Maipo representa un límite importante para las condiciones químicas y físicas de los fluidos termales. Suponiendo que la composición química e isotópica de estos fluidos se pudiera describir como una mezcla entre (i) fluidos de origen profundos (hidrotermales y/o magmático-hidrotermales) y (ii) fluidos meteóricos someros, tanto las características geoquímicas de los fluidos termales como los patrones de flujo calórico indican que la contribución de fluidos profundos disminuye abruptamente al norte del oroclino del Maipo. En este trabajo se concluye que la interacción de las variaciones topográficas de la CP, junto con la variación en el rumbo de las fallas inversas y el cambio del campo de estrés que

deforma actualmente a la CP al norte y sur del oroclino del Maipo (*Cembrano y Lara 2009; Farías et al. 2010*), son los principales responsables del aumento relativo en la contribución de fluidos profundos hacia el sur.

Al norte del oroclino, la mayor carga hidráulica regional creada por las mayores diferencias topográficas y la menor permeabilidad vertical de las zonas de fallas – debido a la interacción entre fallas inversas de alto ángulo pobremente orientadas (rumbo N-S) respecto al campo de estrés compresivo (de orientación E-O) – suprime parcialmente la advección vertical de fluidos profundos y/o la convección de agua meteórica en las zonas de fallas (*López y Smith 1995; 1996*), dando como resultados fluidos con una fuerte signatura meteórica. Por el contrario, al sur del oroclino, la menor carga hidráulica regional generada por la disminución de la topografía, así como la mayor permeabilidad vertical de las fallas – debido a su orientación favorable (rumbo NNE-SSO) respecto a la cinemática de deformación transcurrente de rumbo dextral (de orientación NNE-SSO) que afecta actualmente la CP – genera condiciones favorables para la formación de celdas convectivas de agua meteórica y/o la advección vertical de fluidos profundos (magmáticos y/o hidrotermales) [*López y Smith 1995; 1996*], dando como resultado manifestaciones termales de mayor temperatura, y bajo ciertos casos, fluidos geoquímicamente maduros.

VIII.3 IMPLICANCIAS DEL ESTUDIO

Este estudio dispone de una gran base de datos geoquímicos e isotópicos de los fluidos provenientes de los sistemas volcánicos e hidrotermales de la región Andina de Chile Central, sentando las bases para iniciar el monitoreo geoquímico en los diversos sistemas volcánicos ya estudiados, especialmente de aquellos sistemas con mayor actividad (Planchón-Peteroa, Tupungatito, San José, Tinguiririca). También permite establecer las bases para la evaluación de las características de los reservorios, y por ende, la estimación de la temperatura, forma y de los distintos sistemas hidrotermales presentes en los Andes de Chile Central. Además, permitirá la extensión del estudio global de los sistemas termales de baja entalpía, y por sobre todo, estimar sus potenciales como posibles sitios para el aprovechamiento de la energía termal a nivel local.

Los resultados de esta tesis entregan nuevas herramientas para la prospección de recursos geotermales en los Andes de Chile Central, indicando que al sur del oroclino del Maipo la interacción entre volcanismo y tectónica favorece la existencia de sistemas geotermales de alta entalpía (ej. Calerías, Tinguiririca, Calabozos, Estero del

Volcán, Mariposas) los cuales tendrían que ser considerados para su incorporación a la matriz eléctrica del país debido al promisorio potencial energético estimado para dichos sistemas (desde 168 a 510 MWe; Capítulo VII).

El aprovechamiento directo de los recursos geotérmicos, complementario al uso balneológico, es factible en la totalidad de las manifestaciones termales estudiadas. Este puede ser a través de: calefacción distrital, invernaderos para diversificación de cultivos, procesamiento y secado de alimentos y madera, procesos industriales que requieren calor, mejoramiento de la productividad ganadera, derretimiento de nieve; siendo todas estas ampliamente utilizadas en el mundo (*Lund et al. 2005*). El desarrollo de este tipo de proyecto tiene que estar vinculado a los deseos de desarrollo local de los pobladores que pueden ser beneficiados.

BIBLIOGRAFÍAS

Aguilera F, Tassi F, Darrah T, Moune S, Vaselli O (2012). Geochemical model of a magmatic hydrothermal system at the Lastarria volcano, northern Chile. Bull Volcanology. Bull. Volcanol 74:119–134.

Brantley SL, Agustsdottir AM, Rowe GL (1993) Crater lakes reveal volcanic heat and volatile fluxes. Geol Soc Am Today 3:175–178.

Capaccioni B, Martini M, Mangani F (1995) Light hydrocarbons in hydrothermal and magmatic fumaroles: hints of catalytic and thermal reactions. Bull Volcanol 56:593–600.

Capaccioni B, Aguilera F, Tassi F, Darrah T, Poreda RJ, Vaselli O (2011) Geochemical and isotopic evidences of magmatic inputs in the hydrothermal reservoir feeding the fumarolic discharges of Tacora volcano (northern Chile). J Volcanol Geotherm Res 208:77–85.

Casertano L. (1963). General characteristics of active Andean volcanoes and a summary of their activities during recent centuries. Bulletin of the Seismological Society of America, Vol. 53, Nº6, pp. 1415-1433.

Cembrano, J. and L. Lara (2009). The link between volcanism and tectonics in the southern volcanic zone of the Chilean Andes: A review. Tectonophysics 471(1-2): 96-113.

Contreras-Reyes E, Flueh ER, Grevemeyer I (2010) Tectonic control on sediment accretion and subduction off south-central Chile: Implications for coseismic rupture processes of the 1960 and 2010 megathrust earthquakes. Tectonics 29:1–32.

Cox, S. (2010). The application of failure mode diagrams for exploring the roles of fluid pressure and stress states in controlling styles of fracture-controlled permeability enhancement in faults and shear zones: Geofluids, v. 10, p. 217–233.

Delmelle P, Bernard A, Kusakabe M, Fisher TP, Takano B (2000) Geochemistry of the magmatic-hydrothermal system of Kawah Ijen volcano, East Java, Indonesia. J Volcanol Geotherm Res 97:31–53.

Farías M., Comte D. et al. (2010). Crustal-scale structural architecture in central Chile based on seismicity and surface geology: implications for Andean mountain building. Tectonics, 29, TC3006, http://dx.doi.org/10.1029/2009TC002480.

Futa K. and Stern C.R. (1988). Sr and Nd isotopic and trace element compositions of Quaternary volcanic centers of the southern Andes: Earth and Planetary Science Letters, v. 88, p. 253–263, doi: 10.1016/0012-821X(88)90082-9.

Giambiagi L., Tassara A. et al. (2014). Evolution of shallow and deep structures along the Maipo–Tunuyan transect (33°40′S): from the Pacific coast to the Andean foreland. In: Sepúlveda S. A., Giambiagi L. B., Moreiras S. M., Pinto L., Tunik M., Hoke G. D. y Farías, M. (eds) Geodynamic Processes in the Andes of Central Chile and Argentina. Geological Society, London, Special Publications, 399. http://dx.doi.org/10.1144/SP399.14

Giggenbach WF (1992) Isotopic shifts in waters from geothermal and volcanic systems along margins, and their origin. Earth Planet Sci Lett 113:495–510.

Goff, F. and C. J. Janik (2000). Geothermal Systems. Encyclopedia of Volcanoes. H. Sigurdsson, Houghton, B., McNutt, S., Rymer, H., and Stix, J. San Diego, CA, Academic Press: 817-834.

González-Ferrán O (1995) Volcanes de Chile. Instituto Geográfico Militar, Santiago Militar, 639 p. Santiago

Grevemeyer I, Juan L Diaz-Naveas, Cesar R Ranero, Heinrich W Villinger, Ocean Drilling Program Leg 202 Scientific Party (2003) Heat flow over the descending Nazca plate in central Chile, 32°S to 41°S: observations from ODP Leg 202 and the occurrence of natural gas hydrates. Earth Planet Sci Lett 213:285–298.

Hamza V. M. y M. Muñoz (1996). Heat flow map of South America. Geothermics 25(6): 599-621.

Hildreth W. y Moorbath S. (1988). Crustal contributions to arc magmatism in the Andes of Central Chile: Contributions to Mineralogy and Petrology, v. 98, p. 455–489.

Hilton, D. R., K. Hammerschmidt, S. Teufel and H. Friedrichsen (1993). "Helium isotope characteristics of Andean geothermal fluids and lavas." Earth and Planetary Science Letters 120(3-4): 265-282.

Kay S. M., Godoy E. and Kurtz A (2005). Episodic arc migration, crustal thickening, subduction erosion, and magmatism in the South-Central Andes. Geological Society of America Bulletin 117, 67-88.

Lara, L., Moreno, H., Naranjo, J. (2004). Rhyodacitic fissure eruption in Southern Andes (Cordón Caulle; 40.5°S) after the 1960 (Mw: 9.5) Chilean earthquake: a structural interpretation. Journal of Volcanology and Geothermal Research, 138, 127-138.

López, D. L. and L. Smith (1995). "Fluid Flow in Fault Zones: Analysis of the Interplay of Convective Circulation and Topographically Driven Groundwater Flow." Water Resources Research 31(6): 1489-1503.

López, D. L. and L. Smith (1996). "Fluid flow in fault zones: Influence of hydraulic anisotropy and heterogeneity on the fluid flow and heat transfer regime." Water Resources Research 32(10): 3227-3235.

López-Escobar L., Frey F.A., and Vergara M., (1977). Andesites and high-alumina basalts from the central-south Chile high Andes: Geochemical evidence bearing on their petrogenesis. Contributions to Mineralogy and Petrology, v. 63, p. 199–228.

Lund, J., Freeston, J., Boyd, T., (2005). World-Wide Direct Uses of Geothermal Energy 2005 In: Proceedings of the World Geothermal Congress 2005, Antalya, Turkey, 24-29 April 2005.

Marini, L., G. Ottonello, M. Canepa and F. Cipolli (2000). Water-rock interaction in the Bisagno valley (Genoa, Italy): application of an inverse approach to model spring water chemistry. Geochimica et Cosmochimica Acta 64(15): 2617-2635.

Mariner R.H., Presser T.S., Evans W.C. (1993). Geothermometry and water-rock interaction in selected thermal systems in the Cascade Range and Modoc Plateau, western United States. Geothermics 22, 1-15.

Naranjo J, Haller M, Ostera H, Pesce A, Sruoga P. (1999). Geología y Peligros del Complejo Volcánico Planchón-Peteroa, Andes del Sur (35º15´S), Región del Maule, Chile- Provincia de Mendoza, Argentina. Serv Nac Geol Min, 52

Naranjo J, Haller M (2002). Erupciones principalmente explosivas del volcán Planchón, Andes del sur (35º15'S). Rev Geol Chile 29:93-113

Naranjo J (2012) Principales etapas evolutivas holocenas del volcán Planchón y su reactivación relacionada al megasismo del 27 de Febrero de 2010. XIII Chilean Geologic Congress 5-9 August, Antofagasta, Chile, pp. 440–441

Pasternack GB, Varekamp JC (1997) Volcanic lake systematics I. Physical constraints. Bull Volcanol 58:528–538.

Pritchard ME, Jay JA, Aron F, Henderson ST, Lara LE (2013) Subsidence at southern Andes volcanoes induced by the 2010 Maule, Chile earthquake. Nature Geosci 6(8): 632-636.

Petit-Breuilh M. E. (2004).La historia eruptiva de los volcanes hispanoamericanos (siglos XVI al XX). Serie Casa de los Volcanes Nº8, Exmo. Cabildo Insular de Lanzarote, España, 431 p.

Ramos VA, Cristallini E, Introcaso A (2004) The Andean thrust system latitudinal variations in structural styles and orogenic shortening. AAPG Spec Vol Memoir 82: Thrust tectonics and hydrocarbon systems, pp. 30–50.

Sibson R.H. (2004), "Frictional mechanics of seismogenic thrust systems in the upper continental crust: implications for fluid overpressures and redistribution," American Association of Petroleum Geologists Memoir, 82, 1-17.

Stern, C.R. (1989). Pliocene to present migration of the volcanic front, Andean Southern Volcanic Zone: Revista Geológica de Chile, v. 16, p. 145–162.

Stern C.R. (1991). Role of subduction erosion in the generation of Andean magmas: Geology, v. 19, p. 78–81, doi:10.1130/0091-7613(1991)0192.3.CO:2.

Stern C., H. Moreno, L.López-Escobar,J.E. Clavero, L.E. Lara, J.A. Naranjo, M.A. Parada, M.A. Skewes. (2007). Chilean Volcanoes. In: The Geology of Chile. Geological Society of Chile. Pag.156-157.

Strand K (1995) Semmicrostructural analysis of a volcanogenic sediment component in a trench.slope basin of the Chile margin. In: Lewis SD, Behrmann JH, Musgrave RJ, Cande SC (eds) Proceedings of the Ocean Drilling Program, Scientific Results, 141, pp. 169–180.

Taran YA, Pokrovsky B, Esikov A (1989) Deuterium and oxygen-18 in fumarolic steam and amphiboles from some Kamchatka volcanoes: "andesitic waters". Doklady Akademii nauk SSSR 304:440–443.

Tassi F, Aguilera F, Vaselli O, Medina E, Tedesco D, Delgado Huertas A, Poreda R, Kojima S (2009) The magmatic- and hydrothermal-dominated fumarolic system at the Active Crater of Lascar volcano, northern Chile. Bull Volcanol 71:171–183.

Tassi F, Montegrossi G, Capaccioni B, Vaselli O (2010) Origin and distribution of thiophenes and furans in thermal fluid discharges from active volcanoes and geothermal systems. Int J Mol Sci 11:1434–1457.

Tassi F, Aguilera F, Vaselli O, Darrah T, Medina E (2011) Gas discharges from four remote volcanoes (Putana, Olca, Irruputuncu and Alitar) in northern Chile: a geochemical and isotopic survey. Ann Geophys 54:121–136.

Tormey D.R., Hickey-Vargas R., Frey F.A. and López-Escobar L. (1991). Recent lavas from the Andean volcanic front (33 to 42°S): Interpretations of alongarc compositional variations, in Harmon, R.S., and Rapela, C.W., eds., Andean magmatism and its tectonic setting: Geological Society of America Special Paper 265, p. 57–78.

Tormey D.R., Frey F. and López-Escobar L. (1995). Geochemistry of the active Azufre-Plancho-Peteroa volcanic complex, Chile (35°15′S): Evidence for multiple sources and processes in a Cordilleran arc magmatic system: Journal of Petrology, v. 36, p. 265–298.

Varekamp, JC, Pasternack GB, Rowe GL (2000) Volcanic lake systematics II. Chemical constraints. J. Volcanol Geotherm Res 97:161–179.

von Huene R, Scholl DW (1991) Observations at convergent margins concerning sediment subduction, subduction erosion, and the growth of continental crust. Rev Geophys 29:279–316.

ANEXOS

Journal of Volcanology and Geothermal Research 237–238 (2012) 69–80

Contents lists available at SciVerse ScienceDirect

Journal of Volcanology and Geothermal Research

journal homepage: www.elsevier.com/locate/jvolgeores

Contribution of ground surface altitude difference to thermal anomaly detection using satellite images: Application to volcanic/geothermal complexes in the Andes of Central Chile

Francisco J. Gutiérrez [a,*], Martín Lemus [a], Miguel A. Parada [a], Oscar M. Benavente [a], Felipe A. Aguilera [b]

[a] Departamento de Geología, Universidad de Chile; Centro de Excelencia en Geotermia de los Andes (CEGA-FONDAP 15090013), Chile
[b] Departamento de Geología, Universidad de Atacama; Centro de Excelencia en Geotermia de los Andes (CEGA-FONDAP 15090013), Chile

ARTICLE INFO

Article history:
Received 1 December 2011
Accepted 14 May 2012
Available online 1 June 2012

Keywords:
Thermal anomaly detection
Satellite images
Ground surface altitude
Environmental lapse rate
Geothermal manifestations

ABSTRACT

Detection of thermal anomalies in volcanic-geothermal areas using remote sensing methodologies requires the subtraction of temperatures, not provided by geothermal manifestations (e.g. hot springs, fumaroles, active craters), from satellite image kinetic temperature, which is assumed to correspond to the ground surface temperature. Temperatures that have been subtracted in current models include those derived from the atmospheric transmittance, reflectance of the Earth's surface (albedo), topography effect, thermal inertia and geographic position effect. We propose a model that includes a new parameter (K) that accounts for the variation of temperature with ground surface altitude difference in areas where steep relief exists. The proposed model was developed and applied, using ASTER satellite images, in two Andean volcanic/geothermal complexes (Descabezado Grande-Cerro Azul Volcanic Complex and Planchón-Peteroa-Azufre Volcanic Complex) where field data of atmosphere and ground surface temperature as well as radiation for albedo calibration were obtained in 10 selected sites. The study area was divided into three zones (Northern, Central and Southern zones) where the thermal anomalies were obtained independently. K value calculated for night images of the three zones are better constrained and resulted to be very similar to the Environmental Lapse Rate (ELR) determined for a stable atmosphere ($ELR > 7$ °C/km). Using the proposed model, numerous thermal anomalies in areas of ≥ 90 m $\times$ 90 m were identified that were successfully cross-checked in the field. Night images provide more reliable information for thermal anomaly detection than day images because they record higher temperature contrast between geothermal areas and its surroundings and correspond to more stable atmospheric condition at the time of image acquisition.

1. Introduction

Many workers have utilized satellite imagery to identify geothermal anomalies and to better constrain the underground temperature contribution associated with volcanic systems (e.g. Pieri and Abrams, 2004; Pieri and Abrams, 2005; Murphy et al., 2011), geothermal fields (e.g. Watson, 1975; Hellman and Ramsey, 2004; Hellman and Ramsey, 2004; Coolbaugh et al., 2007; Watson et al., 2008) and shear zones (e.g. Srivastava et al., 2009). Current approaches for geothermal anomaly identification (Urai, 2002; Coolbaugh et al., 2007; Murphy et al., 2011) rely a baseline ground surface temperature, provided by satellite imagery (e.g. Advanced Spaceborne Thermal Emission and Reflection Radiometer; ASTER, NASA's Earth Observing System); from this baseline, various external temperature effects maybe corrected for, such as those derived from atmospheric transmittance, reflectance of the Earth's surface (albedo), topographic effects (surface slope effects derived of sun exposure and shadows), thermal inertia and geographic position effect. Previous studies have recognized that atmospheric temperature variations due to altitude may further affect the adequate detection of geothermal anomalies using remote sensing data (e.g. Warner and Chen, 2001; Urai, 2002; Eneva and Coolbaugh, 2009). However, few attempts have been made to incorporate this effect in recent studies (e.g. Urai, 2002). Indeed, this effect is commonly neglected since relatively flat study areas may be selected so as to minimize altitude variations (e.g. Murphy et al., 2011).

In this study, we propose a new model that includes the effect of altitude differences on ground surface temperature to refine thermal anomaly detection in areas with steep relief and significant elevation differences, but lacking dense vegetation coverage, such as volcanic/geothermal centers in the central Chilean Andes. Our aim is to assess and evaluate the role of elevation in thermal anomaly detection in zones with steep relief by using remote sensing analysis.

The first order effect of altitude considered here is that of temperature variations. One well-documented attempt to quantitatively assess this variation was the introduction of the Environmental Lapse

* Corresponding author.
E-mail address: frgutier@ing.uchile.cl (F.J. Gutiérrez).

0377-0273/$ – see front matter © 2012 Elsevier B.V. All rights reserved.
doi:10.1016/j.jvolgeores.2012.05.016

Rate (*ELR*; for example, see Houghton and Cramer, 1951; Jacobson, 2005). The *ELR* describes the rate of decrease of atmospheric temperature with altitude in a stationary troposphere at a given time and position. This effect is caused by the expansion of air as altitude increases and pressure decreases, performing adiabatic work. This work results in lower internal energy of the air, and hence a decrease in temperature. Theoretical calculations of adiabatic dry *ELR* give values about 9.8 °C/km, whereas the measured dry average *ELR* for the lowest 10 km of the atmosphere is 6–7 °C/km (e.g. Houghton and Cramer, 1951; Srivastava, 1987; Danielson et al., 2003). For moist or saturated atmosphere, the theoretical adiabatic *ELR* is 3.6 °C/km. Hence, measurements of *ELR* are usually between 3.6 and 9.8 °C/km and vary depending on radiation, convection and condensation. If *ELR* is higher or lower than these values, the atmosphere becomes unstable or stable, respectively.

This study was carried out in a large area of about 6500 km^2 that comprises two contiguous volcanic complexes of the Southern Andean Volcanic Zone (SAVZ): Planchón-Peteroa-Azufre and Descabezado Grande-Cerro Azul (Fig. 1). These volcanic complexes belong to the widest region of the Central Chilean volcanic arc, where several volcanic structures, craters, lavas flows and thermal manifestations have been recognized (e.g. Grunder et al., 1987 ; Stern, 2004). The studied area exhibits steep relief with elevations that range from about 800 m a. s. l. to 4,107 m a. s. l.

2. Late Pleistocene–Holocene volcanic complexes and related thermal emissions

The Planchón-Peteroa-Azufre Volcanic Complex (PPA) is a group of three Late Pleistocene–Holocene stratocones, aligned in a 6 km long, N15°E belt. From north to south are: Planchón (4,090 m a. s. l.), Peteroa (3,920 m a. s. l.) and Azufre (3,752 m a. s. l.) (Tormey et al., 1995; Naranjo et al, 1999). PPA consists mainly of andesitic to glassy dacitic lava flows, dacitic to rhyodacitic pyroclastic deposits and lahar flow deposits (Tormey et al., 1995). The youngest unit corresponds to a scoria cone and its single andesitic lava flow, formed during the 1937 eruption (Naranjo et al, 1999). Two major subplinian Holocene eruptions (VEI ~3–4) of 7000 and 1500 years BP were recorded (Naranjo and Haller, 2002). Additionally, at least 15 historical eruptions have been detected since 1660, corresponding mainly to phreatic and phreatomagmatic explosions, frequently associated with lahar generation (e.g. phreatomagmatic explosion during February 1991; González-Ferrán, 1995; Naranjo et al., 1999). Recent eruptions (September 2010 and April 2011) have occurred in the westernmost crater, which is nested in the 4 km diameter caldera located at the summit of Peteroa Volcano.

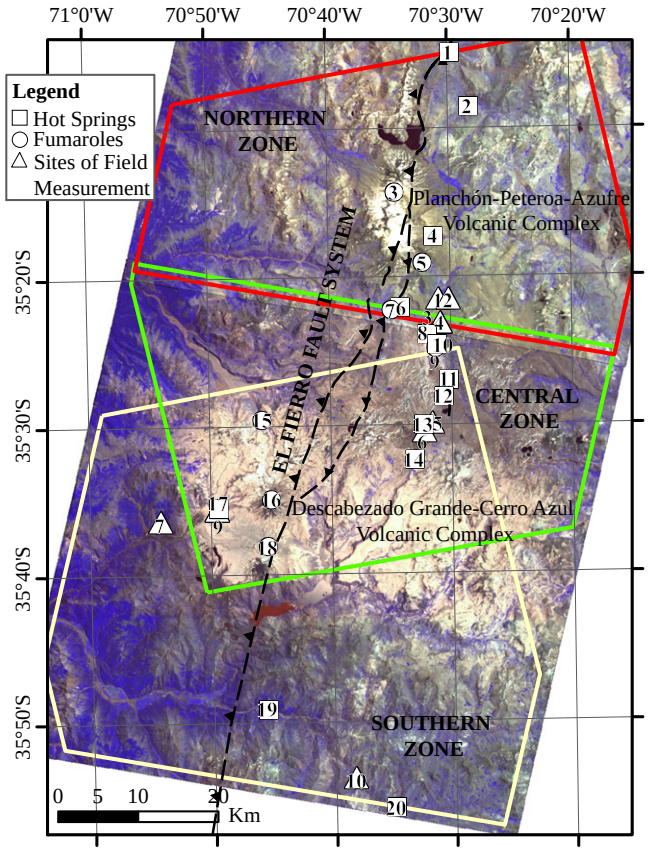

Fig. 1. Radiance satellite image (ASTER 07) of the study area. Main thermal manifestations and sites of field measurements have been numbered as in Tables 1 and 3, respectively. Polygons indicate the Northern, Central and Southern zones.

The Descabezado Grande-Cerro Azul Volcanic Complex (DGCA) is a group of four stratovolcanoes consisting of Descabezado Grande (3,953 m a. s. l.), Cerro Azul (3,788 m a. s. l.), Descabezado Chico (3,276 m a. s. l.) and Calabozos (3,508 m a. s. l.). They consist predominantly of andesite to rhyodacite lava flows and pyroclastic products, although high-alumina basalt to basaltic andesite products dominate the southern part of Calabozos (Grunder and Mahood, 1988). The volcanic edifices have heights from base to summit that vary between 1000 and 1500 m and exhibit steep relief caused by Late Pleistocene–Early Holocene glacial erosion. An explosion crater located at the northern flank of Cerro Azul Volcano named Quizapu originated during the historical plinian eruption in 1932 (Hildreth and Drake, 1992; Stern, 2004; Stern et al., 2007). The eastern part of DGCA is occupied by the Loma Seca Tuff, a series totaling >1000 km^3 of rhyodacitic to andesitic zoned ash flow sheets separated in three units of 0.8, 0.3 and 0.15 Ma (Grunder and Mahood, 1988). The origin of the Loma Seca Tuff has been attributed to Calabozos composite caldera formation (Hildreth et al., 1984).

Mesozoic and Cenozoic units constitute the basement of both PPA and DGCA volcanic complexes. Mesozoic units are mainly exposed in the eastern part of the study area, and correspond to marine and continental sedimentary rocks (Valle Grande, Río Damas, Baños del Flaco, Colimapu and Plan de los Yeuques formations), whereas Cenozoic units correspond to volcanic-continental sedimentary rocks (Abanico-Cura Mallín, Corona del Fraile, Cola de Zorro and Loma Seca formations) and granodiorite plutons (e.g. Haller et al 1985; Grunder et al., 1987; Naranjo et al., 1999).

Geothermal manifestations related to PPA and DGCA complexes (Fig. 1 and Table 1) are located in an area of 100 km^2 and consist of fumarolic fields (Quizapu, Peteroa and Azufre volcanoes, Llolli, Lontué and Puesto Calabozos), crater lakes (Peteroa volcano) and numerous hot springs, boiling-mud and bubbling pools. Water discharges present near-boiling temperatures (88°–92 °C) and three compositional groups of thermal manifestations can be distinguished: (i) chloride hot springs (11,960 ppm > Cl > 330 ppm) with oxide minerals as alteration products (Romeral, San Pedro, Barros Colorado, Médano, Campanario and Puesto Calabozos);(ii) bicarbonate hot springs (1434 ppm > HCO_3 > 69 ppm) with travertine and carbonate deposits (Baños de las Yeguas, Pellejo, Colorado River hot springs, Potrerillo, Tigre Naciente, Aguas Calientes and Descabezado Grande hot springs); and (iii) sulphate waters associated with fumarolic fields (1000 ppm > SO_4) with sulphur precipitation and vuggy silica deposits (Vn Planchón, La Azufrera, Llolli and Lontué fumarlic fields). Hot springs and bubbling pools are aligned in NE–SW and NW–SE trends related to El Fierro fault system (Farías et al., 2010) (Fig. 1).

3. Field methods and data

Solar radiation and atmosphere and ground surface temperatures were measured during two field campaigns (March and April 2010; Fig. 2) in 10 selected sites (complete data list is available in

Table 1
Field data of the thermal manifestations included in this study.

No	Name	UTM-NS	UTM-WE	Elevation m	Maximum T°C	Area m^2
1	Romeral	6116454	363400	1467	6	2
2	San Pedro	6109782	365777	1893	24	400
3	Vn. Planchón	6098941	356550	3440	97	22,500
4	Termas del Azufre	6093503	361373	2492	41	14,194
5	La Azufrera	6090190	360010	2743	88	364,108
6	Baños de la Yegua	6084619	357294	1981	54	2016
7	Llolli	6084259	356168	1972	94.5	111,374
8	El Pellejo	6081287	360693	2136	48.5	80
9	Barros del Colorado	6079574	361772	2282	94.4	6
10	Termas del Río Colorado	6080021	361869	2165	93.3	30
11	Potrerillos	6075582	363392	2382	46	4
12	Termas del Tigre Naciente	6073577	362754	2568	64.9	4
13	Aguas Calientes	6069989	360199	2578	38.9	6240
14	Puesto Calabozos	6065638	359128	2472	80	41,760
15	Lontué	6070434	340030	1988	94.5	1488
16	Vn Descabezado Grande	6060525	341224	3824	20	2,543,410
17	Descabezado Grande hot springs	6059315	334606	1897	29.8	55,414
18	Vn Quizapu	6054669	340856	3107	20	603,512
19	Médano	6034248	340857	968	29.5	600
20	Campanario	6022193	356945	1566	54.5	240

Table 2
Instruments used in the field data collection.

Variable	Instrument	Model/brand
Incident and reflected solar radiation (W/m^2)	2 pyranometers	SP-Lite/Kipp & Zonnen
Temperature (°C)	Solid state thermocouple	TC-107/Campbell Scientific
Remote temperature (°C)	Non-contact infrared thermometer	OAKTON TempTestr® IR
Remote temperature (°C)	Infrared thermocouple sensor	IRTS-P/Campbell Scientific
Net radiation (0.2–100 mm; W/m2)	Net radiometer	NR-Lite/Kipp & Zonnen
Sub-mid heat flux (W/m^2)	Plate heat flux	HFTP3/REBS

Supplementary Material 1), where rocks, unconsolidated deposits and thermal manifestations are exposed. These measurements were acquired with a radiometric station (electrically powered by a solar panel), consisting of a data logger device (CR10X-2M, Campbell Scientific). Instrumental details are given in Table 2. Temperature and radiation were recorded at intervals of 30 s and 5 min, respectively.

Atmospheric and ground surface temperatures were recorded using a solid state thermocouple and an infrared thermocouple sensor, respectively, during 24 h to obtain a daily average value (Fig. 2). In order to check the consistency of atmospheric and ground surface temperature variations within the expected range, internal station temperatures were also recorded (Table 2). The record of the minimum and maximum temperatures of the station was performed with a manual infrared thermocouple at 00:00, 03:00, 12:00 and 14:00 h (local time, GMT −3). Interpolation and extrapolation of temperature data for each site (T^s) were obtained from the following equation:

$$T^s(t) = \alpha_k^s + \sum_{k=1}^{4} \alpha_k^s \sin(2k\pi t) + \alpha_{k+4}^s \cos(2k\pi t) \quad (1)$$

where t is the time (hours), $\alpha_k^s$is a constant (complete list of α_k^s values are available in Supplementary Material 2) that varies with for $k=1$ to 8, and s designs the site number. This function corresponds to a sum of sinusoidal even and odd functions to represent the cyclical nature of the data collected (Fig. 3).

Albedo values were obtained from radiation measurements (up, down and total radiation). Although albedo is an intrinsic property of various materials, and therefore should not to vary within a single location, small variations were observed during sunset and sunrise. Nevertheless, these variations were filtered so that they do not affect albedo calculations.

4. Model for thermal anomaly detection: satellite image processing

ASTER images were acquired from the Land Processes Distributed Active Archive Center (LP DAAC), of NASA's Earth Observing System Data and Information System (EOSDIS) data centers. The images used are: (i) ASTER 1B (ASTER L1A data with the radiometric and geometric coefficients applied); (ii) surface reflectance ASTER 07 (based

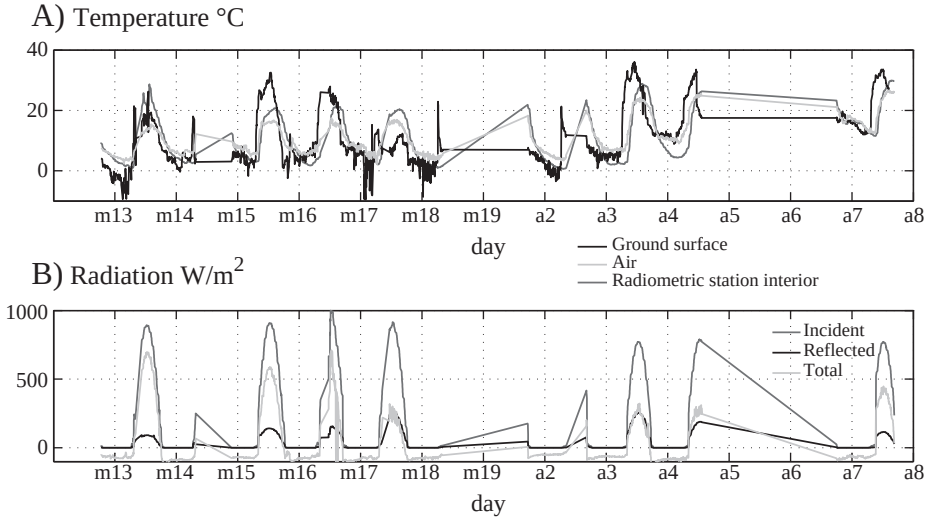

Fig. 2. Field data collected in two field campaigns in March (13th-19th) and April (2nd- 8th) 2010 (see Table 2 for details about variables and instruments used in the data collection), including: (A) Daily temperatures (°C) of the ground surface, atmosphere, and radiometric station interior; and (B) Daily radiation: incident, reflected and total radiation. m = March; a = April. Gap in the recorded temperature and radiation corresponds to the time interval between the two campaigns.

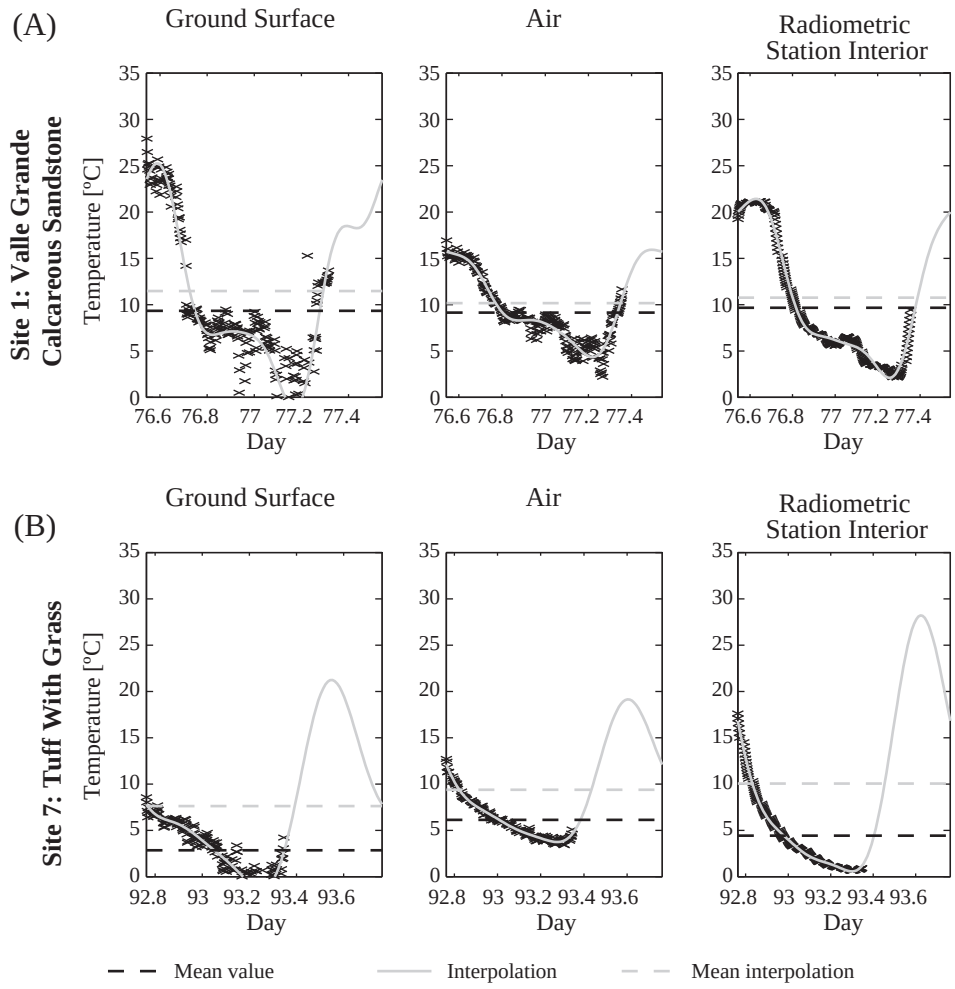

Fig. 3. Temporal record of temperature for the ground surface, air and radiometric station interior (Table 3). (A) Complete temperature data collected in Site 1, where averages of data and interpolation are similar, between 10 ° C and 11 ° C. In (B) data were obtained at Site 7 only at night and early morning, thus the interpolation gives higher values and a more limited range (8–10 ° C) from those measured (3–6 °C). Instruments used for temperature measurements are given in Table 2.

on a look-up table approach of Thome, 1994); and (iii) kinetic temperature ASTER 08 (based on the TES algorithm of Gillespie et al., 1998). We used 2 day and 2 night images of the study area (Table 4), which was divided into three smaller zones where the thermal anomalies were obtained independently: Northern, Central and Southern zones (Fig. 1). A Digital Elevation Model (DEM) was acquired from ASTER GDEM platform of the Earth Remote Sensing Data Analysis Center (ERSDAC). ASTER images were georeferenced and georectified with the DEM (image to image method) with the nearest neighbor resampling method to preserve pixel values and using more than 150 cross-checked control points in order to eliminate quadratic errors of the geographic position.

Current models for ground surface thermal anomaly detection have been obtained from remote sensing analysis (Coolbaugh et al.,

Table 3
Parameters obtained in the selected sites of field measurement: geographic position (UTM WGS84 Zone 19S); spectral bands (R_1, R_2 and R_3) of the ground surface reflectance (ASTER 07); cosine of zenith angle (cos (Z')); kinetic ground surface temperature (ASTER 08) for day and night images; albedo calculated from radiation measurements (A); mean and interpolated (I) temperatures of ground surface (GS), atmosphere (Atm) and radiometric station (RS).

Sites	Name	UTM-WE	UTM-NS	R_1	R_2	R_3	cos(Z')	Kinetic T°C day	Kinetic T°C night	A	GS T°C	AtmT°C	RSI T°C	I GS T°C	I Air T°C	I RSI T°C
1	Valle Grande Calcareous Sandstone	361,983	6,085,776	0.211	0.205	0.281	0.5417	43.85	−1.35	0.2029	9.33	9.14	9.67	11.47	10.17	10.75
2	Oxfordian gypsum	363,262	6,085,721	0.298	0.307	0.398	0.5208	39.05	−1.55	0.2969	4.75	8.79	9.07	5.15	9.12	9.28
3	Valle Grande soil with grass	362,261	6,082,712	0.148	0.12	0.316	0.9583	36.85	−0.65	0.0918	5.36	7.39	4.72	13.96	11.32	8.26
4	Moraine	362,240	6,082,751	0.201	0.177	0.319	0.4194	36.85	−0.65	0.1626	12.23	10.01	10.39	12.68	10.21	10.46
5	Lomas Secas Tuff	361,310	6,070,251	0.253	0.225	0.261	0.8347	46.15	3.45	0.2418	−1.29	4.81	3.51	2.54	7.43	9.89
6	Vn Descabezado lava flow	360,339	6,069,195	0.192	0.177	0.211	0.5035	38.25	8.45	0.1033	8.63	9.19	10.14	10.99	9.84	10.34
7	Tuff with grass	327,391	6,057,655	0.156	0.11	0.322	0.7736	49.25	13.05	0.1314	2.84	6.13	4.43	7.62	9.38	10.05
8	Pumice	334,427	6,059,135	0.41	0.392	0.429	0.7236	45.85	6.85	0.329	13.19	12.37	10.06	14.5	13.46	11.77
9	Obsidiane	334,427	6,059,135	0.41	0.392	0.429	0.7722	45.85	6.85	0.2396	16.61	14.77	11.16	19.18	16.58	13.81
10	Río Maule andesite	351,858	6,025,855	0.179	0.157	0.24	0.7514	45.05	12.75	0.1538	20.31	18.6	18.68	20.48	18.84	19.05

Table 4
Data of ASTER satellite images used for thermal anomaly detection.

Image data	Aster product	Day/night	Date	Time (GMT)	ID CODE
Radiance	L1B	Day	12/1/2009	14:46:20	ASTL1A 090112144620090115037 5
Radiance	L1B	Day	12/1/2009	14:46:29	ASTL1A 090112144629090115037 6
Reflectance	Aster 07	Day	12/1/2009	14:46:20	ASTL1A 090112144620090115037 5
Reflectance	Aster 07	Day	12/1/2009	14:46:29	ASTL1A 090112144629090115037 6
Kinetic Temperature	Aster 08	Day	12/1/2009	14:46:20	ASTL1A 090112144620090115037 5
Kinetic Temperature	Aster 08	Day	12/1/2009	14:46:29	ASTL1A 090112144629090115037 6
Kinetic Temperature	Aster 08	Night	03-23-2008	3:36:42	ASTL1A 080323033642090421080 8
Kinetic Temperature	Aster 08	Night	04-17-2008	3:30:59	ASTL1A 080417033059080419085 7

2007) in areas with nearly flat topography, by subtracting the thermal solar contribution from the temperature (kinetic) provided by ASTER 08 (assumed to be the ground surface temperature). Considering that the study area exhibits deep glacial-fluvial valleys, the effect of ground surface altitude difference on thermal anomaly detection needs to be assessed. For that purpose, we developed and compared two models: i) Model 1, considers only the subtraction of the thermal solar contribution from the ground surface temperature (Coolbaugh et al., 2007), while the thermal effects of altitude difference is neglected; and ii) Model 2, considers both the subtraction of the mentioned thermal effect of altitude and solar contribution from ground surface temperature. The variation of ground surface temperature with altitude (hereafter 'altitude-related thermal gradient') is assumed equivalent to the *ELR*.

The thermal anomaly defined in this study is the temperature difference (ΔT) between the kinetic ground surface temperature (provided by the ASTER 08 without any subtraction) and the model temperature (i.e. calculated temperature of a particular site at a particular moment obtained from the proposed model). In the course of 24 h, the overall ΔT is obtained by combining geothermal anomalies of night (ΔT_n) and day (ΔT_d) by a night weight factor (Wn) given by:

$$\Delta T = Wn \times \Delta T_n + (1 - Wn) \times \Delta T_d \quad (2)$$

Wn factor is obtained by minimizing the thermal inertia effects as follows: (i) minimizing the variance between the mean temperature directly measured in the field (Coolbaugh et al., 2007) and the kinetic temperature image (ASTER 08); or (ii) minimizing the thermal inertia effects in closed water bodies (lakes). The latter is a new method proposed here to correct the effects of thermal inertia, based on the assumption that the water bodies are not affected by geothermal contributions.

A thermal anomaly using day (ΔT_d) and night (ΔT_n) images is obtained by subtracting the 'model' temperature (Tm) from the kinetic ground surface temperature (Tk):

$$\Delta T_{n/d} = \left(Tk_{n/d} - Tm_{n/d}\right) \quad (3)$$

where $Tk_{n/d}$ is the kinetic temperature, provided by the ASTER 08 for day and night, respectively. Therefore, all anomaly values are scaled

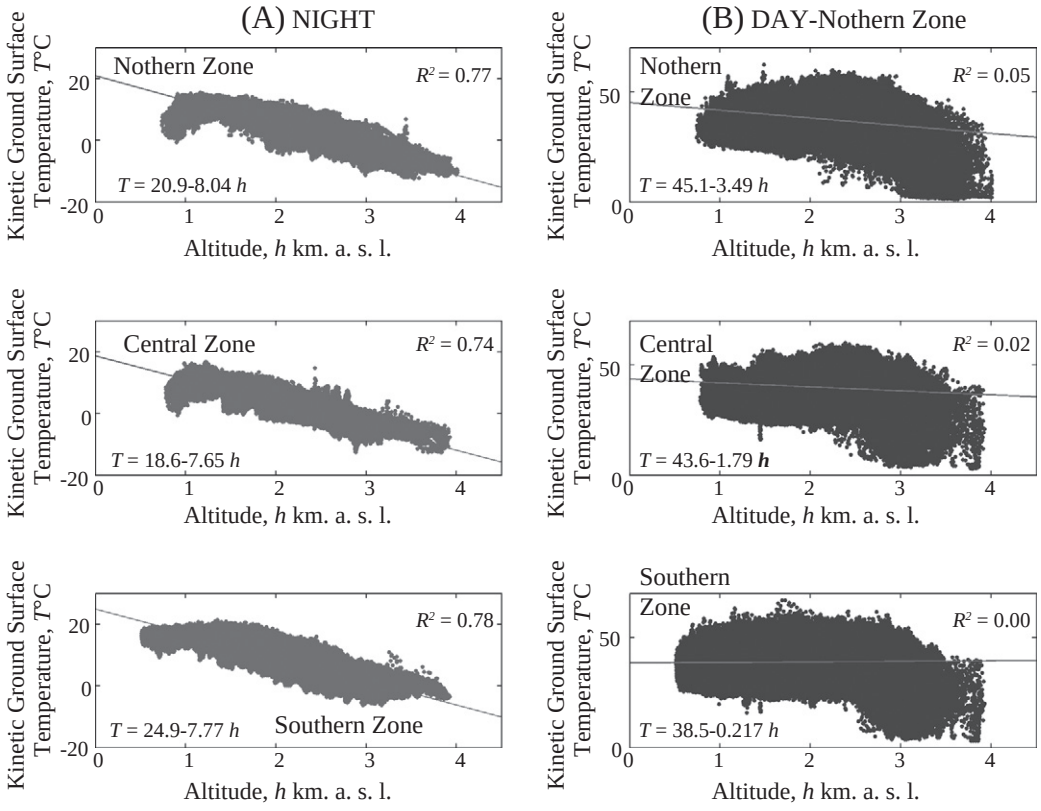

Fig. 4. Kinetic ground surface temperature (ASTER 08) versus altitude (h, altitude in kilometers above the sea level) in the Northern, Central and Southern Zones for: (A) night images and (B) day images. R^2 is the determination coefficient of direct linear regression between kinetic ground surface temperature and altitude.

to the original ASTER 08 kinetic temperature references. *Tm* is obtained by adding to the solar temperature contribution the thermal effect of topographic slope and thermal altitude gradient. The general equation for the 'model' temperature, modified from Coolbaugh et al. (2007), is given by:

$$Tm = a_0 + a_1 \times [1 - A(c, b_0, b_1)] \times \sum_{t=1}^{24} TR(Z(t)) \times \cos\left(Z'(t)\right) \times D(t - t_a) \times \Delta t - K \times h \quad (4)$$

where a_0, a_1, b_0, b_1, c and K are constants; A is the albedo; t is the GMT time; Z is the zenith angle; Z' is the angle between the solar rays and the ground surface normal; TR is the atmospheric transmittance; Δt is the time increment (1 h); t_a is the image acquisition time; D is a decay function, inversely proportional to $t - t_a$; and h is the altitude (ground surface height in kilometers above sea level). The constants a_0, a_1, b_0, b_1 and c are obtained by minimizing the thermal variance ($\Delta T^2_{d/,n}$) by using the least squares method. K is the (ground surface) 'thermal altitude gradient'. Model 1 assumes $K = 0$ °C/km, whereas in Model 2, K is obtained by the minimization process for thermal anomalies of day and night. It is important to recognize that the K parameter in our model is obtained in the solution of the model itself, and hence *a priori* knowledge of this constant is not required (as opposed to, for example, Urai, 2002, where this parameter must be previously determined). Values of Z and $TR(Z(t))$, which depend on latitude, longitude and date, were taken from Finlayson-Pitts and Pitts (2000). The cos(Z') values are calculated directly from a (DEM) from the shaded relief option available on the ENVI® software considering date, time, latitude and longitude.

The decay function (D) was calculated as:

$$D(t) = 1/(t - t_a + 0.9615) - 0.0401 \quad (5)$$

Albedo values were calculated by a simplified calibration equation, where the atmospheric radiance is neglected (Schowengerdt, 1997; Coolbaugh et al., 2007), given by:

$$A = b_1 \times \sum_{w=1}^{3} Wf_w \times \frac{R_w - f_w}{e_w} \times \min\left(\frac{1}{\cos(Z')}, c\right) + b_0 \quad (6)$$

where w design each of the three spectral bands of the ground surface reflectance, or reflectivity; R is the ground surface reflectance (ASTER 07 sub product); e and f are constants; and Wf are weight factors that include the wavelength-dependent solar irradiance (at the top of the atmosphere), atmospheric transmittance, and the bandwidth.

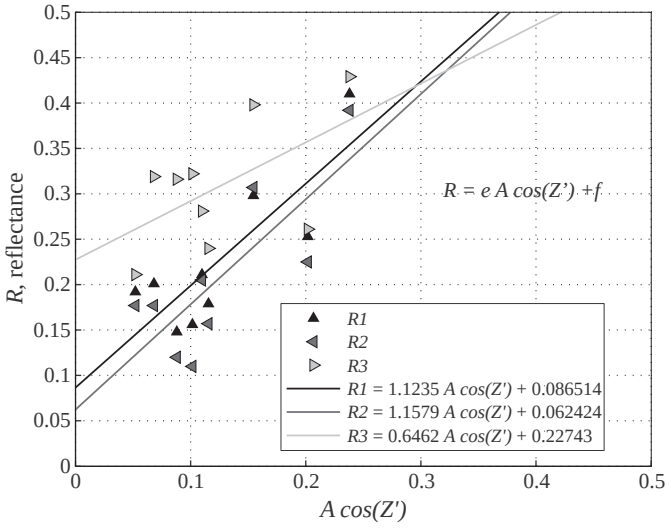

Fig. 5. Reflectance (ASTER 07) versus $A\ cos(Z')$ (Table 3), where A is albedo, calculated from solar radiation measurement, and Z' is the angle between the solar rays and the normal to the ground surface. Linear regressions between these parameters are shown for each of the three spectral bands (R_1; R_2 and R_3; Table 5).

Table 5
Parameters obtained in the albedo calculation for the spectral bands (R_1, R_2 and R_3) of the ground surface reflectance image (ASTER 07).

Parameter	R_1	R_2	R_3
e	1.1235	1.1579	0.6462
f	0.0865	0.0624	0.2274
Wf	0.3891	0.2552	0.3557
Determination coefficient	0.8606	0.8706	0.4718

5. Results

Albedo calculation is based on field measurements at nine sites (Fig. 1; Table 3) following the methodology proposed by Coolbaugh et al. (2007). Albedo values (A cos(Z')) range between 0.05 and 0.24, whereas images of reflectivity (ASTER 07) are between 0.11 and 0.43 (Fig. 5). Results of linear regression (Table 5) indicate values of *e*, between 0.65 and 1.16, and *f* between 0.09 and 0.23. However, in theory the constant *e* should be near one and the constant *f* near zero because all atmospheric absorption and scattering effects are not successfully removed. Coolbaugh et al. (2007) indicate that positive values of *f* can be attributed to atmospheric haze causing thermal disruption in the atmosphere column (e.g. smoke from distant forest fires) at the time of satellite image acquisition. However, the results obtained here are similar ($e = 0.89$ and $f = 0.09$) to those obtained by Coolbaugh et al. (2007) despite no atmospheric haze being detected at the time of satellite image acquisition. Instead, we attribute $f > 0$ to the applied methodology because ground surface reflectance obtained with the SWIR (short wave infrared) of the ASTER images has a resolution of tens of meters (30×30 m, for example), which cannot be obtained by a single field measurement of radiation. In contrast, the calculated albedo values could vary on a metric scale depending on ground surface heterogeneities. Determined coefficients between albedo and reflectivity (Table 5) indicate that the albedo calculation is better fitted with field measurement radiation using bands 1 and 2 rather than band 3.

Correction of thermal inertia (Table 6) was obtained by minimizing the variance between the mean temperature measured in the field and the corresponding weighted temperature from the satellite images (Coolbaugh et al., 2007; Fig. 6). This was effective in the Northern Zone ($Wn = 0.73$) because the obtained variance was low ($\Delta T^2 < 1$), but not in the Central and Southern zones. In fact, in both the Central (where *Wn* values were between 0.69 and 0.93) and Southern (*Wn* ranges between 0.75 and 0.93) zones the variances were extremely high (ΔT^2 values > 50 and > 20, respectively). The correction of thermal inertia by minimization of the thermal inertia effects in water bodies (lakes, Table 7) is therefore our preferred method because it generates a narrow range of *Wn* values in all three zones (Fig. 7).

Thermal anomaly (ΔT) image in each zone was obtained independently for day and night (Table 8). Magnitude and amount of pixels of thermal anomalies using Model 1 and 2 substantially differs (Figs. 8 and 9), indicating that 'altitude-related thermal gradient' (K; Model 2) produces a significant variation of thermal balance. Values of ΔT close to zero are more common when Model 2 is used irrespective of zone. This indicates that ΔT values of this model are given by a lower numbers

Table 6
Values of night weight factor (*Wn*) for thermal inertia correction given by: (i) minimizing the variance (Coolbaugh et al., 2007) and (ii) minimization of the effect of thermal inertia in lakes.

Zone	Northern	Center	Southern
Wn (*i*)	0.7237	0.7802	0.8287
Wn (*ii*)	0.7737	0.7141	0.7979

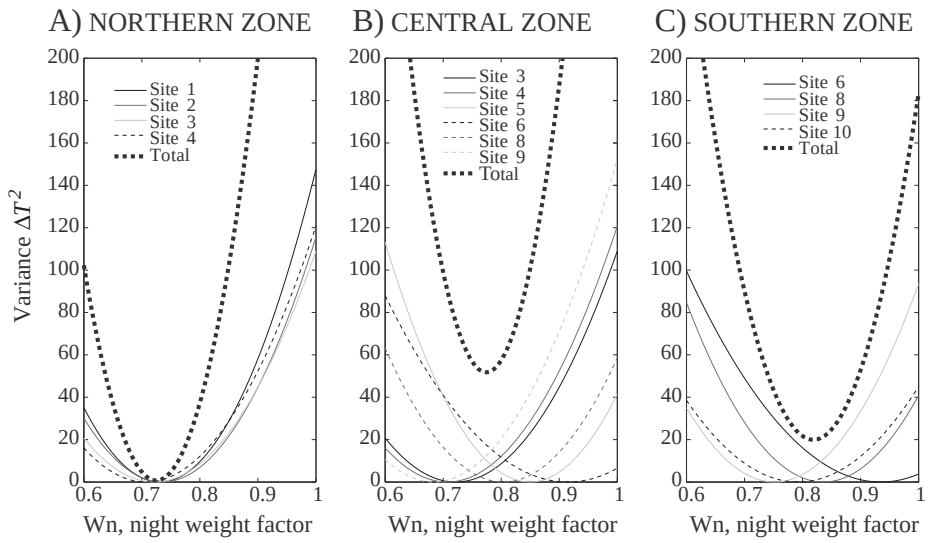

Fig. 6. Variance of thermal anomaly (ΔT^2) per site and total variance, versus night weight factors (Wn) for the correction of thermal inertia: (A) Northern Zone, (B) Central Zone and (C) Southern Zone. The Northern Zone has a total value of 0.72 with a low variance. The other two zones have Wn values range from 0.7 to 0.9 and total variance values are >20.

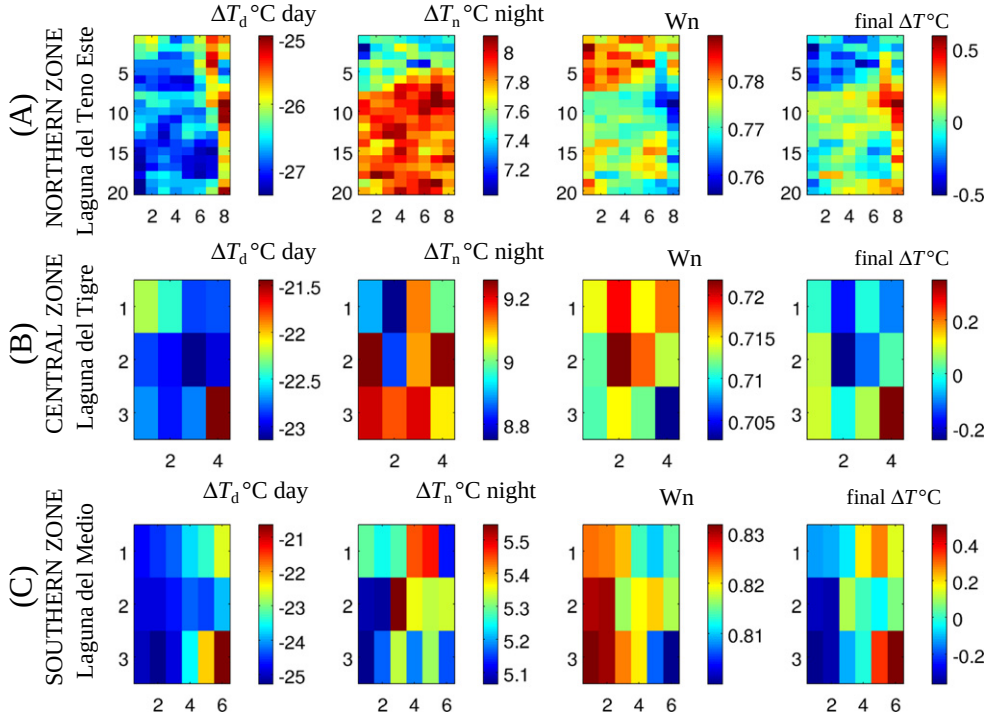

Fig. 7. Representation of thermal anomalies (ΔT) obtained from Model 2 after minimization of the thermal inertia effect in closed water bodies in day and night (Table 6): (A) Northern Zone; (B) Central Zone; and (C) Southern Zone. Numbers in each image correspond to the number of pixels used in the minimization. ΔT values of day and night are combined in a proportion $(1-Wn)$ and Wn, respectively. Final ΔT values are close to zero (<1 °C).

of pixels than Model 1. It is interesting to note that larger differences are obtained in night than day images (Fig. 8). This is because values of K (Table 8) and ELR (Table 9) are higher for night than day, consistent with higher 'altitude-related thermal gradient' at night. ELR values obtained by regression of Model 2 are similar (differences lower than 1 °C) than ELR values obtained by direct linear regression that considers only temperature and altitude (Table 9 and Fig. 4), consistent with its determination coefficients values.

6. Discussion

The new approach proposed here allows us to obtain the K parameter (ground surface altitude-related thermal gradient in °C/km) in the solution of the model itself, and hence *a priori* knowledge of this constant is not required. This important distinction follows directly from the different solution mechanisms between our model and

Table 7
Information of the area (polygonal) of the lakes used for thermal inertia correction. Datum: UTM WGS84 Zone 19S.

Name	Zone	Area m^2	UTM-N	UTM-S	UTM-W	UTM-E
Laguna del Teno Este	North	1,282,319	6,106,620	6,104,857	358,830	359,541
Laguna del Tigre	Center	94,166	6,071,759	6,071,499	362,961	363,214
Laguna del Medio	South	158,322	6,069,941	6,069,664	351,150	351,705

Table 8
Day and night regression parameters of Model 1 and 2.

Model	1	1	1	1	1	1	2	2	2	2	2	2
Zone	North	North	Center	Center	South	South	North	North	Center	Center	South	South
Time	Day	Night	Day	Night	Day	Night	Day	Night	Day	Night	Day	Night
a_0	0.5802	1.342	1.301	−0.1729	1.134	4.212	22.37	20.61	23.04	17.93	20.99	23.64
a_1	0.5946	−0.3122	0.5179	1.565	1.157	1.16	26.54	2.162	10.66	6.388	10.04	5.636
b_0	0.1433	0.03567	1.876	1.092	0.386	4.528	−0.8626	−0.4236	−3.157	−1.361	5.13	2.714
b_1	−0.7682	0.04516	0.5373	−0.3124	0.3399	−1.942	0.001307	0.002525	0.000476	0.006686	0.001848	−0.01284
K							3.287	7.793	2.729	7.449	0.773	7.087
c	0.4845	0.2668	−0.6522	0.01086	−0.5035	0.0389	1.001	12.66	0.9058	0.8848	−0.4414	−1.58

others models, where similar parameters must be previously determined (e.g. 'altitude corrected surface temperature' of Urai, 2002). This illustrates an advantage of our model: this variable is not needed at the time of image acquisition, which is a valuable advancement particularly in zones where meteorological data are scarce. Given a specific altitude, it appears that the temperature of the ground surface and the ambient atmosphere tends to be similar. This may be due to an interdependent relationship; nevertheless, this result allows us to interchange the *ELR* and *K* parameters in Eq. (4). We find that *K* values for night images are between 7.1 and 7.8 °C/km (Table 9),

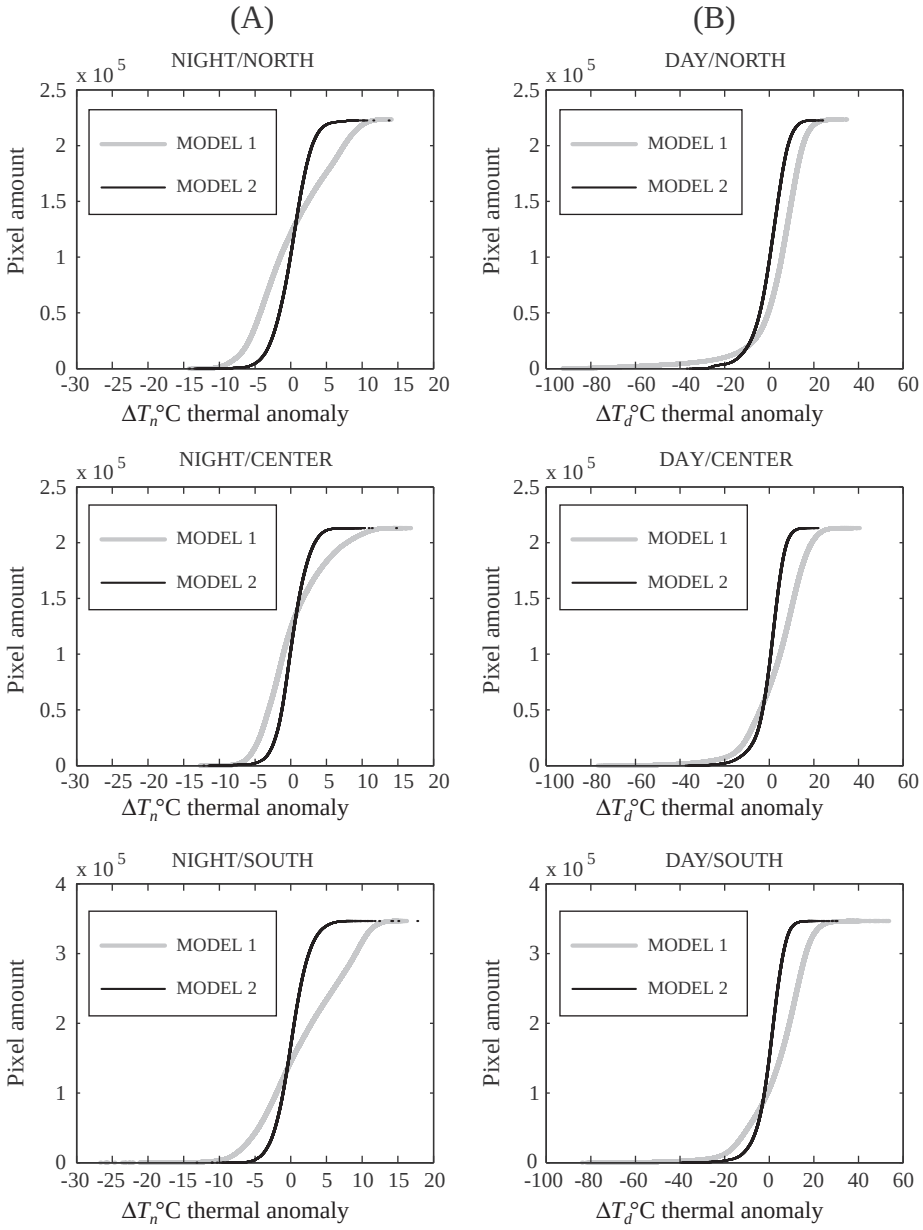

Fig. 8. Thermal anomalies (ΔT) versus amount of pixels sorted from negative to positive thermal anomalies for Model 1 and 2. (A) and (B) correspond to diagrams of thermal anomalies for night (ΔT_n) and day (ΔT_d), of the Northern, Central and Southern Zones, respectively.

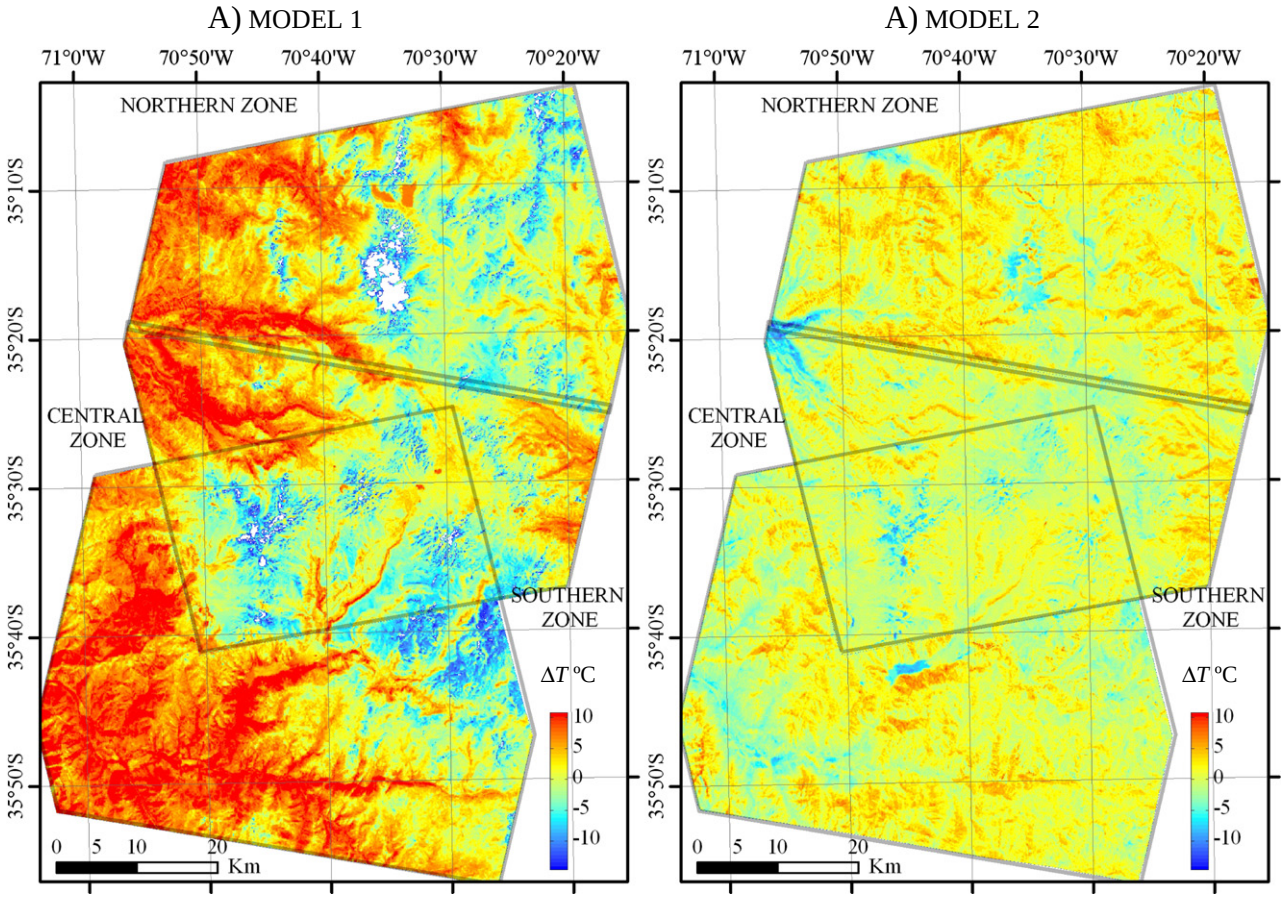

Fig. 9. Thermal anomalies (ΔT) of the study areas for (A) Model 1 and (B) Model 2.

which is consistent with a stable atmosphere stratification, while K values for day images are between 0.2 and 3.5 °C/km, consistent with a highly unstable atmosphere as a direct consequence of solar heating (no other effect on atmosphere turbulence was detected at the time of the image acquisition). We propose a simple way to detect thermal anomalies: first, we exclude the pixels of water bodies, which have high thermal inertia; and second, we select pixels that do not follow the expected 'altitude-related thermal gradient'. Furthermore, since the atmosphere at night is more stable, and there is a higher temperature contrast between thermal manifestations and the surrounding environment, we confirm that night images are more useful than day images for detection of thermal anomalies (e.g. Urai, 2002).

6.1. Size reduction of thermal anomaly area

The proposed model (Model 2) for detecting thermal anomalies requires an integration of several parameters including atmosphere transmittance, reflectivity of the Earth's surface, topography, thermal inertia and 'altitude-related thermal gradient' (K). The latter parameter produces a reduction of pixels related to the thermal anomaly (Figs. 8 and 9) as compared with a model where this parameter is not included (Model 1). It is important to note that a reduction of pixels does not represent a reduction of the threshold of thermal anomaly detection, given by original ASTER images, but rather a change in the size of pixels of the thermal anomaly. The size reduction of pixels obtained from Model 2 in comparison to Model 1, mainly corresponds to those pixels with values of <1 °C (Fig. 8). For example, the size of the thermal anomaly with values near 1 °C decreases between 1.4 and 4.2 times for night images and between 5.0 and 6.5 times for day images, whereas the size of the hottest thermal anomalies has been reduced between 0.0 and 0.1 times for night images and between 0.5 and 0.8 times for day images. From this we infer that hotter anomalies (>1 °C) generally represent real features, and therefore are not significantly reduced. However, cooler anomalies (<1 °C) are often greatly reduced, representing the higher likelihood that they are simply false positives. By comparing the two models, Model 2 shows an important reduction of thermal anomaly magnitude in deep valleys dissecting the western part of the study area, where no thermal manifestation exists (Fig. 9), indicating that the thermal altitude gradient has a fundamental influence in thermal anomaly detection in areas with abrupt topography.

Table 9
Ground surface altitude-related thermal gradient in °C/km (K) values obtained from Model 2 and direct linear regression (DLR) between altitude and kinetic ground surface temperature.

Zone	Northern	Center	Southern
K of Model 2 for day	3.29	2.73	0.77
K of DLR for day	3.49	1.79	0.22
K of Model 2 for night	7.79	7.45	7.09
K of DLR for night	8.05	7.65	7.78

6.2. Limitations and applications of the model

The model proposed here can be useful for thermal anomaly detection at a scale that depends on the size and intensity of thermal anomalies as well the detection limit of satellite images (Murphy et al., 2011). Most of the geothermal manifestations having areas larger than 90 m^2, such as craters or fumarolic fields (Figs. 10, 11 and 12), have been detected as positive geothermal anomalies with this new approach. However, thermal manifestations occupying areas <60 m^2, or having a small thermal anomaly (ΔT<5 °C) are not

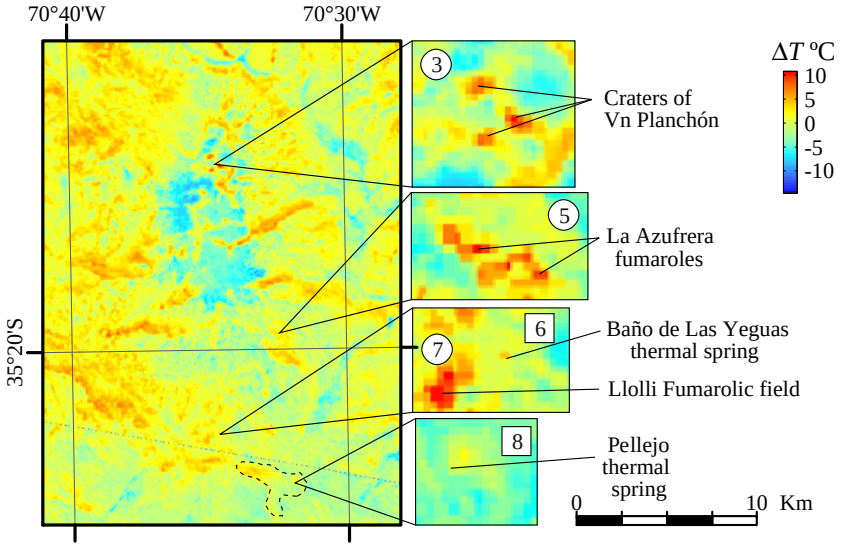

Fig. 10. Thermal anomaly (ΔT) of Planchón-Petreroa Volcanic Complex according to Model 2. Thermal manifestations corresponding to hot springs (squares) and fumaroles (circles) have been numbered as in Table 1. Zoom insets depict a few of the areas with thermal manifestations that were cross-checked with field observations.

identified. This is due to the resolution of the ASTER-based information, which does not allow identification of areas <90 m^2 and/or temperatures below 5 °C above ambient temperature. Because the capability of detection of areas with thermal anomalies depends on its size and maximum temperature, the limitations of this new approach are shown in Fig. 13, where field of detectable and not detectable anomalies are defined. To illustrate the attributes of our proposed model, we apply it to existing areas with geothermal manifestations.

As case examples, well-known fumaroles and hot springs associated with La Azufrera, Llolli, Puesto Calabozos and Descabezado Grande Volcano (Figs. 11 and 12 A–C), were clearly detected. La Azufrera (Figs. 10 and 12A) is located 3 km eastward of Vn Azufre. It consists in a fumarolic field in an area of about 0.34 km^2 (Table 1) with hot springs and mud pools. Temperatures are between 70 °C and 88 °C, pH between 3.94.8 and 6.7 and flow rates are generally low (<1 L/s). Argillic hydrothermal alteration with sulfur and clay deposits and vuggy silica are present. Llolli (Figs. 10 and 12B) is located at 7 km southward of Vn Azufre, along the north bank of the Colorado River. It consists of a fumarolic field in an area of about 0.11 km^2 (Table 1) with hot springs and mud pools. Temperatures are 74.5 °C, pH of about 2, and flow rates are low (<1 L/s). Argillic hydrothermal alteration with sulfur and clay deposits and vuggy silica are also present. Puesto Calabozos (Figs. 11 and 12C) is located 5 km southeastward of Vn Descabezado Chico. It consists of a cluster of hot springs that flow from underneath a lava flow from Descabezado Chico towards the river. Although the area is only about 0.04 km^2 the maximum temperature of hot springs is 80 °C, heating the river enough to allow

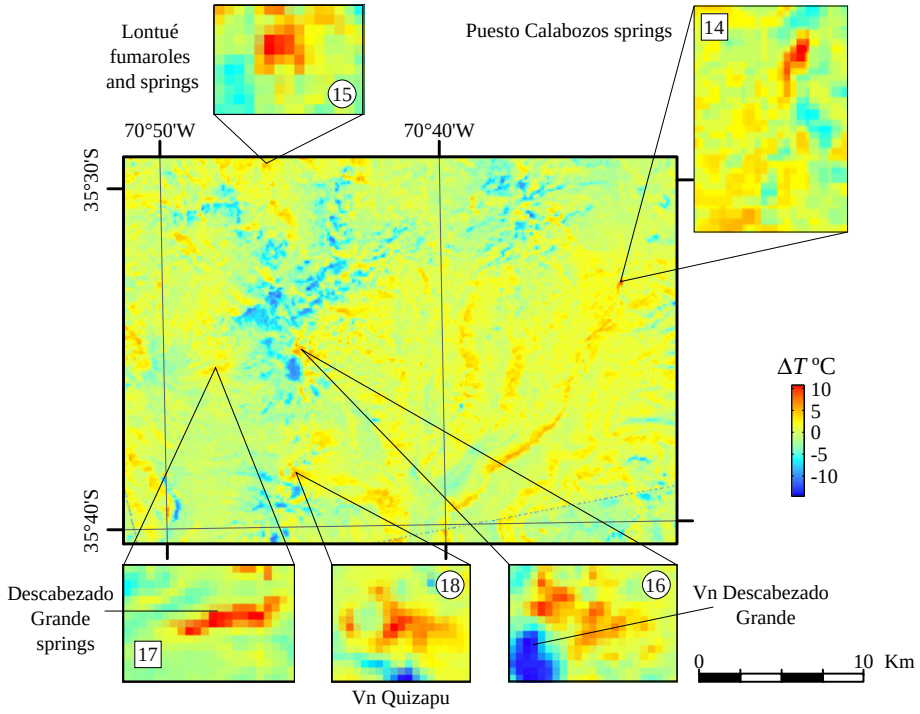

Fig. 11. Thermal anomaly (ΔT) of Descabezado Grande-Cerro Azul Volcanic Complex. Thermal manifestations corresponding to hot springs (squares) and fumaroles (circles) have been numbered as in Table 1. Zoom insets depict a few of the areas with thermal manifestations that were cross-checked with field observations.

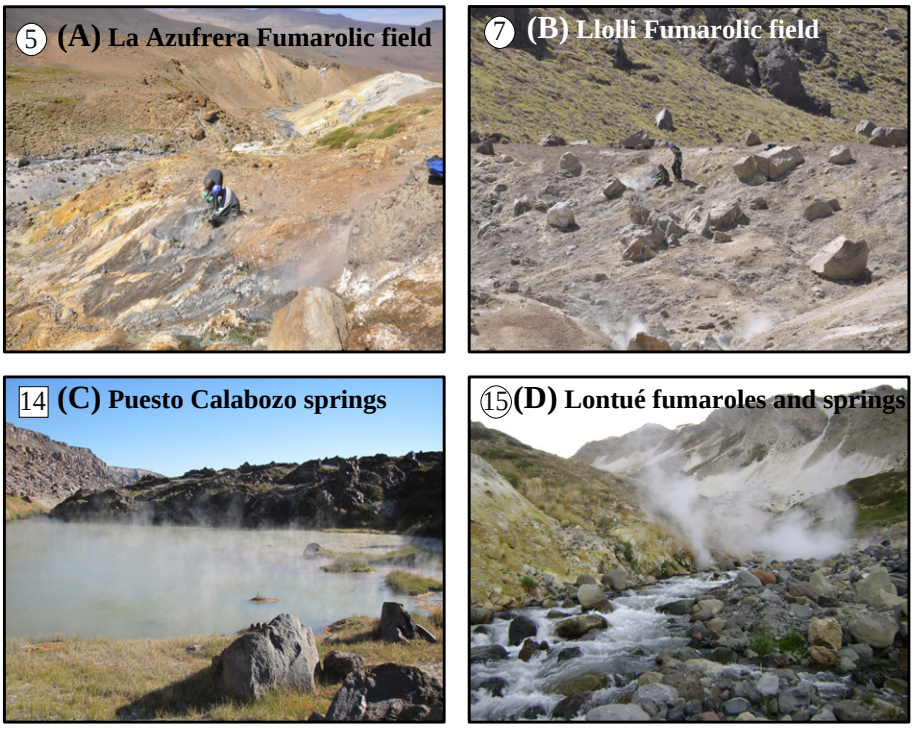

Fig. 12. A–D; examples of thermal manifestations that were cross-checked with thermal anomalies obtained from Model 2.

thermal anomaly detection by remote sensing. Descabezado Grande (Fig. 11) is located 7 km westward of Vn Descabezado Grande. It consists of a cluster of about 20 hot springs of about 20 °C that flow next to the Quizapu lava flow (1846 and 1947 eruption, (Hildreth and Drake, 1992). Unlike the previous cases, the temperature is about 20 °C, only 15 °C above the mean day ambient temperature. However, the big area of about 2.54 km^2 allows thermal anomaly detection by remote sensing. The craters of Volcán Planchón (~ 3,550 m.a.s.l) were identified as a positive thermal anomaly of 10 °C higher than the surrounding ground surface temperature. On the other hand, an unknown geothermal manifestation of about 1488 m^2 and 94.5 °C (Table 1) was discovered in the deep Lontué River valley, about 10 km northward of Vn Descabezado Grande, (Lontué fumaroles and springs; Figs. 11 and 12D) using this new approach. This feature consists of a fumarolic field northeast-elongated, with hot springs and mud pools that cross the Lontue River, which boils at the river shore. Argillic hydrothermal alteration with sulfur and clay deposits and vuggy and sinter silica are present. Additionally, an area of positive thermal anomaly of about 5.2 km^2 (see dashed line in Fig. 10) was detected in a snowed range, despite no record of geothermal manifestation exists. In this case, the effect of the observed thermal anomaly was caused by more rapid melting of the snow cover than in surrounding areas. Hydrothermal fluid circulation probably associated with the Pellejo and Baño de Las Yeguas thermal springs located along the Colorado Valley could explain this anomaly.

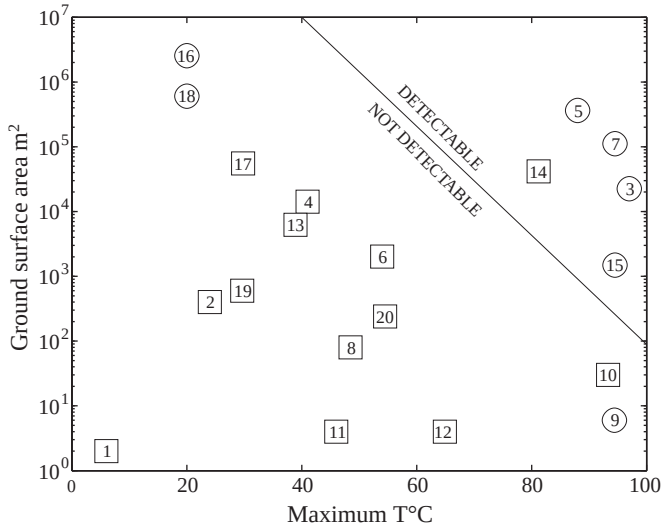

Fig. 13. Ground surface area, where thermal anomalies were detected using Model 2, versus its maximum recorded temperature. The thermal manifestations have been numbered as in Table 1. The line defines the limit of two fields where thermal manifestations are detectable and not detectable using the proposed model.

6.3. Volcanological and geothermal implications

The proposed model allows identification of geothermal anomalies (volcanic craters, hot springs and fumarolic fields) in zones with steep relief by using remote sensing analysis. This procedure is applied here by using satellite images in three different contiguous zones with similar results. Because the proposed method can be used in a wide superficial coverage (about of 100 km, from north to south by 65 km, from west to east), we suggest that this method can be useful to detect and track the evolution of thermal anomalies during a volcanic eruption and in geothermal exploration. During an eruption, the main volcanic products, such as a lava flow, a lava dome or a lava crater, will be easy to detect and monitoring the temperature evolution with this model because they are usually within the areal detection limit (>90 m^2) and have a great temperature contrast with the ambient air (>5 °C). The subsequent thermal anomalies derived from an eruption, such as the temperature increase in rivers and lakes, may also be possibly detected. We also suggest that the proposed method is a useful tool for geothermal exploration. Finally, the proposed method will allow researchers to get a low-cost preliminary look at places of interest, to determine if thermal anomalies might possibly exist. As we show here, known thermal manifestations can be corroborated, and new ones can be discovered. We believe that both of these results are relevant in the Andes, were

volcanological monitoring and geothermal exploration have been advanced in recent years.

7. Conclusion

A previous model (Coolbaugh et al., 2007) of satellite image-based thermal anomaly detection considers the subtraction from the kinetic ground surface temperature (ASTER 08) of: (i) solar-derived thermal effects (atmospheric transmittance, reflectance or albedo), (ii) thermal inertia, and (iii) thermal effect of topography derived from sun exposure and shadows. We propose a new model that additionally includes the thermal effect of altitude difference of the ground surface as an important variable in thermal anomaly detection. This model is particularly useful in detecting thermal anomalies in high-mountain ranges, where steep topography and great differences in altitude exist. The effect of the altitude difference is given by the incorporation of a new parameter (K) in the model temperature expression that reflects the linear relation between ground surface temperature and altitude. Importantly, this parameter is solved for internally, and thus is given by the solution of the model itself. The proposed model was developed and applied in two volcanic complexes (Descabezado Grande-Cerro Azul Volcanic Complex and Planchón-Peteroa-Azufre Volcanic Complex) and allowed detection of thermal manifestations that were successfully cross-checked in the field. Although both day and night images are necessary for thermal anomalies in this detection model, K values calculated for night images are better constrained and closer to the ELR (>7 °C/km) for a stable atmosphere. Additionally, we demonstrate that night images provide more reliable information for thermal anomaly detection than day images because they record higher temperature contrasts between geothermal areas and surroundings.

8. Acknowledgment

This research has been developed by the PBCT-PDA07 project granted by CONICYT (Chilean National Commission for Science and Technology). We thank the Land Processes Distributed Active Archive Center (LP DAAC) of the Earth Observing System Data and Information System (EOSDIS) of NASA for providing the satellite images used for academic purposes in this study. We thank the Department of Geophysics at the University of Chile for the equipment used during this research and Geothermal Academic Program of the Department of Geology at the University of Chile for their support in the development of field campaigns. We thank 4ea for the logistical support in field activities, transportation and feeding in an area of difficult access. We appreciate the comments of Matt Patrick and Sarah Gelman in the review of this manuscript.

Appendix A. Supplementary data

Supplementary data to this article can be found online at http://dx.doi.org/10.1016/j.jvolgeores.2012.05.016.

References

Coolbaugh, M.F., Kratt, C., Fallacaro, A., Calvin, W.M., Taranik, J.V., 2007. Detection of geothermal anomalies using Advanced Spaceborne Thermal Emission and Reflection Radiometer (ASTER) thermal infrared images at Bradys Hot Springs, Nevada, USA. Remote Sensing of Environment 106 (3), 350–359.

Danielson, E.W., Levin, J., Abrams, E., 2003. Meteorology, 2nd ed. McGraw-Hill Higher Education. (558pp.).

Eneva, M., Coolbaugh, M., 2009. Importance of elevation and temperature inversions for the interpretation of thermal infrared satellite images used in geothermal exploration. GRC Transactions 33, 467–470.

Farías, M., Comte, D., Charrier, R., Martinod, J., David, C., Tassara, A., Tapia, F., Fock, A., 2010. Crustal-scale structural architecture in central Chile based on seismicity and surface geology: implications for Andean mountain building. Tectonics 29 (3), TC3006.

Finlayson-Pitts, B.J., Pitts, J.N., 2000. Chemistry of the Upper and Lower Atmosphere—Theory, Experiments and Application (pp. 53-60). (1st Ed.). Academic Press, San Diego CA, (ISBN 0-12-257060-x).

Gillespie, A., Rokugawa, S., Matsunaga, T., Cothern, J.S., Hook, S., Kahle, A.B., 1998. A temperature and emissivity separation algorithm for Advanced Spaceborne Thermal Emission and Reflection Radiometer (ASTER) Images. IEEE Transactions on Geoscience and Remote Sensing 36 (4), 1113–1126.

González-Ferrán, O., 1995. Volcanes de Chile. I.G.M. DE CHILE. (640 pp.).

Grunder, A.L., Mahood, G.A., 1988. Physical and chemical models of zoned silicic magmas: the Loma Seca tuff and Calabozos Caldera, Southern Andes. Journal of Petrology 29 (4), 831–867.

Grunder, A.L., Thompson, J.M., Hildreth, W., 1987. The hydrothermal system of the Calabozos caldera, central Chilean Andes. Journal of Volcanology and Geothermal Research 32 (4), 287–298.

Haller, M., Nullo, F., Proserpio, C., Parica, P., Cagnoni, M., Walker, J., 1985. Major element geochemistry of early Tertiary Andean volcanics (34°-36°S). Comunicaciones 35, 97–100.

Hellman, M.J., Ramsey, M.S., 2004. Analysis of hot springs and associated deposits in Yellowstone National Park using ASTER and AVIRIS remote sensing. Journal of Volcanology and Geothermal Research 135 (1–2), 195–219.

Hildreth, W., Drake, R.E., 1992. Volcán Quizapu, Chilean Andes. Bulletin of Volcanology 54 (2), 93–125.

Hildreth, W.E.S., Grunder, A.L., Drake, R.E., 1984. The Loma Seca Tuff and the Calabozos caldera: a major ash-flow and caldera complex in the southern Andes of central Chile. Geological Society of America Bulletin 95 (1), 45–54.

Houghton, H.G., Cramer, H.E., 1951. Theory of entrainment in convective currents. Journal of Atmospheric Sciences 8 (2), 95–102.

Jacobson, M.Z., 2005. Fundamentals of Atmospheric Modeling, 2nd ed. Cambridge University Press. (ISBN 0-521-83970-X, 656pp.).

Murphy, S.W., Filho, C.R.d.S., Oppenheimer, C., 2011. Monitoring volcanic thermal anomalies from space: size matters. Journal of Volcanology and Geothermal Research 203 (1–2), 48–61.

Naranjo, J.A., Haller, M.J., 2002. Erupciones holocenas principalmente explosivas del volcán Planchón, Andes del sur (35°15′S). Revista geológica de Chile 29 (1), 93–113.

Naranjo, J.A., Haller, M.J., Ostera, H.A., Pesce, A.H., Sruoga, P., 1999. Geología y peligros del Complejo Volcánico Planchón-Peteroa, Andes del Sur (35°15'S), Región del Maule, Chile-Provincia de Mendoza, Argentina. Boletín del Servicio Nacional de Geología y Minería 52, 55.

Pieri, D., Abrams, M., 2004. ASTER watches the world's volcanoes: a new paradigm for volcanological observations from orbit. Journal of Volcanology and Geothermal Research 135 (1–2), 13–28.

Pieri, D., Abrams, M., 2005. ASTER observations of thermal anomalies preceding the April 2003 eruption of Chikurachki volcano, Kurile Islands, Russia. Remote Sensing of Environment 99 (1–2), 84–94.

Schowengerdt, R.A., 1997. Remote sensing, models and methods for image processing (pp. 313−318). (3rd Ed.). San Diego, CA: Academic Press. (ISBN 13: 978-0-12-369407-2; ISBN 10: 0-12-369407-8).

Srivastava, R.C., 1987. A model of intense downdrafts driven by the melting and evaporation of precipitation. Journal of Atmospheric Sciences 44 (13), 1752–1774.

Srivastava, P.K., Majumdar, T.J., Bhattacharya, A.K., 2009. Surface temperature estimation in Singhbhum Shear Zone of India using Landsat-7 ETM+ thermal infrared data. Advances in Space Research 43 (10), 1563–1574.

Stern, C.R., 2004. Active Andean volcanism: its geologic and tectonic setting. Revista geológica de Chile 31 (2), 161–206.

Stern, C.R., Moreno, H., López-Escobar, L., Clavero, J.E., Lara, L.E., Naranjo, J.A., Parada, M.A., Skewes, M.A., 2007. Chilean Volcanoes. In: Moreno, T., Gibbons, W. (Eds.), The Geology of Chile. The Geological Society, London, pp. 147–178.

Thome, K.J., 1994. Proposed atmospheric correction for the solar-reflective bands of the Advanced Spaceborne Thermal emission and Reflection Radiometer. Geoscience and Remote Sensing Symposium. IGARSS. Surface and Atmospheric Remote Sensing: Technologies, Data Analysis and Interpretation., International, Pasadena, California, USA, 1, pp. 202–204.

Tormey, D.R., Frey, F.A., Lopez-Escobar, L., 1995. Geochemistry of the Active Azufre–Planchon–Peteroa Volcanic Complex, Chile (35°15′S): evidence for Multiple Sources and Processes in a Cordilleran Arc Magmatic System. Journal of Petrology 36 (2), 265–298.

Urai, M., 2002. Heat discharge estimation using satellite remote sensing data on the Iwodake volcano in Satsuma-Iwojima, Japan. Earth Planets Space 54 (3), 211–216.

Warner, T.A., Chen, X., 2001. Normalization of Landsat thermal imagery for the effects of solar heating and topography. International Journal of Remote Sensing of Environment 22 (5), 773–788.

Watson, K., 1975. Geologic applications of thermal infrared images. Proceedings of the IEEE 63 (1), 128–137.

Watson, F.G.R., Lockwood, R.E., Newman, W.B., Anderson, T.N., Garrott, R.A., 2008. Development and comparison of Landsat radiometric and snowpack model inversion techniques for estimating geothermal heat flux. Remote Sensing of Environment 112 (2), 471–481.

The origin of fumarolic fluids from Tupungatito Volcano (Central Chile): new insights from volatile compositions

Oscar Benavente[1], Franco Tassi[2], Francisco GutiÃľrrez[1], Orlando Vaselli[2], Felipe Aguilera[3]

[1]Centro de Excelencia en Geotermia de los Andes,Universidad de Chile, Plaza Ercilla, 803, Chile, [2]CNR-IGG, Istituto di Geoscienze e Georisorse Via G. La Pira, 4, Firenze, Italy, [3]Departamento de Geologia, Universidad de Atacama, Copayapu 485, Copiapo, Chile

E-mail: oscar.benavente.zolezzi@gmail.com

Tupungatito is an early Pleistocene – Holocene volcano located 100 km east of Santiago, in the northernmost sector of the South Volcanic Zone (SVZ) in Central Chile. Permanent fumarolic activity occurs at the Tupungatito summit (Gonz á lez – Ferr á n 1995) where three crater lakes are hosted. In this study we present and discuss the very first chemical and isotopic (δ 13C – CO2, R/Ra, and 40Ar/36Ar) composition of fumarolic gases and steam (δ 18O and δ D) collected from this volcano during two sampling campaigns carried out in February 2011 and 2012. The main aims are to investigate the different fluid source regions and the chemical-physical processes controlling fluid chemistry.

The chemical and isotopic data indicate that the discharged gas species and steam are likely produced by mixing processes of fluids between a magmatic source rich in acidic gases (SO2, HCl and HF) and a meteoric – recharged hydrothermal reservoir. The magmatic – hydrothermal fluids at the surface are affected by steam condensation that controls the outlet fumarolic temperatures (<84 ℃) favoring the dissolution of high soluble magmatic gases. The origin of CO2 seems to be mainly related to devolatilization of the subduction carbonates, with a limited contribution from the overlying organic – rich sediments, suggesting that the mantle source is strongly contaminated by the slab sediments. Gas geothermometry based on the kinetically rapid H2 – H2O – CO – CO2 system indicates equilibrium temperatures >200 ℃ at redox conditions more oxidizing than those commonly characterizing hydrothermal reservoirs. Reactions involving CH4 and C2 – C3 alkenes/alkanes pairs, having a relatively slow kinetics, seem to equilibrate at greater depth where temperatures are >200 ℃ and redox conditions consistent with those inferred by the presence SO2 – H2S redox pair, typical of a magmatic fluid environment. A comprehensive conceptual geochemical model describing the circulation pattern of the Tupungatito hydrothermal – magmatic fluids is proposed to show fluid source regions and re – equilibration processes affecting the different gas species occurring at changing chemical – physical conditions as the magmatic – hydrothermal fluids rise up toward the surface.

By comparing the Tupungatito gas geochemical data with those discharging from other volcanic systems located in the northernmost sector of the Chilean Andes, it is possible to asses that i) different climate, ii) amount and composition of the subducted sediment, iii) slab thermal state, and iv) crustal thickness and lithology do not apparently play a significant influence on the gas chemistry.

Central Chile volcanic lakes: the Tupungatito and Peteroa acid crater lakes

Oscar Benavente[1,2], Franco Tassi[3,4], Felipe Aguilera[2,5], Mariano Agusto[6], Alberto Caselli[6], Francisco Gutiérrez[1,2], Orlando Vaselli[3,4], Martin Reich[1,2].

[1] Departamento de Geología, Universidad de Chile, Plaza Ercilla, 803 – 8370450 Santiago (Chile). [2] Centro de Excelencia en Geotermia de los Andes (CEGA), Universidad de Chile, Plaza Ercilla, 803 – 8370450 Santiago (Chile). [3] Dipartimento di Scienze della Terra, Via G. La Pira, 4 – 50121 Firenze (Italy). [4] CNR-IGG Istituto di Geoscienze e Georisorse, Via G. La Pira, 4 – 50121 Firenze (Italy). [5] Departamento de Geología, Universidad de Atacama, Copayapu 485 – 1532296 Copiapó (Chile). [6] Departamento de Geología, Facultad de Ciencias Exactas y Naturales, Universidad de Buenos Aires, Buenos Aires, Argentina

E-mail: obenaven@ing.uchile.cl

Oral presentation

Central Chile volcanism (CCV; 33-36°S) is controlled by dehydration of Nazca plate and subsequent partial melting of the mantle wedge (Hildreth and Moorbath 1984). Among the thirteen volcanoes of the CCV, whose location is structurally controlled by Cenozoic east-verging margin-parallel folds and thrusts, six experienced historical eruptions (Tupungatito in 1987; San José in 1960; Maipo in 1912; Tinguiririca in 1917; Planchón-Peteroa in 1991, 1998, 2010-2011; Quizapu in 1846 and 1932).

Tupungatito (33.4°S-69.8°W; 5600 m.a.s.l.) and Planchón-Peteroa (35.5°S-70.2°W; 4107 m.a.s.l.) are the sole volcanoes of central Chile characterized by permanent fumarolic activity and the occurrence of crater lakes at its summit (González-Ferrán 1995). This study show the preliminary geochemical data of water samples collected from these hyper-acidic volcanic lakes during three campaigns carried out since 2010.

Tupungatito lake water has a temperature, pH and TDS ranging from 32.2 to 35.2 °C, 0.34 to 0.6 and 38.9 to 45.1 g/L respectively. SO_4 and Cl are the mains anions (up to 13.69 and 12.50 g/L respectively), however important concentrations of F are found (up to 0.31 g/L). Ca correspond to the main cation (up to 1.48 g/L), followed by Na, K and Mg (up to 0.8, 0.49 and 0.47 g/L respectively). On the other hand, Planchón-Peteroa lake waters has a pH, temperature and TDS ranging from 1.49 to 2.91, 7.4 to 43.2°C, and 4,58-7,50 g/L respectively. SO_4, Cl and Ca are also the mains ions (3.28, 0.66 and 1.47 g/L respectively) followed by Na, K and Mg (806, 492 and 470 mg/L respectively).

The high SO_4 and Cl concentrations relative to the Ca, Na, K and Mg abundances, as well as the low pH of Tupungatito and Planchón-Peteroa crater lakes are typical of volcanic lakes acting as condensers and calorimeters for acid compounds (e.g. SO_2-H_2S, HCl and HF) and heat released from hydrothermal-magmatic degassing, where the rate of acidification greatly exceeds the rate of neutralization (acid-brine type systems; Varekamp et al. 2000).

Similar results were reported at Copahue volcano (37.51°S-71.1°W; 2997 m.a.s.l) by Varekamp et al. (2003) in the south of Chile. Chemical and physical parameters have been monitored periodically since 2003 at Copahue volcano (Agusto 2011). These features have been contrasted with the surface deformation in this volcanic area (Velez 2012) as part of a monitoring

program at Copahue volcano, being very helpful to understand the evolution of the volcanic-hydrothermal systems in active and quiet periods.

Tupungatito and Planchón-Peteroa volcanoes are the most active volcanoes of central Chile, with nineteen historical eruptions each. The relative low maximum VEI of these volcanoes (2 and 4 for Tupungatito and Planchón-Peteroa respectively), as well as their proximity to Chilean and Argentinian cities, makes their crater lakes suitable to the application of geochemical surveillance and monitored techniques as the crater lake of Copahue volcano.

REFERENCES

Agusto, M., 2011. Estudio geoquímico de los fluidos volcánicos e hidrotermales del Complejo Volcánico Copahue Caviahue y su aplicación para tareas de seguimiento. Tesis Doctoral (inédita) Universidad de Buenos Aires: 270 pp.

González-Ferrán, O. 1995. Volcanes de Chile. Instituto Geográfico Militar, 639 p. Santiago.

Hildreth, W. and S. Moorbath. 1988. "Crustal contributions to arc magmatism in the Andes of Central Chile." Contributions to Mineralogy and Petrology 98(4): 455-489.

Varekamp, J.C., Pasternack, G.B. & Rowe, G.L. 2000. Vol- canic lake systematics. II. Chemical constraints: J. Vol- canol. Geotherm. Res. 97: 161-179

Varekamp, J.C., Flynn, K., Ouimette, A.P., Herman, S., Delpino, D. & Bermudez, A. 2003. Compositional changes in hydrothermal fluids from Copahue volcano, Argentina, during the 2000 eruptions. Pageophs.

Velez, M.L, 2012. Análisis de la deformación asociada al comportamiento de sistemas volcánicos activos: volcán Copahue. Tesis Doctoral (inédita) Universidad de Buenos Aires. 150 pp.

ICMGP - Edinburgh 2013
International Conference on
Mercury as a Global Pollutant

Real-time measurements of gaseous elemental mercury at the summit area of Mt. Etna volcano (Italy): preliminary results

[1]*S. Calabrese, [2]J. Cabassi, [1]M. Bitetto, [3]F. Capecchiaccii, [4]O.M. Benavente Zolezzi, [1,2]F.Tassi, [5]W, D'Alessandro, [1]F. Parello, [2,3]O. Vaselli

(1) DiSTeM -Università degli Studi di Palermo, via Archirafi 36, 90123 Palermo (Italy)
(2) Dipartimento di Scienze della Terra, Via G. Pira 4, 50121 Firenze (Italy)
(3) CNR-IGG Istituto di Geoscienze e Georisorse, Via G. Pira 4, 50121 Firenze (Italy)
(4) Departamento de Geología, Universidad de Chile, Plaza Ercilla 803, 8370450 Santiago (Chile)
(5) Istituto Nazionale di Geofisica e Vulcanologia - INGV Palermo, Via Ugo La Malfa 153, 90146 Palermo (Italy)

sergio.calabrese@gmail.com

INTRODUCTION

Mercury is a highly toxic element whose accumulation can cause adverse effects on both human health and ecological systems. The dominant form of mercury in the atmosphere is gaseous elemental mercury (Hg^0 ~98%), characterized by high stability (residence time 0.5-2 years), low solubility and high volatility. Volcanic emissions are the major natural source of mercury to the atmosphere and constant degassing from open-conduit volcanoes, such as Mt. Etna, can have a significant local environmental impact.


Summit craters from Torre del Filosofo

METHODS

A field study was performed in September 2012 at the summit area of Mt. Etna volcano to investigate atmospheric concentrations of Hg in an area affected by diluted volcanic plume. The study area, Torre del Filosofo, is located at the base of the summit craters at 2,900 m a.s.l. and is visited by hundreds of tourists every day. The area is situated at approximately 1.5 km from the active vents and is often affected by plume fumigation due to its downwind position with respect to the prevailing winds, causing frequent high levels of gaseous volcanic species like SO_2, HCl and HF.

The simultaneous real-time measurements of Hg^0, CO_2, SO_2 and meteorological parameters (air temperature, pressure and relative humidity) were made by coupling a portable Zeeman atomic absorption spectrometer with high frequency modulation of light polarization (Lumex RA-915M) and a multigas analyzer (manufactured by INGV-Palermo). The acquisition of the GPS signal at the same time allowed us to obtain spatial coordinates for each concentration value. All instruments were synchronized and set to high-frequency acquisition (every two seconds). Measurements were carried out along transects-walk (about 2 km path, with a mean speed 1.5 km/h) across the diluted volcanic plume.

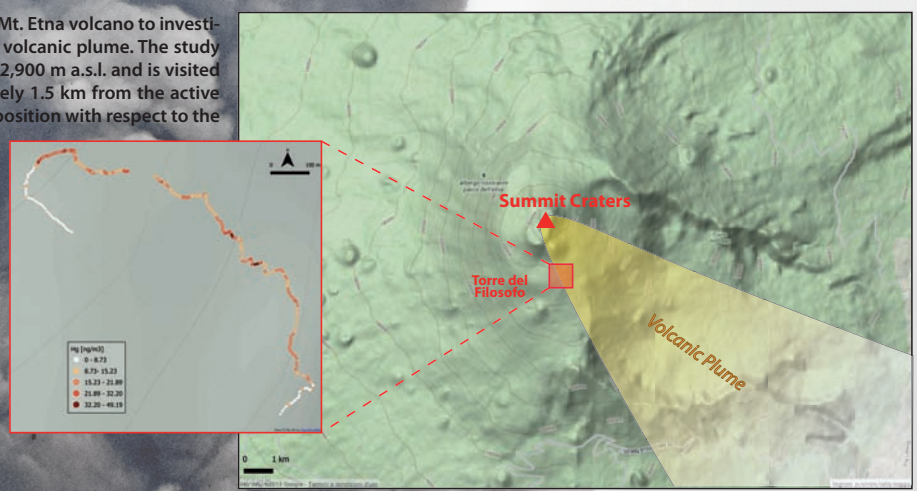

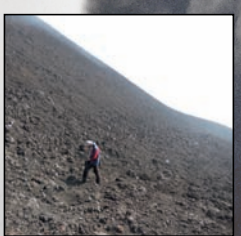

PRELIMINARY RESULTS

Based on about 1,200 measurements, the average concentrations of gaseous mercury inside the diluted-plume amounted to 15-20 ng/m³, with a peak concentration of 75 ng/m³, in contrast to the low values (4-8 ng/m³) measured outside the plume. Concentrations of 200-500 ng/m³ previously measured at the crater rims indicate a substantial dilution of the plume in the study area. The comparison with the SO_2 and CO_2 concentrations (0.8-3 ppm and 320-600 ppm respectively) allowed us to confirm that the anomalous mercury concentrations are directly related to the diluted plume, although the two patterns do not always show a significant correlation. Real-time detection of Hg allowed to highlight high-frequency variability in the continuous signal, probably related to both wind effects and to the air-plume dilution.

Preliminary field tests results of the portable mercury spectrometer were successful and showed its unique capabilities of continuous measurements of mercury in diluted volcanic emissions. This method, associated with other real-time instruments, offers a useful tool to easily map spatial dispersion of volcanic plume and to better evaluate the plume dilution with the distance from active craters.

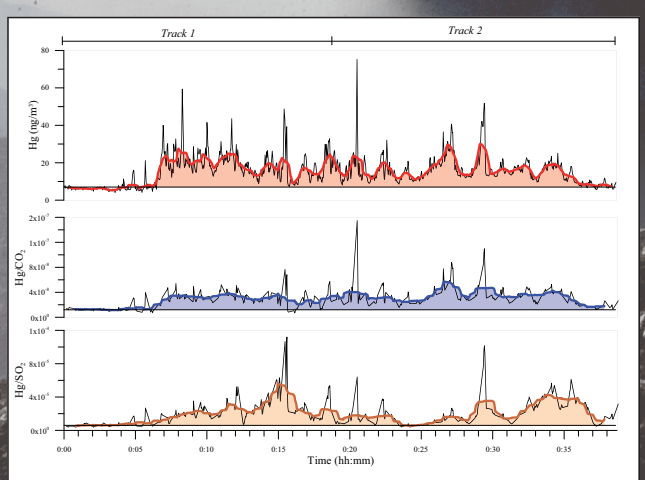

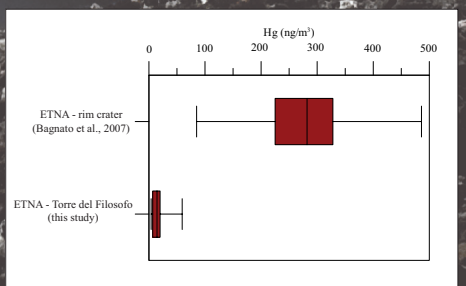

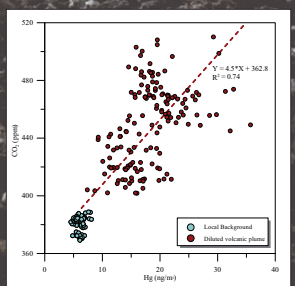

El sistema magmático-hidrotermal asociado al Volcán Tupungatito, Región Metropolitana, Chile

Oscar Benavente[1,2*], Francisco Gutiérrez[1,2], Felipe Aguilera[2,3], Martin Reich[1,2], Franco Tassi[4] y Orlando Vaselli[4].
[1] *Departamento de Geología, Facultad de Ciencias Físicas y Matemáticas, Universidad de Chile, Plaza Ercilla 803, Santiago, Chile.*
[2] *Centro de Excelencia en Geotermia de los Andes (CEGA), Universidad de Chile, Plaza Ercilla 803, Santiago, Chile.*
[3] *Departamento de Geología, Facultad de Ingeniería, Universidad de Atacama, Copayapu 485, Copiapó, Chile.*
[4] *Departamento de Ciencias de la Tierra, Universidad de Florencia, Via La Pira 4,50121, Florencia, Italia.*

** E-mail: oscar.benavente.zolezzi@gmail.com*

Resumen. El Volcán Tupungatito es una caldera con ocho cráteres activos pertenecientes a la parte norte de la Zona Volcánica Sur, 70 km al Este de la ciudad de Santiago (33.4°S, 69.8°W; 5682 m.s.n.m). La fuente de los fluidos presentes es principalmente hidrotermal, con una componente magmática importante. El sistema volcánico esta dominado por un dominio profundo de gas y líquido en equilibrio a 330°C y uno vapor condensado más somero con una temperatura de equilibrio de 230°C.

Palabras Claves: Volcán Tupungatito, Geoquímica de Fluidos volcánicos.

1. Introducción

El volcán Tupungatito (33.4°S, 69.8°W; 5682 m.s.n.m) corresponde a una caldera volcánica localizada en la Región Metropolitana de Chile, 70 km al Este de la ciudad de Santiago (Fig. 1a). Actualmente, el Tupungatito es el volcán más al norte de la Zona Volcánica Sur (ZVS) en presentar actividad solfatárica permanente, incluida la existencia de tres lagunas cratéricas en su interior (Fig. 1b). Éste volcán es uno de los tres centros eruptivos (Tupungatito, San José y Maipo) de la ZVS norte en presentar actividad histórica, y cuya última erupción data del año 1987 (Stern et al., 2007). Producto de la altura de su cráter, el volcán Tupungatito está cubierto de nieve y hielo, actuando como un importante alimentador de los sistemas de drenajes de la alta cordillera. Éstos, en última instancia desembocan en el río Maipo, el cual cruza la ciudad de Santiago (Stern et al., 2007). A pesar de los potenciales riesgos geológicos existentes en una eventual erupción del volcán Tupungatito (e.j. flujo de ceniza, lahares y caída de ceniza), poco se sabe acerca de las características petrológicas de los productos volcánicos del Tupungatito (Hildreth and Moorbarth, 1988; Stern et al., 2007). Adicionalmente, no existen datos monitoreo sismológico del volcán, y tampoco un catastro geoquímico e isotópico de las numerosas manifestaciones termales dentro del cráter.

Este trabajo presenta los primeros resultados de la composición química e isotópica de los gases y aguas recolectadas durante dos campañas de terreno, realizadas durante el mes de Febrero 2011 y Febrero 2012. Junto con el análisis de datos, se discute las principales características geoquímicas de los fluidos emitidos en el volcán Tupungatito, y se formula un modelo conceptual del sistema magmático e hidrotermal.

2. Marco geológico

El volcán Tupungatito se localiza en la Cordillera Principal de la Cordillera de los Andes, donde la geología consiste principalmente en secuencias marinas y volcanoclásticas Meso-Cenozoicas, de Este a Oeste respectivamente (Farías et al., 2010). Estructuralmente esta zona destaca por fallas inversas de alto ángulo asociadas a la inversión de la cuenca de Abanico en la parte Oeste, y fallas inversas asociadas a la faja plegada y corrida de Aconcagua en la porción Este (Farías et al., 2010). Ambos dominios litológicos y estructurales se encuentran en contacto a través del sistema de falla El Diablo (Farías et al., 2010). Depositado disconformemente sobre las deformadas secuencias Mesozoicas se encuentran los más de 6 km^3 de lavas pertenecientes al edificio del Volcán Tupungatito (Hildreth and Moorbarth, 1988), que corresponde a una caldera volcánica compuesta con 8 cráteres activos anidados en su interior (González-Ferrán, 1995). La caldera tiene 5 km de diámetro y una edad Pleistocena reciente (González-Ferrán, 1995). Los productos volcánicos del Tupungatito tienen una composición andesítica a basalto andesítica (Hildreth and Moorbarth, 1988).

La actividad histórica del Tupungatito registra 19 erupciones desde 1829, donde la mayor parte de éstas no superan el índice de explosividad 2 (González-Ferrán, 1995). Por otro lado, los registros históricos muestran que la mayoría de las erupciones del Tupungatito se encuentran temporalmente relacionadas con los grandes eventos tectónicos de Chile central (González-Ferrán, 1995).

3. Resultados

La temperaturas de las fumarolas varían entre 82.5 y 117°C. El contenido de vapor de agua varía entre 72.4 a 75.69 % del volumen total. La composición de la fracción seca del gas se caracteriza por la presencia de CO_2 como el gas más abundante ($\leq$ 973.556 μmol/mol), y la presencia

de gases ácidos como HCl (≤ 0.307 µmol/mol), HF (≤ 0.026 µmol/mol) y SO_2 (≤ 0.215 µmol/mol). Otras especies importantes corresponden a H_2S (≤ 22.217 µmol/mol), N_2 (≤ 4.893 µmol/mol), S (≤ 0.001 µmol/mol), CH_4 (≤ 0.439 µmol/mol), Ar (≤ 0.005 µmol/mol), O_2 (≤ 0.029 µmol/mol), H_2 (≤ 2.415 µmol/mol), He (≤ 0.094 µmol/mol) y CO (≤ 0.0019 µmol/mol). Las concentraciones de los hidrocarburos livianos (ΣC_2-C_7) varían entre 0.0017 y 0.0027 µmol/mol. El contenido de $\delta^{13}C$-CO_2 varía entre -2.92 y -6.84‰ V-PDB. La composición isotópica varía para δD entre -55 y -72‰ V-SMOW, mientras que para $\delta^{18}O$ lo hace entre -3.3 y 0.8‰ V-SMOW. La composición isotópica expresada en R/Ra varía entre 5.19 y 5.45.

La temperatura del agua de la laguna cratérica alcanza los 32.2°C. El pH del agua es de 0.34, el total de sólidos disuelto es de 40 gr/lt y la composición química se caracteriza por la presencia de SO_4 (12589 mg/lt), Cl (12504 mg/lt), Ca (1097 mg/lt), Na (589 mg/lt), K (355 mg/lt) y Mg (305 mg/lt).

4. Discusiones

Las descargas fumarólicas del volcán Tupungatito pueden ser consideradas como el resultado de la mezcla entre dos miembros, uno relacionados a una fuente magmática y el otro a una fuente hidrotermal muy desarrollada.

La fuente magmática está representada por las altas concentraciones de SO_2 y N_2, y la razón N_2/He~800, ambas relacionadas a la deshidratación del slab (Figura 2). Por otro lado, la fuente hidrotermal está representada por la presencia de las altas concentraciones de H_2S y CH_4, y por el desarrollo de lagunas cratéricas dentro del crater, las cuales son las representaciones más someras del sistema hidrotermal (Varekamp et al., 2000). De acuerdo a la composición química de la laguna cratérica, ésta puede ser clasificada como una del tipo activa producto de la alta concentración de SO_4 y Cl y su bajo pH, sugiriendo un importante input de gases ácidos de origen magmático en la génesis laguna.

La composición isotópica de $\delta^{18}O$ and δD de las fumarolas sugiere que el origen de los fluidos se debe al resultado de la mezcla entre aguas andesíticas y aguas meteóricas, mientras que la composición isotópica de He sugiere una mezcla entre un componente mantélico (R/Ra~8) y cortical (R/Ra~0.1).

La composición isotópica de $\delta_{13}C$-CO_2 indica que la principal fuente de carbón es la deshidratación de los sedimentos del slab, con un escaso input mantélico (MORB).

De acuerdo a los cálculos geotermométricos, el volcán Tupungatito es un sistema vapor-líquido en equilibrio, donde el vapor es separado de un acuífero en ebullición a una temperatura de ~330°C. Estos fluidos hacienden y son condensados en el sistema hidrotermal sobreyacente (*scrubbing*), haciendo que los fluidos estén controlados por el buffer hidrotermal (FeO-$FeO_{1.5}$) a una temperatura entre 200 y 250°C.

Este sencillo modelo geoquímico de la evolución de los fluidos, además de explicar bastante bien los datos químicos e isotópicos de los fluidos, entrega información acerca del estado eruptivo del volcán. Producto del abundante agua en la zona, existirá un balance entre el input de energía y masa desde la cámara magmática y el *scrubbing* de esta masa en el cuerpo de agua del sistema hidrotermal (Symonds et al., 2001). De esta manera las condiciones hidrotermales serán siempre una constante encima del volcán, hasta que exista un aumento importante del input energético y másico desde la cámara magmática (e.g. en periodos eruptivos). Muy diferente a lo que acontece en zonas áridas (norte de Chile), donde los volcánes por lo general tienen un sistema volcánico bien desarrollado encima del volcán y el sistema hidrotermal está supeditado a los bordes del volcán, por lo que durante periodos de actividad volcánica y entre éstos, el *buffer* volcánico siempre estará presente (Aguilera et al., 2011; Capaccioni et al., 2011).

Agradecimientos

Los autores agradecen a las siguientes fuentes de financiamiento: (i) MECESUP UCH-0708 por el financiamiento de la beca de doctorado del autor principal, (ii) FONDAP-Centro de Excelencia en Geotermia de los Andes (CEGA), por el financiamiento de los equipos de terreno, el trabajo de campo y la asistencia a congresos y (iii) PBCT-PDA07 por financiar equipo de trabajo y trabajo de campo.

Referencias

Aguilera, F., Tassi, F., Darrah, T., Moune, S., Vaselli, O. 2011. Geochemical model of a magmatic hydrothermal system at the Lastarria volcano, northern Chile. Bulletin of Volcanology..

Capaccioni B. et al. 2011. Geochemical and isotopic evidences of magmatic inputs in the hydrothermal reservoir feeding the fumarolic discharges of Tacora volcano (northern Chile). Journal of Volcanology and Geothermal Research 208 (2011) 77–85.

Chiodini G. and Marini L. 1998. Hydrothermal gas equilibria; the H2O-H2 -CO2 -CO-CH4 system Geochim. Cosmochim. Acta 62(15), 2673-2687.

Farias, M., D. Comte, et al. 2010. "Crustal-scale structural architecture in central Chile based on seismicity and surface geology: Implications for Andean mountain building." Tectonics 29: 22

Giggenbach W.F. and Gougel R.L. (1989). Collection and analysis of geothermal and volcanic water and gas discharges. Inst. Geol. Nucl. Sci. New Zealand, Report n. CD2401, 36-53..

Giggenbach, W.F., 1997. The origin and evolution of fluids in magmatic-hydrothermal systems. In: Barnes, H.L. (Ed.), Geochemistry of Hydrothermal Ore Deposits, 3rd ed. JohnWiley and Sons, New York, NY, USA, p. 972

González-Ferrán, O. 1995. Volcanes de Chile. Instituto Geográfico Militar, 639 p. Santiago

Hildreth, W. and S. Moorbath. 1988. “Crustal contributions to arc magmatism in the Andes of Central Chile.” Contributions to Mineralogy and Petrology 98(4): 455-489.

Stern, C., Moreno, H., López-Escobar, L., Clavero, J., Lara, L., Naranjo, J., Parada, M., Skewes, A. 2007.Chilean Volcanoes. In Geology of Chile, Moreno, T., Gibbons, W. (ed.). Geological Society of London. P. 289-308

Symonds, R.B., Gerlach, T.M. and Reed, M.H., 2001, Magmatic gas scrubbing: implications for volcano monitoring, J. Volcanol. Geotherm. Res. 108, 303-341.

Tassi, F., Aguilera, F., Darrah, T., Vaselli, O., Capaccioni, B., Poreda, R J., Huertas, A Delgado. 2010. Fluid geochemistry of hydrothermal systems in the Arica-Parinacota , Tarapacá and Antofagasta regions (northern Chile). Journal of Volcanology and Geothermal Research. Vol 192. 1-15.

Varekamp, J.C., G.B. Pasternack, and G.L. Rowe Jr. 2000. Volcanic lake systematics II. Chemical constraints, J. Volcanol. Geotherm. Res., 97:161-179.

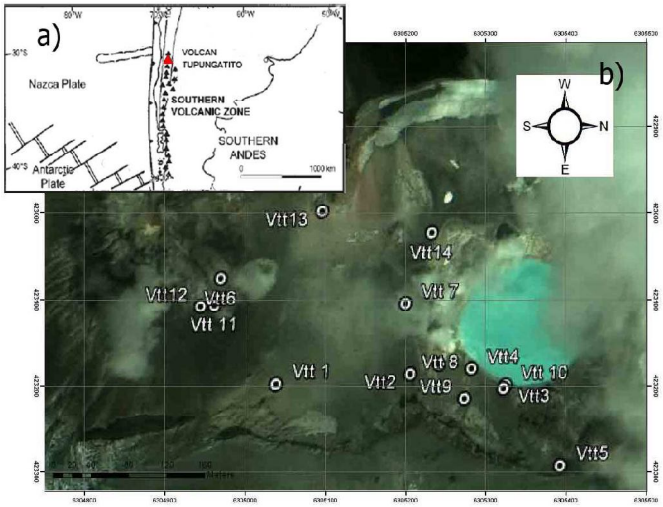

Figura 1. a) Mapa ubicación del volcán Tupungatito en la Zona Volcánica. b) Mapa de los cráteres del volcán Tupungatito y los puntos de muestreo.

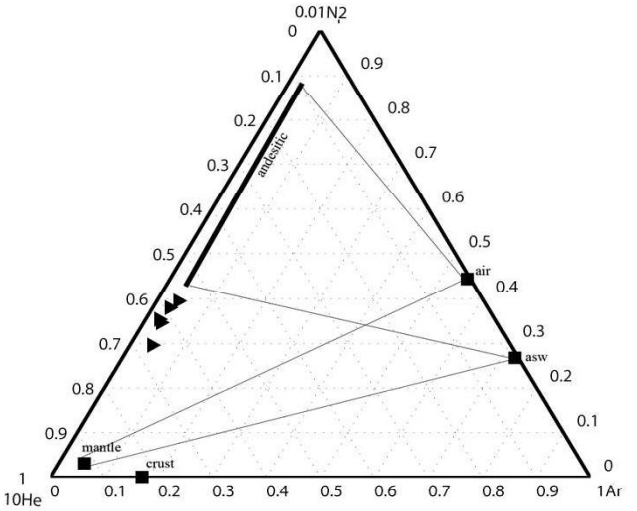

Figura 2. Diagrama triangular de N_2/100-Ar-He*10 de las descargas fumarólicas del volcán Tupungatito (Giggenbach et al., 1997).

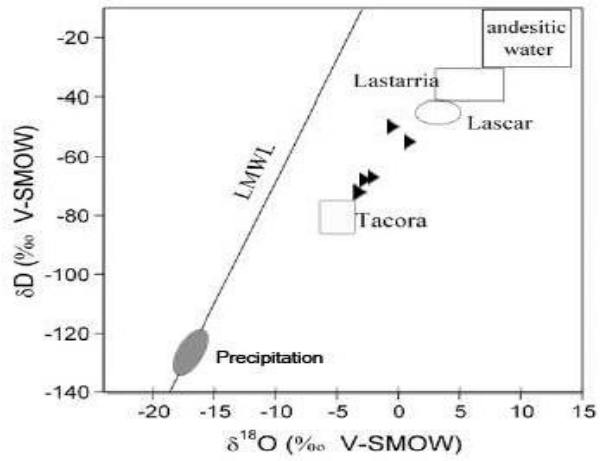

Figura 3. Diagrama binario de $\delta^{18}O$ vs δD para las descargas fumarólicas del volcán Tupungatito.. Con fines de comparación se ponen los campos del volcán Lastarrias, Lascar y Tacora (Capaccioni et al., 2011), además de las precipitación de la zona de estudio y el campo de aguas andesíticas (Giggenbach et al., 1997).

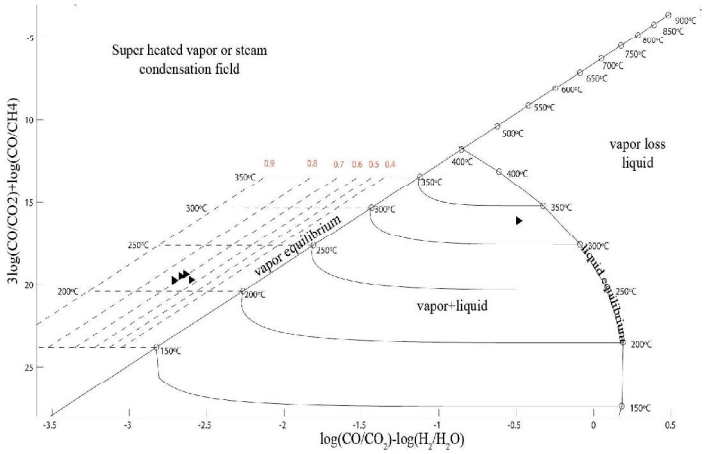

Figura 4. Diagrama binario de de la suma de las razones CO/CO2-H2/H2O v/s CO/CO2+CO/CH4 para las descargas fumarólicas del volcán Tupungatito..

Fluids Geochemistry from Planchón-Peteroa-Azufre volcanic Complex, Southern Volcanic Zone, Chile

Ornella Saltori[1,2]*, Felipe Aguilera[1,2], Mariano Agusto[3], Oscar Benavente[2,4], Franco Tassi[5], Alberto Caselli[3], Francisco Gutierrez[2,4], Marcela Pizarro[1,2]

[1] *Departamento de Geología, Universidad de Atacama, Chile*
[2] *Centro de Excelencia en Geotermia (CEGA), Universidad de Chile, Chile*
[3] *Departamento de Ciencias Geológicas, Universidad de Buenos Aires, Argentina*
[4] *Departamento de Geología, Universidad de Chile, Chile*
[5] *Dipartimento di Scienze della Terra, Università degli Studi di Firenze, Italia*

* *E-mail: o.saltori@gmail.com*

Abstract. Peteroa is a composite stratovolcano located at the border between Chile and Argentina (35 ° 31'W-70 ° 14'S-4,107 m a.s.l.) and belongs to the Planchon-Peteroa-Azufre Volcanic Complex. Peteroa presents 4 craters hosting acidic lakes and 3 of them with fumarolic activity. Several thermal springs, occasionally associated with bubbling gases, were recognized in the surrounding of the volcano. Gas geochemistry suggests the presence of a shallow hydrothermal system, constituted by vapor separated from a boiling aquifer at temperatures from 275°C to 340°C, which is affected by input of deep magmatic species (e.g. SO_2, N_2 and ^3He). A mix of hydrothermal and meteoric end members characterizes surrounding thermal springs, although magmatic input cannot be ruled out. Crater lakes have acidic SO_4^{2+} waters, whereas the thermal springs located within the Gendarmería, El Azufre and External valleys, have a HCO_3^--Na^+ and Cl^--Na^+ composition.

Key words: Fluid geochemistry, crater lake, thermal springs, Peteroa.

1 Introduction and geological setting

Planchon-Peteroa-Azufre Volcanic Complex (PPAVC) is a NE-SW volcanic chain located in the border between Chile and Argentina (35º31'W-70°14'S – 4,107 m s.n.m.) and is part of the Southern Andean Volcanic Zone (SAVZ) (Fig. 1). The 4 km wide caldera summit of the currently active Peteroa volcano show 4 main craters (150-500 m diameter) and a scoria cone (150 m diameter, 60 m height) (Naranjo et al., 1999). Acidic lakes are hosted in the 4 craters, 3 of them showing permanent fumarolic activity. An intense thermal activity characterized by presence of thermal springs can be recognized in: the Vergara Valley (N side), External Valley (NE side), Gendarmeria and Los Azufres valleys (E side), SE flank of Azufre volcano and Colorado Valley (SSE side).

Peteroa volcano is the youngest and smallest (<1 km^3) volcano of the PPAVC, and is formed by calc-alkaline lavas and pyroclastic units, mainly corresponding to andesites and Holocene rhyodacitic tuffs. Differently, Azufre and Planchon volcanoes are composed by basaltic to dacitic lava and pyroclastic flows (Tormey et al., 1995). PPAVC is built above an underlying basement consisting in Cretaceous marine and evaporitic sediments, formed mostly of limestone, conglomerates and sandstones, basaltic to rhyolitic lava flows and pyroclastic rocks (Tertiary) and Middle Tertiary granodiorite plutons (e.g. Haller et al., 1985; Naranjo et al., 1999). PPAVC is related genetically to strike-slip faults W–NW trend, where volcanoes are aligned (Tormey et al., 1995).

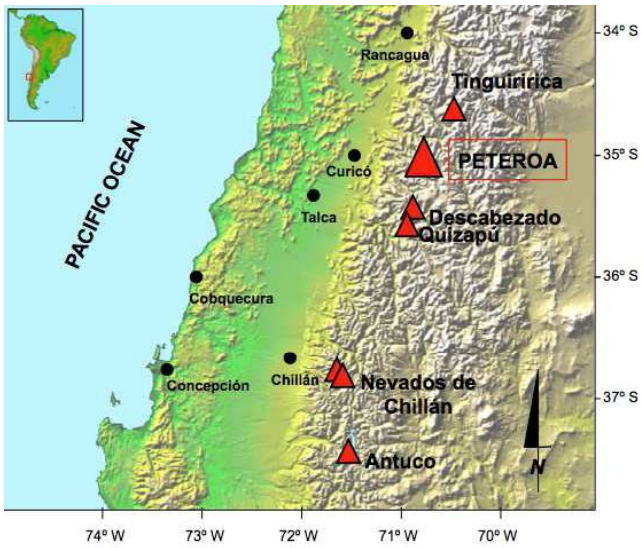

Figure 1. Location map of the study area.

Historical activity of Peteroa volcano includes explosive eruptions in 1762 and 1889–1894 and lava flows in 1837 and 1937. In 1991, the greatest phreatomagmatic eruption of the 20th century occurred. This eruption produced eruptive columns as high as 1,000 and 2,000 m above the crater, being dispersed to E-NE by 80 km approximately. Lahars occurred in the W side of volcano (BGVN, 1991; Gonzalez-Ferrán, 1995; Naranjo et al., 1999). The last eruptive cycle started during September 2010, with sporadic phreatic explosions in October 2010, February, April and May 2011.

This study presents chemical and isotopic data of gas and water from fumaroles, crater lakes and thermal springs related to PPAVC for period 2010-2011. The main aim is

to determine the geochemical characteristics of the hydrothermal-magmatic system in the PPAVC.

3 Results

3.1 Gas composition

Gas samples from fumaroles and bubbling pools present temperatures that ranging from 87.7 to 102.1°C, and 24 to 46.2, respectively. Water vapor ranged from 78.19 to 96.15% vol., and from 0.95 to 3.49% vol., for fumaroles and bubbling pools, respectively. Gas composition (excepting water vapour) is dominated by CO_2 (up to 997,000 µmol/mol), and is characterized by presence of SO_2 (up to 0.550 µmol/mol), HCl (up to 0.385 µmol/mol) and HF (up to 0.021 µmol/mol), with the exception of Barros Colorado fumarole and those gas samples collected from the bubbling pools of the surrounding valleys. Significant concentrations of H_2S (up to 35.4 µmol/mol), N_2 (up to 8.14 µmol/mol), CH_4 (up to 1.58 µmol/mol), H_2 (up to 0.384 µmol/mol) and CO (up to 0.015 µmol/mol), where also measured in the fumaroles. Oxygen, Ar and He have concentrations up to 0.64, 0.15 and 0.0078 µmol/mol, respectively. Light hydrocarbons concentrations (ΣC_2–C_7) ranges from 0.0094 to 2.90 µmol/mol. The $\delta^{13}C$-CO_2 values range from -13.21 to -2.02‰ V-PDB. The δD and $\delta^{18}O$ values in water of condensate samples range from -106 to -73‰ and from -14.7 to -3.5‰ V-SMOW, respectively. Helium isotopes composition expressed as R/R_a range between 3.27 and 7.11.

3.2 Water composition

Water samples from bubbling pools and springs have temperature, pH and TDS that range from 2.3 to 77.2°C, 1.49 to 7.92 and 107 to 11,663 mg/L. The concentration of main anions, HCO_3^-, SO_4^{2-} and Cl^-, range from 7 to 1,334 mg/L, 2.1 to 3,288 mg/L and 0.04 to 5,135 mg/L, respectively. The more abundant cations are Na^+ (from 5.3 to 3,674 mg/L), K^+ (from 1.7 to 462 mg/L), Ca^{2+} (from 16 to 674 mg/L) and Mg^{2+} (from 4 to 377 mg/L). Concentrations of NO_3^- are up to 3.64 mg/L, whereas those of F^-, Br^- and Li^+ are up to 39.2, 5.81 and 1.96 mg/L, respectively. The δD and $\delta^{18}O$ values of waters vary from -106 to -74‰ and from -14.7 to -9.5 ‰ V-SMOW, respectively.

4 Discussion

4.1 Gas geochemistry

Gases from Peteroa craters, Colorado Valley and all thermal springs are result of mixing from two end members: i) Hydrothermal and ii) magmatic sources (Fig. 2). In the case of Peteroa craters discharges, the presence of high temperature gas like SO_2, and other acid gases like HCl and HF, suggest input of fluids from a magmatic source. In fact, Peteroa crater fumaroles present high R/Ra ratios, ranging between 6.78 and 7.11. Although Colorado Valley and diverse thermal springs discharges are dominated by input of hydrothermal fluids (Fig. 2), R/Ra ratios suggest contributions of 40 to 46% of magmatic helium (^3He). In fact, N_2/Ar ratios for Colorado Valley discharges (>500) are higher than Air (84), indicating a no atmospheric source for N_2. According to Giggenbach (1996), N_2 in subduction zones is related to sediments released from subducting slab, consequently, N_2 excess can be attributed to a magmatic source. Accordingly, subducted sediments sources originate $\delta^{13}C$-CO_2 composition. Thermal springs discharges are affected by meteoric fluids, scrubbing its original compositions, being especially strong in the farthest springs (e.g. External Valley) (Fig. 2).

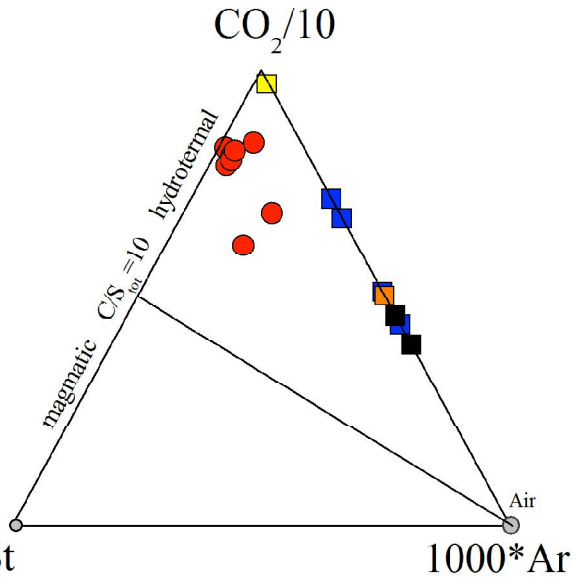

Figure 2. 1000*Ar-CO_2/10-St ternary diagram for PPAVC gases. Red circles: Peteroa crater; Black squares: Gendarmería Valley; Blue squares: Los Azufres Valley; Orange squares: External Valley; Yellow Square: Colorado Valley

4.2 Water geochemistry

Accordingly to Fig. 3, crater lake samples show typical acid SO_4^{2-}-(Cl^-)-Ca^{2+} waters, produced by dissolution of gases like SO_2, H_2S and HCl. Waters from Gendarmería and External valleys correspond to HCO_3-(SO_4^{2-})-Na^+, with relatively high contents of Mg^{2+}. Colorado Valley shows two different water groups, the first corresponding to HCO_3^--Na^+ waters, while the second (Río Colorado Spring) shows a Cl^--Na^+ composition, typical waters fed from geothermal reservoirs. Waters from Vergara Valley have a Cl^--Na^+-(Ca^{2+}) composition and can be attributed to waters from a geothermal reservoir.

The water composition in Peteroa crater condensates is consequence of a mix between “andesitic water” and a

meteoric source related to local precipitation (Fig. 4). In the cases of Peteroa crater lakes, Colorado Valley and thermal springs, are dominated by meteoric water.

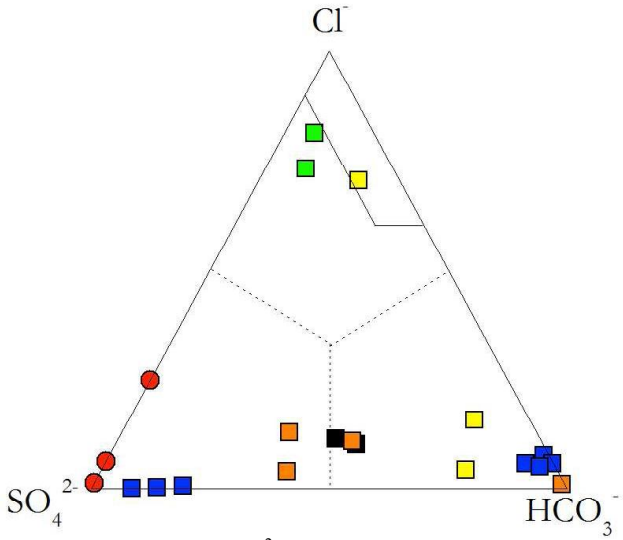

Figure 3. HCO_3^- - Cl^- - SO_4^{2-} ternary diagram for PPAVC waters. Red circles: Peteroa crater lakes; Black squares: Gendarmería Valley; Blue squares: Los Azufres Valley; Orange squares: External Valley; Yellow Square: Colorado Valley; Green squares: Vergara Valley.

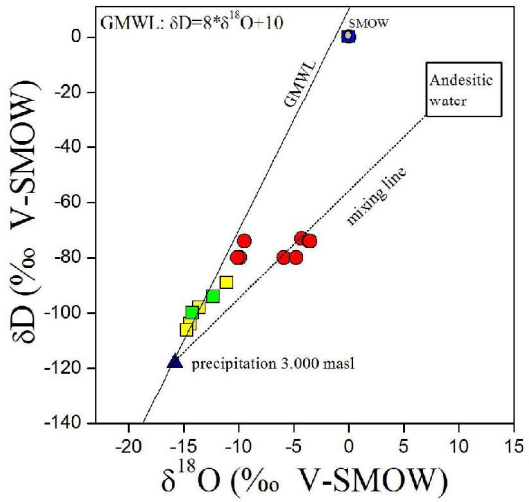

Figure 4. $\delta^{18}O$–δD diagram for fumarolic condensates from PPAVC. Symbols as Fig. 4

Acknowledgements

This work has been funded by FONDECYT Nº 11100372 y FONDAP 15090013 – Centro de Excelencia en Geotermia (CEGA).

References

Bulletin of Global Volcanism Program. 1991. Peteroa. Volcanic Activity Reports. BGVN 16:01. http://www.volcano.si.edu

Giggenbach, W. 1996 Chemical composition of volcanic gases. In: Scarpa M, Tilling RJ (eds) Monitoring and mitigation of Volcanic Hazards. Springer, Heidelberg, pp 221–256

González-Ferrán, O. 1995. Volcanes de Chile. Instituto Geográfico Militar, 639 p. Santiago

Haller, M., Nullo, F., Proserpio, C., Parica, P., Cagoni, M., Walker, J. 1985. Major element geochemistry on early Tertiary Andean volcanic (34º-36ºS). Comunicaciones, Vol. 35, 97-100

Naranjo J., Haller M., Ostera H., Pesce A., Sruoga P. 1999. Geología y Peligros del Complejo Volcánico Planchon-Peteroa, Andes del Sur (35º15´S), Región del Maule, Chile- Provincia de Mendoza, Argentina. Servicio Nacional de Geología y Minería, Boletín No 52.

Tormey D., Frey F., López L. 1995.Geochemistry of the Active Azufre-Planchón-Peteroa Volcanic Complex, Chile (35º15'S): Evidence for Multiple Sources and Processes in a Cordilleran Arc Magmatic System. Journal of Petrology, Vol. 36: 265-298

Eruptive activity of Peteroa Volcano for period 2010-2011, Southern Volcanic Zone, Chile

Felipe Aguilera*[1], Jorge Romero[1,2], Francisco Gutierrez[3], Mariano Agusto[4], Ornella Saltori[1], Oscar Benavente[3], Alberto Caselli[4], Marcela Pizarro[1]

[1] *Departamento de Geología, Universidad de Atacama, Chile*
[2] *Geohiggins, Museo Regional de Rancagua, Chile*
[3] *Departamento de Geología, Universidad de Chile, Chile*
[4] *Departamento de Ciencias Geológicas, Universidad de Buenos Aires, Argentina*

E-mail: felipe.aguilera@uda.cl

Abstract. Peteroa corresponds to a composite stratovolcano located in the border between Chile and Argentina (35º31'W-70°14'S-4,107 m a.s.l.) and belongs to the Planchon-Peteroa-Azufre Volcanic Complex. Peteroa started a new eruptive period (VEI 1-2) during 4 January 2010, when phreatics explosions generated white coloured column of 500 m altitude above crater. Four eruptive stages have been recognized, being the second and fourth the most intense. The main activity, occurred in its westernmost crater, is characterized by phreatic eruptions, which generated columns that reached up 1.5 km above the crater and plumes that extended by 170 km. Main plumes directions were ESE and NNW. Ash fall deposits were identified in the SE flank of the volcano, covering an area of ~200 km^2, with thickness that varied from 4 m to 1 mm. Fall deposit corresponds to dark grey tephra, with grain-size varying from coarse to fine ash and constituted totally by lithics fragments. No juvenile fragments are present. Statistical analysis shows a multi modal deposit, with high contents of fine ash.

Key Words: Phreatic explosions, ash fall deposit, Peteroa volcano

1 Introduction

Planchon-Peteroa-Azufre Volcanic Complex (PPAVC) is a NE-SW volcanic chain located in the border between Chile and Argentina (35º31'W-70°14'S – 4,107 m s.n.m.) and is part of the Southern Andean Volcanic Zone (SAVZ) (Fig. 1). The actual active volcano corresponds to Peteroa, which is distinguished by its 4 km caldera-type crater that hosts 4 craters (150-500 m diameter) and a scoria cone (150 m diameter, 60 m height) (Naranjo et al., 1999). Acid lakes are hosted in 4 craters, while permanent fumarolic activity is present in 3 of them. In the areas that surround the volcano may notice an intense thermal activity with the presence of thermal springs, which often have an intense bubbling gas.

This work describes the characteristics of recent eruptive activity of Peteroa volcano (2010-2011) based on local witnesses information, visual observation of the authors, Southern Andes Volcanic Observatory (OVDAS) internal reports and webcam data, satellite and fall deposit analysis.

2 Geological and volcanological setting

Peteroa volcano is the youngest and smallest (<1 km^3) volcano of the complex, and is formed by calc-alkaline lavas and pyroclastic units, corresponding mainly to andesites and Holocene rhyodacitic tuffs. Differently, Azufre and Planchon volcanoes are composed by basaltic to dacitic lava and pyroclastic flows (Tormey et al., 1995). PPAVC is built above an underlying basement consisting in Cretaceous marine and evaporitic sediments, formed mostly of limestone, conglomerates and sandstones, basaltic to rhyolitic lava flows and pyroclastic rocks (Tertiary) and Middle Tertiary granodiorite plutons (e.g. Haller et al., 1985; Naranjo et al., 1999). PPAVC is related genetically to strike-slip faults W–NW trend, where volcanoes are aligned (Tormey et al., 1995).

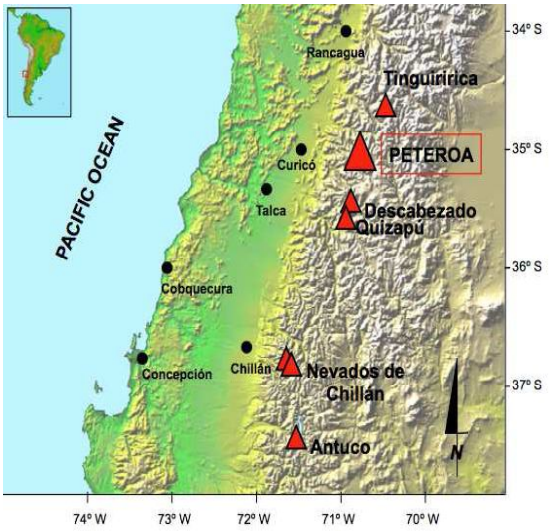

Fig 1. Location map of the study area.

3 Historic eruptive chronology

The historical activity is characterized by the permanent emission of gas from different fumarolic fields. However, sporadic gas column is emitted (~200 m above crater), normally during the summer, probably associated to ice melting. At least 13 historical eruptions have been observed since 1660, corresponding mainly phreatic and

phreatomagmatic, and being frequently associated to those eruptions the generation of lahars (Gonzalez-Ferran 1995). The last eruption occurred during February 1991, when a phreatomagmatic explosion generated eruptive columns between 1.000 and 2.000 m above the crater, which were dispersed to E-NE by 80 km approximately, while lahars were generated in the W side of volcano (BGVN 1991; Gonzalez-Ferran 1995; Naranjo et al 1999).

4. Eruptive chronology

4.1 Stage 1

First report of activity (SERNAGEOMIN, 2010) from Peteroa volcano indicates that a white plume ~250 m above the crater started at 4 January 2010. Phreatic explosions in the acid crater lake of the westernmost crater, that produced a ~500 m of altitude white column, was observed from the authors between 23 and 26 February 2010.

4.2 Stage 2

During 4 September 2010, a 1.2 km of altitude above the crater dark-grey eruptive column was emitted from the westernmost crater (SERNAGEOMIN-OVDAS, 2010a). The plume was dispersed to N by 30 km and ash fall was reported in the NW and NE flanks. Between 6 September and 10 November 2010 diverse explosions produced light to dark-grey eruptive columns, which altitude that varied from 200 to 1,500 m above the crater (Fig. 2). The plumes were dispersed mainly to ESE and NNW, reaching up 170 km of distance (Fig. 3).

4.3 Stage 3

Between 11 November 2010 and first week of February 2011 were emitted steam columns with altitudes ranging 200-300 m above crater (SERNAGEOMIN-OVDAS 2010b, c and 2011a). Visual observations at the eruptive crater during November 2010 evidenced the absence of acid crater lake.

4.3 Stage 4

The period between second week of February and 5 May 2011, a permanent steam column was emitted, with altitude between 200 and 650 m above the crater. Visual observations during March 2011 indicate that a new acid crater lake appeared in the active crater, although littler than February 2010 lake. Explosions were observed the second week of February, 18 March, 16, 17, 18, 19, 21, 25, 26, 27, 28 and 29 April, and 5 May 2011 (SERNAGEOMIN-OVDAS, 2011b, c, d and e). Eruptive columns reached up 1.2 km above the crater, while plumes were dispersed to mainly to SE, reaching up 22 km of distance.

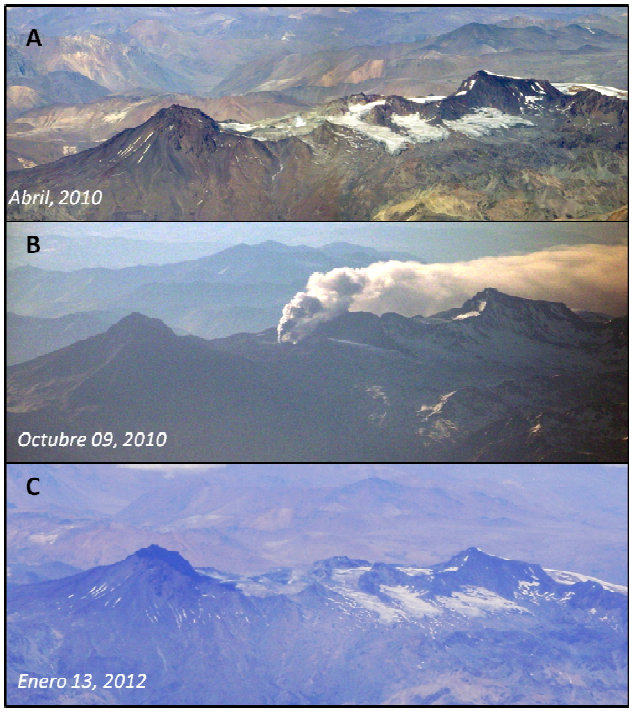

Figure 2. Peteroa volcano during pre eruptive (A), eruptive (B) and post eruptive (C) stages. View from the West. Photos by Victor Marfull and Hector Moyano.

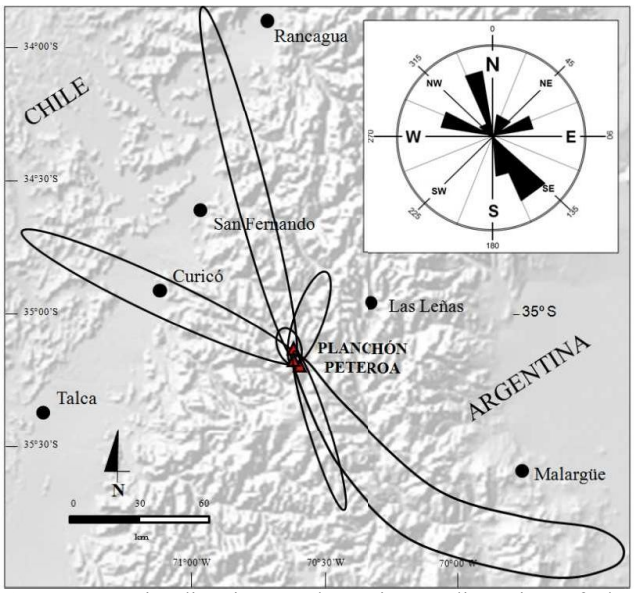

Figure 3. Main directions and maximum dispersion of the eruptive plumes generated during 2010-2011 period

4. Fall deposit analysis

A total area of ~200 km^2 was covered by ash fall, being deposited mainly in the SE flank of volcano, where ~90% of ash was deposited during the second stage. Thickness of ash deposit varies from 4 m on the SE border of active crater to 1 mm, 80 km SE from Peteroa crater.

During March 2011, fall deposit was sampled on the SE border of active crater. Fall deposit corresponds to dark grey tephra, with grain-size varying from coarse to fine ash (2 to <0.075 mm) and constituted totally by lithics fragments. Lithics correspond to poorly vesicular andesitic lava (40-20% vol.), glassy lava fragments (35-10% vol.), and quartz (35-15% vol.), plagioclase (15-8% vol.) and pyroxene (2% vol.) crystals. No juvenile fragments are present in the ash fall deposit. Statistical analysis shows a multi modal deposit, with high contents of fine ash. Ash fall deposit characteristics suggest a typical phreatic eruption.

5. Conclusions

The new eruptive period of Peteroa volcano (January 2010-May 2011) is characterized by four stages, being the second and fourth the most intense. The activity have been characterized by occurrence of phreatic eruptions, which generated columns that reached up 1.5 km above the crater and plumes dispersed to ESE and NNW reaching up 170 km of distance over Argentina. Ash fall deposit, constituted exclusively by lithics fragments and grain-size distribution trending to fine ash is compatible with typical phreatics eruptions. Consequently, have been estimated that 2010-2011 eruptive period correspond to low magnitude event, with a VEI 1-2.

Acknowledgments

This work has been funded by FONDECYT Nº 11100372 (FA) and PBCT-PDA07 (FG) projects. The group is warmly grateful of Constanza Nicolau by her help in the ash analysis, Victor Marfull (POVI) for aerial photographs, Cristobal Bayer, Juan José Oliva, local horse riders Don Aburto and Miguel for their help during the field trip, and Gendarmería Argentina (Paso Vergara) for February 2011 eruption data.

References

Bulletin of Global Volcanism Program. 1991. Peteroa. Volcanic Activity Reports. BGVN 16:01. http://www.volcano.si.edu

González-Ferrán, O. 1995. Volcanes de Chile. Instituto Geográfico Militar, 639 p. Santiago

Haller, M., Nullo, F., Proserpio, C., Parica, P., Cagoni, M., Walker, J. 1985. Major element geochemistry on early Tertiary Andean volcanic (34º-36ºS). Comunicaciones, Vol. 35, 97-100

Naranjo J., Haller M., Ostera H., Pesce A., Sruoga P. 1999. Geología y Peligros del Complejo Volcánico Planchon-Peteroa, Andes del Sur (35º15´S), Región del Maule, Chile- Provincia de Mendoza, Argentina. Servicio Nacional de Geología y Minería, Boletín No 52.

SERNAGEOMIN. 2010. Actividad fumarólica en volcán Planchón. SERNAGEOMIN reporte interno

SERNAGEOMIN-OVDAS. 2010a. Reporte Especial Nº 2, Actividad volcánica Región del Maule, Grupo volcánico Planchón-Peteroa, 6 de Septiembre de 2010. Observatorio Volcánico de los Andes del Sur

SERNAGEOMIN-OVDAS, 2010b. Reporte Nº 11, Actividad volcánica REGIÓN DEL MAULE, Noviembre de 2010. Observatorio volcanológico de los Andes del Sur

SERNAGEOMIN-OVDAS, 2010b. Reporte Nº 12, Actividad volcánica REGIÓN DEL MAULE, Diciembre de 2010. Observatorio volcanológico de los Andes del Sur

SERNAGEOMIN-OVDAS, 2011a. Reporte Nº 13, Actividad volcánica REGIÓN DEL MAULE, Enero de 2011. Observatorio volcanológico de los Andes del Sur

SERNAGEOMIN-OVDAS, 2011b. Reporte Nº 14, Actividad volcánica REGIÓN DEL MAULE, Febrero de 2011. Observatorio volcanológico de los Andes del Sur

SERNAGEOMIN-OVDAS, 2011c. Reporte Nº 15, Actividad volcánica REGIÓN DEL MAULE, Marzo de 2011. Observatorio volcanológico de los Andes del Sur

SERNAGEOMIN-OVDAS, 2011d. Reporte Nº 16, Actividad volcánica REGIÓN DEL MAULE, Abril de 2011. Observatorio volcanológico de los Andes del Sur

SERNAGEOMIN-OVDAS, 2011e. Reporte Nº 17, Actividad volcánica REGIÓN DEL MAULE, Abril de 2011. Observatorio volcanológico de los Andes del Sur

Tormey D., Frey F., López L. 1995. Geochemistry of the Active Azufre-Planchón-Peteroa Volcanic Complex, Chile (35º15'S): Evidence for Multiple Sources and Processes in a Cordilleran Arc Magmatic System. Journal of Petrology, Vol. 36: 265-298

Los sistemas hidrotermales de Chile central (33-36°S)

Oscar Benavente[1,2*], Felipe Aguilera[2,3], Francisco Gutiérrez[1,2], Franco Tassi[3], Martin Reich[1,2] y Orlando Vaselli[4].
[1] *Departamento de Geología, Facultad de Ciencias Físicas y Matemáticas, Universidad de Chile, Plaza Ercilla 803, Santiago, Chile.*
[2] *Centro de Excelencia en Geotermia de los Andes (CEGA), Universidad de Chile, Plaza Ercilla 803, Santiago, Chile.*
[3] *Departamento de Geología, Facultad de Ingeniería, Universidad de Atacama, Copayapu 485, Copiapó, Chile.*
[4] *Departamento de Ciencias de la Tierra, Universidad de Florencia, Via La Pira 4,50121, Florencia, Italia.*

** E-mail: oscar.benavente.zolezzi@gmail.com*

Resumen. La génesis de los sistemas hidrotermales de Chile central se relaciona a la transferencia de masa y energía desde las cámaras magmática de los volcanes cuaternarios, la interacción con las rocas de la cordillera principal y la dilución con agua meteórica. Dos dominios de manifestaciones termales se identifican: alta y baja cordillera. Las manifestaciones termales de alta cordillera corresponden a campos fumarólicos, manantiales calientes y fríos, piscinas burbujeantes y piscinas de barro, mientras que las de baja cordillera corresponden a manantiales fríos. Las variaciones longitudinales y latitudinales en el tipo, química e isotopía de las manifestaciones termales se pueden explicar por la cercanía a la estructura volcánica y el estado termal de la corteza.

Palabras Claves: Sistemas hidrotermales, Geotermia. Geoquímica de Fluidos.

1 Introducción

A pesar del gran potencial geotérmico estimado para Chile (16.000 MW; Lahsen, 1986; Lahsen et al., 2010), la falta de políticas gubernamentales y el escaso conocimiento científico acerca de los sistemas geotérmicos Andinos, han impedido una desarrollo fructífero en la exploración y explotación de este recurso. Chile central (33-36°S) es un buen ejemplo de esto. Esta zona se caracteriza por un gran potencial geotérmico, ya que convergen características geodinámicas que favorecen la ocurrencia de sistemas geotermales, como (Gupta y Roy, 2007): (i) fuentes de calor dada por las cámaras magmática producto del volcanismo cuaternario, (ii) recarga de agua meteórica favorecida por el clima, y (iii) fallas y fracturas que permiten la circulación de fluidos a través de la corteza. A pesar del gran potencial geotérmico de Chile central (4000 W), actualmente sólo existen dos zonas en las cuales se han hecho pozos exploratorios (Tinguiririca y Calabozos), lo que se condice bien con el escaso conocimiento de base sobre los sistemas geotermales de la zona (Benavente y Gutiérrez, 2011; Martini, 2008; Hauser, 1997; Grunder et al., 1987).

Este trabajo presenta un avance en el conocimiento general de los sistemas hidrotermales de Chile central en base a los resultados analíticos de la composición química e isotópica de las diferentes manifestaciones termales obtenidos hasta el momento, así poder entender el desarrollo de los sistemas geotermales en Chile central (33°-36°S), su relación genética con el volcanismo Cuaternario, y la influencia del estilo estructural que controla tanto espacial como temporalmente su ocurrencia.

2 Geología

Chile central es una franja de 500 km pertenecientes a la parte norte de la Zona Volcánica Sur (ZVS), cuyos rasgos morfoestructurales principales que la caracterizan corresponden a franjas Norte-Sur, que de Oeste a Este son (Figura 1): Cordillera Costa (CC), Depresión Central (DC), y Cordillera Principal (CP); siendo éste último el lugar más importante en este trabajo, ya que es donde se ubica el volcanismo actual y la mayoría de las manifestaciones termales.

La geología de la CP se puede dividir en dos franjas principales (Figura 1; Farías et al., 2010): la zona occidental correspondiente a un basamento de rocas volcánico-sedimentarias e intrusivos (ej. lavas, tobas, conglomerados, granitoides) de edad Cenozoica; y la zona oriental correspondiente a rocas sedimentarias marino-continentales (ej. areniscas, conglomerados, calizas, yesos) de edad Mesozoica.

Estructuralmente la CP también se puede dividir en dos, coincidiendo con la división de la geología (Figura 1). En la parte Oeste existen fallas inversas pertenecientes al sistema de falla Pocuro-San Ramón (SFPS) asociadas a la inversión de la Cuenca de Abanico (Farías et al., 2010 y referencias en él). En cambio, las estructuras desarrolladas en la parte Este de la CP son fallas inversas asociadas a las fajas plegadas y corridas de Aconcagua (FPCA) entre los 33º-34ºS y Malargue (FPCM) entre los 34º-37ºS (Farías et al., 2010). Las dos franjas de la CP se encuentran en contacto a través de fallas al sistema de falla El Diablo-Las Leñas Espinoza-El Fierro (SFELE), que corresponde a fallas inversas con vergencia Este, asociada la inversión de la cuenca de abanico (Farías et al., 2010 y referencias en él).

3 Distribución de las manifestaciones termales

En Chile central diferentes áreas hidrotermales activas han sido identificadas y caracterizadas (Grunder et al., 1987; Hauser, 1997; Benavente y Gutiérrez, 2011), dando cuenta

de los diferentes tipos de manifestaciones termales existentes (manantiales fríos y calientes, piscinas burbujeantes, piscinas de barro, fumarolas y lagunas cratéricas). La mayoría de éstas manifestaciones se encuentran en la CP, donde espacialmente están controladas por la existencia de los diferentes sistemas de falla existentes (Figura 1).

En la parte Oeste de la CP, a lo largo del SFPS, sólo manantiales fríos pueden ser encontrados. La parte central de la CP, a lo largo del SFELE, se caracteriza por sus volcanes activos con lagunas cratéricas y/o fumarolas, campos fumarólicos, piscinas de barro, manantiales burbujeantes y manantiales calientes y fríos. Finalmente, asociado tanto a la FPCA y la FPCM posee tanto piscinas burbujeantes, como manantiales fríos y calientes.

Un rasgo llamativo en las manifestaciones termales de Chile central es la ocurrencia variable de campos fumarólicos, en donde en la porción norte (33-34.5°S) no existen fumarolas catastradas a excepción de las encontradas sobre los volcanes Tupungatito y San José. En cambio en la porción sur (34.5-36°S) al menos 4 campos fumarólicos han sido catastrados (Grunder et al., 1987; Benavente y Gutiérrez, 2011; Clavero et al., 2011) además de los ubicados sobre los volcanes con actividad fumarólica (Tinguiririca, Planchón-Peteroa y Quizapu).

4 Resultados

La temperatura de salida de las manifestaciones termales varía entre 6 y 98.2°C, el total de sólidos disueltos (TSD) varía entre 170 y 42000 mg/lt y el pH de las aguas varía entre 0.34 y 9.3. Los elementos mayores de las aguas están caracterizados por la presencia de Cl (1.6 - 14959 mg/lt), HCO_3 (5.4 - 1434.4 mg/lt), SO_4 (2.4 – 12598 mg/lt), Na (21.3 – 9950 mg/lt), Ca (1.1 – 1818 mg/lt), K (1.3 – 728.7 mg/lt), Mg (0 – 376.5 mg/lt) y SiO_2 (11.5 – 267.4 mg/lt). El contenido de $\delta^{36}S\text{-}SO_4$ es variable entre 0.01 y 19.7‰ (Hauser, 1997). La composición isotópica del agua varía para δD entre -50.9 y -117.7‰ V-SMOW y para $\delta^{18}O$ entre -15.8 y -4.23‰ V-SMOW. La composición isotópica de $\delta^{13}C\text{-}CO_2$ (V-PDB) y de He expresada en Ra/R, en los gases disueltos en las manifestaciones termales varían entre -14.3 y -5.9‰, y 0.68 y 1.27‰ respectivamente.

5 Discusiones

Basado en la distribución espacial y en la química de las manifestaciones termales de Chile central, dos dominios son reconocidos: Alta y Baja Cordillera (AC, BC). El dominio de AC comprende todas las manifestaciones termales asociadas con los centros volcánicos y yacen sobre las trazas de los sistemas de falla El Diablo-Las Leñas Espinoza-El Fierro y las fajas plegadas y corridas de Aconcagua y Malargue. Éstas manifestaciones tienen una temperatura variable entre 6 - 98.2°C, pH variables entre 0.3 - 7.6 y un TSD que varía entre 180 y 42000 mg/lt. La composición de estas aguas es diversa existiendo aguas cloruradas salinas neutras (con TSD de hasta 35000 mg/lt), aguas bicarbonatadas con pH variables entre 5.8 - 8, aguas sulfato-cloruradas salinas ácidas (con TDS de hasta 42000 mg/lt), y aguas sulfato-ácidas (Figura 2). Por otro lado, el dominio de BC comprende todas las manifestaciones termales asociadas al sistema de falla San Ramón-Pocuro, cuya temperatura varía entre 18.2 y 28°C y su TSD no supera los 1000 mg/lt. La composición de estas aguas es mayoritariamente bicarbonatada sódica con un pH que varía entre 7 y 9 (Figura 2).

De acuerdo a la razón R/Ra y los valores isotópicos de $\delta_{13}C\text{-}CO_2$, los fluidos termales de ambos dominios (AC y BC) provienen sólo del sistema hidrotermal. Mientras que la composición isotópica de $\delta^{18}O$ y δD muestran que el origen de las aguas se debe a la circulación de agua meteórica.

La razón molar de los elementos $(Na+Ca+Mg+K)/(Cl+SO_4+HCO_3/2+SiO_2)$ es similar a 1 para las manifestaciones termales de ambos dominios (exceptuando las de las lagunas cratéricas), sumado a los valores isotópicos de $\delta^{36}S\text{-}SO_4$, se observa la influencia litológica de la zona (e.g. yeso, caliza, feldespatos) en la composición química e isotópica de las aguas.

La geotermometría de las aguas cloruradas muestra que existen variaciones importantes de las temperaturas de equilibrio de Norte a Sur. Entre los 33-34°S las manifestaciones de la AC tienen temperaturas de equilibrio variables entre 100 y 150° estimadas por los geotermómetros de mayor cinética de reacción (Na-K y Na-K-Mg), y entre 200 y 250°C para los geotermómetros de menor cinética de reacción (Na-K-Ca). En cambio entre los 34-36°S las temperaturas estimadas por los geotermómetros de mayor cinética de reacción varía entre 200 y 250°C, y los de menor cinética de reacción varían entre 300-350°C.

Con los datos obtenidos hasta el momento se puede plantear que los sistemas hidrotermales de Chile central son producto de la transferencia de masa y energía desde las cámaras magmáticas cuaternarias y la posterior interacción de éstos con la roca circundante y el agua meteórica en diferentes proporciones. Ésto explicaría de buena manera las diferencias longitudinales del tipo de manifestaciones existentes entre la BC y AC, a pesar que la química e isotopía de las aguas insinúan un origen común. Es así como en la AC la distribución de las manifestaciones termales es la típica de sistemas volcánicos activos (e.g. aguas cloruradas periféricas, aguas sulfato-ácidas en las zona del *upflow*, y aguas bicarbonatadas entre ambas zonas; Gupta y Roy, 2007), mientras que las manifestaciones pertenecientes a la BC son en su mayoría aguas bicarbonatadas sódicas que

podrían se explicadas por la interacción y dilución de las de las aguas cloruradas profundas con aguas meteórica y rocas carbonatadas, durante la circulación a través del sistema de falla Pocuro-San Ramón. Por otro lado, las diferencias Norte-Sur existentes en las temperaturas de equilibrio de las manifestaciones termales maduras y la ocurrencia de campos fumarólicos podrían ser explicadas por (i) variaciones en el input magmático desde las cámaras magmáticas a los sistemas hidrotermales respectivos (Benavente y Gutiérrez, 2011; Clavero et al., 2011) y/o (ii) variaciones en el estado termal de la corteza producto de la disminución del espesor cortical de Norte a Sur, o de la profundidad de la cámara magmática.

Agradecimientos

Los autores agradecen a las siguientes fuentes de financiamiento: (i) MECESUP UCH-0708 por el financiamiento de la beca de doctorado del autor principal, (ii) FONDAP-Centro de Excelencia en Geotermia de los Andes (CEGA), por el financiamiento de los equipos de terreno, el trabajo de campo y la asistencia a congresos y (iii) PBCT-PDA07 por financiar equipo de trabajo y trabajo de campo. (iv) FONDECYT Iniciación en Investigación Nº11100372 "Role of climate, continental crust and subducted sediments in the degassing style and fluid composition of Andean volcanoes" a cargo del Dr. Felipe Aguilera, por financiar trabajo de campo. (v) CONICYT "Programa de pasantías en el extranjero para investigadores; profesionales del sector privado; profesionales y funcionarios de instituciones públicas" por el financiamiento de la pasantía para el análisis de las muestras en la Universidad de Florencia.

Referencias

Benavente, O. and Gutiérrez, F. (2011): "Magmato-hydrothermal systems associated to Planchón-Peteroa and Descabezado Grande-Quizapu-Cerro Azul volcanix complex, VII Region, Chile." Society for Geology Applied to Mineral Deposits, Antofagasta, Chile.

Cembrano, J. and L. Lara (2009). "The link between volcanism and tectonics in the southern volcanic zone of the Chilean Andes: A review." Tectonophysics 471(1-2): 96-113.

Clavero J., Pineda G., Mayorga C., Giavelli A., Aguirre I., Simmons S., Martini S., Soffia J., Arriaza R., Polanco E., Achurra L., 2011. Geological, Geochemical, Geophysical and First Drilling Data from Tinguiririca Geothermal Area, Central Chile. GRC Transactions, Vol. 35.

Farias, M., Comte,D. et al., 2010. Crustal-scale structural architecture in central Chile based on seismicity and surface geology: Implications for Andean mountain building. Tectonics 29: 22.

Grunder, A., Thompson, J., Hildreth, W., 1987. The hydrothermal system of the Calabozos caldera, central Chilean Andes, Journal of Volcanology and Geothermal Research, Volume 32, Issue 4, Pages 287-298.

Gupta, H. and Roy, S. (2007). Geothermal Energy: An alternative resource for the 21ST century, Elservier publications.

Hauser, A. (1997). Catastro y caracterización de las fuentes de aguas minerales y termales de Chile. Servicio Nacional de Geología y Minería, Boletín Nº 50, 90 p.

Lahsen, A. (1986). Origen y potencial de energía geotérmica en los Andes de Chile. In: J.Frutos, R. Oyarzún, and M. Pincheira (Eds) Geología y Recursos Minerales de Chile, Univ. de Concepción, 423–438.

Lahsen, A., Muñoz, N. and Parada, M.A. (2010). Geothermal Development in Chile. Proceedings World Geothermal Congress, Bali, Indonesia.

Martini, S. (2008). Sistemas estructurales y recursos geotermales en la Cordillera Principal de Chile central: 32°30' – 34°00' de Latitud Sur. Memoria para optar al título de Geólogo. Departamento de Geología, Universidad de Chile.

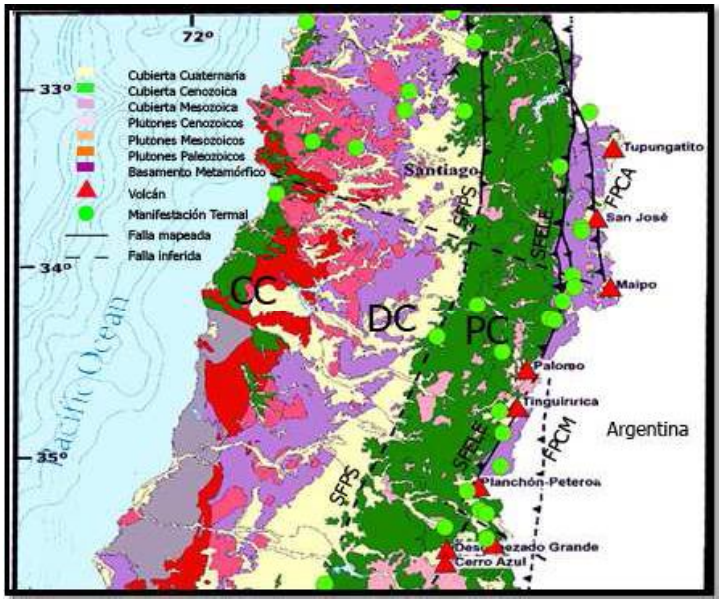

Figura 1. Geología de Chile central (33-36ºS). Modificado de Cembrano and Lara (2009).

Magmatic-Hydrothermal system associated to Planchón-Peteroa and Descabezado Grande-Quizapu-Cerro Azul volcanic complexes

Oscar Benavente, Francisco Gutiérrez
Departamento de Geología, Universidad de Chile, Plaza Ercilla 803, Santiago, Chile
Corresponding author: oscar.benavente.zolezzi@gmail.com, obenaven@ing.uchile.cl

Abstract. Thermal manifestation associated to Planchón-Peteroa and Descabezado Grande-Quizapu-Cerro Azul volcanic complexes can be explained by a close relationship between a magmatic-hydrothermal systems and faults from the Malargue Fold Thrust and Belt. Two possible reservoir can be distinguish at different depth. The deeper one has temperatures near 350ºC and is controlled mainly by a mixture of volcanic and hydrothermal fluids. Instead the shallow has a temperatures range between 100-140ºC and is mainly controlled by hydrothermal system.

Keywords: Fluids geochemistry, Volcanism, Geothermal exploration.

1 Introduction

Calabozos Caldera Complex (CCC) and Planchón-Peteroa (PPVC) and Descabezado Grande-Quizapu-Azul (DGQAVC) volcanic complexes, are located between 35-36ºS, at Maule's region, Chile. This complexes belong to the volcanic arc of the Transitional Southern Volcanic Zone (TSVZ; Figure 1), which correspond to a sector of 300 km long (34.4-37ºS), where the actual volcanic arc reach a width of 150 km and the crust depth range between 35-40 km (Hildreth & Moorbath, 1988).

The time-spatial control of the VCPP-VCDGQA-CCC and the active hydrothermal system associated are determinate by NW-SE and NE-SW structures (Cembrano y Lara, 2009; **¡Error! No se encuentra el origen de la referencia.**) that develop along the Malargue fold thrust and belt (MFTB). The MFTB is a thick-skinned fold thrust and belt in this zone, composed by a series of basement blocks that limit zone with thin-skinned internal deformation (Dicarlo y Cristallini, 2007). In this way PPVC and DGQAVC lies over inverse fault that put in contact Meso-Cenozoic unit with NE-SW striking (Cembrano, 2009), whereas that CCC, uses NW-SE and NE-SW structures for its emplacement.

Previews studies of the active hydrothermal systems associated with CCC (Thompson et al., 1983; Grunder et al., 1987) relate the thermal manifestation (i.e. hot springs and fumaroles) with fault associated to the collapse and resurgence of the caldera complex. Along the thermal manifestation it can be distinguish two principal groups: (i) the ones associated with the fault that control the volcanism and, (ii) the ones associated with caldera's edges structures. For both groups a maximum temperature of 250ºC has been estimated by quartz geothermometers and the enthalpy-chlorine diagrams (Thompson et al., 1983; Grunder et al., 1987).

The aim of this study is to understand the contribution of volcanism in the origin of the active thermal manifestation in the zone, base on the geological, structural, geophysics superficial information, and gas-water geochemical. For this purpose we collected a total of 24 water and 6 gas samples from hot spring, bubbling pools, fumaroles and meteoric water. We analyzed cations, anions and stable isotope (^{18}O-^{2}H) in water samples, and soluble and insoluble gas species.

2 Results and Discussion

The main results are: (i) The origin of the fluids from the fumaroles, hot springs, bubbling pools are depth circulation of meteoric water that are heated by shallows magmatic chambers (4 km). This can be seen by $\delta^{2}H$-$\delta^{18}O$ ratio in water samples and from relative content of N_2-He-CO_2 in gas samples. (ii) The origin of the water dissolved component can be explained by water-rock interaction based on molar ratio showing dissolution trends of the main minerals present in the zone (i.e. gypsum, calcite, dolomite, feldspar). Despite this, water samples that were taken near to fumaroles present SO_4 and CO_2 anomalous concentrations that doesn't follows the dissolution trend. (iii) Quartz, chalcedony and multimineral equilibrium geothermometers show equilibrium temperatures that range between 100º-140ºC, instead the geothermometers with slow kinetic reaction like Na-K-Ca and He-CH_4 for water and gases samples respectively, estimates maximum temperatures of 350ºC for a some samples.

Due to the different temperatures estimated by the geothermometers and the geology, is possible to infer the existence of two reservoir at different depth. The deeper one would reach temperature near to 350ºC, where water would rise throw a permeable zone associated to faults of the MFTB. In its rise, thermal water would mix with meteoric water and interact with the host rock changing the equilibration temperatures of the faster kinetic reaction geothermometers (i.e. quartz, chalcedony, Na-K, multimineral equilibrium). Therefore, on sectors where faults reach surface is possible to find active thermal manifestation with evidence of equilibrium from the deeper reservoir (samples 9, 15, 17, 19, 35). Meanwhile where faults does not reach surface due to the impermeable volcanic cover, water would flow laterally having sufficient time to reequilibrate also the slower kinetic reaction geothermometers like

Na-K-Ca and He-CH_4, erasing all evidence from deeper reservoir (samples 1, 2, 3, 6, 7, 8, 10, 30 y 39).
The conceptual model proposed can be represented in a better way on enthalpy-chloride diagrams (Figure 2ab). The upflow fluids (samples 9, 15 and 35) represent water arising directly from fault, and can be modeled by mixing of parent water at 350ºC and meteoric water. Instead, the outflow fluids (samples 36, 17 and 19) also represent water arising from fault zone, but the parent water comes from the boiling of the 350ºC water and are located in the peripheral part of the systems. On the other hand, samples 1, 2, 3, 6, 7, 8, 10, 30, 39 are waters that flow laterally due to impermeable volcanic rocks and do not follow the mixing lines. Those can be affected by heat transfer from the crust, increasing water temperature (without mass transfer "chlorine") producing a negative superficial thermal anomaly (Figure 2c).

3 Conclusions

This work has two main conclusions: (1) Thermal manifestation associated to PPVC, DGVC and CCC can be explained by close relationship between a magmatic-hydrothermal systems and faults from the MFTB. (2) Geothermometry and superficial thermal anomaly shows the existence of two reservoir beneth lavas and tuff belong to CCC. The deeper one reach temperature near 350ºC, and the shallow one has temperatures range 100º to 140ºC.

Acknowledgements

Authors would like to thank Universidad de Chile for the necessary facilities and support to carry out this work, and CONICYT`s PBCT proyect PDA-07 for the financial support.

References

Cembrano J. and Lara L., 2009. The link between volcanism and tectonics in the southern volcanic zone of the Chilean Andes: A review, Tectonophysics, Volume 471, Issues 1-2, Pages 96-113.
Dicarlo, D.J. y Cristallini, E. 2007. Estructura de la margen norte del río Grande, Bardas Blancas, Provincia de Mendoza. Revista de la Asociación Geológica Argentina 62: 187-199.
Grunder A., Thompson J., Hildreth W., 1987. The hydrothermal system of the Calabozos caldera, central Chilean Andes, Journal of Volcanology and Geothermal Research, Volume 32, Issue 4, Pages 287-298.
Hildreth W. and Moorbath S., 1988. Crustal contributions to arc magmatism in the Andes of Central Chile. Contributions to Mineralogy and Petrology 98: 455 - 489.
Thompson, J.M., 1975. Selecting and collecting termal springs for chemical analysis: A method for field personneL.U.S. Geol. Surv., Open-File Rep. 75-68, 12 pp.

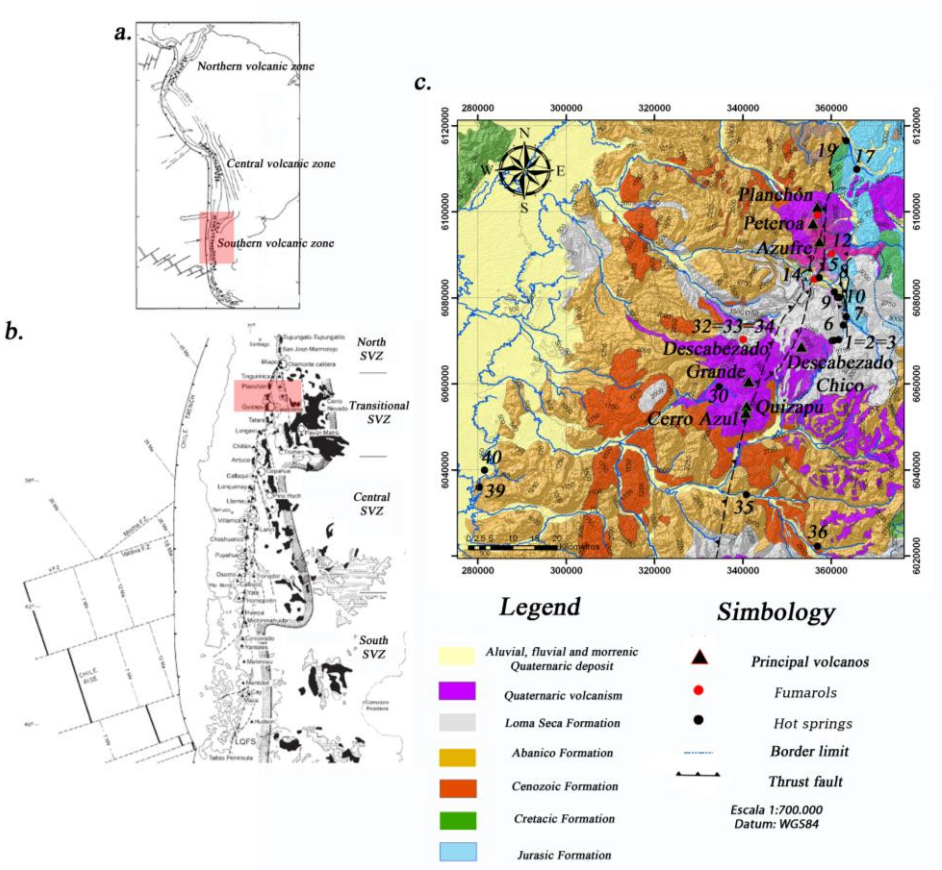

Figure 1. a: Andean volcanic zone (modified from Parada et al., 2007). **b**: South volcanic zone (modified from Parada et al., 2007). **c:** Geological map from the study zone. Samples 1, 2 y 3 aguas calientes spring; 6 tigre naciente spring; 7 potrerillo spring; 8 pellejo spring; 9 tierra humeante del colorado spring; 10 quebrada de los colores spring; 12 azufre fumaroles; 14 Llolli fumaroles; 15 Baños de la Yegua spring; 17 san pedro spring; 19 romeral spring; 30 descabezado grande spring; 32, 33 y 34 valle

del estero del volcán fumaroles; 35 medano spring; 36 campanario spring; 39 panimávida spring; 40 quinamávidas spring.

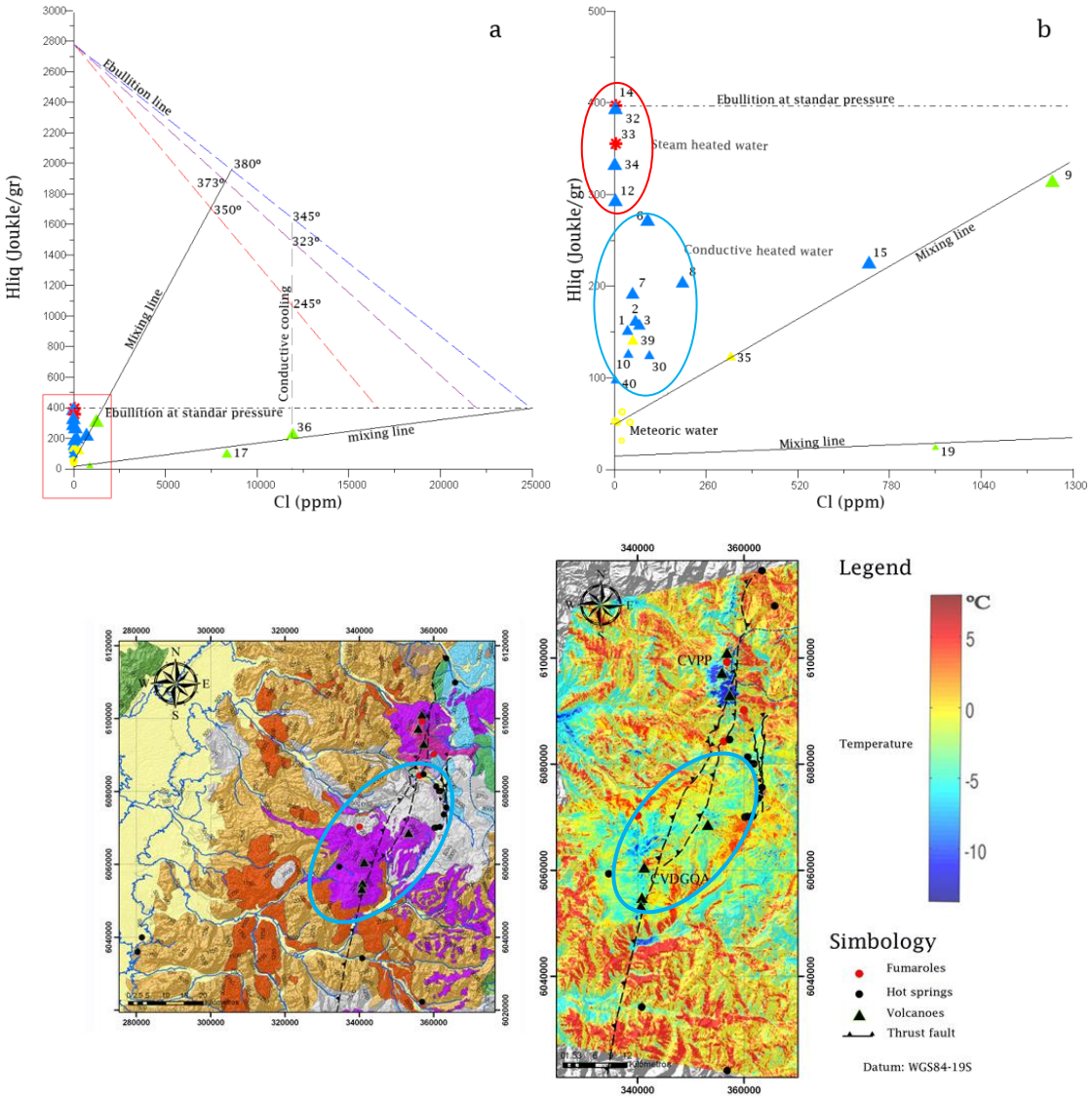

Figure 2. a. Chloride-enthalpy diagrams for water samples. b. is the zoom of the red rectangle on Figura 2.a. On green triangles chloride waters; yellow triangles sulfate-chloride waters; blue triangles bicarbonate waters; red asterisks acid-sulfate waters, yellow circles meteoric waters. c: Possible reservoir and superficial thermal anomalies.

MAGMATO-HYDROTHERMAL SYSTEMS ASSOCIATED TO PLANCHÓN-PETEROA AND DESCABEZADO GRANDE-QUIZAPU-CERRO AZUL VOLCANIC COMPLEXES, VII REGION, CHILE.

Oscar Benavente*, Francisco Gutiérrez
Departamento de Geología, Universidad de Chile, Plaza Ercilla 803, Santiago, Chile.
*Corresponding author: obenaven@ing.uchile.cl; oscar.benavente.zolezzi@gmail.com
Tel: (56 2) 9780627, (56 9) 76775156

INTRODUCTION

Calabozos Caldera Complex (CCC) and Planchón-Peteroa (PPVC) and Descabezado Grande-Quizapu-Azul (DGQAVC) volcanic complexes, are located between 35-36ºS, at Maule's region, Chile. This complexes belong to the volcanic arc of the transitional south volcanic zone (TSVZ), which correspond to a sector of 300 km (34.4-37ºS) where the arc has a width of 150 km and the crust has a depth of 35-40 km (Hildreth & Moorbath, 1988).

The time-spatial control of the CVPP-CVDGQA-CCC and the active hydrothermal system associated are determinate by NW-SE and NE-SW structures (Cembrano, 2009; Figure 1) that develop along the Malargue fold thrust and belt (MFTB). The MFTB is a thick-skinned fold thrust and belt in this zone, composed by a series of basement blocks that limit zone with thin-skinned internal deformation (Dicarlo y Cristallini, 2007). In this way PPVC and DGQAVC lies over inverse fault that put in contact Meso-Cenozoic unit with NE-SW striking (Cembrano, 2009), whereas that CCC, uses NW-SE and NE-SW structures for its emplacement.

Previews studies of the active hydrothermal systems associated with CCC (Thompson et al., 1983; Grunder et al., 1987) relate the thermal manifestation (i.e. hot springs and fumaroles) with fault associated to the collapse and resurgence of the caldera complex. Along the thermal manifestation it can be distinguish two principal groups: (i) the ones associated with the fault that control the volcanism and, (ii) the ones associated with caldera's edges structures. For both groups a maximum temperature of 250ºC has been estimated by quartz geothermometers and the enthalpy-chlorine diagrams.

The aim of this study is to understand the contribution of volcanism in the origin of the active thermal manifestation in the zone, base on the geological, structural and geophysics superficial information, and gas-water geochemical, considering a bigger area than the latter authors. For this purpose we collected a total of 24 water and 6 gas samples from hot spring, bubbling pools, fumaroles and meteoric water. We analyzed cations, anions and stable isotope (^{18}O-^{2}H) in water samples, and soluble and insoluble gas species.

RESULTS AND DISCUSSIONS

The main results are: (i) The origin of the fluids from the fumaroles, hot springs, bubbling pools are depth circulation of meteoric water that are heated by shallows magmatic chambers (4 km). This can be seen by $\delta^{2}H$-$\delta^{18}O$ ratio in water samples and from relative content of N_2-He-CO_2 in gas samples. (ii) The origin of the water dissolved component can be explained by water-rock interaction based on molar ratio showing dissolution trends of the main minerals present in the zone (i.e. gypsum, calcite, dolomite, feldspar). Despite this, water samples that were taken near to fumaroles present SO_4 and CO_2 anomalous concentrations that doesn't follows the dissolution trend. (iii) Quartz, chalcedony and multimineral equilibrium geothermometers show equilibrium temperatures that range between 100º-140ºC, instead the geothermometers with slow kinetic reaction like Na-K-Ca and He-CH_4 for water and gases samples respectively, estimates maximum temperatures of 350ºC for a some samples.

Due to the different temperatures estimated by the geothermometers and the geology, is possible to infer the existence of two reservoir at different depth. The deeper one would have temperature near to 350ºC, where water would rise throw a permeable zone associated to faults of the MFTB. In its rise, thermal water would mix with meteoric water and interact with the host rock changing the equilibration temperatures of the faster kinetic reaction geothermometers (i.e. quartz, chalcedony, Na-K, multimineral equilibrium). Therefore, on sectors where faults reach surface is possible to find active thermal manifestation with evidence of equilibrium from the deeper reservoir (samples 9, 15, 17, 19, 35). Meanwhile where faults does not reach surface due to the impermeable volcanic cover, water would flow laterally having sufficient time to reequilibrate also the slower kinetic reaction geothermometers like Na-K-Ca and He-CH_4, erasing all evidence from deeper reservoir (samples 1, 2, 3, 6, 7, 8, 10, 30 y 39).

The conceptual model proposed can be represented in a better way on enthalpy-chloride diagrams (Figure 2). The upflow fluids (samples 9, 15 and 35) represent water arising directly from fault, and can be modeled by mixing of parent water at 350ºC and meteoric water. Instead, the outflow fluids (samples 36, 17 and 19) also represent water arising from fault zone, but the parent water comes from the boiling of the 350ºC water and are located in the peripheral part of the systems. On the other hand, samples 1, 2, 3, 6, 7, 8, 10, 30, 39 are waters that flow laterally due to impermeable volcanic rocks and do not follow the mixing lines. Those can be affected by heat transfer from the crust, increasing water temperature but without mass transfer (chlorine).

CONCLUSIONS

In this way the thermal manifestation associated to PPVC, DGVC and CCC can be explained by close relationship between a magmato-hydrothermal systems and faults from the MFTB.

ACKNOWLEDGEMENT

Authors would like to thank Universidad de Chile for the necessary facilities and support to carry out this work, and CONICYT`s PBCT proyect PDA-07 for the financial support.

REFERENCES

Cembrano J. and Lara L., 2009. The link between volcanism and tectonics in the southern volcanic zone of the Chilean Andes: A review, Tectonophysics, Volume 471, Issues 1-2, Pages 96-113.

Dicarlo, D.J. y Cristallini, E. 2007. Estructura de la margen norte del río Grande, Bardas Blancas, Provincia de Mendoza. Revista de la Asociación Geológica Argentina 62: 187-199.

Grunder A., Thompson J., Hildreth W., 1987. The hydrothermal system of the Calabozos caldera, central Chilean Andes, Journal of Volcanology and Geothermal Research, Volume 32, Issue 4, Pages 287-298.

Hildreth W. and Moorbath S., 1988. Crustal contributions to arc magmatism in the Andes of Central Chile. Contributions to Mineralogy and Petrology 98: 455 - 489.

Thompson, J.M., 1975. Selecting and collecting termal springs for chemical analysis: A method for field personneL.U.S. Geol. Surv., Open-File Rep. 75-68, 12 pp.

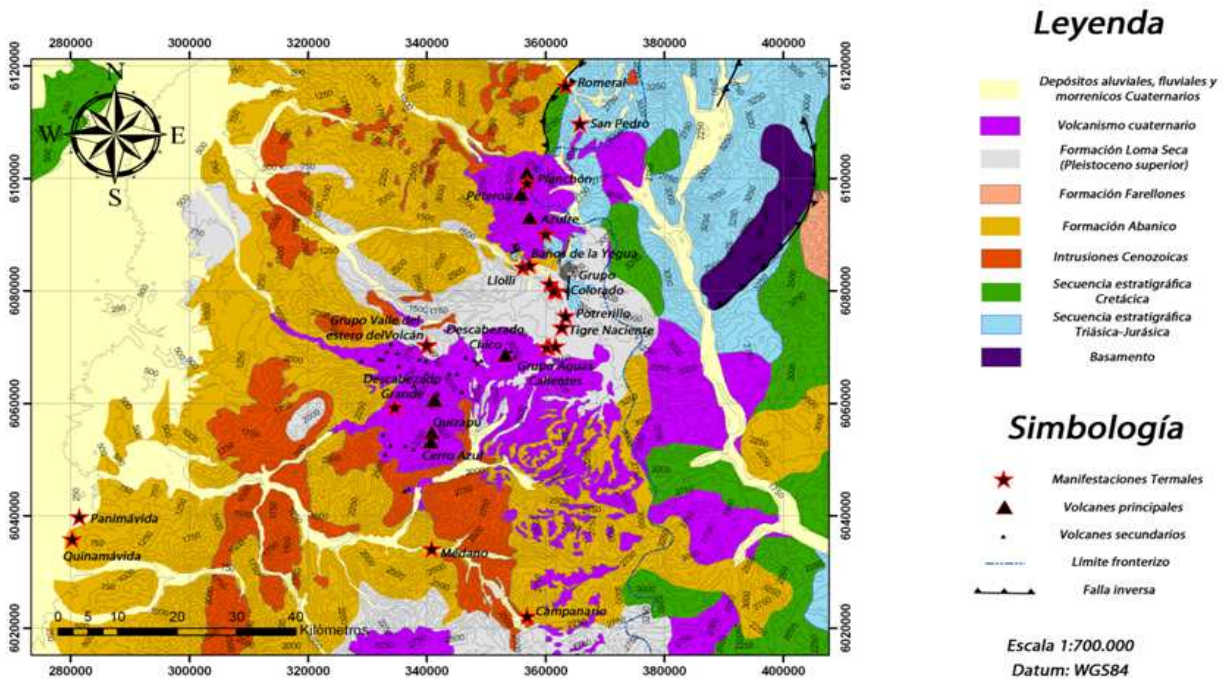

Figure 1: Geological map from the study zone. Samples 1, 2 y 3 aguas calientes spring; 6 tigre naciente spring; 7 potrerillo spring; 8 pellejo spring; 9 tierra humeante del colorado spring; 10 quebrada de los colores spring; 12 azufre fumaroles; 14 Llolli fumaroles; 15 Baños de la Yegua spring; 17 san pedro spring; 19 romeral spring; 30 descabezado grande spring; 32, 33 y 34 valle del estero del volcán fumaroles; 35 medano spring; 36 campanario spring; 39 panimávida spring; 40 quinamávidas spring.

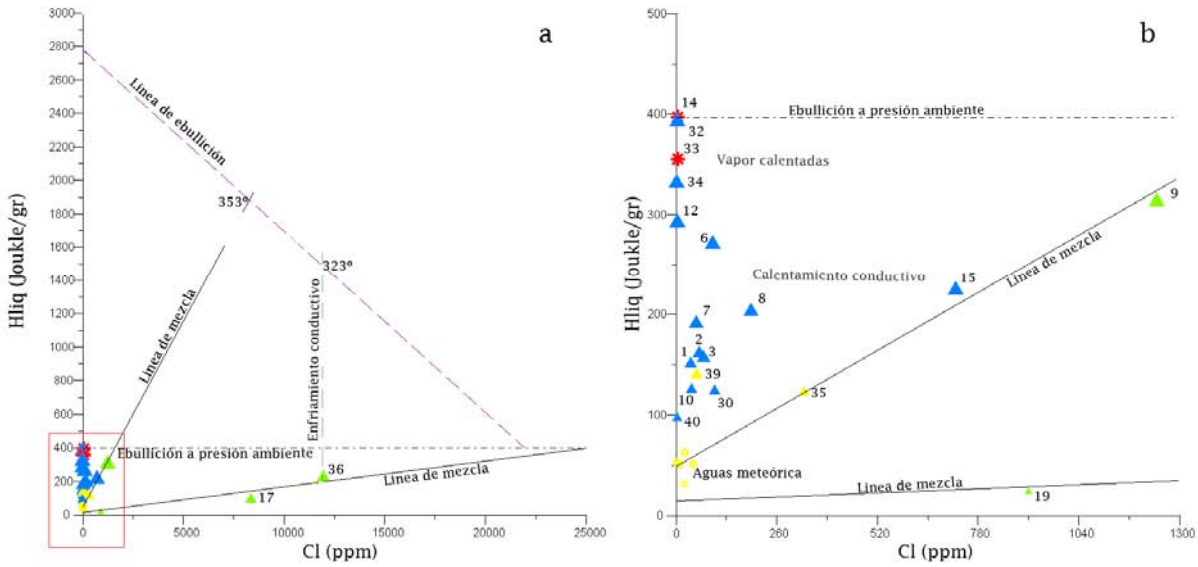

Figure 2: Chloride-enthalpy diagrams for water samples. On green triangles chloride waters; yellow triangles sulfate-chloride waters; blue triangles bicarbonate waters; red asterisks acid-sulfate waters, yellow circles meteoric waters.